AGARD-CP-567

AGARD-CP-567

# AGARD

ADVISORY GROUP FOR AEROSPACE RESEARCH & DEVELOPMENT
7 RUE ANCELLE, 92200 NEUILLY-SUR-SEINE, FRANCE

DTIC
ELECTE
JUL 19 1995
B

**AGARD CONFERENCE PROCEEDINGS 567**

# Propagation Assessment in Coastal Environments

(l'Évaluation de la propagation en régions côtières)

*Papers presented at the Sensor and Propagation Panel Symposium, held in Bremerhaven, Germany 19-22 September 1994.*

DISTRIBUTION STATEMENT A
Approved for public release;
Distribution Unlimited

19950718 004

**NORTH ATLANTIC TREATY ORGANIZATION**

Published February 1995

*Distribution and Availability on Back Cover*

AGARD-CP-567

# AGARD

**ADVISORY GROUP FOR AEROSPACE RESEARCH & DEVELOPMENT**
7 RUE ANCELLE, 92200 NEUILLY-SUR-SEINE, FRANCE

**AGARD CONFERENCE PROCEEDINGS 567**

# Propagation Assessment in Coastal Environments

(l'Évaluation de la propagation en régions côtières)

Papers presented at the Sensor and Propagation Panel Symposium, held in Bremerhaven, Germany 19-22 September 1994.

North Atlantic Treaty Organization
*Organisation du Traité de l'Atlantique Nord*

# The Mission of AGARD

According to its Charter, the mission of AGARD is to bring together the leading personalities of the NATO nations in the fields of science and technology relating to aerospace for the following purposes:

- Recommending effective ways for the member nations to use their research and development capabilities for the common benefit of the NATO community;
- Providing scientific and technical advice and assistance to the Military Committee in the field of aerospace research and development (with particular regard to its military application);
- Continuously stimulating advances in the aerospace sciences relevant to strengthening the common defence posture;
- Improving the co-operation among member nations in aerospace research and development;
- Exchange of scientific and technical information;
- Providing assistance to member nations for the purpose of increasing their scientific and technical potential;
- Rendering scientific and technical assistance, as requested, to other NATO bodies and to member nations in connection with research and development problems in the aerospace field.

The highest authority within AGARD is the National Delegates Board consisting of officially appointed senior representatives from each member nation. The mission of AGARD is carried out through the Panels which are composed of experts appointed by the National Delegates, the Consultant and Exchange Programme and the Aerospace Applications Studies Programme. The results of AGARD work are reported to the member nations and the NATO Authorities through the AGARD series of publications of which this is one.

Participation in AGARD activities is by invitation only and is normally limited to citizens of the NATO nations.

The content of this publication has been reproduced
directly from material supplied by AGARD or the authors.

Published February 1995

Copyright © AGARD 1995
All Rights Reserved

ISBN 92-836-0013-4

*Printed by Canada Communication Group*
*45 Sacré-Cœur Blvd., Hull (Québec), Canada K1A 0S7*

# Theme

With the decreased probability of a global war, military emphasis has shifted to regional conflicts. Such conflicts are likely to involve coastal areas and multi-national forces including sub-surface, surface, land and air units. Low intensity and limited objectives operations place high-precision requirements on surveillance and weapon systems and demand highly reliable communications. For example, weapons using accurate electro-optical guidance systems can be used to minimize civilian casualties. Fleet units in coastal waters are vulnerable to attacks from the shore and need to have reliable detection capabilities against incoming missiles. Communications must accommodate high-data rates needed by modern command and control systems and must be jam-resistant.

Coastal areas are frequently characterized by a complex propagation environment which is difficult to model and predict. For example, radio propagation predictions must include both water and terrain surfaces as well as the refractivity structure affected by both domains. This requires models which consider spatial and temporal atmospheric structure, surface conductivity, sea clutter and terrain effects. For electro-optical propagation assessment, aerosols usually are a mixture of marine and land sources which makes the prediction of their extinction properties difficult; in addition, their temporal and spatial structure can be very complex and variable.

Development, testing and validation of models and sensing techniques require complex measurement campaigns. Several such campaigns conducted by Research Groups 8 (Panel 3 and 4) of the Defense Research Group of NATO provided valuable data presented in the Symposium.

Assessment of electromagnetic and electro-optical propagation in coastal environments requires propagation modeling in inhomogeneous environments, direct and remote sensing of the critical environmental parameters, forecasting of the temporal and spatial structure of environmental parameters, and the development of tactical decision aids to exploit or mitigate the effects of the propagation environment.

Topics covered:

- Radio Propagation Modeling
- Electro-optical Propagation Modeling
- Remote and Direct Sensors and Sensing Techniques
- Modeling and Prediction of the Propagation Environment
- Sensor Technology and Systems Aspects
- Measurement Campaigns


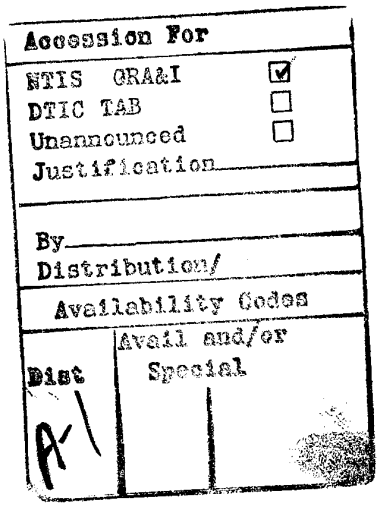

# Thème

La probabilité de la déclaration d'une guerre mondiale étant moindre aujourd'hui, les efforts militaires se sont tournés plutôt vers les conflits régionaux. De tels conflits concerneront probablement des régions côtières et impliqueront des forces multinationales comprenant des unités sous-marines, terrestres et aériennes.

La réussite des opérations de faible intensité et à objectifs limités dépend de l'acquisition de systèmes d'armes et de surveillance de haute précision, ainsi que de réseaux de télécommunications hautement fiables. Pour citer un exemple, des armes intégrant des systèmes de guidage électro-optiques de précision peuvent être utilisés pour réduire au minimum le nombre de victimes parmi la population civile. Des unités de la marine navigant dans les eaux côtières sont vulnérables à des attaques lancées de la côte et doivent être équipées de moyens de détection ou de missiles fiables. Les équipements de télécommunications doivent fonctionner aux débits élevés exigés par les systèmes de commandement et de contrôle modernes et ils doivent être protégés contre le brouillage intentionnel.

Les régions côtières sont souvent caractérisées par des environnements à propagation complexes qui sont difficiles à modéliser et donc de prévoir. Pour citer un exemple, les prévisions de propagation radioélectrique doivent tenir compte des surfaces terrestres et maritimes, ainsi que de la structure de réfringence des deux domaines. La modélisation doit donc tenir compte des structures atmosphériques spatiales et temporelles, de la conductivité superficielle, du fouillis de mer et des effets de terrain. Pour ce qui est de l'évaluation de la propagation électro-optique, les aérosols sont normalement composés d'un mélange d'origine maritime et terrestre, ce qui rend difficile la prévision de leures caractéristiques d'extinction; en outre, leur structure spatiotemporelle peut être très complexe et variable.

Le développement, les essais et la validation des modèles et des techniques de détection requièrent des campagnes de mesures complexes. Un certain nombre de telles campagnes, réalisées par le groupe sur la recherche pour la défense de l'OTAN (le GRD), ont eu pour résultat des données de valeur, qui ont été présentées lors du symposium.

L'évaluation de la propagation électromagnétique et électro-optique en régions côtières requiert la modélisation de la propagation en milieux hétérogènes, la détection et la télédétection des paramètres critiques du milieu, la prévision de la structure temporelle et spatiale de ces paramètres, et le développement d'aides à la prise de décisions tactiques pour exploiter ou mitiger ces effets du milieu de propagation.

Les sujets suivants étaient examinés:

— la modélisation de la propagation radioélectrique
— la modélisation de la propagation électro-optique
— les techniques de détection et de télédétection
— la modélisation de la prévision du milieu de propagation
— la technologie de détection et les aspects systèmes
— campagnes de mesures.

# Sensor and Propagation Panel

**Chairman:** Prof. D.H. HÖHN
FGAN
Forschungsinstitut für Optik
Schloss Kressbach
D-7400 Tübingen
Germany

**TECHNICAL PROGRAMME COMMITTEE**

**Co-Chairmen:**

Dr. J.H. Richter (US)
Dr. K.H. Craig (UK)

**Programme Committee Members:**

Dr. S.D. Burk (US)
Mr. F. Christophe (FR)
Ir. H.J.M. Heemskerk (NE)
Prof. H. Jeske (GE)
Mr. A. Junchat (FR)
Dr. G. de Leeuw (NE)
Dipl.-Ing. R. Makaruschka (GE)
Mr. J. D. Turton (UK)

**PANEL EXECUTIVE**

Lt. Colonel R. Cariglia, IAF

**Mail from Europe:**
AGARD-NATO
ATTN: SPP Executive
7, rue Ancelle
92200 Neuilly-sur-Seine
France

Phone: 33-1-47.38.57.68

**from North America:**
AGARD NATO/SPP
PSC 116
APO AE 09777

Fax: 33-1-47.38.57.99

# Preface

Modern military conflicts are likely to involve coastal environments. Such regions are characterized by complex and rapidly varying propagation conditions that must be known and predictable for sophisticated aerospace applications involving a wide range of flight vehicles. In response to this need, the meeting covered sensing, modeling, and operational assessment techniques for military operations in coastal environments. It specifically addressed important aerospace applications like missile defense and satellite remote sensing. For the latter, innovative techniques were described to use GPS signals for remote sensing of refractivity structure and use of active and passive satellite sensors for inferring radio ducting conditions. High emphasis was given to operational applications. An entire session was devoted to environmental prediction systems that are crucial for conduct and planning of military operations. Other examples of direct operational concern were radio coverage concepts and handbooks for transferring NATO ship-shore-ship data and an electrooptical tactical decision aid for point defense and strike warfare. The meeting also devoted two sessions to field trials conducted by DRG research groups. The meeting offered high-quality technical papers of direct concern to the mission of SPP and AGARD. Numerous questions following the papers indicated interest, involvement and technical appreciation by most of the participants. The meeting was attended by over 100 people and 42 papers were presented.

Gratefully acknowledged are cooperation and assistance received by the members of the technical program committee. The SPP Executive, LTC R. Cariglia and the SPP Secretary, Ms. Stephanie Branch deserve special thanks for their excellent planning and execution of the meeting and their help in preparing the proceedings. Prof. E. Schweicher and Dr. D. Dion graciously helped with the translation of question and answers.

Major credit for this very successful meeting goes to Dr. H.J. Albrecht for selecting and organizing the meeting in a German coastal region and to the officers and staff of the Marine-Ortungsschule for superbly hosting and efficiently supporting all activities.

J.H. Richter and K.H. Craig
Co-Chairmen

# Contents


| | Page |
|---|---|
| **Theme/Thème** | iii/iv |
| **Sensor and Propagation Panel** | v |
| **Preface** | vi |
| **SESSION I — SENSORS AND SENSING TECHNIQUES**<br>**Session Chairman: H. Jeske** | |
| **Structure, Variability, and Sensing of the Coastal Environment**<br>by J.H. Richter | 1 |
| **Tropospheric Refractivity Profiles Inferred From Low Elevation Angle Measurements of Global Positioning System (GPS) Signals**<br>by K.D. Anderson | 2 |
| **Lidar Measurements of Refractive Propagation Effects**<br>by C.R. Philbrick and D.W. Blood | 3 |
| **Remote Measurement of Atmospheric Refraction Conditions in the Coastal Region**<br>by K.L. Davidson and C.H. Wash | 4 |
| **Étude bistatique du comportement polarimétrique des océans**<br>par F. Daout, A. Khenchaf, Y. Hurtaud et J. Saillard | 5 |
| **Paper 6 withdrawn** | |
| **SESSION II — RADIO PROPAGATION MODELING AND MEASUREMENTS**<br>**Session Chairman: R. Makaruschka** | |
| **Atmospheric Data Resolution Requirements for Propagation Assessment: Case Studies of Range-Dependent Coastal Environments**<br>by G.D. Dockery and J. Goldhirsh | 7 |
| **Fast PE Models for Mixed Environments**<br>by M.F. Levy | 8 |
| **Terrain and Refractivity Effects in a Coastal Environment**<br>by A.E. Barrios | 9 |
| **Modeling Nonperfect Reflection from the Sea for Range-Dependent Ducting Conditions**<br>by H.V. Hitney | 10 |
| **A Propagation-Based Model of Terrain Effects for Ship-Board Radar Applications**<br>by J.P. Reilly and C.C. Lin | 11 |
| **Prévision de la Couverture Radar au Vois inage d'une Côte**<br>by M. Fournier | 12† |
| **Operational Support for a Range-Dependent Radio Propagation Model**<br>by J. Cook, G. Vogel and G. Love | 13 |


† Not available at time of printing

SESSION III — EO PROPAGATION MODELING AND MEASUREMENTS
Session Chairman: A. Junchat

Paper 14 withdrawn

**Refraction Effects on EO System Detection Ranges in Coastal Environments** 15
by D. Dion

**Comparison of Simultaneous 3-5 and 8-12 μm Transmission Measurements Near the Ocean Surface** 16
by H.T. Bull and D.R. Jensen

**Radiance of the Ocean Horizon** 17
by C.R. Zeisse

SESSION IV — MEASUREMENT CAMPAIGNS I: MAPTIP
Session Chairman: D. Jensen

**Summary of the Marine Aerosol Properties and Thermal Imager Performance Trial (MAPTIP)** 18
by D.R. Jensen, G. de Leeuw and A.M.J. van Eijk

**Characterisation of Atmospheric Properties During MAPTIP** 19
by A.M.J. van Eijk, F.H. Bastin, F.P. Neele, G. de Leeuw and J. Injuk

**Aerosol Profiles Near the Sea Surface During MAPTIP** 20
by S.G. Gathman

**Aerosol Maps Made During MAPTIP** 21
by S.G. Gathman and D.R. Jensen

**UMIST Observations of Accumulation Mode Aerosol Concentrations and Composition During MAPTIP** 22
by M.H. Smith

**Impact of Coastal Environment on Point Target Detection** 23
by K. Stein, A. Kohnle, W. Schuberth and R. Jantzen

**MAPTIP: Canada's Measurements of Refraction Effects** 24
by J.L. Forand, D. Dion and J. Beaulieu

**Surface Layer Turbulence and Aerosol Profiles During MAPTIP** 25
by K.L. Davidson, P.A. Frederickson and G. de Leeuw

**Polarization Enhancement of Contrast in Infrared Ship/Background Imaging** 26
by A.W. Cooper, W.J. Lentz, P.L. Walker and P.M. Chan

SESSION V — MEASUREMENT CAMPAIGNS II: LORIENT, VOCAR
Session Chairman: H. Heemskerk

**Overview of NATO/AC 243/Panel 3 Activities Concerning Radiowave Propagation in Coastal Environments** 27
by F. Christophe, N. Douchin, Y. Hurtaud, D. Dion, R. Makarushka, H. Heemskerk and K. Anderson

**LORIENT Campaign 1993 — The Dutch Contribution** 28
by R.B. Boekema

**Modélisation des profils verticaux d'indice de réfraction et de $Cn^2$ en atmosphère marine** 29
by J. Claverie, Y. Hurtaud, Y. de Fromont, A. Junchat

**An Overview of an Intensive Observation Period on Variability of Coastal Atmospheric Refractivity** 30
by R.A. Paulus

**Effects of Spatial and Temporal Variability of Atmospheric Refractivity on the Accuracy of Propagation Assessments** 31
by L.T. Rogers

**Refractive Variability During VOCAR 23 August to 03 September 1993** 32
by R.A. Helvey

**Use of Satellite Imagery and Other Indicators to Assess Variability and Climatology of Oceanic Elevated Ducts** 33
by R. Helvey, J. Rosenthal, L. Eddington, P. Grieman and C. Fisk

**SESSION VI — SENSOR TECHNOLOGY AND SYSTEMS ASPECTS**
**Chairman: F. Christophe**

**HF Antenna Concept Covering North and Baltic Sea to Transfer NATO Ship Shore Ship (SSB) Data** 34*
by D. Borgmann and B. Strauch

**Operational Handbook for LF/HF/UHF/Radio Reception in the Coastal Area of the North and Baltic Sea Based on Different Propagation Assessments** 35*
by D. Borgmann and J. Ott

**Direct Verification of Duct Presence in the Mediterranean Sea** 36
by C. Coveri, A. Pratesi and A. Riccobono
**(PAPER NOT AVAILABLE FOR PUBLICATION)**

**Operational Sensor Performance Prediction and Analysis** 37*
by M. Moore and D. Lewis

**A FLIR Case Study Using the Electro-Optical Tactical Decision Aid (EOTDA) MARK III** 38
by C.P. McGrath

**SESSION VII — MODELING AND PREDICTION OF THE PROPAGATION ENVIRONMENT**
**Charimen: S. Burk and J. Turton**

**An Assessment of the Operational Potential of the Meteorological Office Mesoscale Model for Predicting Royal Navy Radar Performance** 39*
by P.A. Tunnicliffe, B. Robinson, S. Bevan and J.D. Turton

**Mesoscale Modeling of Refractive Conditions in a Complex Coastal Environment** 40
by S.D. Burk, W.T. Thompson

**High Resolution Meteorological Grid for Clear Air Propagation Modeling in Northern Coastal Regions** 41
by S. Lystad and T. Tjelta

**A Microwave Propagation Model Coupled to an Air Mass Transformation Model** 42
by G.E. Grandin

* Published in Classified Supplement

**Climatic Mapping of Refractivity Parameters from Radiosonde Data** 43
by K.H. Craig and T.G. Hayton

**IR/RF Refractivity Profiles Over Coastal Water** 44
by G. de Leeuw, F.P. Neele and A.M.J. van Eijk

**Paper 45 withdrawn**

# Structure, Variability, and Sensing of the Coastal Environment

**Juergen H. Richter**
Ocean and Atmospheric Sciences Division
NCCOSC RDTE DIV 54
53570 SILVERGATE AVE
SAN DIEGO CA 92152-5230
USA

## SUMMARY

Radar observations of coastal atmospheric structures and propagation data are presented to illustrate temporal and spatial variability of the propagation environment. Sensing of radio refractivity has historically been accomplished with direct sensing techniques such as radiosondes. While direct sensing techniques provide good data for propagation assessment purposes, remotely sensed data would be more desirable. Various direct and remote sensing techniques and an assessment of their potential operational usefulness are reviewed. Included are radiosondes, refractometers, radar sounders, lidars, satellite-based sensors, and radiometric and radio propagation techniques. The need for and feasibility of providing three-dimensional, time-varying refractivity fields for propagation assessment are addressed.

Aerosol extinction is often the atmospheric parameter limiting electrooptical systems performance. For proper performance assessment, slant path extinction must be known. For several decades, attempts have been made to infer aerosol extinction from lidar backscatter measurements. A discussion of selected lidar techniques and their limitations is presented.

## 1. INTRODUCTION

Modern sensor and weapon systems rely on propagation of electromagnetic or electrooptical energy in an inhomogeneous atmosphere. Especially, a coastal propagation environment often exhibits complex spatial structures with high temporal variability that need to be understood for both sensing and modeling applications. An example of a sensor system affected by propagation anomalies are radars detecting targets far beyond the normal radio horizon or encountering holes in coverage. Systems operating in the visible or infrared wave bands can be rendered totally ineffective in the presence of clouds or fog. A quantitative assessment of the impact of the propagation medium on a system requires an adequate description of the relevant atmospheric parameters which can be obtained through sensing, numerical modeling or a combination of both. In the following, various techniques for sensing radio refractivity and aerosol extinction are described.

## 2. RADIO REFRACTIVITY

### 2.1 Structure and variability

Before addressing sensing techniques, it is important to establish *what* needs to be sensed, how *accurate* measurements ought to be and how *often* and *where* data should be taken.

Radio refractivity $N$ ($N$=[n-1]$10^6$; n = refractive index) in the atmosphere is given by

$$N=77.6[P/T+4810e/T^2] \quad (1)$$

where $P$ is the atmospheric pressure (hPa), $T$ the temperature (K) and $e$ the partial water vapor pressure (hPa). Under most atmospheric conditions, refractivity is primarily dependent on the partial water vapor pressure. Sensing efforts for radio refractivity are, therefore, mainly concerned with the vertical distribution of water vapor in the atmosphere.

For radio propagation assessment purposes, the absolute accuracy of $N$ is less important than vertical refractivity gradients and their height. Based on experience in anomalous radio propagation assessment, the height of refractive layers should be known with an accuracy of some 10 m and $N$-unit changes across a layer to approximately one $N$-unit.

Answering the question of how *often* and *where* refractivity profiles should be taken requires an understanding of the temporal and spatial behavior of atmospheric refractivity. One of the best tools to visualize atmospheric refractivity structure is a special radar built for exactly that purpose (Richter, 1969). The radar is a vertically-pointing frequency-modulated, continuous-wave (FM-CW) radar which senses the turbulence structure parameter $C_n^2$ for the refractive index. While the relationship between $C_n^2$ and the refractivity profile is not simple, strong radar echoes are most often associated with steep vertical refractivity gradients. Temporal and spatial changes of radar echoes are, therefore, an excellent description of temporal and spatial variations of layers in the vertical refractivity profile. An example is shown in figure 1 where a

*Paper presented at the Sensor and Propagation Panel Symposium on "Propagation Assessment in Coastal Environments" held in Bremerhaven, Germany 19-22 September 1994.*

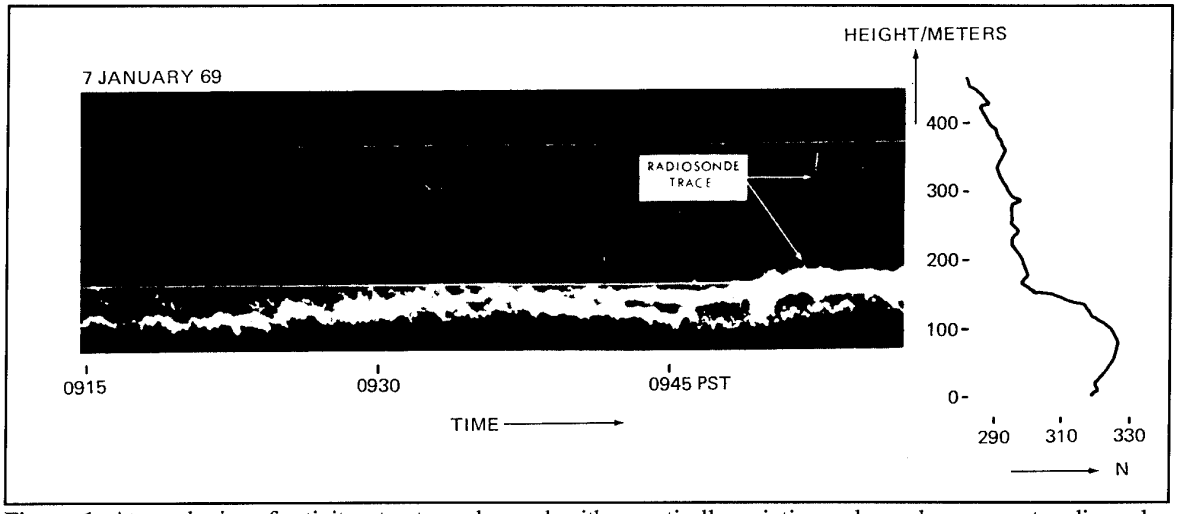


**Figure 1.** Atmospheric refractivity structure observed with a vertically pointing radar and concurrent radiosonde-derived refractivity profile.

vertically pointing FM-CW radar located in San Diego senses undulating layers that are associated with strong gradients in the directly-sensed refractivity profile. Several distinct, undulating layers can be seen. Radar observations of complex refractivity structures are not confined to a marine environment. Figure 2 is an example of FM-CW radar observations obtained in a desert environment by Eaton et al. (1994) showing complex, multy-layered wave structures (point echoes are returns from insects). Another example is shown in figure 3, where an FM-CW radar and a colocated acoustic echosounder are operated simultaneously (Noonkester and Richter, 1980). The $C_n^2$ measured by the radar is mostly dependent on moisture fluctuations while the acoustic sounder-measured $C_n^2$ depends primarily on temperature fluctuations. Both sounders reveal a consistent picture of atmospheric structure: convective activity below an inversion layer that

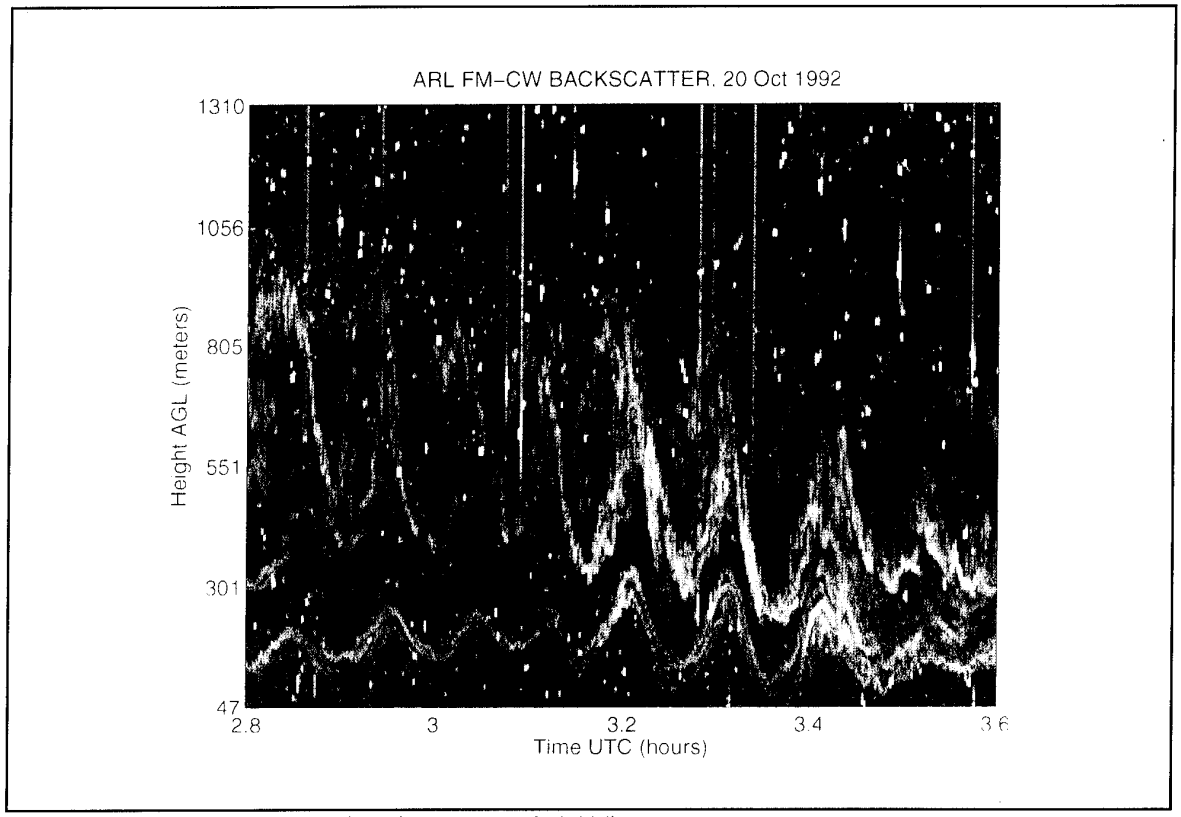


**Figure 2.** FM-CW radar observations by Eaton et al. (1994)

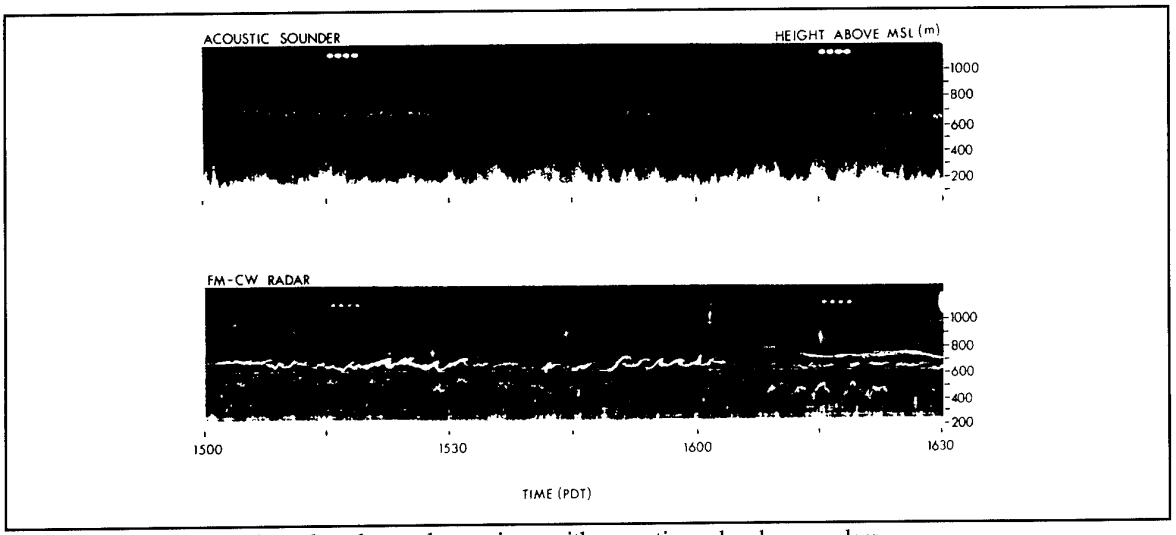


**Figure 3**. Simultaneous boundary layer observations with acoustic and radar sounders.

undulates between 600-700 m. Figures 1-3 convey a picture of a dynamic refractivity structure consistent with propagation measurements, which, when influenced by atmospheric refractive layers, vary (fade) with time. Figures 4-7 illustrate signal variability and suggest fundamental limitations to instantaneous signal-level

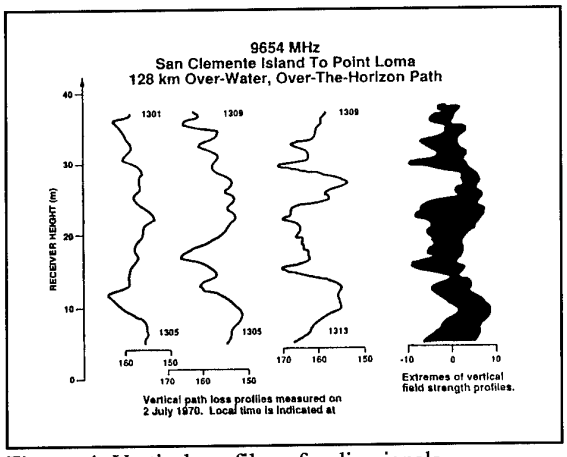


**Figure 4**. Vertical profiles of radio signals.

predictability. Figure 4 shows 9.6 GHz signals for a 128 km over-water, over-the-horizon path measured with a receiver which was moved vertically between 5 and 38 m above the surface. The numbers at the tops and bottoms of the three individual traces indicate the start and stop time for the measurements. Acquisition of the three individual profiles took 4 minutes each. Even though the three profiles are separated by not more than 12 minutes, they have little resemblance to each other. The upper and lower envelopes of signal variability for the entire measurement period are shown on the right side of the figure indicating almost 20 dB variability. This number may be considered large and disappointing for high-fidelity assessment purposes. However, this variability is superimposed on 50 - 60 dB signal enhancements over standard atmospheric conditions (in figure 4, the transmitter was located 10 m above sea level, troposcatter loss is 215 dB; free space loss is 154 dB). This illustrates an important point: the quality of propagation and environmental models should be judged by their ability to predict average signal enhancements (or decreases) rather than short term fluctuations; the latter may appear large by themselves but are really small compared to the overall effect. Figure 5 (reproduced from Dockery and Konstanzer, 1987) addresses the same point using state-of-the art range-dependent refractivity measurements and range-dependent propagation models. Refractivity profiles

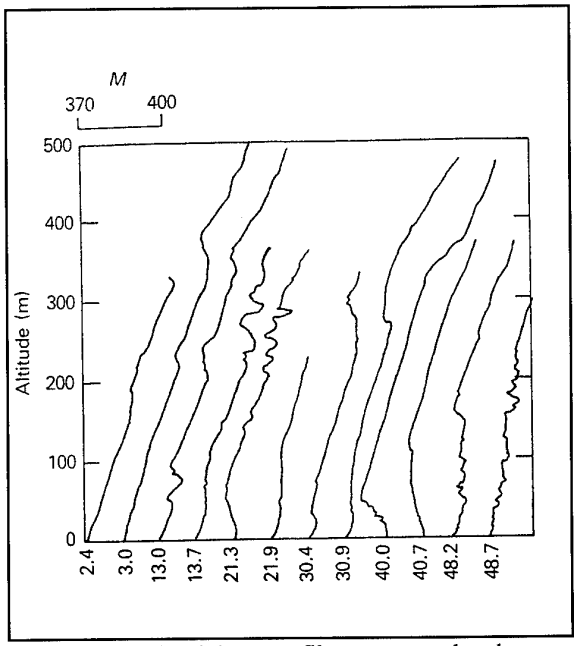


**Figure 5**. Refractivity profiles measured along a propagation path (Dockery and Konstanzer, 1987)

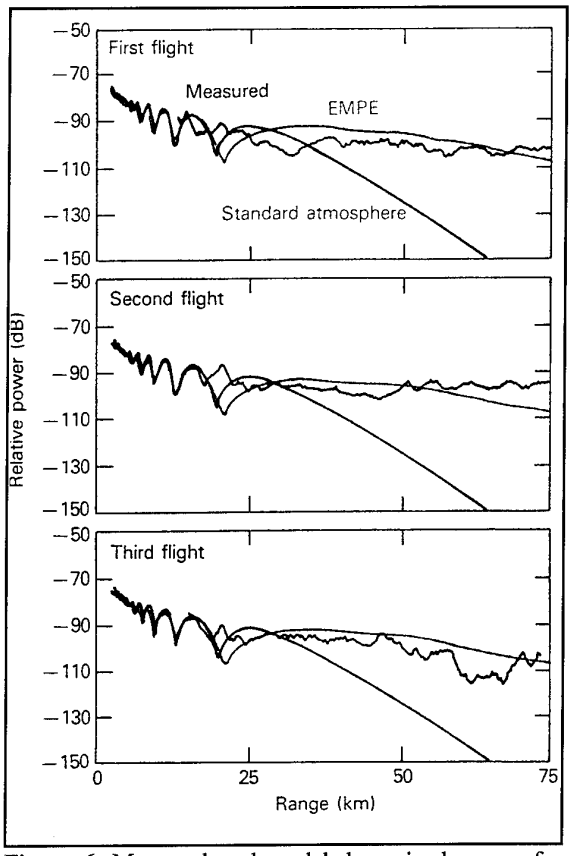


**Figure 6.** Measured and modeled received power for the refractivity conditions of figure 5.

calculated from helicopter-borne temperature and humidity measurements (figure 5) show a variable refractivity environment along a propagation path. These profiles were used with the range-dependent propagation code EMPE (Ko et al., 1983) to calculate path loss at 5.65 GHz as a function of range. Figure 6 shows measured path loss values (from an aircraft flying at a constant altitude of 31 m), calculations based on the helicopter measurements, and, for comparison purposes, path loss for a standard atmosphere. For all three cases in figure 6, the propagation calculations predict the general signal enhancement for beyond-the-horizon ranges but disagree at certain ranges with the measurements by as much as 20 dB.

Occasionally, the environment varies so rapidly that measuring such a variability is not feasible. Even if it were, the rapid changes would make accurate propagation predictions impossible. Two examples given by Anderson (1993) illustrate stable and variable refractivity environments. Anderson investigated low-altitude, short-range radar detection capabilities under evaporation ducting conditions. A shore-based 9.4 GHz radar at 23.5 m above mean sea level tracked a calibrated target at 4.9 m above the sea. Figure 7 shows radar data (propagation loss) for target ranges between 3-17 km. The measurements cluster around what propagation models predict for the 7-8 m evaporation duct present (for this evaporation duct strength, signal levels between approximately 7-15 km are below those plotted for a standard atmosphere). The same radar measurements repeated on another day are shown in figure 8. Propagation loss levels show instantaneous variations of up to 20 dB. The reason for this variability was an elevated refractive layer responsible for an approximately 50 m thick surface-based duct that dominated the propagation mechanism. This elevated layer apparently fluctuated sufficiently to cause the highly-variable propagation loss values. Figure 2 serves as a reminder of possible refractivity complexity and variability. There is no way of either measuring or modeling such highly variable refractivity structures for instantaneous signal strength predictions. This means there will be situations for which an accurate instantaneous sensor performance assessment cannot be provided. Fortunately, such highly variable situations are rare (a subjective estimate is that they occur less than 10% of the time) and techniques may be developed to make the operator aware of such situations and perhaps bracket the expected variability. For the majority of the

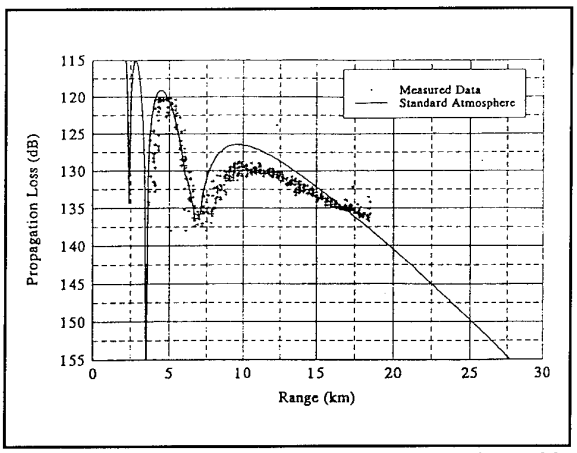


**Figure 7.** Propagation loss measurements under stable atmospheric conditions.

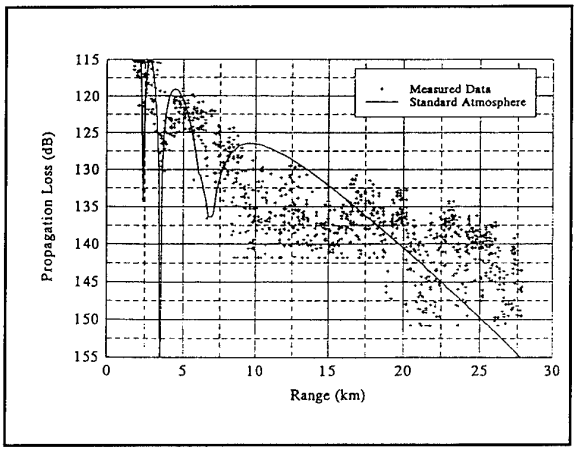


**Figure 8.** Propagation loss measurements under variable refractivity conditions.

situations encountered, the assumption of horizontal homogeneity is reasonable. It was found that calculations of propagation enhancements based on a single vertical profile were correct in 86% of the cases. A similar conclusion has been reached from years of shipboard experience with the US Navy's Integrated Refractive Effects Prediction System (Hitney et al., 1985).

Additional excellent quantitative refractivity and propagation data have recently been obtained during a program in the southern California coastal area named VOCAR [Variability of Coastal Atmospheric Refractivity, (Paulus, 1994)]. The major objective of this program is the development of a data assimilation system which provides refractivity nowcasts and forecasts based on both sensed data and meteorological numerical models. Such a data assimilation system is the only hope for an operational refractivity assessment and forecasting system. One component of VOCAR was the simultaneous and continuous measurement of a radio signal radiated from the northern tip of San Clemente Island (SCI) and received simultaneously at Pt. Mugu (133 km path) and at San Diego (127 km path). These propagation paths are nearly identical in length but are located in different areas of the S. California Bight. Variations in signal levels over the two paths are a precise measure of path-integrated refractivity conditions and their temporal changes; in addition, cross-correlation between the signals over the two paths gives quantitative data concerning horizontal homogeneity of refractivity conditions (Rogers, 1994a,b).

In conclusion, it is very important to realize and appreciate the temporal and spatial variability of atmospheric refractivity structure for any sensing and forecasting effort. For most applications, horizontal homogeneity is a reasonable assumption. Therefore, single profiles of refractivity measured either directly or remotely are adequate for propagation assessment purposes. Most promising is a data assimilation system, which combines sensed and numerically modeled data.

## 2.2 Direct Sensing Techniques

### *Radiosondes*

Radiosondes have been, and still are, the most frequently used direct sensing technique for obtaining radio refractivity profiles. Ever since the slow-response lithium chloride humidity sensor was replaced with the carbon element some 35 years ago (thin film capacitors are used today), the radiosonde has provided satisfactory vertical humidity profiles under most conditions. A commonly used radiosonde system today consists of a Vaisala RS 80 series radiosonde and suitable receivers. The specified accuracy of the sensors is 0.5 hPa for the pressure, 0.2 °C for temperature and 2% for relative humidity (humidity lag is 1 s for 6 m/s flow at 1000 hPa, +20 °C). The radiosonde package itself weighs less than 200 g and can be launched with a 100 g balloon. The radiosonde senses temperature, humidity and pressure continuously but each of the sensors is selected in succession for relaying the information to the ground station. The duration of the measurement sequence is approximately 1.5 s. This results in non-continuous temperature and humidity profiles which can cause problems when the sonde ascends through very sharp vertical humidity gradients while transmitting other data. Such problems are not very common and rarely significant for operational assessments; they can be avoided for special applications by either more rapid switching schemes or continuous profile measurements (i.e., launching more than one radiosonde with one of the sondes transmitting humidity only). The radiosonde can also be equipped with navigation receivers (Omega or LORAN C) which permits sensing of winds. Incorrect surface values represent one problem encountered with radiosondes. The launch point may be affected by surface heating (or by a local heat source in the case of shipboard launches) and lead to systematic errors (Helvey, 1983). Shipboard-induced surface heating errors can be avoided by dropsondes (released by aircraft and descending by parachute) or by launching the radiosonde sensor package with a small rocket and obtaining the measurements during parachute descent away from the ship (Rowland and Babin, 1987). These techniques measure the profiles away from the ship down to the ocean surface. They do not, however, measure (as sometimes erroneously stated) humidity profiles responsible for evaporation ducting. Another shortcoming of radiosonde-measured profiles is the non vertical flight path of the balloon (and parachute) and the time it takes to measure one profile. Both the non vertical sampling path and temporal changes during the measurement do not necessarily provide an accurate vertical profile. This must be considered when comparing true vertical, instantaneous profile measurements (e.g., lidar profilers) with radiosonde data.

### *Microwave Refractometers*

Unlike radiosondes, microwave refractometers measure radio refractivity directly. Ambient air is passed through a microwave cavity whose resonant frequency is a function of both the dimensions of the cavity and the refractive index of the air within the cavity. If the dimensional changes of the cavity are kept very small, the refractive index of the air within the cavity can be accurately determined from the measurement of the resonant frequency of the cavity. The operating frequency of microwave refractometers is usually around 10 GHz. Microwave refractometers have been used as early as 1952 and have been installed operationally in the US Navy's E-2C airborne surveillance aircraft (designated AN/AMH-3, Airborne Microwave Refractometer). In research operations, microwave refractometers are often deployed from helicopters. Microwave refractometers are considered the most accurate sensor for radio refractivity and have usually very rapid response times. Their disadvantages are relatively high cost and weight.

*Evaporation Duct Sensors*

An important ducting phenomenon over oceans is the evaporation duct. This duct is caused by a rapid decrease in humidity right above the ocean surface. A measurement of the instantaneous vertical humidity profile is difficult because humidity decreases from saturation directly at the surface (relative humidity 100%) to its ambient value within the first few centimeters above the surface. The instantaneous ocean surface is perturbed by wave motions and an average surface height is defined only when the instantaneous height is averaged over time. In addition, individually measured profiles are characterized by temporal fluctuations which are of the same order as the vertical changes of interest. Therefore, individually measured profiles are not meaningful for evaporation ducting assessment unless they are averaged over time (on the order of one minute). Lack of understanding of these basic micrometeorological properties has resulted in many inappropriate profile measurement proposals and attempts. Relationships have been developed which permit reliable evaporation duct height determination from four simple "bulk" measurements: sea-surface temperature and air temperature, relative humidity, and wind speed measured at a convenient reference height (usually 5-10 m) above the surface (Jeske, 1973). These four measurements are usually made with standard meteorological sensors (e.g., psychrometer for humidity, anemometers for wind and thermometers [thermistors, thermocouples] for temperature). For sea-surface temperature, a hand-held radiometer may provide more convenient and accurate data (Olson, 1989). Over two decades of experience in evaporation ducting assessment based on bulk measurements have provided satisfactory and consistent results. Operational assessment of evaporation ducting effects is less affected by uncertainties in relating bulk measurements to profiles than by range-variations in the duct.

## 2.3 Remote Sensing Techniques

*Radar Techniques*

Radar observations of atmospheric refractivity structures are almost as old as radars themselves (Cowell and Friend, 1937). The first radar specifically designed for the study of refractivity structure was introduced by Richter (1969). The radar provided continuous observations of atmospheric refractivity structures with an unprecedented range resolution of one meter. Observations with this radar helped settle the question of the nature of radar returns from atmospheric refractivity and revealed a detailed picture of temporal and spatial refractivity variations unknown before (Fig. 1-3). To this day, there is no other remote sensor capable of providing a more detailed picture of the dynamics and structure of atmospheric refractivity. The radar, however, does not sense the refractivity profile but rather the structure parameter $C_n^2$ of the structure function describing the turbulent perturbation of atmospheric refractivity. Gossard and Sengupta (1988) derived a relationship between refractivity gradient and $C_n^2/C_w^2$ where $C_w^2$ is the structure parameter of the vertical component of the turbulent wind velocity field (measured from the turbulent broadening of the Doppler spectrum). This relationship allows, in principle, retrieval of refractivity profiles from radar measurements. In practice, retrievals are limited by the presence of clouds or other particulates contaminating the radar data. Additional difficulties are that the broadening of the Doppler spectrum may be due to effects other than turbulence and the need for data with high signal-to-noise ratios. It appears that a combination of remote sensors such as radar (with Doppler capability), acoustic echo sounder, and Radio Acoustic Sounding System (RASS), may sense data which will result in accurate refractivity profiles (Gossard, 1992).

*Lidar Techniques*

Two lidar techniques have been used successfully to measure atmospheric profiles of water vapor: differential absorption lidars (DIAL) and Raman-scattering lidars.

DIAL uses the strong wavelength-dependent absorption characteristics of atmospheric gases. For radio refractivity, water vapor is of interest (oxygen is used for temperature profiling). A tunable laser is tuned to the resonance of an absorption line and then tuned off resonance. The ratio of the range-gated lidar signal permits determination of the atmospheric water vapor profile (Schotland, 1966; Collis and Russell, 1976; Measures, 1979).

Raman-scattering lidars utilize a weak molecular scattering process which shifts the incident wavelength by a fixed amount associated with rotational or vibrational transitions of the scattering molecule (Melfi et al., 1969; Cooney, 1970). The ratio of the Raman-scattered signal for the water-vapor shifted line to the signal from nitrogen is approximately proportional to the atmospheric water vapor mixing ratio (Melfi, 1972).

An example of a water vapor profile measured with a Raman lidar is shown in figure 9 (Blood et al., 1994; Philbrick, 1994). The instrument used for measuring those data is a 532 nm, 0.6 Joule/pulse, 7 ns pulse width, 20 Hz pulse repetition frequency lidar. The lidar profiles are integrated over 30 min and the range resolution of the data set is 75 m. The solid trace in figure 9 represents the lidar and the dashed trace the radiosonde data. The agreement is excellent considering that the balloon profile is not the true instantaneous vertical profile and the lidar data are time averaged.

Even though water vapor profiling based on differential absorption and Raman scattering has been demonstrated some 25 years ago, no instruments for routine ground-based use are commercially available yet. The reason is that neither technique will produce profiles reliably under all conditions. Daytime background radiation

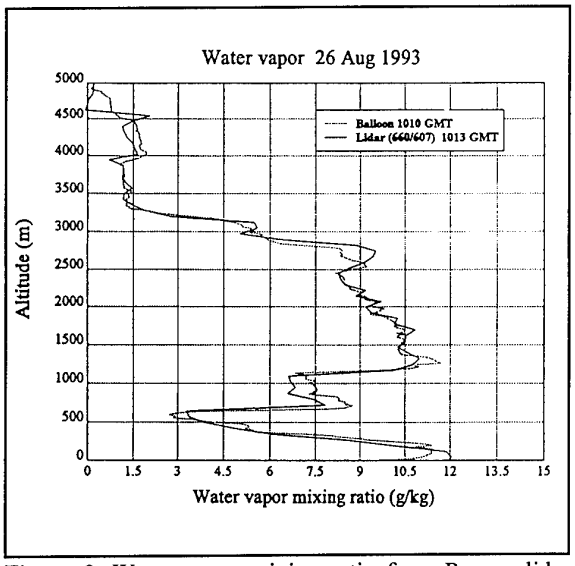


**Figure 9**. Water vapor mixing ratio from Raman lidar measurement (solid) and radiosonde (dashed).

decreases the signal-to-noise ratio and so does extinction by aerosols. For cost and eye-safety reasons, there is a limit of how powerful the emitted radiation can be. For Raman-scattering lidars, various attempts have been made to use the so-called solar-blind region (230-300 nm) to reduce daytime background noise (Cooney et al., 1980; Petri et al., 1982; Renaut and Capitini, 1988). Extinction by aerosols is a fundamental problem for any remote sensing technique (active or passive) using ultraviolet, visible or infrared radiation. In a marine environment the most severe ducting conditions occur when a strong temperature inversion is present. Stratus clouds form frequently when there is a strong temperature inversion. The height of the rapid humidity decrease occurs just above the top of the stratus cloud which means the laser energy has to penetrate the cloud from below and travel back to the ground-based receiver.

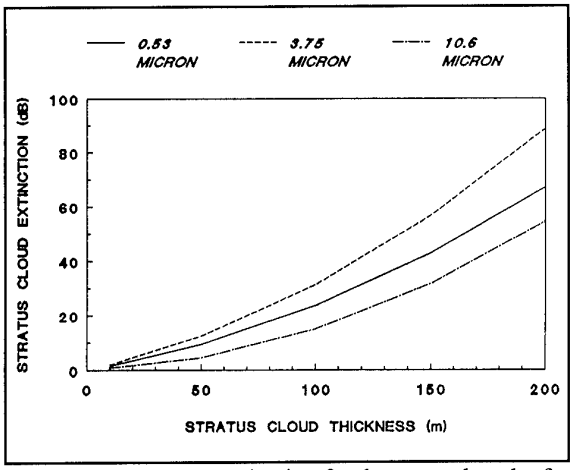


**Figure 10**. Two way extinction for three wavelengths for a signal penetrating a stratus cloud of a given thickness based on Noonkester (1985).

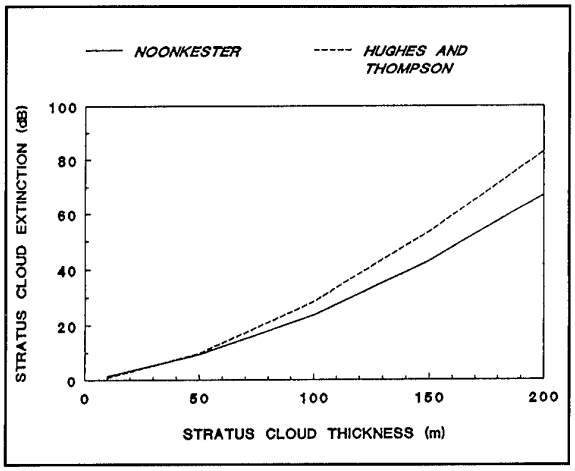


**Figure 11**. Two way extinction for 0.53 microns for a signal penetrating a stratus cloud of a given thickness [solid line based on Noonkester (1985), dashed line on Hughes and Thompson (1984)]

Figure 10 shows the additional attenuation a laser signal encounters by travelling through a stratus cloud of a given thickness. The extinction curves in figure 10 are based on dropsize measurements of stratus clouds having a mixture of marine and continental aerosols using a linear regression line fit to the data (Noonkester, 1985). Hughes and Thompson (1984) applied a power law fit to the same data which results in higher extinction values as shown in figure 11 for 0.53 microns. From figures 10 and 11, one can see that a vertically pointing, ground-based 530 nm lidar system may loose as much as 43-54 dB in signal when penetrating a 150 m thick stratus cloud. It is doubtful that any realistic lidar could handle such attenuation values.

An interesting attempt to deduce water vapor profiles from lidar measurements of aerosol backscatter is described by Hughes et al. (1992). The technique is based on a correlation between aerosol dropsize distribution and relative humidity. However, this technique will also not work under high extinction (clouds) conditions.

### *Radiometric Techniques*

Radiometric techniques are widely used in remote sensing for determining temperature and humidity profiles (Ulaby et al., 1981; 1986; Janssen, 1993). They are passive and are, therefore, ideally suited for situations where active emissions are undesirable. The downwelling sky radiometric or brightness temperature in the zenith direction $T_B(\nu)$ is related to the water vapor profile $\rho_v(z)$

$$T_B(\nu)=\int_0^\infty W_\rho(\nu,z)\rho_v(z)dz \qquad (2)$$

where the weighting function for water vapor, $W_\rho(\nu,z)$ is given by

$$W_\rho(\nu,z)=\kappa_\nu(z)\frac{T(z)}{\rho_\nu(z)}e^{-\tau_\nu(z)} \qquad (3)$$

$T(z)$ is the atmospheric temperature profile, $\tau_\nu$ the optical thickness, $\nu$ the frequency, and $\kappa_\nu(z)$ the absorption coefficient (which is approximately the water vapor absorption coefficient for measurements taken in the vicinity of water vapor absorption lines and under clear sky conditions). Radiometric retrieval techniques are not well suited for obtaining rapidly varying parameters. They provide better results for retrieving temperature profiles since temperature profiles have a smaller relative variability about their mean profile than humidity profiles. For anomalous radio propagation assessment, height and gradient of humidity profile changes are important; presently available microwave radiometry methods are far from producing humidity profiles with a vertical resolution suitable for anomalous propagation assessment. Figure 12 shows an example of a radiometrically retrieved water vapor profile and a radiosonde profile. The strong vertical gradient around 200 mb above the surface as well as the fluctuations below are not evident in the radiometrically sensed profile (Westwater and Decker, 1977).

Other attempts to measure humidity profiles have recently been made using a high resolution interferometer sounder (HIS) operating in the 5 - 20 $\mu$m band (Rugg, 1992).

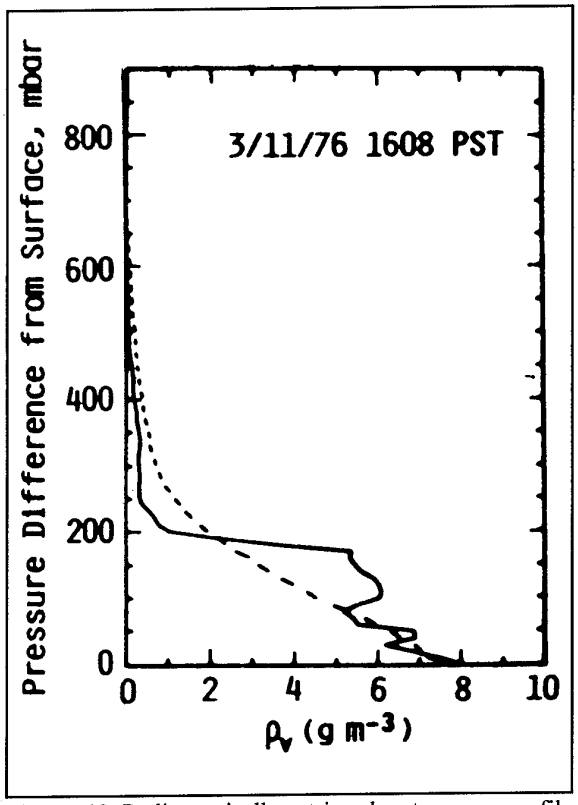


**Figure 12.** Radiometrically retrieved water vapor profile $\rho_v(z)$ (dashed) and radiosonde profile (solid).

While this technique showed some minor improvements compared to microwave radiometry, it still does not produce humidity profiles with a resolution suitable for radio propagation assessment purposes. Figure 13 shows

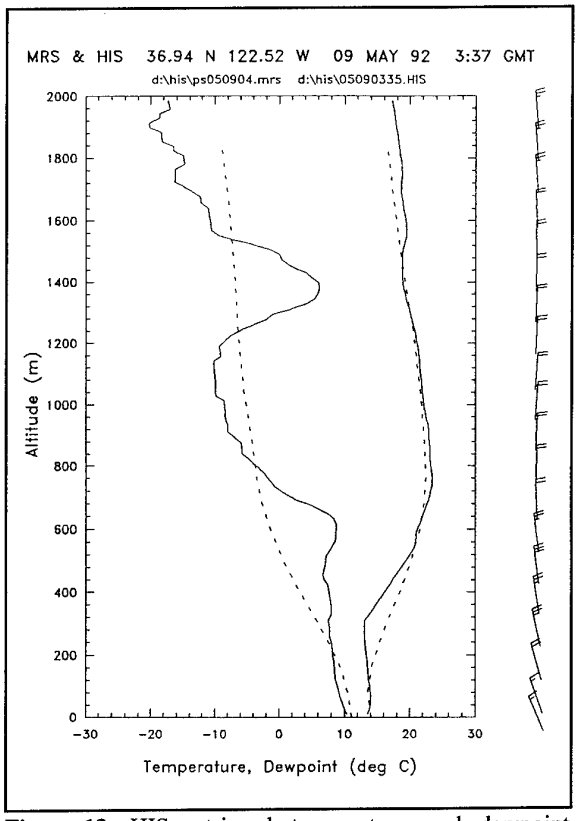


**Figure 13.** HIS retrieved temperature and dewpoint profiles (dashed) and MRS (Mini Rawin System) (solid).

a comparison of temperature and dewpoint profiles retrieved from the HIS to radiosonde measurements (Wash and Davidson, 1994). The radiometrically retrieved temperature profile is in good agreement with the radiosonde while the radiometrically retrieved dewpoint profile misses the vertical gradients that are crucial to propagation assessment.

In conclusion, microwave and infrared radiometry, *by themselves*, are presently not capable of retrieving vertical humidity profiles with an accuracy necessary for radio propagation assessment purposes. However, radiometry can play an important role as one component in a data assimilation system consisting of sensed and modeled fields.

### *Satellite Sensing Techniques*

Because of the potential for global coverage, refractivity sensing from satellites would be very desirable. In principle, all of the above mentioned remote humidity profile (refractivity) sensors could be deployed from satellites and some already are (radiometers). Because of the limitations of the remote refractivity sensors discussed

above, none are likely to provide the desired information by themselves. For determining evaporation duct heights, which require no continuous profile data but only four surface or near-surface parameters, Cook (1992) has proposed a scheme of combining satellite-sensed (ocean surface temperature, near-surface wind speed, and radiometry) data with outputs from numerical weather models in data assimilation systems. This kind of an approach is very likely to become more important in the future (Wash and Davidson, 1994). Additional interesting techniques have been proposed to use satellite data such as visible and infrared imagery to *infer* ducting conditions. Rosenthal and Helvey (1992) have pioneered subjective and objective techniques and demonstrated remarkable success in relating cloud patterns to ducting conditions in the Southern California off-shore area. Their approach assumes an inversion-dominated weather regime with low stratus or stratocumulus clouds that are lowest and flattest over the eastern parts of the subtropical oceans where the overlying inversion is lowest and strongest. They developed statistical relationships between cloud patterns and radiosonde-derived ducting conditions. They also derived an objective duct height estimate by correlating radiosonde statistics to cloud-top temperatures deduced from infrared imagery (Helvey and Rosenthal, 1994).

***Radio Propagation Techniques***

One remote sensing technique of high potential for operational assessment involves monitoring known radio transmitters. Especially in coastal regions, one usually finds an abundance of land-based transmitters which can be passively monitored off-shore. Signal levels of known emitters may be related to refractivity structure. Hitney (1992) used refractivity profile statistics in the S. California coastal region to derive correlations between radio signals and height of the trapping layer, which usually coincides with the base of the temperature inversion in this region. This single-path, single-frequency method can undoubtedly be improved by using multiple paths and multiple frequencies. Part of the above mentioned VOCAR effort addresses remote sensing based on propagation data (Paulus, 1994; Rogers, 1994a,b).

Shipboard radars may sense returns from the sea surface and, in the presence of ducting, these sea-surface clutter returns may be modified by atmospheric refractivity. An example is clutter rings that are caused by multiple bounces of a radar signal between an elevated refractive layer (responsible for a surface-based duct) and the sea surface. In that case, the height of the reflecting layer (height of the duct) can be calculated from the geometry involved. Much more difficult is separation of the combined effects of sea-clutter enhancement and evaporation ducting. The ocean-surface properties affecting clutter (such as wind speed and direction) are not necessarily related to evaporation duct parameters and both effects are measured simultaneously. No reliable technique has been proposed to separate the two effects, which is necessary before shipboard radars may be used as evaporation duct sensors.

Another technique involves radio signals emitted from satellites in an attempt to relate refractive bending to refractivity structure. The bending effect is only significant within a few degrees of the horizon and, therefore, primarily of interest over oceans where unobstructed horizons are found. Refractivity structure may be deduced from a shift in the observed interference pattern when compared to standard conditions (Anderson, 1982). Anderson (1982) had moderate success inferring refractivity profiles but not with sufficient reliability to recommend the technique for routine use. This technique is presently being reexamined using Global Positioning System (GPS) signals which have much higher phase stability than previously available.

One very important aspect of remote sensing using radio propagation data is that the *path-integrated* effect of refractivity can be measured *instantaneously* to any degree of desired accuracy. The accuracy of data assimilation systems based on remote and direct sensors, numerical meteorological models, and other information is very difficult to verify experimentally because this requires extensive measurements in both space and time. Modelers have argued that their models are better than our present ability to measure the temporal and spatial structure of interest. That argument does not apply to careful radio propagation measurements; any data assimilation system addressing refractivity can and should be objectively and quantitatively evaluated by propagation data.

**2.4 Data Assimilation Systems**

It is obvious from the foregoing that there is no single sensing technique that can provide the needed refractivity information continuously and reliably. Neither can it be expected that such a technique will ever be available. Even if it were, for military applications an ability to forecast propagation conditions is as important as a nowcasting capability. Meteorological mesoscale models are presently available with 20 km horizontal grid spacing and 30 levels total in the vertical; there are ten grid points in the first 500 m with a 25 m spacing near the surface and 75 m near 500 m. Newer models being tested now have a 10 km grid spacing and a total of 36 levels in the vertical (Burk et al., 1994; Thompson et al., 1994). A data assimilation system comprising such models and utilizing remotely and directly sensed refractivity data is undoubtedly the right approach to describe and forecast refractivity conditions. A major objective of the previously mentioned VOCAR program is providing a data base to evaluate a data assimilation system under development by the US Navy.

## 3. AEROSOL EXTINCTION

### 3.1 Structure and Variability

The high emphasis on smart weapons with electrooptical (EO) sensors is putting increasing demands on assessment of atmospheric EO effects. In comparison to refractivity assessment where the spatial scales of interest are in the tens to hundreds of km, for EO applications the scales of interest are usually an order of magnitude less. Also, atmospheric variability can be much larger for EO systems than for those dependent on radio refractivity. For example, the extinction of a cloud may be many hundreds of dB above clear conditions, which poses a particularly challenging problem for real-time prediction of EO propagation conditions through broken clouds. To illustrate the complexity of EO propagation assessment, an example is presented which does not even involve clouds (Richter and Hughes, 1991). Figure 14 shows predicted and measured detection ranges for an airborne thermal imaging system (Forward Looking Infrared or FLIR) against a large ship target. The scatter in figure 14 is indicative of the uncertainty in many parameters contributing to detection range calculations: there is the

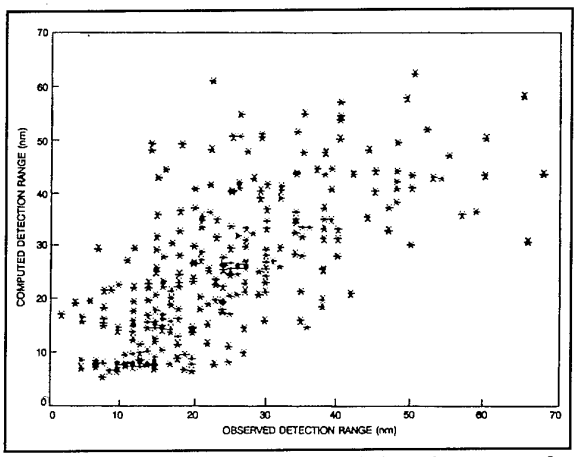


**Figure 14**. Observed and calculated detection ranges for a thermal imaging system.

subjective element of the operator to call a signal on the screen a detection; the general condition and calibration of the complex hardware involved; the adequacy of meteorological data, which may come from other locations and taken at different times; the validity of models that translate observed meteorological data into parameters important for EO propagation such as aerosol extinction; and the variability of all factors affecting propagation along the path. Considering the potential contribution that each of the above uncertainties may have on the detection range calculation, the scatter in figure 14 is not unexpected. It is, however, unacceptable for the operational use of thermal imaging systems and steps need to be taken to reduce the scatter and provide more precise detection range predictions.

There are four atmospheric parameters which affect EO propagation: (a) molecular extinction; (b) turbulence; (c) refraction; and (d) extinction (i.e., absorption and scattering) by aerosols. Molecular extinction by the various gases found in the atmosphere is well understood for most EO systems applications. Molecular extinction can be quite severe in certain spectral regions, which EO systems either avoid or sometimes exploit. Atmospheric turbulence may degrade the coherence of a high-resolution image or change the precise position of a laser beam and thereby limit the performance of a system. Refraction may bend the propagation of optical energy and may, for example, shorten or extend the optical horizon. In the following, only the question of sensing aerosol extinction is addressed since aerosol extinction is by far the most significant limitation for EO sensors and also it is the most difficult to measure and predict.

### 3.2 Direct Sensing Techniques

Detection and sizing of aerosol particles can be done by passing an air sample through a laser beam and measuring the scattered radiation. An example is the family of "Knollenberg" drop-size spectrometers available from Particle Measuring Systems. An evaluation of these devices was done by Jensen et al. (1983). Usually more than one drop-size spectrometer is needed since no single instrument is capable of measuring aerosol distributions ranging from submicron to tens of microns in diameter with number densities (numbers of aerosols per unit volume) spanning more than 12 orders of magnitude over these size ranges. Other methods to determine aerosol concentration and sizes include impaction devices, cloud chambers, electrostatic mobility devices and centrifuges. Other instruments measure the combined molecular and aerosol volume scattering (nephelometers and visibility meters) and extinction (transmissometers). The above instruments are delicate and expensive optical instruments and not suited for all applications. In particular, unlike the radiosonde, they are neither light-weight nor expendable, which limits vertical profiling to tethered balloons or aircraft. The above instruments may be impractical even for point-measurements such as the measurement of large aerosols close to the ocean, which are important for near-horizon passive infrared (IR) detection of low-flying anti-ship missiles. De Leeuw (1986a; 1986b) used a Rotorod™ impactor to collect near-surface large aerosols for analysis under a microscope. The Rotorod™ (available from Sampling Technologies, Los Altos, California) is a volumetric, rotating-arm impaction device capable of obtaining quantitative aerosol data in the 10 - 100 micron size range.

### 3.3 Remote Sensing Techniques

*Lidars*

The desire for vertical or slant-path extinction profiles prompted numerous attempts to employ lidars as described by Richter and Hughes (1991). The utility of a monostatic lidar system as a remote sensor for obtaining temporal and spatial information about the dynamic processes of the atmosphere is well established

(Noonkester et al., 1972). By measuring the power backscattered from a laser pulse at a given range to a receiver, the movement and relative concentrations of naturally occurring aerosols, industrial pollutants or battlefield obscurants can be monitored and the bases of clouds determined. Remote mapping of wind velocities and flow patterns over large portions of the atmosphere can also be carried out. In these applications, the lidar is used as a tracer of aerosols that scatter the incident radiation rather than as a probe for studying the aerosols' optical properties.

For a given aerosol size distribution, extinction can be determined from Mie theory assuming that aerosols scatter and absorb radiation as if they were spheres of known refractive indices. For example, in the well-mixed marine boundary layer, relative humidities are usually high enough that most of the aerosols are hydrated, taking on a spherical shape. But above the boundary layer, where relative humidities are lower, aerosols may be non-spherical. In such cases, the optical properties predicted for spheres may differ by as much as an order of magnitude from those observed.

The single-scatter lidar equation is given by the relation

$$S(r)=\ln[P(r)r^2]=lnK+\ln\beta(r)-2\int_0^r \sigma(r')dr' \qquad (4)$$

In this equation $P(r)$ is the power received from a scattering volume at range $r$, $K$ is the instrumentation constant, and $\beta(r)$ and $\sigma(r)$ are the volumetric backscatter and extinction coefficients, respectively. In differential form this equation is

$$\frac{dS(r)}{dr}=\frac{1}{\beta(r)}\frac{d\beta(r)}{dr}-2\sigma(r) \qquad (5)$$

The solution of equation (5) requires knowing or assuming a relationship between $\beta(r)$ and $\sigma(r)$. However, if the atmosphere is homogeneous, the extinction coefficient can be simply expressed in terms of the rate of change of signal with range, i.e., $\sigma = -½\,[ds(r)/dr]$. A plot of $S(r)$ vs. $r$ would then yield a straight line whose slope is $-2\sigma$. However, horizontally homogeneous conditions are not generally found.

An assumed relationship between backscatter and extinction coefficients can be eliminated by comparing the powers returned from a volume common to each of two lidars located at opposite ends of the propagation path. For this double-ended lidar configuration, the range-dependent extinction coefficient can be shown (Hughes and Paulson, 1988) to be related to the slope of the difference in the range compensated powers measured by the two lidars at the common range $r$ by equation (6). However, the receiver gain of both lidars must be accurately known since it affects the slope characteristics

$$\sigma(r)=-\frac{1}{4}\frac{d}{dr}[S(r)_1-S(r)_2] \qquad (6)$$

of the individual S(r) curves. Although the double-ended technique has practical limitations for tactical situations, e.g., for slant path measurements at sea, it is feasible to use it in aerosol studies and to evaluate various single-ended schemes for measuring extinction. Hughes and Paulson (1988) used the double-ended lidar configuration over a 1 km inhomogeneous slant path to demonstrate that if the value of $C(r)$ varies with range, but is assumed to be a constant, single-ended algorithms will not allow range-dependent extinction coefficients to be determined with any assured degree of accuracy even if the initial boundary values are specified. If, however, the manner in which $C(r)$ varies is specified, single-ended inversion techniques reproduce the double-ended measurements remarkably well. It is, therefore, concluded that range-dependent extinction coefficients cannot be determined from simple, single-ended lidar measurements with any assured degree of accuracy unless either the backscatter/extinction coefficient ratio is known along the propagation path or the atmosphere is horizontally homogeneous.

For a single-ended lidar to become a useful operational tool, innovative concepts need to be pursued. A single-ended lidar technique has been proposed by Hooper and Gerber (1986; 1988) to measure optical depths when used looking down from an aircraft or satellite at the ocean surface and when the reflection properties of the surface are known. In this technique, two detectors are used: one with a narrow field-of-view, which measures the power directly reflected off the rough ocean surface and another with a wide field-of-view where the directly reflected photons are blocked (aureole detector). Bissonette and Hutt (1989) described a technique based on the simultaneous measurement of lidar returns at different fields of view. By ratioing these returns, the need for a backscatter-to-extinction relationship is eliminated. So far, none of these techniques have been widely accepted. Finally, even if a lidar would produce reliable extinction profiles at one wavelength, the question remains of how to extrapolate the data to other wavelength bands.

***Satellite Techniques***

Griggs (1983) and Durkee et al. (1986) inferred aerosol optical thickness using satellite radiance measurements over oceans. Their technique is based on a linear relationship between the upwelling radiance measured by a satellite over the ocean and the optical depth of the atmosphere. This approach is applicable over water surfaces since they have a low reflectance (close to zero) so that the upwelling radiance is essentially all due to atmospheric scattering. Over land surfaces (which have a much larger albedo), the upwelling radiance is mostly reflected from the surface and is less sensitive to change in atmospheric aerosols. This technique provides global

atmospheric optical depth data but is only useful over oceans.

### 3.4 Data assimilation systems

No single sensing technique is available that provides accurate, three-dimensional, time varying aerosol extinction. Vertical aerosol distributions over water can be related to commonly observed meteorological parameters (Gathman, 1989; Gathman and Davidson, 1993). A data assimilation system which combines sensed extinction data and aerosol profiles calculated from numerical meteorological mesoscale models is presently the best approach to provide extinction data. Such systems are under development but will, initially, not have the resolution desired for EO systems performance assessment.

## 4. CONCLUSIONS

Direct sensing techniques for vertical refractivity (humidity) profiles are well established, are relatively easy to obtain, inexpensive, and provide useful results for propagation assessment purposes. Lidar remote sensing techniques provide excellent vertical refractivity (humidity) profiles when background noise and aerosol extinction are low. Techniques involving satellite sensors or sensing of satellite signals show promise in the future. Direct sensing of aerosol extinction is also well established even though the instrumentation is delicate and expensive. Attempts to remotely sense aerosol extinction profiles using lidar techniques have not yet resulted in generally available instrumentation that would provide data with adequate and assured accuracy. The best approach to obtaining both refractivity and aerosol extinction is the development of data assimilation systems which combine sensed data and data derived from high-resolution meteorological mesoscale models.

## ACKNOWLEDGEMENTS

This work was supported by the Office of Naval Research.

## REFERENCES

Anderson, K.D., Inference of refractivity profiles by satellite-to-ground RF measurements, Radio Science, Vol. 17, No. 3, pp. 653-663, 1982

Anderson, K.D., Radar detection of low-altitude targets in a maritime environment, NCCOSC RDTE DIV (NRaD) TR 1630, Vol. 1 and 2, 1993

Bissonette, L.R., and D.L. Hutt, Remote sensing of the aerosol scattering coefficient with a multi-field-of-view lidar, AGARD CP-453, pp.39.1-3913, 1989

Blood, D.W, S. McKinley, C.R. Philbrick, R. Paulus, and L.T. Rogers, Lidar measured refractive effects in a coastal environment, Proc. IGARSS '94, Vol 1, pp. 394-398, 1994

Burk, S.D., W.T. Thompson, J. Cook, and G.G. Love, Mesoscale modeling of refractive conditions during the VOCAR experiment, Proc. IGARSS '94, Vol 1, pp. 402-404, 1994

Collis, R.T.H., and P.B. Russell, Lidar measurement of particles and gases by elastic backscattering and differential absorption, Chapter 4 in *Laser Monitoring of the Atmosphere,* (E.D. Hinkley, ed.), Springer, 1976

Cook, J., A "Virtual Sensor" for evaporation ducts - The impact of data uncertainties, AGARD CP-502, pp. 9.1-9.10, 1992

Cooney, J.A., Remote measurements of atmospheric water vapor profiles using the Raman component of laser backscatter, J. Appl. Meteor., 9, pp. 182-184, 1970

Cooney, J.A., K. Petri, and A. Salik, Acquisition of atmospheric water vapor profiles by a solar blind Raman lidar, in *Atmospheric Water Vapor,* (Deepak, Wilkerson, Ruhnke, ed.), Academic Press, New York, pp. 419-431, 1980

Cowell, R.C., and A.W. Friend, Tropospheric radio wave reflections, Science, Vol. 86, pp. 473-474, 1937

de Leeuw, G., Size distributions of giant aerosol particles close above the sea level, J. Aerosol. Sci, Vol. 17, No. 3, pp, 293-296, 1986a

de Leeuw, G., Vertical profiles of giant particles close above the sea surface, Tellus, 38 B, pp. 51-61, 1986b

Dockery, G.D., and G.C. Konstanzer, Recent advances in prediction of tropospheric propagation using the parabolic equation, Johns Hopkins APL Tech. Dig., Vol. 8., No. 4, pp. 404-412, 1987

Durkee, P.A., D.R. Jensen, E.E. Hindman, and T.H. Vonder Haar, The relationship between marine aerosol particles and satellite-detected radiance, J. Geoph. Res., Vol 91, No. D3, pp. 4063-4072, 1986

Eaton, F.D., S.A. McLaughlin, and J.R. Hines, A new FM-CW radar for studying planetary boundary layer morphology, accepted for Radio Science, 1994

Gathman, S.G., A preliminary description of NOVAM, the Navy Oceanic Vertical Aerosol Model, NRL Rep. No. 9200, 1989

Gathman, S.G., and K.L. Davidson, The Navy oceanic vertical aerosol model, NCCOSC RDTE DIV, TR 1634, 1993

Gossard, E.E., and N. Sengupta, Measuring gradients of meteorological properties in elevated layers with a surface-based Doppler radar, Radio Science, Vol. 23, No. 4, pp. 625-639, 1988

Gossard, E.E., Relationship of height gradients of passive atmospheric properties to their variances: applications to the ground-based sensing of profiles, NOAA TR ERL 448-WPL 64, 1992

Griggs, M., Satellite measurements of tropospheric aerosols, Adv. Space Res., Vol. 2, No. 5, pp. 109-118, 1983

Helvey, R.A., Radiosonde errors and spurious surface-based ducts, Proc. IEE, Vol. 130, Part F, No. 7, pp. 643-648, 1983

Helvey, R. and J. Rosenthal, Guidance for an expert system approach to elevated duct assessment over the northeastern Pacific Ocean, Proc. IGARSS '94, Vol 1, pp. 405-409, 1994

Hitney, H.V., J.H. Richter, R.A. Pappert, K.D. Anderson, and G.B. Baumgartner, Tropospheric radio

propagation assessment, Proc. IEEE, Vol. 73, No. 2, pp. 265-283, 1985

Hitney, H.V., Remote sensing of refractivity structure by direct radio measurements at UHF, AGARD CP-502, pp. 1.1-1.5, 1992

Hooper, W.P., and H. Gerber, Down looking lidar inversion constrained by ocean reflection and forward scatter of laser light, Appl. Opt., 21, 689, 1986

Hooper, W.P., and H. Gerber, Monte Carlo simulations of laser-generated sea surface aureole, Appl. Opt., 27, 5111, 1988

Hughes, H.G., and M.R. Paulson, Double-ended lidar technique for aerosol studies, Appl. Opt., 27, 2273, 1988

Hughes, H.G., and B.L. Thompson, Estimates of optical pulse broadening in maritime stratus clouds, Optical Eng., Vol. 23, No. 1, pp. 38-42, 1984

Hughes, H.G., M.R. Paulson, and J.H. Richter, Radio refractivity profiles deduced from aerosol lidar measurements, AGARD CP-502, pp. 6.1-6.6, 1992

Janssen, M.A., *Atmospheric Remote Sensing by Microwave Radiometry*, Wiley, New York, 1993

Jensen, D.R., R. Jeck, G. Trusty, and G. Schacher, Intercomparison of Particle Measuring Systems, Inc.'s particle-size spectrometers, Optical Eng., Vol. 22, No. 6, pp. 746-752, 1983

Jeske, H., State and limits of prediction methods of radar wave propagation conditions over the sea, in *Modern Topics in Microwave Propagation and Air-Sea Interaction,* D. Reidel, Boston, 1973

Ko, H.W., J.W. Sari, and J.P. Skura, Anomalous microwave propagation through atmospheric ducts, Johns Hopkins APL Tech. Dig., 4, pp. 12-26, 1983

Measures, R.M., Analytical use of lasers in remote sensing, Chapter 6 in *Analytical Laser Spectroscopy,* (N. Ometto, ed.), John Wiley and Sons, 1979

Melfi, S.H., J.D. Lawrence, and M.P. McCormick, Observations of Raman scattering by water vapor in the atmosphere, Appl. Phys. Lett., 15, pp.295-297, 1969

Melfi, S.H., Remote measurements of the atmosphere using Raman scattering, Appl. Optics, 11, pp.1605-1610, 1972

Noonkester, V.R., D.R. Jensen, and J.H. Richter, Simultaneous FM-CW radar and lidar observations, Prepr. 15th Radar Meteorology Conf., pp.335-340, 1972

Noonkester, V.R., Profiles of optical extinction coefficients calculated from droplet spectra observed in marine stratus cloud layers, J. Atm. Sci., Vol. 42, No. 11, pp.1161-1171, 1985

Noonkester, V.R., and J.H. Richter, FM-CW radar sensing of the lower troposphere, Radio Science, Vol. 15, No. 2, pp. 337-353, 1980

Olson, J., Shipboard measurements of air-sea temperature in the evaporation duct, Naval Ocean Systems Center, TR 1313, Dec. 1989

Paulus, R.A., VOCAR: An experiment in variability of coastal atmospheric refractivity, Proc. IGARSS '94, Vol.1, pp.386-388, 1994

Philbrick, C.R., Lidar measurements of water vapor concentration in the troposphere, Proc. IGARSS '94, Vol. 4, pp. 2043-2045, 1994

Petri, K., A. Salik, and J. Cooney, Variable-wavelength solar-blind Raman lidar for remote measurement of atmospheric water-vapor concentration and temperature, Appl. Optics, Vol. 21, No. 7, pp. 1212-1218, 1982

Renaut, D., and R. Capitini, Boundary layer water vapor probing with a solar-blind Raman lidar: validations, meteorological observations and prospects, J. Atmos. and Oceanic Technology, 5, pp. 585-601, 1988

Richter, J.H., High resolution tropospheric radar sounding, Radio Science, Vol 4, No. 12, pp. 1261-1268, 1969

Richter, J.H., and H.G. Hughes, Marine atmospheric effects on electro-optical systems performance, Opt. Eng., Vol 30, No. 11, pp. 1804-1820, 1991

Rogers, L.T., Statistical assessment of the variability of atmospheric propagation effects in the southern California coastal area, Proc. IGARSS '94, pp. 389-393, 1994a

Rogers, L.T., Effects of spatial and temporal variability of atmospheric refractivity on the accuracy of propagation assessments, AGARD CP 567, pp. 31.1-31.7, 1994b

Rosenthal, J., and R. Helvey, Refractive assessments from satellite observations, AGARD CP-502, pp.8.1-8.9, 1992

Rowland, J.R., and S.M. Babin, Fine-scale measurements of microwave refractivity profiles with helicopter and low-cost rocket probes, Johns Hopkins APL Technical Digest, Vol 8, No. 4, pp. 413-417, 1987

Rugg, S.A., An investigation of the ground-based high-resolution interferometer sounder (GB-HIS) in a coastal marine environment, Thesis, Naval Postgraduate School, Monterey, 1992

Schotland, R.M., Some observations of the vertical profile water vapor by means of a laser optical radar, *Proc. Fourth Sym. on Remote Sensing of the Propagation Environment,* U. of Michigan, Ann Arbor, 1966

Thompson, W.T., S.D. Burk, J. Cook, and G.G. Love, Variations in coastal atmospheric refractivity induced by mesoscale processes, Proc. IGARSS '94, Vol 1., pp. 410-412, 1994

Ulaby, F.T., R.K. Moore, and A.K. Fung, *Microwave Remote Sensing,* Volume I: Microwave Remote Sensing Fundamentals and Radiometry, Addison-Wesley, Reading, 1981

Ulaby, F.T., R.K. Moore, and A.K. Fung, *Microwave Remote Sensing,* Volume III: From Theory to Applications, Artech House, Norwood, 1986

Wash, C.H., and K.L. Davidson, Remote measurements and coastal atmospheric refraction, Proc. IGARSS '94, Vol. 1, pp.397-401, 1994

Westwater, E.R and M.T. Decker, Application of statistical inversion to ground-based microwave remote sounding, in *Inversion Methods in Atmospheric Remote Sounding* (A. Deepak, ed.), Academic Press, New York, pp. 395-428, 1977

## DISCUSSION

**C. R. PHILBRICK** (Comment)
The $N_2$ Raman technique does give us now the opportunity to obtain the true extinction. The double-ended backscatter lidar experiment of your group provides a beautiful example of a way to use the backscatter signal to obtain true extinction. The missing information on forward scatter comes from the second backscatter profile. In the case of $N_2$ Raman, the forward scatter information comes from the relative decrease in the molecular scatter of the succeeding volume element. The $N_2$ Raman Technique is presently limited to a relative narrow range of optical density however and it cannot provide information in strong cloud layers.

**U. LAMMERS**
In order to predict tropospheric radio wave propagation accurately, the spatial and temporal distribution of meteorological parameters has to be known quite accurately. Has there been progress made recently, both in the accuracy and affordability of measuring these meteorological parameters directly?

**AUTHOR'S REPLY**
I discussed in my talk status and promise of various sensing techniques. Improving the accuracy of direct sensing techniques will not result in improved radio propagation predictions for the reasons given in the paper.

# Tropospheric Refractivity Profiles Inferred From Low Elevation Angle Measurements of Global Positioning System (GPS) Signals

**Kenneth D. Anderson**
Ocean and Atmospheric Sciences Division
NCCOSC RDTE DIV 543
53170 WOODWARD ROAD
SAN DIEGO CA 92152-7385
USA

## SUMMARY

Propagation assessment tools, such as the Engineer's Refractive Effects Prediction System, provide a near real-time capability to evaluate the performance of radar and communication systems and include tactical decision aids that can be used to mitigate or exploit atmospheric effects on propagation. However, a crucial factor for these analytical tools is a thorough knowledge of the spatial distribution of refractivity. Quantifying the refractivity structure is a difficult problem especially in the littoral zone where the sharp contrast between land and sea strongly contributes to both spatial and temporal variability.

A technique to remotely sense the vertical refractivity profile of the lower atmosphere is examined. This technique infers the refractive structure from ground-based measurements of GPS satellite signals as the satellite rises or sets on the horizon. There are obvious advantages to this concept. Results from a series of satellite-to-ground signal measurements are presented and compared to "ground truth" measurements made using radiosondes and an instrumented aircraft.

## 1. INTRODUCTION

Modern naval microwave communication and sensor system performance can be greatly affected by the spatial distribution of the refractive index in the lower atmosphere. A famous example of refractive effects on signal propagation is the WW II sighting of the Arabian coast with a 200 MHz radar from India 1700 miles away [*Freehafer*, 1951]. Although a strong refractive gradient can confine an electromagnetic wave within a vertically thin layer such that over-the-horizon fields may be many tens of decibels higher than expected, conditions have been observed where radars could not detect a surface target that was optically visible [*Freehafer, op. cit.*].

In recent years, considerable effort has been put forth to create computer-based systems to assess refractive effects on signal propagation in the lower atmosphere [*Hitney and Richter*, 1976]. These assessment tools provide a near-real-time capability to evaluate the performance of radar and communication systems and include tactical decision aids for mitigation or exploitation of atmospheric propagation effects. However, a crucial factor for these analysis tools is a thorough knowledge of the spatial distribution of refractivity.

Conventional direct atmospheric sensing by radiosondes or airborne microwave refractometers is inconvenient and expensive. In addition, these sensors measure the refractivity in a limited volume of space. A radiosonde rising through the atmosphere measures refractivity along the line of its ascent. Although typical correlation scales for refractivity are tens of km in the horizontal, tens of m in the vertical, and hours in time, typical propagation problem scales are tens to hundreds of km in the horizontal, one to ten km in the vertical, and hours in time. Generally, without additional radiosonde or refractometer measurements, horizontal homogeneity in the refractive structure is a necessary assumption.

A technique to infer the vertical refractive profile of the lower atmosphere from ground-based measurements of GPS satellite signals as the satellite rises or sets on the horizon has obvious advantages. First, the inferred profiles will be representative of the integrated refractive effects along the range-height path instead of a single time and space line representation of refractivity. Second, with the completion of the GPS constellation, there are a number of times per day (84 at most) when a GPS satellite will rise or set on the horizon. A receiver located near the equator will see rise and set locations nearly uniformly distributed in azimuth. As the receiver latitude approaches either pole, there will be fewer and fewer rise and set locations in the direction of the pole. A third advantage to this concept is the leveraging of a multi-billion dollar system that is fully functional. The satellites are in place, the signal structure is well known, the hardware is mature, and the receivers are commercially available. Lastly, the concept is one that can easily be automated. Ideally, a GPS receiver and a small computer are all that is needed for processing. A microcomputer has the computational horsepower to control the receiver, process the data, infer the profile, and even transfer the profile to propagation assessment computer systems.

*Paper presented at the Sensor and Propagation Panel Symposium on "Propagation Assessment in Coastal Environments" held in Bremerhaven, Germany 19-22 September 1994.*

This is a fresh look at the problem of inferring the refractive profile from monitoring satellite signals as described by *Anderson* [1982] and patented by *Hitney* [1978]. For example, the upper plot of figure 1 shows the modeled and observed interference pattern (Lloyd's Mirror effect) where the abscissa is ground range to the satellite subpoint (in km) and the ordinate is propagation loss. The observed data (dotted line) are from a set of measurements made on 28 July 1978 at the Naval Command, Control and Ocean Surveillance Center, RDT&E Division (NRaD) using signals from the *Wideband* satellite (see *Anderson, op. cit.*). The transmission frequency was 1239 MHz and the satellite was in a nominal 1000 km polar orbit. The modeled interference pattern (solid line) is derived from the refractivity profile measured at the receiver site with a radiosonde and a unique propagation model [*Hitney*, 1993] that combines ray optic and parabolic equation

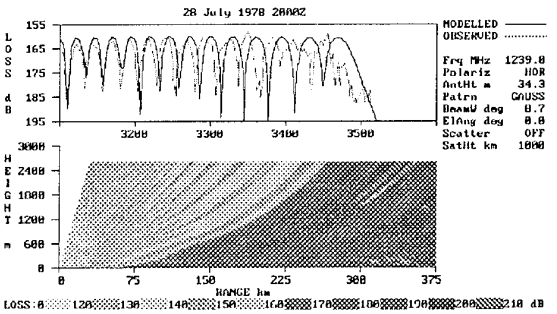


**Figure 1.** Measured and modeled data from the PRISM experiment.

methods to evaluate the wave equation for propagation on satellite-to-ground paths. At the closest subsatellite ranges (highest elevation angles), the predicted and observed interference pattern are in excellent agreement. At the farthest subsatellite ranges, the patterns are different, which likely indicates that the refractivity profile measured near the receiver is not representative of the conditions along the path.

The bottom plot on figure 1 is a range-height diagram of propagation loss for the same case. Small changes in the refractivity profile 70 to 80 km down range from the receiver could have a large effect on the stretching or contraction of the interference pattern at long subsatellite ranges. Unfortunately, the refractive conditions at these distances were not measured in 1978. However, the data displayed in figure 1 clearly shows that there are reasonable possibilities of estimating the effective refractive profile from RF measurements along a satellite-to-ground path.

The generally good agreement between measured and modeled data encouraged the development of an effort to infer the vertical refractivity profile from GPS signal measurements. In the following paragraphs, the selection of a GPS receiver is examined, the propagation model is reviewed, and comparisons of modeled to measured data are presented.

## 2. SELECTION OF A GPS RECEIVER

In 1978, the measurement equipment needed to monitor and record the *Wideband* satellite signals occupied three racks. Today, high performance, multi-channel, GPS receivers are smaller than a brief case and are readily available. However, one problem in selecting a GPS receiver is that the manufacturers specifications are almost exclusively related to geodetic capabilities where the satellites are generally well above the horizon. Detection and tracking of GPS signals when the satellite is near the horizon is one of the most stressful cases for the receiver; it is crucial to the success of inferring the refractivity.

A market survey of equipment manufacturers was conducted in early summer of 1993. From this survey, three manufacturers responded with equipment that could be usable. The manufacturers and equipment are listed in table 1. Allen Osborne Associates, Inc. (AOA) and Trimble Navigation Ltd. graciously loaned their equipment free of charge for testing at NRaD. Ashtech, Inc. agreed to rent their equipment for a nominal fee. All three companies provided excellent technical support during the tests.

| Company | Equipment |
|---|---|
| Allen Osborne Associates | Turbo Rogue |
| Ashtech | MD XII C |
| Trimble Navigation | 4000 SSE |

**Table 1.** GPS receivers examined.

Figure 2 is a typical display of the signal-to-noise (SNR) ratio for the C/A, P1, and P2 code loops extracted from the AOA receiver as a satellite was rising above the horizon. The abscissa is the geometric elevation angle between the satellite and the receiver, which was located at an orthometric height of 42 meters. C/A and P1 code are transmitted on the same frequency, L1, at 1575.42 MHz. P2 code is transmitted on a lower frequency, L2, at 1227.60 MHz.

The interference pattern is readily observable for elevation angles greater than about one degree. At lower angles, only portions of the pattern are observed. This is expected as the digital lock loop breaks lock when no signal is present (in a null) and, after some period of time, the loop reacquires the signal after the signal has exceeded a SNR threshold enabling the loop to lock. For a rising satellite, the "half pattern" is toward higher elevation angles. For setting satellites, the half pattern is toward lower elevation angles.

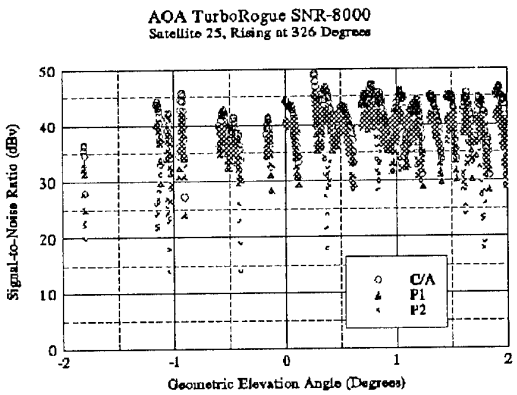


**Figure 2.** AOA Turbo Rogue receiver measurements made on 10 August 1993 at NRaD.

Measurements using the Trimble 4000 SSE are typified by the data displayed in Figure 3. The raw SNR data from this unit are expressed in counts and are plotted as decibels relative to one count for comparison with the AOA receiver data. On L1, the Trimble unit first acquires the C/A code then switches to track the P1 code. Compared to the AOA SNR plot, the sparse data from the Trimble unit indicate that extraction of the interference pattern is much more difficult. In addition, the P2 data are not nearly as complete compared to AOA P2 data.

The Ashtech MD XII receiver monitors only P code; C/A code processing is not available. Figure 4 shows a typical set of data from the Ashtech unit for a rising satellite. Like the Trimble unit, the MD XII raw SNR for the P code loops are expressed in counts. However, unlike the Trimble unit, the dynamic range of the P2 count is small, ranging between 0 and 10 in integer steps. It is unlikely that any information on the P2 loop could be used to construct an interference pattern. While the P1 loop data indicates the interference pattern at least as well as the Trimble unit, the Ashtech MD XII does not seem to be able to acquire the signal much before the time when the satellite is at zero degrees. This "fault" appears to be associated with the firmware control of the receiver (that is, it suspected that the firmware doesn't begin to look for the satellite until the satellite is close to or exceeding zero degrees elevation). *Rocken and Meertens* [1992] also indicate that the Ashtech receiver does not lock and track at very low elevation angles.

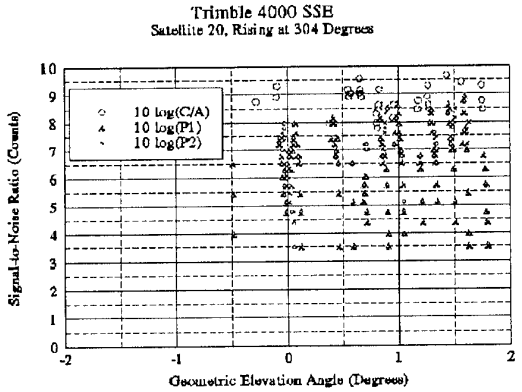


**Figure 3.** Trimble receiver measurements made on 22 August 1993 at NRaD.

Although not ideal as a GPS receiver for this effort (see *Anderson*, 1994), the Turbo Rouge receiver is considered the "best" receiver of the three high performance, geodetic quality receivers that were tested. A precise positioning service (PPS) receiver was ordered from AOA for delivery to NRaD by the end of April 1994. However, AOA has only been able to ship a standard positioning service (SPS) receiver; approval for AOA to deliver a PPS receiver is pending with the GPS Joint Program Office (JPO), which is the controlling agency for GPS.

Before examining results obtained with the SPS receiver, the next section will review the propagation modeling.

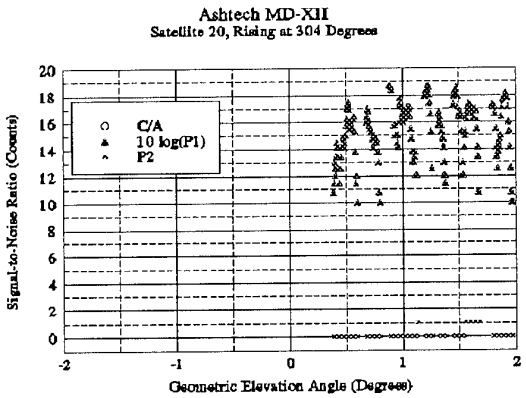


**Figure 4.** Ashtech receiver measurements made on 25 August 1993 at NRaD.

## 3. PROPAGATION MODELING

Modifications that extend the Radio Physical Optics (RPO) propagation model [*Hitney*, 1992] to handle ground-to-satellite paths are described in an earlier AGARD paper [*Hitney*, 1993]. A split-step parabolic equation (PE) model is used for low elevation angles and low terminal heights. An extended-optics method is used to trace a family of rays originating at the top of the PE region at elevation angles determined by ray-optics methods. The propagation factor $F$ (the ratio of the field strength to the free-space field strength) is computed by the PE model at the top of the PE region and is kept constant along each ray.

To trace a ray from the top of the PE region to the satellite, the refractivity at all altitudes must be known. The refractivity model consists of four regions: A linear region that extends from the surface to a altitude of 4.85 km; an exponential region that extends from 4.85 km to 50 km where the relationship between altitude and refractivity follows a model proposed by *Bean and Dutton* [1968] (this model, at 4.85 km, has a refractive gradient equal to the gradient expected in an adiabatic atmosphere, which is typical of over-ocean conditions); an ionospheric region that extends from 50 to 1000 km where refractivity is described by *Flattery and Ramsay* [1975]; and, finally, a constant region that extends from 1000 km to the satellite altitude (approximately 20,200 km) where the refractivity is assumed to be zero.

The change in ground range (from the receiver, along the surface of the earth, to the nadir point of the satellite) is related to the change in satellite altitude by

$$\Delta r \approx \frac{a^2 c_a}{\rho_a^2 \sqrt{1 - \frac{a^2 c_a^2}{\rho_a^2}}} \Delta\rho \qquad (1)$$

where $a$ is the earth's radius (6378.135 km), $c_a$ is the average value of the ray characteristic that is expected in all refractive conditions ($c_a = 0.99775$), $\rho_a$ is the average of the distance from the earth's center (EC) to the satellite, $\rho_s$, and the EC distance to a normalized altitude of 20183.103 km, $\rho_n$, and $\Delta\rho = \rho_n - \rho_s$. Equation 1 is the ground range adjustment needed to simulate moving the satellite from its actual altitude to a normalized altitude (GPS satellite altitudes vary ±400 km from $\rho_n$). This adjustment allows RPO calculations to be done at only one altitude, saving considerable complexity. The approximation differs from exact by at most ±80 meters, which is considered negligible in this analysis.

The following section examines some of the results that have been obtained and compares them to modeled results.

## 3. MEASUREMENTS AND COMPARISONS

GPS satellite signal measurements were made on 6 and 8 June 1994, 20 and 21 July 1994, and on 27 and 28 July 1994. Surface and upper-air meteorological measurements were made near the receiver site, which was approximately 32 meters above the ocean with a clear view of the horizon from due south, through west, to nearly due north. In addition to the meteorological measurements at the receiver site, an instrumented aircraft was flown at a constant altitude (about 30 meters above the ocean surface) to measure air temperature, dew point temperature, sea surface temperature, atmospheric pressure, and altitude. At designated points along a radial to or from the receiver site, the aircraft ascended to an altitude of about 500 meters in a spiral motion and then descended in the same motion to its original altitude. Vertical profiles of refractivity were measured at about 7 km due west of the receiver site, at about 50 km due south or west from the receiver, and at about 100 km due south or west of the receiver.

As of January 1994, nearly all of the GPS satellites have encryption of their signals enabled. An SPS receiver cannot determine the SNR of the P code loop when P code is encrypted. During the first five measurement periods, only one GPS satellite was not encrypted. On 28 July 1994, GPS JPO disabled encryption on all 24 satellites for some special testing and multiple satellites were available to assess the accuracy of the propagation models. Although only data from 28 July will be examined, results are comparable to results obtained on the earlier days.

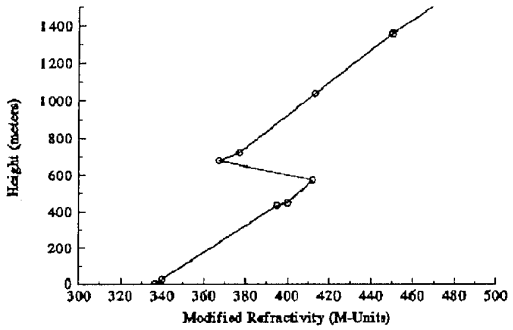


**Figure 5.** The refractive profile measured near the receiver on 28 July 1994 at 1933Z.

Figure 5 shows the modified refractivity profile that was measured on 28 July 1994 at 1933Z. This profile was measured by a balloon-launched radiosonde package that was launched from a position near the receiver site. The data from the radiosonde were recorded and processed by a Vaisala Mini Rawin System (MRS).

Figure 6 shows the modified refractivity profiles that were measured by the aircraft as it was traveling on a east-west radial from the receiver site. Compared to the profile in Figure 5, these profiles are similar in that they all show a moderate elevated duct.

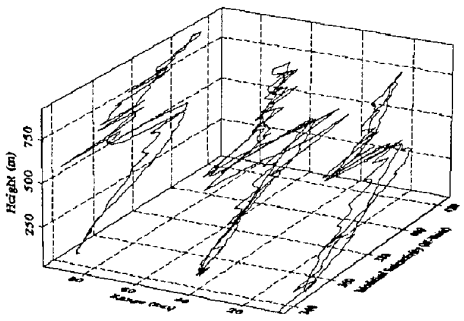


**Figure 6.** Modified refractivity profiles measured by the aircraft on 28 July 1994. Radial is due west from the receiver.

Table 2 lists the estimated range dependent height and modified refractivity pairs (in a form that is suitable for input to RPO). At range 0, there is an elevated trapping layer extending from 572 to 678 meters that forms an elevated duct whose base is located at 225 meters. As range increases, the base of the trapping layer, the thickness of the layer, and the intensity (M-unit difference between the top and bottom of the layer) all decrease. However, there is a reasonable indication of horizontal and temporal homogeneity.

| Range | 0 km | Range | 45 km | Range | 90 km |
|---|---|---|---|---|---|
| Height | M-Units | Height | M-Units | Height | M-Units |
| 0 | 336.7 | 0 | 336.7 | 0 | 336.7 |
| 572 | 412.0 | 420 | 391.1 | 420 | 391.1 |
| 678 | 367.0 | 526 | 346.9 | 470 | 370.7 |
| 772 | 393.0 | 620 | 372.9 | 620 | 390.2 |
| 2772 | 653.0 | 2620 | 632.9 | 2620 | 650.2 |

**Table 2.** Estimated refractivity profiles for 28 July 1994.

Figure 7 compares the measured propagation loss (crosses) to the computed propagation loss (solid line) for the L2 frequency of satellite 25 as it was rising at the horizon. The computed propagation loss uses the range 0 (range independent) profile from Table 2. For the higher elevation angles where the subsatellite range is less than about 8400 km, there is excellent agreement between the measured and calculated loss. However, at the lower elevation angles (greater subsatellite range), where shape of the refractivity profile will have the greatest influence, there is substantial difference. The presence of measured data at about 8650 km indicates that there may have been a surface-based duct at the time when the satellite was rising. One concern is the "missing" data between about 8550 and 8650 km. Is this data missing because the signal was too weak to receive or is the data missing because the receiver's firmware was not actively searching for the signal? It is suspected that the data gap was caused by the firmware.

Figure 8 compares the measured propagation loss to the computed propagation loss for the L2 frequency of satellite 22 as it was rising. At the higher elevation angles, there is excellent agreement between the measured and calculated results, which is similar to the results shown in Figure 7. Again, as in Figure 7, the signal appears before it is expected indicating the presence of a surface-based duct. Between 8420 and 8490 km, there is a gap in the data; it is suspected that the gap is caused by the P2 loop becoming unlocked, the receiver losing the signal, and the firmware not actively searching for the signal until sometime later. The explanation for the 10 to 15 dB decrease in SNR between 8400 and 8420 km is not known at this time.

## 4. CONCLUSIONS

Techniques to infer the vertical refractivity profile from measurements of GPS signals as the satellite rises or sets on the ocean horizon are being examined. Results of comparing modeled to measured propagation loss where the modeled data is calculated from knowledge (or estimates) of the refractive conditions are very encouraging.

## ACKNOWLEDGMENT

This work is sponsored by the Office of Naval Research.

## REFERENCES

Anderson, K.D., Inference of refractivity profiles by satellite-to-ground RF measurements, *Radio Sci.*, 17, pp. 653-663, May 1982.

Anderson, K.D. An evaluation of three GPS receivers for use in the GPS sounder, NCCOSC RDTE DIV Tech. Rept. 1637, April 1994.

Bean, B.R., and E.J. Dutton, *Radio Meteorology*, Dover Publications, Inc. 1968.

Flattery, T.W., and A.C. Ramsay, Derivation of total electron content for real time global applications, in *Effect of the Ionosphere on Space Systems and Communications*, J.M. Goodman, Ed., Naval Research Lab., 1975.

Freehafer, J.E., Tropospheric refraction, in *Propagation of Short Radio Waves*, D.E. Kerr, Ed., New York, McGraw-Hill, pp. 9-22, 1951.

Hitney, H.V., and J.H. Richter, Integrated refractive effects prediction system (IREPS), *Nav. Eng. J.*, 88, pp. 257-262, April 1976.

Hitney, H.V., Means for determining the refractive index profile of the atmosphere, U.S. Patent 4,093,918 of 6 June 1978.

Hitney, H.V., Hybrid ray optics and parabolic equation methods for radar propagation modeling, IEE Conf. Pub. 365, *Radar 92*, pp. 58-61, 12-13 October 1992.

Hitney, H.V., Modeling tropospheric ducting effects on satellite-to-ground paths, AGARD CP-543, pp. 16-1 to 16-5, October 1993.

Rocken, C. and C. Meertens, UNAVCO receiver tests, UNAVCO Memo, 8 November 1992.

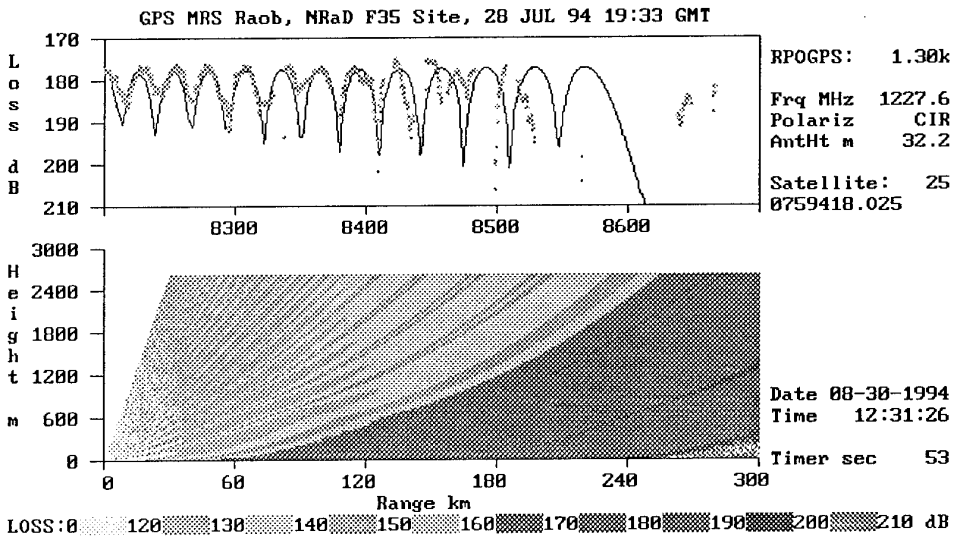


**Figure 7.** Measured and calculated propagation loss for satellite 25 rising at 1845Z.

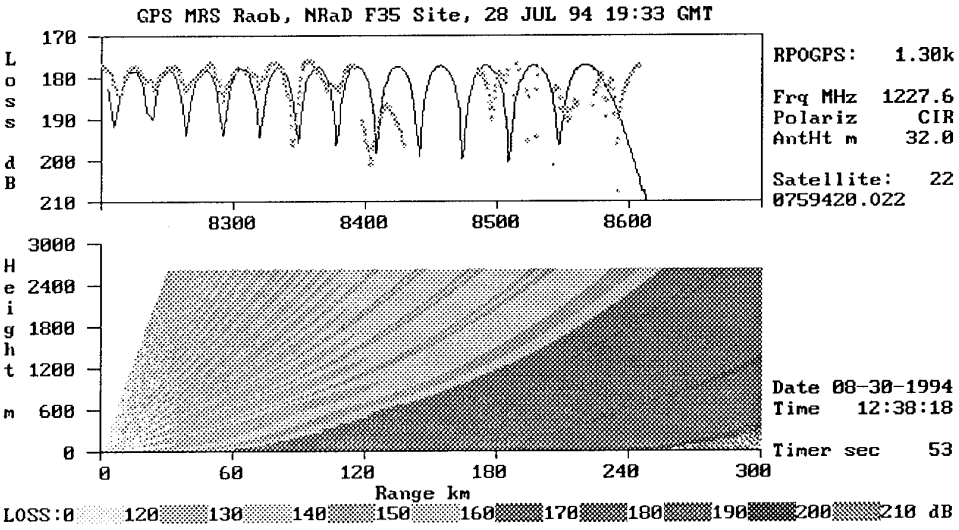


**Figure 8.** Measured and calculated propagation loss for satellite 22 rising at 2052Z.

## DISCUSSION

**N. DOUCHIN**

1. As you certainly know, we did a similar work as yours some years ago, but with the intention of characterizing the evaporation duct. What is your opinion about the possibility to characterize the evaporation duct using satellites?

2. What is your strategy for the determination of the receiving antenna height in case of a very rough sea surface?

**AUTHOR'S REPLY**

1. Evaporation duct effects on GPS signal propagation are relatively small and may be difficult to extract from measurements. I don't think that GPS is a good system to infer evaporation duct height or profiles.

2. In a rough sea, I think that one can adjust the height of the receiver antenna such that the modeled interference pattern matches the measured pattern at high ($>$ 2 degrees) elevation angles. This should give the effective height.

# LIDAR MEASUREMENTS OF REFRACTIVE PROPAGATION EFFECTS

**C. R. Philbrick and D. W. Blood**
Applied Research Laboratory/Penn State University
P.O. Box 30, State College, PA 16804 USA
(814) 863-7682 - FAX (814) 863-8783

## 1. SUMMARY

A multi-wavelength Raman lidar has been developed and used to measure the profiles of atmospheric properties in the troposphere under a wide range of geophysical conditions. The instrument measures the two physical properties which contribute to the refractive index at radio frequencies, water vapor concentration profiles from vibrational Raman measurements and neutral density determined from rotational Raman temperature profiles and surface pressure. The LAMP lidar instrument is transportable and has been used to make measurements at several locations in addition to our local Penn State University site, including shipboard measurements between Arctic and Antarctic and in the coastal environment at Point Mugu, CA. Lidar measurements of the atmospheric refractive environment, which are of particular interest, were made during 1993 at Point Mugu, CA, including the period of Project VOCAR (Variability of Coastal Atmospheric Refractivity). Both the lidar and balloon tropospheric measurements have been used for analyses of the propagation conditions by employing the Navy's RPO, IREPS and EREPS PC programs and comparisons have been made with the measured propagation conditions. On the short term (hour-to-hour throughout a day), the lidar derived profiles permit the examination of refractive layer stratification for guided-wave mode propagation.

## 2. INTRODUCTION

During the VOCAR program of 1993, lidar measurements of the coastal atmospheric profiles of water vapor and temperature were made at Point Mugu, CA (see description of the VOCAR program, Ref 1). One of the primary purposes was to produce refractivity profiles of the lower troposphere during variable coastal atmospheric conditions to verify that lidar measurements, as well as balloon/radiosonde measurements of the atmospheric refractivity could be used as input to propagation models for evaluation of the propagation effects which are known to range from normal atmospheric propagation to highly ducted radiowave propagation in this ocean and coastal region. A useful overview of the RF propagation characteristics and models for the lower atmosphere is available (Ref 2) and the particular propagation characteristics of the coastal environment have been discussed in this volume (Ref 3).

Penn State University/Applied Research Laboratory was invited to participate in the VOCAR program, which involved a wide variety of meteorological sensors coordinated for the purpose of characterizing the spatial and temporal variability of the refractive environment at sea, and along the California coastline. The portable research instrument, referred to as the PSU/LAMP lidar (Ref 4), was placed strategically at the Point Mugu NAWC during the 1993 program, near the Geophysics Division, where the weather station is located and where frequent balloon launchings of radiosondes were carried out during the intensive data collection periods.

The LAMP lidar transmitter uses a Nd:YAG laser which has an output of 1.5 j at 20 Hz at the 1064 nm fundamental output. The beam is passed through a doubling crystal and a mixing crystal to produce the 532 and 355 nm, or 266 nm, beams which are used for the lidar measurements. The primary receiver is a 42 cm diameter Cassegrain telescope. The low altitude backscatter signals of the visible and ultraviolet beams can be detected as analog signals and digitized at 10 MSps to provide 15 meter resolution from the surface to 25 km, or detected as photon count signals with 75 m altitude resolution. The high altitude signals, obtained by photon counting techniques, are accumulated into 500 nanosecond range bins to provide 75 meter resolution, from 20 to 80 km. The high altitude detector also contains low altitude photon counting channels which measure the first Stokes vibrational Raman signals of the $N_2$ and the $H_2O$ Raman scatter. The low altitude detector has eight channels to measure the backscatter signal at two laser fundamental lines, two $N_2$ Raman lines, two $H_2O$ water vapor lines and two segments of the rotational Raman envelope. The transmitter, receiver, detector, and data system combination have been integrated into a standard shipping container, which serves as a field laboratory.

A recent review (Ref 5) of the vibrational and rotational Raman scattering techniques has clearly shown that these approaches have the capability of measuring the minor species and structure properties, as well as the optical properties, of the lower atmosphere, even in the presence of a small amount of interference from the background aerosol environment. The Raman technique measures the profiles of water vapor from the ratio of Raman vibrational backscatter signals of water vapor to those of nitrogen. The lidar has been used to obtain water vapor profiles from molecular Raman vibrational scattering at several wavelengths and temperature profiles from Raman rotational scattering at 528 and 530 nm. The water vapor measurements have been made using the vibrational Raman backscatter intensity from the 660/607 ratio from the 532 nm, 407/387 ratio from 355 nm, or the 294/283 ratio from 266 nm laser radiation. Having two sets of measurements allows additional examination of the small scale structure and the wavelength dependence of the correction for aerosol differential extinction. The quadruple (266 nm) Raman scatter signals have been examined and used for daytime measurements where the troposphere is shielded from wavelengths below 300 nm (solar blind region) by the stratospheric ozone absorption. These ultraviolet measurements are slightly complicated by the need to make corrections for the absorption of tropospheric ozone.

The profiles of water vapor and temperature, and ground based pressure data, were averaged and used to compute profiles of refractivity, N and modified refractivity, M, at 75 m resolution in the lower tropospheric region (0-5000 m). The lidar data is stored at one minute intervals and the temporal variation of refractive index is typically examined at intervals of 30 minutes. The profiles are analyzed for refractive layer structures which influence electromagnetic wave propagation over the ocean and near-coastal regions. Under summer atmospheric conditions, periods of persistent surface-based ducting (trapping layers) of horizontally propagating radio waves are frequently observed. The effects of ducts over the ocean path environments were sensed by measured signal levels on several ocean and coastal radio paths monitored by NCCOSC/NRaD at VHF and UHF bands during the measurement campaign (Ref 6).

## 3. PROPAGATION EFFECTS IN A COASTAL ENVIRONMENT

For the entire VOCAR period, NCCOSC/NRaD established and operated a radio path signal monitoring network of several VHF and UHF transmission source signals at both Point Mugu and San Diego, CA (Ref 6). The multiple source signals were sampled,

*Paper presented at the Sensor and Propagation Panel Symposium on "Propagation Assessment in Coastal Environments" held in Bremerhaven, Germany 19-22 September 1994.*

through the use of a programmable spectrum analyzer, and processed for a continuous synoptic monitoring of the received signal level every 15 minutes. Available ATIS (Automatic Terminal Information System) transmissions from both commercial and military airports were monitored and recorded. In addition, separate VHF and UHF continuous wave transmissions dedicated to the VOCAR program, were installed at San Clemente Island, and monitored at the two reception points on a routine basis. These two path lengths were nearly identical, however with different ocean path directions. The San Clemente Island-to-Point Mugu path distance is 132 km.

Figures 1 and 2 show a seven day segment of both the San Clemente Island (SCI) UHF (374.95 MHz), and VHF (143.09 MHz) received signal level histories at Point Mugu, CA, during the VOCAR intensive data collection period of August 1993. PSU Lidar operations were conducted on a daily basis during each night-to-daytime period of the VOCAR program. The five such operational periods (which will be discussed further) are highlighted in the figures. It is observed that the signal levels varied over a 40-50 dB range during the period from August 25 to September 1. The sequence of days analyzed illustrate the major changes in near-surface propagation and refractive effects that occurred during VOCAR. The five lidar operation day periods analyzed were in a period with major changes in the atmospheric conditions. These ranged from days with greatly enhanced propagation to days with standard propagation and losses beyond the horizon. During periods of surface refractive ducting (so-called anomalous) conditions the beyond-line-of-sight paths exhibited very strong signal levels reaching and exceeding that of free space propagation. Under standard refractive conditions, low signal strengths were received as would be predicted during non-ducting tropospheric conditions.

## 4. LIDAR MEASUREMENTS OF REFRACTIVITY

The primary measurements by lidar for this study consisted of water vapor and temperature profiles obtained by Raman (vibrational and rotational) line ratio spectral measurement techniques discussed. Examples of the lidar-measured parameters are shown in Figures 3 and 4 respectively, starting at 1013 UT on the 26th of August 1993. The photon counts were accumulated in 75 meter range/altitude bins and over one minute intervals. The profiles shown, however consist of 30 such interval accumulations combined, and therefore represent a 30 minute averaged period. The statistical error bars (+/- standard deviation) are shown on the solid lines for the lidar measurements. The near time balloon (radiosonde profile) measurements, expressed in the same units (g/kg) for water vapor and (degree K) for temperature, are shown as dashed lines in the figures for comparison with the lidar measurements. The balloon and lidar atmospheric measurements, although agreeing very well in general, often times show slight departures in measured profile details attributable to the different temporal and spatial sampling of the drifting balloon versus the perfectly vertical (single location) profile of the lidar. The measured temperature and water vapor, together with an atmospheric pressure value derived from an integration of the hydrostatic equation using the lidar measurements, constitute the inputs to the standard and accepted equation for refractivity. Although measured by lidar to above 5000 m altitudes, only the lower tropospheric region profile from the surface to 1500 m is presented in this analysis to describe the refractive conditions for near-surface propagation.

The computed refractivity (N) and modified refractivity (M) profiles, corresponding to the water vapor and temperature data of Figures 3 and 4, are shown in Figure 5. On 26 August 1993, the rapid decrease in water vapor combined with the temperature inversion (positive lapse rate) produced gradients in refractivity sufficient for the trapping of horizontally propagating electromagnetic waves. The strong ducting conditions start very near the surface and the duct height extends to nearly 600 m above the surface. Figure 5 at 1013 UT is just one of the entire sequence of 30 minute accumulated profiles taken throughout the lidar operation period on this date. The entire series of M-profiles on 26 August is portrayed in the Figure 6 three dimensional surface plot of modified refractivity versus altitude and time.

Similar conditions existed on 27 August, Figures 7 and 8, except that the surface based duct height is lower, extending only to 350 m instead of 600 m. Referring back to Figures 1 and 2, the enhanced received signal levels are comparable on the two days. On 28 August, the ducting condition tends to lift from the surface with a surface based elevated duct to heights of 425 m, as evident in Figures 9 and 10. The corresponding signal levels drop by at least 10 dB on this date. Surface-based ducting has ceased by August 29th , and the Figures 11 and 12 show only an elevated duct conditions remains in the altitude region of 350 to 500 m in the time period of 0800 UT. Once more, the signal levels as indicated in Figures 1 and 2 have dropped further by about 10 dB from the previous day.

Finally, by 31 August, evidence of even an elevated duct is gone, and the profile data of Figure 13 shows a lack of any elevated duct. The time history is shown in Figure 14 with a long sequence of stable refractive conditions and little variability. The signal levels have now reached the lowest levels of up to 40 dB below the strongly enhanced conditions of 26 August when ducting near the surface occurred.

## 5. RESULTS OF PROPAGATION MODELING USING LIDAR PROFILES

The propagation conditions may be analyzed in more detail by using the Navy's RF propagation modeling programs such as IREPS, EREPS and RPO (Refs 7, 8, and 9), which have been incorporated into PC applications. The lidar profiles have been prepared as input to these programs, originally designed for radiosonde input and for refractive effects assessment. The five days and two frequencies constitute a set of 10 measurement-days which have been analyzed to evaluate the qualitative aspects of the changing refractive effects and the propagation loss characteristics that would have been predicted, given the lidar profile data as an input.

Table 1 shows the predicted propagation loss as would have been obtained by IREPS, the first propagation analysis tool developed (Ref 7), and by the recent RPO (Radio Physical Optics) program provided by NCCOSC/NRaD (Ref 9). The 132 km San Clemente Island to Pt. Mugu over ocean path is analyzed for comparison by the two programs. The early IREPS software only crudely analyzes the propagation losses, and inadequately solves for the field for long beyond-the-horizon distances (loss relative to free space, 5th column of Table 1). The RPO program, however, provides a more precise measure of the propagation losses by computing the field strength at any range and elevation from a source transmission, given refractive profiles as input which are representative of the path conditions. Although RPO will accept a range-dependent set of refractivity profiles, the profiles from the Point Mugu lidar are input as a single profile representative of the path, although measured and obtained at the path endpoint only. Further, the lidar profiles shown in Figures 5, 7, 9, 11, and 13 have been piece-wise smoothed (linear) to simplify the data entry into RPO and IREPS. The latter is not a requirement for RPO, however. The RPO predicted losses relative to free space and the total path losses are given in the 6th and 7th columns respectively. Note that the total path losses from 8/26 to 8/31 span a 40 dB range of differences.

The coverage and loss plots of RPO are instructive in terms of understanding where physically the signals propagate and what waveguide modal effects contribute to a signal enhancement or to

an excessive loss over the propagation path. Figure 15 shows the propagation loss contour output of RPO for the UHF frequency (374.95 MHz) on 8/26. The contours are for 2.5 dB steps of increasing loss on a height versus range display. During surface-based ducting, the EM wave propagates within the duct to great ranges beyond the curvature of the earth. Figure 16 shows the loss versus height at the fixed range corresponding to the receiver distance from the source transmitter (132 km in this case). Notice that enhancements or deficits in signal can occur very rapidly with receiving antenna height change. The receiving antenna at Pt. Mugu in this case is at 30.5 m, very near the bottom portion of the curve. Figure 17 shows the loss as a function of range with a constant height antenna at 30.5 m, that used for VOCAR. Figures 18, 19 and 20 represent the same plots showing the VHF signal level (143.09 MHz) variations predicted for 8/26. Notice that at this frequency, the free space losses are not reached even though the ducted signals are enhanced above that for standard refractive profile environments.

Table 2 also shows the RPO computed losses but compares them with the observed losses at UHF and VHF (column 4) from Figures 1 and 2. The VOCAR signal path losses have been scaled from the signal level data of Figures 1 and 2 with approximate levels and extremes within +/- 3 hours of the specific lidar collection date interval using the available 15 minute sampled signal level data. The RPO predictions (using lidar data profiles as input) are shown in column 5 in dB relative to free space. The differences between the scaled observed signal and the predicted RPO level are shown in column 6. On individual dates and times the RPO prediction using a single profile and a relatively approximate scaling of data, the path losses can only be estimated to with about +/- 10 dB. Overall, however the average of the ten frequency measurement-day differences which were either too high or to low is less than one dB.

The lidar atmospheric sensor has proven to provide good temporal and vertical sampling of refractive variability. The path-integrated signal level variability, however, depends upon the horizontal homogeneity of the refractivity profile. The spatial homogeneity or variability of refractive index has been examined further during VOCAR by multiple sensors, aircraft flights, and other techniques (Ref 10). The widespread characterization of refractive ducting through changing weather fronts has been explored through the use of GOES satellite imagery (Ref 11).

One can conclude that on the whole, the propagation predictions based on a single lidar profile are useful to provide first order estimates of the losses that can occur on a propagation path. This has been applied to time periods when persistent refractive conditions have occurred, indicative of widespread stability. An arbitrary refractive profile is obtained to represent the prevailing conditions, and horizontal homogeneity is assumed over the path. Further analysis will be required to determine if improvement below +/-10 dB case-by-case level can be achieved with a more detailed time history of the lidar and signal level data sets. The general features of widely varying day-to-day signal levels are predicted in accordance with the observed signal levels with conditions ranging from strong surface-based ducting to the absence of ducting in the lower tropospheric refractive profile.

## 6. ACKNOWLEDGEMENTS

Special appreciation for the support and encouragement of this work goes to Dr. Juergen Richter, CDR. Dave Markham and CDR. Pete Ranelli. The opportunity to directly compare the lidar derived refractivity to the measurements of electromagnetic wave ducting was made possible by efforts of H. Hitney, R. Paulus and T. Rogers of NCCOSC NRaD. J. Rosenthal, J. Borgen and R. Helvey of the meteorological office of Geophysics Division, Safety Officer G. Wadley of the Naval Air Warfare Center at Point Mugu, CA, and W. Lee of SPAWAR contributed much to the success of the project. The efforts of D. B. Lysak, Jr., R. E. Erdley, T. J. Kane, J. Jenness, T. Petach, T. D. Stevens, P. A. T. Haris, Y.-C. Rau, S. Rajan, B. Mathason, M. O'Brien, S. C. McKinley, S. Maruvada, G. Evanisko, G. Pancoast, W. W. Moyer and E. Harpster have contributed much to the success of this project.

## 7. REFERENCES

1. Paulus, R.A., "An overview of an intensive observation period on Variability of Coastal Atmospheric Refractivity," NCCOSC RDTE DIV., US, AGARD CP 567, pp 30.1, 1994.

2. Radio Wave Propagation Modeling, Prediction and Assessment, AGARD-AG-326, Ed. by Juergen H. Richter, NOSC/OASD, US, NATO/AGARD Monograph No. 326, ISBN 92-835-0598-0, December 1990.

3. Richter, J.G., "Structure, variability and sensing of the coastal environment," NCCOSC RDTE DIV., US, AGARD CP 567, pp. 1.1, 1994.

4. Philbrick, C.R., D.B. Lysak, T.D. Stevens, P.A.T. Haris, and Y.-C. Rau, "Atmospheric measurements using the LAMP lidar during the LADIMAS campaign," 16th International Laser Radar Conference, NASA Publication 3158, 651-654, 1992.

5. Philbrick, C.R., "Raman lidar measurements of atmospheric properties," Proceeding of the SPIE Symposium on Atmospheric Propagation and Remote Sensing III, Vol 2222, 922-931, 1994.

6. Rogers, L.T., "Effects of spatial and temporal variability of atmospheric refractivity on the accuracy of propagation estimates," NCCOSC RDTE DIV., US, AGARD CP 567, pp. 31.1- 31.7, 1994.

7. Hitney, H.V., J.H. Richter, R A. Pappert, K.D. Anderson, and G.B. Baumgartner, Jr., "Tropospheric radio propagation assessment," Proc. IEEE, Vol. 73, No. 2, pp. 265-283, Feb. 1985.

8. Engineer's Refractive Effects Prediction System (EREPS), Tech. Doc. 2648, NCCOSC RDTE Div., US Navy/NRaD, San Diego, CA, US, May 1994.

9. Hitney, H.V., "Hybrid ray optics and parabolic equation methods for radar propagation modeling," in Radar 92, IEEE Conference Proceedings No. 365, pp. 58-61, 1992.

10. Helvey, R., and L.W. Eddington, "Refractive variability during VOCAR 23 Aug.- 03 Sep. 1993, NAWCWPNS, US, AGARD CP 567, pp. 32.1, 1994.

11. Rosenthal, J., R. Helvey, and P. Greiman, "Satellite inferences of elevated duct variability over the eastern pacific during VOCAR," NAWCWPNS, US, AGARD CP 567, pp. 33.1, 1994.

Table 1. Predicted propagation loss data using RPO and IREPS based on using lidar profiles of refractivity at Point Mugu for the San Clemente Island to Point Mugu path (132 km).

| Date (1993) | Time (UT) | Frequency (MHz) | Free Space Path Loss (dB) | IREPS** Loss (dB>f.s.) | RPO Loss (dB>f.s.) | RPO Total Path Loss (dB) |
|---|---|---|---|---|---|---|
| 8/26 | 1013 | (U) 374.9 | 126.3 | +3 | +2.5 | 123.8 |
| | | (V) 143.1 | 117.9 | -8 | -13.2 | 131.1 |
| 8/27 | 1025 | (U) " | 126.3 | +3 | +10.2 | 116.1 |
| | | (V) " | 117.9 | -6 | -7.8 | 125.7 |
| 8/28 | 0906 | (U) " | 126.3 | +3 | -19.1 | 145.4 |
| | | (V) " | 117.9 | -8 | -26.7 | 144.6 |
| 8/29 | 0800 | (U) " | 126.3 | -43* | -28.0 | 154.3 |
| | | (V) " | 117.9 | -41* | -33.2 | 151.1 |
| 8/31 | 0945 | (U) " | 126.3 | -46* | -43.2 | 169.5 |
| | | (V) " | 117.9 | -43* | -45.7 | 163.6 |

*Tropospheric-scatter-limited per IREPS program only
** very approximate losses from IREPS program

Table 2. Propagation loss data for San Clemente Island to Point Mugu, with measured and RPO predicted values based on atmospheric measurements of lidar profiles at Point Mugu.

| Date (1993)/ Time (UT) | VOCAR Frequency (MHz) | Free Space Path Loss (dB) | VOCAR Sig. Path Losses* (dB>f.s.) | RPO Loss (dB>f.s.) | dB Diff sig/ pred loss | RPO Total Path Loss (dB) | Obs. Total Path Loss (dB) |
|---|---|---|---|---|---|---|---|
| 8/26 /1013 | (U) 374.9 | 126.3 | -2 +/-10 dB | +2.5 | -5 | 123.8 | 128.3 +/-10 dB |
| | (V) 143.1 | 117.9 | -21 +/-9 | -13.2 | -8 | 131.1 | 138.9 +/-9 |
| 8/27 /1025 | (U) " | 126.3 | -.5 +/-9 | +10.2 | -11 | 116.1 | 126.8 +/-9 |
| | (V) " | 117.9 | -17.5 +/-4.5 | -7.8 | -10. | 125.7 | 135.4 +/-4.5 |
| 8/28 /0906 | (U) " | 126.3 | -13.5 +/-6.5 | -19.1 | 5.6 | 145.4 | 139.8 +/-6.5 |
| | (V) " | 117.9 | -34 +/-6 | -26.7 | 7.3 | 144.6 | 151.9 +/-6 |
| 8/29 /0800 | (U) " | 126.3 | -23 +/-6 | -28.0 | 5 | 154.3 | 159.8 +/-6 |
| | (V) " | 117.9 | -37 +/-6 | -33.2 | -4 | 151.1 | 154.9 +/-6 |
| 8/31 /0905 | (U) " | 126.3 | -33.5 +/-4.5 | -43.2 | 9.7 | 169.5 | 159.8 +/-4.5 |
| | (V) " | 117.9 | -43 +/-7 | -45.7 | 2.7 | 163.6 | 160.9 +/-7 |
| | | | Overall | Avg. diff | -.74 | dB | |

* approx. 6 hour median and extremes (+/- 3 hours of 15min. samples about Lidar collection interval)

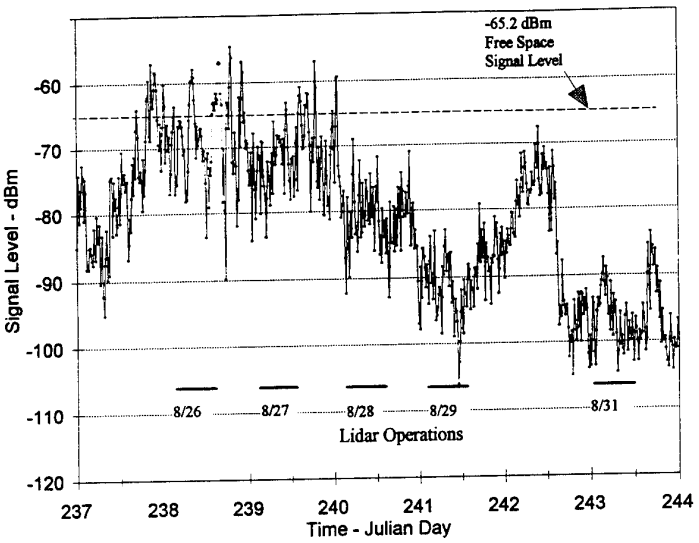


Figure 1. VOCAR received signal level at UHF for San Clemente Island to Point Mugu path (132 km) showing variability over an 8 day period, 15 minute samples.

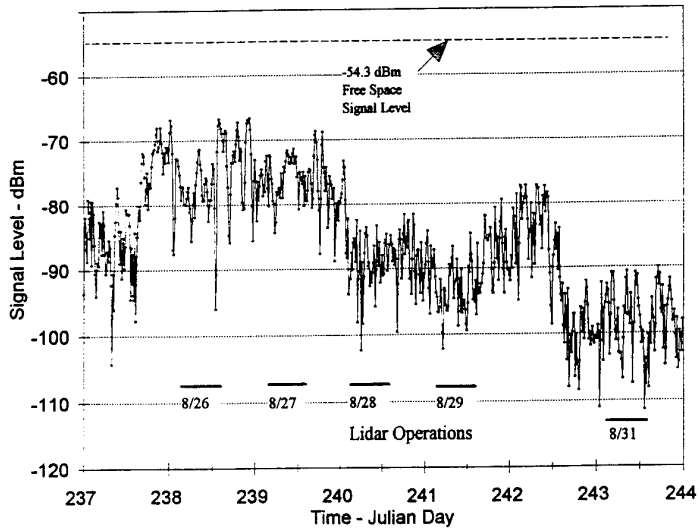


Figure 2. VOCAR received signal level at VHF for San Clemente Island to Point Mugu path (132 km) showing variability over an 8 day period, 15 min samples.

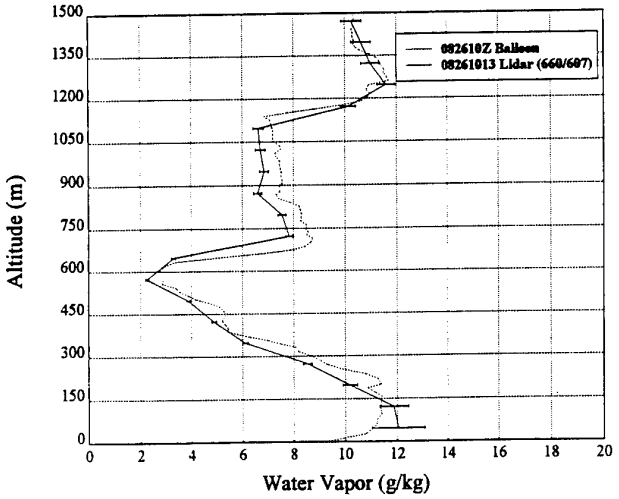


Figure 3. Example of lidar water vapor profile on 26 August 1993.

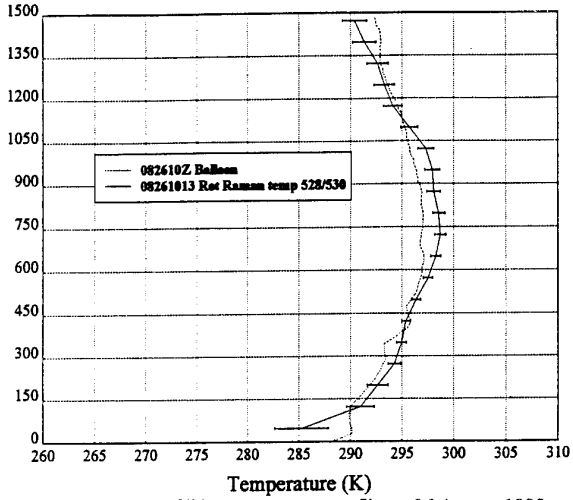


Figure 4. Example of lidar temperature profile on 26 August 1993.

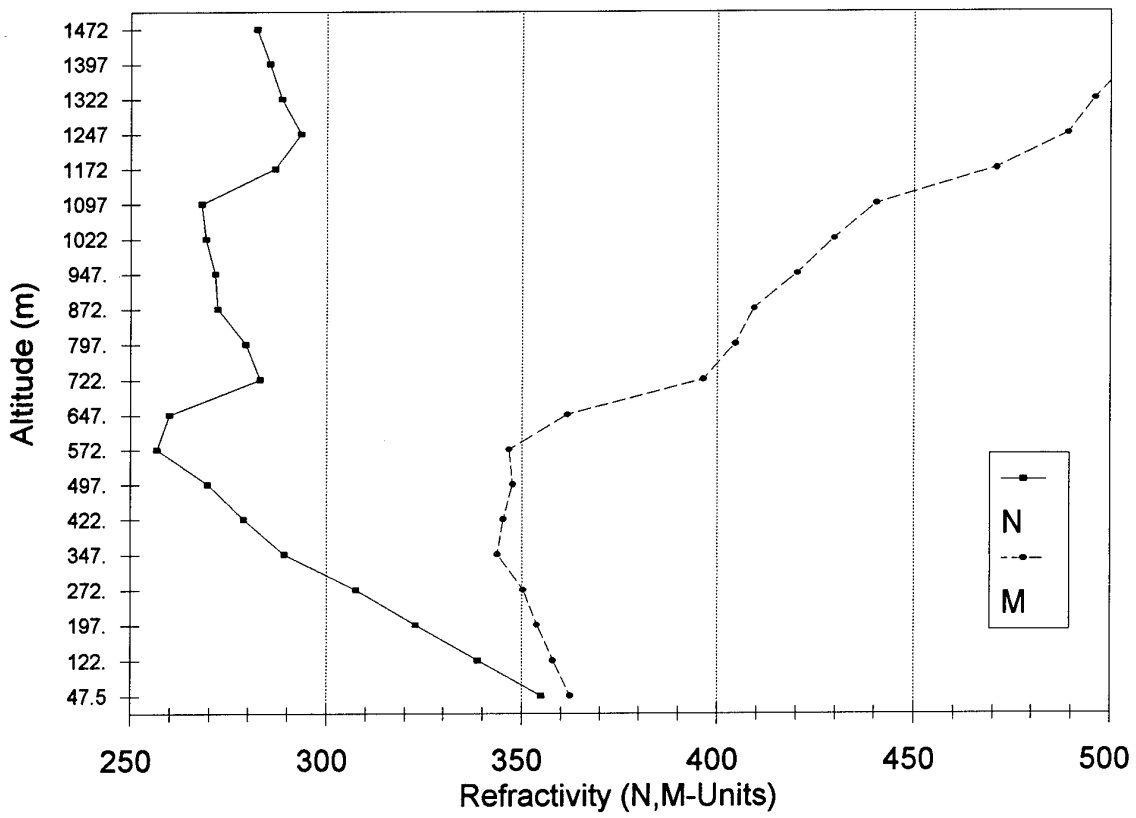


Figure 5. Refractive profiles on 26 August 1993 (1013Z) at Point Mugu showing a surface based duct to 600 m.

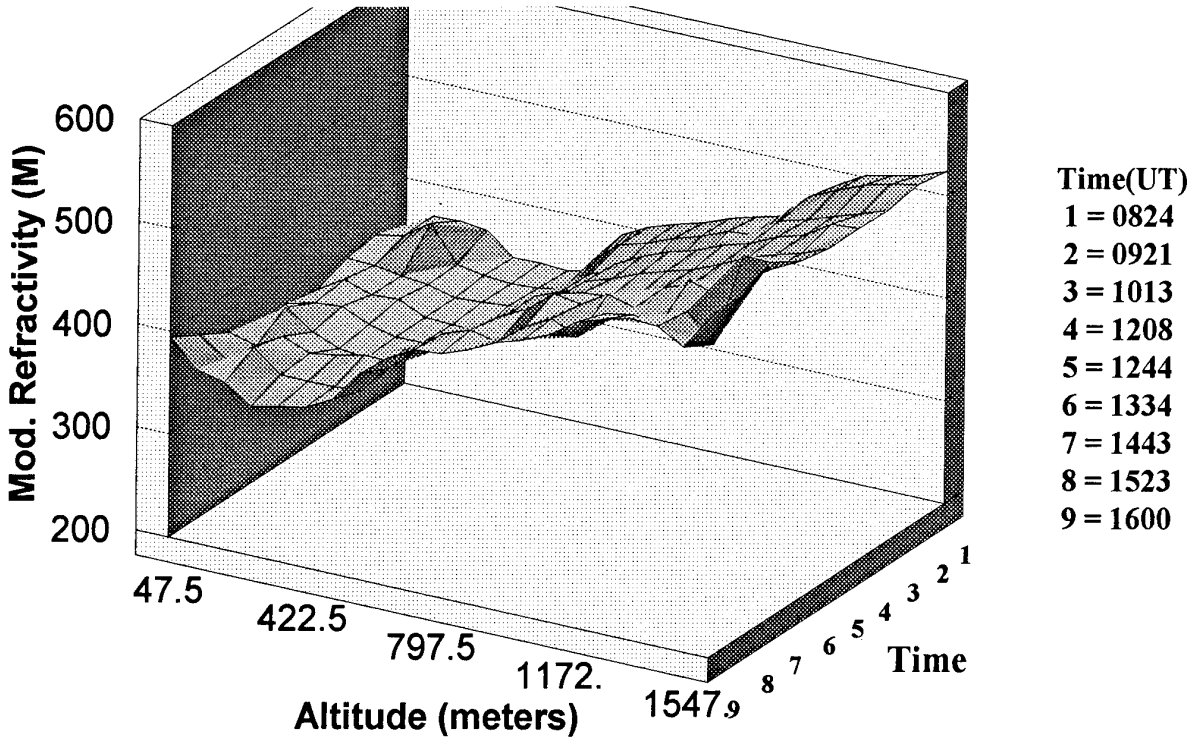


Figure 6. Surface contour of modified refractivity from lidar data on 26 August 1993.

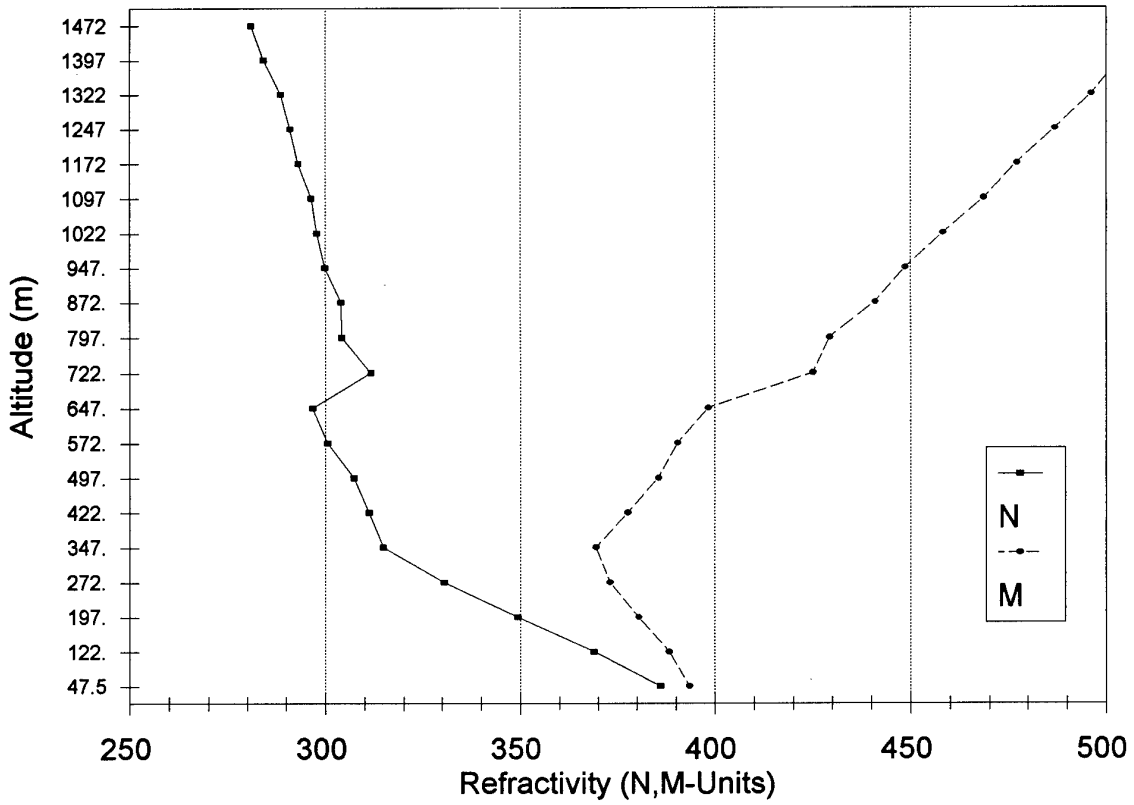


Figure 7. Refractive profiles on 27 August 1993 (1025Z) at Point Mugu showing a surface based duct to 350 m.

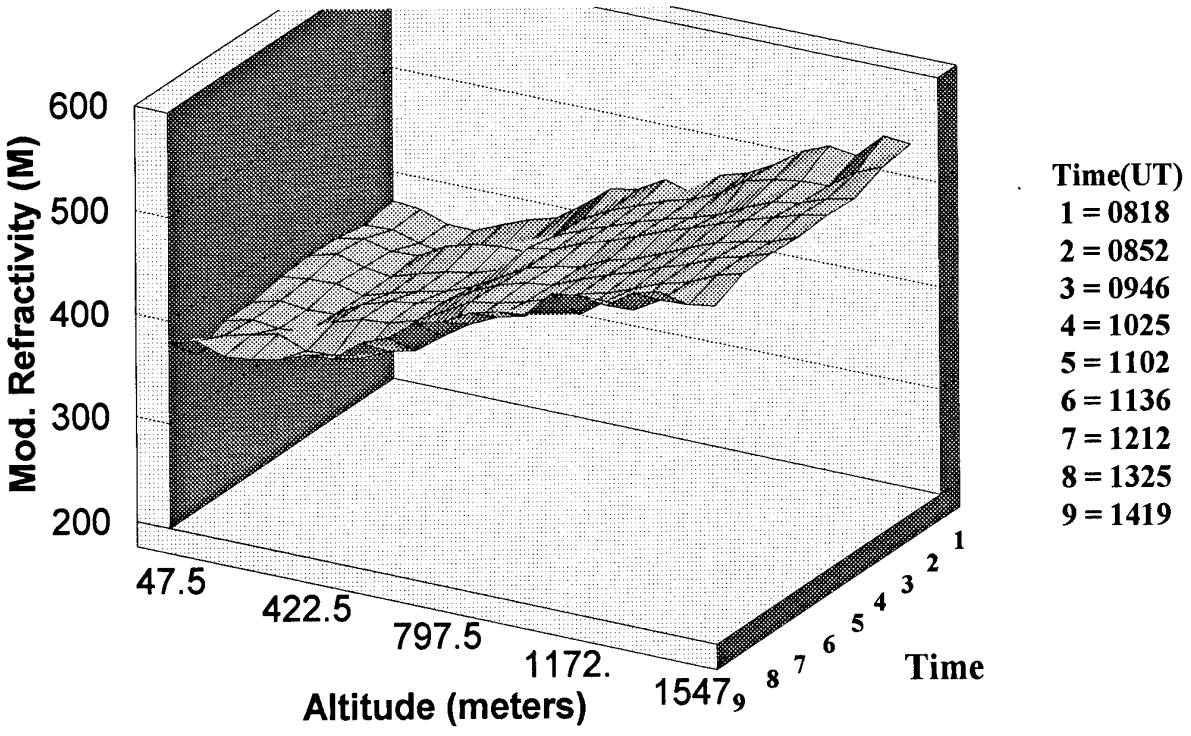


Figure 8. Surface contour of modified refractivity from lidar data on 27 August 1993.

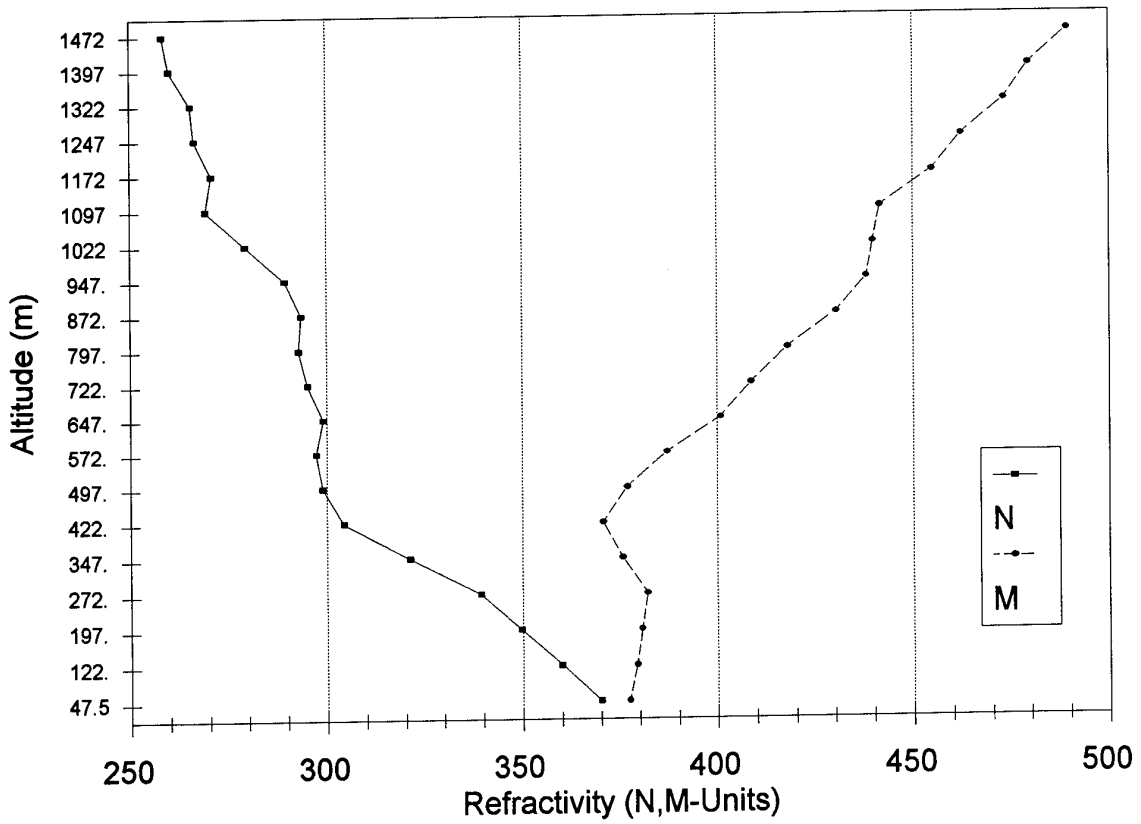


Figure 9. Refractive profiles on 28 August 1993 (0906Z) at Point Mugu showing a surface-based elevated duct at 425 m.

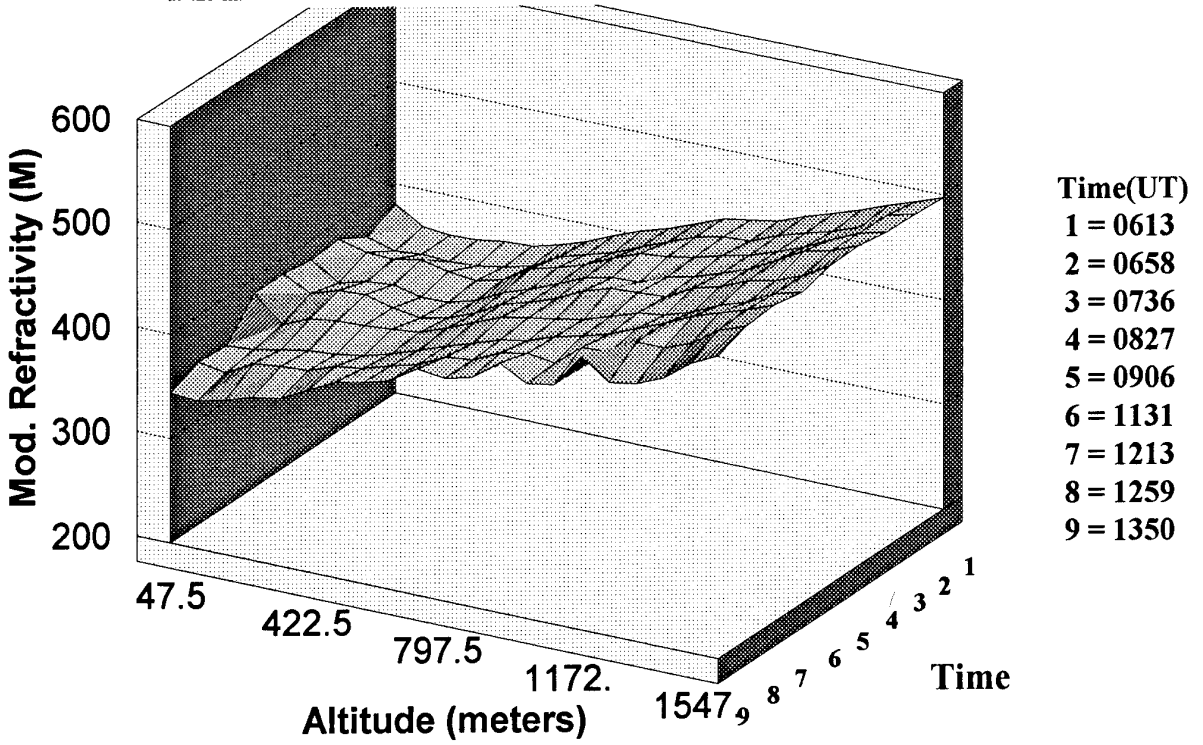


Figure 10. Surface contour of modified refractivity from lidar data on 28 August 1993.

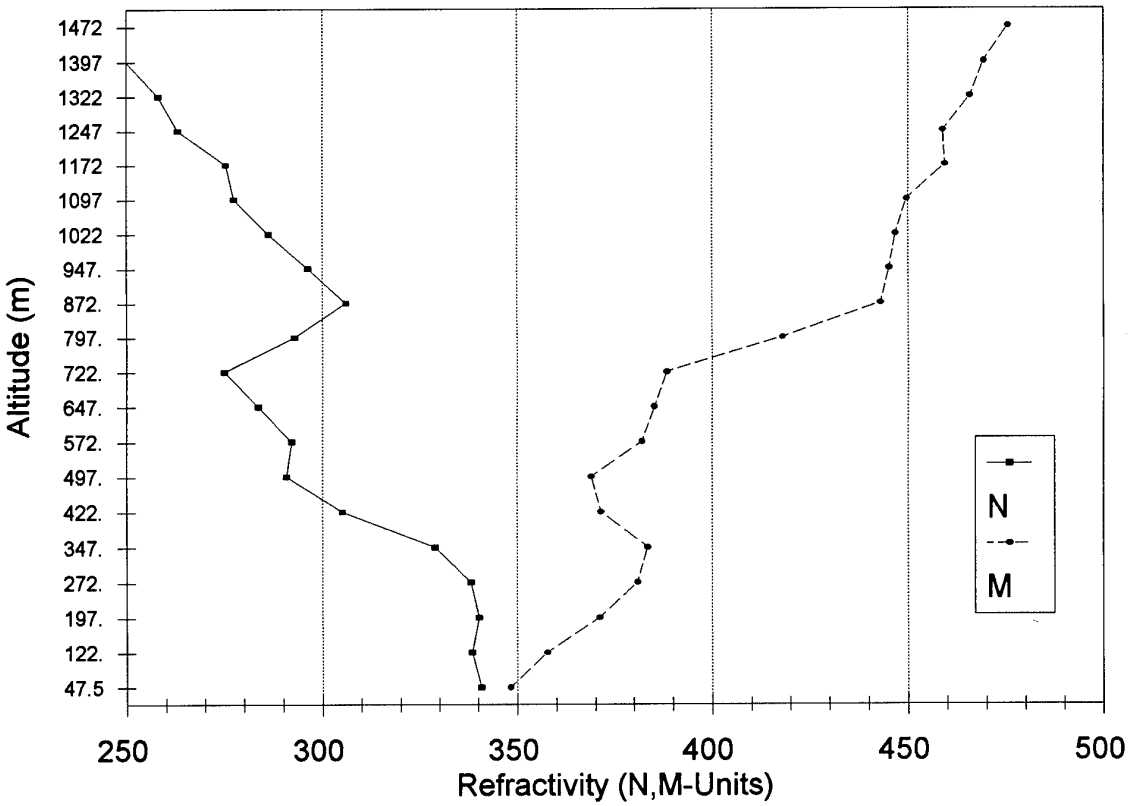


Figure 11. Refractive profiles on 29 August 1993 (0800Z) at Point Mugu showing an elevated duct 350-500 m.

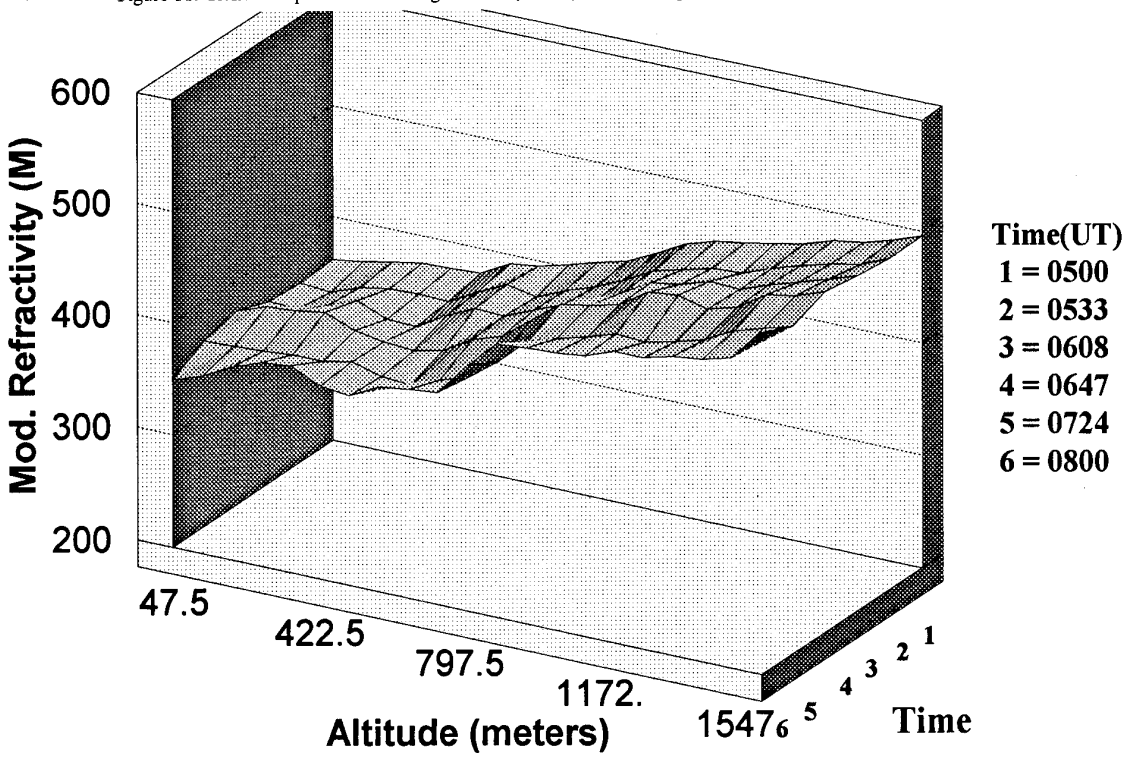


Figure 12. Surface contour of modified refractivity from lidar data on 29 August 1993.

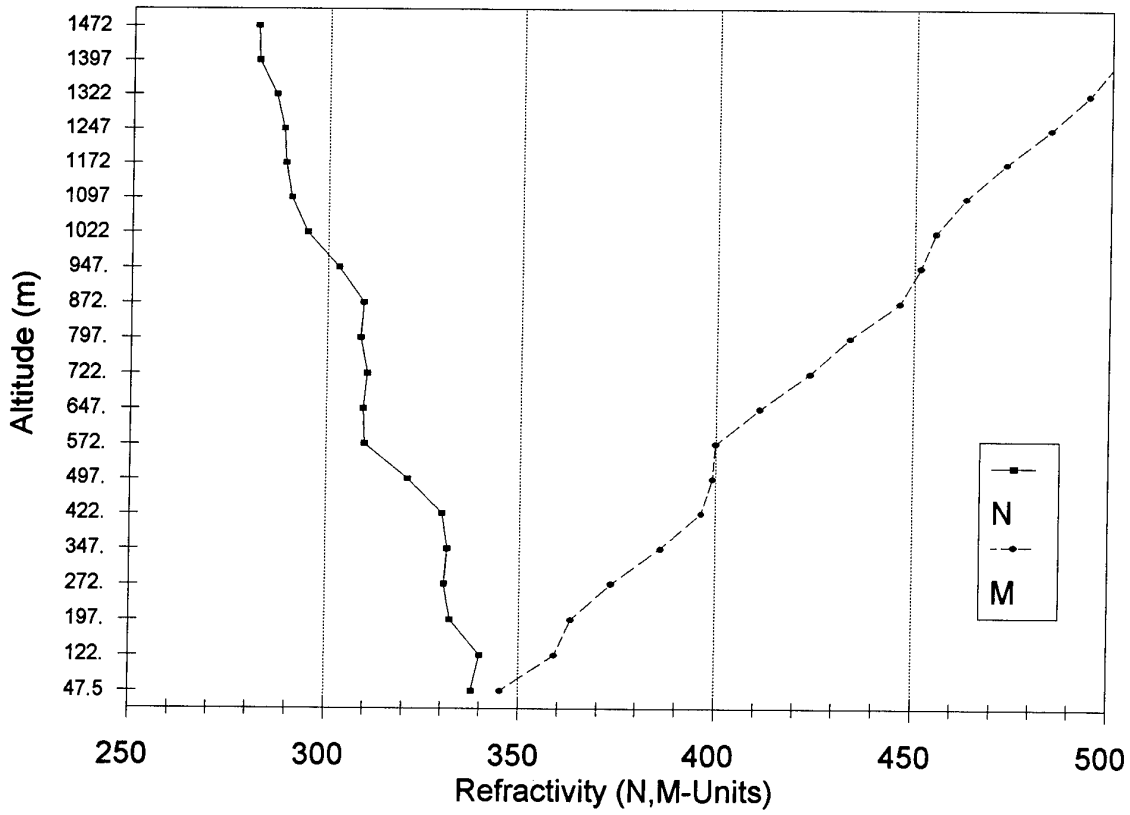


Figure 13. Refractive profiles on 31 August 1993 (0945Z) at Point Mugu showing non-anomalous conditions.

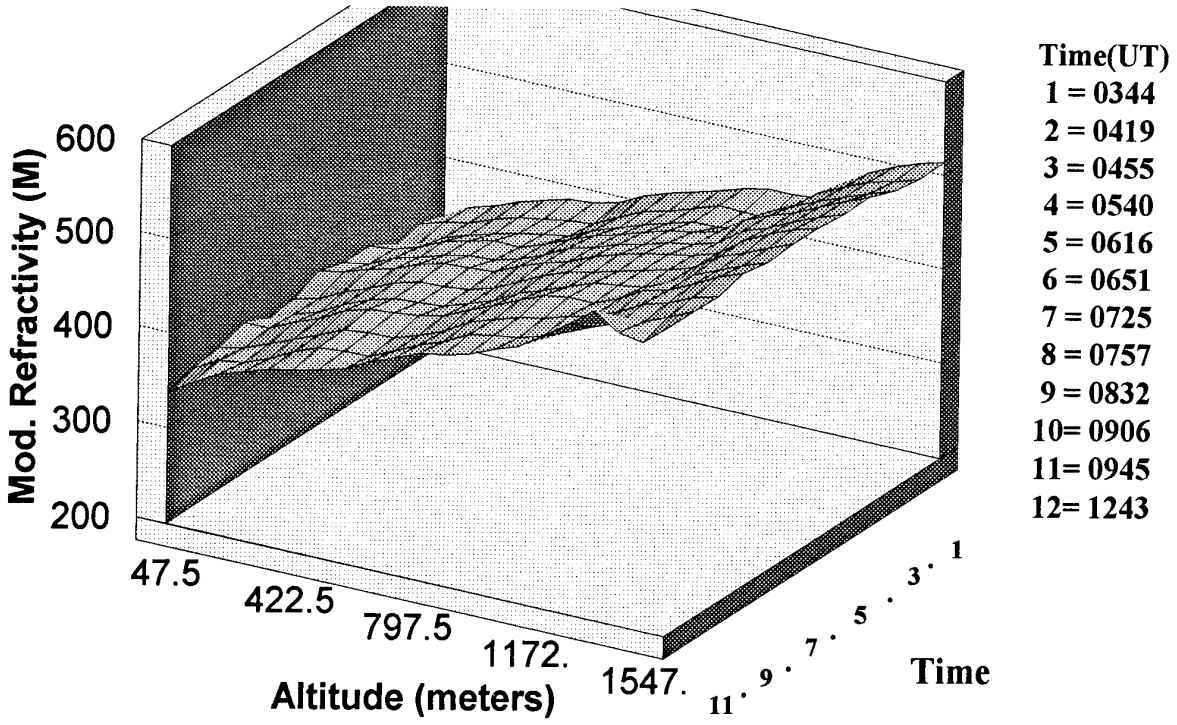


Figure 14. Surface contour of modified refractivity from lidar data on 31 August 1993.

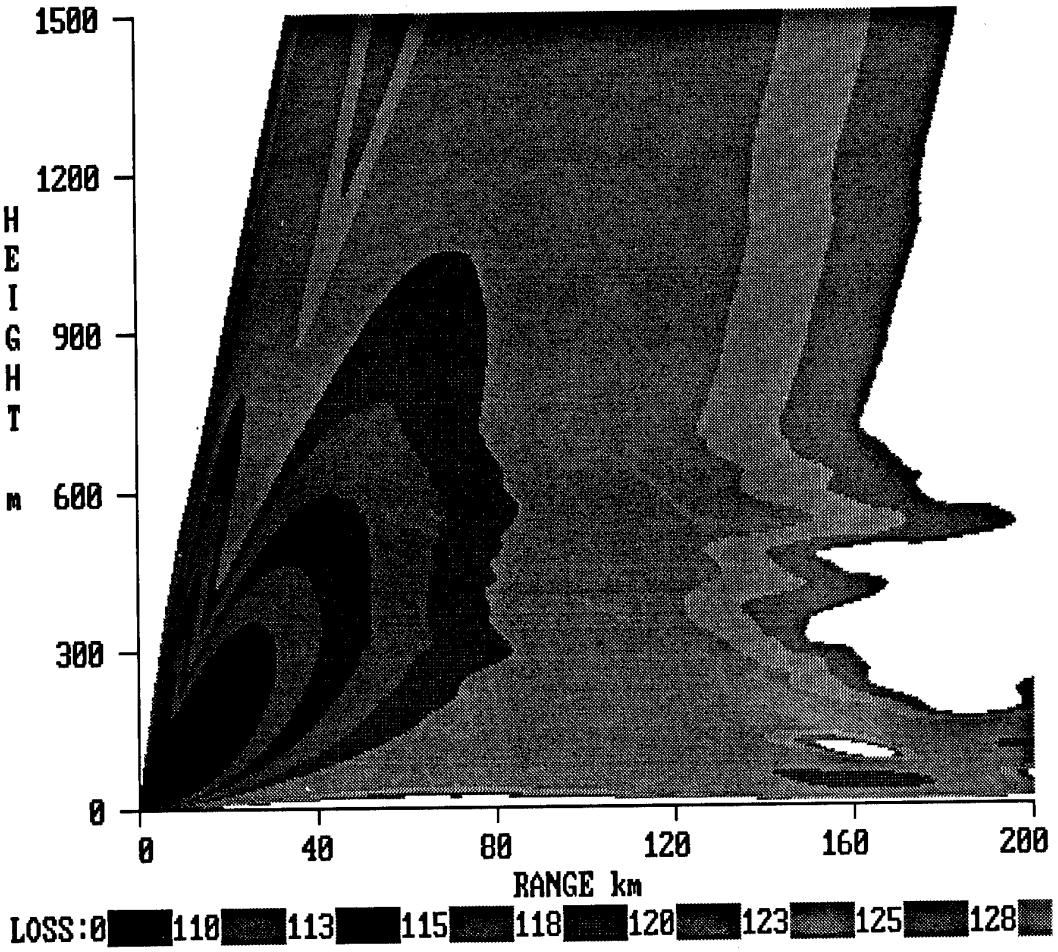


Figure 15. An example of propagation loss coverage calculated from RPO at UHF (374.9 MHz) based on lidar profiles at 1013Z on 26 August 1993.

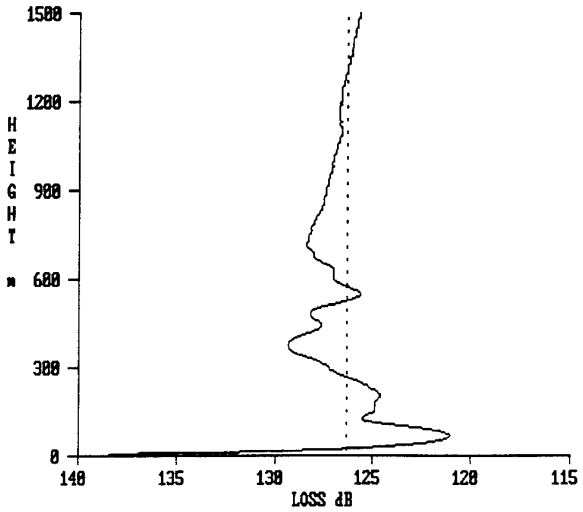


Figure 16. Calculation from RPO of UHF signal loss versus height relative to free space loss (for fixed antenna at 30.5 m) for conditions at 1013Z on 26 August 1993.

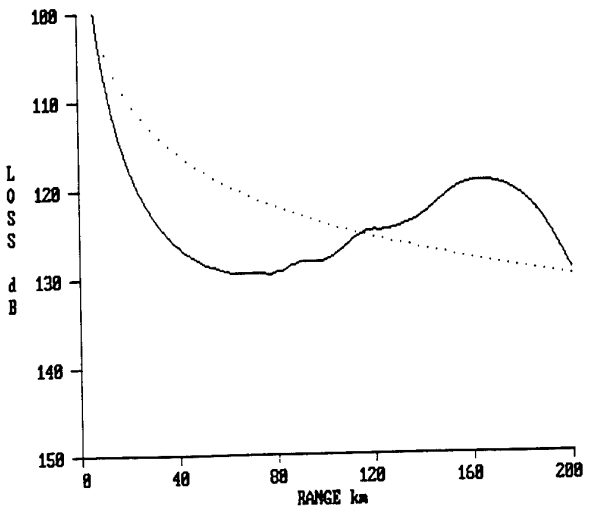


Figure 17. Calculation from RPO of UHF signal loss versus range at 30.5 m height relative to free space loss (dotted) for conditions at 1013Z on 26 August 1993.

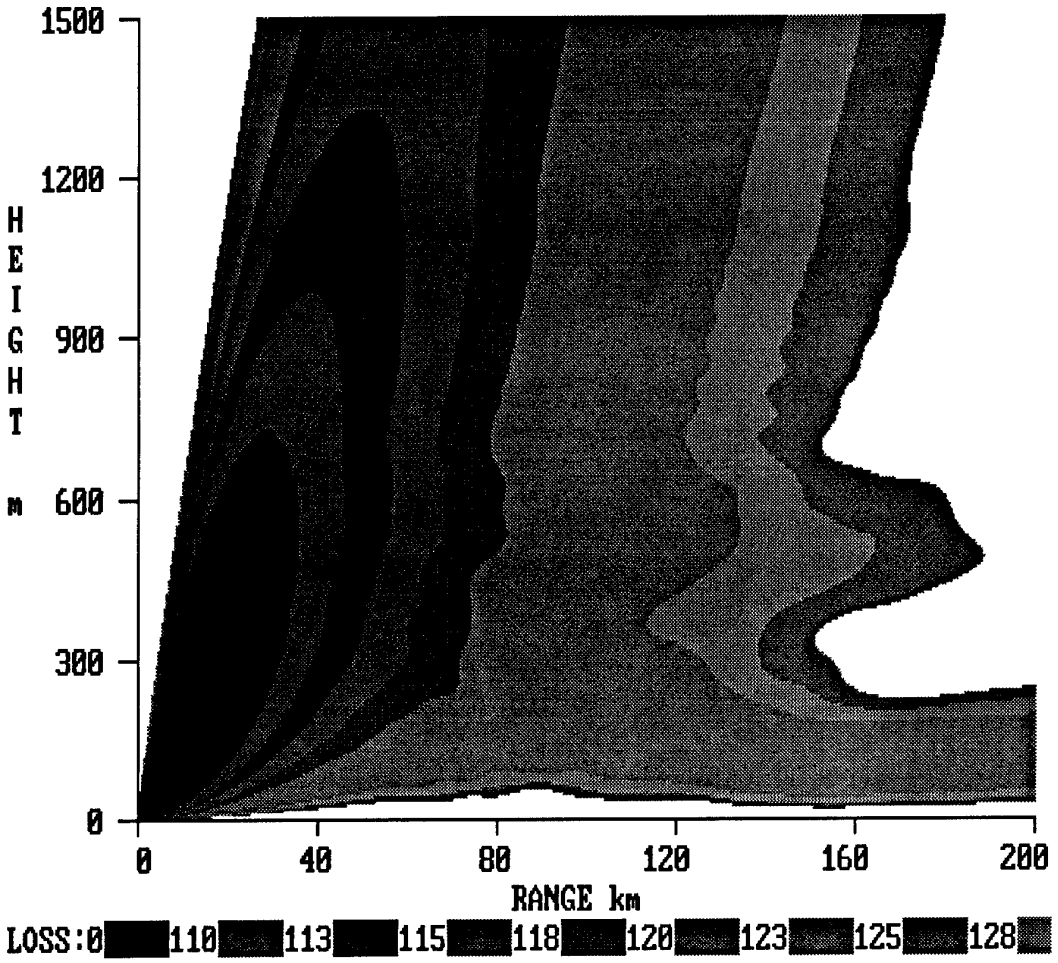


Figure 18. An example of propagation loss coverage calculated from RPO at VHF (143.1 MHz) based on lidar profiles at 1013Z on 26 August 1993.

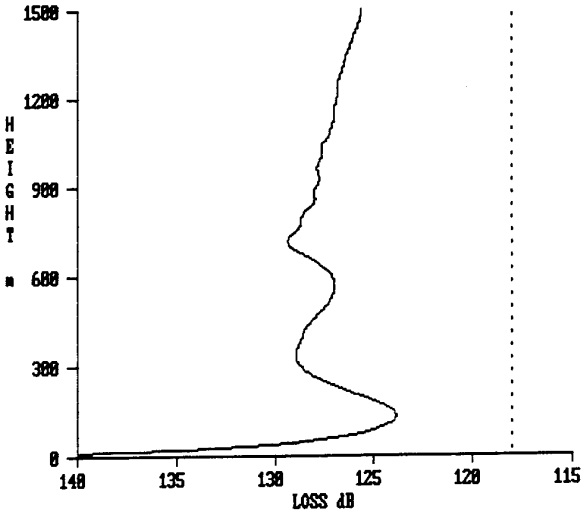


Figure 19. Calculation from RPO of VHF signal loss versus height relative to free space loss (for fixed antenna at 30.5 m) for conditions at 1013Z on 26 August 1993.

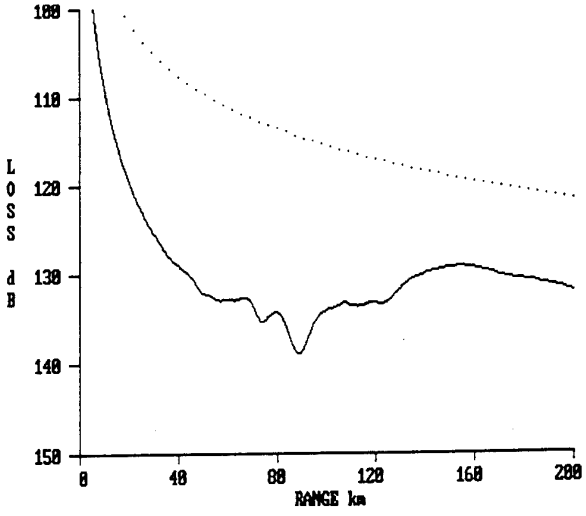


Figure 20. Calculation from RPO of VHF signal loss versus range at 30.5 m height relative to free space loss (dotted) for conditions at 1013Z on 26 August 1993.

## DISCUSSION

**K.H. CRAIG**
How effective is the Raman lidar technique at tracking sharp temperature gradients? The same types of ducting layers over land can be caused by temperature inversions without significant water vapor effects.

**AUTHOR'S REPLY**
The rotational Raman technique provides an accurate way of measuring the temperature in narrow layers along the profile. At present we are limited to 75 m resolution elements, but should be able to measure the temperature gradients which are thicker than 75 meters.

**J. ROSENTHAL**
Regarding Dr. Craig's question concerning abilities of the lidar to detect temperature variations, it is common in coastal environments to have strong vertical moisture variations whenever a strong temperature inversion is present; this makes it more difficult to isolate the temperature sensitivity. However, the lidar is capable of detecting just the temperature variations.

**AUTHOR'S REPLY**
Yes, our present data set does not really contain strong temperature gradients, but we should be able to measure them adequately.

# Remote Measurement of Atmospheric Refraction Conditions in the Coastal Region

**K. L. Davidson**
**C. H. Wash**
Department of Meteorology
Naval Postgraduate School
589 Dyer Rd., Room 254
Monterey, CA 93943-5114
USA
Tel: 408.656.2309 Fax: 408.656.3061 EMail: davidson@osprey.nps.navy.mil

## SUMMARY

Marine atmospheric boundary layer (MABL) and ocean surface properties remotely sensed by airborne and ground-based sensors are compared with coastal in situ measured refractive conditions. Near-surface refractive conditions are influenced by near-surface turbulence (wind speeds), by surface temperature (SST), and by overlying air dryness. All the latter can be estimated within operational and research satellite data. Humidity and temperature gradients at the top of the boundary layer can be related to remotely sensed cloud properties and to ground-based infrared High Resolution Interferometer Sounder (HIS) measured profiles. Studies were performed in coastal (Norwegian, California) regions. In situ and ground-based remote data were obtained from ship mounted systems. Other remote data were from aircraft and from operational (NOAA, DMSP) and research (ERS-1) satellite borne sensors. In examined cases, remotely sensed information yields reasonable assessments of refractive conditions immediately above the surface but not of the structure at the top of the boundary layer. Remote data describe high resolution horizontal and temporal variations, important in the coastal, but not described by point measured in situ data.

## 1. INTRODUCTION

Two important and spatially variable [on the orders of kms] features of the coastal region are the radar and radio frequencies influencing elevated refractive layers at the top of the marine layer and the surface-layer evaporation duct. Both are caused by vertical gradients of temperature (increase) and humidity (decrease). For radar/radio frequencies humidity is the most important. Because of temporal and spatial variability of both of these, it is necessary to pursue any approach that would remotely yield quantitative information on them. Elevated trapping layers affecting radio/radar waves are prevalent over ocean areas because of the relatively high specific humidity of the underlying "marine layer". The trapping layer can be the consequence of both synoptic scale meteorological and local coastal circulations. Synoptic scale features are the high pressure system associated subsidence of dry air. Local influences are those that exist in coastal zones. Differential advection of dry air above the boundary layer from adjacent coastal regions would cause the important large decrease in humidity above the surface. In either case, horizontal variations occur in both the height and strength of the trapping layer which could be either elevated or surface based, depending on the layer strengths and heights. In situ measurements of the elevated trapping layer requires radiosonde launches or aircraft profiles, neither are sufficient.

The evaporation duct is surface based and is persistent over ocean areas because of the rapid decrease of moisture immediately above the surface. Information on coastal region evaporation duct strengths will often be required 50-100 km beyond the location of local measurements. Surface layer flux-profile scaling theory yields a general empirical expression for the evaporation duct height (strength) in terms of well established velocity, temperature, humidity, and buoyancy scaling parameters [1]. The parameters can be calculated from routine shipboard measured or possibly from remotely sensed properties of the overlying airflow and the surface.

We believe interpretation of data from satellite-borne sensors is critical to assessment of spatial variations of the evaporation duct. As described, the imagery has to yield information on the sea-surface temperature, the dryness of the overlying air, and the mixing. Further these variations have to be determined at scales of the order of kilometers. Because of the rapidly increasing capabilities of satellite sensors the approach has to address sensors on operational NOAA and DoD satellites and to future operational sensors now being deployed on research satellites.

Geernaert [1] reviewed the application of operational and future satellite borne remote sensors sensing of refraction properties in the MABL. These include the low-frequency microwave radiometer (LFMR), the special sensor microwave imager (SSM/I), the altimeter (ALT), the scatterometer (NSCAT), the oceanographic synthetic aperture radar (SAR), and the advanced very high resolution radiometer (AVHRR). All sensors but the LFMR have been deployed. THE NSCAT and SAR sensors are deployed on research (non-operational) satellites and NPS was involved in experiments during 1988 and 1991 to calibrate and validate their applications. The others are deployed and currently operational.

In this paper we present results from examinations of multi-channel AVHRR, airborne and ship based scatterometers, and airborne and satellite borne C-band SARs as well as a "Ground-Based" High Resolution Interferometer Sounder, GB-HIS.

## 2. GB-HIS DETECTION OF LAYERS

In the coastal zone there is a need to continuously estimate MABL properties important to refraction. One approach involves the use of the Ground-Based Interferometer Sounder (GB-HIS) which measures atmospheric radiance in the infrared spectrum (3.3 to 18.2 μm) passively with very high spectral resolution. These measurements are used to retrieve near-continuous temperature and water vapor profiles for the low troposphere [2].

*Paper presented at the Sensor and Propagation Panel Symposium on "Propagation Assessment in Coastal Environments" held in Bremerhaven, Germany 19-22 September 1994.*

During the past several years, GB-HIS data has been successfully gathered in numerous field experiments. The data summarized here are from (1) two research vessel cruises by the R/V Point Sur off the central California coast on 8-10 May 1991 and 8-11 May 1992 and (2) a coastal site at the Naval Air Station at Point Mugu, California during the Variation Of Coastal Atmospheric Refractivity (VOCAR) experiment in August and September 1993. In situ radiosonde data was gathered at approximately 3 to 6 h intervals to validate the GB-HIS and better understand the coastal environment.

A thorough evaluation of the GB-HIS data has been completed, [3] and [4]. These studies found that the strengths of the GB-HIS are its ability to measure the thermal structure of the MABL and monitor the changes in the low-level inversion that caps the MABL. Figure 1 shows a comparison of temperature and dew point profiles retrieved from the GB-HIS to radiosonde measurements for a typical coastal sounding. Note the accuracy of the GB-HIS temperature profile and that the capping inversion is smoothed-out.

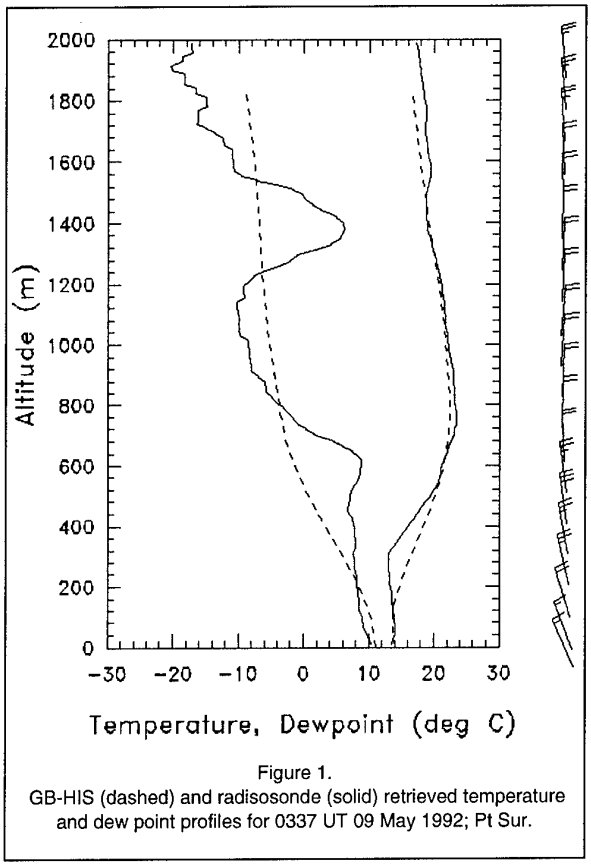


Figure 1.
GB-HIS (dashed) and radisosonde (solid) retrieved temperature and dew point profiles for 0337 UT 09 May 1992; Pt Sur.

The ability of the GB-HIS to monitor the thermal structure of the low troposphere was illustrated in all three data sets. During the Pt Sur 1991 cruise, the GB-HIS resolved the dramatic lifting of the marine inversion during a frontal passage and captured the development of a deep, well-mixed boundary layer following the front. During the Pt Sur 1992 cruise, the GB-HIS observed changes of the marine inversion induced by local land breeze circulations. Finally, the Pt Mugu 1993 GB-HIS data resolved diurnal oscillations of the coastal boundary layer.

The primary weakness of the GB-HIS is its inability to resolve the observed detailed moisture structure of the coastal boundary layer. Although the general larger scale vertical moisture gradients are present in the retrievals, all of the narrow moist and dry zones during the experimental period are not captured. This is illustrated also on Figure 1. Note the smooth GB-HIS dew point curve in comparison to the detailed moisture structure measured by the radiosonde.
These difficulties in moisture retrievals pose a serious problem for determining and monitoring refractive trapping layers in the three data sets. Resolving sharp moisture gradients are critical to estimate refractivity profiles. Figure 2 illustrates the modified refractivity profiles, M, for a sounding shown earlier. Note the smoother M structure from the GB-HIS data. The conclusion from the three coastal data sets was that the GB-HIS estimates of refractive were poor. Current research studying the impact of marine aerosols on the moisture retrievals and improving the retrieval coefficients may lead to improved GB-HIS moisture profiling in the future.

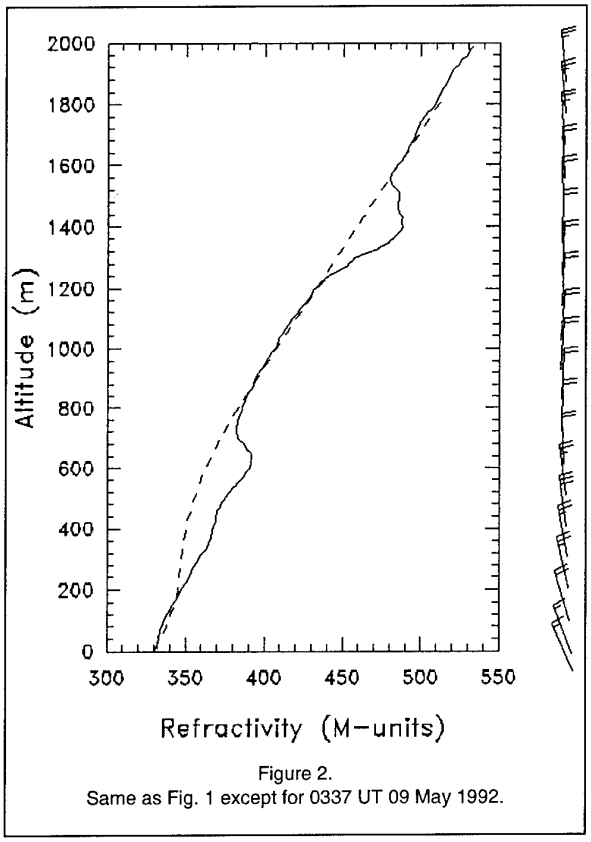


Figure 2.
Same as Fig. 1 except for 0337 UT 09 May 1992.

## 3. ERS-1 SAR DETECTION OF REFRACTIVE CONDITIONS

Investigations with satellite borne active sensors are being performed with the 1991 launched European Space Agency ERS-1 C-band scatterometer and synthetic aperture radar (SAR) and the scatterometer. We believe we are the only group examining the capability of these sensors characterize high spatial variation in refractive conditions. The in situ data for this examination were obtained during the NORwegian Continental Shelf EXperiment conducted during an ERS-1's calibration/validation phase in November 1991 (NORCSEX'91). NORCSEX'91 occurred from 7 to 28 November off the west coast of Norway. ERS-1 SAR passes over the experiment site were every 3 days. The Haltenbanken site was located in almost the exact center of the SAR swath which has a width of 100 km.

In situ atmospheric and surface data pertinent to refraction descriptions were collected from the University of Bergen R/V Haakon Mosby (HM). Surface layer wind, temperature, and humidity and surface temperature were measured continuously from the HM and radiosondes were launched with every pass of the ERS-1. Remote sensing (scatterometer) as well as meteorological, and oceanographic (ADCP and SEASOR) observations were also conducted from ship simultaneously on an almost 24 hours a day basis. Descriptions of sensed ocean surface features during NORCSEX'91 and their relation to air-sea interaction have been presented, [5] and [6], for periods related to refraction in the following sections.

### 3.1 SAR Sensing of Evaporation Duct Variations

On 13 November 1991 a wind front was imaged by ERS-1 SAR (at 2110 UT) and transited by the HM (at 2230 UT). A step change in backscatter intensity (from ~ -18 dB to - 5 dB) in the SAR derived intensity scan across the front, Figure 3. The spatial distance of the SAR detected wind regime change is 10's of meters, certainly less that 50 meters.

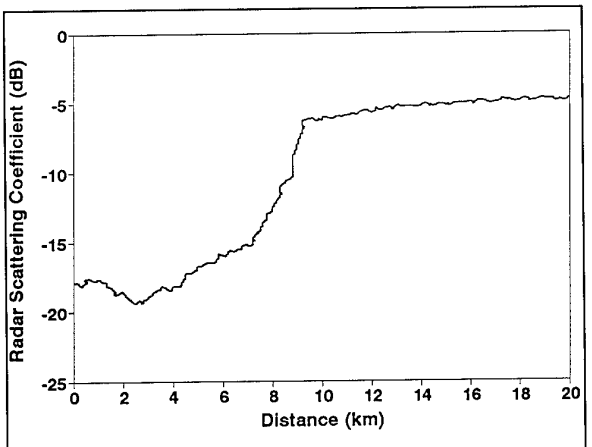


Figure 3.
ERS-1 C-band SAR backscatter response scan of 2110 UT 13 November 1991.

The HM was operating in the SAR image region from a period 3 hours before the SAR take to 3 hours after. A rapid increase (frontal boundary) in the shipboard measured backscatter occurred at about 2130 UT. Wind, temperature and humidity information is shown in Figure 4. Winds were light (2-3 m/s) in the vicinity of the SAR detected front, for the period from 1800 to 2100 UT. A 1 °C increase in sea surface temperature (8 °C to 9 °C) occurred, the relative humidity increased gradually, and the wind had changed direction by ~ 90 deg. in the transition region of the front.

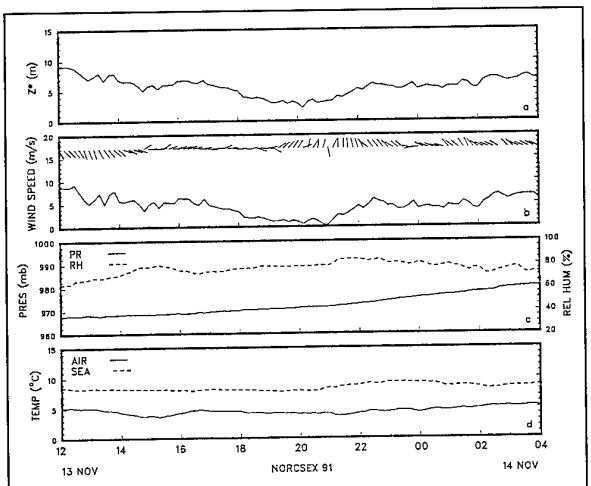


Figure 4.
HM time series from 11/13/1220 to 11/14/0400 of (a) evaporation duct thickness, (b) wind speed and direction (barbs), (c) barometric pressure and relative humidity, and (d) air and sea temperature.

The calculated evaporation duct thickness (Z*) decreased during the low wind speed period. The duct thickness was correlated with the wind speed. The duct thickness changes are important to operational radars since a calculated minimum frequency significantly affected would have increased from near 10 GHz to above 100 GHz when the duct thickness decreased from 10 to 2 meters.

The reason for such a large backscatter change when there isn't a large change in wind speed is still under investigation. Possibilities are that a threshold wind speed exists argument or that the direction change of the backscatter elements caused it. We believe that in this case the large backscatter change is a result of both the threshold wind and the direction change, because the change was 10-15 dB.

The detection of low wind conditions is important because any wind mixing plays an critical role in the evaporation duct strength under such conditions. This is particularly the case when the air is warmer than the water. Under such conditions a wind decrease would cause evaporation duct strengths (thickness) to increase considerably. In this case the air temperature (~ 4 °C) was 4-5 °C less than the sea temperature and remained study during this period. With such thermally unstable conditions, a drop in wind speed leads to increased convective mixing. Evaporation duct heights were calculated using surface layer flux profile expressions that account for this.

### 3.2 SAR Information and the Occurrence of Elevated Refractive Layers.

NORCSEX'91 SAR images also revealed distinct high resolution coherent backscatter manifestation of wind rows caused by variations of the vector wind across organized large eddies, i.e. "roll vortices", in the planetary boundary layer, PBL, [6]. The wind-induced low-wavenumber structure relation to boundary layer features are described by existing physical models, [7] and [8]. Such SAR detected features were examined by Gerling [9] with SEASAT SAR spectra and used to extract wind direction.

Two-dimensional pattern recognition (FFT spectral) processing of SAR images enable quite accurate quantification of the existence of and the orientation, and separation scales of the wind rows. Low-wavenumber spectra for two ERS-1 ascending pass images, one from near 11/10/21 and the other near 11/16/21, are shown in Figures 5a and 5b. A visual examination of the images, not shown here, clearly reveals that the one corresponding to Figure 5a had distinct row structure and the one corresponding to Figure 5b did not.

The spectrum in Figure 5a, corresponding to an image (from 10 November) with visual rows, contains a sharp, well- defined dominant peak aligned along a south-southwest to north-northeast direction. The dominant wave number image has coherent structure separations, read from the inner concentric circles, near 3000 meters. The axis of the role would be perpendicular to this alignment along the general direction of the wind. The 3000 meter separation would be associated with 1500 meter depth roles if the role "pair" had 1:1 aspect ratio. The depth of the rolls gives the top of the marine layer and hence height of the large humidity gradient. The aspect ratio has nominal values from 3 to 5:1, i.e., the vortices are flattened circles distorted by mean wind shear [8]. The 16 November image spectrum (Figure 5b) doesn't have a distinct dominant wave number. Instead it has two marginally distinct wave numbers with southwest to northeast alignments. Further, the separations are greater than for those on 10 November.

Rawinsondes were launched from the HM near the ERS-1 overpass times on the 10th and 16th, when the HM was within the image. Temperature, dew point temperature, N and vector wind profiles for these launches are shown in Figures 6 and 7. The HM shipboard surface layer measurements and the radiosonde profiles provide parameters relevant to the coherent structure occurrence, [9]. Measured and calculated parameters for times soon after each overpasses are listed in Table 1. The axis direction listed in Table 1 pertains to the FFT determined wavenumber orientation of coherent structures, Figs. 5a and 5b, and has a clear meaning for rows associated with image yielding spectrum in Figure 5a. However for spectrum in Figure 5b, it describes alignment of cellular structures. $Z_i$ is the depth of the lowest mixed-layer estimated from the radiosonde profile and L is the Monin-Obukhov stability length calculated from mean surface-layer and surface wind, temperature, and humidity values using exchange coefficients, [5].

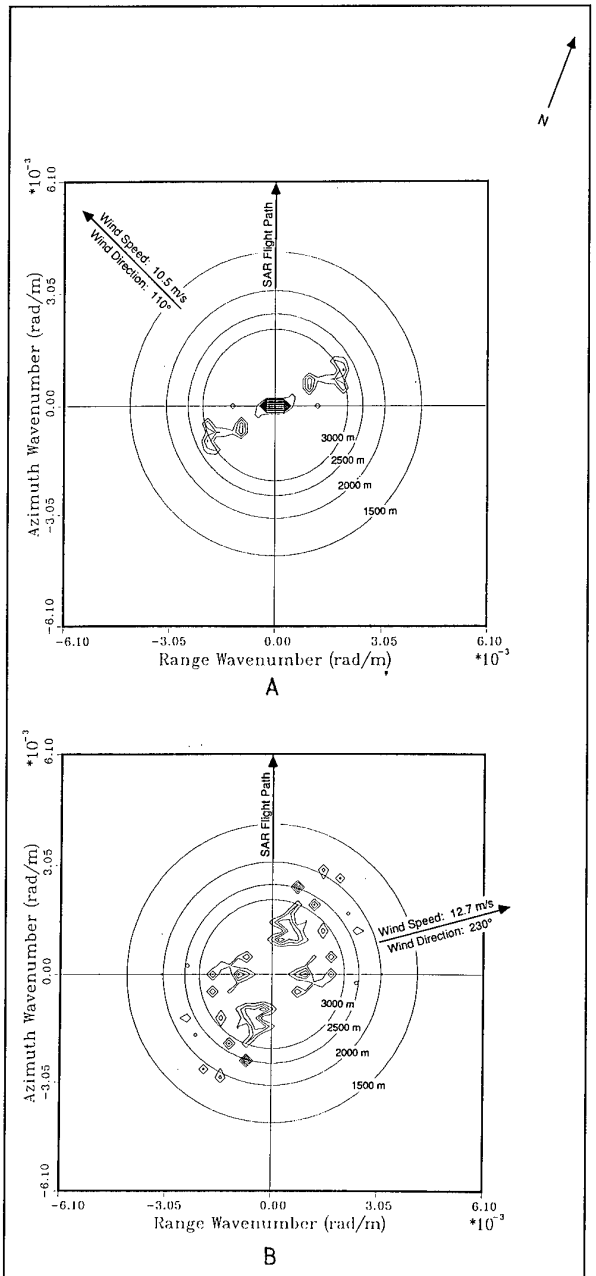


Figure 5.
ERS-1 SAR low-wavenumber wave spectrum for (a) 21:10:96 UT on 10 November 1991 and (b) 22:28:21 UT on 16 November 1991. Measured wind speed and direction are superimposed. From [6].

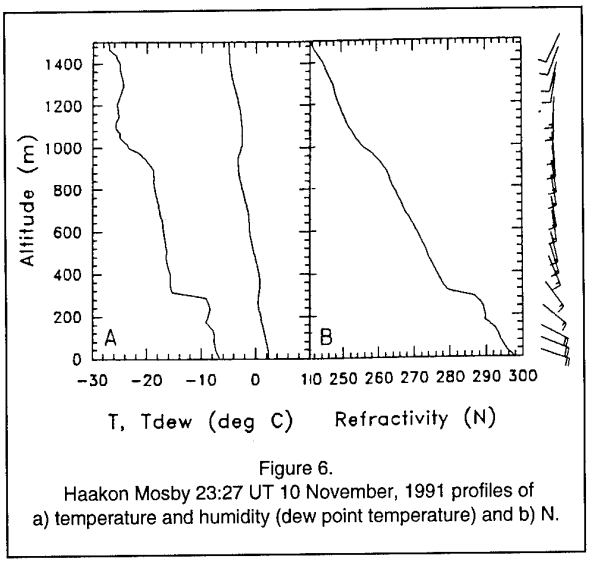


Figure 6.
Haakon Mosby 23:27 UT 10 November, 1991 profiles of a) temperature and humidity (dew point temperature) and b) N.

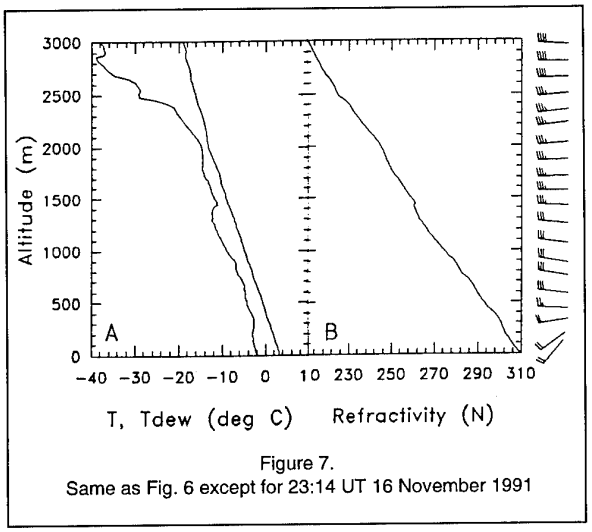


Figure 7.
Same as Fig. 6 except for 23:14 UT 16 November 1991

Table 1.
MABL parameters

| Date/Time(UT) | 11/10/2 | 11/16/22 |
|---|---|---|
| $U_{10}$ (m/s) | 8.9 | 9.0 |
| $T_{air}$ (°C) | 2.7 | 3.4 |
| $T_{sea}$ (°C) | 9.4 | 8.8 |
| $U_{10}$ dir (deg) | 137 | 232 |
| axis (deg) | 143 | 289 |
| L (m) | -34 | -45 |
| $Z_i$ (m) | 300 | 2500 |
| $Z_i/L$ | -9 | -56 |

An important consideration in view of the values in Table 1 and physical scaling for roll occurrence is that the occurrence of roll versus cellular structures is based on the value of $Z_i/L$, [10]. The $Z_i/L$ range for roll occurrence is, $-25 < Z_i/L < -5$, and for cell occurrence is, $Z_i/L < -25$. Hence, the SAR detected surface patterns agree with the $Z_i/L$ predictions for these cases. Further, the primary influence on the $Z_i/L$ ratio being within or outside of the roll range, -9 or -56, is the mixed layer depth, being 300 or 2500, rather than L, being -34 or -45 m.

On the 10th, $Z_i/L$ was -34 or within a range associated with roll occurrence, the coherent structure separation was approximately 3 km, the rawinsonde profile has a mixed-layer extending up to 0.3 km, Figure 6. This layer had a moderate to strong capping inversion due to off-shore flow. This mixed layer would yield an aspect ratio near 5, within the range or on the low side of those normally reported. The N profile exhibits a distinct refractive layer at the top of this layer.

The 16th profile, Figure 7, shows no temperature inversion below 3 km. A mixed layer depth of near 2.5 km is almost discernible in the humidity (dew point temperature) profile. There is little evidence of a refractive layer in the N profile. The corresponding spectrum, Figure 5b, was ambiguous on the wave number for coherent structure. The $Z_i/L$ value for this time indicated that deep convection was associated with coherent structures having "cellular" versus "roll" surface patterns, [10]. Hence, the SAR detected low-wavenumber structure is related to mixing properties of the overlying boundary layer in this case even if they were not determined by "roll vortices".

## 4. MULTISPECTRAL RESULTS

MABL structure varies dramatically in the coastal zone. In this area remote sensing approaches offer the only approach to estimate variations in the vertical temperature and moisture profiles that influence refraction. The development of satellite-based MABL characterization methods are valuable for regional analyses. Methods using sounder systems are limited by broad weighting functions and thus can not resolve the sharp temperature and moisture gradients at the top of boundary layer. These gradients are critical to refractive assessment.

Currently a multispectral approach using visible and IR data is being tested to indirectly estimate important variables such as the depth of the MABL, surface moisture and sea- surface temperature. The method relies on previously developed techniques for estimating aerosol optical depth and total column water vapor. Approaches for estimating aerosol optical depth have been developed, [11] and [12]. The approach uses the red-visible radiance measurements of the NOAA AVHRR (channel 1) and the direct relation between of this radiance to optical depth. Satellite measurements of water vapor variations are also employed. The method of Dalu [13] that estimates total column water vapor to the difference between split window brightness temperatures from the NOAA AVHRR (channels 4 and 5). Since both estimates are derived from the same sensor, the boundary layer estimates can be derived from a single satellite data source.

The method is based on three assumptions about the MABL:

1) The MABL is well-mixed,

2) aerosol optical depth variations are due to particles in the MABL, and

3) total water vapor is confined to the MABL.

Satellite estimates of optical depth and column water vapor are both related to the MABL height and moisture. An iteration method was devised to solve for the MABL height and surface relative humidity for clear regions in a satellite pass using the AVHRR data, [14] and [15]. Sensitivity estimates using a model atmosphere indicated the method is reliable when the MABL satisfies the assumptions of the technique, [15].

This approach has been used to map the MABL for the VOCAR period, [16]. To accomplish this, the assumption that the total water vapor is confined to the MABL was relaxed. Instead, an estimate of the percentage of water vapor in the MABL was used. This is viewed to have been an important improvement to the technique for those climatological regions where significant water vapor is found above the marine inversion.

Figure 8 shows a satellite analyses of MABL depth with corresponding radiosonde derived MABL depths for 27 August 1993, [16]. There is a slope of the MABL depth with shallow values to the west and deeper value along the eastern portion of the coastal region. This slope is confirmed by the radiosonde data. This case is one with significant mid-tropospheric water vapor and indicates that the method will work when the fraction of MABL moisture is estimated. In this case, this percentage is estimated to be 25%.

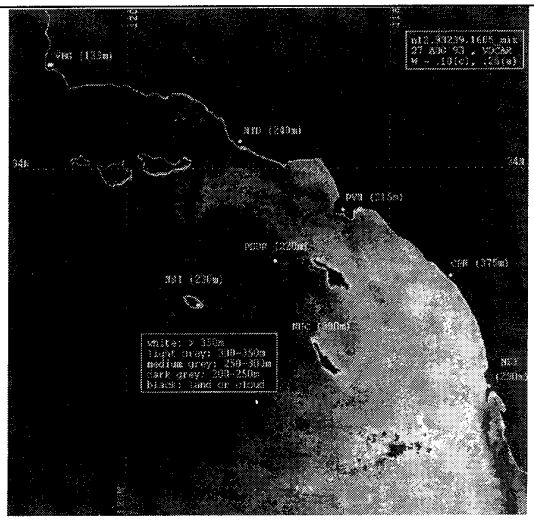

Figure 8
Multispectral MABL depth (m) for 16:06 UT 27 August 1993 compared to VOCAR radiosonde derived values (xxx), from [16].

The multispectral approach applicable for clear regions has been merged with an approach (IR Duct) based on the stratus cloud top IR temperature and assuming well-mixed profiles below cloud bases, Rosenthal and Helvey [17]. A merging of clear and cloud approaches is necessary to map the MABL depths over coastal regions, which normally have partial clear and stratus covered regions. Figure 9 shows merged predictions for two transects within the field described by Figure 8. Station identifiers in Figure 8 provide a guide to the two coast-overwater-coast transects in Figure 9 ; from VBG-NSI-NUC-NZY (Figure 9a) and from NTD-PSUR-NUC-NZY (Figure 9b).

IR-Duct determined MABL (cloud-covered) depths in Fig 9 agree well with the multispectral determined MABL (clear) depths. There is good agreement of the merged satellite determined values with the general downward slope from east to west. There is good agreement between the bottom of the radiosonde profile inferred trapping layer (boxes inserted above station identifier) and the satellite multi-sensor determined MABL depth. For 6 coastal stations (3 coast locations, 2 island locations, and one ship location), the latter correctly predicted the presence of elevated layers and further MABL depths within 25% of observed trapping layer base.

## 5. CONCLUSIONS

We have described how remotely sensed information can be related to refractive conditions at and above the ocean surface in coastal regions. Some of this information is now available from sensors on operational satellites and some is available on experimental satellites, ERS-1 and -2. No one passive or active satellite borne sensor directly described the responsible refractivity gradients. However, knowledge of what causes and modifies the gradients can be applied to remotely sensed information to estimate the probable occurrence and nature of significant refractive conditions. Different types of remotely sensed data, when fused together or merged with some in situ observed or predicted information, offers the promise of mapping refractive conditions in the coastal regions.

## 6. ACKNOWLEDGEMENTS

In situ data collection were supported by NRaD (VOCAR) and by NRL-SSC (NORCSEX'91). Refraction related analyses and interpretations were supported by NRaD. We acknowledge very important and contributions by NORCSEX'91 collaborators at the NANSEN Environmental and Remote Sensing Center (NERSC), Bergen, NO and at the Environmental Research Institute of Michigan (ERIM), and by NPS staff (K. Jones, P. Frederickson, T. Neta) and students (D. Walsh) participating with the VOCAR and NORCSEX'91 projects.

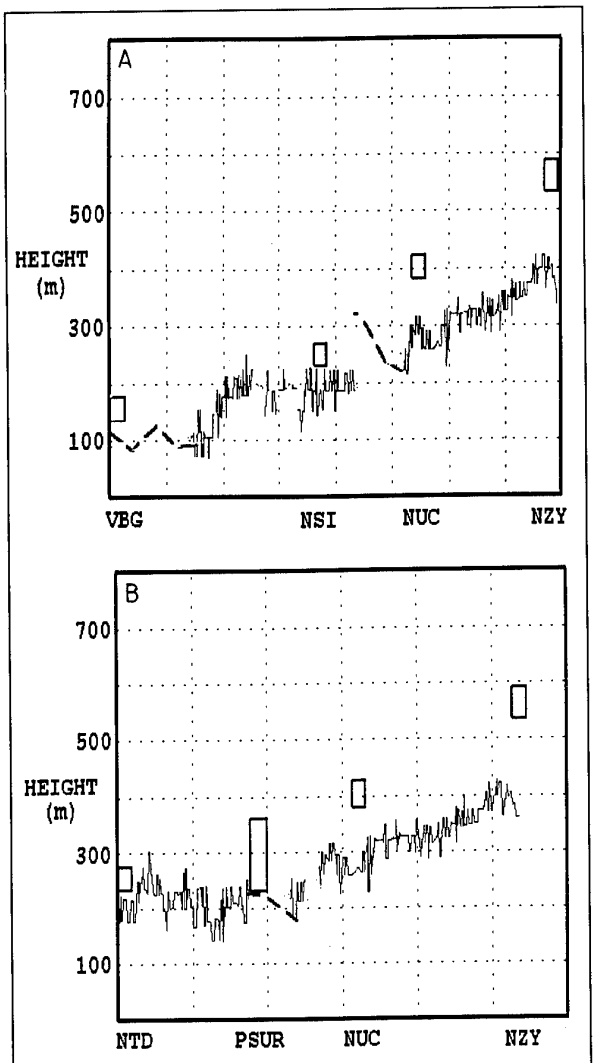


Figure 9.
Satellite-derived MABL depth transects for (a) VBG-NSI-NUC-NZY and (b) NTD-PSUR-NUC-NZY. Continuous line from multispectral and dashed line from IR-Duct technique. Boxes are radiosonde trapping layers.

## 7. REFERENCES


1. Geernaert, G. L., "Remote Sensing of Evaporation Ducts for Naval Warfare," Naval Research Laboratory Report, NRL Report 9228, 1989, 25 pp.

2. Smith, W. L., H. E. Revercomb, H. B. Howell, H. M. Woolf, R. O. Knuteson and M. T. Decker, "GAPEX, a Ground-based Atmospheric Profiling Experiment," Bull. Amer. Met. Soc., 71, 1990, pp 310-318.

3. Rugg, S. A., "An Investigation of the GB-HIS in a Coastal Marine Environment," Masters Thesis, Naval Postgraduate School, Monterey, CA, 1992, 91 pp.

4. Ledesma, R. R., "Coastal Boundary Layer and Refractivity Measurements Using the GB-HIS," Masters Thesis. Naval Postgraduate School, Monterey, CA, 1993, 73 pp.

5. Davidson, K. L., R. G. Onstott, and P. A. Frederickson, "Shipboard Studies of L-, C-, AND X-Band Backscatter and Surface Wind Forcing during NORCSEX'91," Oceans'93 (Special Session on Oceanic Microwave Remote Sensing), Victoria, British Columbia, Canada, 18-21 October 1993, 1993, pp I-13 to I-24.

6. Davidson, K. L., J. A. Johannessen, R.A. Shuchman, and R. A. Brown, "Analysis and Interpretation of ERS-1 SAR detected Wind Rows Relative to Observed Air-Sea Interaction Processes," Oceans'93 (Special Session of Synthetic Aperture Radar, SAR), Victoria, British Columbia, Canada, 18-21 October 1993, 1993, pp III-19 to III-24.

7. Brown, R. A., " A Secondary Flow Model for the Planetary Boundary Layer", J. Atmos. Sci., 27, 1970, pp 742- 757.

8. Mourad. P. D. and R. A. Brown, "Multi-scale Large Eddy States in Weakly Stratified Planetary Boundary Layers", J. Atmos. Sci., 47, 1990, pp 414-438.

9. Gerling, T. W., "Structure of the Surface Wind Field from the SEASAT SAR", J. Geophys. Res., 91, 1986, pp 2308- 2320.

10. Etling, D., and R. A. Brown, "Roll Vortices in the Planetary Boundary Layer: A review," Boundary-Layer Meteorology, 65, 1993, pp 215-248.

11. Griggs, M., "Satellite Measurements of Tropospheric Aerosols," Adv. Space. Res., 2, 1983, pp. 109-118.

12. Durkee, P. A., D. R. Jensen, E. E. Hindman and T. H. VonderHaar, "The Relationship Between Marine Aerosol Particles and Satellite-Detected Radiance," J. Geophys. Res., 91, 1986, pp 4063-4072.

13. Dalu, G., "Satellite Remote Sensing of Atmospheric Water Vapor", Intl. J. Remote Sensing, 7, 1986, pp 1089-1097.

14. Kren, R. J., "Estimation of Marine Boundary Layer Depth and Relative Humidity with Multispectral Satellite Measurements", Masters Thesis. Naval Postgraduate School, Monterey, CA, 1987.

15. Smolinski, S. P., "Marine boundary layer depth and relative humidity estimates using multispectral satellite measurements," Masters Thesis, Naval Postgraduate School, Monterey, CA, 1988, 70 pp.

16. Walsh, D. J., "Multispectral NOAA Marine Atmospheric Boundary Layer (MABL) Estimates During VOCAR", Masters Thesis, Naval Postgraduate School, Monterey, CA, 1994, 106 pp.

17. Rosenthal, J. and R. Helvey, "Refractive Assessments from Satellite Observations," AGARD CP-502. 1992, pp 8.1-8.9.

## DISCUSSION

**M.F. LEVY**

1. Can $Z_i$ be estimated from satellite measurement?

2. What is the vertical resolution for HIS profiling?

**AUTHOR'S REPLY**

1. $Z_i$ is the depth of the mixed-layer, or aerosol and water vapor containing marine layer, and can be estimated from both passive and active remote sensing. Passive (radiative) approaches are based on optical depth and cloud-top temperature properties of the boundary. If skies are clear, the multi-spectral method using satellite-borne sensors has been shown to yield reasonable estimates of $Z_i$. With clear skies, ground based remote sensing with high resolution interferometer sounding (HIS) has also yielded reasonable estimates of $Z_i$. If the mixed layer is stratus covered and no middle or high clouds exist, satellite IR sensor (AVHRR) derived cloud-top temperatures have been interpreted for $Z_i$ values. This is decribed by Helvey et al., paper #33, in these proceedings.

Active (radar) approaches are based on roughness properties of the surface. Wind rows can be detected by SAR under both clear and cloudy skies. Since coherent structures (e.g. rolls) in the boundary layer have certain ranges for the height to width aspect ratios, SAR determined separation of wind rows can be interpreted for likely mixed-layer depths.

2. An estimated near-surface representative spacing would be 50 to 70 meters. The vertical resolution would increase with increased density of molecules responsible for the upwelling irradiance. Hence the resolution near the surface is highest and will decrease with height as the pressure gradient decreases.

# ETUDE BISTATIQUE DU COMPORTEMENT POLARIMETRIQUE DES OCEANS

*F. Daout, A. Khenchaf, Y. Hurtaud* et J. Saillard*
*Lab. SEI/S2HF, IRESTE, Université de Nantes, La Chantrerie, CP 3003,*
*44087, Nantes Cedex 03, FRANCE*
*Tel. 40 68 30 43, Télécopie 40 68 32 33*
** Centre d'Electronique de L'ARmement, Division GEOS/SOP*
*35 170 Bruz*

**RESUME**

*Les régions côtières sont souvent caractérisées par des environnements à propagation complexe qui sont difficiles à modéliser. En utilisant les caractéristiques polarimétriques d'une cible et du milieu environnant, il est possible d'augmenter la discrimination d'un radar.*

*L'article proposé s'inscrit dans le cadre général de la télédétection océanographique et des liaisons hertziennes au-dessus de la mer. Il concerne dans un premier temps, une étude sur les méthodes de diffusion par la surface océanique, puis dans un deuxième temps, la recherche de la signature polarimétrique de la surface de la mer en fonction des divers paramètres d'observation et de plusieurs modèles théoriques de diffusion. Une méthode d'optimisation polarimétrique est développée pour augmenter la fiabilité d'une liaison hertzienne ou pour accroître la discrimination d'une cible radar.*

**ABSTRACT**

*This paper covers the general topic of remote sensing and radio propagation above the sea surface. A study concerning scattering methods on the oceanic surface is first presented, followed by the search of the polarimetric signature of the sea surface, as a function of the observation parameters and some theoritical scattering models.*

*A technique of polarimetric optimization is finally developed to increase the reliability of the radio link as well as to improve the radar accuracy.*

## 1. INTRODUCTION

Pour décrire l'effet de la réflexion d'une onde électromagnétique par une surface rugueuse, il est nécessaire de choisir un modèle approprié. Les méthodes les plus utilisées [1] peuvent être classées en deux catégories:

- théorie basée sur l'approximation de Kirchhoff,
- théorie des petites perturbations.

En télédétection marine, ou dans le cadre d'une liaison hertzienne au-dessus de la mer, le critère de détection est basé sur la puissance de l'onde diffusée par une cible: or l'onde électromagnétique diffusée par un objet est une grandeur vectorielle transportant une information polarimétrique due au diffuseur.

La signature polarimétrique [2] d'une cible représente la variation de la puissance diffusée en fonction des différentes combinaisons des états de polarisation choisis à l'émission et à la réception.

La connaissance de la signature polarimétrique de la surface de la mer peut permettre l'extraction des cibles noyées dans le bruit.

Cependant, cette identification n'est valable que sous certaines conditions de mesures (*gamme de fréquence, position de la cible, direction d'illumination, etc...*). Le terme "signature polarimétrique" est à considérer avec précaution car il ne représente sectoriellement qu'un invariant de la cible quelles que soient, son attitude le long de l'axe de visée du radar, la fréquence d'émission, la base orthogonale des vecteurs de polarisation, et la méthode utilisée pour calculer le champ diffusé. Dans la troisième partie de ce papier, l'influence de ce choix sur la signature polarimétrique d'une surface est montrée. Un bref rappel sur les méthodes de diffusion par une surface rugueuse est proposée dans la deuxième partie.

Dans la dernière partie de cet article, une méthode d'optimisation polarimétrique est présentée. elle s'applique dans le cadre d'une liaison bistatique au-dessus de la mer, elle consiste à choisir une polarisation optimale de l'antenne de réception afin de minimiser l'influence du champ diffusé par la mer.

## 2. MODELES THEORIQUES DE DIFFUSION

L'étude de la diffusion d'une onde électromagnétique par une surface rugueuse a été initialisée depuis de nombreuses années. Aucune solution exacte n'a encore été obtenue à ce jour. Des techniques numériques telle que la méthode des moments ont été utilisées pour obtenir une solution quasi-exacte, mais en général, ces méthodes sont prohibitives en temps de calcul et ne sont généralement utilisées que pour évaluer la précision et le domaine de validité des méthodes approchées plus grossières.

Habituellement, la précision des modèles approchés est suffisante et ceux-ci sont plus simples à mettre en oeuvre. Bien qu'ils ne soient valables qu'à l'intérieur d'un domaine de rugosité, ces modèles sont utilisés dans de nombreuses situations.

*Paper presented at the Sensor and Propagation Panel Symposium on "Propagation Assessment in Coastal Environments" held in Bremerhaven, Germany 19-22 September 1994.*

Dans ce paragraphe, nous présentons un ensemble de techniques concernant la diffusion d'une onde électromagnétique par une surface rugueuse aléatoire. Nous commençons par introduire des modèles polarimétriques de diffusion par une surface rugueuse, basés sur l'approximation de Kirchhoff (*phase stationnaire, approximation scalaire*) et sur la méthode des petites perturbations.

**2.1. Approche de Kirchhoff**

Sous l'approche de Kirchhoff, le champ diffusé est écrit en terme de champ tangent à la surface rugueuse. Le champ à la surface est alors approché par la valeur du champ diffusé par un plan au voisinage du point considéré.

Cette méthode est appelée l'approximation du plan tangent. Son domaine de validité correspond à une surface dont chaque point possède un rayon de courbure supérieur à la longueur d'onde.

L'approximation de Kirchhoff est basée sur le second théorème de Green où le champ en chaque point à l'intérieur d'une surface libre peut être exprimé en fonction du champ tangentiel sur la surface. Cette considération est formulée mathématiquement par Stratton et Chu et modifiée pour le champ lointain par Silver [1], ainsi le champ diffusé peut s'écrire sous la forme:

$$\vec{\hat{E}}^s = K\hat{n}_s \wedge \int \{\hat{n} \wedge \vec{\hat{E}} - \eta_1 \hat{n}_s \wedge (\hat{n} \wedge \vec{\hat{H}})\} e^{jk\hat{r}\cdot\hat{n}_s} ds \qquad (1)$$

où $\hat{n}_s$: vecteur unitaire dans la direction du champ diffusé,

$\hat{n}$: vecteur unitaire normal,

$k$: constante d'onde,

$\eta_1$: impédance intrinsèque du milieu où $\vec{\hat{E}}^s$ est évalué,

$K = -jk\dfrac{e^{-jkR_o}}{4\pi R_o}$ ,

$R_o$: distance du centre illuminé au point d'observation,

$\vec{\hat{E}}$: champ électrique total,

$\vec{\hat{H}}$: champ magnétique total.

Pour déterminer le champ diffusé, il faut commencer par exprimer les composantes tangentielles des champs $\hat{n} \wedge \vec{\hat{E}}$ et $\hat{n} \wedge \vec{\hat{H}}$ pour chacune des réalisations de la surface en fonction du champ incident $\vec{\hat{E}}^i$ en utilisant l'approximation de Kirchhoff.

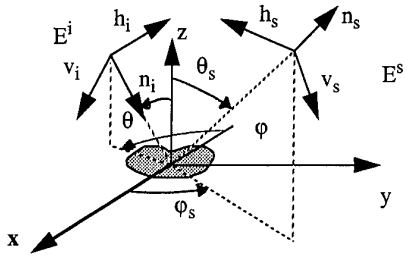


Fig 1.Géométrie de la diffusion

Sous cette approximation, les champs à la surface dépendent de l'orientation de la surface (*caractérisée par l'orientation de sa normale locale*), des caractéristiques physiques du milieu (*température et salinité*) et de la géométrie de la diffusion (*angles d'incidence et angles d'observation*).

Même sous l'approximation du plan tangent, le champ diffusé s'exprime en fonction d'une intégrale de surface difficile à résoudre analytiquement. D'autres hypothèses simplificatrices sont alors nécessaires.

*2.1.1 Domaine haute fréquence - Phase stationnaire*

La solution haute fréquence (*Optique Géométrique*) est obtenue en utilisant l'approximation de la phase stationnaire. Son domaine de validité correspond à des surfaces qui ont un rayon de courbure moyen et un degré de rugosité important vis-à-vis de la longueur d'onde.

Pour résoudre (1) il est nécessaire d'utiliser l'approximation dite phase stationnaire: la diffusion a lieu uniquement le long de la direction spéculaire.

Le champ diffusé est calculé à partir de (1) sur l'aire illuminée (Fig 1.), avec un facteur de phase $exp\{-jk\hat{n}_i \cdot \hat{r}'\}$ par rapport au champ incident.

Mathématiquement, l'approximation est obtenue à partir de la phase $Q$:

$$Q = k(\hat{n}_s - \hat{n}_i) \cdot \hat{r}' = q_x x' + q_y y' + q_z z' \qquad (2)$$

avec:

$q_x = k(\sin\theta_s \cos\varphi_s - \sin\theta\cos\varphi)$

$q_y = k(\sin\theta_s \sin\varphi_s - \sin\theta\sin\varphi)$

$q_z = k(\cos\theta_s + \cos\theta)$

$\hat{r}' = (x', y', z')^T$: distance du point au centre de la cible

La phase est dite stationnaire si:

$$\begin{cases} \dfrac{\partial Q}{\partial x'} = 0 = q_x + q_z \dfrac{\partial z'}{\partial x'} \\ \dfrac{\partial Q}{\partial y'} = 0 = q_y + q_z \dfrac{\partial z'}{\partial y'} \end{cases} \quad (3)$$

A partir de ces relations, les pentes sont exprimées en fonction de $q_x$, $q_y$ et $q_z$:

$$\begin{cases} \dfrac{\partial z'}{\partial x'} = -\dfrac{q_x}{q_z} \\ \dfrac{\partial z'}{\partial y'} = -\dfrac{q_y}{q_z} \end{cases} \quad (4)$$

L' hypothèse de stationnarité simplifie l'évaluation des quantités $\hat{n} \wedge \vec{E}$, $\hat{n} \wedge \vec{H}$ et élimine leur dépendance vis-à-vis des variables d'intégration. Ainsi pour une polarisation d'émission $q$ et une polarisation de réception $p$, les composantes du champ diffusé sont données par l'expression (5):

$$E^s_{pq} = K I_1 E_0 U_{pq} \quad (5)$$

avec:

$K = -\dfrac{jk\exp\{-jkR_0\}}{4\pi R_0}$,

$I_1 = \dfrac{q}{|q_z|} \iint \exp\{jq_x x' + jq_y y' + jq_z z(x', y')\}\, dx'\, dy'$

$q^2 = q_x^2 + q_y^2 + q_z^2$

$E_o$:module du champ incident,

$U_{pq}$: terme de polarisation,

$z(x, y)$ : surface aléatoire illuminée.

Une étude bistatique des coefficients de diffusion de la surface maritime nous a permis d'évaluer l'influence de la salinité, de la température et de la rugosité sur l'intensité du champ diffusé.

Sous cette approximation, seules les facettes ayant une orientation spéculaire vis-à-vis du faisceau incident diffusent. Dans le cas de la rétrodiffusion, seulement celles possédant une orientation perpendiculaire au faisceau incident contribuent. L'angle d'incidence locale (Fig 2.) est tel que $\theta_l = 0°$ ce qui implique:

$$\begin{aligned} Rv &= Re^{j\varphi_v} \\ Rh &= Re^{j\varphi_h} \end{aligned} \quad (6)$$

avec $R = |Rv(0)| = |Rh(0)|$.

Ainsi les termes de polarisation croisés sont nuls et les es coefficients de copolarisation ont la même amplitude .

L'influence du degré de rugosité se fait sentir sur le coefficient de rétrodiffusion de deux manières différentes (Fig 3.):

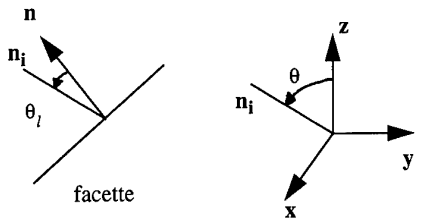


Fig 2.Orientation d'une facette - angle d'incidence locale

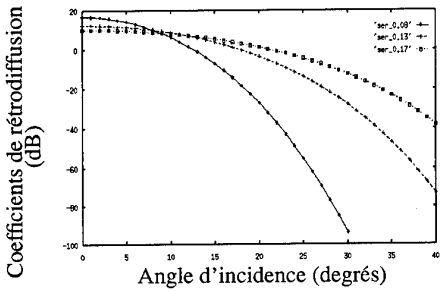


Fig 3.Coefficient de rétrodiffusion ($\sigma_{vv} = \sigma_{hh}$) en fonction de θ pour plusieurs états de mer - mer faible (ser_0.08), mer forte (ser_0.13) tempête (ser_0.17) - et pour une mer standard (Salinité S= 35 ppm et Température T= 20 °C) - Fréquence = 10 GHz

* pour une incidence normale θ inférieure à 10°, le coefficient de rétrodiffusion est maximal par mer plate et décroît quand la vitesse du vent augmente (*état de la mer*);

* pour θ supérieur à 10° la tendance s'inverse et le coefficient de rétrodiffusion augmente avec la vitesse du vent.

En incidence verticale, et par vent nul (*mer calme*), l'onde est réfléchie comme sur un miroir; quand le vent augmente, le nombre de facettes de réflexion spéculaire devient plus faible et le coefficient de rétrodiffusion diminue.

Pour θ supérieur à 10°, le nombre de facettes contribuant à une réflexion spéculaire augmente avec le vent, il en est de même pour le coefficient de rétrodiffusion.

Le comportement des coefficients de diffusion sous l'hypothèse de la phase stationnaire rejoint les résultats expérimentaux observés (Fig 4.et Fig 5.).

Pour la bande de fréquence utilisée (*8 à 20 GHz*), l'influence de la température, de la salinité et de la fréquence reste négligeable. En considérant des fréquences plus faibles (*inférieures à 1 GHz*), il devient nécessaire de prendre en

compte les variations de la salinité [4].

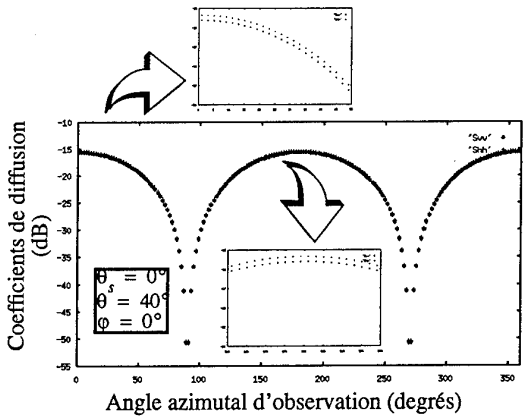


Fig 4.Coefficients de diffusion $\sigma_{hh}$ (Shh) et $\sigma_{vv}$ (Svv) en fonction de $\varphi_s$ pour une mer standard (T=20°C et S=35ppm) - pour une fréquence de 13.9 GHz et un état de mer faible à modéré - pour un angle d'incidence de 40°.

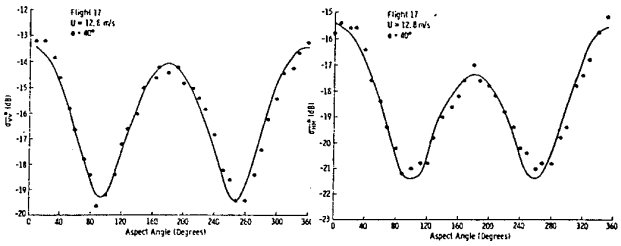


Fig 5.Coefficients de diffusion $\sigma_{hh}$ et $\sigma_{vv}$ en fonction de $\varphi_s$ pour $\theta = 40°$ (extrait de Fung 1979 [3])

Si le degré de rugosité diminue, la surface tend vers un plan. La méthode ne peut plus s'appliquer et commence à fournir des résultats erronés.

Une autre approche est alors nécessaire: c'est l'approximation scalaire.

*2.1.2. Optique physique -L'approximation scalaire*

Cette approche consiste à décomposer les termes de l'intégrale obtenue à partir de (1) dans *2.1.1.* autour des termes de pente nulle. Pour être valable, la surface doit posséder un rayon de courbure important et un écart-type des pentes faible par rapport à la longueur d'onde. Il faut également que les coefficients de Fresnel varient lentement par rapport à la surface. L'hypothèse d'un écart-type des pentes faibles simplifie l'expression de la normale locale à la surface. La dernière hypothèse permet un développement en série des coefficients de Fresnel au voisinage des pentes nulles. On montre dans ce cas que le champ diffusé s'écrit:

$$E^s_{pq} = KE_o \int \overline{U}_{pq} exp\{jQ\}\, ds' \tag{7}$$

Où $Q$ est la fonction de phase définie ci-dessus, les termes $\overline{U}_{pq}$ sont des fonctions de la géométrie de la diffusion, des coefficients de Fresnel modifiés et des pentes de la surface. On montre qu'ils peuvent être mis sous la forme

$$\overline{U}_{pq} = a_0 + a_1 Z_x + a_2 Z_y \tag{8}$$

où les $a_i$ dépendent de la polarisation. Les termes $Z_x$ et $Z_y$ désignent les pentes de la surface exprimées dans les directions $x$ et $y$.

Sous ces hypothèses et après simplification, les coefficients de diffusion peuvent être écrits comme la somme d'une composante cohérente (*terme* $\sigma^s_{pqc}$) et d'une composante diffuse (*termes* $\sigma^s_{pqn}$ *et* $\sigma^s_{pqs}$):

$$\sigma^s_{pq} = \sigma^s_{pqc} + \sigma^s_{pqn} + \sigma^s_{pqs} \tag{9}$$

Dans le cas d'une surface gaussienne d'écart-type $\sigma$ et de fonction de corrélation gaussienne de longueur de corrélation $l$, l'équation (9) se décompose ainsi:

$$\sigma^s_{pqc} = \pi k^2 |a_o|^2 \delta(q_x)\,\delta(q_y)\, exp\{-q_z^2\sigma^2\} \tag{10}$$

$$\sigma^s_{pqn} = \left(\frac{l}{2}\right)^2 \pi k^2 |a_o|^2 exp\{-q_z^2\sigma^2\} \cdot \sum_{n=1}^{\infty} \frac{(q_z^2\sigma^2)^n}{n!\,n} exp\left\{-\frac{(q_x^2+q_y^2)\,l^2}{4n}\right\} \tag{11}$$

$$\sigma^s_{pqs} = -(k\sigma)^2 \frac{q_z}{2} exp\{-q_z^2\sigma^2\}\, Re[a_0(q_x a_1^* + q_y a_2^*)] \cdot \sum_{n=1}^{\infty} \frac{(q_z^2\sigma^2)^{n-1}}{n!\,n} exp\left\{-\frac{(q_x^2+q_y^2)\,l^2}{4n}\right\} \tag{12}$$

Dans le cas d'une surface plane, le terme $q_z\sigma$ tend vers zéro, seule la composante cohérente (*ou spéculaire*) existe.

Quand le degré de rugosité augmente, la composante cohérente diminue au profit des composantes diffuses [5].

En comparant cette méthode à celle de la phase stationnaire, des résultats semblables sont obtenus (Fig 6.) notamment si les produits $k\sigma$ et $kl$ sont importants (*respectivement de l'ordre de 1.5, 22*).

Un comportement identique a été observé vis-à-vis de la température, la salinité et la fréquence.

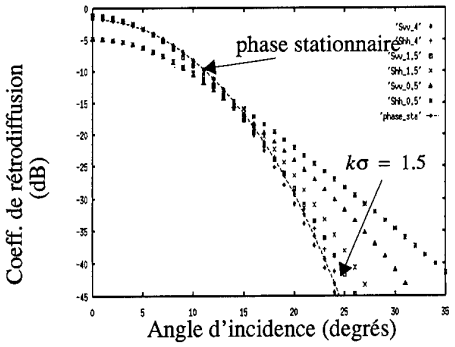


Fig 6.Coefficients de rétrodiffusion $\sigma_{hh}$ (Shh) et $\sigma_{vv}$ (Svv) en fonction de l'angle d'incidence $\theta$ pour, plusieurs valeurs de $k\sigma$, un degré de rugosité égale à 0.1 et une constante diélectrique égale à 1.6

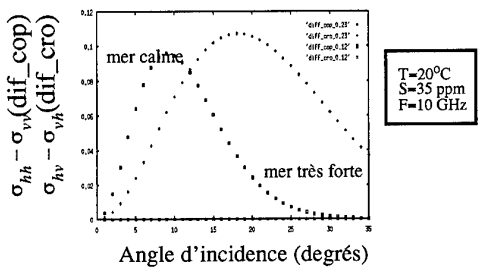


Fig 7.Différence entre les termes de polarisation croisés (diff-cro) et entre les termes copolarisés (diff-cop) en fonction de $\theta$, pour une mer standard, une fréquence de 10 GHz et pour deux états de mer: mer calme et mer très forte.

Néanmoins des différences ont été observées en ce qui concerne les termes copolarisés en rétrodiffusion: les termes $\sigma_{hh}$ et $\sigma_{vv}$ ne sont plus égaux (Fig 7.).

Cette différence est imputable au comportement des coefficients de réflexion de Fresnel qui ne varie plus "lentement" au voisinage de l'angle de Brewster.

De même en comparant les coefficients de diffusion, une différence existe entre les termes de polarisation croisés (*sous l'hypothèse de la phase stationnaire $\sigma_{hv}$ est toujours identique à $\sigma_{vh}$*).

Dans l'approximation de Kirchhoff, la dimension horizontale de la surface doit être plus grande que la longueur d'onde mais aucune restriction n'est imposée à l'écart-type de la surface.

Dans la première partie de ce paragraphe (*approximation de la phase stationnaire*), on a supposé que le degré de rugosité est important. Dans la seconde partie, l'approximation scalaire à été présentée, elle permet de traiter des surfaces possédant des pentes faibles.

L'approximation de Kirchhoff doit être complétée par la méthode des petites perturbations.

**2.2 Méthode des petites perturbations**

La méthode des petites perturbations est basée sur l'hypothèse que les champs diffusés et transmis par ou à travers une surface rugueuse, peuvent être représentés par une superposition d'ondes planes d'amplitude inconnue se propageant vers le récepteur.

Cette représentation, connue aussi sous le nom de l'approximation de Rayleigh, repose sur l'hypothèse d'une variation des hauteurs de la surface faible vis-à-vis de la longueur d'onde. Il est alors possible d'écrire le champ diffusé sous forme de série. Sous cette hypothèse et en utilisant les conditions aux limites, les amplitudes inconnues des champs sont déterminées.

Compte-tenu des hypothèses faites, cette méthode est seulement applicable à des surfaces peu rugueuses.

Le développement est souvent limité au premier ordre à cause de la complexité des calculs pour les ordres supérieurs.

Cette technique est valable pour des incidences plus importantes contrairement aux deux techniques précédentes.

Les coefficients de diffusion (*au premier ordre*) s'écrivent [6]:

$$\sigma_{pq}^{s} = 8\left|k^2\sigma\cos\theta\cos\theta_s\alpha_{pq}\right|^2 W(k_x + k\sin\theta, k_y) \qquad (13)$$

avec:

$$W(k_x, k_y) = \frac{1}{2\pi}\int_{-\infty}^{\infty}\int \rho(u,v)\,exp\{-j(k_x u + k_y v)\}\,dudv,$$

$\rho$: fonction de corrélation de la surface,

$\alpha_{pq}$: terme de polarisation.

Une étude bistatique des coefficients de diffusion de la surface océanique nous a permis de mesurer l'influence de la salinité, de la température et de la rugosité sur l'intensité du champ diffusé.

Ainsi, nous avons constaté que le coefficient de rétrodiffusion n'est significatif que pour des angles d'incidence supérieure à 20°. Les termes copolarisés $\sigma_{hh}$ et $\sigma_{vv}$ sont différents. Les termes de polarisations croisées sont nuls (*approximation d'ordre 1*).

L'augmentation de l'état de mer provoque un accroissement des coefficients de rétrodiffusion (Fig 8.). Elle modifie également la pente de ces coefficients vis-à-vis de $\theta$: une mer

forte entraîne une décroissance plus rapide de $\sigma_{pp}$ que pour une mer faible. En polarisation horizontale ce phénomène est plus important.

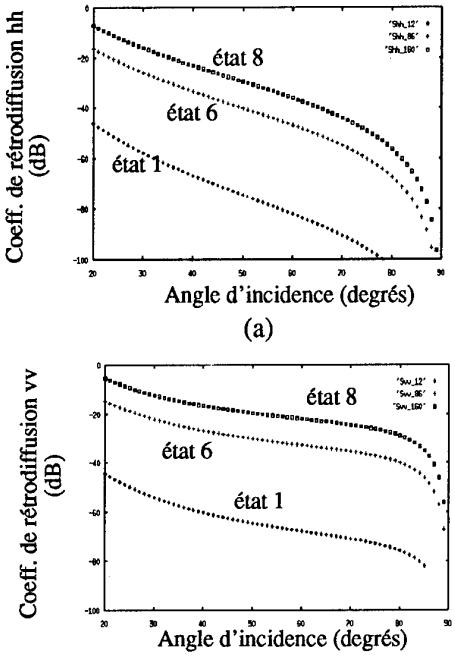


Fig 8.Coefficients de rétrodiffusion (- (a) - $\sigma_{hh}$ et - (b) - $\sigma_{vv}$ ) en fonction de $\theta$ pour plusieurs états de mer - mer faible (état 1 - U*=12 cm/s), mer forte (état 6 -U*=86 cm/s) tempête (état 8 - U*=160 cm/s) - et pour une mer standard (Salinité S= 35 ppm et Température T= 20 °C) - Fréquence = 10 GHz

L'influence de la température est importante sur le coefficient $\sigma_{vv}$ pour des angles d'incidences rasantes (Fig 9.). Elle reste négligeable en polarisation horizontale.

Le même phénomène est observé vis-à-vis de la salinité, mais son influence est très faible (*inférieur à 7 °/o*) pour des fréquences supérieures à 4 GHz.

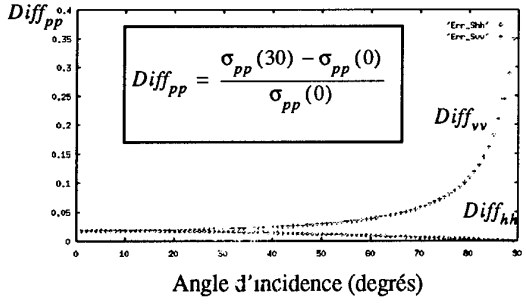


Fig 9.Influence de la température sur les coefficients de rétrodiffusion en fonction de $\theta$ pour une mer forte (état 6), deux températures T=0°C et T=30°C - salinité S=35ppm - Fréquence = 10 GHz

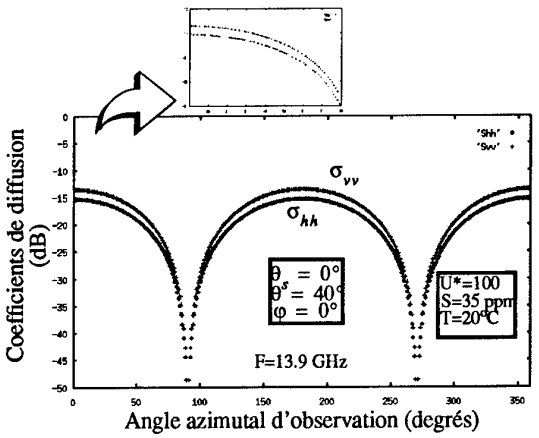


Fig 10.Coefficients de diffusion $\sigma_{hh}$ (Shh) et $\sigma_{vv}$ (Svv) en fonction de $\varphi_s$ pour une mer standard (T=20°C et S=35ppm) - pour une fréquence de 13.9 GHz un vent de fricition de 100 cm/s et un angle d'incidence de 40°.

Le comportement des coefficients de diffusion sous l'hypothèse de la méthode des petites perturbations (Fig 11.) rejoint les résultats expérimentaux observés.

L'influence de l'angle d'observation $\theta_s$ et la constante diélectrique $\varepsilon_r$ est notable en propagation avant [5].

La fréquence et l'état de la mer modifient l'amplitude des coefficients de diffusion. Leur influence est plus importante en rétrodiffusion.

## 3. COMPORTEMENT POLARIMÉTRIQUE

L'exploitation de l'information polarimétrique véhiculée par les ondes électromagnétiques a longtemps été négligée au profit d'informations purement scalaires. Mais depuis un certain nombre d'années, on assiste à une augmentation des recherches dans ce domaine, notamment, dans le domaine du radar.

Dans la première partie de ce paragraphe, la signature polarimétrique de surface rugueuse est présentée ainsi que la typologie des courbes obtenues dans le cas de plusieurs modèles théoriques de diffusion (*méthode de Kirchhoff, méthode des petites perturbations*) et pour diverses géométries d'observations (*étude bistatique*). Dans la dernière partie, une méthode d'optimisation polarimétrique est présentée pour augmenter la fiabilité d'une liaison hertzienne ou accroître la discrimination d'une cible radar.

Une onde électromagnétique plane est caractérisée par sa polarisation décrite par la trajectoire (Fig 12.) de son vecteur champ électrique dans un plan tranverse à sa direction de propagation (*plan d'onde*).

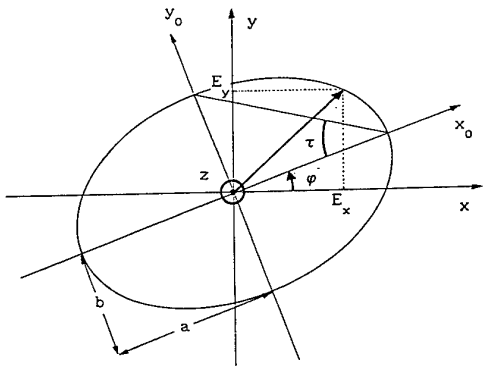


Fig 11.La polarisation d'une onde est définie par les paramètres $\phi$ (*orientation*) et $\tau$ (*ellipticité*) de son ellipse de polarisation.

Quand une cible radar est illuminée, l'onde diffusée possède un état de polarisation qui porte de l'information sur la nature du diffuseur (*signature polarimétrique*).

Une cible radar se comporte comme un modificateur de polarisation; le changement de polarisation au niveau de l'objet est décrit par une relation matricielle.

Dans le cas d'une cible canonique, la matrice de diffusion [S] décrit la relation linéaire amplitude/phase entre l'onde diffusée $E^s$ et l'onde incidente $E^i$.

$$E^s = [S]E^i \tag{14}$$

Si l'onde diffusée par la cible n'est pas monochromatique, les composantes du champ reçu peuvent être considérées comme des variables aléatoires résultant d'une sommation incohérente de l'ensemble des diffuseurs contenus dans la zone éclairée. Dans ce cas la matrice [S] perd sa signification. Il est nécessaire d'utiliser une représentation en puissance, la plus usuelle est la matrice de Mueller moyenne $\langle [M] \rangle$. Il est possible de montrer que la matrice $[M]$ est liée à la matrice de diffusion $[S]$. On peut dire qu'à chaque matrice $[S]$ correspond une matrice de Mueller $[M]$, mais, l'application n'est pas bijective.

Il existe des cas (*diffusion par une surface aléatoire*) qui ne peuvent être décrits par une transformation du type (14) quoique descriptible par la matrice de Mueller.

### 3.1. Signature polarimétrique

La matrice de Mueller moyenne $\langle [M] \rangle$, résultant d'un moyennage temporel des mesures, est caractéristique de la cible. Elle dépend de la géométrie d'observation, de la fréquence, des paramètres physiques et comportementaux de la cible mais elle est indépendante de l'état de polarisation de l'onde incidente et de l'onde reçue.

La signature polarimétrique [2] d'une cible représente la variation de la puissance diffusée en fonction des différentes combinaisons des états de polarisation choisis à l'émission et à la réception.

#### *3.1.1. Phase stationnaire*

La matrice de Mueller est construite à partir d'une matrice qui matérialise la dépolarisation. Il est possible d'extraire un terme constant multiplicatif $C_1$ de la matrice de Mueller. Dans cette constante apparait l'influence du degré de rugosité de la surface. De ce fait, la signature polarimétrique d'une surface est indépendant (*dans le cas de cette méthode*), de l'agitation du milieu éclairé. Quel que soit l'état de la mer, la signature polarimétrique est identique car elle est normalisée.

Le terme $C_1$ s'exprime ainsi:

$$C_1 = \frac{(kE_o)^2}{(4\pi R_0)^2} \cdot \frac{2\pi A_o q^2}{q_z^4 \sigma^2 |\rho''(0)|} exp\left\{ -\frac{q_x^2 + q_y^2}{2q_z^2\sigma^2|\rho''(0)|} \right\} \tag{15}$$

#### *3.1.2 Approche scalaire*

La matrice de Mueller se construit à partir des coefficients de polarisation $a_i$ et des coefficients de Fresnel modifiés. Comme précédemment, il est possible de faire apparaître un terme constant en facteur:

$$\langle E_{pq} E_{uv}^* \rangle = C_2 (a_i a_j^*) \tag{16}$$

$C_2$ est une constante qui dépend de l'aire éclairée, de la géométrie de la diffusion et du degré de rugosité de la surface.

Dans le cas d'une surface gaussienne d'écart-type $\sigma$ et de fonction de corrélation gaussienne de longueur de corrélation $l$, cette constante s'exprime ainsi:

$$C_2 = \frac{(kE_o)^2}{16\pi R_o^2} A_o l^2 exp\{-(q_z\sigma)^2\} \cdot \sum_{n=1}^{\infty} \frac{(q_z\sigma)^{2n}}{n!\,n} exp\{-\frac{(q_x^2 + q_y^2) l^2}{4n}\} \tag{17}$$

La rugosité de la surface module donc globalement l'ensemble des termes de la matrice de Mueller

#### *3.1.3 Méthode des petites perturbations*

La matrice de Mueller se construit à partir des termes $\langle E_{pq} E_{uv}^* \rangle$. Pour une géométrie et un type de surface fixé, l'intensité $\langle E_{pq} E_{uv}^* \rangle$ est proportionnelle aux termes de polarisation:

$$\langle E_{pq} E_{uv}^{*} \rangle = C_3 (\alpha_{pq} \alpha_{uv}^{*}) \quad (18)$$

Le coefficient $C_3$ est une constante qui dépend de la rugosité et de la surface ainsi que de la géométrie de la diffusion.

$$C_3 = \frac{2A_o (E_o)^2}{4\pi R_o^2} (k^2 \sigma \cos\theta \cos\theta_s)^2 W(k_x + k\sin\theta, k_y) \quad (19)$$

### 3.2. Application

Nous allons étudier dans ce paragraphe, les variations de la puissance diffusée en fonction de la surface (*paramètre physique et géométrique*) et de la polarisation de l'antenne de réception.

L'analyse de ces variations nous permet de trouver une polarisation optimale de l'antenne de réception afin de minimiser la puissance diffusée par la surface de la mer. Pour cela considérons une antenne de réception avec des éléments ajustables qui permettent de régler l'état de polarisation de l'antenne (*notamment l'orientation $\phi_{re}$ de sa base de polarisation -Fig. 12*). La géométrie du site est fixée $(\theta, \theta_s, \varphi, \varphi_s)$.

Le vecteur de Stockes $g_{re}$ associé à la polarisation de l'antenne peut être exprimé en fonction du vecteur de Stockes $g_r$ associé à l'onde incidente reçue par l'antenne:

$$g_{re} = [T_{re}] g_r \quad (20)$$

Avec:

$$[T_{re}] = \begin{bmatrix} 1 & 0 & 0 & 0 \\ 0 & \cos 2\phi_{re} & -\sin 2\phi_{re} & 0 \\ 0 & \sin 2\phi_{re} & \cos 2\phi_{re} & 0 \\ 0 & 0 & 0 & -1 \end{bmatrix} \quad (21)$$

La puissance reçue s'exprime ainsi:

$$P = \frac{1}{2} g_{re}^T [M]^T g_r = \frac{1}{2} g_r^T [T_{re}]^T [M]^T g_r \quad (22)$$

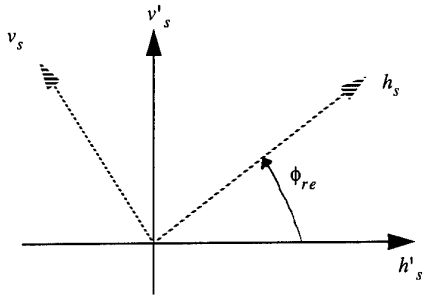


Fig 12.Base de polarisation de l'antenne de réception

On cherche alors à minimiser cette puissance. Les extremums vis-à-vis de $\phi_{re}$ sont obtenus en calculant la dérivée $\frac{dP}{d\phi_{re}}$, ce qui laisse entrevoir un calcul fastidieux.

Compte-tenu de la remarque précédente, c'est-à-dire que l'ensemble des paramètres $\langle S_{pq} S_{uv}^{*} \rangle$ suivant la même évolution en fonction du degré de rugosité. On constate que quelque soit l'état de la mer, la puissance minimale est toujours obtenue pour le même état de polarisation de l'antenne de réception.

L'influence de la constante diélectrique (*c'est à dire de la variation de la température et de la salinité de la surface de la mer*) reste très faible dans la bande de fréquence 8-20 GHz.

Sur La figures 13 est présenté un exemple de recherche de minimum $(\phi_{re})_{min}$ pour une géométrie donnée. Elle montre la variation de la puissance diffusée en fonction de l'angle $\phi_{re}$.

### 3.3. Résultats

Les figures 14,15 et 16 représentent la variation de la puissance diffusée par la mer, en fonction des différentes combinaisons des états de polarisation choisis à l'émission et à la réception, pour différents modèles théoriques de diffusion.

Chaque figure est obtenue pour un angle d'incidence et d'observation de 20° et une mer standard (*salinité $S = 35ppm$ et température $T = 20°C$*).

Si nous comparons les trois modèles, nous observons des résultats comparables pour l'approche scalaire et la méthode des petites perturbations. Ces deux méthodes ont des conditions de validité proche (*surface peu rugueuse*) bien qu'elles ne soient pas applicables pour une même plage d'incidence.

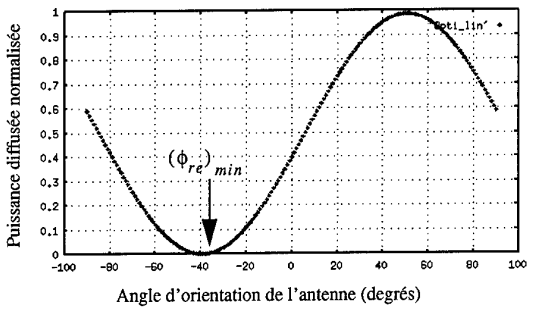


Fig 13.Puissance diffusée normalisée reçue par l'antenne dans le cas des petites perturbations en fonction de l'angle d'orientation de l'antenne de réception $\phi_{re}$ - Mer standard ($T = 20°$, $S = 35ppm$) et pour $\varphi = 0°$, $\varphi_s = 60°$, $\theta = 30°$ et $\theta_s = 60°$ - Polarisation incidente linéaire à 22, 25°

La méthode de la phase stationnaire présente un comportement différent. La signature co-polarisé (*même état de polarisation à l'émession et à la réception*) est peu influencée par l'angle d'azimut $\varphi_s$. Pour un angle d'incidence et d'observation de 20°, la surface se comporte comme une plaque. Néanmoins pour $\varphi_s$ = 90°, un maximum de puissance est observé pour un état de polarisation vv. Le minimum est toujours observé pour un état de polarisation circulaire. La signature cross-polarisée (*état de polarisation à l'émetteur et au récepteur orthogonal*) présente un comportement étrange pour des angles $\varphi_s$ proche de 90°. Dans ce cas, l'énergie est répartie de façon uniforme (Fig 14-f2) dans le plan $(\tau, \phi)$, c'est-à-dire qu'elle est indépendante de l'état de polarisation.

Les Figures 15 et 16 sont comparables sauf dans le cas de la rétrodiffusion (*Fig.15.a1 et Fig.16.a1*). Ainsi un maximum de puissance est observé pour une polarisation vv avec la méthode des petites perturbations, tandis que ce maximum correspond à une polarisation hh dans le cas de l'approche scalaire. Le minimum de puissance correspond toujours à des états de polarisation circulaire

## 4. CONCLUSION

Dans cet article, deux approches pour calculer l'intensité du champ diffusé, ont été développées: la méthode des petites perturbations et l'approximation de Kirchhoff. Cette dernière suppose qu'en tout point de la surface, le profil peut être remplacé par un plan tangent infini en ce point, ce qui impose implicitement un rayon de courbure grand devant la longueur d'onde en chaque point de la surface.

Deux approximations peuvent être faites pour la résolution de ce problème: la solution de l'optique géométrique, dite également phase stationnaire et celle de l'optique physique, dite approximation scalaire.

L'approximation de la phase stationnaire repose sur l'hypothèse que le champ diffusé provienne uniquement des points spéculaires, ce qui se traduit mathématiquement par une condition de stationnarité sur la phase. L'énergie alors diffusée est proportionnelle à la probabilité d'avoir des pentes réfléchissantes de façon spéculaire. Cette approximation nous a permis de calculer théoriquement, puis numériquement, les coefficients de la matrice de diffusion bistatique. On montre que ces coefficients ne dépendent que des pentes de la surface.

L'approximation scalaire est basée sur un écart-type des pentes faibles vis-à-vis de la longueur d'onde et sur des variations lentes des coefficients de Fresnel par rapport à leur position sur la surface.

L'approximation de Kirchhoff est complétée par la méthode des petites perturbations, cette technique impose deux conditions: l'écart type de la surface et la longueur de corrélation doivent être faibles devant la longueur d'onde. Ainsi les champs peuvent être développés en série de Fourier dont les coefficients à l'ordre n sont déterminés par les conditions aux limites.

Pour chaque méthode, une étude bistatique des coefficients de diffusion de la surface océanique nous a permis de mesurer l'influence de la salinité, de la température et de la rugosité sur l'intensité du champ diffusé.

Une étude polarimétrique nous a permis de montrer que les éléments de la matrice de Mueller sont tous influencés de la même façon par le degré de rugosité de la surface. La différence d'évolution entre ces coefficients est à attribuée á la constante diélectrique de la surface et à la géométrie de la diffusion. Cette différence se traduit par une modification de la typologie et de la topologie des signatures polarimétriques.

Cette remarque parait étonnante, en effet l'indépendance de la signature polarimétrique vis-à-vis de la rugosité tend à montrer que la rugosité globalement ne dépolarise pas. Elle provoque uniquement une modulation globale de l'amplitude des termes de la matrice de Mueller. Les seuls éléments dépolariseurs sont la constante diélectrique du milieu et la géométrie de la diffusion.

Nous avons montré qu'il est possible, quelles que soient les conditions de validité de minimiser les effets de diffusion dus à la mer. La polarisation linéaire optimum est une fonction qui semble ne dépendre que seulement de la géométrie de la diffusion.

## 5. REMERCIEMENTS

Les auteurs souhaitent exprimer leur remerciement au CELAR (*Centre Electronique de L'ARmement, Division GEOS/SOP, Bruz, France*) pour son soutien.

## 6. REFERENCES

[1] F.T.Ulaby, R.K.Moore, A.K.Fung, "Microwave remote sensing - Active and passive", vol. II, Adison-Wesley publishing company, 1982.

[2] C. Elachi, J.J. Van Zyl, H.A. Zebker, "Imaging radar polarization signatures - Theory and observation", Radio Sciences, vol 22, N 4, pp 529-543, July-August 1987.

[3] R.K.Morre, A.K.Fung, "Radar determination of wind at sea", Proceedings of the IEEE, vol. 67, No 11, pp 1504-1521, November 1979.

[4] F.Daout, A.Khenchaf, J.Saillard, "The effect of salinity and temperature on the electromagnetic field scattered by sea water", Ocean'94 Osates, Brest, 13-16 September 94.

[5] A.Khenchaf, F.Daout, J.Saillard, "Champ diffusé par une surface rugueuse: lien entre le champ moyen, les composantes cohérentes et incohérentes", JINA 94, Nice, November 8-10 1994.

[6] F.Daout, A. Khenchaf, J.Saillard, 'Diffusion d'une onde électromagnétique par la surface océanique', D.G.A., C.E.L.A.R. , Convention N 01/3/SA.AR, juin 1994.

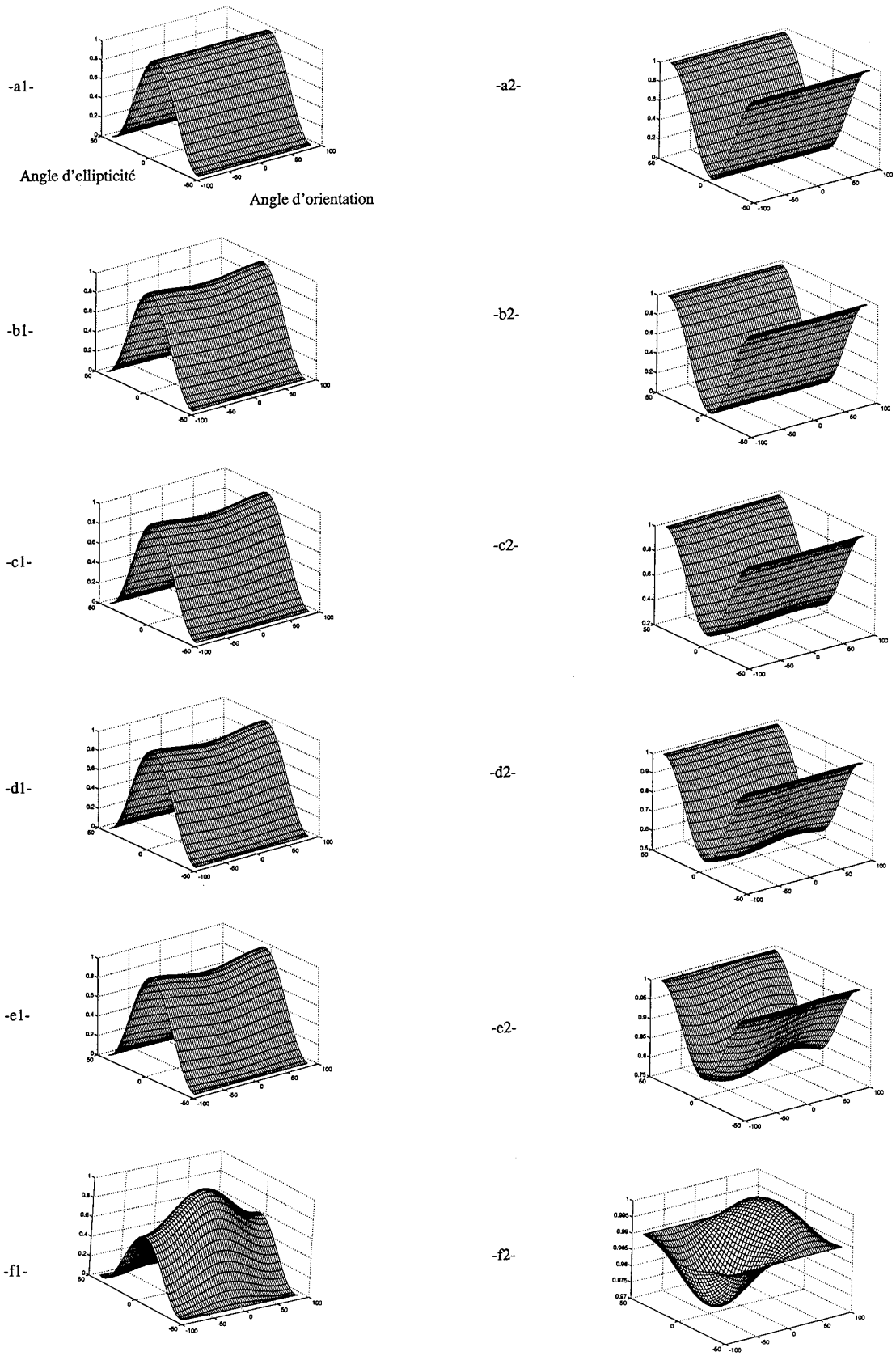


Fig.14. Signature polarimétrique théorique de la surface de la mer ($T = 20°$, $S = 35ppm$)- méthode de la phase stationnaire -(1) signature co-polarisée, (2) signature cross-polarisée - Angle d'incidence et d'observation $\theta = \theta_s = 20° - \varphi = 0°$ - (a) $\varphi_s = 180°$ (rétrodiffusion), (b) $\varphi_s = 0°$ (propagation avant), (c) $\varphi_s = 30°$, (d) $\varphi_s = 45°$, (e) $\varphi_s = 60°$, (f) $\varphi_s = 90°$.

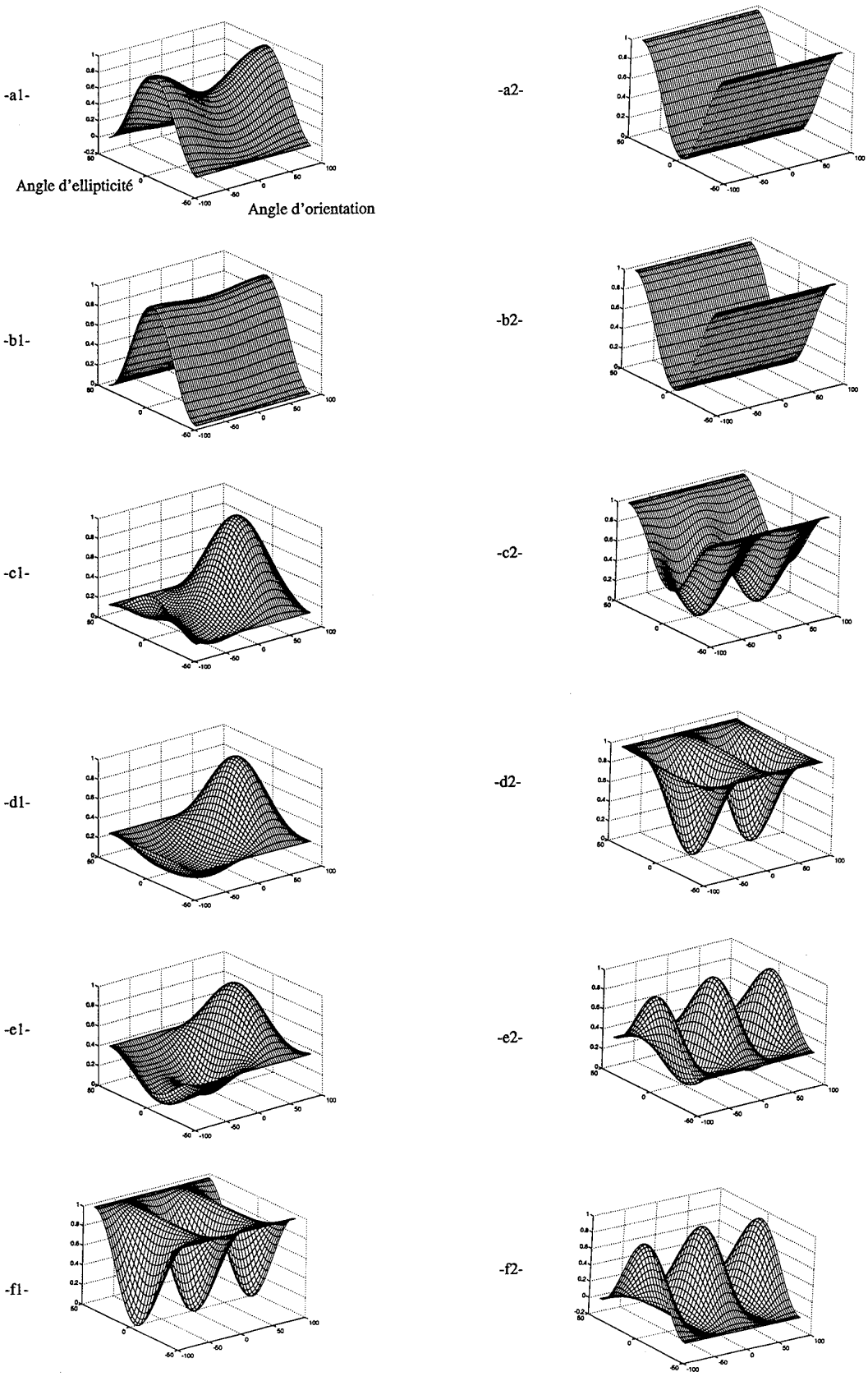


Fig.15. Signature polarimétrique théorique de la surface de la mer ($T = 20°$, $S = 35ppm$)- méthode scalaire -(1) signature co-polarisée, (2) signature cross-polarisée - Angle d'incidence et d'observation $\theta = \theta_s = 20°$ - $\varphi = 0°$ - (a) $\varphi_s = 180°$ (rétrodiffusion), (b) $\varphi_s = 0°$ (propagation avant), (c) $\varphi_s = 30°$, (d) $\varphi_s = 45°$, (e) $\varphi_s = 60°$, (f) $\varphi_s = 90°$.

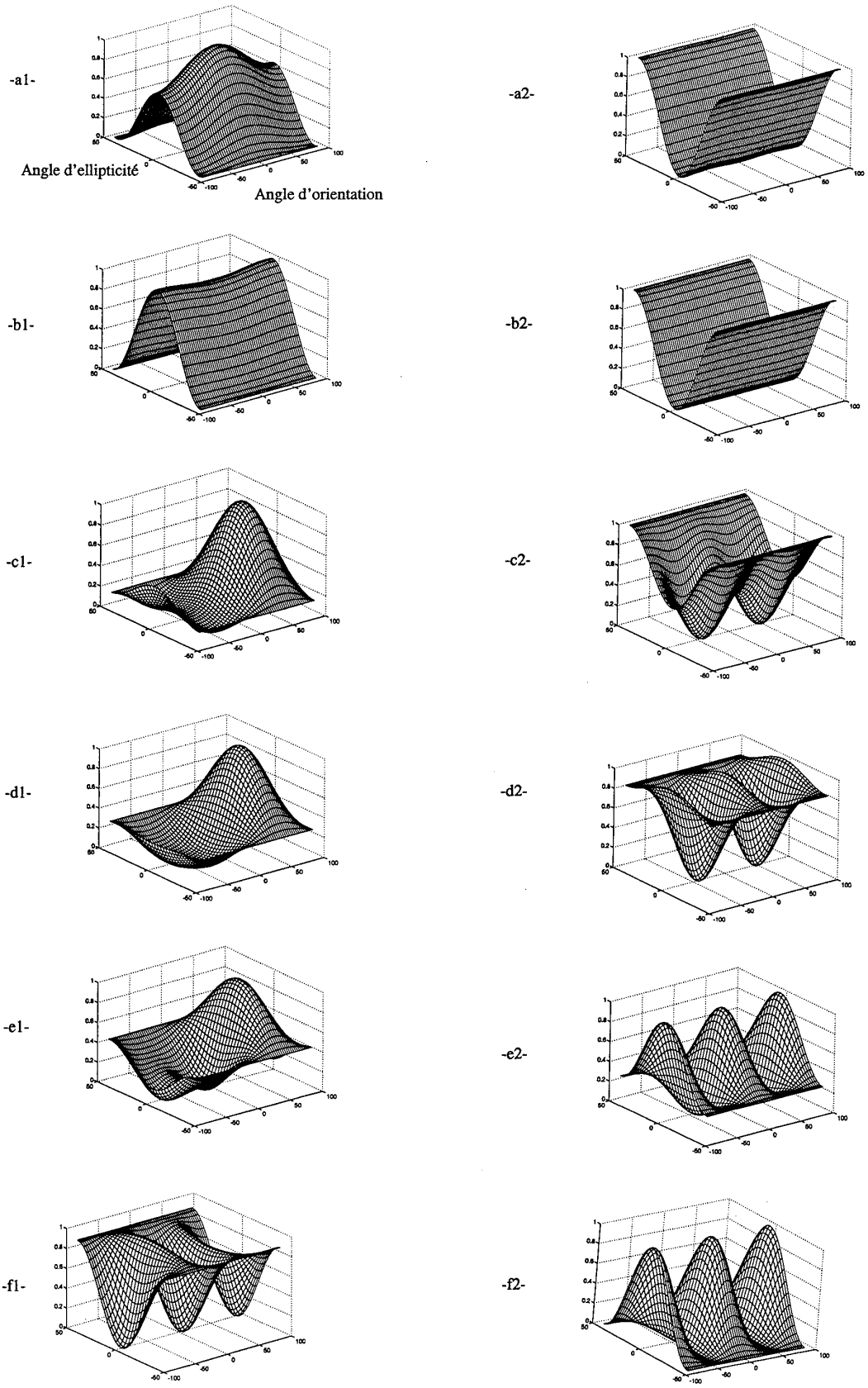


Fig.16. Signature polarimétrique théorique de la surface de la mer ($T = 20°$, $S = 35ppm$)- méthode des petites perturbations -(1) signature co-polarisée, (2) signature cross-polarisée - Angle d'incidence et d'observation $\theta = \theta_s = 20° - \varphi = 0°$ - (a) $\varphi_s = 180°$ (rétrodiffusion), (b) $\varphi_s = 0°$ (propagation avant), (c) $\varphi_s = 30°$, (d) $\varphi_s = 45°$, (e) $\varphi_s = 60°$, (f) $\varphi_s = 90°$.

## DISCUSSION

**E. SCHWEICHER**

Quand vous avez parlé des 3 conditions aux limites, vous avez dit qu'elles vous fournissaient 6 équations permettant de trouver 6 inconnues. Or je ne trouve que 5 équations: chacune des 2 équations avec produits vectoriels me donne 2 équations scalaires et la divergence me donne une équation, ce qui me fournit 5 équations en tout et pas 6 équations. Où est mon erreur?

*When you spoke about the 3 boundary conditions, you stated that those conditions give you 6 equations to determine the 6 unknowns. I only find 5 equations, because each of the 2 equations including vectorial products give me 2 scalar equations while the divergence equation gives me a single equation. Therefore, I have 5 equations and 6 unknowns. Where is my error?*

**AUTHOR'S REPLY**

Le champ sur la surface est calculé sur la partie supérieure de l'interface et sur le domaine inférieur. Le relation de divergence nous fournit donc deux équations. (Une sur le milieu supérieur et une sur le domaine inférieur).

*The field at the surface is calculated above and below the interface. The divergence relation furnishes two equations (one equation for the medium above and one equation for the medium below).*

# ATMOSPHERIC DATA RESOLUTION REQUIREMENTS FOR PROPAGATION ASSESSMENT: CASE STUDIES OF RANGE-DEPENDENT COASTAL ENVIRONMENTS

**G. Daniel Dockery**
**Julius Goldhirsh**

The Johns Hopkins University, Applied Physics Laboratory
Johns Hopkins Road
Laurel, Maryland 20723-6099, U.S.A

## 1. ABSTRACT

With the proliferation of efficient, accurate, range-dependent propagation models, the largest remaining challenge in shipboard environmental assessment is obtaining high-resolution atmospheric data for use in these models. Due to the difficulty of acquiring data in all directions from a ship, it is particularly important to establish what horizontal separation between atmospheric profiles is adequate for accurate shipboard assessment. It is equally important to determine the minimum acceptable resolution in the vertical direction. In order to begin to investigate these spatial sampling requirements, this paper examines two sets of high-resolution atmospheric data collected along the east and west coast of the U.S. These data were collected by an instrumented helicopter in support of U.S. Navy propagation experiments and tests. The sampling necessary to represent significant atmospheric structures is discussed, and an accurate propagation model is used to examine the sensitivity of propagation predictions to vertical and lateral data resolution. Results are presented for 3 and 10 GHz to examine the frequency dependence of resolution effects.

## 2. INTRODUCTION

The basic impacts of environmental conditions on the operation of shipboard radiating systems have been understood for some time (Refs. 1-4), and methods to model these effects, particularly those associated with atmospheric refractivity, are now relatively mature (Refs. 5-9). In fact, there is an apparent consensus among organizations working on environmental assessment for naval applications that microwave propagation in near-horizontal directions should be represented using the parabolic wave equation (PE) solved with a suitable numerical technique, such as Fourier split-step or implicit finite difference algorithms. This approach has been demonstrated to provide excellent agreement with measured signal levels when sufficient atmospheric refractivity data are available for use in the PE algorithm (Refs. 10 and 11).

With the successful development of accurate propagation models, the challenge has shifted to obtaining the high-resolution, in situ atmospheric data necessary for effective system performance predictions. The most serious difficulties in this area arise from the need to accurately characterize horizontal variations in the refractive environment because this necessitates acquiring data at multiple ranges and azimuths, as well as at several heights. Potential methods of obtaining information about horizontal variations include frequent flights by aircraft (manned or remotely piloted) equipped with atmospheric sensors or dropsondes (Ref. 12), or using three-dimensional remote sensing techniques (e.g., radar or laser sounding) from surface ships, aircraft, or satellites (Refs. 13-16). Currently, however, each of these approaches is plagued by either logistic or technological limitations, and the impact of these limitations is directly related to the spatial and temporal measurement resolution required by a given propagation assessment application.

The goal of this paper is to provide an initial study of the sensitivity of propagation estimation accuracy to atmospheric data resolution. This is a difficult topic to address in a general manner because the sensitivity of propagation predictions will depend on the source-observer geometry, radiated frequency, and type of atmospheric condition. Furthermore, criteria for acceptable propagation prediction accuracy will depend strongly on the function of the system for which the predictions are made. The question of "adequate resolution" is thus treated in a relative sense in this study.

## 3. ATMOSPHERIC REFRACTIVE CHARACTERISTICS

Atmospheric refractive conditions are frequently described by fitting them into one of the following categories: standard refraction (often represented as an effective earth radius of 4/3 times the physical earth radius), subrefraction (shortened horizon relative to standard), superrefraction (extended horizon), surface ducting, and elevated ducting. Generally, the smallest and most severe refractive structures are associated with surface ducting, so these conditions will be the focus of the present atmospheric data resolution study. It is assumed that data requirements that support ducting characterization will also support accurate characterization of the other conditions mentioned above.

It is convenient to represent atmospheric refractive conditions in terms of vertical profiles of modified refractivity, M, which is related to the usual refractive index, n, as follows:

$$M = (n - 1 + z/a_e) \times 10^6$$

where z is the altitude and $a_e$ is the physical earth radius. Using this quantity, ducting or trapping layers are immediately identified as regions where the vertical derivative of M is negative. In contrast, a standard atmosphere exhibits a vertical M-gradient of +118/km.

Surface ducting refers to any refractive condition that traps energy (i.e., rays) over extended ranges in proximity of the earth's surface. There are two basic categories of surface ducting: those caused by evaporation just above the sea surface, and those resulting from humidity trapped below a stable temperature inversion. In this paper, the former will be referred to as evaporation ducts and the latter termed (rather arbitrarily) surface-based ducts.

Evaporation ducts are small (typically less than 30 meters high) but persistent features of the marine environment, which can

*Paper presented at the Sensor and Propagation Panel Symposium on "Propagation Assessment in Coastal Environments" held in Bremerhaven, Germany 19-22 September 1994.*

have substantial impacts on propagation at frequencies above 1 GHz. These ducts are rarely determined directly via standard methods for measuring a vertical refractivity profile due to the statistical nature of the duct. Rather, evaporation duct refractivity profiles are typically calculated using a few simple measurements (e.g., air temperature, relative humidity, wind speed, and sea surface temperature) in a meteorological model (Refs. 17 and 18). Although accurate characterization of the evaporation duct is important, this study will focus on the surface-based duct as this condition is likely to have more severe data resolution requirements. Future work will address measurement accuracy and resolution requirements for evaporation duct characterization.

Surface-based ducts occur when a stable atmospheric condition results in a temperature inversion and a sufficient amount of water vapor is trapped below that inversion. This condition causes a rapid decrease in refractive index with increasing height leading to waveguide-like trapping. It is also possible for a stable atmosphere in the presence of higher-altitude moisture to cause the water vapor content and refractive index to increase with altitude, resulting in extreme subrefraction (Ref. 19). Although temperature inversions are often referred to as the characterizing feature of surface-based ducts, it is the humidity gradient that dominates microwave refractivity.

As will be demonstrated below, surface-based ducts often exhibit features that vary rapidly with height, and important structures may occupy only a small height region. At the same time, the shape and height of refractive structures may vary substantially with range, particularly in coastal regions. Finally, refractive conditions can change rapidly in time, either due to diurnal variations or to the movement of weather fronts. These are the characteristics that will drive atmospheric data resolution requirements. Measurement requirements in surface-based ducting conditions will be the subject of the remainder of this paper, although discussion of temporal variability is deferred to future papers.

## 4. REFRACTIVITY DATA BASE

Since 1984, JHU/APL has collected thousands of atmospheric profiles during propagation experiments and in support of U.S. Navy exercises. The majority of these data have been obtained using a civilian helicopter equipped with atmospheric sensors which collect temperature, pressure, humidity versus altitude, and a dual-antenna radar altimeter to measure altitude accurately (Ref. 12). Altitude is measured accurately using a dual-antenna radar altimeter. The atmospheric sensors are mounted forward, under the nose of the helicopter in a reverse-flow probe; a minimum forward airspeed of 110 km/h has been determined to be sufficient to keep the probe out of the down-wash from the helicopter rotor.

During experiments, the measurement procedure involves executing helicopter flights along the propagation path between the radiating sensor of interest and the receiver or calibrated reflector. A "sawtooth" pattern in altitude is flown with data being recorded at a 2-Hz rate on each descent. This data rate, and a descent rate of 100 to 150 meters per minute, results in data being recorded nominally every 1 meter in altitude. Also, profile altitudes of 150 to 450 meters result in average range separations between atmospheric profiles of 3.5 to 11 km. Due to possible variabilities in time, every attempt is made to collect atmospheric data within 30 minutes of any signal measurement.

## 5. METHODOLOGY

### 5.1. Atmospheric Data Processing and Propagation Calculations

Data collected in the above manner, when used in conjunction with evaporation duct information and propagation and system performance models, have provided excellent agreement with observed signal levels and system performance (e.g., Ref. 10). For this reason, these helicopter-acquired atmospheric data will be taken as the baseline, or "ground truth" for this study. This is equivalent to assuming that the helicopter measurements have sampled the atmosphere on a fine enough grid to support perfect reconstruction of propagating signals. Of course, reconstructions using these data are not perfect due to fine scale atmospheric fluctuations and temporal variability, but analyses of experiments such as those described in Refs. 10 and 11 have demonstrated typical low-altitude signal prediction to within 5 dB for ranges as large as 75 km.

One critical step in generating propagation predictions using measured helicopter data is the use of an atmospheric data conditioning algorithm to filter out small-scale fluctuations and construct a physically reasonable range-interpolation between adjacent refractivity profiles. The algorithm used in this study is called LARRI (Large-scale Atmospheric Refractivity Range Interpolator), and it is described in more detail in Ref. 10. LARRI automatically performs the following steps: (1) smooths the individual refractivity profiles, (2) extrapolates to the surface and to a user-specified height if necessary, (3) fits line segments to the smoothed profiles, (4) identifies and categorizes profile structures, (5) finds best possible match of refractivity structures between adjacent profiles, and (6) interpolates between profiles while preserving matched structures. LARRI is used routinely in the analysis of test data to prepare helicopter measurements for use in propagation models; examples illustrating LARRI's operation are included below.

The propagation model used here is called TEMPER (Tropospheric Electromagnetic Parabolic Equation Routine), which is based on the Fourier split-step numerical solution of the parabolic wave equation (Refs. 5 and 6). TEMPER is also a routine part of JHU/APL's post-test analysis procedure, and has been extensively validated against measured data and other propagation models. Parabolic equation models, such as TEMPER, are the only models that have thus far demonstrated robust performance in complicated range-varying refractive environments.

The methodology used in this paper is to choose two sets of helicopter data collected in coastal environments, and to exercise LARRI and TEMPER using these data; this establishes a baseline propagation factor for a hypothetical radiating system operating in the chosen environments. Results are presented for frequencies of 3 and 10 GHz, and an antenna height of 20 m, which is representative of many shipboard radiating systems. The study focuses on altitudes below 150 m where refractive effects on propagation are most severe. Although propagation factor results vary substantially as the antenna height is changed, resolution discussions using the 20-m antenna results are expected to be valid for antenna heights between 10 and 50 m. Finally, the transmitting antenna was arbitrarily chosen to be located at the position of the farthest refractive profile from shore and directed toward the shore along the helicopter measurement path.

Propagation factor results at these frequencies exhibit sharp nulls due to various interference phenomena, including multipath interference from surface reflections, and interference between

competing modes within surface ducts. The exact location and depth of these nulls is very sensitive to the environment, and differences of several tens of dB can be caused at a given observation point by slight shifts in these features. The authors do not consider the precise prediction of these interference features to be important for most applications because they occur in small regions of space and are likely to be moving in actual environments. The nature of these features at 4.7 GHz can be examined in Ref. 11. In this paper, all propagation factor results were averaged over approximately 2 km in range and 15 m in altitude prior to being presented. Thus, every point on each propagation factor curve is the average of all TEMPER data in a 2000-m by 15-m box centered on that point. At these frequencies, TEMPER typically generates results on a 200-m in range by 0.4-m in height grid. These averaging intervals were chosen to remove deep interference nulls while preserving low-altitude propagation factor features.

### 5.2. Chosen Study Cases

As previously described, a helicopter measurement flight results in a series of refractivity profiles in a vertical plane. When processed by LARRI and used in TEMPER, "ground truth" propagation factors are produced for these two-dimensional environments. In this paper, we consider sets of profiles measured near San Nicolas Island off the coast of Southern California on 19 March 1988 (Figure 1), and off the coast of Norfolk, Virginia on 26 April 1994 (Figure 2). The rationale for selecting these sets of profiles is that they provide examples of surface-based duct conditions with differing characteristics in two different coastal regions. The Norfolk data involve simple surface-based ducts with moderate heights (100-150 m), while the San Nicolas profiles exhibit low and moderate altitude ducts (35-110 m) with a significant amount of structure. Also, both cases show considerable lateral inhomogeneity.

### 5.3. Vertical and Lateral Resolution

The sensitivity of propagation factor predictions to measurement resolution is examined by manipulating the raw atmospheric data to reduce vertical and lateral resolution, and subsequently repeating LARRI and TEMPER calculations. The "spoiled" results are then compared with the "ground truth" calculations to determine the impact of the simulated degradation in measurement resolution. The lateral resolution is degraded by systematically reducing the number of helicopter profiles used in the propagation calculations. As the limiting case, calculations were made using a single profile and assuming that the atmosphere is laterally homogeneous. This case, of course,

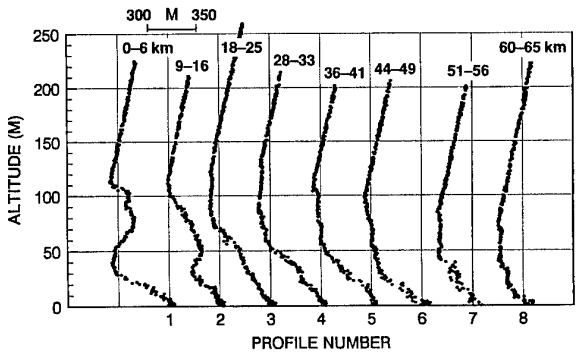


Figure 1. Refractivity profiles collected with instrumented helicopter near San Nicolas Island, California on 19 March 1988. The modified refractivity scale for the first profile is shown.

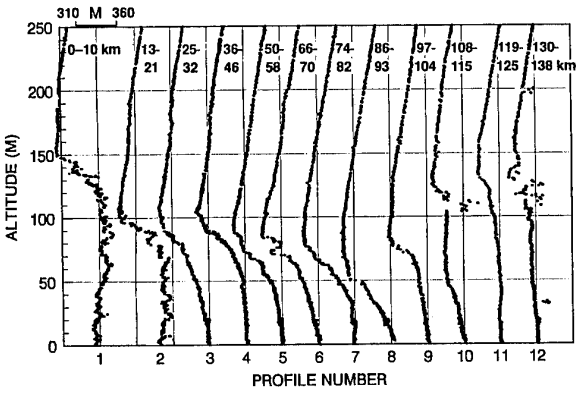


Figure 2. Refractivity profiles collected with instrumented helicopter near Norfolk, Virginia on 26 April 1994. The modified refractivity scale for the first profile is shown.

corresponds to making a single in situ measurement in the vicinity of the radiating sensor.

In order to decouple vertical and lateral effects, the vertical resolution sensitivity is examined by choosing a single profile, assuming this profile applies at all ranges, and systematically removing data points from this profile. The average vertical resolution of the raw data is reduced by nominal factors of 10, 30, and 50 in the following discussions.

## 6. RESULTS

### 6.1. San Nicolas Island Measurements

The unprocessed helicopter-based refractivity data are presented in Figure 1 for the chosen San Nicolas case. For a given height, measurements are separated by an average of approximately 9 km, with 2 to 3 km between the end of one sounding and the beginning of the next. Figure 3 presents the smoothed and interpolated profiles generated by LARRI for use in TEMPER for the San Nicolas Island case; the blending and interpolation of refractivity structures is clear in this figure. LARRI generated a processed profile approximately every 2 km. The output spacing for these profiles is a user-specified parameter, which is generally chosen to be somewhat smaller than the range separation between measurements to avoid losing information. After reading in the LARRI-processed profiles, TEMPER performs a simple interpolation of these data onto its internal calculation grid, which is typically much finer in both range and altitude.

The first profile of Figure 1 exhibits two distinct ducting layers

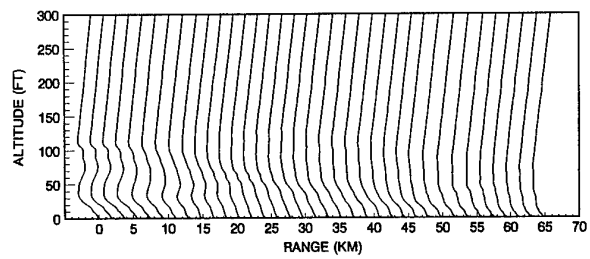


Figure 3. The San Nicolas Island refractivity data after processing by LARRI.

at 35 m and 110 m, while the last profile shows a smooth 75-m surface duct. The ranges are referenced to the northwest coast of San Nicolas, from which location the helicopter flew in a west-northwest direction at a heading of 300 degrees true. The winds at the time of this measurement were out of the north-northeast at 4 m/s resulting in a crossing wind on the helicopter flight path and no appreciable "shadowing" due to San Nicolas Island.

**6.1.1.** *Vertical Resolution Results (San Nicolas Island)*
The refractivity profile measured between 59 km and 65 km from the coast of San Nicolas (first profile in Figure 1) is chosen as the single profile for the vertical resolution calculations. The "baseline" is thus generated by smoothing this profile with LARRI and using the resulting profile at all ranges in TEMPER. The average vertical spacing between helicopter data over the first 150 m of the sounding is 0.6 m.

Lower resolution measurements were simulated by retaining only every ith (e.g., i=10, 30, 50) measurement from the original sounding, and repeating the LARRI and TEMPER calculations with the modified sounding. Keeping every 10th, 30th, and 50th point results in vertical resolutions of 6 m, 18 m, and 30 m, respectively. The original and thinned profiles, after smoothing by LARRI, are plotted in Figure 4. The systematic degradation of the original data is evident, with only the 6-m case being a relatively faithful reproduction of the 0.6-m profile. The profile with 30-m resolution is a weak, 100-m surface duct that exhibits none of the structure of the original data.

TEMPER propagation factor calculations were performed for each of the profiles in Figure 4 using a 20-m antenna height and frequencies of 10 GHz and 3 GHz; vertical polarization was chosen arbitrarily for all results, but the polarization has no impact on the resolution study. In order to investigate the effects of degrading measurement quality, vertical propagation factor slices were examined at ranges of 30 km and 50 km, and horizontal slices at heights of 30 m and 100 m. The results for the 10 GHz frequency are shown in Figures 5 through 8.

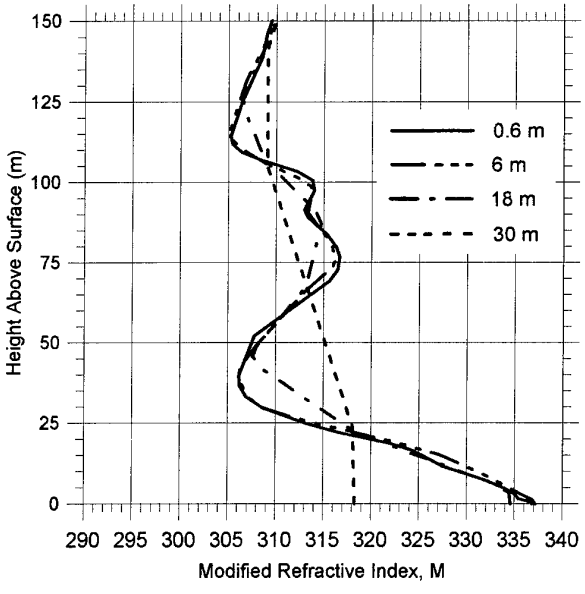


Figure 4. Full- and reduced-resolution San Nicolas profiles beginning with profile 1 from Figure 1 (after LARRI processing).

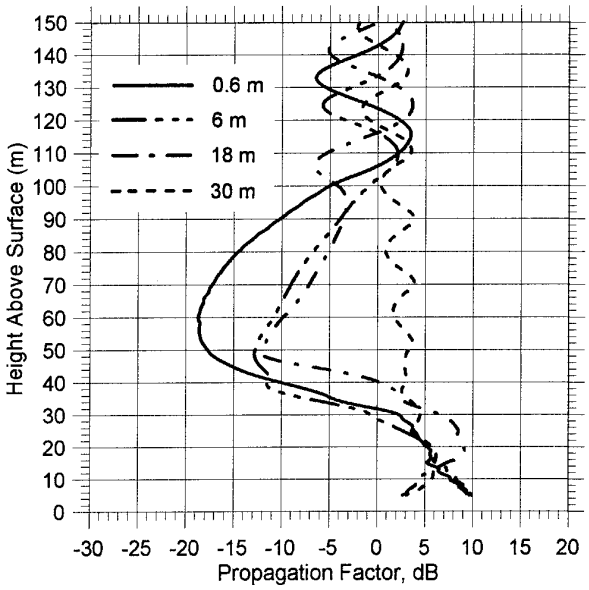


Figure 5. 10 GHz propagation factor calculations at 30 km using the San Nicolas profiles of Figure 4.

At 30 km range (Figure 5), the propagation factor for the original profile exhibits a fade region of 15 dB or more between 45 m and 80 m. This is essentially the altitude region between the two ducting layers in the refractivity profile. One of the reasons this region has less relative power is that the profile is actually subrefractive between 40 and 70 m, causing rays to rapidly bend up and out of this area. At 30 km (Figure 5), the 30-m resolution results show very little structure through this region, which is consistent with the over-simplified refractivity profile in Figure 4. The two intermediate resolutions are deviating from the baseline by 5 to 10 dB between 50 and 95 m at 30 km. The 6-m resolution results are noticeably better than the 18-m results below 40 m.

At 50 km (Figure 6), the 30-m resolution results remain poor in

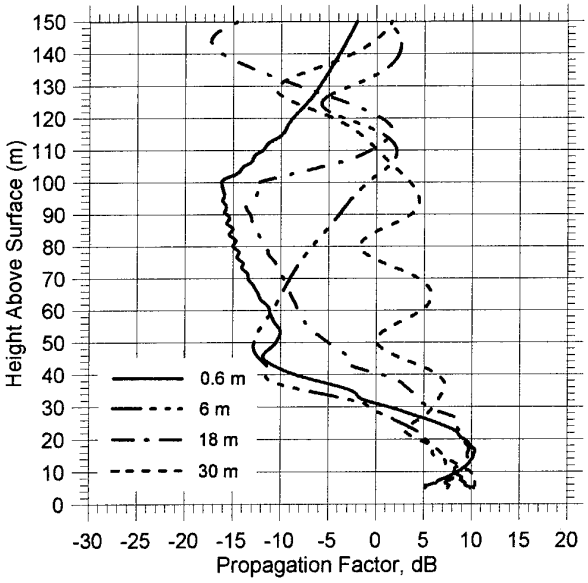


Figure 6. 10 GHz propagation factor calculations at 50 km using the San Nicolas profiles of Figure 4.

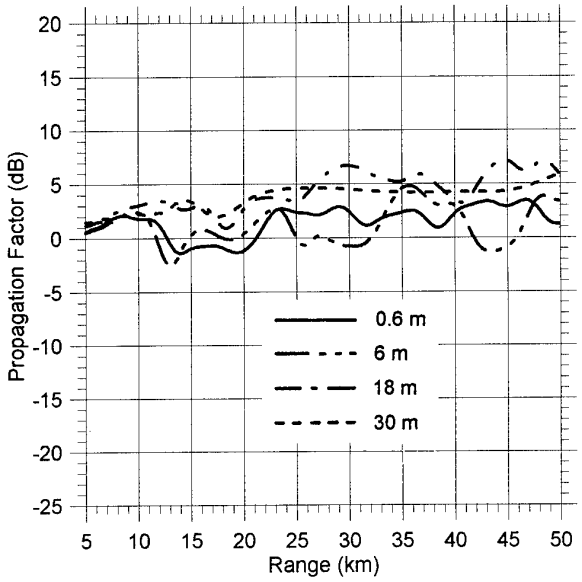


Figure 7. 10 GHz propagation factor calculations at 30 m altitude using the San Nicolas profiles of Figure 4.

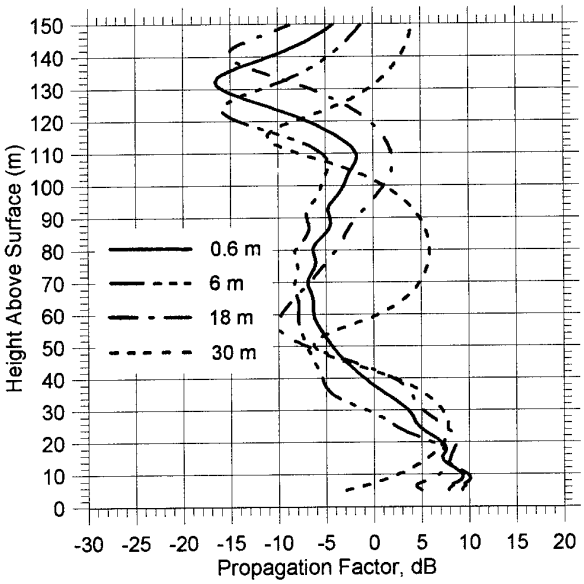


Figure 9. 3 GHz propagation factor calculations at 30 km using the San Nicolas profiles of Figure 4.

the 35-120 m region, and the 6-m and 18-m curves are in poorer agreement with the baseline than they were at 30 km. A 15-dB error is observed at 100 m for the 6-m curve, and similar errors are noted at 110 m and 145 m for the 18-m curve. Due to the dominant nature of the lowest ducting layer, and the fact that the antenna is below the top of this layer, all of the results are within 5 dB below 25 m, but none of the degraded-resolution results are providing the proper behavior as a function of height at 50 km.

Based on Figures 5 and 6, one would expect reasonable agreement between all results at 30 m and much poorer agreement at 100 m. This expectation is borne out in Figures 7 and 8. The 30-m curve is remarkably near the baseline curve at 30 m, and in fact all of the curves stay within 5 dB of the 0.6-m result over the entire range. At 100 m, however, the 30-m resolution results are clearly the worst, and the intermediate-resolution results also degrade beyond 25 to 30 km. The 18-m resolution curve exhibits an error of 10 dB at 35 km, and the 6-m curve is off by 12 dB at 50 km.

The above calculations and comparisons were repeated for 3 GHz, and the results are presented in Figures 9 through 12. As would be expected for a longer wavelength, Figures 9 and 10 show less sensitivity to decreasing resolution than did Figures 5 and 6. At both ranges, only the 30-m curve deviated from the baseline by more than 5 dB over a significant region.

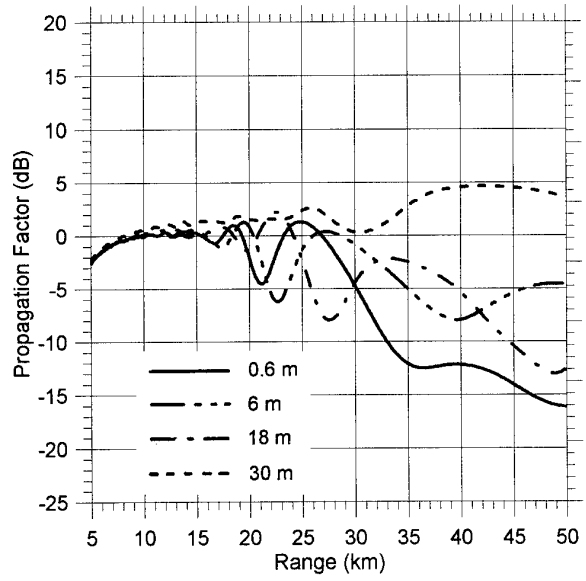


Figure 8. 10 GHz propagation factor calculations at 100 m altitude using the San Nicolas profiles of Figure 4.

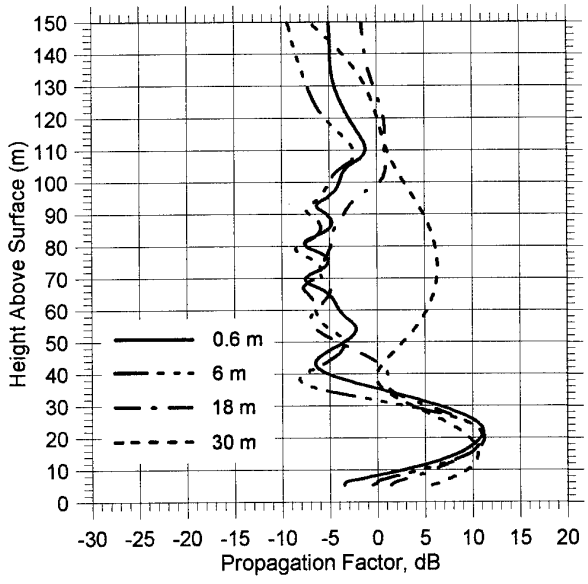


Figure 10. 3 GHz propagation factor calculations at 50 km using the San Nicolas profiles of Figure 4.

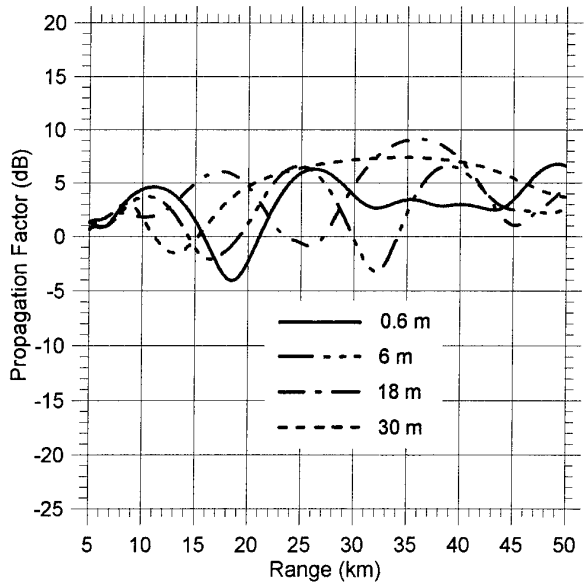


Figure 11. 3 GHz propagation factor calculations at 30 m altitude using the San Nicolas profiles of Figure 4.

Interestingly, the horizontal slice at 30 m in altitude (Figure 11) displays somewhat larger deviations from the baseline for the 6-m and 18-m resolution cases than in Figure 7, with both curves showing errors larger than 5 dB over range intervals of 2-5 km. These errors are slowly oscillating, however, and are never greater than 10 dB. At an altitude of 100 m (Figure 12), the 6-m resolution curve does noticeably better than the 18-m curve, and the 30-m curve has the poorest agreement.

**6.1.2.** *Lateral Resolution Results (San Nicolas Island)*
Measurements with degraded lateral resolution were simulated by using a decreasing number of the available soundings and repeating LARRI and TEMPER calculations at 10 GHz and 3 GHz. The baseline uses all eight profiles shown in Figure 1.

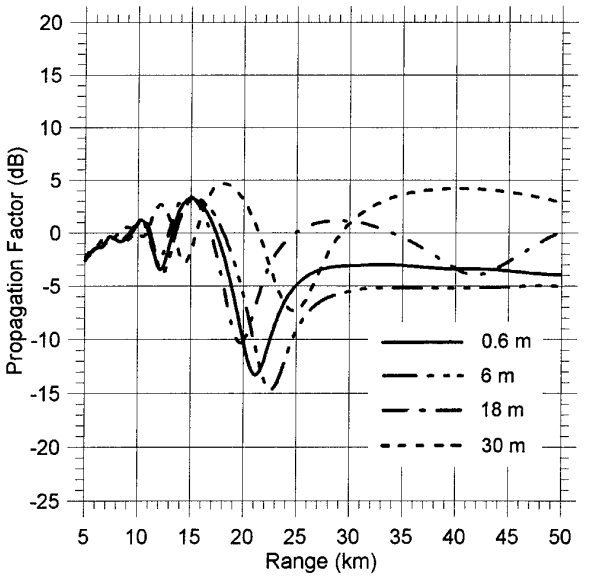


Figure 12. 3 GHz propagation factor calculations at 100 m altitude using the San Nicolas profiles of Figure 4.

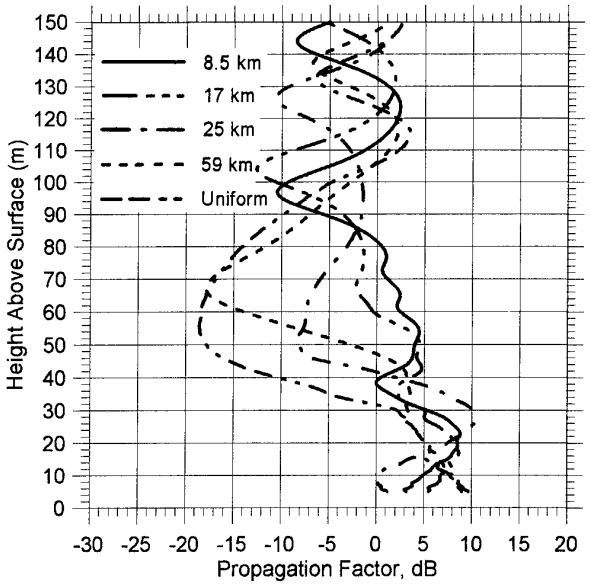


Figure 13. 10 GHz propagation factor calculations at 30 km using various lateral resolutions with the San Nicolas Island data.

Referring to the profile numbers in Figure 1, the degraded resolution cases use four profiles (1, 3, 5, 7), three profiles (1, 4, 7), two profiles (1, 8), and profile number 1 alone. The corresponding average lateral resolutions are 8.5 km (baseline), 17 km, 25 km, 59 km, and none (uniform). Propagation factor results were examined at the same range and altitude locations as before.

The 10 GHz results are presented in Figures 13 through 16. At 30 km, the uniform curve stands out as being in the poorest agreement with the baseline, with 10-20 dB deviations everywhere between 40 m and 90 m. However, none of the

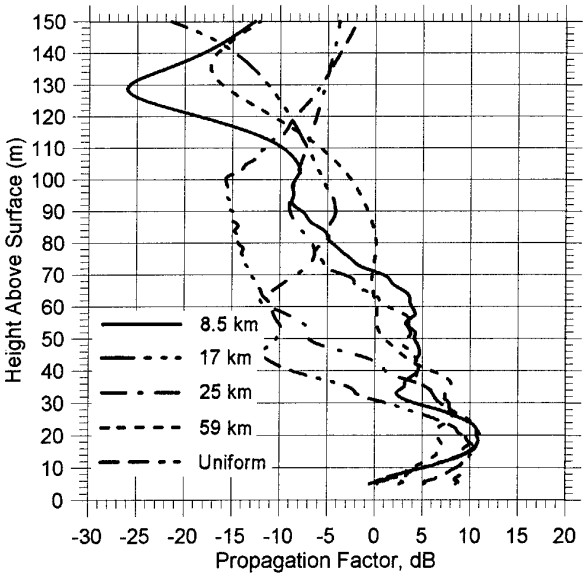


Figure 14. 10 GHz propagation factor calculations at 50 km using various lateral resolutions with the San Nicolas Island data.

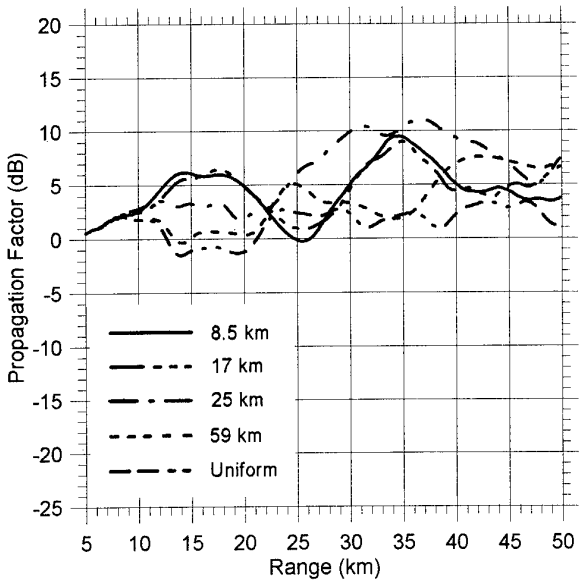


Figure 15. 10 GHz propagation factor calculations at 30 m altitude using various lateral resolutions with the San Nicolas Island data.

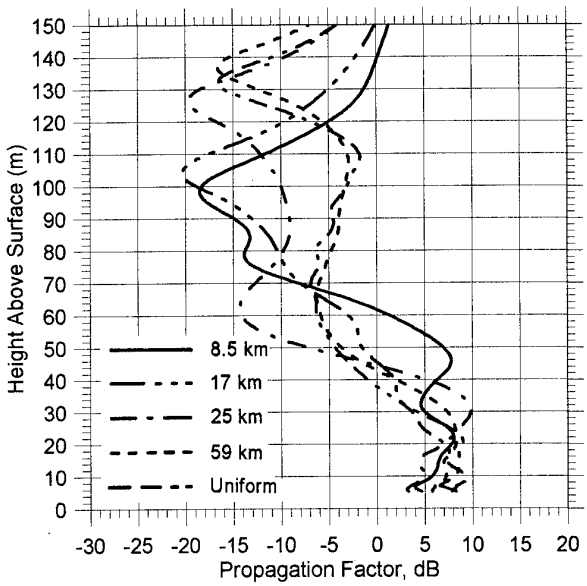


Figure 17. 3 GHz propagation factor calculations at 30 km using various lateral resolutions with the San Nicolas Island data.

reduced-resolution results are in good agreement with the baseline since they are all "out of phase" with the high-resolution curve. In fact, the 2-profile curve is at least as good as the 3- and 4-profile results. At 50 km (Figure 14), none of the lower-resolution curves are in reasonable agreement with the baseline above 30 m.

Figure 15 presents propagation factor versus range at the 30-m altitude. Although none of the lower-resolution curves are way off, except perhaps the 2-profile case beyond 40 km, the best agreement is observed for the 3- and 4-profile cases, as would be expected. At an altitude of 100 m (Figure 16), agreement with the baseline is poor for all the cases beyond 25 km. Regions where several of the curves agree, such as at 36 km, appear to be fortuitous rather than significant.

Figures 17 through 19 present lateral resolution results for 3 GHz. The 30-km results in Figure 17 show the 4-profile cases providing good agreement with the baseline below 30 m where deviations of less than 5 dB are observed. Similarly, at 50 km (Figure 18), the 17-km resolution case shows good agreement below 30 m and above 90 m. The lower-resolution curves exhibit much poorer agreement at both ranges. The range-slice at 30 m altitude (not shown) revealed behavior essentially

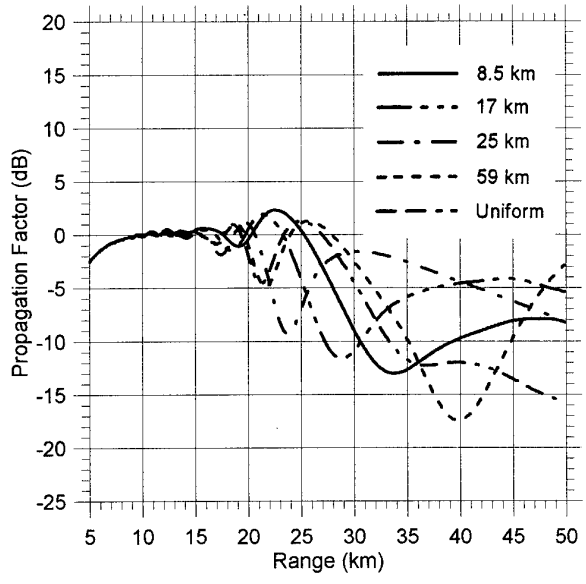


Figure 16. 10 GHz propagation factor calculations at 100 m altitude using various lateral resolutions with the San Nicolas Island data.

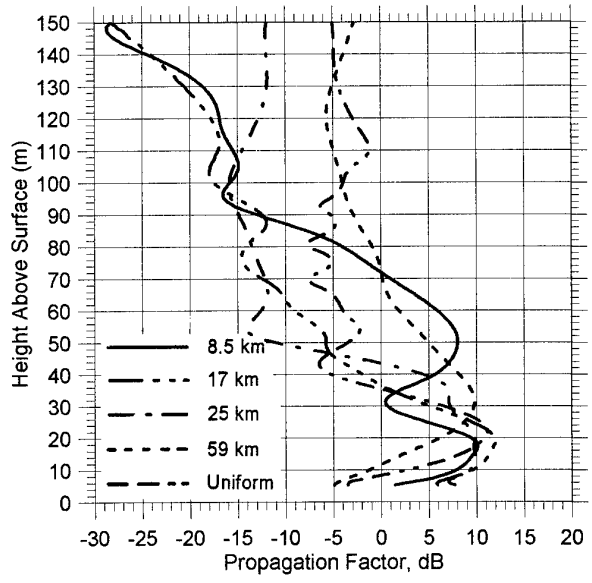


Figure 18. 3 GHz propagation factor calculations at 50 km using various lateral resolutions with the San Nicolas Island data.

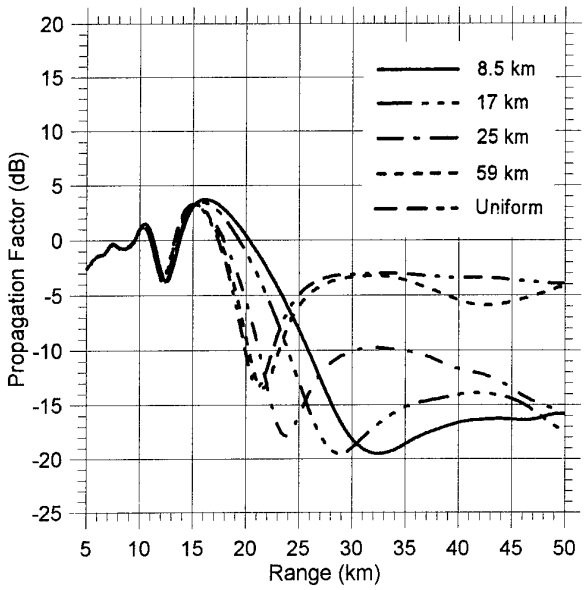


Figure 19. 3 GHz propagation factor calculations at 100 m altitude using various lateral resolutions with the San Nicolas Island data.

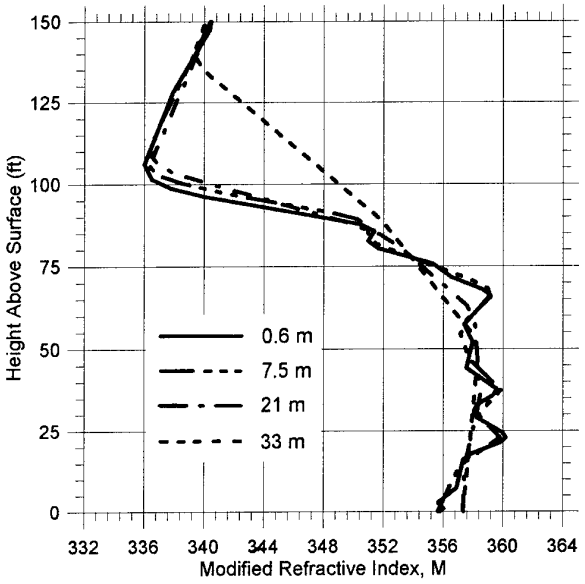


Figure 20. Full- and reduced-resolution profiles from Norfolk, Virginia beginning with profile 1 from Figure 2 (after LARRI processing).

similar to that of previous 30-m plots. At 100 m altitude (Figure 19), however, the 17-km resolution case was the only one to show good agreement with the baseline. The lower-resolution curves exhibited deviations of 5-15 dB over range intervals of many kilometers, with no indication of predicting range trends correctly.

### 6.2. Norfolk Measurements

Comparisons of the type just described have also been performed using the helicopter data collected near Norfolk, Virginia (Figure 2). Twelve soundings were performed on this particular flight with the average spacing between soundings being 12 km. The ranges shown are measured from the coast near Virginia Beach, Virginia and increase in a southeast direction (120 degrees true). The surface winds were out of the southwest at 3 m/s, resulting in an off-shore flow.

The refractivity profiles exhibit substantial lateral variation, beginning with a 150-m surface duct at the coast, decreasing to a stronger 50-m duct at 50 km, and rising back up to 150 m by 130 km. The two profiles farthest from the coast display larger fluctuations in the ducting layer than the closer profiles indicating an increased level of turbulence in this region. This was a common feature during this test period, and suggests that the longer-range measurements may have been reaching warmer surface water associated with the Gulf Stream. This is consistent with surface temperature maps for this region on 26 April 1994.

#### 6.2.1. *Vertical Resolution Results (Norfolk)*

Profile number 2 (Figure 2) was chosen for the vertical resolution study due to its classic surface-based duct shape and because it has a relatively strong refractivity gradient at the top of the ducting layer. As was the case with the San Nicolas profile, the average vertical spacing in the original helicopter data is 0.6 m. Lower-resolution measurements were simulated by retaining every 12th, 35th, and 55th point to obtain effective data resolutions of 7.5 m, 21 m, and 33 m, respectively. Figure 20 presents the resulting refractivity profiles for these cases.

In contrast with the previous example, noticeable misrepresentation of the original profile occurs only in the 33-m resolution case. Coincidentally, the 7.5-m and 21-m profiles each have a point very near the original duct height of 105 m. Because this is a coincidence, one must allow for the possibility that two points separated by 21 m could have just as easily "straddled" this altitude resulting in a poorer representation of the original profile. Nevertheless, the dominant structure in this profile is considerably larger than important features in the San Nicolas Island data, and it is reasonable to expect that the sensitivity to resolution will be somewhat less.

Vertical propagation factor comparisons at 30 km and 50 km are

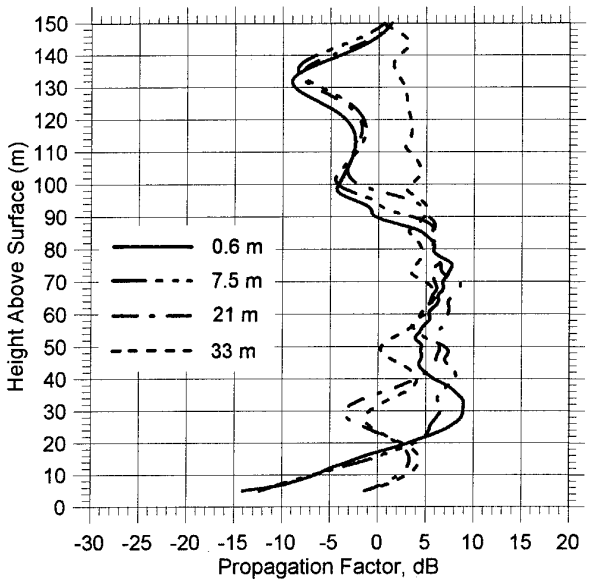


Figure 21. 10 GHz propagation factor calculations at 30 km using the Norfolk profiles of Figure 20.

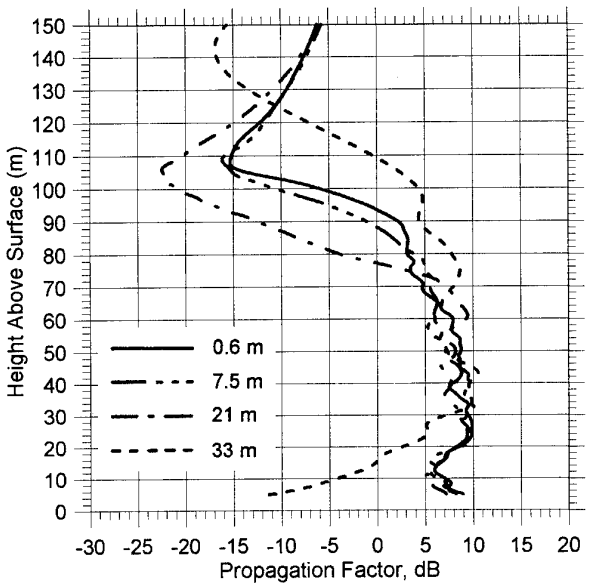


Figure 22. 10 GHz propagation factor calculations at 50 km using the Norfolk profiles of Figure 20.

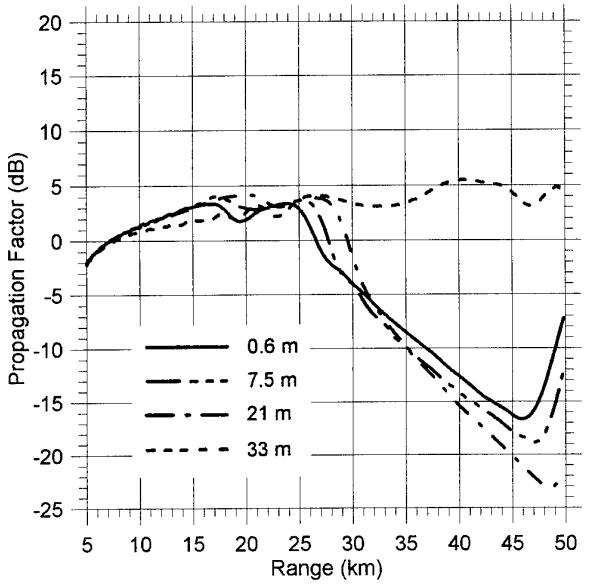


Figure 24. 10 GHz propagation factor calculations at 100 m altitude using the Norfolk profiles of Figure 20.

presented in Figures 21 and 22. The 33-m resolution results are clearly the worst at both ranges. Peak deviations at 30 km (Figure 21) are 13 dB and 12 dB at 5 m and 30 m heights, respectively. At 50 km (Figure 22), the 21-m resolution case shows peak deviations of 5-15 dB between 80 m and 110 m. The 7.5-m resolution results agree very well with the full resolution case at both ranges.

The range-slices at altitudes of 30 m and 100 m are shown in Figures 23 and 24. In Figure 23, the 7.5-m resolution results agree well with the baseline, but both the 21-m and 33-m results have sizeable regions of disagreement. At 100 m (Figure 24), the 7.5-m and 21-m curves are within 5 dB and 10 dB of the baseline curve, respectively. The 33-m curve shows deviations as large as 20 dB.

The above calculations were also repeated for a frequency of 3 GHz; results are shown for the 50-km vertical slices and the 100-m horizontal slices in Figures 25 and 26, respectively. The agreement for the 7.5-m and 21-m curves is slightly improved over the 10 GHz results, but the 33-m curve is still quite poor. The 21-m results still exhibit deviations above 5 dB near 90 m in Figure 25 and near 45-50 km in Figure 26. For this particular profile, the above comparisons indicate that the 7.5-m resolution measurements produce good propagation factor predictions.

**6.2.2** Lateral *Resolution Results (Norfolk)*

Measurements with reduced lateral resolution were again simulated by making calculations using subsets of the available

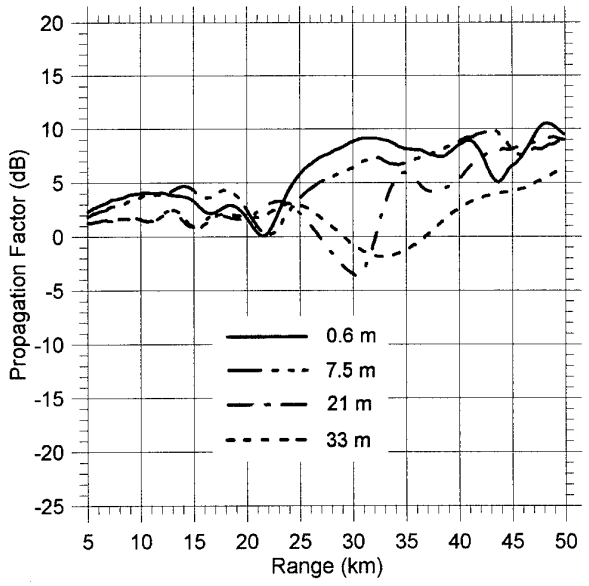


Figure 23. 10 GHz propagation factor calculations at 30 m altitude using the Norfolk profiles of Figure 20.

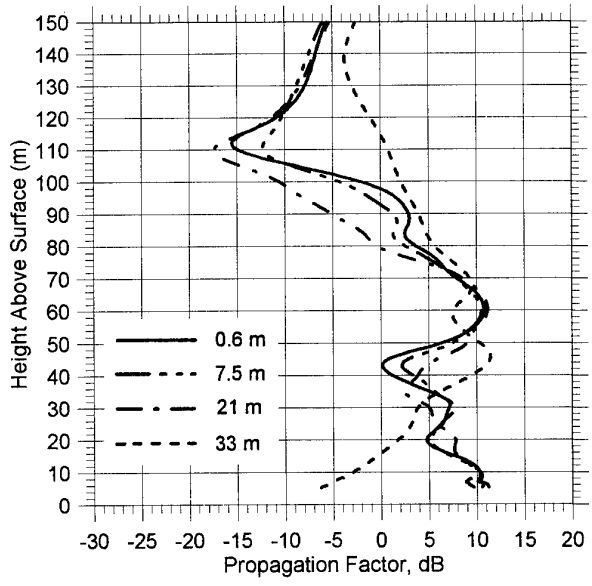


Figure 25. 3 GHz propagation factor calculations at 50 km using the Norfolk profiles of Figure 20.

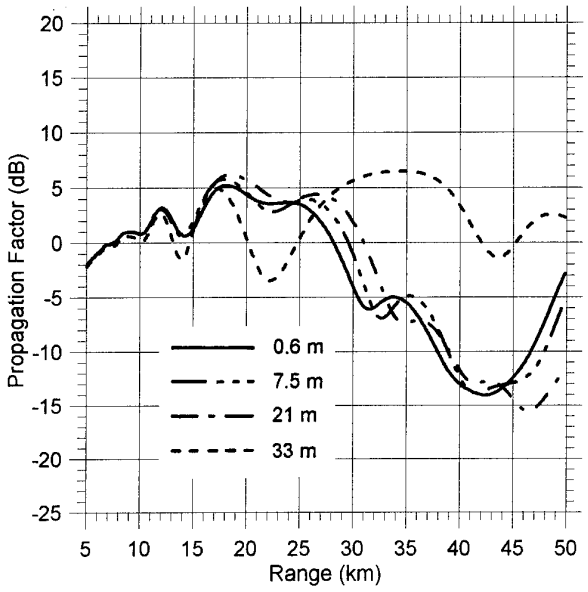


Figure 26. 3 GHz propagation factor calculations at 100 m altitude using the Norfolk profiles of Figure 20.

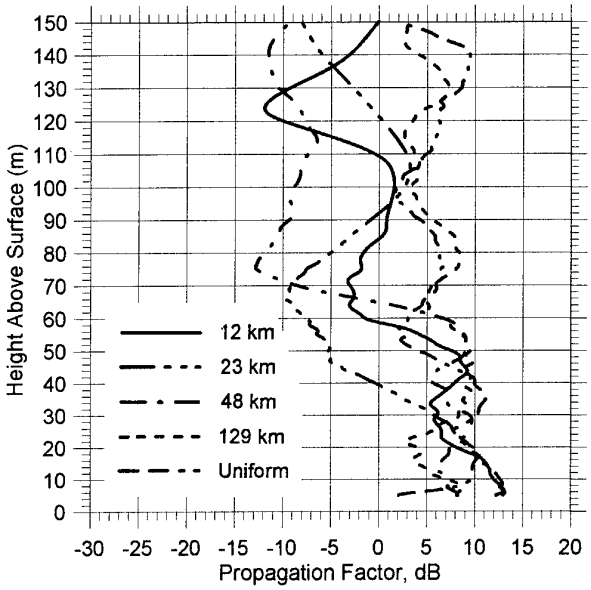


Figure 28. 10 GHz propagation factor calculations at 90 km using various lateral resolutions with the Norfolk data.

profiles. For the Norfolk data, cases were constructed using all twelve profiles, six profiles (1, 3, 5, 7, 9, 11), three profiles (1, 5, 9), two profiles (1, 12), and profile number 1 alone. The corresponding average lateral resolutions are 12 km, 23 km, 48 km, 129 km, and none (uniform).

The lateral resolution results at 10 GHz and 3 GHz are presented in Figures 27 through 32. Since the first and last refractivity profiles are separated by 129 km, vertical propagation factor cuts are examined at ranges of 50 km and 90 km. Surprisingly, the 10 GHz vertical cuts indicate that the 23-km resolution curve (first level of spoiled resolution) gives the poorest agreement between 30 m and 140 m at 50 km (Figure 27) and between 40 m and 170 m at 90 km (Figure 28). This result is further amplified in the 100-m altitude curves in Figure 29 between 30 km and 70 km in range. This unexpected result arises due to erroneously efficient ducting that occurs for this particular subset of profiles (i.e., 1, 3, 5, 7, 9, 11). Note that 100 m in altitude is just above the duct height for the central group of profiles in Figure 2; namely, profiles 3 through 9. If the ducting layer descends with range at the proper rate, trapping within the duct can be very efficient and propagation fading above the duct can be severe. In the present situation, removing every second profile results in more efficient trapping than do the baseline or 48-km cases. The 129-km and uniform cases have neglected all of the central profiles, which have the lower duct heights, causing the 100-m altitude to be below the resulting duct height.

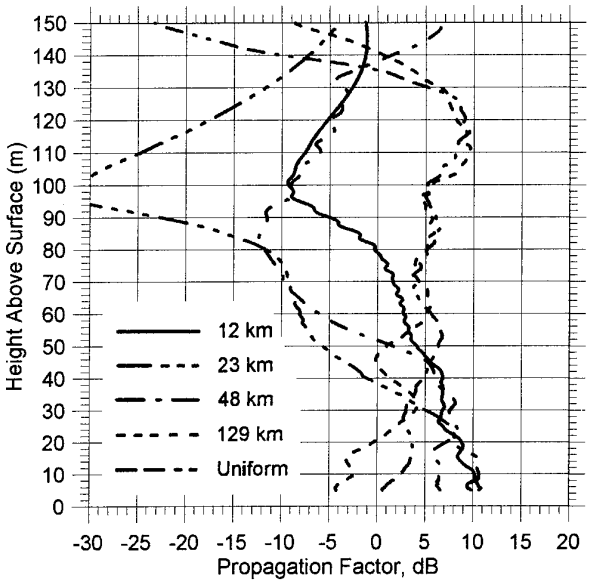


Figure 27. 10 GHz propagation factor calculations at 50 km using various lateral resolutions with the Norfolk data.

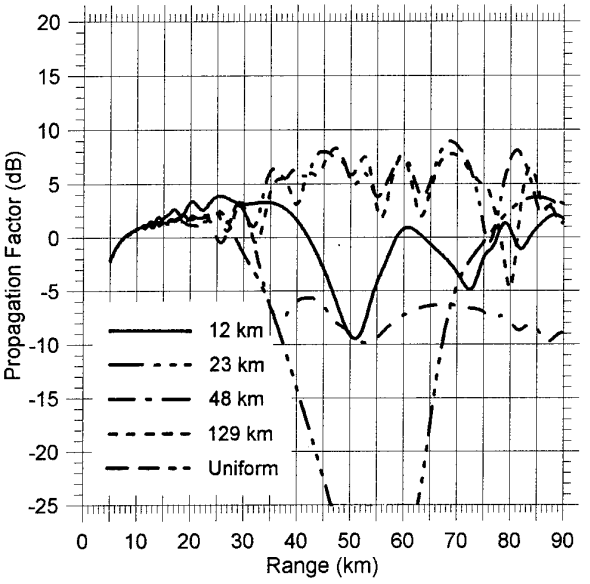


Figure 29. 10 GHz propagation factor calculations at 100 m altitude using various lateral resolutions with the Norfolk data.

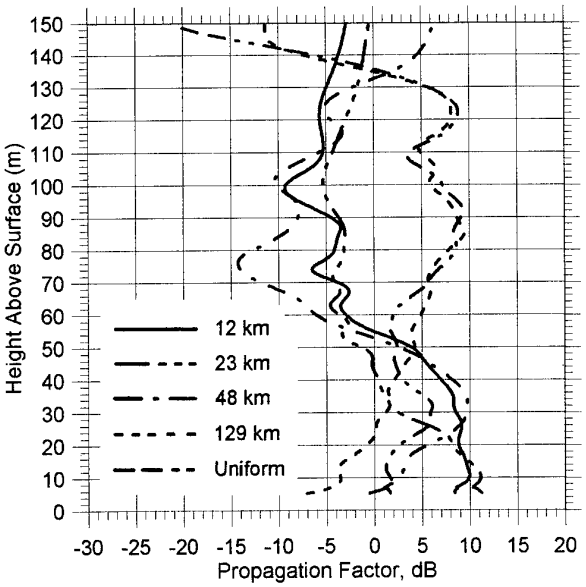


Figure 30. 3 GHz propagation factor calculations at 50 km using various lateral resolutions with the Norfolk data.

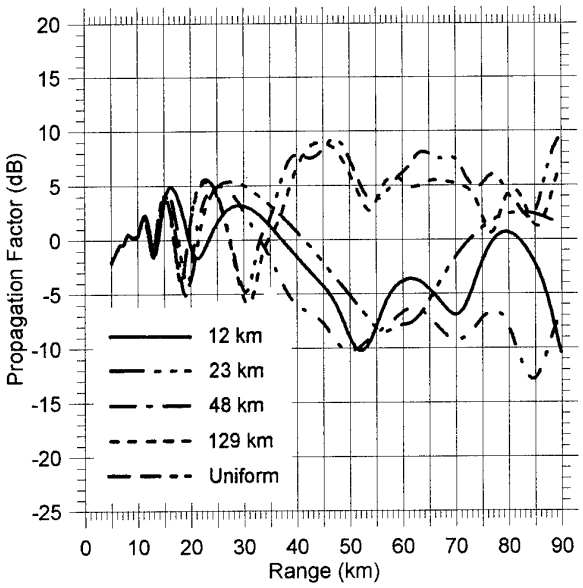


Figure 32. 3 GHz propagation factor calculations at 100 m altitude using various lateral resolutions with the Norfolk data.

Unlike the 10 GHz case, the 3-GHz results (Figures 30 through 32) exhibit the expected behavior in that the first level of spoiled resolution (23-km) agrees best with the baseline. In general, the 3 GHz curves show smaller deviations from the baseline as the resolution decreases than do the 10 GHz results.

## 7. CONCLUDING COMMENTS

This study is intended only to be the beginning of an effort to quantify the sensitivity of propagation predictions to measurement resolution. However, the refractivity data used in this study are examples of an important class of refractive conditions; namely, laterally inhomogeneous, low-altitude surface ducts. The importance of this class of conditions arises because it is the most difficult to characterize accurately, and it can have huge impacts on the performance of surface-based sensors and communication systems. Such conditions are not unusual in coastal regions, and many more examples could have been presented had space permitted.

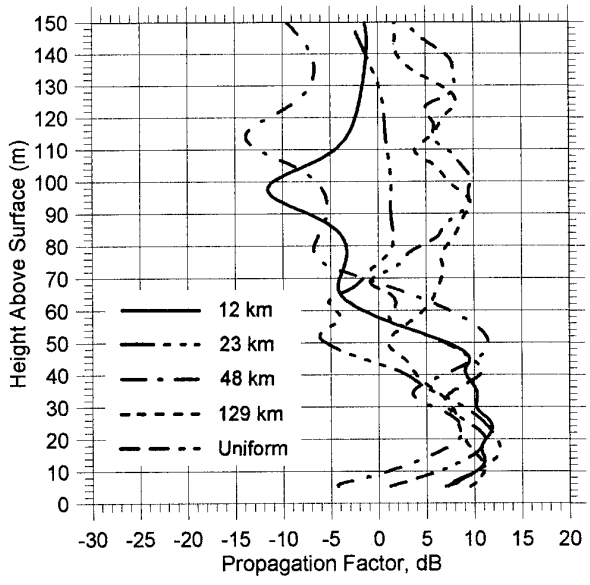


Figure 31. 3 GHz propagation factor calculations at 90 km using various lateral resolutions with the Norfolk data.

Based on 10 GHz propagation in the March 19, 1988 San Nicolas conditions, one would conclude that to maintain a propagation prediction accuracy of 5 dB in the low-altitude region requires a vertical resolution of at least 6 m, and a lateral resolution of less than 17 km. The Norfolk example, taken alone, would suggest that 10 m vertical resolution is sufficient, but that lateral resolution of 17 km or less is again required. Also, the 3 GHz results were somewhat less sensitive to degrading resolution than the 10 GHz calculations. Finally, a 5-dB criteria may be too strict for many propagation assessment applications; if, for example, it is only necessary to predict propagating signal levels to within 15 dB, the resolution can be relaxed considerably.

As borne out by the above study of both data sets, the effects of degrading lateral resolution are considerably harder to predict based on intuition than are those associated with vertical resolution. Depending on the relative locations of the antenna and trapping layers, the propagation factor can be quite sensitive to the rate at which the heights of layers vary. For instance, a slowly rising or falling ducting layer can substantially increase the efficiency of trapping energy, causing much less energy to escape or "leak" out of the duct (Ref. 20). As a result of such effects, conclusions regarding lateral resolution requirements must be made carefully, after examining many types of conditions and geometries.

One cannot establish atmospheric data resolution requirements based only on the cases presented here as a virtually infinite combination of refractivity structures and transmit geometries are possible. If the San Nicolas conditions happen to be a severe case, then one would like to know the probability of encountering such conditions before establishing an atmospheric data requirement that would be very difficult to satisfy. Many more cases need to be examined in order to identify the characteristics of conditions that require higher measurement

resolutions, and to develop some confidence that the full range of effects that can be encountered has been examined. Future work will address these issues, as well as the issues of temporal variability and evaporation duct measurement requirements.

## 8. ACKNOWLEDGMENTS

The authors would like to thank Bert Musiani for his assistance in developing software to simulate lower-resolution helicopter soundings. This work was supported by the AEGIS Shipbuilding Program, PMS-400 under Navy Contract N00039-94-C-0001.

## 9. REFERENCES

1. Hitney, H. V., J. H. Richter, R. A. Pappert, K. D. Anderson, and G. H. Baumgartner, Jr., "Tropospheric Radio Propagation," Proc. IEEE, Vol. 73, No. 2, 1985, pp. 265-283.

2. Ko, H. W., J. W. Sari, and J. P. Skura, "Anomalous Microwave Propagation Through Atmospheric Ducts," Johns Hopkins APL Tech. Dig., Vol. 4, No. 1, pp. 12-16, 1983.

3. Dockery, G. D., and E. R. Thews, "The Parabolic Equation Approach to Predicting Tropospheric Propagation Effects in Operational Environments," AGARD Conference Proceedings No. 453: Operational Decision Aids for Exploiting or Mitigating Electromagnetic Propagation Effects, AGARD-CP-453, 1989, pp. 18-1 through 18-9.

4. Reilly, J. P., and G. D. Dockery, "Influence of Evaporation Ducts on Radar Sea Return," IEE Proceedings, Pt. F, Vol. 137, No. 2, 1990, pp. 80-88.

5. Dockery, G. D., "Modeling Electromagnetic Wave Propagation in the Troposphere Using the Parabolic Equation," IEEE Trans. Ant. Propag., Vol. 36, No. 10, 1988, pp. 1464-1470.

6. Kuttler, J. R. and G. D. Dockery, "Theoretical Description of the Parabolic Approximation/Fourier Split-Step Method of Representing Electromagnetic Propagation in the Troposphere," Rad. Sci., Vol. 26, No. 2, 1991, pp. 381-393.

7. Craig, K. H., "Propagation Modelling in the Troposphere: Parabolic Equation Method," Electron. Lett., Vol. 24, No. 18, 1988, pp. 1136-1139.

8. Hitney, H. V., "Hybrid ray optics and parabolic equation methods for radar propagation modeling," Proceedings: International Conference, Radar 92, Brighton, England, 12-13 October 1992, pp. 58-61.

9. Barrios, A. E., "A Terrain Parabolic Equation Model for Propagation in the Troposphere," IEEE Trans. Ant. Prop., Vol. 42, No. 1, 1994, pp. 90-98.

10. Dockery, G. D., and G. C. Konstanzer, "Recent Advances in Prediction of Tropospheric Propagation Using the Parabolic Equation," Johns Hopkins APL Tech. Dig., Vol. 8, No. 4, 1987, pp. 404-412.

11. Goldhirsh, J., G. D. Dockery, and B. H. Musiani, "Fade statistics and propagation events at C band for two overwater, line-of-sight propagation paths over a 1-year period," Rad. Sci., Vol. 27, No. 6, 1992, pp. 813-828.

12. Rowland, J. R., and S. M. Babin, "Fine-Scale Measurements of Microwave Refractivity Profiles with Helicopter and Low-Cost Rocket Probes," Johns Hopkins APL Tech. Dig., Vol. 8, No. 4, 1987, pp. 413-417.

13. Melfi, S. H., D. Whiteman, and R. Ferrare, "Observation of Atmospheric Fronts Using Raman Lidar Moisture Measurements," J. Appl. Meteor., Vol. 28, September 1989, pp. 789-806,.

14. Grant, W. B., "Differential absorption and Raman lidar for water vapor profile measurements: a review," Opt. Eng., Vol. 30, No. 1, 1991, pp. 40-48..

15. Gossard, E. E., and N. Sengupta, "Measuring gradients of meteorological properties in elevated layers with a surface-based Doppler radar," Rad. Sci., Vol. 23, No. 4, 1988, pp. 625-639.

16. NATO AGARD Conference Proceedings, No. 502, "Remote Sensing of the Propagation Environment," Cesme, Turkey, 30 September-4 October 1991.

17. Gossard, E. E., "The height distribution of refractive index structure parameter in an atmosphere being modified by spatial transition at its lower boundary," Rad. Sci., Vol. 13, No. 3, 1978, pp. 489-500.

18. Paulus, R. A., "Practical application of an evaporation duct model," Rad. Sci., Vol. 20, No. 4, 1985, pp. 887-896, 1985.

19. Goldhirsh, J., G. D. Dockery, and J. H. Meyer, "Three years of C-band signal measurements for over-water, line-of-sight links in the Mid-Atlantic coast, part 2: meteorological aspects of sustained deep fades," Rad. Sci., 1994, in press.

20. Hitney, H. V., "Whispering gallery effects in the troposphere," Rad. Sci., Vol. 27, No. 6, 1992, pp. 893-898.

## DISCUSSION

**M.F. LEVY**
Is the spatial resolution sufficient to achieve accurate results? In view of the large variability of the results, would it be sounder to assume horizontal homogeneity?

**AUTHOR'S REPLY**
One could argue that, based on the 10 GHz results, the lateral resolution in the helicopter data is still insufficient. However, the 3 GHz results exhibit better behavior. Historically, 3 GHz radar performance has been accurately predicted using these helicopter data. It is my expectation that 10 GHz signals would be predicted accurately by helicopter measurements of sufficient lateral resolution. Whether predictions using a single profile are sufficient will depend on the application. In any case, we need to look at many more cases before drawing general conclusions.

**J.H. RICHTER**
Did you make measurements down to the ocean surface and include evaporation ducting that is important for the 10 GHz propagation?

**AUTHOR'S REPLY**
The helicopter sounding typically extended down to 3 meters above the sea. In this study, the profiles were extrapolated linearly to the surface and evaporation ducting was neglected. Of course, we could not make this assumption if we were comparing predictions with measured signals. We are planning to investigate environmental data requirements for evaporation ducts in the future.

**K.D. ANDERSON**
What are your comments regarding degrading significant features in the profiles instead of degrading at fixed height or range intervals?

**AUTHOR'S REPLY**
With regard to measurement approaches, we were assuming direct-sounding methods which generally have uniform vertical spacing. Other remote sensing techniques or meteorological models may have thresholds associated with the size or strength of atmospheric features that can be represented. For these methods, a different type of data requirement study, such as you suggested, might be more appropriate.

# FAST PE MODELS FOR MIXED ENVIRONMENTS

**M.F. Levy**
Rutherford Appleton Laboratory
Chilton, Didcot
Oxfordshire OX11 0QX
U.K.

## 1. SUMMARY

We derive non-local boundary conditions for use with PE methods to compute the coverage diagram of surface or airborne sensors. With these boundary conditions, the PE integration domain can be truncated in height, with large savings in execution times. One of our NLBCs can be applied even when the source is above the domain of interest: this provides an efficient tool for computing the coverage diagram of an airborne source. The truncated PE method has been validated against traditional PE techniques, and should provide a robust and fast way of predicting propagation effects in complex environments for both surface and airborne sensors.

## 2. INTRODUCTION

Parabolic equation techniques have been for some years the dominant tool for computing coverage diagrams in the presence of anomalous refraction [4,2]. More recently, PE techniques have been generalized to the case where irregular terrain effects are present as well [8,13,1]. Certainly PE methods are an ideal tool for propagation predictions in a coastal environment, since they can cope simultaneously with the effects of atmosphere and terrain.

The drawback with PE methods is that they can be computationally intensive, thus limiting their usefulness in operational situations. An excellent way of speeding-up computation times was introduced by Hitney [7]: the idea of RPO (Radio Physical Optics) is to limit the use of the PE to a domain as small as possible, and to use much faster ray-trace techniques to extend the solution to larger heights and angles of propagation. Another tool, the horizontal parabolic equation (HPE) was then derived [9,10], giving a full-wave method to extend the PE solution to large heights.

A typical coastal situation is shown in Figure 1: an evaporation duct is present oversea, and terrain variations must be taken into account overland. Above height $H$, the propagation medium is 'standard' (no terrain perturbations and a well-mixed atmosphere).

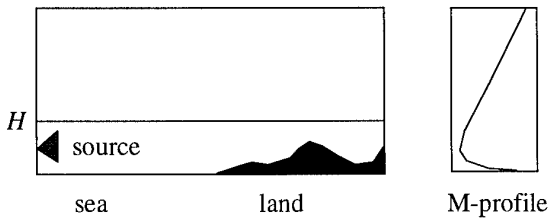


Figure 1. Coastal environment

If field values are required in the whole domain of Fig. 1, they can be computed with 'pure' vertical PE (VPE) as shown in Fig. 2a, but for large domains the computing times become prohibitively long. It certainly makes sense to reserve the computer-intensive vertical PE for heights below $H$ and to use faster techniques above to extend the solution. This is shown in Figure 2b, where a vertical PE algorithm is used below $H$, and HPE is used above. This can be combined with RPO-type methods to limit the use of the PE to small propagation angles.

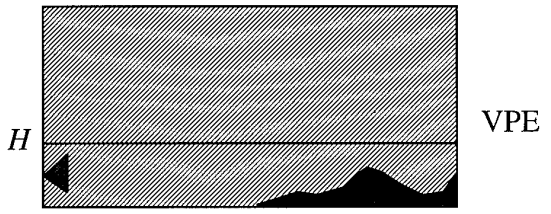


a. Traditional PE method

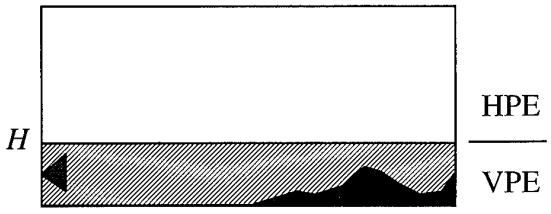


b. Hybrid PE method

Figure 2. PE methods

Hybrid techniques already provide considerable improvements in execution times. However they work by extending a previously computed solution, which up to now was calculated with traditional PE algorithms. This is the area where there is much scope for improvement.

In this paper we derive novel boundary conditions for use with PE methods, which allow very efficient calculations for the heights below $H$. Figures 1 and 2 show the case of a source below $H$, the only case that can be dealt with with traditional PE methods. Our new techniques can also be used for sources above $H$, thus providing a fast tool for computing the coverage diagram of an airborne source.

## 3. NON LOCAL BOUNDARY CONDITIONS

All PE methods need the specification of boundary conditions at the top and bottom of the integration domain. At the ground/air interface, this can be done with surface impedance expressions. The problem at the 'sky' boundary of the domain is that it must represent at a finite distance the fact that energy radiates outwards to infinity. Until recently, PE

*Paper presented at the Sensor and Propagation Panel Symposium on "Propagation Assessment in Coastal Environments" held in Bremerhaven, Germany 19-22 September 1994.*

models implemented the radiation boundary condition by using a larger domain with an absorbing upper layer (see Fig. 3a). This technique has two major drawbacks: it introduces parasitic reflections from the top of the domain, and it increases computation times.

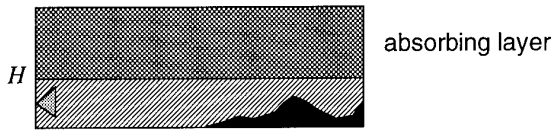


a. Traditional PE: local BC with enlarged domain

b. PE with NLBC and unchanged domain

Figure 3. Boundary conditions for PE methods

It is tempting to implement directly the radiation boundary condition in a truncated domain. Attempts to do this failed until it was realized that local boundary conditions cannot be adequate. A local boundary condition only involves the field and its derivatives at the boundary point considered, whereas a non-local boundary condition (NLBC) also involves the field and its derivatives at other boundary points. It turns out that perfectly transparent NLBCs are available for several propagation problems, allowing the solution of the wave equation on a truncated domain to escape the domain without any parasitic reflection. Then PE integration can be limited to the region below $H$, which contains the perturbations of the propagation medium. This is illustrated in Fig. 3b.

The key is of course the non-locality, which takes into account the global nature of the solution, and not just its local properties. In the parabolic equation frame work, the NLBC at a given range involves all the **previous** ranges (but not **subsequent** ranges, hence the marching character of PE solutions is preserved). Fig. 4a illustrates the traditional local BC, setting the field to zero at some large height $H_m$, which is only possible by inserting an absorbing layer. In Fig. 4b, the non-local BC at a given range depends on all previous ranges, and does not require an artifical absorbing layer.

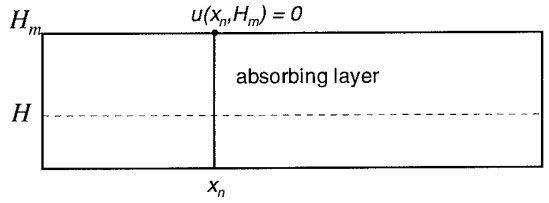


a. local BC at range $x_n$

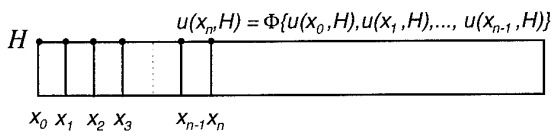


b. NLBC at range $x_n$

Figure 4. Local and non-local BC.

Perfect boundary conditions for a truncated domain were first derived for the elliptic wave equation [5]. In 1991, Marcus introduced an NLBC suitable for use with the parabolic approximation of the wave equation in underwater acoustics problems [12]. This NLBC, that we shall call NLBC1, was also used successfully for waterwave and radiowave applications [3,13]. NLBC1 is applicable to cases where the antenna is below the boundary, and the refractive index is constant above the boundary, which means that its usefulness is limited in radiowave propagation applications.

New work by the author has provided NLBCs for two important cases:

- NLBC2: antenna located below the boundary, with a linear refractive index above the boundary.
- NLBC3: antenna above or below the boundary, with a constant refractive index above the boundary.

This latter NLBC is very important in practice, since it can be used for fast calculation of the field of an airborne source. This is illustrated in Figure 5. With traditional PE methods, the coverage is computed by brute force, in a domain that extends well above the source in height (Fig. 5a). With an appropriate NLBC, integration can stop at height $H$, provided all the anomalous refractive index features and of course all the terrain heights are below $H$ (Fig. 5b). The energy coming down from the source is included in the boundary condition. This NLBC gives large improvements in execution times, particularly for high sources.

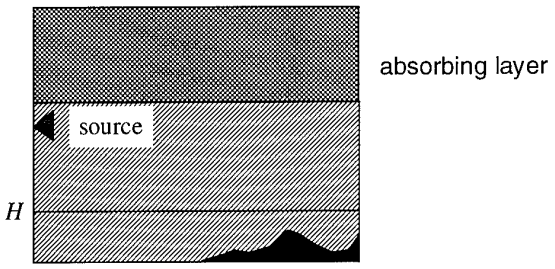


a. Traditional PE method: domain must include source and absorbing layer

b. PE with NLBC: no need to include source for low altitude coverage

Figure 5. PE methods for high altitude source

In the next section, we outline the mathematical derivation of NLBCs.

## 4. MATHEMATICAL BACKGROUND

We start with the standard parabolic equation,

$$\frac{\partial^2 u}{\partial z^2} + 2ik\frac{\partial u}{\partial x} + k^2\left(n^2 - 1\right)u = 0 \qquad (1)$$

For a fixed height $z$, let $U(p,z)$ be the Laplace transform of $u(x,z)$ with respect to range $x$.

We denote by $\varphi(z)$ the field at zero range. If the refractive index above height $H$ does not depend on range, then for any $z$ greater than $H$ the Laplace tranform $U$ satisfies

$$\frac{\partial^2 U}{\partial z^2}(p,z)+\left(2ikp+k^2\left(n^2-1\right)\right)U(p,z)=2ik\varphi(z) \tag{2}$$

The idea is to solve Eqn. 2 in closed form, and to compute the partial derivative in $z$ of the solution at the boundary height $H$. An inverse Laplace transform then gives the required NLBC. We now briefly describe the three NLBCs mentioned in the previous section.

### 4.1. Null starter, no atmophere

This is NLBC1, which was first derived by Marcus. Assume that the refractive index is constant equal to 1 above $H$, and that $\varphi$ is zero above $H$ (null starter). Then the bounded solution of equation 2 is

$$U(p,z)=U(p,H)\exp\left((-1+i)\sqrt{kp}(z-H)\right) \tag{3}$$

Computing the partial derivative in $z$ at height $H$, we find

$$\frac{\partial U}{\partial z}(p,H)=(-1+i)\sqrt{k}\,pU(p,H)\frac{1}{\sqrt{p}} \tag{4}$$

We now invert this expression to get

$$\frac{\partial u}{\partial z}(x,H)=(-1+i)\sqrt{\frac{k}{\pi}}\int_0^x\frac{\partial u}{\partial x}(\xi,H)\frac{d\xi}{\sqrt{x-\xi}} \tag{5}$$

Eqn. 5 can be discretized as in [3], and the resulting difference equation can easily be incorporated in a finite difference scheme.

### 4.2. Null starter, linear atmosphere

We now use the Earth flattening transformation which allows us to work with much more convenient coordinates: $z$ is now the height above the Earth surface, and $x$ is the ground range. Equations 1 and 2 are still valid if we replace $n$ with the modified refractive index $m=n+z/a$, where $a$ is the Earth radius.

We assume for simplicity that $m(H) = 1$. Assume that $m$ satisfies for $z$ greater than $H$:

$$k^2\left(m^2(z)-1\right)=\alpha(z-H) \tag{6}$$

where the slope $\alpha$ is positive. In fact, the derivation is still valid when $m$ is piecewise linear provided $m$ increases with height above $H$. Hence this technique can be applied whenever the atmosphere above $H$ is well-mixed, taking for $\alpha$ twice the modified refractive index slope at $H$.

The algebra is now more complicated, as the solutions of Eqn. 2 are written in terms of Airy functions.

We put $W_1(z)=\mathrm{Ai}\left(ze^{2i\pi/3}\right)$ and

$$\zeta_p(z)=-\left(\alpha k^2\right)^{1/3}(z-H)-2ikp\left(\alpha k^2\right)^{-2/3} \tag{7}$$

If we assume that $\varphi$ is zero above $H$, the bounded solution of Eqn. 2 is

$$U(p,z)=U(p,H)\frac{W_1\left(\zeta_p(z)\right)}{W_1\left(\zeta_p(H)\right)} \tag{8}$$

As before, we compute the partial derivative in $z$ to get

$$\frac{\partial U}{\partial z}(p,H)=-\left(\alpha k^2\right)^{1/3}U(p,H)\frac{W_1'\left(\zeta_p(H)\right)}{W_1\left(\zeta_p(H)\right)} \tag{9}$$

The problem is now to find the inverse Laplace transform of

$$\frac{W_1'\left(\zeta_p(H)\right)}{pW_1\left(\zeta_p(H)\right)}$$

This requires knowledge of the zeros of the Airy function and of its growth [14], and some factorization theorems which allow the representation of the Airy function as an infinite product [15]. Skipping the mathematics, we find that

$$\frac{\partial u}{\partial z}(x,H)=\int_0^x\frac{\partial u}{\partial x}(\xi,H)w(x-\xi)d\xi \tag{10}$$

where the function $w$ is given by

$$w(x)=-i\frac{\alpha k}{2}\sum_{j=1}^{\infty}\frac{e^{p_j x}}{p_j}-\left(\alpha k^2\right)^{1/3}\frac{\mathrm{Ai}'(0)}{\mathrm{Ai}(0)} \tag{11}$$

The $\left(p_j\right)$ are given by

$$p_j=\left(\alpha^2 k\right)^{1/3}\frac{e^{-i\pi/6}}{2}a_j \tag{12}$$

where the $\left(a_j\right)$ are the zeros of the Airy function. This is NLBC2, which is again easy to incorporate into a finite difference scheme.

### 4.3. Arbitrary starter, no atmosphere

This case is very important, as it allows the speedy calculation of coverage diagrams for airborne sources. We start again with Eqn. 2, assuming the refractive index $n$ is equal to 1 above the boundary height $H$. This time we have to integrate a non-homogeneous differential equation. We shall not give the derivation in detail here (it can be found in [11]). It involves the use of mathematical tools like the theory of 'distributions' (a kind of generalized functions) [6].

It turns out that when the starter field is sufficiently nice (which is always the case in practice), the following NLBC holds:

$$\frac{\partial u}{\partial z}(x,H)=(-1+i)\sqrt{\frac{k}{\pi}}\int_0^x\frac{\partial u}{\partial x}(\xi,H)\frac{d\xi}{\sqrt{x-\xi}} \tag{13}$$
$$+(1-i)\sqrt{\frac{k}{\pi x}}\int_H^{\infty}\varphi'(z-H)e^{ik(z-H)^2/2x}dz$$

This is NLBC3. This is perhaps the most intriguing of the NLBCs discussed here: the coverage diagram at heights below $H$ can be computed even for a source well above $H$ by carrying out the PE integration **on heights less than $H$ only**. The information about energy coming from the source above

the boundary is entirely contained in the Fresnel-like integral term.

## 5. USE OF NLBCS

In this section, we give a few examples of the use of PE models with NLBCs. It should be said that these NLBCs have only been implemented very recently, and that the algorithms are by no means optimized. The timings given here already show the great power of these methods, but they can certainly be improved. In what follows, TRUNCPE (for 'truncated' PE domain) is our NLBC implementation of the finite-difference PE. We compare results with a split-step PE model (PCPEM package, Signal Science Ltd) and a finite difference PE model (FDPEM package, Signal Science Ltd). All the software runs on a PC with a transputer card.

It should be borne in mind that the PCPEM and FDPEM timings include the computation of results up to altitudes well above the source, which puts them at a disadvantage if the source is high and only low altitude coverage is required. If high altitude coverage predictions are also wanted, some appropriate HPE method is needed to extend the TRUNCPE solution, and a fair comparison should add HPE execution times to the TRUNCPE ones.

### 5.1. Evaporation duct with NLBC2

We start with an example of the use of NLBC2, the boundary condition which works with flattened earth coordinates. We have used a 10 m evaporation duct, and a 10 GHz antenna located at a height of 20 m. The domain of interest is 100 km in range by 30 m in height. Here we use a Gaussian beamshape for the source, with a beamwidth of 0.2 degrees.

Note that a compromise must be reached between a large beamwidth, for which the aperture is small and the initial field negligible above 30 m, and a smaller beamwidth which allow faster PE integration. A relatively small beamwidth is usually adequate for looking at ducting effects. If higher angle coverage is required, a hybrid method like RPO [7] can be used.

Figure 6 shows the coverage diagram obtained with TRUNCPE. Note that the boundary is perfectly transparent, with no parasitic reflections.

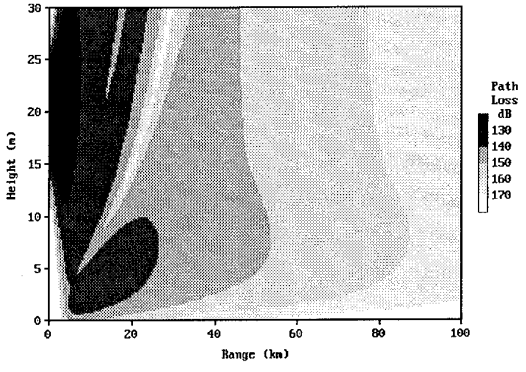


Figure 6. TRUNCPE coverage diagram (10 m duct)

Figure 7 shows a comparison of path loss results at a height of 20 m between PCPEM and TRUNCPE. The PCPEM results have been offset by 20 dB for legibility, otherwise the two curves are practically undistinguishable. The execution times were 11 seconds for TRUNCPE and 3 minutes for PCPEM.

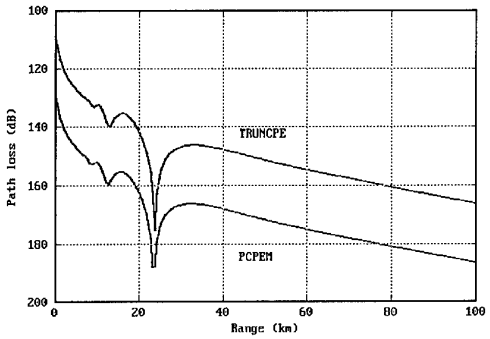


Figure 7. Path loss vs range comparisons at 20 m

### 5.2. Vacuum case with NLBC3

Here we use NLBC3, which assumes the refractive index is constant above the boundary (hence flattened Earth coordinates cannot be used), but allows the source to be located below, on or above the boundary. We shall concentrate on sources above the boundary, since this is probably the most interesting case for operational use. Here we have a 3 GHz source located at a height of 500 m. The domain of interest is 200 km by 30 m, so the source is well above the boundary. The output resolution is 1 km in range, and 0.250 m in height.

Figure 8 shows the TRUNCPE coverage diagram. Note how the energy enters the domain of interest at a range of about 30 km. The boundary condition, which carries the source information, allows this incoming energy to be well represented. Again the boundary condition is perfectly transparent. It should be noted here that integration could in fact start at any range less than about 30 km, since in this case the field and its derivatives are negligible on the horizontal boundary before that range.

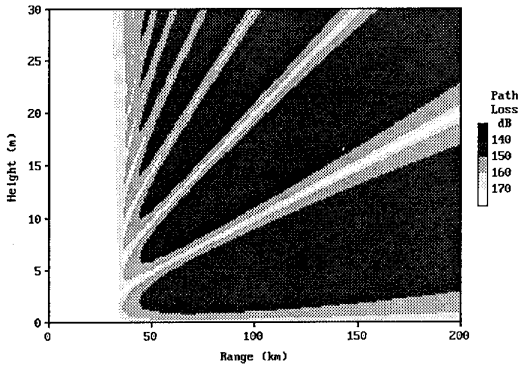


Figure 8. TRUNCPE coverage diagram (Tx at 500 m)

Figure 9 shows a comparison of TRUNCPE and PCPEM at range 100 km. Again the PCPEM results have been offset by 20 dB for legibility. The timings here are 53 seconds for TRUNCPE and 10 minutes for PCPEM.

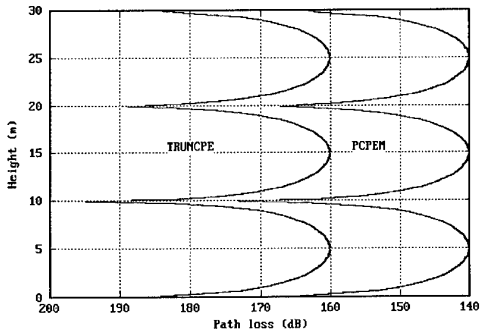


Figure 9. Path loss vs height comparisons at 100 km

### 5.3. X-band examples with NLBC3

Here we use a 10 GHz source located at an altitude of 200 m, with the same domain as in the previous section. In order to emphasize that NLBCs may be used with arbitrary refractive index variations below the boundary, we show the case of vacuum, and a ducting case. The ducting layer is between 0 and 20 m, with a strength of 5 N-units. Figures 10 and 11 show the coverage diagrams for these two cases.

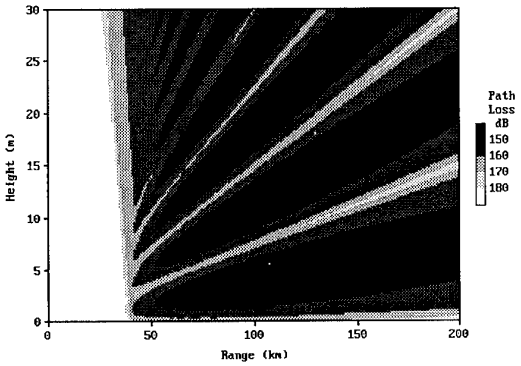


Figure 10. TRUNCPE results (Tx at 200 m, vacuum)

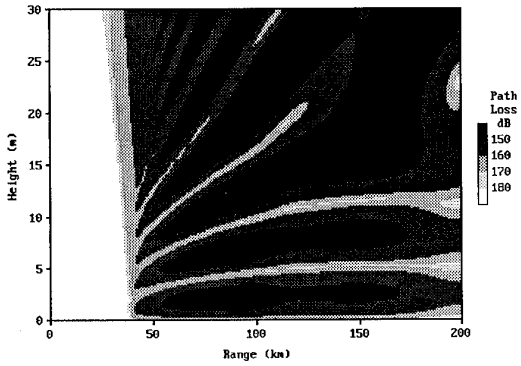


Figure 11. TRUNCPE results (Tx at 200 m, duct)

Again NLBC3 has represented adequately the energy coming in from the source above, and has no difficulty coping with the perturbations due to the duct. Each of these runs took 63 seconds. It should be emphasized here that integration times for TRUNCPE do not depend on source height, unlike PE algorithms with local boundary conditions: for the latter algorithms, the integration domain must include the source, and execution times depend roughly linearly on source height.

### 5.4. Irregular terrain example with NLBC3

In this example we show how to represent the Earth with NLBC3: since we are constrained by the fact that the refractive index must be constant above the boundary, we have to represent the Earth explicitly. We can include standard atmospheric effects above the boundary by using 4/3 Earth coordinates. There is no problem with including irregular terrain. In Figure 12, we have used a 3 GHz source located at 200 m above terrain height. This is a coastal path, with land starting at 30 km.

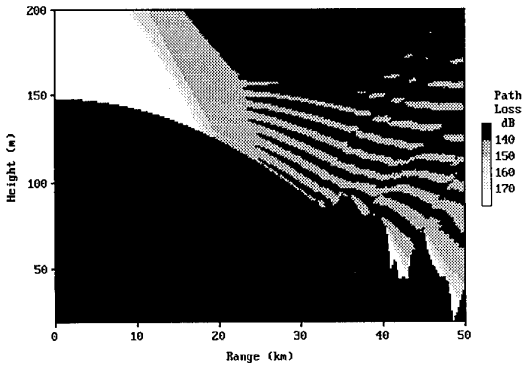


Figure 12. Irregular terrain with NLBC3 (Tx at 200m agl)

We could also have included anomalous refraction effects: the only constraint is that the refractive index should not depend on range above the boundary. This is easily achieved even in a range-dependent environment by offsetting the refractive index profiles. This corresponds to a phase offset of the PE solution on each vertical: it does not affect the field amplitude, nor the relative phases on each vertical, and the absolute phase is easily retrieved if necessary.

Figure 13 shows path loss against range comparisons at a height of 25 m above terrain, between TRUNCPE and FDPEM. The FDPEM results have been offset by 20 dB. The slight differences are due to the fact that TRUNCPE currently uses a fixed range step, whereas FDPEM uses an adaptive range step. Execution times were 28 seconds for TRUNCPE and 5 minutes for FDPEM.

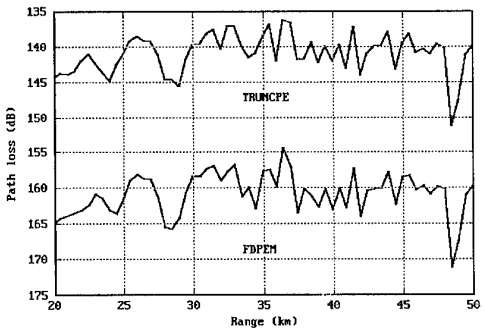


Figure 13. Path loss vs range (height agl 25 m)

This approach is workable for relatively short paths, but Figure 12 shows that the integration domain can become quite large for long paths, because of the large changes in the

Earth $z$-coordinate. However it could also be useful for high sources and long paths if the Earth was represented with **increasing** heights, and integration was started at the range where energy reaches the domain. Obviously the best solution would be to derive an NLBC suitable for use with flattened Earth coordinates and an arbitrary starter field, since the integration domain could then be limited to fixed heights above the Earth surface.

## 6. FUTURE WORK

There is still some work to be done in optimizing the implementation of the various NLBCs. In particular we believe that greater numerical stability can be achieved in NLBC3 if the incident field is decomposed into plane waves, for which the solution can be expressed exactly in terms of Fresnel integrals.

However the most important remaining problem is that of finding an NLBC valid for a linear atmosphere and an arbitrary starter field. Indeed this would allow the fast computation of low altitude coverage for airborne sources, even at very large ranges. Quite complicated holomorphic functions are involved here, but there is quite good hope of a workable solution.

A related problem is that of extending the HPE method to deal with the case of a non-zero starter. Then path loss against range values for an airborne source can be calculated at higher altitudes of interest by using the HPE reconstruction method. This looks straightforward enough for the constant case, but more difficult in the linear case.

## 7. CONCLUSIONS

We have derived several non-local boundary conditions for use with PE algorithms. Their main property is that they allow 'clean' truncation of the PE integration domain, thus giving large execution speed-ups. An important application is the calculation of coverage diagrams for airborne sources, but speed-ups are also obtained for surface-based sensors. This paper demonstrates the usefulness of NLBCs, but further work is required to reap the full potential of these methods.

## 8. ACKNOWLEDGMENTS

I am very grateful to Dr. R.G. Haydon of Brasenose College, Oxford, who provided invaluable suggestions on the mathematical aspects of this research.

This work has been funded as part of the National Radio Propagation Programme by the Radiocommunications Agency of the Department of Trade and Industry, U.K.

## 9. REFERENCES

[1] A.E. Barrios, A terrain parabolic equation model for propagation in the troposphere, IEEE Trans. AP, vol. 42, pp. 90-98, 1994.

[2] K.H. Craig and M.F. Levy, Parabolic equation modelling of the effects of multipath and ducting on radar systems, IEE Proc.-F, vol. 138, pp. 153-162, 1991.

[3] R.A. Dalrymple and P.A. Martin, Perfect boundary conditions for parabolic water-wave models, Proc. R. Soc. London A, vol. 437, pp. 41-54, 1992.

[4] G.D. Dockery, Modeling electromagnetic wave propagation in the troposphere using the parabolic equation, IEEE Trans. AP, vol. 36, pp. 1464-1470, 1988.

[5] D. Givoli, Non-reflecting boundary conditions, J. Comp. Phys., vol. 94, pp. 1-29, 1991.

[6] P. Henrici, Applied and computational complex analysis, vol. 2, Wiley-Interscience, 1977.

[7] H.V. Hitney, Hybrid ray optics and parabolic equation methods for radar propagation modeling, Proceedings of Radar 92, IEE, Conf. Pub no 365, pp. 58-61, 1992.

[8] M.F. Levy, Parabolic equation modelling of propagation over irregular terrain, Elec. Lett., vol 26, pp. 1153-1155, 1990.

[9] M.F. Levy, Combined effects of atmosphere and terrain on UHF/microwave paths, AGARD CP 543, paper 15, 1994.

[10] M.F. Levy, Horizontal parabolic equation solution of radiowave propagation problems on large domains, to appear in IEEE Trans. Antennas Propag.

[11] M.F. Levy, Non-local boundary conditions for radiowave propagation, submitted for publication.

[12] S.H. Marcus, A generalized impedance method for application of the parabolic approximation to underwater acoustics, J. Acoust. Soc. Am., vol. 90, pp. 391-398, 1991.

[13] S.H. Marcus, A hybrid (finite difference--surface Green's function) method for computing transmission losses in an inhomogeneous atmosphere over irregular terrain, IEEE Trans. AP, vol. 40, pp. 1451-1458, 1992.

[14] F.W.J. Olver, Introduction to Asymptotics and Special Functions, Academic Press, 1974.

[15] E.C. Titchmarsh, The theory of functions, Oxford University Press, 1939.

# Terrain and Refractivity Effects in a Coastal Environment

**Amalia E. Barrios**
Ocean and Atmospheric Sciences Division
NCCOSC RDTE DIV 543
53170 WOODWARD ROAD
SAN DIEGO, CA 92152-7385
USA

## SUMMARY

Results from the VOCAR (variability of coastal atmospheric refractivity) experiment, performed in the southern California coastal area, are presented and compared with a terrain parabolic equation model called TPEM. Both homogeneous and range dependent refractivity environments are considered.

## 1. INTRODUCTION

Much emphasis has been given lately to radio field prediction in coastal environments. Currently, well established propagation models exist that have been shown to predict, fairly accurately, radio signals over water [1, 2, 3]. However, in a coastal environment, when one or both terminals are located a short distance inland, the smooth earth assumption that these models employ fails to account for terrain effects on these propagation paths.

An experiment was performed recently along the southern California coast in which RF signals from military and civilian Automatic Terminal Information Service (ATIS) transmitters were received at two locations on the southern California coastline. Some of the propagation paths were entirely over water while others were partially over land. Many of the inland transmitters were obstructed by very high cliffs and/or mountainous terrain typical of the California coastline. Even when the propagation path was more than 90% over water, predictions based on a smooth earth assumption fail to agree with measured data.

A split-step parabolic equation model that can account for terrain effects, called TPEM, has been previously described [4, 5] and is used here to investigate the signals that were measured from transmitters located several kilometers inland.

## 2. EXPERIMENT

In 1993, an experiment to characterize the variability of coastal atmospheric refractivity (VOCAR) was performed in the southern California coastal area. Signals from 14 military and civilian transmitters located along the coastline between San Diego and Santa

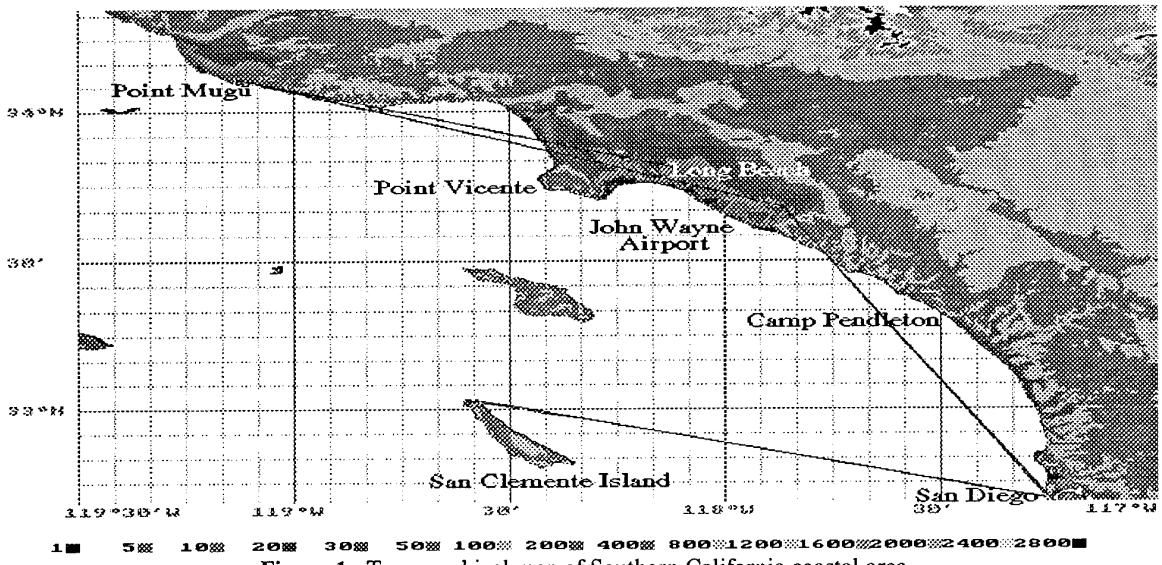


**Figure 1.** Topographical map of Southern California coastal area

*Paper presented at the Sensor and Propagation Panel Symposium on "Propagation Assessment in Coastal Environments" held in Bremerhaven, Germany 19-22 September 1994.*

Barbara were constantly being measured by receivers on the coast at the Naval Command, Control and Ocean Surveillance Center, Research Development Test and Evaluation Division in San Diego (NRaD) and at the Naval Air Warfare Center Weapons Division in Point Mugu (NAWCWPNS). Additional transmitters were placed on San Clemente Island and were also received at San Diego and Point Mugu.

During an intense measurement period between August 23 and September 3, 1993, signals were constantly being received over these land/water propagation paths. Observations taken over a few of the paths will be presented. The propagation paths and the surrounding area are shown in Figure 1. The topography information shown in this figure, and the terrain elevation information used by TPEM for all paths discussed in this paper, is from the Digital Terrain Elevation Data (DTED) database provided by the Defense Mapping Agency. Both receivers at NRaD and at NAWCWPNS were located at 30.5 m above mean sea level. Below is a table of the operating frequencies and antenna heights (above mean sea level) of the transmitters located inland.

| Location | Frequency (MHz) | Antenna Height (m) |
|---|---|---|
| Long Beach Airport | 127.75 | 17.1 |
| John Wayne Airport | 126.0 | 24.4 |
| San Clemente Island | 268.6 | 66.7 |

**Table 1**. Location, frequency, and antenna heights of ATIS transmitters shown in Fig. 1.

Radiosondes were launched approximately 4 to 5 times daily at North Island in San Diego, Point Mugu, San Clemente Island, Camp Pendleton and Point Vicente.

### 3. RESULTS

The first path considered is that from San Clemente Island to San Diego. Signals were received from a transmitter located at the Naval Auxilary Landing Field (NALF) on the island approximately two kilometers inland. A small mountain peak, roughly 137 m high and located between NALF and the shore, lay in direct line from the transmitter to the receiver at NRaD. The propagation path is 127 km long and although most of the path is over water, the presence of this peak created a substantial reduction in signal received at San Diego.

Radiosondes taken at North Island were used as refractivity inputs to RPO [3] and TPEM. RPO is a hybrid ray optics/PE model that assumes smooth earth and does not account for terrain. The results, along with observations for the ten day period in August and September, are shown in Figure 2. RPO underestimated the propagation loss by roughly 20 dB and in some instances, by as much as 40 dB, whereas, TPEM showed very good agreement. The free space and troposcatter thresholds are shown for reference. The troposcatter

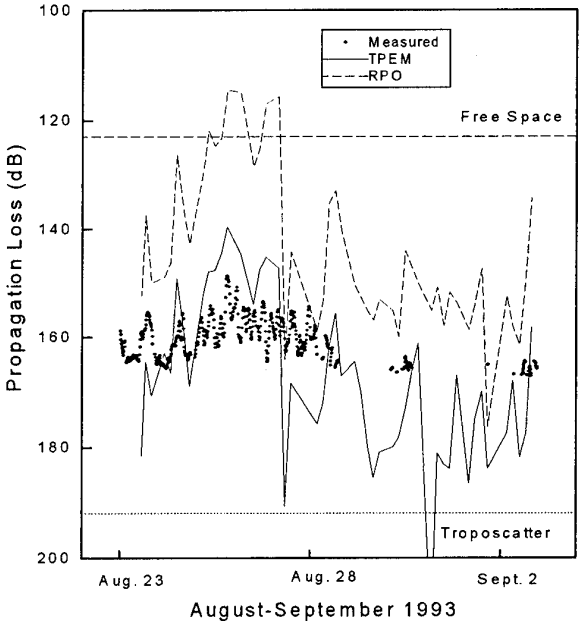


**Figure 2.** TPEM and RPO results vs. measurements for San Clemente Island to San Diego path using North Island soundings.

threshold was determined based on the model by Yeh[6]. Between August 29 and September 3 signal levels were generally too low to be detected, and during this time period TPEM predicted very low signal levels.

For the John Wayne Airport to San Diego propagation path there is a substantial mountain range, roughly 300 m at its peak, from 3 km out to 15 km away from the transmitting antenna. The remainder of the path is over

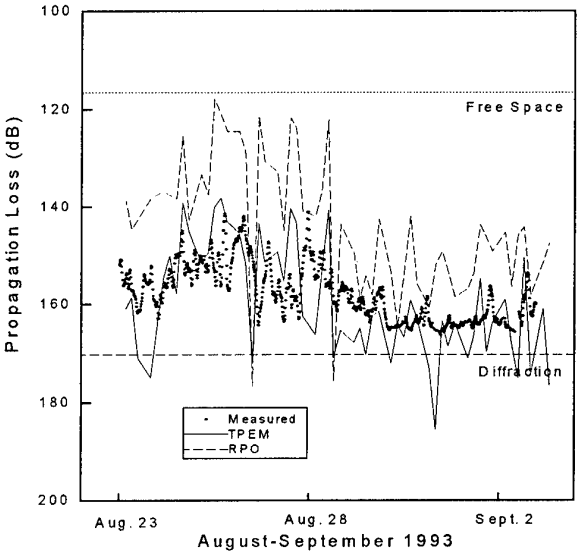


**Figure 3.** TPEM and RPO results vs. measurements for John Wayne to San Diego path using Camp Pendleton soundings.

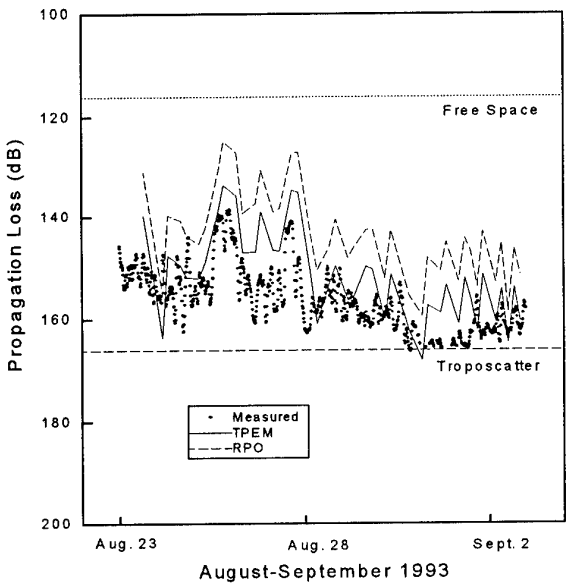


**Figure 4.** TPEM and RPO results vs. measurements for John Wayne Airport to Point Mugu path using Point Mugu soundings.

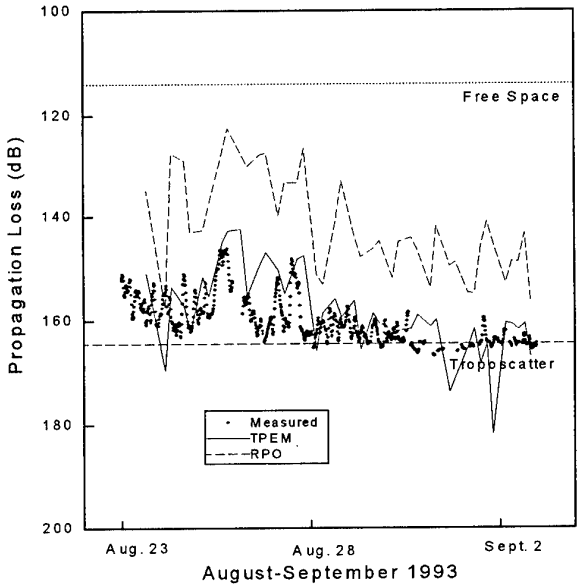


**Figure 5.** TPEM and RPO results vs. measurements for Long Beach to Point Mugu path using Point Mugu soundings.

water with the entire path being 123 km long. Refractivity profiles measured throughout the ten day period at Camp Pendleton were used as environmental inputs to RPO and TPEM. A comparison of their predictions against measured data is shown in Figure 3.

A substantial reduction in signal level due to the mountain range is apparent. Again, RPO underestimates the losses by approximately 10 to 20 dB while TPEM shows very good agreement. The diffraction threshold in this case was determined based on a standard atmosphere environment over the same terrain path.

Refractivity profiles measured at Point Mugu were used for the two propagation paths from John Wayne Airport to Point Mugu and Long Beach to Point Mugu. The terrain path from John Wayne Airport to Point Mugu is roughly 129 km. The path begins over the Los Angeles basin area and the remainder of the path is over water with some small mountain peaks near the receiving end at Point Mugu. Figure 4 shows RPO and TPEM results, along with observations, for this path. The terrain profile did not consist of very large obstructions and was relatively smooth, with most terrain elevation features having a height of 50 m or less. One would expect that a smooth earth assumption in this case would be adequate and that results from RPO would be in close agreement with observations. In fact, RPO and TPEM results differ by only 5 to 10 dB. However, in comparison with measurements, TPEM still gives a much better match to the data.

The path from Long Beach Airport to Point Mugu, a distance of 100 km, starts with fairly smooth terrain but contains some high coastal mountain peaks near the receiving end at Point Mugu. Results are shown in Figure 5. Here again, the presence of these peaks causes a significant reduction in received signal. TPEM shows very good agreement with observations, while RPO differs by as much as 20 to 30 dB.

Clearly, for all of the propagation paths discussed in Figs. 2-5, the terrain had a significant effect on the field. The smooth earth assumption results, given by RPO, did not adequately model what was observed. Also, since the signal levels measured were usually well above troposcatter and diffraction levels, this indicates the refractivity had a major effect on the field as well. The refractivity profiles used in Figs. 2-5 were taken from one site only and were either at the receiving end of, or midway along, the path; and the atmospheric environment for these cases was assumed to be homogeneous. Refractivity measurements were taken at more than one location along each path. The atmosphere can change drastically at land/sea boundaries where anamolous conditions are attributable to very different mechanisms over land than over water. How much improvement, if any, would there be between predicted and measured fields if range dependent refractivity environments were considered?

Results from TPEM for the San Clemente Island to San Diego path for homogeneous and range dependent environments are shown in Figure 6. The measured data is shown as a solid line and all information is given in terms of the percentage of time in which the propagation loss exceeds the abscissa value. The North Island curve represents results from TPEM assuming homogeneous

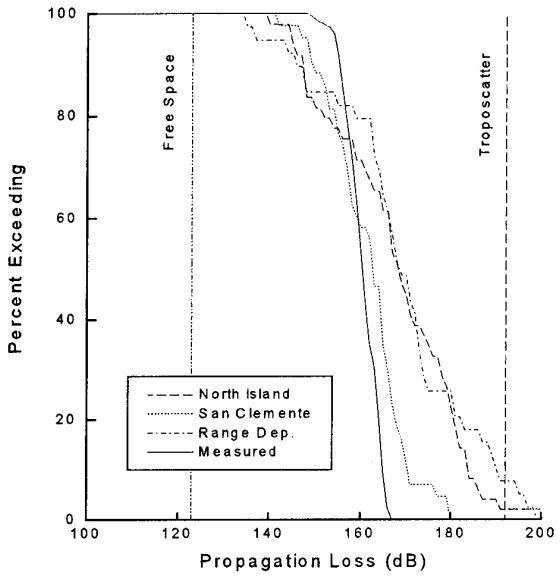


**Figure 6.** Distribution for San Clemente Island to San Diego path for homogeneous and range dependent refractivities.

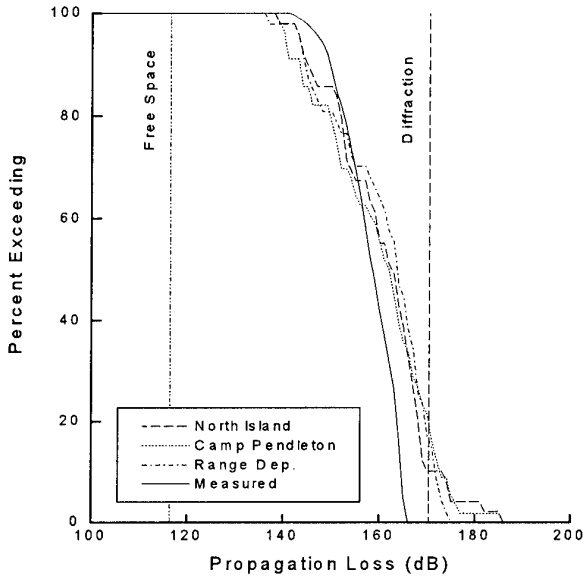


**Figure 7.** Distribution for John Wayne Airport to San Diego path for homogeneous and range dependent refractivities.

environments based on soundings at North Island (this corresponds to Fig. 2). Similarly, the San Clemente Island curve represents results from TPEM assuming homogenous environments based on soundings measured at San Clemente Island. Lastly, soundings from both of these locations taken at roughly the same time of day (no further than 30 minutes apart) were used for the range dependent result. The results given by the San Clemente Island soundings produced the best agreement with observations, particularly at the higher loss values. In fact, the range dependent curve gives the worst agreement overall. However, as mentioned earlier, during the last 5 days of the measurement period, signals could not be detected. Therefore, large discrepancies, specifically at the higher loss values, may be due to lack of sufficient samples.

For the path from John Wayne Airport to San Diego, results from homogeneous environments based on North Island and Camp Pendleton soundings agreed with measurements just as well as those using the range dependent environments, as shown by Figure 7. The range dependent environment for this path assumed horizontal homogeneity between John Wayne Airport and Camp Pendleton based on Camp Pendleton soundings, and then range dependent refractivity between Camp Pendleton and San Diego based on Camp Pendleton and North Island soundings.

In Figure 8, results using range dependent environments gave slightly better agreement at the lower loss values for the John Wayne Airport to Point Mugu path. All TPEM results were computed without accounting for troposcatter losses, therefore one would expect the range dependent curve to follow more closely the measured curve at the higher loss values when troposcatter is included. The two curves representing homogeneous refractivity based on Point Vicente and Point Mugu soundings performed equally well, though they do not match the measured data very closely at the lower loss values. Here, the range dependent results assumed horizontal homogeneity from John Wayne Airport to Point Vicente based on Point Vicente soundings, then range dependent refractivity from Point Vicente to Point Mugu based on their respective soundings.

Figure 9 shows the distribution curves for the Long Beach to Point Mugu path. As in Fig. 8, the range dependent result assumed horizontal homogeneity from Long Beach to Point Vicente, then treated the environment as range dependent from Point Vicente to Point Mugu. The range dependent curve shows excellent agreement at the lower loss values. As mentioned earlier in regards to Fig. 8, closer agreement is expected at the higher loss values when including troposcatter losses.

In Figs. 6-9, the assumption of a homogeneous refractivity environment, using whatever soundings were available, gave fairly good agreement with observations. For three of the four propagation paths, little difference is seen in the distribution results when using a sounding midway or at one end of the path. Only on the San Clemente Island to San Diego path (Fig. 6) was there much better agreement when using soundings from San Clemente Island than from North Island, but this large discrepancy may be due to insufficient observation samples during the last 5 days of the meaurement period. In fact, using range dependent environments based on

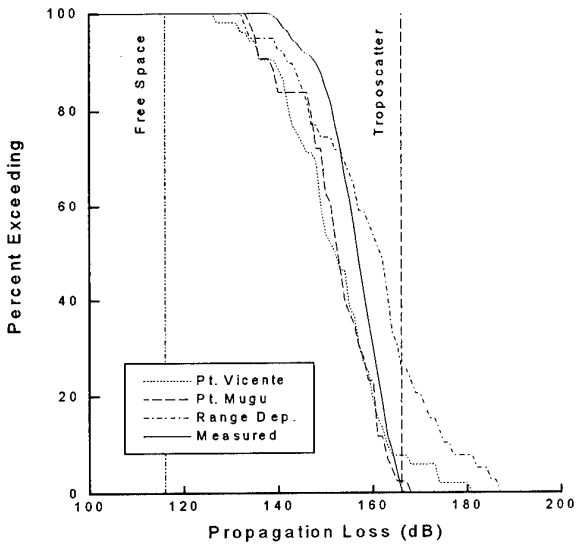


**Figure 8.** Distribution for John Wayne Airport to Point Mugu path for homogeneous and range dependent refractivities.

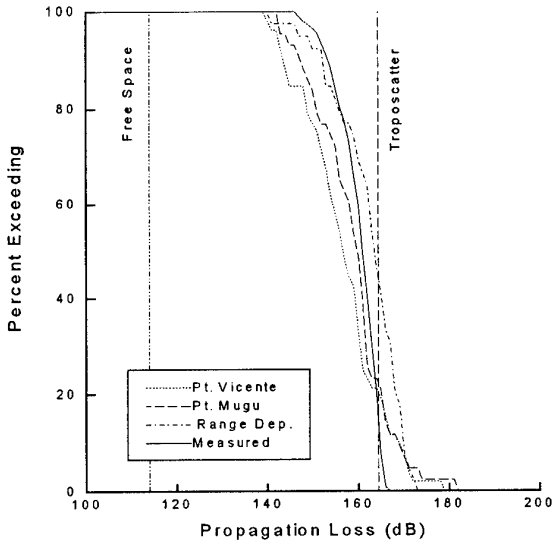


**Figure 9.** Distribution for Long Beach to Point Mugu path for homogeneous and range dependent refractivities.

the available soundings along the path did not produce any substantial improvements. A slight improvement occurred in only two of the paths, Figs. 8 and 9, when using range dependent refractivity environments.

## 4. CONCLUSIONS

It has been shown that in a coastal environment, fields are greatly affected by the presence of terrain even when propagation paths are primarily over water. Another major effect on the field is, of course, the refractivity environment. Horizontally homogeneous refractivity environments based on soundings taken at midway and at either end of the path showed good agreement with measured data. However, attempting to describe the atmosphere as accurately as possible by modeling a range dependent environment did not significantly improve comparisons with observations. While it is certainly worthwhile to describe the atmosphere as well as possible when soundings are available along the path, one is not at a great disadvantage to rely only on soundings taken at one location on the path.

## ACKNOWLEDGEMENT

This work was sponsored by the Office of Naval Research.

## REFERENCES

1. Craig, K.H., "Propagation modeling in the troposphere: Parabolic equation method", Electron. Lett., 24, 1989, pp. 1136-1139.

2. Kuttler, J.G. and Dockery, G.D., "Theoretical description of the parabolic approximation/Fourier split-step method of representing electromagnetic propagation in the troposphere", Radio Sci., Mar-Apr. 1991, pp. 381-393.

3. Hitney, H.V., "Hybrid ray optics and parabolic equation methods for radar propagation modeling", "Radar 92", IEE Conf. Pub. 365, Oct. 1992, pp. 58-61.

4. Barrios, A.E., "Terrain modeling using the split-step parabolic equation method", "Radar 92", IEE Conf. Pub. 365, Oct. 1992, pp.66-69.

5. Barrios, A.E., "A Terrain Parabolic Equation Model for Propagation in the Troposphere", IEEE Trans. on Ant. and Prop., 42, 1, Jan. 1994, pp. 90-98.

6. Yeh, L.P., "Simple Methods for Designing Troposcatter Circuits", IRE Trans. on Comm. Systems, CS-8, 3, Sept. 1960, pp. 193-198.

## DISCUSSION

**D. DION**
Since radiosonde data, that were used for describing the horizontal inhomogeneity, do not provide information on near-surface conditions, what type of surface profiles were assumed?

**AUTHOR'S REPLY**
No surface refractivity information was included, such as evaporation duct measurements, because the frequencies of these transmitters are too low for the evaporation duct to have any effect on the propagated field.

**J. TURTON**
1. The results suggested that range dependent behavior was not particularly important - did the meteorological measurements show significant range dependent behavior? (That probably explains why it doesn't really matter whether you use the profile at the transmitter or receiver end in the calculations.)

2. Would these conclusions hold in a much more range dependent, inhomogeneous atmosphere?

**AUTHOR'S REPLY**
1. Radiosonde measurements did not show a lot of range dependent behavior indicating the atmosphere was fairly homogenous.

2. Not necessarily so. The main emphasis here is that the two major effects are terrain features along the path and refractivity. Even if the atmosphere were varying horizontally, range dependency would probably be a secondary effect.

# Modeling Nonperfect Reflection from the Sea for Range-Dependent Ducting Conditions

**Herbert V. Hitney**
Ocean and Atmospheric Sciences Division
NCCOSC RDTE DIV 543
53170 WOODWARD ROAD
SAN DIEGO CA 92152-7385
USA

## SUMMARY

This paper describes an approximate method to account for nonperfect reflection from the sea that uses a simple technique to modify a parabolic equation (PE) model based on sine fast Fourier transforms (FFTs). Although the method is an approximation, it gives good results compared to other more rigorous models, and is very efficient. Comparisons of results for ducting conditions that are homogeneous with range using the approximate, waveguide, and mixed transform PE methods are presented to evaluate the approximate method.

The approximate method is easily extended to range-dependent ducting and roughness conditions likely to be encountered in coastal environments. To evaluate these cases, a comparison is made of approximate method results and results from a mixed-transform PE model for vertical polarization.

## 1. INTRODUCTION

The split-step PE method has proven to be an efficient and accurate radio propagation model for conditions where the vertical refractive-index profile changes with range [1-3]. The simplest and most efficient PE models are those that assume perfect reflection from the lower boundary and are based on sine FFTs. For propagation over the sea, these models give outstanding results for horizontal polarization and smooth sea conditions, since there is virtually perfect reflection from the sea. For conditions of nonperfect reflection, such as for vertical polarization or rough sea conditions, these sine-FFT PE models still give very good results for environmental conditions that do not include surface or surface-based ducts. For these ducting conditions, which cause a strong interaction between the trapping and reflecting mechanisms, nonperfect reflection from the sea becomes a potentially important effect which is not accounted for by the sine-FFT PE models.

Hitney [4] has proposed an approximate method to account for vertical polarization and rough surface effects under surface ducting conditions by using a slight modification to a sine FFT PE model. This modification adjusts the PE calculation with a boundary loss factor at each range step, where the loss factor is determined by the reflection coefficient appropriate to the polarization and surface roughness for the maximum grazing angle trapped in the duct. This method was developed for integration into the Radio Physical Optics (RPO) model [5]. RPO is a range-dependent over-water hybrid ray optics and PE model for operational propagation assessment systems that emphasizes computational efficiency.

In this paper a waveguide program known as MLAYER (for multi-layer, since it accepts multiple levels in the refractivity profile) [6-7], is used as a standard or "ground truth" model. Although MLAYER only models horizontally homogeneous refractivity profiles, it does treat the effects of nonperfect reflection from the lower boundary in a theoretically rigorous manner based on the Fresnel reflection coefficient modified for surface roughness by the Miller-Brown model [8]. This model is given by

$$R = R_0 \exp\left[-2(2\pi g)^2\right] I_0\left[2(2\pi g)^2\right] \qquad (1)$$

where $R$ is the rough-surface coherent reflection coefficient, $R_0$ is the ordinary Fresnel reflection coefficient, $I_0$ is the modified Bessel function, and the "apparent ocean roughness" $g$ is given by

$$g = (\sigma_h \sin\psi)/\lambda \qquad (2)$$

where $\sigma_h$ is the standard deviation of the sea-surface elevation, $\psi$ is the grazing angle, and $\lambda$ is the electromagnetic wavelength. The relationship of $\sigma_h$ to wind speed is derived from the Phillips' saturation curve spectrum [9] and is given by

$$\sigma_h = 0.0051\, u^2 \qquad (3)$$

where $u$ is wind speed in meters per second.

The approximate method was developed based on observations that results from MLAYER could be matched by results from a slightly modified PE model. The modification consists of multiplying the magnitude of the lowest field point in the PE model by a boundary loss factor $B$ between 0 and 1 immediately prior to each PE range step calculation. For example, Figure 1 shows results from the MLAYER waveguide model for a 24-m evaporation duct environment described in Table 1. The frequency is 9 GHz, the transmitter height is 25 m, and the range is 500 km. Figure 1 shows propagation loss

*Paper presented at the Sensor and Propagation Panel Symposium on "Propagation Assessment in Coastal Environments" held in Bremerhaven, Germany 19-22 September 1994.*

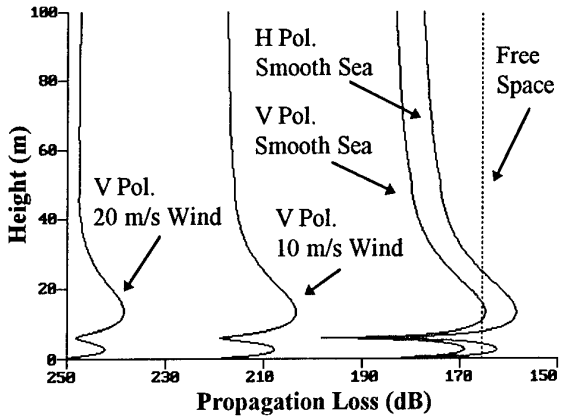


**Figure 1.** MLAYER results for the 24-m evaporation duct of Table 1. Frequency is 9 GHz, transmitter height is 25 m, and range is 500 km.

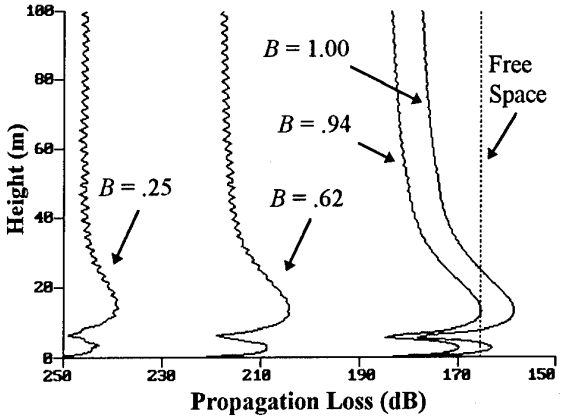


**Figure 2.** RPO results for various boundary loss factors $B$ for the same conditions as Figure 1.

| Height (m) | $M$ units |
|---|---|
| 0.000 | 0.00 |
| 0.135 | -20.40 |
| 0.223 | -21.89 |
| 0.368 | -23.37 |
| 0.607 | -24.84 |
| 1.000 | -26.29 |
| 1.649 | -27.71 |
| 2.718 | -29.08 |
| 4.482 | -30.35 |
| 7.389 | -31.49 |
| 12.182 | -32.39 |
| 20.086 | -32.90 |
| 24.000 | -32.95 |
| 33.115 | -32.78 |
| 54.598 | -31.59 |
| 90.017 | -28.66 |
| 148.413 | -22.86 |

**Table 1.** Profile of modified refractivity in relative $M$ units versus height for a 24-m evaporation duct.

versus receiver height for both horizontal and vertical polarization over a smooth sea and for vertical polarization with 10 m/s and 20 m/s wind. Rough surface cases for horizontal polarization result in loss values a few dB less than the vertical polarization cases shown. Figure 2 shows results from RPO utilizing the four boundary loss factors indicated. It is clear that a suitable boundary loss factor can be found that simulates the waveguide results. Many similar cases of surface ducts have been tried with comparable results.

In the previous paper [4] the model development was described, and one independent homogeneous test case was analyzed. Model results were also compared with a three week time series of propagation loss measurements at 37 GHz over a fixed path characterized by variable evaporation duct heights and wind speeds. These results showed that RPO with the roughness model matched the measurements much better than RPO without the roughness model, especially for high wind speed cases.

This paper builds on the previous work and analyzes one more independent homogeneous case and one range-dependent environment. The ability of this approximate model to work in range-dependent environments is important for coastal applications, where either the refractivity profile or the surface roughness is likely to change along the propagation path. The mixed sine and cosine FFT PE model TEMPER [10] (version 1.0A) is used here as a "ground truth" model for range-dependent environments. The treatment of vertical polarization in TEMPER is based on theoretically rigorous methods and is hence assumed correct. Since the version of TEMPER used here does not include rough surface effects, the analysis of range-dependent effects is limited to smooth sea conditions.

## 2. MODEL

The modification for nonperfect reflection multiplies the magnitude of the lowest field point in the PE model by a boundary loss factor $B$ immediately prior to each PE range step calculation. The semi-empirical relationship for $B$ developed in [4] is given by

$$B = \left|R(\psi)\right|^{131\,\delta x/x_s} \tag{4}$$

where $R$ is the Fresnel reflection coefficient from (1), $\psi$ is the maximum grazing angle that can be trapped by the surface duct, $\delta x$ is the PE range step, and $x_s$ is the skip distance of a ray with grazing angle $\psi$ in the duct. The coefficient 131 was determined by an iterative process to best match results from MLAYER. The maximum grazing angle is computed from ray optics theory using

$$\psi = \sqrt{2 \times 10^{-6}\left(M_0 - M_m\right)} \tag{5}$$

where $M_0$ is the modified refractivity at the surface and $M_m$ is the minimum modified refractivity on the profile. The skip distance is computed using a simple ray trace procedure on each linear modified refractivity segment of the profile.

## 3. RANGE INDEPENDENT ENVIRONMENT

The model was applied to several range-independent, or homogeneous, surface ducting environments that are independent of the environments used to develop the model to further evaluate its ability to simulate nonperfect reflection. Many cases that were tried were inconclusive, since vertical polarization or rough surface results did not substantially differ from the horizontal polarization smooth sea case for any of the models. One case that did show a substantial difference is a 12-m evaporation duct described in Table 2. The case studied is for 12 GHz with an antenna height of 10 m and a maximum range of 250 km. Figure 3 shows propagation loss versus receiver height from the MLAYER program. Figure 4 shows the corresponding results from RPO with the modification. A comparison of these two figures shows that RPO matches MLAYER well for vertical polarization over a smooth sea and vertical polarization with 10 m/s of wind. However, RPO underestimated the loss by about 10 dB compared to MLAYER for vertical polarization and 20 m/s of wind. Figure 5 shows TEMPER results for this same case for vertical and horizontal polarization over a smooth sea. These results are virtually identical to the MLAYER and RPO results shown in Figures 3 and 4.

| Height (m) | *M* units |
|---|---|
| 0.000 | 0.00 |
| 0.068 | -9.16 |
| 0.112 | -9.91 |
| 0.184 | -10.65 |
| 0.303 | -11.38 |
| 0.500 | -12.11 |
| 0.824 | -12.81 |
| 1.359 | -13.50 |
| 2.241 | -14.14 |
| 3.695 | -14.71 |
| 6.091 | -15.16 |
| 10.043 | -15.41 |
| 12.000 | -15.43 |
| 16.558 | -15.35 |
| 27.299 | -14.76 |
| 45.009 | -13.29 |
| 74.207 | -10.39 |

**Table 2.** Profile of modified refractivity in relative *M* units versus height for a 12-m evaporation duct.

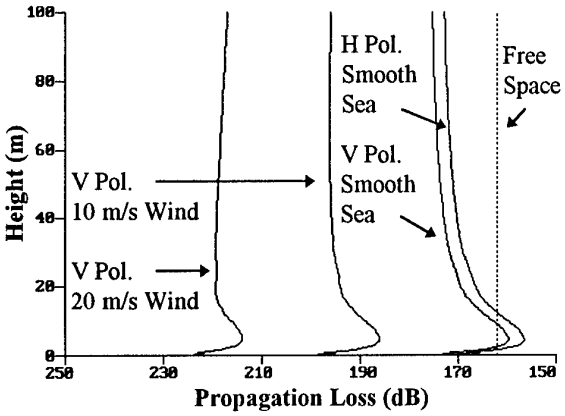


**Figure 3.** MLAYER results for the 12-m evaporation duct of Table 2. Frequency is 12 GHz, transmitter height is 10 m, and range is 250 km.

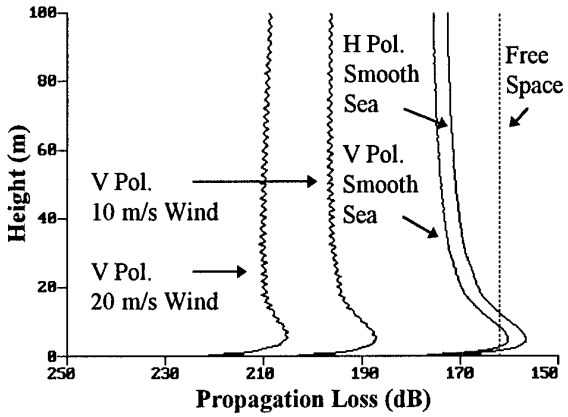


**Figure 4.** RPO results for the 12-m evaporation duct. Frequency is 12 GHz, transmitter height is 10 m, and range is 250 km.

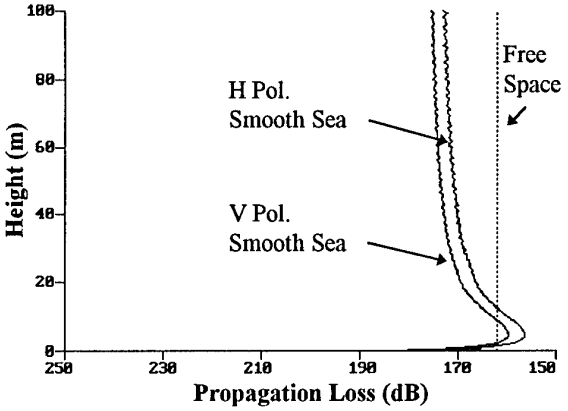


**Figure 5.** TEMPER results for the 12-m evaporation duct. Frequency is 12 GHz, transmitter height is 10 m, and range is 250 km.

One of the cases from which equation (4) for *B* was derived also shows some error in accurately accounting for rough surface effects. This case is the 46-m surface duct described by Table 3 for a frequency of 10 GHz with a transmitter height of 25 m and a range of 500 km. Figure 6 shows the MLAYER results for this case and Figure 7 shows the corresponding RPO results. A comparison of these figures shows the RPO model to be working well for vertical polarization over a smooth sea,

| Height (m) | *M* units |
|---|---|
| 0.0 | 350.000 |
| 45.7 | 334.677 |
| 1524.0 | 506.710 |

**Table 3.** Profile of modified refractivity in *M* units versus height for a 46-m surface duct.

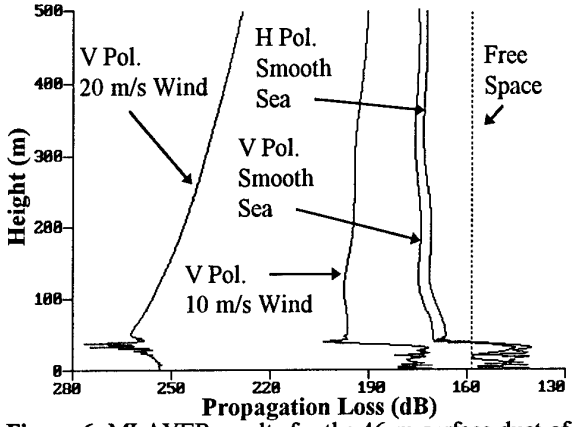


**Figure 6.** MLAYER results for the 46-m surface duct of Table 3. Frequency is 10 GHz, transmitter height is 25 m, and range is 500 km.

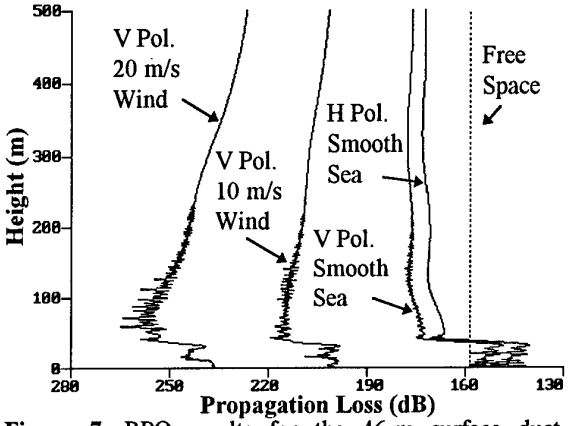


**Figure 7.** RPO results for the 46-m surface duct. Frequency is 10 GHz, transmitter height is 25 m, and range is 500 km.

but it overestimates the loss for the 10 m/s wind case, and is also in error at some altitudes for the 20 m/s wind case.

In both of the previous cases, and many other cases tried but not reported on, the RPO boundary loss model performed well for vertical polarization over a smooth sea. In all of these cases the reflection coefficient $R$ is between 0.9 an 1.0. For the rough surface cases, where $R$ can be as low as 0.1, the performance is not as good, although the trends with increasing wind speed are certainly correct.

## 4. RANGE DEPENDENT ENVIRONMENT

To test how well the RPO boundary loss method works in range dependent environments, several comparisons were made to the TEMPER model for both horizontal and vertical polarization over a smooth sea. Similar to the range independent cases, it was difficult to find test cases that showed substantial differences between the two polarizations, from which a conclusion could be drawn. One case tried that does show a moderate difference is an evaporation duct that increases from 12 to 24 meters over a range of 100 km. The modified refractivity profiles are those described in Tables 1 and 2. Both TEMPER and RPO interpolate the heights and modified refractivity values linearly with range between specified profiles. The frequency is 9 GHz, the transmitter height is 25 m, and the range is 100 km. Figure 8 shows the results from TEMPER and Figure 9 shows the results from RPO. Both models give nearly equal results, and show vertical polarization to result in about 3 dB greater loss than the horizontal polarization case. Also shown in these two figures are the results for the vertical polarization case for a homogeneous environment which assumes the 12-m evaporation duct at all ranges. Clearly, the effects of range dependency are far greater than the polarization effects for this example. RPO also matched the TEMPER results for this homogeneous case very well.

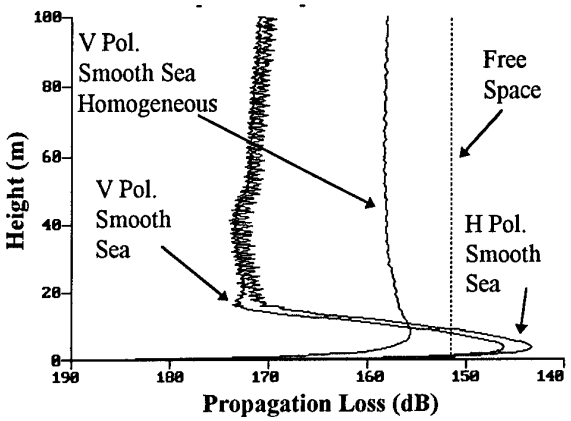


**Figure 8.** TEMPER results for the range-dependent 12- to 24-m evaporation duct. Frequency is 9 GHz, transmitter height is 25 m, and range is 100 km.

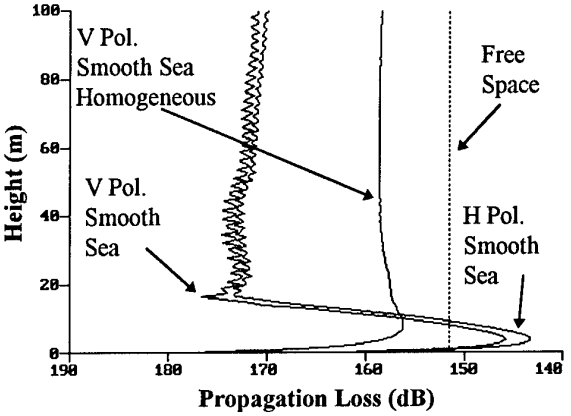


**Figure 9.** RPO results for the range-dependent 12- to 24-m evaporation duct. Frequency is 9 GHz, transmitter height is 25 m, and range is 100 km.

## 5. CONCLUSIONS

Based on comparison to more rigorous models, the approximate method appears to work very well for vertical polarization and reasonably well for surface

roughness. In addition, the method seems to work well in range-dependent environments. Although more extensive testing should be performed, it is recommended that this model, or a similar one, be permanently incorporated into RPO.

**ACKNOWLEDGMENT**

This work is sponsored by the Office of Naval Research.

**REFERENCES**

1. Dockery, G.D., "Modeling Electromagnetic Wave Propagation in the Troposphere Using the Parabolic Equation," IEEE Trans. Antennas Propagat., 36, 10, October 1988, pp 1464-1470.
2. Craig, K.H., "Propagation Modeling in the Troposphere: Parabolic Equation Method," Elec. Lett., 24, 18, 1988, pp 1136-1139.
3. Barrios, A.E., "Parabolic Equation Modeling in Horizontally Inhomogeneous Environments," IEEE Trans. Antennas Propagat., 40, 7, July 1992, pp 791-797.
4. Hitney, H.V., "Modeling Surface Effects with the Parabolic Equation Method," in "International Geoscience and Remote Sensing Symposium (IGARSS '94)," Digest Vol. IV, IEEE Cat. No. 94CH3378-7 (ISBN 0-7803-1497-2), 8-12 August 1994, pp 2322-2325.
5. Hitney, H.V., "Hybrid Ray Optics and Parabolic Equation Methods for Radar Propagation Modeling," in "Radar 92," IEE Conf. Pub. 365, 12-13 October 1992, pp 58-61.
6. Baumgartner, G.B., "XWVG: A Waveguide Program for Trilinear Tropospheric Ducts," Naval Ocean Systems Center TD 610, June 1983.
7. Baumgartner, G.B., H.V. Hitney, and R.A. Pappert, "Duct propagation modelling for the integrated-refractive-effects prediction system (IREPS)," IEE Proc., Pt. F, 130, 7, December 1983, pp 630-642.
8. Miller, A.R., R.M. Brown, and E. Vegh, "New derivation for the rough-surface reflection coefficient and for the distribution of sea-wave elevations," IEE Proc., Pt. H, 131, 2, April 1984, pp 114-116.
9. Phillips, O.M., "Dynamics of the Upper Ocean," London, Cambridge Univ. Press, 1966.
10. Kuttler, J.R. and G.D. Dockery, "Theoretical description of the parabolic approximation/Fourier split-step method of representing electromagnetic propagation in the troposphere," Radio Sci., 26, 2, March-April 1991, pp 381-393.

## DISCUSSION

**M.F. LEVY**
How is the skip distance calculated in range-dependent environments?

**AUTHOR'S REPLY**
The skip distance is computed based on the range-dependent vertical refractivity profile. However, this profile is considered to be locally range-independent for this computation.

# A PROPAGATION-BASED MODEL OF TERRAIN EFFECTS FOR SHIP-BOARD RADAR APPLICATIONS

J. P. Reilly
C. C. Lin
The Johns Hopkins University
Applied Physics Laboratory
Johns Hopkins Road
Laurel, MD 20723 USA

## SUMMARY

In this paper, a site-specific approach is presented to characterize terrain and target visibility and terrain clutter as seen by a shipboard radar in a coastal environment. The method takes into account the location of the ship, the particular terrain topography, the radar parameters, and the propagation effect. The method incorporates refractive index models of the atmosphere surrounding the radar, an optical ray-trace model, an electromagnetic parabolic equation model, and a data base of terrain elevations. The model can simulate illumination and shadow regions of both surface clutter and elevated targets. Simulated clutter results are shown to compare favorably with clutter data measured at S-band. This correspondence is evident in geographic patterns and statistical distribution of clutter on directly illuminated terrain surfaces.

## 1.0 INTRODUCTION

A ship-board radar in a coastal region is subject to complications not encountered in the open ocean. These complications include terrain shadowing of air targets over land, and clutter returns from terrain. Terrain shadowing occurs in geographic patterns dictated by specific terrain contours, resulting in regions of attenuated radar signal strength that can compromise detection and tracking. Terrain clutter can obscure a target's signal, even when it is not in shadow, and even when the clutter is at a range distant from the target. Both terrain shadowing and clutter are significantly affected by the characteristics of electromagnetic propagation, which can be quite complicated in the coastal region.

Existing models for land clutter are typically empirical ones. For instance, tables and empirical formulas are available in which reflectivity for generic types of terrain is related to various radar parameters [1] - [6]. Typically some statistical measure is given, such as mean or median reflectivity ($\sigma_o$), often along with parameters of some statistical model. Such models suffer from a number of deficiencies. These deficiencies include inability to account for site-specific terrain features, geographic patterns of clutter, propagation conditions, or target shadowing. Other researchers have developed models that account for site-specific terrain features [7], [8], but these models fail to account for arbitrary propagation conditions, and do not represent target shadowing.

The model described here overcomes these deficiencies. Features of the model include 3-D refractive index specifications, an optical ray-trace model, an electromagnetic parabolic equation model, and a data base of terrain elevations known as DTED (Digital Terrain Elevation Data), which is published by the Defense Mapping Agency. The data base provides terrain elevations on a 100 m grid for much of the earth's land mass. The model can accept refractivity inputs that vary in three dimensions, if such detailed data is available. Alternatively, a single profile of refractive index versus altitude may be used to represent a uniformly stratified atmosphere, i.e., a condition in which the refractive index versus altitude is constant over the radar coverage area.

The terrain effects model is presently configured with varying levels of complexity and fidelity. A "Terrain Visibility Routine" (TEVIR) calculates regions of the terrain or of the air space above the terrain that is subject to direct illumination by the radar. TEVIR-I performs such calculations for an atmosphere characterized by a linear refractivity profile, of which the standard atmosphere is a specific case. TEVIR-I performs calculations using calculations of straight line ray trajectories over a round earth having an equivalent earth radius dictated by the refractivity slope. In the case of the standard atmosphere, the equivalent earth radius is a factor of 1.33 greater than the true earth radius. TEVIR-II can use arbitrary refractivity profiles, which can include profiles that vary in both range and azimuth from the radar location. TEVIR-II makes use of an optical ray-trace routine. A third variant called the RADSCAT (Radar Scattering) model determines propagation effects using an electromagnetic parabolic equation method. This method involves a full-wave calculation of the total electromagnetic field. The parabolic equation is numerically solved in RADSCAT by the Fourier Split-step method, using the computer model known as TEMPER developed at the Johns Hopkins Applied Physics Laboratory [9], [10]. The RADSCAT model with TEMPER provides numerical calculations of the propagation factor, and accounts for radar refraction, multipath, and diffraction. The more complex RADSCAT model is used to calculate quantitative radar clutter data. Like TEVIR-II, RADSCAT can accept three dimensional refractivity inputs.

## 2.0 VISIBILITY MAPS

### 2.1 General Considerations

With consideration of propagation effects, we determine terrain visibility by one of two methods: an optical ray-trace program, and an electromagnetic parabolic equation model (TEMPER). In both methods, electromagnetic energy is assumed to be perfectly reflected from water surfaces, but absorbed by terrain.

The optical ray-trace method integrates propagation differential equations along a ray trajectory. In the ray-trace method, rays are launched at closely spaced elevation angles. Typically both positive and negative angles are included; the negative ones are reflected from the water surface. The range of angles needed to simulate radar visibility will depend on the beamwidth of the radar, the maximum altitude of terrain peaks, and their range to the radar. In a typical simulation of a ship-board radar, ray angles of $\pm 2°$ usually sufficiently account for all rays that intersect terrain. The trajectory of each ray is calculated for a particular refractivity profile. Once a ray encounters a land surface, that surface is considered illuminated for subsequent ranges along an equal azimuth slice until the terrain slope becomes negative. For ranges beyond the negative terrain slope, the terrain is considered to be in shadow until the another ray intersects the terrain surface. By repeated application of this algorithm, one can identify directly illuminated regions along a radial slice; with slices along various azimuths, one can identify directly illuminated areas of terrain. The accuracy of the resulting plot improves as we increase the density of rays within the elevation launch angles, and as we increase the density of azimuth slices. For a typical application, we obtain satisfactory results with elevation ray spacing of about 0.02°, and azimuth spacing of about 0.5 °.

The number of ray calculations can become quite large. For example, using $\pm 2°$ elevation coverage with 0.02° spacing, and 90° azimuth coverage with 0.5° spacing, there are 36000 ray trajectories to be computed if the refractivity profiles are unique

*Paper presented at the Sensor and Propagation Panel Symposium on "Propagation Assessment in Coastal Environments" held in Bremerhaven, Germany 19-22 September 1994.*

along each azimuth slice. For a uniformly stratified atmosphere, however, the number of calculated rays need be only 200 by employing the same set of trajectories at each azimuth angle.

One can often evaluate the potential severity of terrain clutter problems by examining a terrain visibility map showing the regions of terrain that are directly illuminated (i.e., not in shadow). Often the distribution and extent of visible terrain sufficiently indicate the probable impact of clutter. In such cases a ray trace solution obtained by TEVIR-I and -II may be sufficient for radar performance evaluation.

In this section, we will examine propagation effects using refractivity profiles illustrated in Fig. 1. Profiles A and B were measured by the Pacific Missile Test Center (PMTC) off the coast of California over a three-day period in June, 1990. Strong surface-based ducts were persistent during this period. Profile C was measured off the coast of California by Applied Physics Laboratory personnel during the summer of 1992. Surface-based duct heights of 500, 600, and 1000 ft apply to profiles A, B, and C respectively. The profiles include evaporation ducts at the surface. An additional profile representative of a standard atmosphere is also shown in Fig. 1. When using the profiles of Fig. 1, we retain the evaporation duct for propagation over the sea. However, we assume that the evaporation duct does not exist over land. For overland applications, we delete the evaporation duct, and extrapolate the refractivity profile above that duct to the surface. The refractivity profiles shown here have been constructed from temperature, pressure, and humidity constituents, using relationships given in [12]. The evaporation duct profile has been constructed using the marine boundary model with a neutrally buoyant condition as described in [11]

### 2.2 Terrain Visibility - Ray Trace Solutions for Stratified Atmosphere

Figure 2 illustrates an example of a DTED terrain profile and ray trajectories for a standard atmosphere refractivity profile. The highlighted areas are those in direct illumination, according to the algorithm described in Sect. 2.1. Figure 3 illustrates a terrain visibility diagram for a radar located in the Red Sea with standard atmosphere propagation. The region shown is characterized as "high relief terrain", having terrain peaks of 8200 ft. Figure 4 illustrates a ray diagram for a refractivity profile involving a uniformly stratified 600 ft surface-based duct (identified as "profile 6" in [12]). Figure 5 shows the same area as in Fig. 3, but with a 600-ft surface-based duct.

By comparing Figs. 3 & 5, one sees significant differences in the patterns of visible terrain under standard atmosphere and ducting conditions. Clearly, much more terrain is directly illuminated with the 600-ft duct than with the standard atmosphere. However, the maximum extent of the clutter is similar in the two cases. The increased density of illuminated terrain under ducting may be explained by the downward refraction of radar energy, which illuminates features that might otherwise be hidden, as suggested in Fig. 4. The terrain at great distances is illuminated primarily by rays which escape the duct and intersect high altitude terrain features. For that reason, there is not a large difference in the maximum extent of visible terrain in the two cases shown here.

Figure 6 illustrates terrain visibility with propagation via a 1000-ft surface-based duct (profile C) near the coast of Saudi Arabia. In this example, the terrain is characterized as low-to-medium relief, with peaks of about 1000 ft. With the radar situated 70 nm from the coast (Part *a*), the directly-illuminated terrain is confined to a narrow band about 20 nm wide along the coast. However, by moving the radar to a location that is 25 nm more distant (Part *c*), the directly illuminated terrain extends to about 75 nm from the coast (Part *d*) - a significant increase relative to Part *b*. The extended visibility in Part *d* occurs because of the opportunity for reflected paths from the ocean surface to intersect distant terrain as indicated in Part *c*.

### 2.3 Terrain Modified Refractivity Profiles.

The atmospheric constituents that govern refractivity are temperature, pressure, and humidity-parameters which will be subjected to terrain influences. Consequently, a more realistic atmospheric model would include terrain-related modifications to the refractivity profiles, in contrast to the simple stratified atmospheric assumptions employed in the previous examples. In order to illustrate the ability to represent terrain influences, we simulated an adiabatic sea breeze (ASB) model in which a sea breeze transports the air mass from the sea to the land [12]. We assumed that as the air mass is raised in altitude, it undergoes adiabatic expansion (i.e., heat is neither added nor subtracted. We assumed knowledge of temperature, pressure and humidity versus height profiles over the sea, and that the temperature, pressure, and humidity constituents are transformed via an adiabatic process as the air mass is transported over the land. As the air mass is moves inland, we calculated new constituent profiles along range increments $\Delta R$. We then interpolated the constituents between calculated profiles using a linear interpolation procedure. In Fig. 5 of reference [12], the ASB model was applied to Profile A with a ship position in the Red Sea as in Fig. 5 of this paper. Comparing the visibility diagrams generated by the ASB and stratified atmosphere models, one could observe differences in specific regions. However, the overall density and range extent of illuminated terrain are similar in the two cases considered. For other classes of terrain relief, however, one might expect greater differences between a stratified atmosphere and an ASB process.

It is not our intention to represent the ASB model as a realistic case, but rather to demonstrate the ability of our visibility models to incorporate the interaction of terrain and atmospheric processes. Although the ASB process introduces additional complexities into the refractivity model, it is nevertheless a simplification of the physical processes present in coastal meteorology. We have ignored a number of phenomena likely to be important, such as boundary layer phenomena, heat inputs from the terrain, and more complex air movement patterns.

### 2.4 Visibility of Air Targets.

Besides clutter processes discussed above, terrain shadowing can limit the ability of the radar to detect and track overland targets. It is often useful to evaluate target shadowing limitations using a target visibility diagram as illustrated in Fig. 10. This example applies to air targets over former Yugoslavia, for a ship position approximately 25 nm off the coast. The calculated visibility applies to a standard atmosphere assumption. It is assumed that the air target flies at a constant height above the terrain. The shaded regions indicate where an air target at several different heights would be directly illuminated by the radar. The coded regions should be interpreted as being cumulative, e.g., the shaded region applying to 10000 ft also includes the regions for lower altitude targets. This visibility diagram was produced by calculating ray trajectories, and applying a visibility algorithm similar the one used to determine terrain visibility (see Sect. 2.1).

### 2.5 Application of Electromagnetic Propagation Routine

The ray trace methods discussed above provide relatively fast qualitative solutions. The Electromagnetic Parabolic Equation Routine (TEMPER) provides more detailed quantitative calculations of the total electromagnetic field using the Fourier split-step method [9], [10]. Inputs to TEMPER include the radar frequency, polarization, antenna elevation beam pattern, antenna elevation pointing angle, and refractivity profiles (index of refraction versus height). The refractivity profiles may vary with range if such detailed information is available. In our applications, the relevant output of TEMPER is the one-way or

two-way propagation factor $F^2$ or $F^4$, where $F = |E/E_o|$, $E_o$ is the free-space field, and $E$ is the field under the assumed conditions. We have adapted TEMPER to simulate a lower terrain boundary by setting the calculated field to zero at and below the terrain boundary at each range increment [13]. The first non-zero field value above the terrain surface is attributed to the surface field strength. This procedure is an approximation, albeit an imperfect one, to a perfectly absorbing boundary. With this method, the TEMPER calculation will be unique for each azimuth slice.

Figure 11 illustrates a TEMPER solution using a particular terrain slice as a lower boundary. The magnitude of $F^2$ has been coded on a gray scale. The solution includes diffraction zone values within regions that would be considered in shadow according to the ray-trace algorithm. This example was generated using Profile B to specify refractivity - the same profile used in the ray diagram of Fig. 4. Other relevant parameters applying to Fig. 11 are: S-band, vertical polarization, 1.5° beamwidth, 0° antenna pointing angle.

By applying the TEMPER program to each azimuth slice, a terrain visibility map may be obtained. Although the TEMPER method does not explicitly determine shadowed terrain, one can obtain a terrain visibility map by applying a threshold to $F^2$. In reference [13] a visibility map was generated by applying a threshold of -6 dB to $F^2$. By comparing that visibility diagram with the one determined with the ray method (Fig. 5), one sees very little difference.

### 2.6 Terrain Boundary Assumptions

Both ray-trace and TEMPER methods make use of perfectly absorbing boundaries. In principle, it would be possible to extend our models to include reflecting boundaries. In the case of the ray method, one might calculate a reflected path after a ray encounters the terrain, taking into account the terrain slope in determining the reflected launch angle. In the case of TEMPER, one might consider using a finite impedance lower boundary, such as has been studied elsewhere [14], [15].

Not only is our implementation of an absorbing boundary much simpler than alternatives using reflecting boundaries, but one can advance arguments for preferring an absorbing boundary. One argument is that reflected rays are very unlikely to return energy to the surface at a more distant range. One can justify this assertion by realizing that in most cases of practical interest, those rays that are launched at more than a degree (or less) penetrate most practical ducts, and are therefore not refracted back to the surface. Consequently, terrain slopes of more than one degree would not return reflected energy to more distant surface locations. Secondly, energy will tend to be diffusely reflected because realistic terrain is typically very rough compared with radar wavelengths. Consequently, a specular reflection or smooth surface calculation may be unwarranted. Thirdly, absorption at the boundary due to finite impedance will diminish what energy is reflected.

In order to adequately assess the impact of terrain boundary assumptions, more modeling efforts are required. Work continues at the Applied Physics Laboratory to develop finite impedance boundary applications, which we will eventually apply to our terrain effects models.

## 3.0 CLUTTER CALCULATIONS

### 3.1 General Relationships

Clutter magnitude depends on both radar system parameters and terrain parameters. Radar system parameters include transmitter power, frequency, antenna gain, and resolution size (both range and azimuth). Terrain parameters comprise type, roughness, reflectivity, and location relative to the radar. Clutter power can be expressed by:

$$P_c = \frac{P_t G^2 \lambda^2 \sigma_o F^4 A_c}{(4\pi)^3 R^4 L} \qquad (1)$$

where $P_c$ is returned clutter, $P_t$ is transmitted power, $G$ is antenna gain, $\lambda$ is radar wavelength, $\sigma_o$ is the clutter reflectivity of a radar cell, $F^4$ is the two-way propagation factor, $A_c$ is the area of an illuminated cell, $R$ is range to the clutter cell, and $L$ represents various losses.

By using the "constant-gamma" model, the clutter reflectivity is defined as

$$\sigma_o = \frac{1}{n}\sum_i^n \sigma_{oi} = \frac{1}{n}\sum_i^n \gamma \sin \psi_i \qquad (2)$$

where $n$ is the number of DTED facets (defined in [12]) within a radar cell, $\sigma_{oi}$ ($m^2/m^2$) is the reflectivity of the $i$th facet, $\psi_i$ is the grazing angle at the $i$th facet, and $\gamma$ is the normalized reflectivity ($m^2/m^2$), which is pre-defined and depends on the radar frequency and the type of terrain. We use the following frequency relationship in our model:

$$\gamma = \gamma_r \left(\frac{f}{f_r}\right)^k \qquad (3)$$

where $\gamma_r$ is a reference value applicable to a particular radar frequency $f_r$; according to [1], we use the frequency scaling $k = 0.5$. While some data suggest that $\gamma$ and $k$ vary with both terrain relief and cultural development [1], [7], we presently use the same values for both high and low relief terrain, namely $\gamma_r = 0.17$ at $f_r = 3.0$ GHz, and $k = 0.5$. The $\gamma_r$ value has been increased relative to our previous estimates [12], [13] to conform with the measurements presented in Section 4.0. We have not varied $\gamma_r$ with terrain relief, reasoning that terrain relief factors due to large-scale shadowing may be adequately accounted for in our DTED-based method. We recognize, however, that the specification of $\gamma_r$ for our model as a function of terrain type and frequency requires further investigation and clarification. Additional subjects requiring clarification include grazing angle and radar frequency relationships. These subjects are discussed further in the following section.

Generally one characterizes clutter in terms of the reflectivity parameter $\sigma_o$, which is expressed as a unitless quantity ($m^2/m^2$); $\sigma_o$ is usually determined by measuring returned clutter power, and solving for $\sigma_o$ using Eq. (1). Since one typically lacks detailed knowledge of the propagation factor at the clutter source, it is customary to assume $F^4 = 1$ in this calculation. Recognizing the difficulty of separating reflectivity and propagation factor, we will characterize clutter reflectivity in terms of the combined parameter $\sigma_o F^4$.

### 3.2 Parametric Variations

***3.2.1 Grazing angle:*** Many clutter models assume that the backscatter coefficient $\sigma_o$ increases with increasing grazing angle [1] - [5], a trend in accordance with rough surface scattering theory [16] - [18]. Others have proposed a relationship based on depression angle of the radar antenna pattern, rather than grazing angle of the incident energy [6], [7]. According to depression angle advocates [7], the backscatter from terrain is dominated by processes involving vertically oriented features (e.g., trees, cultural features, etc.) and associated "micro-shadowing", rather than the rough surface mechanisms of theoretical models, and that general rough surface theory does not apply to most terrain. There are difficulties in defining appropriate angles in either view. Both depression and incidence angles will be affected by atmospheric refractivity properties. And grazing angles will further be affected by the fine structure of terrain slopes. In general, such details may not be accurately known.

Our present model uses a grazing angle relationship according to Eq. (2), where the grazing angle is defined by the slope of a ray from the ray-trace method and the terrain slope of a DTED directly illuminated cell. For shadowed regions, the grazing angle is approximated using the incidence angle of the previous ray and the local terrain slope. If the grazing angle in the shadow zone is negative (i.e., negative terrain slope exceeds ray inclination), we replace $\psi_i$ with a minimum value in Eq. (2). In this paper, the DTED terrain slope is determined as the slope along a 2-dimensional slice. A more accurate definition of terrain slope would consider the 3-dimensional slope of terrain. However, the error in backscatter coefficients by using a more simply determined 2-dimensional slope is not excessive[12]. We consider the subject of viewing angle relationships to require further research and clarification.

***3.2.2 Gamma Parameter:*** Clutter reflectivity is often characterized using the parameter $\gamma$ of Eqs. (2) and (3); $\gamma$ is usually determined experimentally, and may be separately specified for various terrain relief and cultural development classifications [1]. Past descriptions of $\gamma$ can be only an initial guide for our applications for two reasons. First, most experimental data on $\gamma$ apply to average reflectivity over an entire radar resolution cell, whereas in our applications, we apply $\gamma$ to smaller DTED cells within a radar resolution cell. Consequently, we would expect the appropriate $\gamma$ value in our model to be different than the larger scale value determined in previous studies. Secondly, Previous descriptions of $\gamma$ include only generic classifications of terrain, whereas in our model, the terrain slopes and shadowing features are separately determined for every DTED cell. Consequently, we hypothesize that aspects of terrain roughness might be accounted for in a DTED-based approach using DTED terrain slopes, and the same value of $\gamma$ might apply to various terrain relief classifications. This hypothesis will have to be examined in future experimental studies of the sort presented in Section 4.

Our initial model evaluations [12], [13] used $\gamma = 0.055$ at S-Band - a value derived from previously published data [1]. However, based on data presented in Section 4, that value has been increased to $\gamma = 0.17$ for application to our model. It will be necessary to conduct additional measurements before we can determine the experimental error in that estimate, or can confidently specify $\gamma$ for other radar frequencies and terrain types.

### 3.3 Example Calculation of radar clutter

Figure 12 shows the results of the RADSCAT land clutter model for an S-Band radar with the following parameters: 0° antenna elevation pointing angle, 1.5° beamwidth (both azimuth and elevation), horizontal polarization, 1 μs pulse width, 62 ft antenna height. The top panel of the figure is the land profile at a particular radar look direction. The highlighted surfaces are visible by radar, as determined by the ray-trace program. Note that the land profile presents only one slice of terrain. Within a radar beamwidth, the terrain profiles could vary, especially at large distances from the radar. In our simulations, we generally compute at least two slices within each beamwidth. The second panel shows the one-way propagation factor, $F^2$, computed by TEMPER with Profile B from Fig. 1. The third panel shows the land clutter strength $\sigma_o F^4$ versus range. When $\sigma_o$ is computed by Eq. (2), the incident angle within a shadowed region is assumed to be the same as that of the last ray on the illuminated surface. The bottom panel depicts the returned clutter power calculated by:

$$P_c = K \frac{\sigma_o F^4 A_c}{R^4} \qquad (4)$$

For convenience of calculation and plotting, we evaluate (4) using $K = 10^{10}$, determined with $A_c$ having units of $(\text{nm})^2$, and $R$ having units of nm. The Figure shows clutter power not only from directly illuminated terrain, but also from shadowed regions due to diffraction.

One can construct a clutter map by repeating the calculations shown in Fig. 12 at incremental azimuth angles. Figure 13 illustrates a radar clutter map of $\sigma_o F^4$; the assumed propagation condition and radar location are those used in the visibility diagram of Fig. 5. The radar parameters in this example are: S-Band, 3° beamwidth, 0° elevation pointing angle, 2 μs pulse width, 62 ft antenna height. In the figure, the magnitude of $\sigma_o F^4$ is indicated with a gray scale. The azimuth increment is 0.5°.

### 3.4 Statistical Representation

The Weibull distribution is often used to represent the statistical distribution of terrain clutter. Statistical representations of terrain clutter can, however, be ambiguous and lead to misinterpretation. Consequently, one must be circumspect in interpreting and applying statistical clutter models. A major reason for this ambiguity is the influence of the minimum threshold used in the statistical data base, a parameter which is usually unstated in descriptions of experimental clutter data.

The selection of a lower limit in simulated data is arbitrary. Since the model has no absolute lower limit on $\sigma_o F^4$, one could set a lower threshold to exclude weak clutter data. The effect would be to alter the statistical parameters of the resulting data base. As a practical matter, a similar issue will be present with measured data. Radar measurements will be limited to clutter cells that exceed a minimum signal to noise ($S/N$) ratio, and this minimum will be a function of the sensitivity of the radar, including transmitter power, antenna gain, noise figure, and other parameters. To illustrate this point, imagine that clutter measurements are made by two radars that differ in sensitivity, but are identical in all other respects. If we set a threshold at some multiple of $S/N$, the more sensitive radar would include more data points with small values of $\sigma_o F^4$, and would have a smaller average $\sigma_o F^4$.

We illustrate this situation in Figures 14 and 15, which give simulated cumulative count distributions of $\sigma_o F^4$ for low and high relief terrain, both with $\gamma = 0.055$. Three radars are represented which differ only in frequency. The high relief terrain (Fig. 14) applies to the Red Sea area with the radar looking eastward towards mountainous terrain in the azimuth sector 50 - 60°, and a maximum range of 60 nm. In the low relief terrain case (Fig. 15), the radar is situated in the Persian Gulf 10 nm from the coast at 29.1° latitude and 48.3° longitude. The observed region covers the low relief terrain of Kuwait and Saudi Arabia in the sector 260 - 270°, with a maximum range of 60 nm. The simulated data include shadowed terrain illuminated through diffraction, and do not have an absolute minimum value. Because of enhanced diffraction at longer wavelengths, small values of clutter are enhanced as the frequency band is lowered. However, the reverse is true at large values of $\sigma_o F^4$, where clutter is enhanced as frequency is increased because of the scaling law given in Eq. (3).

Table 1 summarizes the averages of $\sigma_o F^4$ and number of cells ($N$) exceeding the threshold when various thresholds are applied to the data of Figs. 14 and 15. From these data, one might infer that $\sigma_o F^4$ has a frequency scaling law that depends both on threshold and terrain relief. A terrain relief dependency was also indicated in the measurements of Billingsley [7] who found $\sigma_o F^4$ to increase with increasing radar frequency in low relief farmland, but to decrease with increasing radar frequency in high-relief mountainous terrain.

In comparing simulation results with measurements, it is important to understand the difference in statistical properties of simulated and measured data. Whereas the model provides statistical expectations, i.e., statistical averages of reflectivity from individual radar cells, actual measurements include statistical fluctuations about these averages. The simulation results can be said to belong to a simple statistical distribution, whereas measurements will follow a compound distribution (see subsequent discussion in connection with Fig. 21).

## 4.0 EXPERIMENTAL VERIFICATION

### 4.1 Data Collection and Processing

Terrain clutter measurements were collected by a shipboard radar near the coast of southern California and northern Washington in May and June, 1993. Both areas have mountainous high-relief terrain, but differ significantly with respect to the nature of the terrain cover. The measured area of Northern Washington has a moist climate, and is heavily forested, with relatively little cultural development. Southern California is semi-arid, sparsely vegetated, and has much more cultural development. There was scattered light rain during the testing period in northern Washington; in southern California, the weather was clear and dry.

Pertinent radar parameters are: S-band, horizontal polarization, 1.6° beamwidth (azimuth and elevation), 0° elevation pointing angle, 3.0 μs pulse width, and 120 ft antenna height. Clutter data were recorded by a data collector having a 40-dB dynamic range. In order to cover the full measurement range required for our tests, data were sequentially collected with attenuation levels of 80, 60, 40, 20, and 0 dB, and later merged for expanded dynamic range. In the data merging process, a 17 dB lower limit and 37 dB upper limit was used at each attenuator setting to eliminate system noise and saturated data respectively. The clutter-to-noise ratio of the merged data ranged from 17 to 117 dB. The process of data collection at the five attenuator settings consumed approximately 4 - 6 minutes. In the merged data file, each clutter measurement has been attributed to a fixed radar cell, despite the fact that the ship speed was approximately 10 knots during the data collection period. This extended data collection process effectively creates a smearing effect. The data collector is capable of acquiring measurements over an extended azimuth and range sector. In these tests, the azimuth and range sectors were approximately 130° and 63 nm respectively. Considering the range resolution (0.24 nm), azimuth resolution (1.6°) and attenuator settings (5), more than $10^5$ measurements comprise a single range/azimuth data set. Multiple data sets were transferred to tape for later analysis.

Atmospheric data were collected using an instrumented helicopter which measured temperature, pressure, and humidity versus height. The helicopter flew a series of saw-tooth patterns from the ship over the water, thereby allowing a sequence of profiles to be constructed as a function of range from the ship. Atmospheric data were not collected over land. These data were later processed to determine a series of profiles of refractivity index versus height. In both the May and June exercises, measured refractivity did not deviate significantly from a standard atmosphere condition. As a general rule, however, propagation in marine or coastal environments can deviate significantly from standard atmosphere conditions, resulting in significant variations in terrain clutter as seen by a ship-board radar (see Section 2.0).

The tests did not include absolute calibration of the radar power. In relating radar measurements to absolute reflectivity, we relied on specified radar parameters.

### 4.2 Comparison of Measurement and Model: Geographic Patterns

Figure 16 illustrates several features of the measured and simulated reflectivity data. The upper panel shows a terrain profile determined from the DTED data base for a single azimuth direction (106.34°) with the ship positioned in southern California. The highlighted regions represent directly illuminated terrain, as determined with the ray-trace algorithm described in Section 2.1. The terrain profile shown is only one representation of the terrain contour within a radar beamwidth. Within a beamwidth, the terrain height will vary at a fixed range, especially at the greater limits of range. The middle panel shows the one-way propagation factor determined from the TEMPER program described in Section 2.5. The lower panel shows measured values of $\sigma_o F^4$ versus range (dotted line), and modeled data (solid line), where the simulated data was obtained with two azimuth slices per radar beamwidth. The broken line shows the magnitude of $\sigma_o F^4$ necessary to equal system noise. As a general rule, measurements below the noise limit are not possible.

Figure 17 shows wide-area views of measured clutter in southern California. In Fig. 17, magnitudes of $\sigma_o F^4$ have been coded on a gray scale; these magnitudes were derived from measurements of radar power using Eq (1). This picture provides one example out of many such data sets collected during the exercise. Corresponding model data is shown in Figs. 18 and 19. Figure 18 was derived from the terrain visibility routine (TEVIR) using the ray-trace algorithm described in Section 2.0. Figure 19 was derived from the RADSCAT program, described in Section 3.0.

By overlaying the measurement and simulation maps, one observes very good correspondence between the geographic patterns of measured and modeled data. The predicted areas of terrain illumination in from the ray-trace routine (Fig. 18) correspond well with the contours of measured clutter above -20 dB in Fig. 17 This suggests that the strong clutter measurements are associated with directly illuminated terrain.

In order to obtain the indicated geographic correspondence, it was necessary to reduce the calculated range of the modeled data by 4% - an adjustment necessary for the data of both southern California and northern Washington. We do not presently understand the reason for the range discrepancy, although we are investigating several possibilities. In terms of radar timing precision, 4% is a very large range error. On the other hand, it is possible that timing errors may have been present in the data collection process, which might explain the range discrepancy. Another possibility is that the DTED data base, or the simulation process itself contains range errors.

### 4.3 Statistical Representation

*4.3.1 Southern California Data.* Figure 20 illustrates the cumulative distribution of measured and modeled reflectivity ($\sigma_o F^4$) in southern California . The vertical axis gives the number of radar cells exceeding the value of $\sigma_o F^4$ shown on the horizontal axis. The upper broken line applies to measured data, the other lines apply to simulated data using the method described in Section 3.0, with $\gamma = 0.17$. The modeled data includes calculated effects of various horizontal antenna side lobe levels. Side lobe effects were determined by integrating clutter from cells along a constant azimuth slice, but reduced in magnitude by the assumed side lobe level, and adding the integrated side lobe clutter to the calculated main beam value. A side lobe level of -80 dB approximates that of the experimental system.

For $\sigma_o F^4$ greater than -40 dB, the measured and simulated results in Fig. 20 agree quiet well. For weaker clutter, however, the model predictions are significantly below measurements. It was suspected that the lack of correspondence of weaker clutter might

occur primarily in shadow (diffraction) regions. In order to test this hypothesis, we examined the distribution of measured and simulated clutter applying to radar cells that contained at least a portion of directly illuminated terrain as indicated by the ray-trace method. The resulting distributions are shown in Fig. 21. Two distributions are shown for the modeled data: one applies to the calculated values of $\sigma_o F^4$, following the convention shown in Fig. 20; the other is obtained by random numbers drawn from a Raleigh power distribution, in which the mean value is defined by the calculated $\sigma_o F^4$ for that cell. This simulates a compound distribution as described previously. When comparing statistical distributions, the compound distribution is expected to more accurately simulate the measured data.

It is seen that the measured and modeled distributions in Fig. 21 correspond very well, suggesting that the model performs quite well when directly illuminated surfaces are contained within the radar cell. The median value of $\sigma_o F^4$ is -23 dB for both measured and modeled data; the Weibull $a$-parameter is 1.7 for the measurements and the modeled compound distributions. These values compare favorably with previously published data at S-band [1].

*4.3.2 Northern Washington Data.* Figure 22 plots the cumulative distribution of $\sigma_o F^4$ applying to northern Washington. As noted in Section 4.2, these measurements were complicated by the presence of light scattered rain, which is estimated to provide median reflectivity of about -50 dB. In Fig. 22 no attempt has been made to model the rain. As with the southern California data, good correspondence between measured and modeled data is seen for strong returns, particularly those above -30 dB. Below about -40 dB, the model under predicts clutter returns. The discrepancy between measurement and model for weak clutter is greater in Fig. 22 than in Fig. 20, presumably a result of the influence of scattered rain in Fig. 22.

### 4.4 Investigation of Differences Between Measurement and Model

The statistical distribution of measured and simulated clutter appear to correspond well for relatively strong clutter, or for radar cells having directly illuminated surfaces. For weaker clutter, or that pertaining to shadow zones, the model appears to under predict the measured data. We are investigating several possibilities for this discrepancy. The following describes potential sources of discrepancy that are being considered.

*4.4.1 Antenna pattern effects.* The side lobes of an experimental system can increase the occurrence of relatively weak clutter. Azimuth side lobes, as seen in Fig. 20, do increase relatively weak clutter, but not to an extent sufficient to bring the measurement and model in complete correspondence. The experimental system also had elevation side lobes and cross-talk between vertically separated beams. The effects of these elevation side lobes and cross-talk were simulated, and found to reduce the difference between measured and modeled data. We note that at the trailing edges of strong clutter peaks, the measured clutter tends to exceed the simulated data (see Fig. 16). The effects of vertical antenna beam cross-talk appeared to account for the trailing edge effects. Despite this improvement, significant differences remained measured and modeled data below -40 dB.

*4.4.2 Position smearing effects.* As described in Section 4.1, data collection at five attenuator settings took place over a period of 4 - 6 minutes, during which time the ship maintained a velocity of about 10 knots. In order to investigate the possible smearing effects of position changes during the data collection period, we plan to simulate a data base which contains such smearing effects.

*4.4.3 Diffraction representation.* As described in Section 2.5, terrain effects are incorporated into the TEMPER electromagnetic routine using an approximation to a perfectly absorbing boundary. We considered the possibility that the terrain boundary method implemented in TEMPER might not adequately represent diffraction zone effects. In other work by J. D. Huffaker at our laboratory, a reflecting boundary was implemented into TEMPER. The reflecting boundary model was compared with the simpler method used in our clutter model. In one example derived for high-relief terrain, the reflecting boundary resulted in reduced propagation within diffraction regions. This would result in even lower calculations of $\sigma_o F^4$ than with our absorbing boundary approximation. Another simplification in the model is that the terrain boundary is a two-dimensional, rather than three-dimensional as in the real world. The use of a 2-D approximation will introduce errors into the simulation.

*4.4.4 Other possibilities.* Another possible source of error is that multiple scattering processes (due to the three-dimensional aspects of the terrain) are not included in the simulation.

## 5.0 DISCUSSION

This paper discusses a model for terrain effects on ship-board radar performance that accounts for site-specific terrain features, and propagation effects. Both terrain shadowing and clutter can be simulated. The method can accommodate atmospheric data that varies in three dimensions, if such detailed information is available. Site specific terrain contours are described through the DTED data base, which is provided by the Defense Mapping Agency. The model is configured with varying degrees of complexity.

Relatively simple, but fast methods are provided with TEVIR-I and -II. TEVIR I computes terrain and target shadowing, where the propagation can be represented as straight line propagation over a round earth with an equivalent earth radius factor. Atmospheric profiles fitting this category can be represented by a constant gradient of the index of refraction versus height. The "standard atmosphere" is one example fitting into this category. TEVIR II also determines terrain and target shadowing, but with arbitrary atmospheric inputs.

The RADSCAT method employs an electromagnetic parabolic equation method to calculate the propagation factor. RADSCAT includes both refraction and diffraction effects, and can simulate terrain shadowing and backscatter. This method can accept refractivity that varies in three dimensions. Whereas the RADSCAT method provides much more detailed information, it is also takes much more time to execute as compared with the TEVIR methods.

Variations in atmospheric refractivity can significantly alter patterns of terrain clutter and shadowing. The effects will depend structure of atmospheric refractivity, as well as terrain relief. With a surface-based duct for instance, it is possible to markedly increase the density of directly illuminated terrain, or to greatly extend the range extent over which strong clutter is returned.

The RADSCAT and TEVIR models were compared with radar measurements taken off the west coast of the U.S. from an S-band radar. The correspondence between measured and simulated clutter is very good for relatively strong clutter. This correspondence is evident in the geographic patterns and statistical distribution of clutter returns in both northern Washington and southern California. Although the terrain has similar mountainous relief in the two locations, the composition of the terrain is quite different. In the measurement area of northern Washington, the terrain is forested, with little cultural development. In southern California, the terrain is semi-arid, with significant cultural development present, particularly along

the coast. Despite the differences in terrain composition, the clutter returns on directly illuminated surfaces were similar in the two locations.

Within shadowed regions, the model predicts generally lower clutter strengths as compared with measurements. We are presently investigating several hypotheses that might explain the discrepancy. Primary considerations include: (a) smearing due to platform motion during the measurement interval, (b) inadequate representation of diffraction, (c) multiple scattering effects, (d) data collection response dynamics.

Although the simulated patterns of strong clutter corresponded very well to measurements, there was approximately a 4% discrepancy in the range to geographic features. We are investigating the possibility of timing errors in the measurements, or of errors in the simulation.

Future improvements in the model will incorporate the *Digital Feature Analysis Data* (DFAD) data base of terrain composition. This data base, also published by the Defense Mapping Agency, indicates features such as vegetation, structures, roads, bridges, power lines, etc. With such data, it is possible to better predict backscatter, and the effects of both natural and cultural features.

## ACKNOWLEDGMENTS

Measurements were planned and executed through the efforts of P. Econ, R. Phillippi, D. Dockery, and J. Roulette. This work has been supported through the US Navy AEGIS Shipbuilding Program, PMS-400; radar verification data was provided by the Area AAW Systems Division, SEA 91W3.

## REFERENCES

[1] F. E. Nathanson, J. P. Reilly, and M. N. Cohen, *Radar Design Principles*, Second Ed., McGraw-Hill Inc., 1991.

[2] M. W. Long, *Radar Reflectivity of Land and Sea*, Artech House, Dedham MA, 1983.

[3] F. T. Ulaby and M. C. Dobson, *Handbook of Radar Scattering Statistics for Terrain*, Artech House, Norwood MA, 1989.

[4] D. K. Barton, "Land clutter models for radar design and analysis," *Proc. IEEE*, 73 (2), 1985: 198 - 204.

[5] J. W. Henn, D. H. Pictor, and A. Webb, "Land clutter study: low grazing angles (backscattering)," in J. Clarke (ed.), *Advances in Radar Techniques,* Peter Peregrines Ltd., London, 1985: 222 - 226.

[6] N. C. Currie and S. P. Zehner, "Millimeter wave land clutter model, "In J. Clarke (ed.), *Advances in Radar Techniques*, Peter Peregrines Ltd., London, 1985: 227 - 231.

[7] J. B. Billingsley, "Radar ground clutter measurements and models Part I: spatial amplitude statistics," *AGARD Conference Proceedings on Target & Clutter Scattering and their Effects on Military Radar Performance, AGARD-CP-501*, NATO Electromagnetic Wave Propagation Panel Meeting, Ottawa, Canada, May 1991, DTIC# AD-P006373, 1.1 - 1.15.

[8] Ayasli, S., "SEKE: A computer model for low altitude radar propagation over irregular terrain," IEEE Trans. Ant. Prop., AP-34 (8), 1986: 1013 - 1023.

[9] G. D. Dockery, "Modeling electromagnetic wave propagation in the troposphere using the parabolic equation," *IEEE Trans. Ant. Prop.*, 36 (10), 1988: 1464 - 1470.

[10] J. R. Kuttler and G. D. Dockery, "Theoretical description of the parabolic approximation: Fourier split-step method of representing electromagnetic propagation in the troposphere," *Radio Science*, 26 (2), 1991: 381 - 393.

[11] H. V. Hitney, A. E. Barrios, and G. E. Lindem, "Engineers refractive effects prediction system (EREPS). Revision 1.00, Users Manual," Document AD202443, Naval Oceans Systems Center, San Diego, CA, 1988.

[12] J. P. Reilly, C. C. Lin, and S. A. Rudie, "Land clutter and shadowing with consideration of propagation in coastal regions," *Proc. Radar '92*, Brighton England, Oct. 1992: 26 - 29.

[13] C. C. Lin and J. P. Reilly, "Radar terrain clutter model with consideration of propagation effects," *Proc. 23 rd European Microwave Conf.*, Madrid Spain, 6 - 9 Sept., 1993: 478 - 482.

[14] S. W. Marcus, "A hybrid (finite difference - surface Green's function) method for computing transmission losses in an inhomogeneous atmosphere over irregular terrain,", *IEEE Trans. Ant. Prop.*, 40 (12), 1992: 1451 -1458.

[15] M. F. Levy, "Parabolic equation modeling of propagation over irregular terrain," *Electronics Letters*, 26 (15), 1990: 1153 - 1155.

[16] P. Beckman, "Scattering by composite rough surfaces," Proc. IEEE, Aug. 1965: 1012 - 1015.

[17] D. E. Barrick, "Rough surface scattering based on the specular point theory," IEEE Trans. Ant. Prop., AP-16 (4): 449 - 454.

[18] P. Beckman and A. Spizzochino, *The Scattering of Electromagnetic Waves from Rough Surfaces*, Artech House, Norwood MA, 1987.

[19] K. D. Ward, "A radar sea clutter model and its application to performance assessment," *International Conference, Radar-82*, London, Oct. 18 - 20, 1982.

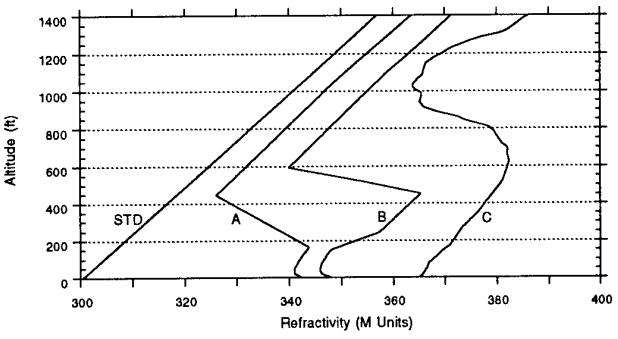


Figure 1 Measured Refractivity Profiles

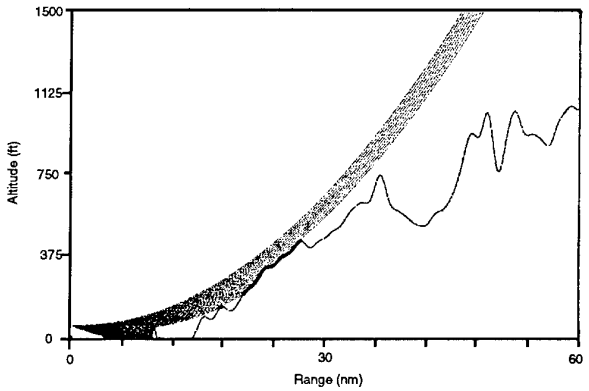


Figure 2. Illustration terrain and ray-trace profile with standard atmosphere.

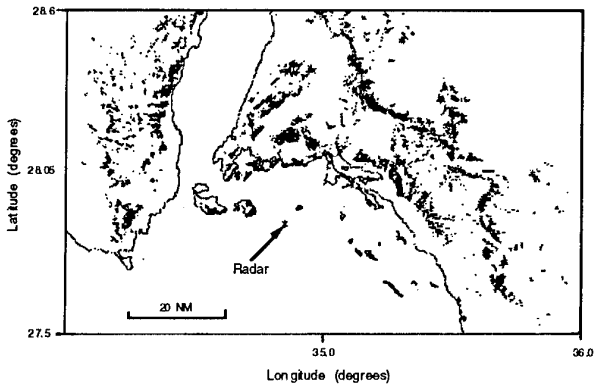


Figure 3. Terrain visibility determined by ray-trace method for a radar located in the Red Sea, standard atmosphere.

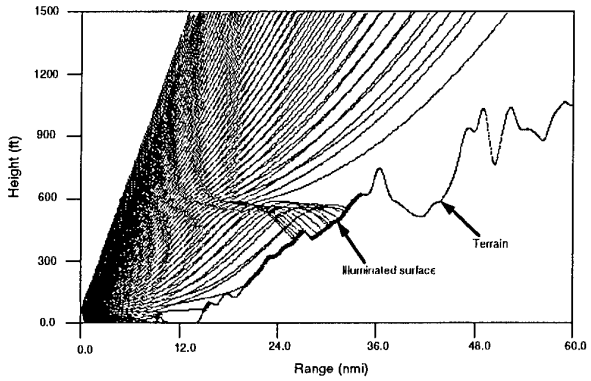


Figure 4. Illustration of Terrain and Ray-trace Profile with a 600-ft Surface Duct

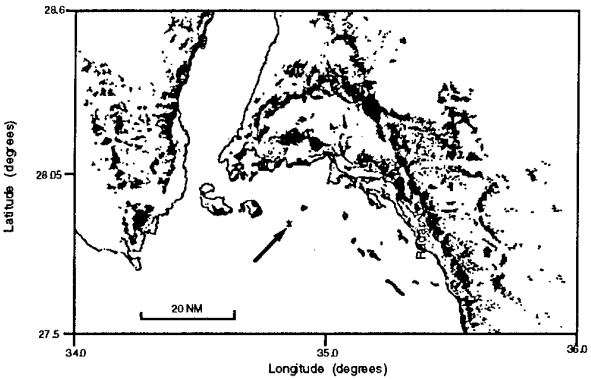


Figure 5. Terrain visibility determined by ray-trace method for a radar located in the Red Sea, 600 ft surface-based duct, uniformly stratified atmosphere.

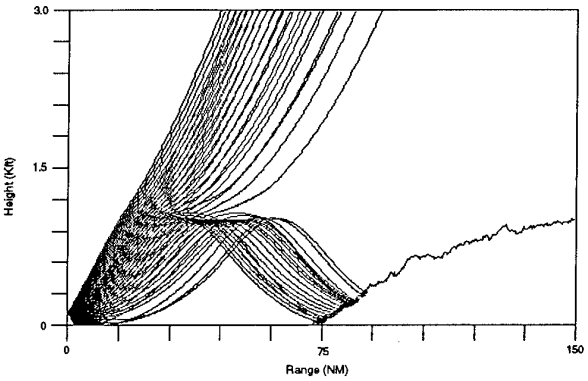


Figure 6. Ray diagram for operation near Saudi Arabia - 1000 ft surface-based duct, radar 70 nm from coast.

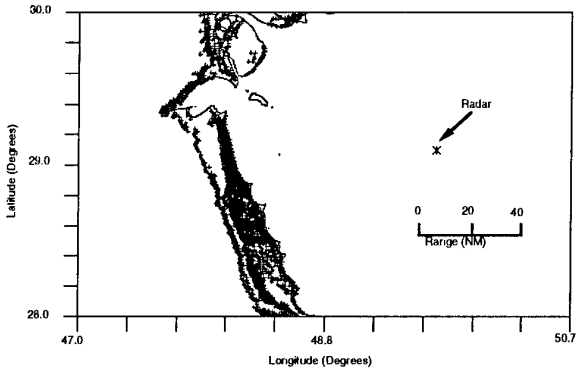


Figure 7. Terrain visibility diagram for operation near Saudi Arabia, 1000 ft surface-based duct, radar 70 nm from coast.

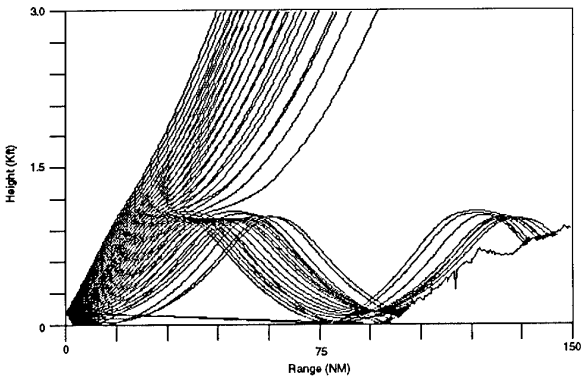


Figure 8. Conditions as in Figure 6; radar 95 nm from coast.

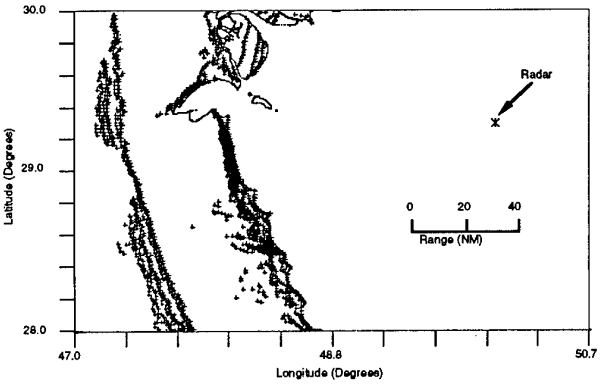


Figure 9. Conditions as in Figure 7; radar 95 nm from coast.

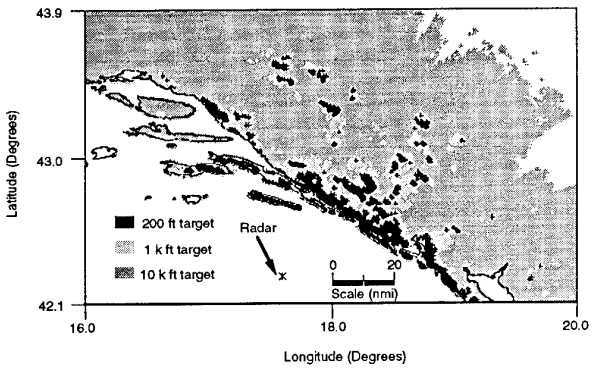


Figure 10. Visibility of Air Target for a Ship Position Off the Coast of Former Yugoslavia - Standard Atmosphere.

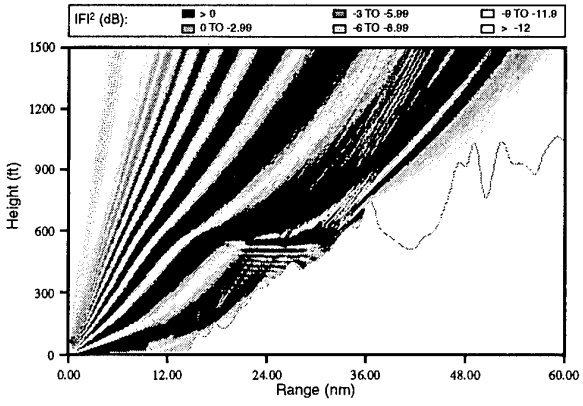


Figure 11. Illustration of Terrain and Propagation Factor Profile with a 600 ft. Surface-Based Duct.

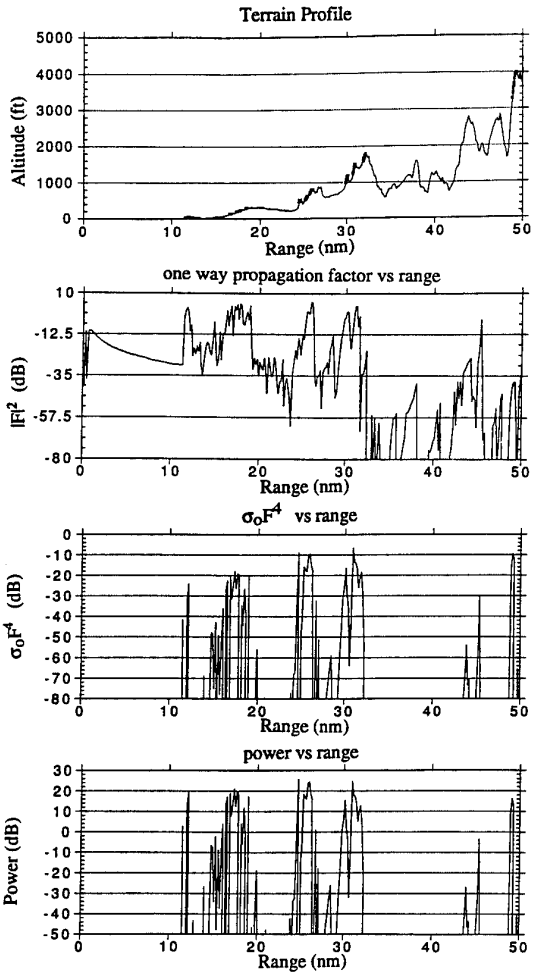


Figure 12. Land Clutter Return of a S-Band Radar Simulation under Heavy Surface Duct Propagation Condition.

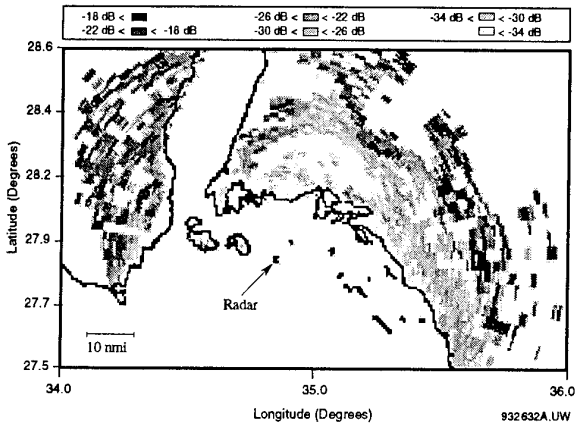


Figure 13. Illustration of Radar Clutter Map ($\sigma_0 F^4$).

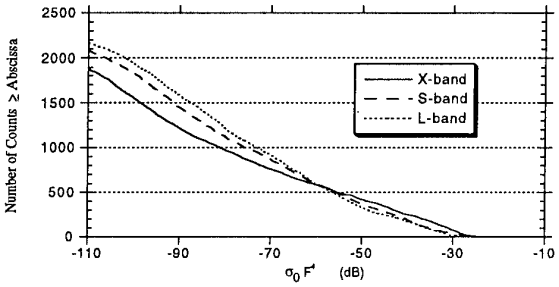


Figure 14. Cumulative distribution of simulated $\sigma_0 F^4$ in low relief terrain.

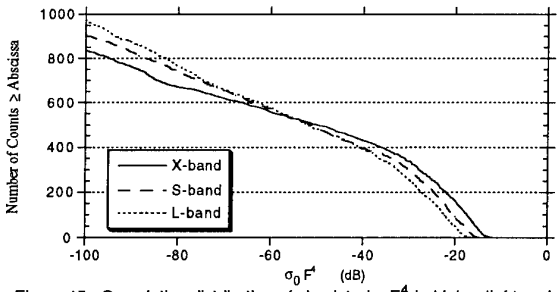


Figure 15. Cumulative distribution of simulated $\sigma_0 F^4$ in high relief terrain.

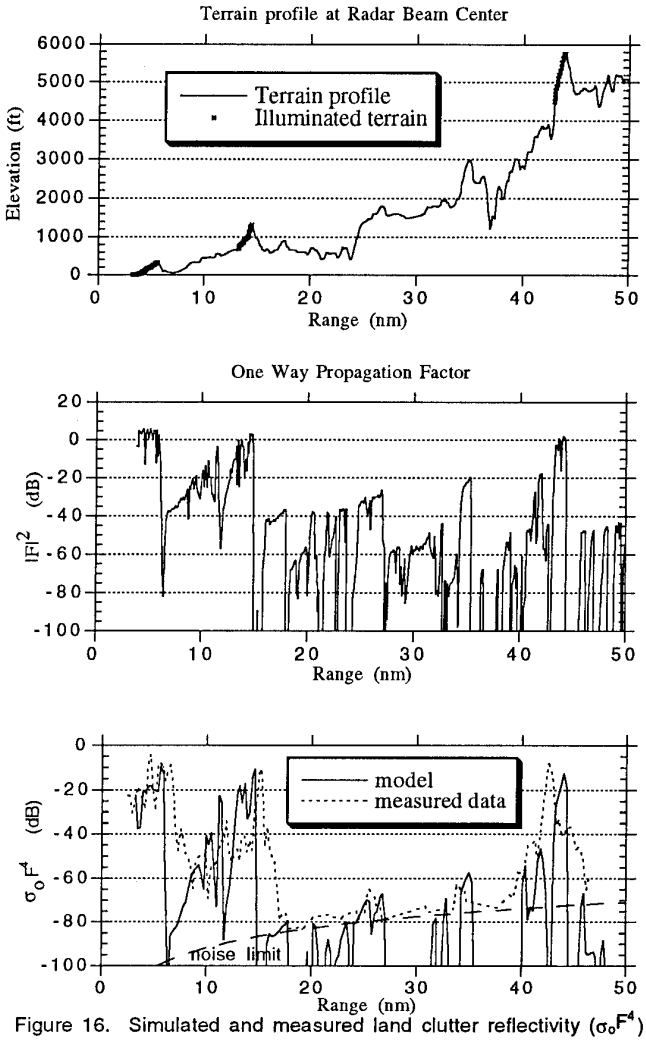


Figure 16. Simulated and measured land clutter reflectivity ($\sigma_o F^4$) with corresponding terrain profile.

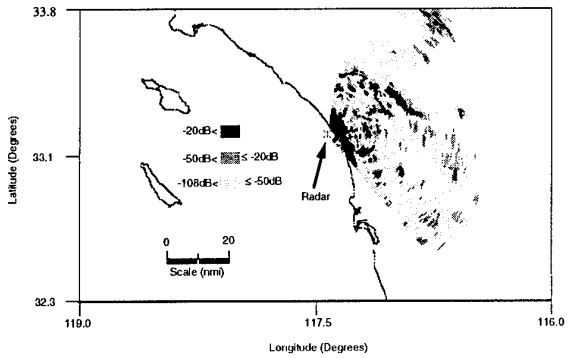


Figure 17. Measured Clutter Reflectivity ($\sigma_o F^4$) at the Coast of S. Cal. within 63.0 nm.

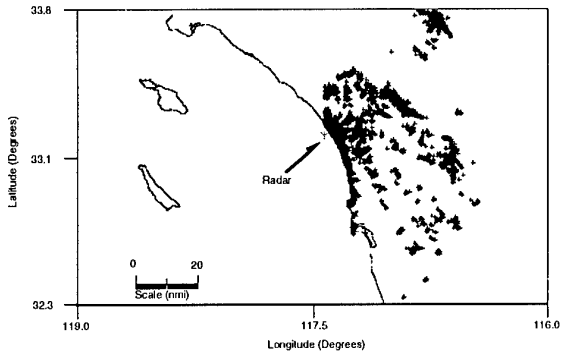


Figure 18. Terrain Visibility Map Predicted with the Ray-Trace Method (Standard Atmosphere, Ant. Ht=120 ft).

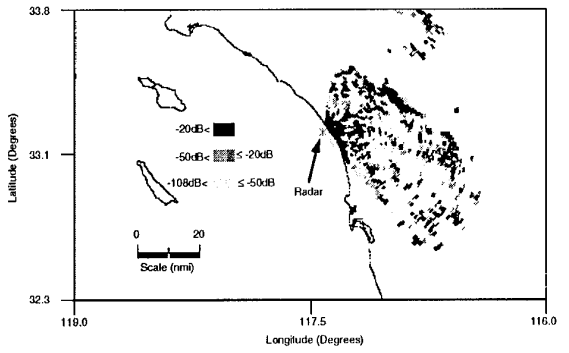


Figure 19. Map of simulated clutter reflectivity ($\sigma_0 F4$) at the coast of southern California using RADSCAT method. Standard atmosphere propagation.

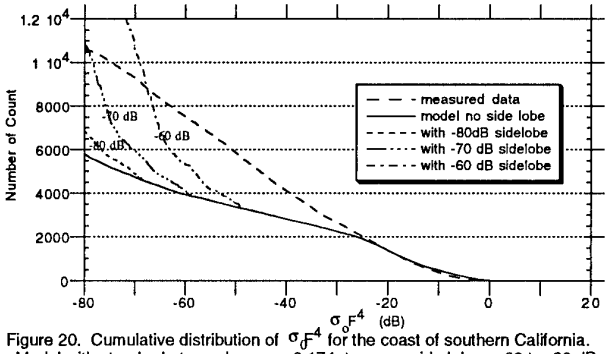


Figure 20. Cumulative distribution of $\sigma_0 F^4$ for the coast of southern California. Model with standard atmosphere, $\gamma$=0.174, two-way side lobe = -60 to -80 dB.

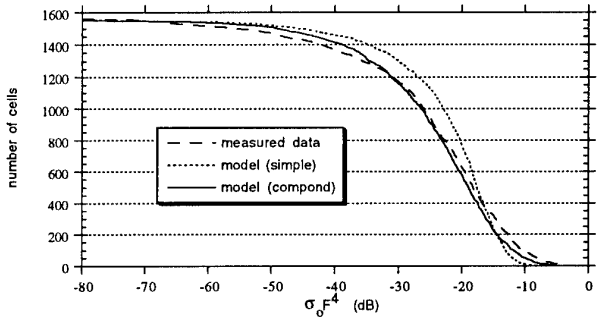


Figure 21. Cumulative distribution of $\sigma_0 F4$ applying to radar cells containing directly illuminated terrain for coast of southern California.

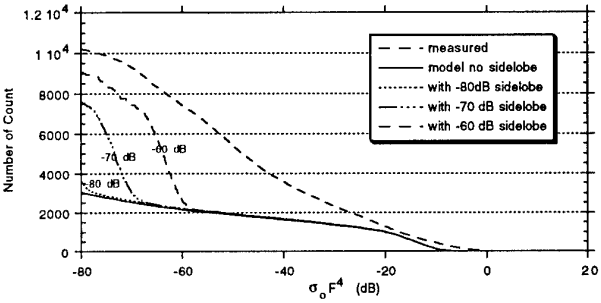


Figure 22. Cumulative distribution of $\sigma_0 F4$ for the coast of northern Washinton. Model with standard atmosphere, $\gamma$ =0.174, two-way side lobe = -60 to -80 dB.

**Table 1. Statistics of $\sigma_0 F^4$ with variation of threshold and radar frequency (1.5° beamwidth, 1 μs pulse width, 62' antenna height)**

| Threshold (dB) | L-Band Mean (dB) | L-Band N | S-Band Mean (dB) | S-Band N | X-Band Mean (dB) | X-Band N |
|---|---|---|---|---|---|---|
| **High Relief Terrain** | | | | | | |
| 40 | -34.3 | 568 | -32.0 | 551 | -29.3 | 549 |
| 30 | -37.9 | 647 | -36.4 | 641 | -32.5 | 607 |
| 20 | -42.3 | 739 | -40.5 | 721 | -35.7 | 660 |
| 10 | -47.3 | 843 | -44.8 | 804 | -40.3 | 730 |
| 0 | -50.6 | 912 | -48.5 | 872 | -45.8 | 817 |
| -10 | -53.0 | 963 | -51.6 | 929 | -49.5 | 875 |
| **Low Relief Terrain** | | | | | | |
| 40 | -42.0 | 418 | -41.8 | 462 | -39.1 | 483 |
| 30 | -48.3 | 683 | -46.5 | 631 | -43.5 | 627 |
| 20 | -53.9 | 971 | -52.2 | 908 | -47.7 | 768 |
| 10 | -59.7 | 1294 | -57.9 | 1177 | -54.0 | 992 |
| 0 | -66.1 | 1684 | -65.0 | 1549 | -61.5 | 1286 |
| -10 | -70.7 | 1980 | -70.7 | 1889 | -70.0 | 1678 |

Note: Threshold refers to C/N ratio for hypothetical radar system.

## DISCUSSION

**C.R. PHILBRICK**
Please comment on the frequency, type, and accuracy of the meteorology measurements that you used as input to your model calculations. Could your observation about the differences between the measured and modelled radar coverage have been due to the spatial or temporal resolution of the meteorology data set that was input to the model?

**AUTHOR'S REPLY** I'd like to refer the question to Dan Dockery who was responsible for the measurements.

**D. DOCKERY**
Helicopter-based atmospheric measurements were made between the ship and a point 20 km inland from the coast. These were high resolution measurements made within 30 minutes of the presented radar data. Standard atmosphere conditions were measured throughout this test and were used in the analysis. The confidence that the data discrepancies are not caused by refraction is high.

# Operational Support for a Range-Dependent Radio Propagation Model

**John Cook, Gerard Vogel and Gary Love**
Naval Research Laboratory
Marine Meteorology Division
7 Grace Hopper Avenue
Monterey, CA 93943-5502
USA

## ABSTRACT

The emerging new standard in the U.S. Navy for range-dependent radio propagation assessment is the Radio Physical Optics (RPO) model developed at the Naval Command, Control and Ocean Surveillance Center, RDT&E Division (NRaD). RPO allows one to compute the expected radio propagation loss field as a function of height along a desired bearing, provided the atmospheric propagation conditions are specified along the path. This paper describes an architecture being developed to operationally support RPO. In developing this architecture, a number of unique constraints and considerations have been dealt with to provide RPO with cross-sections of atmospheric propagation conditions. First, forecast grids from a mesoscale weather data assimilation/prediction model are accessed to provide the best estimate of the current and future refractive and meteorological conditions over the area of interest. Based on conditions near the surface, high-resolution profiles of refractivity in the evaporation duct are calculated and appended onto the bottom of the model forecast profiles. This completes the specification of refractivity down to the sea surface. These refractivity profiles are then processed by a unique algorithm that matches similar refractivity structures from profile-to-profile and reformats the data to support the indexing scheme required by RPO. After RPO has been run, the propagation loss results can be displayed and thresholded to provide expected coverage against specific targets. An example will be shown where multiple RPO runs are used to suggest positioning of available assets to maximize coverage.

## 1. INTRODUCTION

The atmosphere significantly affects electromagnetic (EM) propagation, particularly when strong vertical temperature and humidity gradients are present. Anomalous propagation conditions, such as trapping layers, can greatly enhance detection and reception ranges, but, because of the concentration of energy by the layer, detectability in areas adjacent to the layer can be significantly reduced. Atmospheric data defining these layers are sparse over marine regions. However, recent advances in the development of numerical weather prediction models are encouraging the use of gridded forecast data for propagation assessment because these models have shown promise in forecasting such features (Burk *et al.*, 1994 and Thompson *et al.*, 1994).

Recently, RPO, a range dependent propagation model, has been developed which overcomes the high computational burden traditionally associated with the solution to the EM parabolic equation (Hitney, 1992). Reliable refractivity fields are required as input to RPO. Observing refractivity using radiosonde profiles provides good vertical resolution, but lacks horizontal coverage. Conversely, satellite remote sensing techniques provide good areal coverage, but have poor vertical resolution. Boundary parameters, however, such as sea surface temperature, can be measured accurately using remote sensing techniques. These measurements can be integrated with other observations to develop a realistic representation of the atmosphere using a numerical weather prediction/data assimilation system. Such a system periodically updates a short-term model forecast using local data to produce meteorological fields (including refractivity) that are consistent with known physical relationships. Levy and Craig (1991) have demonstrated that the UK Meteorology Office mesoscale model is capable of providing these refractivity forecasts and this has fueled development of a linkage between a Navy mesoscale weather prediction model and RPO. Automated data processing of the linked mesoscale model output and RPO allows multiple runs with variable parameters which can be used to suggest positioning to maximize coverage and to anticipate changes of radar settings and thresholds.

## 2. DESCRIPTION OF THE ARCHITECTURE

The architecture being developed and tested to run RPO operationally starts with a refractivity data base over marine areas produced by a high resolution mesoscale weather prediction model. Preprocessing software extracts refractive cross sections from the data base along propagation radials and then combines the model profiles with very high resolution near-surface refractivity profiles representative of the surface evaporation duct. These combined refractivity profiles are then processed by a unique algorithm that matches refractivity structures in adjacent profiles that result from common layers.

### 2.1 Mesoscale Model

The mesoscale weather prediction model used here to provide the data sets of atmospheric parameters is a version of the Navy Regional Operational Atmospheric Prediction System (NORAPS) described by Hodur (1987). NORAPS is run operationally at the Fleet

*Paper presented at the Sensor and Propagation Panel Symposium on "Propagation Assessment in Coastal Environments" held in Bremerhaven, Germany 19-22 September 1994.*

Numerical Meteorology and Oceanography Center (FNMOC) using boundary conditions supplied from the Navy global model. A NORAPS domain may be 1000 to 3000 km on a side. Typically, for data assimilation and forecasting in support of refractivity, the version of NORAPS that is run includes a high resolution vertically-nested grid and second-order closure boundary layer physics (Burk and Thompson, 1989). In the mesoscale data assimilation scheme, the previous model forecast is used as a starting point and observed data is then incorporated in order to initialize the next model forecast. In this way, details of atmospheric structure are maintained from one model forecast to the next and are modified using available data. This process is repeated periodically to maintain an updated forecast based on the most current conditions.

### 2.2 Cross Section Extraction

Figure 1a is an example of a vertical cross section of modified refractivity (a series of M-unit profiles as a function of range) extracted out of a NORAPS data base. The profiles are defined at the horizontal resolution of the model (typically 20 km) along a great circle propagation path emanating radially from the transmitter at an arbitrary azimuth. Multiple radials around the same location can be extracted automatically. In addition, collocated near-surface values of air temperature, dew point temperature, wind speed, pressure, and sea surface temperature are extracted for input to the evaporation duct profile generation algorithm. This algorithm is based on the method developed in Cook and Burk (1992) and results in detailed (0.1 m vertical resolution) model profiles of modified refractivity through the first 40 m altitude of the marine surface layer. This high resolution profile is then sampled and interleaved with the bottom of the corresponding NORAPS profile to create a combined profile. As shown in Figure 2, the computed evaporation duct height defines the maximum altitude extent of the profile sampling. The other points that are sampled are at 0.1, 0.2, 0.5, 1, 2, and 5 m altitude, and the point at half the evaporation duct height is also sampled. If no evaporation duct occurs within the 40 m altitude range, only the points at the six fixed levels are sampled. Each interleaved profile is then sorted by height and duplicate levels removed. Thus, at this point, the cross section may consist of a series of profiles with varying numbers of unique vertical levels. Interleaving the model and evaporation duct profiles in this manner may, however, create subtle inconsistencies in the vertical refractivity gradients of the combined profiles. This may occur because the model fields represent a physically consistent integration of atmospheric physical and dynamic processes, while the evaporation duct profiles reflect theoretical expressions valid only in a homogeneous, steady-state, surface layer. Methods of reducing the inconsistencies in the refractivity gradients are currently being assessed.

### 2.3 Refractivity Structure Matching Algorithm (RSMA)

To prepare the combined refractivity cross sections for RPO, RSMA was developed by Vogel (1991). After processing by RSMA, the cross sections meet two important RPO input data requirements: a) every profile has the same number of levels, and b) the nth level in any one profile is matched with the nth level in all the other profiles. The matching up of refractive structures in adjacent profiles that result from common layers is accomplished in three steps. First, each point on each M-unit profile is categorized as being one of 31 structural types, based on the refractivity gradients above and below the point, and the change of these gradients across the point. The first and last points of each profile are assigned the same structural type category to ensure that the tops and bottoms of all profiles are always matched up.

Figure 1b shows the results of the next step where the primary structural type categories in adjacent profiles, within physically reasonable bounds (i.e., an altitude window), are matched up based on a hierarchical classification scheme containing 114 paired structure types. The categories are ordered in such a way that structures considered most likely to affect propagation are matched first. Many possible pairings are considered minor and are not used in RSMA.

The primary matching proceeds by iteratively considering all 144 hierarchical categories at each point in each profile by scanning the portion of the next down range profile within a computed altitude window for the appropriate match. The size of the window is dependent on both the distance between profiles and the altitude of the point being matched. If more than one match is found within the altitude window, then the point in the down range profile nearest in altitude is chosen. Above about 1000 m, the vertical resolution of NORAPS exceeds the window size and sloping layer connections are not allowed. After each point of each profile is checked, the next hierarchical category is considered. Since this is an iterative scheme, already matched profile pairs limit subsequent matching opportunities by restricting the upper or lower bounds of the down range altitude window. This restricts layers from unrealistically crossing each other.

The final step in RSMA pairs up all the points unmatched after the primary matching. This secondary matching process sweeps through the profiles twice, first down range and then back. All available unmatched points between primary matched levels are paired, with points closest in relative altitude between the primary matched points paired first. As shown in Figure 1b, not all profiles have the same number of unmatched points between primary matched pairs. During the sweeps through the profiles, if the number of unmatched points in the two profiles are not the same, proportionally

spaced points are interpolated into the profiles. However, because of the limitations imposed by the primary matched layers, this process can generate more unmatched points. By sweeping through the profiles twice, in opposite directions, the excess points get paired with interpolated points during the second, reverse, pass. In this manner, all the profiles end up with the same number of points with the nth level in any one profile matched to the nth level in all the other profiles. Figure 1c shows the results of RSMA after both primary and secondary matching. When RPO interpolates the refractivity at intermediate ranges, it does so within the bounding quadrilaterals defined by the solid and dashed lines connecting points with the same index between profiles.

At this point, the refractivity data are ready for input into RPO. RPO also requires information about the transmitter characteristics, such as frequency, polarization, antenna height, beam pattern, beam width, and elevation angle. These data are supplied from a small file keyed to an identifier associated with a particular transmitter. Figure 3 is an example of propagation loss computed by RPO along radials in the four cardinal directions about a common location, simulating an antenna scanning in azimuth. A trapping layer that rises and strengthens locally from southwest to northeast results in extended ranges along the north and east radials.

## 3. EXAMPLE APPLICATION

For the purposes of demonstrating the application of automated data extraction and RPO execution described above, the following scenario was developed which highlights radar detection of incoming missiles and provides recommendations for optimal sensor platform placement.

### 3.1 Scenario

Figure 4a shows the location of the scenario in the littoral region off the coast of California, as might represent an actual naval exercise. The circle labeled "Aircraft Carrier" represents one high-value unit plus unmodeled escort and support ships gathered offshore. Two screen ships (represented by the crossed arrows) are placed between the fleet and the shore, to protect against shore launched or air launched missiles threatening the fleet. The assigned screen ship positions are 100 to 130 km offshore with an intership distance of 275 km. To remain covert, the high value unit does not use its radars to search for threat missiles, it relies on the screen ships for initial detection.

The threat is modelled as a uniform target originating from the line between 37.2N 121.8W and 41.7N 125.1W, travelling at 250 $ms^{-1}$, at an altitude of 100 m, in the direction of the high-value unit assumed to be at 37.5N 126.5W. The shaded area corresponds to the threat probability at six minutes into the simulation. Darker shading is higher probability. The radar search is limited to the region between missile launch and 185 km from the high value unit. The 185 km safe range constraint is the closest point of approach to the high value unit required for threat detection to ensure adequate defense.

### 3.2 Environmental Situation

The surface analysis shows a trough and weak cold front approaching the northern California coast with the axis of the trough well to the west. In terms of refractive conditions, in the air ahead of the front an inversion capped boundary layer has developed. The temperature and humidity gradients associated with the inversion cause strong trapping below about 200 m. Near the coast the boundary layer is deeper and well mixed with a weak inversion and trapping layer causing elevated ducting at about 375 m.

### 3.3 Homogeneous Conditions

Typically, a single radiosonde acquired at the location of the high value unit is used to measure the atmosphere at one point and then that environment is assumed to exist everywhere throughout the region of interest. Figure 4b is a map showing the combined cumulative probability of detection (POD) of the threat missiles at an altitude of 100 m when the forecast refractivity profile from NORAPS at the high value unit is assumed to apply everywhere. Therefore, RPO calculated propagation loss for the radars on both screen ships assumes the same refractive structure. A simple model is used to relate the loss values to the cumulative POD of the missiles at the specified 185 km safe range. This prediction shows that adequate detection exists for all possible areas of the threat (the dark shaded area corresponds to greater than 90% cumulative POD), but is erroneous because the refractive conditions are not homogeneous.

### 3.4 Heterogeneous Conditions

In this assessment, the NORAPS data are used to construct fully 3-D heterogeneous propagation assessments around each of the two screen ships. The map of Figure 4c again shows the combined cumulative POD of the missiles for the two screen ships. The poor detection effectiveness, especially on the part of the southern most ship, provides a serious coverage gap through which missiles could easily approach within 100 km or less of the high value unit, without detection. This is due to the different atmospheric propagation conditions between the main fleet location and the screen ships. The cumulative POD for the missiles is 0.62 for these screen ship positions.

### 3.5 Optimized Positions

An iterative computer algorithm was used to determine the optimum positions of the two screen ships given the line-of-threat and heterogeneous environmental conditions forecast by NORAPS. Figure 4d shows the recommended positions which are farther offshore and

the southern ship's position is much farther north. This moves both ships back into a region where conditions are much more favorable for detecting the threat. The cumulative POD for the missiles has been increased from 0.62 to 0.92.

## 4. SUMMARY

This paper showed how output from a mesoscale weather prediction model could be used to forecast atmospheric refractivity and provide input to the RPO model. The architecture being developed to automatically sample the data base, process the data by appending the evaporation duct profile near the surface and linking up common refractive layers from profile-to-profile was discussed. An example showing the coupling of mesoscale weather forecast data to RPO and optimizing screening ship locations based on the heterogeneous refractive conditions illustrated the impact that the complex coastal environment can have on propagation predictions. Applications such as this provide insight into atmospheric effects and propagation subtleties which would otherwise be extremely difficult to comprehend, and can benefit decision makers. An initial operational demonstration of this architecture is scheduled to be conducted in early 1995, with RPO being run on board ship. The environmental data base used will be created by analyzing local data using the NORAPS forecasts as a first guess. The demonstration is designed to test all of the functional components described above in addition to operational computational and communications resources.

## ACKNOWLEDGEMENTS

This work is sponsored by the Office of Naval Research, Program Element 0602435N. The RPO model was provided by H.V. Hitney of the Naval Command, Control and Ocean Surveillance Center and the sensor platform optimization work was conducted by Daniel H. Wagner Associates, Inc., under Contract No. N00014-92-C-6036.

## REFERENCES

Burk, S.D., W.T. Thompson, J. Cook, and G.G. Love, "Mesoscale modeling of refractive conditions during the VOCAR experiment," Proc. IGARSS, Pasadena, Ca., 1994.

Burk, S.D. and W.T. Thompson, "A vertically nested regional numerical weather prediction model with second-order closure physics," *Mon. Wea. Rev.*, **117**, pp. 2305-2324, 1989.

Cook, J. and S. Burk, "Potential refractivity as a similarity variable," *Boundary Layer Meteorol.*, **58**, pp. 151-159, 1992.

Hitney, H., "Hybrid ray optics and parabolic equation methods for radar propagation modeling," Proc. IEE Inter. Radar Conf., Brighton, England, 1992.

Hodur, R.M., "Evaluation of a regional model with an update cycle," *Mon. Wea. Rev.*, **115**, pp. 2707-2718, 1987.

Levy, M.F. and K.H. Craig, "Use of mesoscale models for refractivity forecasting," AGARD CP 502, pp. 7.1-7.12, 1991.

Love, G.G. and J. Cook, "Impacts of weather model forecasts on tactical environmental decision aids," NRL Review, Naval Research Lab., pp. 206-210, 1994.

Thompson, W.T., S.D. Burk, J. Cook, and G.G. Love, "Variations in coastal atmospheric refractivity induced by mesoscale processes," Proc. IGARSS, Pasadena, Ca., 1994.

Vogel, G.N., "Specification for a refractivity structure matching algorithm," NOARL Tech. Note 191, Naval Research Lab., 1991.

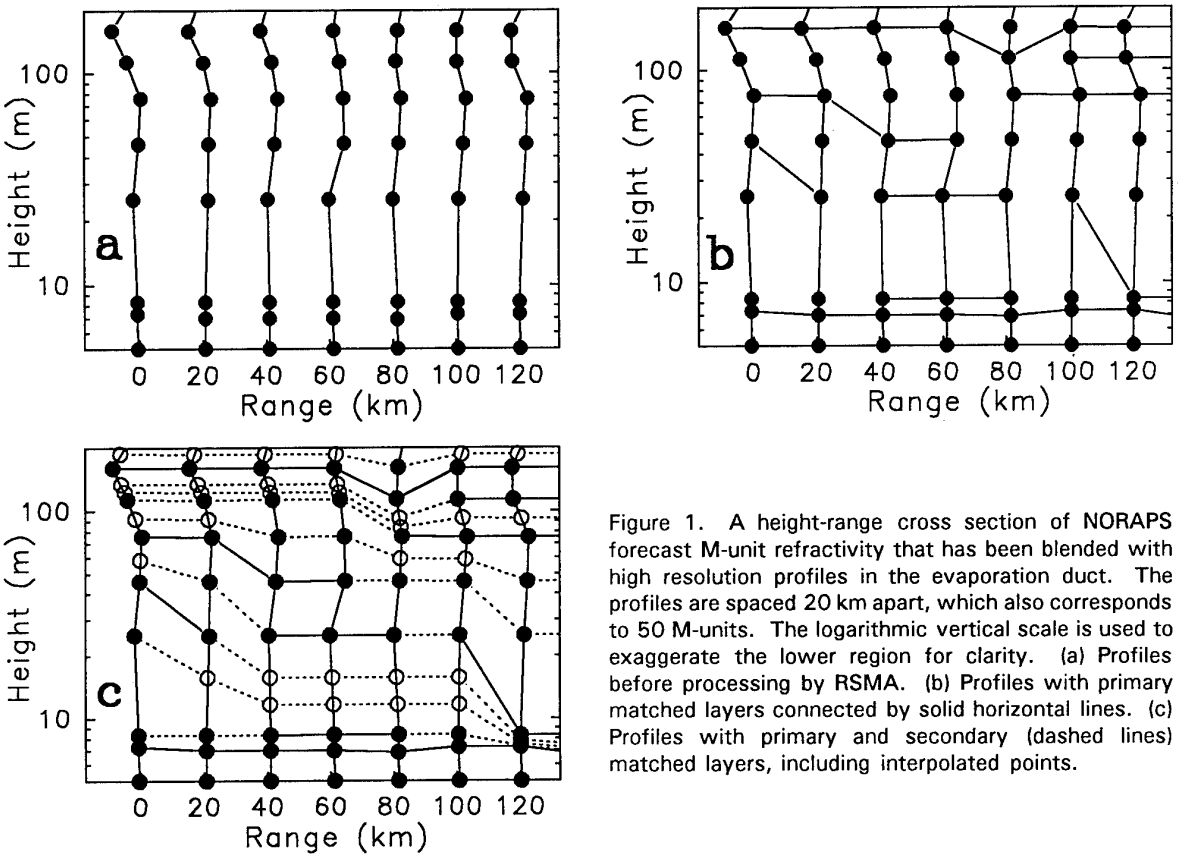


Figure 1. A height-range cross section of NORAPS forecast M-unit refractivity that has been blended with high resolution profiles in the evaporation duct. The profiles are spaced 20 km apart, which also corresponds to 50 M-units. The logarithmic vertical scale is used to exaggerate the lower region for clarity. (a) Profiles before processing by RSMA. (b) Profiles with primary matched layers connected by solid horizontal lines. (c) Profiles with primary and secondary (dashed lines) matched layers, including interpolated points.

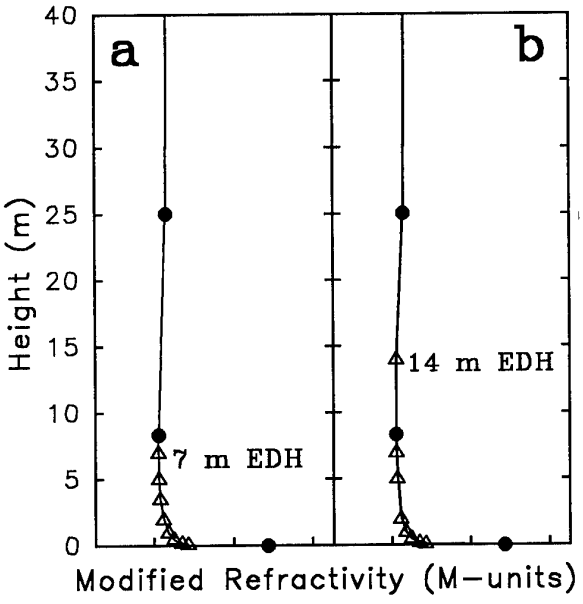


Figure 2. Two examples of evaporation duct profile data (open triangles) interleaved with NORAPS forecast refractivity data (filled circles). (a) A 7 m evaporation duct height (EDH) where all the points occur below the lowest NORAPS level. (b) A 14 m EDH where the highest point occurs between two NORAPS levels.

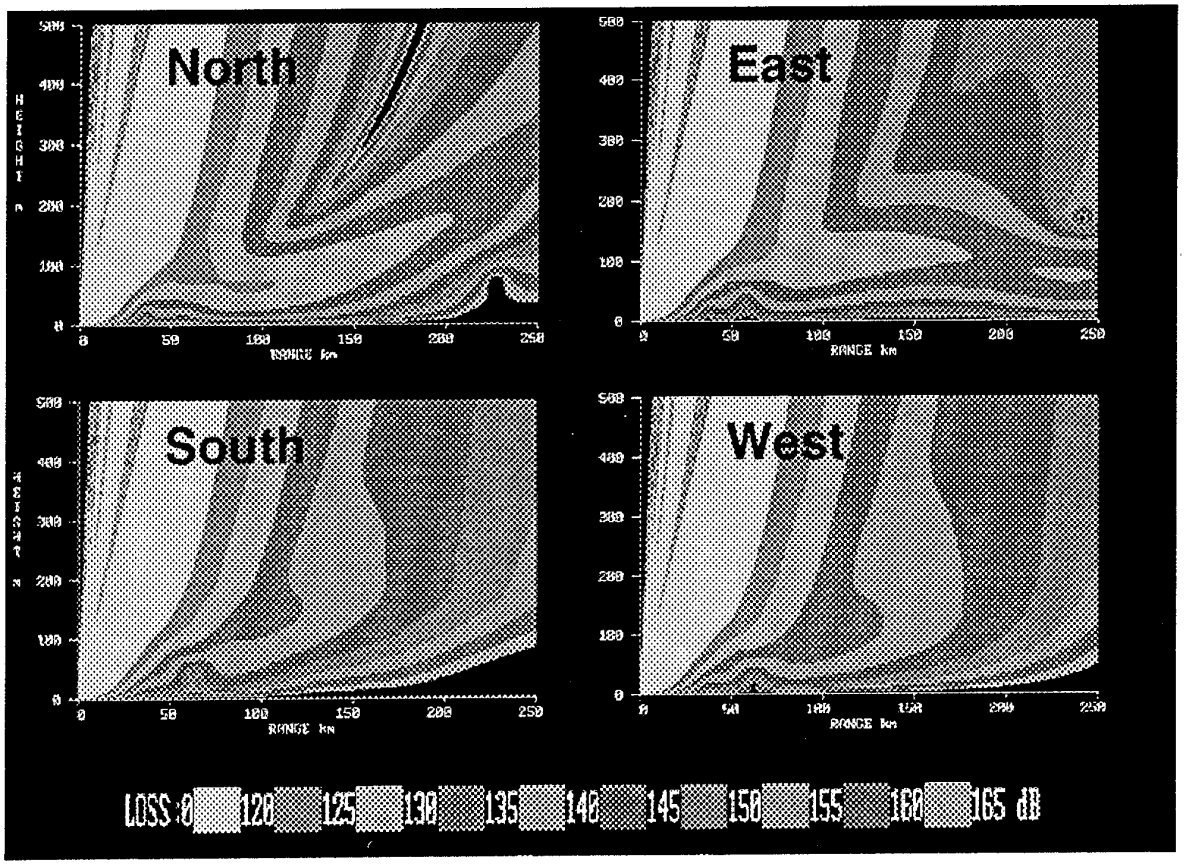


Figure 3. The predicted propagation loss from RPO for four radial cross sections about a common location (from Love and Cook, 1994).

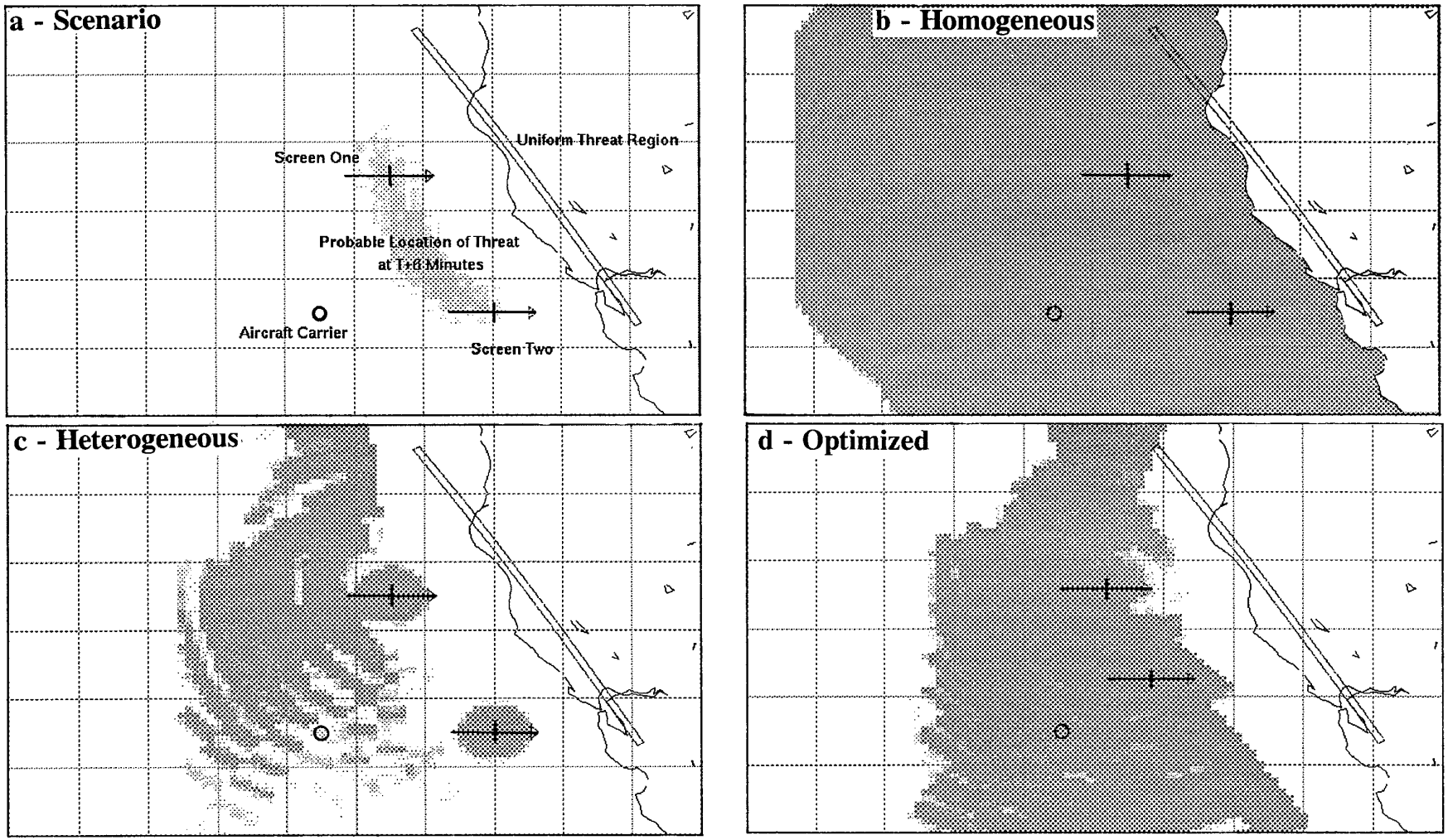


Figure 4. Map showing the locations of the "Aircraft Carrier" high value target (circle), screen ships (crosses), and threat region (line). (a) The shaded region is the probability distribution of the positions of the threat missiles at six minutes into the simulation. (b) Shaded area represents the combined cumulative probability of detection (POD) from the two screen ships of the threat missiles at 185 km from the target assuming homogeneous environmental conditions based on the profile at the target. (c) Heterogeneous environmental conditions from NORAPS used at the locations of the screen ships. (d) Optimized ship locations including heterogeneous environmental conditions.

## DISCUSSION

**M.F. LEVY**
How do you merge evaporation duct data with upper-air data? In particular what happens if a surface duct is present?

**AUTHOR'S REPLY**
If a local minimum is found in the M-unit refractivity profile in the lowest 40 m then the evaporation duct profile is merged with the meso-scale model data. If the stability is such that no minimum is found below 40 m (for example, if a deep surface duct is present), then the evaporation duct profile is not merged with the meso-scale model data. The evaporation duct algorithm is self-contained and has error checks so the developmental assumptions are not violated.

# Refraction Effects on EO System Detection Ranges in Coastal Environments

**Denis Dion**
Defence Research Establishment Valcartier
P.O. Box 8800, Courcelette, Québec
Canada G0A 1R0

## 1. SUMMARY

Atmospheric refraction can significantly affect the detection range performances of electro-optical (EO) systems against low-level targets in coastal environments. Negative air-sea temperature difference (ASTD) conditions, which produce subrefraction, impose an absolute limit of detection range shorter than the terrestrial horizon, while positive ASTD conditions, which produce superrefraction, allow radiation to propagate beyond the horizon. For subrefraction conditions, an approximate formula is given for estimating the detection range limit as a function of ASTD, wind speed and sensor-target elevations. Under superrefraction, the detectability is degraded by the refraction-induced ray spreading near the sea surface. This refraction loss, which depends on the weather conditions and the sensor-target elevations, is discussed.

## 2. INTRODUCTION

Under nonrefractive conditions - where the index of refraction of air can be considered invariant - EO radiation follows straight-line trajectories, and thence, the maximum detection ranges are limited by the terrestrial horizon. However, most of the time, the index of air rapidly varies with elevation near the sea surface and, depending on the conditions, this variation can significantly affect the detection range performances of EO systems due to the bending of rays, as introduced by Dion and Leclerc few years ago [1].

In the marine surface layer, the vertical variation of the index dominates, and in most cases the horizontal variations can be neglected over the EO detection ranges. The refraction conditions can be divided into two families which are characterized by the sign of the vertical index variation (gradient) at the sea surface: subrefraction conditions, when the gradient is positive, and superrefraction conditions, when the gradient is negative. Figure 1 shows ray diagrams for EO systems under typical sub- and superrefraction conditions. The dashed line shows the range limitation due to the earth curvature (versus target height), hereafter denoted horizon-limited range (HLR). For a given sensor and target height, HLR can be obtained using:

$$\begin{aligned} \mathrm{HLR} &= \sqrt{2a}\left[\sqrt{h_s}+\sqrt{h_t}\right] x\, 10^{-3} \\ &\approx 3.57\left[\sqrt{h_s}+\sqrt{h_t}\right] \end{aligned} \qquad (1)$$

where HLR is expressed in kilometers while the sensor height $h_S$, the target height $h_t$ and the earth radius $a$ are expressed in meters ($a \approx$ 6 370 000 m) [2].

As shown in Fig. 1, under subrefraction, the upward bending of the radiation imposes an absolute limit of detection range shorter than HLR. In contrast, under superrefraction conditions, the rays are bent downward, making possible detection of targets well beyond the horizon. The ray crossing and the caustic observed in the subrefraction diagram are due to the exponential nature of the index gradient near the surface [1].

In the IR and the visible, the index gradient of air is dominantly dependent upon the temperature gradient in the operational windows of EO systems (where absorption is low). As the index gradient is inversely proportional to the temperature gradient, negative temperature gradients produce subrefraction, whereas positive temperature gradients produce superrefraction. The negative surface temperature gradient conditions (subrefraction) are by far the most frequent ones in open sea. In coastal environments, they normally prevail when maritime air is present (e.g. when the atmospheric conditions are driven by the sea wind). The positive surface temperature gradients (superrefraction) are infrequent on a world average basis. However, near the coasts, depending on the region of the world and the season, their occurrence can be very significant when the air mass is continental; more precisely, they are likely to occur when warm continental air is blown, from the land, over cool water.

In this paper, the effects on detection range performances are discussed separately for the two families of conditions, starting with subrefraction. Under subrefraction conditions, good estimates of the refraction-limited ranges can be obtained using approximate formulae fitted on calculated values. A formulae expressed as a function of ASTD and wind speed is presented in Section 3. In Section 4, the loss of detectability produced by refraction under superrefraction is discussed.

## 3. MAXIMUM INTER-VISION RANGES UNDER SUBREFRACTION CONDITIONS

For subrefractive conditions, we use the expression maximum inter-vision range (MIVR) to denote the absolute detection range limit imposed by refraction for a given sensor and target height. In Fig. 1, the caustic boundary constitutes, at the same time, the MIVR versus target height curve. EO detection beyond these ranges is physically impossible as no rays can go beyond. In a nonrefractive atmosphere, the MIVRs would correspond exactly to the HLRs (see Fig. 1).

*Paper presented at the Sensor and Propagation Panel Symposium on "Propagation Assessment in Coastal Environments" held in Bremerhaven, Germany 19-22 September 1994.*

Using the air-sea temperature difference (ASTD) to simply characterize the atmosphere's vertical temperature variation, Fig. 2 shows the MIVR variation relative to HLR with respect to ASTD for various wind speeds. These results are for a sensor and a target located 10 m above the sea surface. As given by (1), in this case, the HLR is 22.6 km. In the graphic, the points were obtained by using the Canadian WKD marine boundary layer model [2] - a model which gives vertical refractivity profiles - in conjunction with ray tracing. The relative humidity is taken to be 80% and the reference heights for the temperature and wind speed are 12 and 19.5 m, respectively, which correspond to the standard measurement elevations on board a ship. The graphic shows that significant decrease of detection range can be caused by refraction when ASTD and wind speed are relatively large; for instance, as shown in the figure, for the geometry considered, the detection range limit is about 22% of HLR (thus MIVR = .22 x HLR = 17.6 km) when ASTD is -4 °C and the wind speed is 15 m/sec.

The WKD-based predictions of MIVRs have so far proved appreciably accurate over a diversity of ASTD, wind speed conditions and target-sensor elevations [4] [5]. The MIVR predictions, as shown in Fig. 2, can be considered valid for low-level targets unless the atmosphere is highly inhomogeneous along the propagation path. In most cases, the horizontal variations of the atmospheric conditions over refraction-shortened detection ranges are not likely to significantly affect MIVR predictions. In Ref. [5], predictions made using a single vertical index profile proved satisfactorily accurate even under the experimented inhomogeneous conditions. The MIVR predictions shown in Fig. 2 apply in the visible as well as in the IR 3-5 and 8-12 μm windows as the refractivity gradients can be considered constant over the operational wavebands of EO systems.

In Fig. 2, one notes that MIVRs slightly greater than HLR are obtained for 0 °C ASTD. This light superrefraction effect is due to the atmospheric pressure gradient [1]. We also note that MIVR variations tend to converge as the wind speed increases. Although not shown in Fig. 2, the MIVRs become almost invariant with respect to wind for speeds greater than 15 m/sec. Furthermore, we note that the MIVR variations can be as much sensitive to wind as to ASTD depending on the conditions.

The apparent smooth parabolic-like MIVR variations observed versus ASTD for the different wind speeds allows one to derive approximative formulae for estimating MIVR. Curves in Fig. 2 are polynomial fits on MIVR calculations for the different wind speeds considered. In a second step, fits can be performed over wind speeds to obtain the coefficients of the MIVR-versus-ASTD functions for any wind speed. This second fit (over wind speeds) includes a difficulty due to the discontinuity caused by the crossing of MIVR curves at mid-wind velocity (about 9.5 m/sec) for low ASTDs, as observed in Fig. 2.

Having a MIVR solution for one sensor-target geometry, the MIVRs for any sensor height-target height combinations can be found by exploiting the near-linear variation of MIVR with respect to the height parameter, $H$:

$$H = \sqrt{h_s} + \sqrt{h_t} \qquad (2)$$

where $h_S$ and $h_t$ are the sensor and the target heights expressed in meters, respectively. This linear variation is shown in Fig. 3a and b which present MIVR with respect to $H$ for various ASTDs and wind velocities. Figure 3b, which shows the curves against normalized axis, outlines the discrepancies between slopes. The slope variation can lead to significant MIVR differences for large $\Delta H$s, and thence, it must be taken into account in the calculations of MIVRs.

Therefore, one can look for describing MIVR variations under subrefraction conditions with a function of ASTD and wind velocity (neglecting the pressure and humidity gradient effects) borrowing the form of the effective-earth-radius expression originally developed for RF applications [2]. However, unlike the original form which was derived assuming linear index gradients, a factor, $\Gamma$, is required to account for the sensor height-target height geometry effect discussed above. Thence, the general expression for MIVR can write:

$$MIVR = K_0 \sqrt{\frac{1}{1 + \Phi(\Delta, \omega)}} \cdot \Gamma(H, \Delta, \omega) \qquad (3)$$

where MIVR is expressed in kilometers, $\Delta$ is ASTD in degrees, $\omega$ is the wind speed in m/sec, $H$ is given by (2) and $K_0$ is a constant = 22.405. Expressions for $\Phi$ and $\Gamma$ are given in APPENDIX.

Figure 4 exhibits the distribution of the errors obtained running the proposed expression (3) over 200 cases, for ASTDs ranging from 0 to -8 degrees; wind speeds ranging from 1 to 20 m/sec and for sensor and target heights going from 5 to 20 m. We note that errors obtained are less than 0.4 km in 90 % of the cases considered. This accuracy is certainly sufficient for EO system studies where other factors, often more significant factors, are much less accurately known (e.g. transmittance, sea and sky background radiances, etc.). It is interesting to note that 0.5 km corresponds approximately to the predictions errors obtained from the MAPTIP experiment under the best conditions [5]; under the worst horizontally varying conditions experimented at MAPTIP, the prediction errors were about twice greater. Calculations of MIVRs using (3) can be very useful in target detection simulations, for instance, for screening out quickly physically undetectable targets without getting through profiles computations and ray tracing.

## 4. REFRACTION LOSSES UNDER SUPERREFRACTION CONDITIONS

Under typical superrefraction conditions, ray diagrams show virtually no distinct range limitations, as shown in Fig. 1, and so the MIVR concept does not apply. However, one notes that the ray density (thence, the intensity of the radiation) decreases rapidly near the surface from about the horizon, which produces a loss of detectability. The rate of decrease of the radiation intensity versus range depends on the refractive conditions and the sensor-target elevations.

To describe this refraction loss, one can define a new parameter, hereafter called "refractance", which gives the radiation intensity (due to the geometrical spreading) relative to $1/R^2$, which is normally assumed in any system studies. Like for the MIVR, the refractance is not wavelength dependent. In the calculation of subpixel target detection, one can show that the refractance, $\rho$, directly affects the contrast, $C$, and so the signal-to-noise ratio, $SNR$:

$$SNR = \frac{C}{NEI} = \rho \frac{A_t}{R^2}[N_t' + N_p - N_b'] \qquad (4)$$

where:

$NEI$ is the noise equivalent irradiance ($W/m^2/sr$);

$A_t$ is the apparent target area ($m^2$);

$R$ is the slant range between detector and target (m);

$N_t'$ is the attenuated target irradiance ($W/m^2/sr$);

$N_p$ is the path radiance ($W/m^2/sr$); and,

$N_b'$ is the attenuated background irradiance ($W/m^2/sr$).

Figure 5 shows the refractance versus range for two different superrefraction conditions, for a sensor located 22.5 m above water. The HLR is also shown. When refraction is neglected, $\rho$ is usually considered equal to 1 for $R <$ HLR and equal to 0 for $R >$ HLR. The refractance curves in Fig. 5 were obtained using WKD in conjunction with the DREV ray tracing technique which incorporates ray-intensity calculation [6].

During a measurement campaign conducted in Sylt (Germany) jointly with the Netherlands and Germany in June 1992, tracking of targets moving away from the observer was experimented under the conditions considered for the solid line in Fig. 5 [7]. The arrow indicates where the target located 2.8 m above water was lost during the tracking session. Note that, in this case, the maximum detection range is about 1.5 x HLR, which is significant. This result does demonstrate that limiting detection at HLR, as it is usually done in EO system studies, may lead to excessively pessimistic performance predictions, especially for coastal environments where these conditions can be frequent. It is worth mentioning that clear and warm weathers, favorable for extended detection ranges, prevailed during daytime for more than 8 consecutive days during the Sylt campaign [8].

Figure 5 also shows the refractance under a different atmospheric condition (dashed line) where the refractance decreases more slowly. One shall be careful in interpreting these curves and shall not conclude that the maximum detection range would be necessarily significantly greater in the case of the dashed curve. It must be stressed that the graphic presents exclusively the effect of refraction. Radiation that reaches low-level targets beyond the horizon has to propagate very near the surface over long distances, and so the detection range is likely to be dominantly dependent upon the surface aerosols density under most conditions.

A rigorous experimental validation of refractance prediction curves is difficult and tricky. In particular, the assumption of horizontal homogeneity, which is made here, may lead to sizeable errors especially when long ranges are considered. Evaluating refractance may also imply that all complementary factors affecting the contrast, especially the transmittance, are accurately known. However, the over-spreading of rays that occurs near the surface under superrefraction produces an image compression and the compression ratio is an indirect, though valid, measurement of ray intensity. Although very few measurements of compression ratio have been made so far, they have been in agreement with predictions when the conditions could be assumed homogeneous. An example was presented by Dion et al. a few years ago [4].

To give indications of the refractance variation with respect to the strength of the superrefraction conditions, Fig. 6 shows the predicted ranges where the refractance reaches 0.8 and 0.5, respectively under various ASTD and wind speed conditions. Note that some refraction losses are obtained at ranges less than the horizon. This can also be observed in Fig 5. Long detection range capability due to refraction implies in turn some losses of detectability at shorter distances.

Plots for two refractances, as given in Fig. 6, inform about the rate of decrease of the refractance versus range with respect to the ASTD and wind speed conditions. We see that the sensitivity to wind increases rapidly with ASTD. We also note that, as the wind speed decreases, the potential-range performances increase very rapidly. However, it must be mentioned that the stability length, the Monin-Obukhov stability length, $L$, which can be seen as a measure of the model validity, decreases with decreasing wind speed. In Fig. 6, curves stop at conditions where $L$ gets lower than 15 m; this is an arbitrary criterion since good profile predictions can be obtained for lower $L$ values.

The effect of sensor and target elevations is in relation to the "optical" duct height. As defined in the RF, the duct height corresponds to the elevation where the modified air refractivity goes to a minimum (or, in other words, where its gradient passes through 0). Figure 7 shows the duct height for the visible and the IR versus ASTD and wind speed. Here again, curves stop at conditions where the stability length gets lower than 15 m. Like in the RF, better refractance performances is obtained when both the sensor and the target are below the duct height. However, one notes that, for EO systems, under most conditions the duct height is much lower than the sensor heights of interest for ship defence applications. Moreover, it has to be mentioned that when the target is slightly above the duct, where a "hole" is produced, the refractance falls off rapidly.

## 5. CONCLUSIONS

In coastal environments, the near-sea surface refraction effects on detection range of low-level targets can be significant, and so, techniques are required to efficiently take them into account in the calculation of detection range performances of EO systems. Subrefraction conditions, that are likely to occur when the air mass is maritime, induces an abrupt detection range limit which can be reliably predicted and readily estimated using

approximative formulae; an expression was derived as a function of ASTD and wind velocity. Warm continental air blowing over cool coastal water can produce superrefraction which can lead to significantly extended detection range. Under these conditions, assuming that the detection ranges are limited by the horizon (as it is usually done) can greatly underestimate the system performances. The use of "refractance" has been proposed to take into account the refraction losses under superrefraction conditions in the calculation of detection ranges of EO systems.

## 6. REFERENCES


1. Dion, D. and Leclerc, B., "Investigation of the Air Refractivity Effects on IR Sensors in the Marine Boundary Layer", DREV-R-4570/90, August 1990.

2. Skolnik, M.I., "Introduction to Radar Systems", McGraw-Hill Book Company, 1970.

3. Low, T.B. and Hudak, D.R., "Final Report on the Development and Testing of a Marine Boundary Layer Model", KelResearch Corp., Report under DSS contract #W7701-8-2419/01-XSK, September 1990.

4. Dion, D., Forand, J.L., Fournier, G.R. and Pace, P., "Experimental Data on Near-Surface Refraction Effects at Optical Wavelengths", Optics of the Air-Sea Interface: Theory and Measurements, Lesland Estep, Editor, Proc. SPIE 1749, 1993.

5. Forand, J.L., Dion, D. and Beaulieu, J., "MAPTIP: Canada's Measurements of Refraction Effects", presented at 2nd Symposium of the AGARD Sensor and Propagation Panel on "Propagation Assessment in Coastal Environments", Bremerhaven, Germany, 19-22 September, 1994.

6. Blanchard, A., "Phase and Intensity Ray Tracing to Study the Propagation of Coherent Radiation in the Atmosphere and other Media", DREV-R-4699/93, January 1993.

7. Dion, D. and Beaulieu, J., "Sylt '92 Campaign: The Complementarity of Radar and EO Sensors", private communication, December 1993.

8. De Leeuw, G., Neele, F.P. and Van Eijk, A.M.J., "IR/RF Refractivity Profiles over Coastal Water", presented at 2nd Symposium of the AGARD Sensor and Propagation Panel on "Propagation Assessment in Coastal Environments", Bremerhaven, Germany, 19-22 September, 1994.


## 7. APPENDIX: APPROXIMATE MIVR FUNCTION

Under subrefraction conditions, equation (3) can be used for estimating MIVR, where:

$$\Phi = \alpha\Delta^2 + \beta\Delta + \gamma \qquad (5)$$

where:

$$\begin{aligned} \alpha &= -10^{-3}\left(2.159 + 8.4\ log(\omega)\right) \quad ;\omega < 9.5\ m/sec \\ &= -10^{-2}\left(1.3921 - 0.037454\ \omega\right) \quad ;\omega \geq 9.5\ m/sec \end{aligned} \qquad (6)$$

$$\begin{aligned} \beta &= -10^{-2}\left(1.5 + 3.6\omega - 0.19\ \omega^2\right) \quad ;\omega < 9.5\ m/sec \\ &= -10^{-1}\left(2.184 - 0.0098395\ \omega\right) \quad ;\omega \geq 9.5\ m/sec \end{aligned} \qquad (7)$$

$$\begin{aligned} \gamma &= 0 \quad ;\omega < 9.5\ m/sec \\ &= -0.02 \quad ;\omega \geq 9.5\ m/sec \end{aligned} \qquad (8)$$

where $\Delta$ is the air-sea temperature difference in degrees and $\omega$ is the wind speed in m/sec. For wind speeds less than 0.5 m/sec, the value 0.5 m/sec shall be used in the calculation.

In (3), the function $\Gamma$, which accounts for the effect of the sensor and target heights, is given by:

$$\Gamma = \left(H^* - 1\right)\left(1.1 - S\cdot\Delta\right) + 1 \qquad (9)$$

where:

$$H^* = \frac{H}{6.3246} \qquad (10)$$

where $H$ is given by (2) and:

$$S = 0.0175 + 0.0375\left[1 - exp\left(-(\omega-1)/2.5\right)\right]. \qquad (11)$$

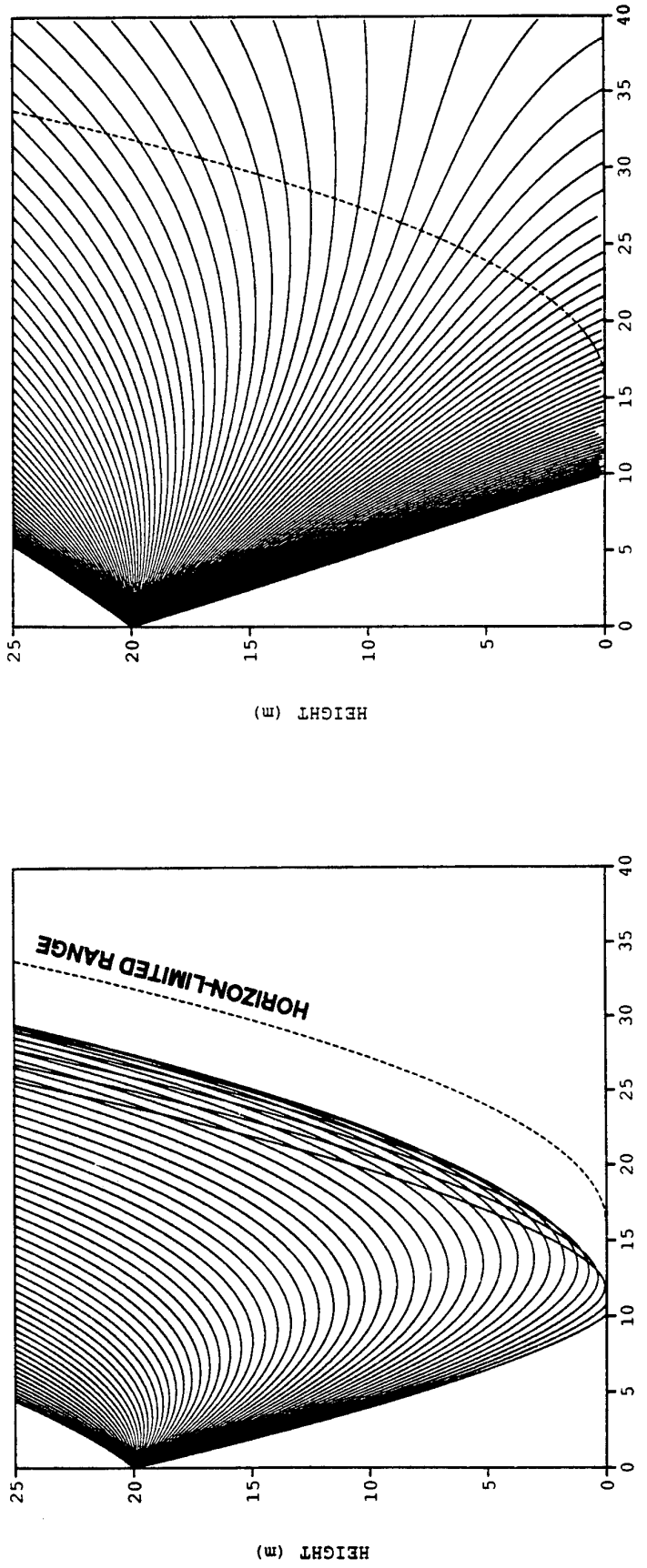


Fig. 1 - Ray diagram for typical sub- and superrefraction conditions

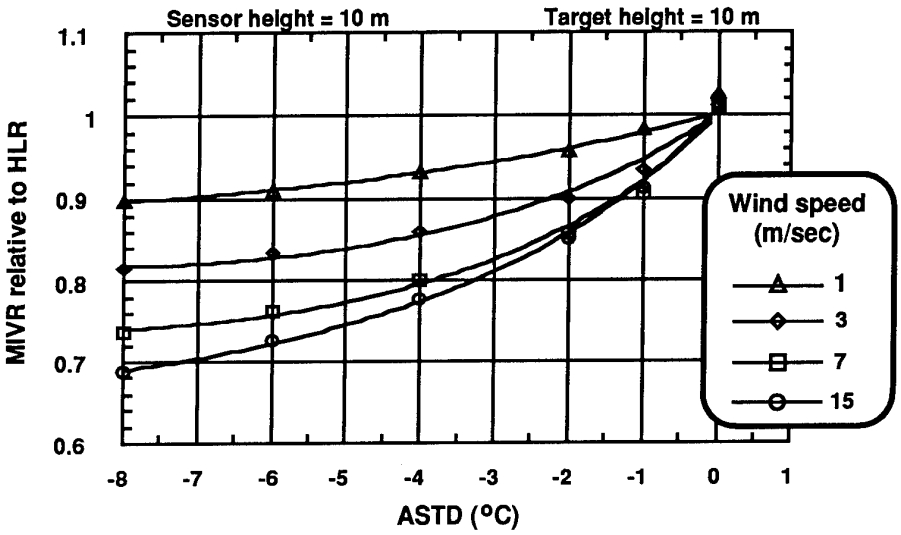


Fig. 2 - MIVR (relative to HLR) versus ASTD for different wind speed conditions

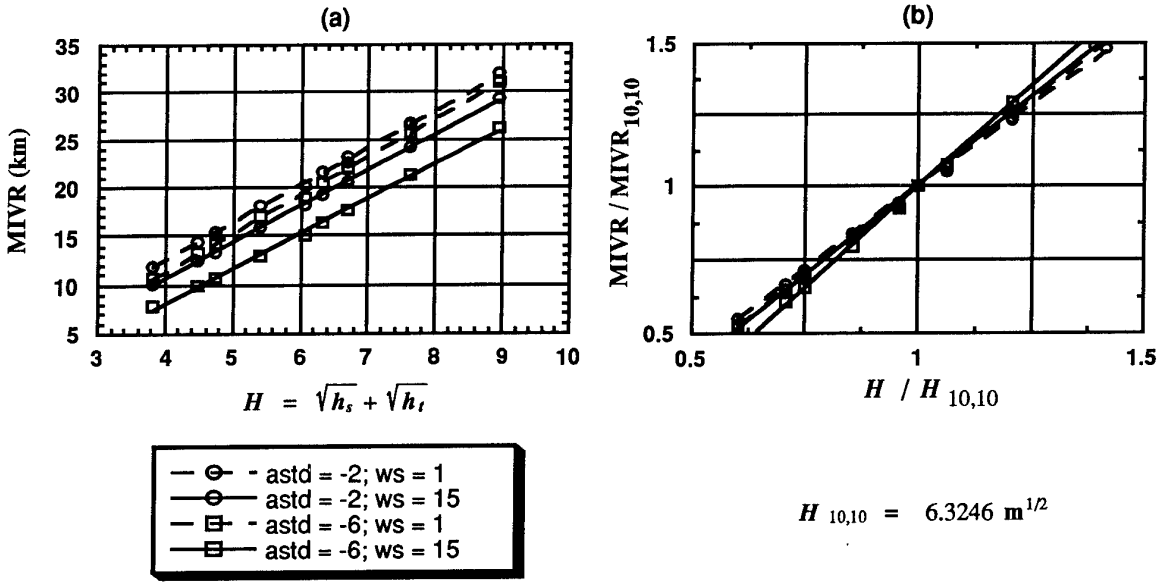


Fig. 3 - MIVR with respect to the sensor-target height parameter $H$ for various ASTD and wind speed conditions; the wind speed (ws) is in m/sec; $H$ (10,10) and MIVR(10,10) are the $H$ and MIVR values for a sensor and a target located 10 m above the sea surface

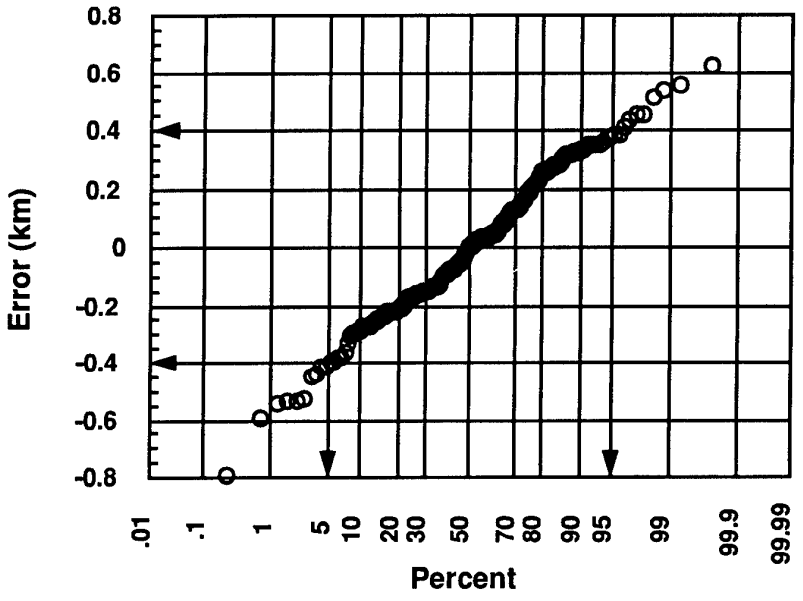


Fig. 4 - Distribution of the errors obtained using the approximate MIVR expression

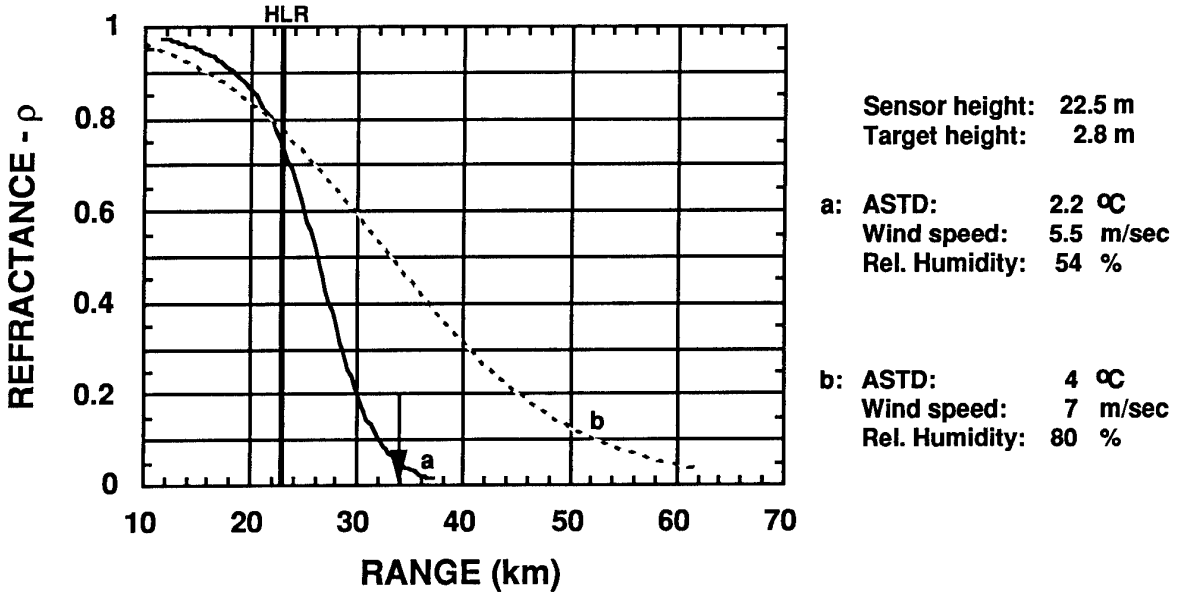


Fig. 5 - Refractance versus range for two refractivity conditions

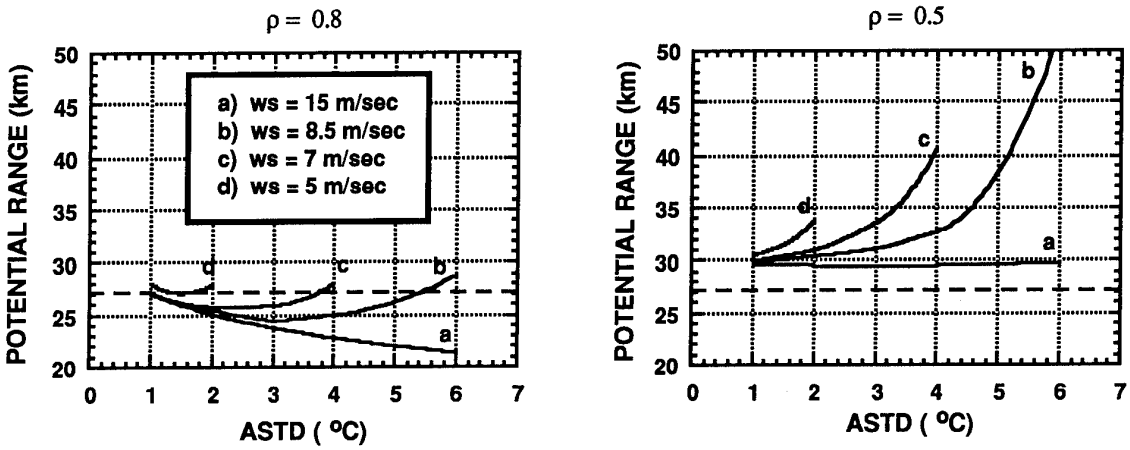


Fig. 6 - Potential range performance versus ASTD and wind speed for ρ = 0.5 and 0.8, respectively; the sensor height is 20 m and the target height is 10 m; ws stands for wind speed

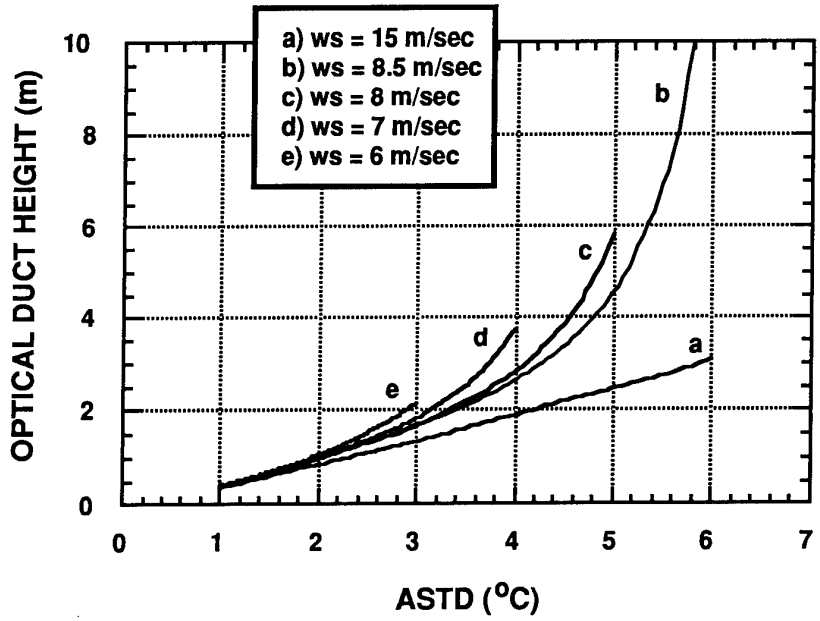


Fig. 7 - "Optical" duct height versus ASTD for different wind speed conditions; ws stands for wind speed

## DISCUSSION

**D. DOCKERY**

You have discussed cases where upward ray bending causes MIVRs to be shorter than the geometric horizon, and cases where downward ray bending causes propagation beyond the horizon. Are there not also cases between these two extremes?

**AUTHOR'S REPLY**

Under non-refractive conditions (i.e. when the refractive index of air can be considered spatially invariant), rays are straight lines and MIVRs correspond to the geometrical horizon. Sub-refraction (produced when ASTD $< 0$ °C) prevents rays from reaching the horizon due to the upward bending phenomenon. When the ASTD is positive (theoretically for an ASTD greater than about -0.5°C due to the pressure gradient effect) rays go beyond the horizon. In general, under significantly positive ASTD conditions, propagation well beyond the horizon is made possible and the MIVR concept does not apply; in this case, the use of "refractance" is proposed to describe the refraction effects. However, for slightly positive ASTD conditions (ASTD $\approx$ 1.5°), there are limit conditions which make the evaluation of both the MIVR and the refractance difficult (potentially inapplicable).

# COMPARISON OF SIMULTANEOUS 3-5 AND 8-12μm TRANSMISSION MEASUREMENTS NEAR THE OCEAN SURFACE

**H. T. Bull**
Department of Aerospace Engineering
California State University, Long Beach, CA 90840
USA

**D. R. Jensen**
Ocean and Atmospheric Sciences Division
NCCOSC RDTE DIV 543
53170 Woodward Road
San Diego, CA 92152-7385
USA

## ABSTRACT

A comparative transmissometer has been developed for evaluating the simultaneous transmission characteristics for near ocean surface transmissions in the 3-5 $\mu$m and 8-12 $\mu$m bands. This transmissometer is a special purpose instrument designed for simultaneously measuring the changes in transmission of the 3-5 $\mu$m and 8-12 $\mu$m transmission bands. The transmissometer has been operated over the San Diego Bay, California, to determine the transmission characteristics for near ocean propagation paths. Observed propagation characteristics for both the 3-5 $\mu$m and 8-12 $\mu$m bands are compared and discussed as a function of existing sea states and meteorological conditions. The observed transmission characteristics for the two wave bands are compared with LOWTRAN calculations. Rapid fluctuations in received signal strength, their power spectra, and correlation coefficients are also discussed.

## 1. INTRODUCTION

With the present interest in using Forward Looking Infrared (FLIR) detection systems within the marine boundary layer (MBL), and particularly within meters of the ocean surface, it is important to obtain detailed information of the effects of the atmosphere on the 3-5 and 8-12 μm FLIR wavelength bands. This information is particularly important for predicting the performance of electro-optical systems operating against low flying aircraft and surface targets when approaching from beyond the horizon. The Atmospheric Transmission/Radiance computer code, LOWTRAN [1,2], is the primary tool used for assessing the propagation characteristics of EO systems. With the inclusion of the Navy Aerosol Model, NAM [3-10], into LOWTRAN 6 [1] and an upgraded version of NAM into LOWTRAN 7 [2], users are now able to determine the effects of aerosols on EO propagation in a maritime environment. This model has proven to be a useful tool in predicting atmospheric transmission in the marine atmosphere along horizontal paths at shipboard levels (above 10 m). Recent studies have shown that NAM in its present forms should not be extrapolated into the region very near the ocean surface (below 10 m) for predicting atmospheric properties [11, 12]. This marine surface layer (MSL) is largely affected by the local sea state, meteorological conditions, and low level aerosol generation sources. Of particular concern is the effect on infrared transmission characteristics due to the MSL meteorological conditions and the whitecapping/surf generated aerosol.

Transmission characteristics in the MSL may be significantly different from that within the MBL. Experiments are needed to determine the relative advantages of the 3-5 and 8-12 μm systems for the cases of extended horizons where humidity and aerosol effects can be the determining factors in system performance. An experimental comparative transmissometer has been developed for evaluating the simultaneous transmission characteristics for near ocean surface transmissions in the near and far wavelength bands. It is a special purpose instrument designed for simultaneously measuring the relative changes in transmission of the 3-5 and 8-12 μm atmospheric transmission windows. The transmissometer has been operated during an initial observation period over the San Diego Bay, San Diego, CA. The design of the comparative transmissometer, the initial observations, comparisons with LOWTRAN calculations, power spectral analysis of the 3-5 and 8-12 μm received signals, and the resultant near surface aerosol modeling effort will be discussed. The overall objective of this comprehensive investigation is to determine the EO propagation characteristics in the MSL from fair to highly disturbed weather and on all time scales from milliseconds to seasons. The propagation characteristics which are reported in this paper are the following:

1. Transmission variations in the 3-5 and 8-12 $\mu$m atmospheric windows (averaged over 5 minutes) compared with in-situ meteorological data.

2. Observed transmission variations in the 3-5 and 8-12 μm bands compared to LOWTRAN calculations.

3. Correlation between the received 3-5 and 8-12 μm rapidly varying signal (averaged over 10 milli-seconds), and the corresponding 3-5 and 8-12 μm power spectra.

## 2. INSTRUMENTATION

The prototype of a "comparative transmissometer" has been installed and operated over the San Diego Bay. The path length is 7 km and the height of the IR source and receiver is 3 and 3.4 m above mean sea level, respectively. The path has a southern exposure to the open ocean between 180° and 270° (referenced to the receiver). The geographical location of the transmissometer path over the San Diego Bay is shown in Figure 1. A block diagram of the transmissometer is shown in Figure 2. A brief description of the design criteria and specifications for the transmissometer follows.

Two different infrared sources were used with the comparative

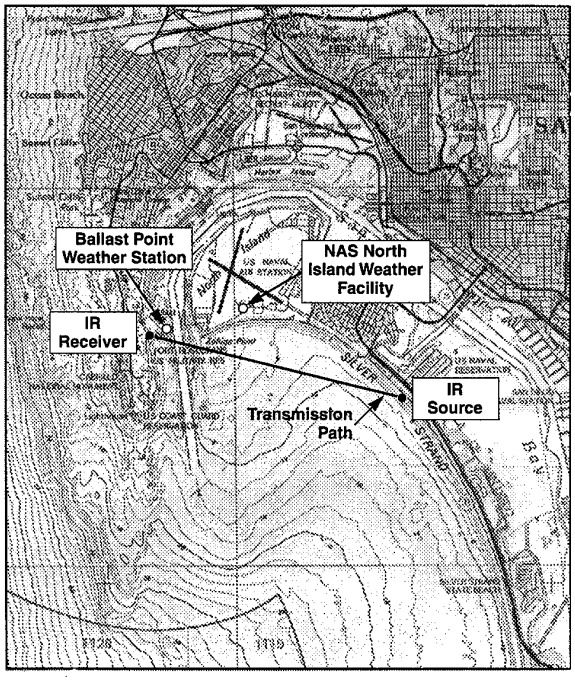


Figure 1. Geographic locations transmission path.

*Paper presented at the Sensor and Propagation Panel Symposium on "Propagation Assessment in Coastal Environments" held in Bremerhaven, Germany 19-22 September 1994.*

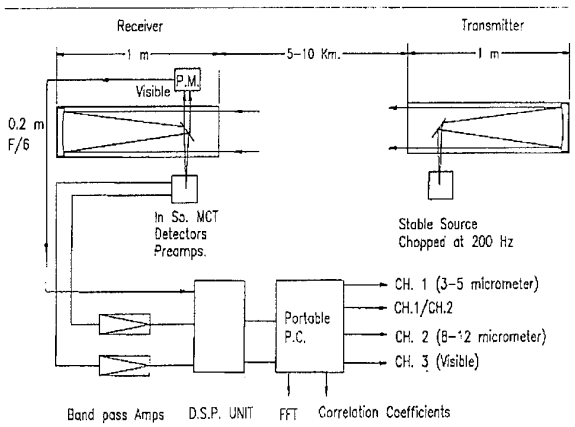


Figure 2. Comparative transmissometer block diagram.

transmissometer at different times. One source was a wide-angle point source and the other a collimated one. The wide-angle point source (2 kw) has the advantage of having no pointing requirements and a guaranteed uniformity in the far field. The collimated infrared source (10 watts) consists of a wire filament encased in a ceramic housing with a 2 mm diameter exit aperture. The radiation is modulated by a conventional chopper at 200 Hz for both sources. The collimator consists of a Newtonian telescope with a 20 cm f/6 parabolic primary mirror. Both sources operate at a temperature of 1200 °K. The mounting platform is a very stable robust structure mounted just beyond the high water line (Figure 1). The radiant and mechanical stability of the IR sources is such that any variations in the received signal resulted from changes in the atmospheric transmission, not changes in the source. It was also determined that moderate wind speeds and air temperature variations have negligible effects on either the wide-angle or the collimated source.

The IR receiver consists of a 20 cm f/6 parabolic primary mirror Newtonian telescope fitted with a 1 mm x 1mm InSb/MCT sandwiched detector. A sandwiched detector is used to guarantee that the field of view for the two channels is identical and that all the received signals follow the same propagation path apart from any differential refraction and diffraction effects. This is important since the relative changes of the 3-5 and 8-12 μm transmission is the principal output of the instrument. The detectors simulate the spectral response of imaging devices used in surveillance operations. The receiver dewer has a twelve holding time for the liquid nitrogen. The receiver is mounted on a stable platform and bolted to concrete pads on a rocky shore (Figure 1). A pointing stability of than one milliradian/month is obtained with this mounting.

Low noise preamplifiers were used making the receiver detector noise limited. The amplifiers are tuned to 200 Hz to match the chopping frequency of the sources. The useful dynamic range of this system is approximately 10:1. The low signal/noise ratio has a limiting effect on the measurement of the atmospheric seeing characteristics which produce the intensity fluctuations. With a 50Hz bandwidth centered on 200 Hz, the signal/detector noise ratios are 20 and 8 in the 3-5 and 8-12 μm channels, respectively. However, the seeing noise is usually an order of magnitude greater than the detector noise. The low signal to noise ratio obtained when a 50 Hz bandwidth is used dictates that the intensity fluctuation power spectra have to be averaged at this stage to get reliable estimates of the composition of seeing noise.

The digital signal processing unit is preceded by an RMS converter and an A/D converter. The signal processing involves rectifying the 200 Hz carrier signal to give the intensity fluctuations of the received signal. Data processing of the 3-5 and 8-12 μm signal are then made utilizing a portable PC computer, i.e., data averaging, ratioing, power spectral analysis, and cross correlations. Long term averages (5 minutes) and short term averages (10 milli-seconds) are recorded.

The effective spectral response of the transmissometer, Figure 3, is dictated by that of the sandwiched detector elements (InSb and MCT), the infrared source, and the atmospheric transmission. The spectral response of the present system is therefore not completely uniform over the spectral bands of interest. The response of the InSb and MCT detectors lessen the amount of the 2.3 μm radiation that would be observed in the 3-5 and 8-12 μm channels.

The output of the comparative transmissometer contains the relative changes in transmission between the two infrared 3-5 and 8-12 μm windows for a specific path as a function of meteorological conditions. Absolute transmission is not measured thus avoiding the complexity and cost of making absolute transmission calibrations. This system appears adequate for the relative comparisons of the 3-5 and 8-12 μm signals over extended meteorological conditions.

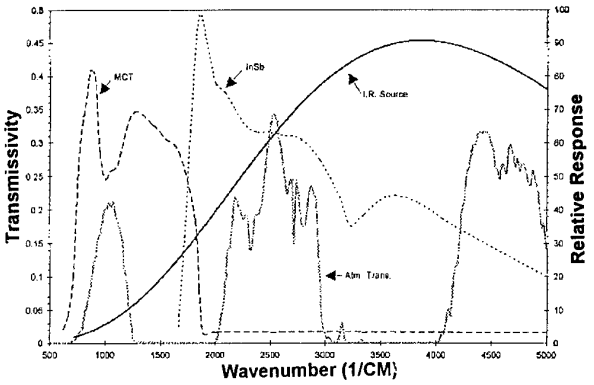


Figure 3. Atmospheric IR transmissivity and instrument spectral functions.

## 3. MEASUREMENTS

The focus of the comparative transmissometer measurements is to identify the relative changes which occur in the infrared atmospheric transmission windows with respect to changes in wind speed, air mass type, existing sea state, and differing meteorological conditions. The transmissometer has been in operation over the San Diego Bay's 7 km transmission path (Figure 1) intermittently since August 1993. Standard meteorological measurements of air temperature, relative humidity, sea surface temperature, wind speed and direction, and visibility were made by the Naval Pacific Meteorological and Oceanography Facility North Island at the Naval Air Station North Island (Figure 1) . Similar meteorological measurements were made near the western end of the transmission path at Ballast Point (Figure 1). Unfortunately in this data set only fair weather conditions were encountered during the operational periods thus eliminating possible correlations with high winds and seas. Figure 4 shows the raw 3-5 and 8-12 μm band transmission data for a twenty eight hour period starting at 0323 GMT on 1 June 1994. Relative changes in the received signal strengths for the two wave bands (averaged over 5 minutes) can be observed. However, comparison of the 3-5 and 8-12 μm raw data cannot be made as the transmission values are not absolute. To circumvent this, the initial data point for each of the two wave bands have been normalized to the fair weather LOWTRAN transmission calculations corresponding to the measured meteorological data from the NAS North Island weather station (Figure 5). The air mass factor was not measured but was estimated from the prevailing wind direction. The use of LOWTRAN permits a direct comparison of the received signals in the 3-5 and 8-12 μm atmospheric transmission bands (relative to LOWTRAN) to be made for determining the differences in the transmission characteristics. The 3-5 μm band has a higher transmissivity throughout the data period than the 8-12 μm band though the 3-5 μm variability is higher ($0.07 \leq$ transmissivity $\leq 0.70$). The 8-12 μm signals were mostly constant throughout the time period. Considering the fact that the 8-12 μm channel is nearly constant and is not showing the

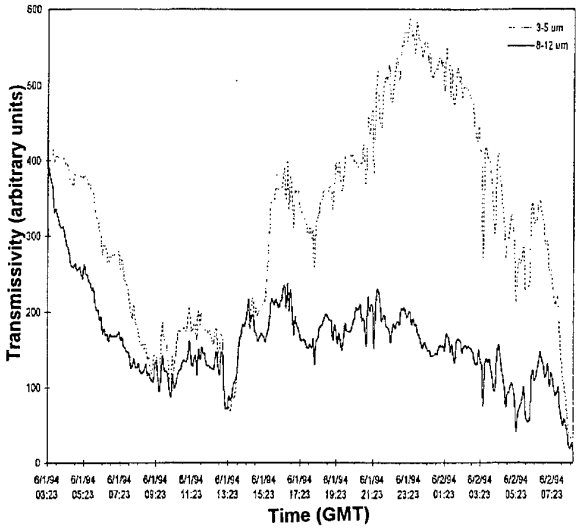


Figure 4. Raw comparative transmissometer data for June 1-2, 1994.

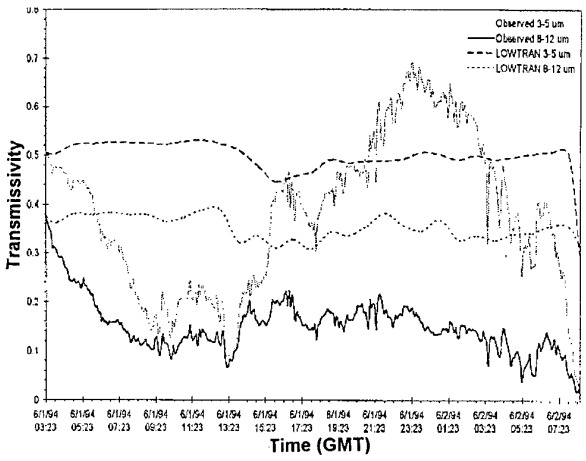


Figure 5. Observed Changes in IR transmission (normalized to LOWTRAN) for June 1-2, 1994.

same variations as the 3-5 μm band, it suggest that an attenuation mechanism exists which seriously degrades the 3-5 μm band while the 8-12 μm remains essentially unaffected.

Figures 6, 7, 8 show the corresponding meteorological data from the NAS North Island and the Ballast Point meteorological observation stations. Comparing the observed changes in the IR transmission for the 3-5 μm band with the meteorological data (Figures 6, 7, 8), shows that the low transmission values correspond to the periods of higher relative humidity, lower wind speeds, and cooler air temperature. The opposite is true for the higher transmission values. Even though some differences in the absolute values exist between the near mid-path inland meteorological observation station with those observed on the western end of the transmission path, the variational patterns are the same. The 8-12 μm transmission values do not show these same correlations and remains at a lower value through the measurement period.

The LOWTRAN calculated transmissivity for this data period (1-2 June 1994) is shown in Figure 5 for the wave bands. The LOWTRAN calculations (using the hourly meteorological averages from NAS North Island) are nearly constant in both bands with the 3-5 μm band having higher transmissivity than the 8-12 μm band. This agrees with the measured data. LOWTRAN predicted less than a 10% change in the transmission for both bands and does not, as one would expect, describe

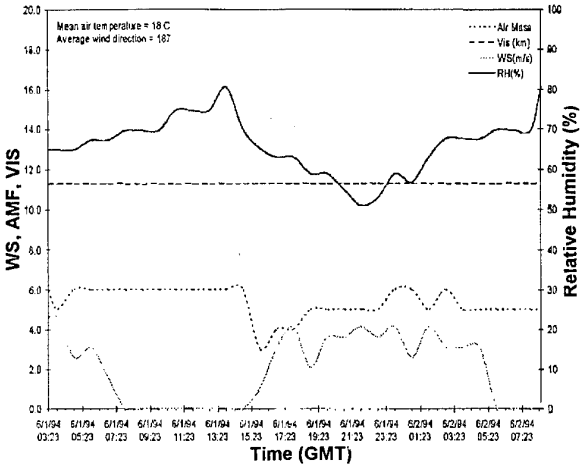


Figure 6. Meteorological data for June 1-2, 1994.

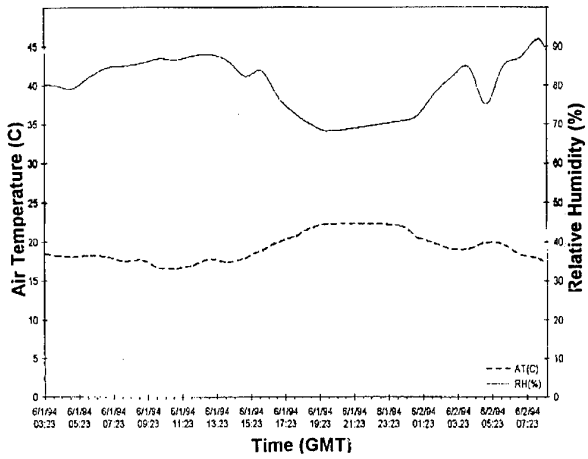


Figure 7. Air temperature and relative humidity for June 1-2, 1994 (Ballast Point).

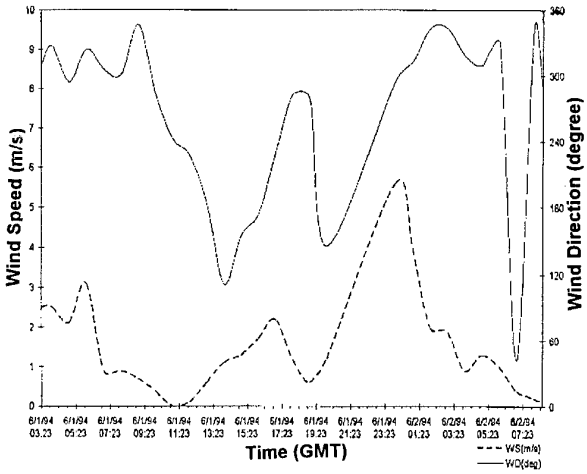


Figure 8. Wind speed and direction for June 1-2, 1994 (Ballast Point).

the rapid fluctuations observed in the 3-5 and 8-12μm bands. Also, the relative amplitudes of the calculated and received transmissivities did not agree. The tracking of the changes in transmission using LOWTRAN calculations when based on standard hourly meteorological observations is not usually in good agreement with the observed changes.

The degree and type of signal variations observed where the 3-5 μm wave band shows large variation and the corresponding 8-12 μm band remains constant is typical of the light sea fog and misty conditions. When the sea mist or fog is more dense, both channels are equally effected as shown in the 5-12 August 1994 IR transmission data (Figure 9). The corresponding meteorological data is shown in Figure 10. On 5, 6, and 7 August fog events occurred where the visibility was reported to be near zero. Corresponding to these events, the 3-5 and 8-12 μm channels showed significant reduction in the received signal strengths. From 7-12 August the 3-5 and 8-12 μm signals showed a cyclic pattern and appears to correlate with the cyclic variations of the relative humidity. The recorded visibility (Figure 10) does not show periods of intense reduced visibility after 7 August. However, the over water transmissometer path could be affected by a coastal fog that did not extend inland and was not observed by the meteorological observation station located at NAS North Island weather station. It is interesting to note that periods of increased 3-5 and 8-12 μm signal strength after 7 August corresponded with increasing winds and decreased relative humidity (or conversely with decreasing winds and increased humidity). Having a fog band that lies along the coast, not penetrating inland, during conditions of low winds is a typical pattern in a coastal environment (no on-shore flow). This would explain the cyclic pattern of the IR data in terms of increased attenuation due to fog and mist along the propagation path.

The LOWTRAN transmission calculations for the 5-12 August 1994 data period are also shown in Figure 9. The 3-5 μm transmissions are better than for those of the 8-12 μm throughout the data period. LOWTRAN calculation do trace the heavy fog events but do not show the apparent cyclic nature after 7 August.

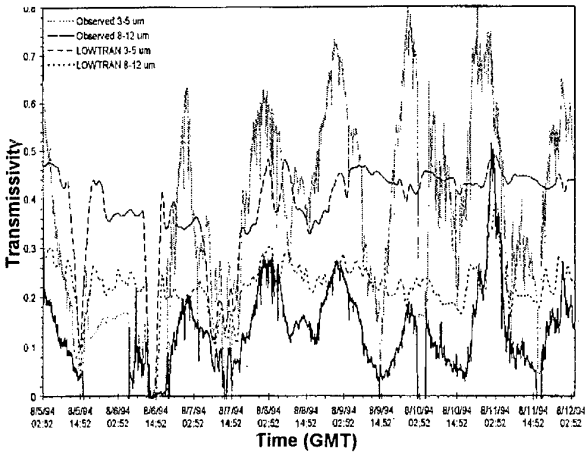


Figure 9. Observed Changes in IR transmission (normalized to LOWTRAN) for August 5-12, 1994.

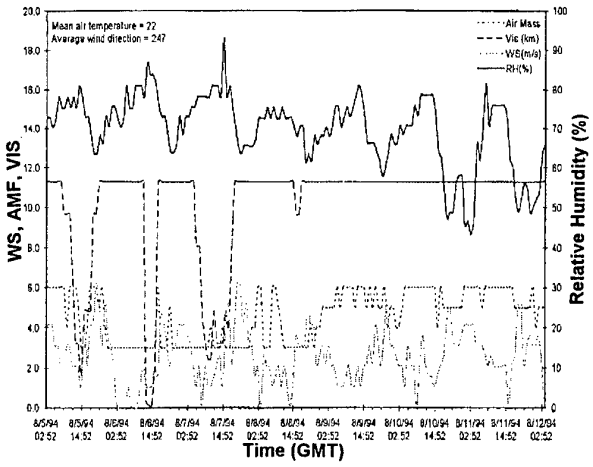


Figure 10. Meteorological data for August 5-12, 1994.

The LOWTRAN comparisons with the measured 3-5 and 8-12 μm band transmission characteristics (Figures 5 and 7) show significant discrepancies when used for predicting the effects of the MSL on IR transmission. The critical LOWTRAN input parameters which determine these characteristics are the visibility, air mass factor, humidity, and aerosol content. Our results show that the meteorological support measurements must be taken near or on the transmission path and include measurements of visibility and air mass factor. Also, the aerosol models used in LOWTRAN for determining the aerosol content must be developed to include the MSL. The development of the Advanced Navy Aerosol Model (ANAM) to describe the aerosol content in the first 10 m above the ocean was the objective of the MAPTIP experiment [13] and a Coastal Aerosol Model (CAM) has been proposed for representing the MSL in the coastal environment [14]. The existing NAM model in LOWTRAN was developed to represent the MBL above 10 m. To account for aerosols generated by surf and wind generated white caps in the coastal MSL additional aerosol models must be added to NAM.

Correlation between the 3-5 and 8-12 μm channels on a very short time scale (milli-seconds) may be useful data in the development of software for the search and track IRST systems [17]. Detection sensitivities and/or the rejection of false alarms may be enhanced by using the statistical properties of the intensity fluctuations in the transmitted infrared beams. An example of the fluctuations is shown in Figure 11. Fluctuations in the propagation characteristics can produce intensity nose up to 50% of the mean signal level. Correlation coefficients between the two channels were calculated for Figure 11, and found to be between 0.5 and 0.75 when the averaging time of 10 milli-seconds was used. However, actual correlation coefficients will be significantly greater than these values because of the large component of the uncorrelated detector noise in the present system. An example of the power spectra is shown in Figure 12.

## 5. CONCLUSIONS

Inspection of the transmissometer data taken over many days show that there is a significant variability in transmission even under fair weather synoptic conditions. These variations can be correlated with the in-situ meteorological measurements. However, the tracking of the relative changes in transmission with LOWTRAN calculations that are based on the standard hourly meteorological observations is usually not in good agreement. The data shows a discrepancy between the relative measured and LOWTRAN calculated transmissions values and suggests that models within LOWTRAN need to be modified to represent the coastal marine MSL environment.

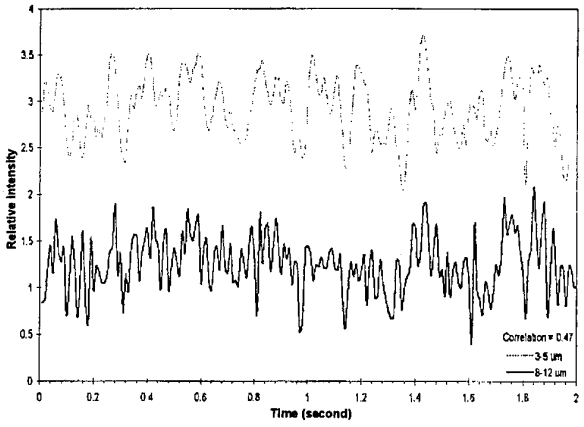


Figure 11. Intensity fluctuations of transmitted IR beams.

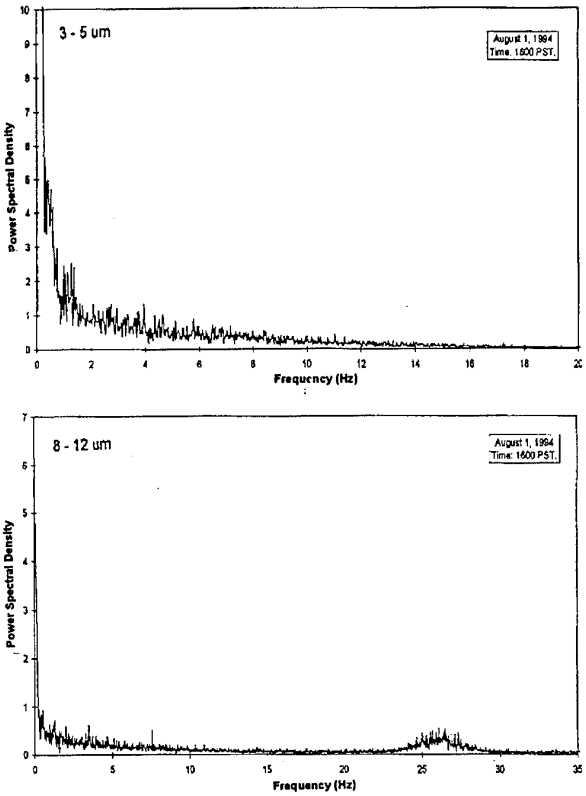


Figure 12. Averaged power spectrum of intensity fluctuations of 3-5 (top) and 8-12 μm (bottom) transmitted beams.

In order to predict the transmissivity in the marine surface layer on a short time scale to better than 30%, the meteorological conditions need to be more specified relative to the on path characteristics. This is especially true in terms of visibility and air mass factor. The role of coastal fogs and mist is of major significance in the near infrared. As the visual ranges reduces from 20 km to 3 km the 3-5 μm transmissions are greatly reduced while the 8-12 μm was observed to be reduced by less than a factor of two. The 3-5 μm band generally offers higher transmissitivities than for the 8-12 μm band but suffers larger variability for light fog and misty conditions.

## 6. FUTURE WORK ON MSL TRANSMISSION MEASUREMENTS AND MODELING

The measurement program will be developed further to include the following aspects:

1. Transmissometer measurements at San Diego will incorporate more accurate assessment of visibility, air mass factor and will include aerosol size distribution measurements. Operations will also be made for a wider range of weather conditions, i.e., higher wind speeds, increased white capping, and higher sea states.

2. A second transmissometer range is to be established over a surf line will and used to identify significant propagation characteristics arising from breaking waves and high surf.

3. A transmissometer parallel to the present path but at a higher elevation above the ocean surface will be used to isolate the effects within the MSL by serving as a continuous reference transmission path outside the surface layer.

4. A collaborative effort for IR transmission analysis and data exchange is planned with the Australian Department of Defence, Defence Science and Technology Organization (DSTO) through the University of Western Australia. The DSTO transmission path is 3 km long from HMAS Sterling to Carnac Island, Western Australia. This transmission path is well exposed to the open ocean and strong winds occur regularly. The air mass is usually well defined as either maritime or continental.

5. Transmissometer data during high winds and sea state will be used to develop/evaluate aerosol models being developed to represent the MSL.

6. The transmissometer source and the detector will be reconfigured and made more weather proof and automated for continuous operation in all weather conditions. The source and detector are to be improved by using a special condensing cone within the detector housing. This will allow the source temperature to be reduced to 500° K to equalize the radiant power in the two atmospheric windows. The detector will also be fitted with filter to remove the 2.3 μm radiations. The visible channel will also be made a permanent feature to replace the standard meteorological observations of visibility.

## 7. ACKNOWLEDGMENTS

The computer program for extinction modelling and for the data processing has been performed by Khalid Rubayi and Stanley Chen of California State University, Long Beach. The numerous and helpful discussions which have been held with S.G. Gathman, H. Hughes, and C. Zeiss of NRaD are gratefully acknowledged. This work was support by the Office of Naval Research.

## 8. REFERENCES

1. Kneizys, F.X., E.P. Shettle, W.O. Gallery, J.H. Chetwynd, Jr., J.H. Abreu, J.E.A. Selby, S.A. Clough and R.W. Fenn, "Atmospheric Transmittance/Radiance: Computer Code LOWTRAN 6," Air Force Geophysical Laboratory Technical Report No. 83-0187, August 1983.
2. Kneizys, F.X., E.P. Shettle, L.W. Abreu, J.H. Chetwynd, G.P. Anderson, W.O. Gallery, J.E.A. Selby, and S.A. Clough, "Users Guide to LOWTRAN 7," Air Force Geophysical Laboratory Technical Report No. 88-0177, Aug 1988.
3. Gathman, S.G., "Optical Properties of the Marine Aerosol as Predicted by the Navy Aerosol Model," Opt. Eng. 22, 57-62, 1983.
4. Gathman, S.G., "Optical Properties of the Marine Aerosol as Predicted by a BASIC Version of the Navy Aerosol Model", NRL Memo Report #5157, 1983.
5. Gathman, S.G., "Navy Hygroscopic Aerosol Model" In: Hygroscopic Aerosol, L.H. Ruhnke & A. Deepak, editors, A. Deepak publisher, Hampton, VA., p93, 1984.
6. Hughes, H.G., "Evaluation of the LOWTRAN 6 Navy Maritime Aerosol Model Using 8 to 12 micron Sky Radiances," Opt. Eng., Vol. 26, #11, 1155-1160, 1987.
7. Battalino, T.E. and R.A. Helvey "Air Mass Parameterization in the Navy Aerosol Model," Geophysical Sciences Technical Note # 103, PMTC, Point Mugu, CA, 1985.
8. Gerber, H.E., "Relative-Humidity Parameterization of the Navy Aerosol Model (NAM)," NRL Report #8956, December 1985.
9. Hughes, H.G. and M.R. Paulson, "Lidar Technique for Adjusting Aerosol Model Number Densities to Existing Conditions," NOSC TD #1637, September 1989.
10. Smith, M.H. and D.R. Bates, "Radon Concentrations over the North East Atlantic," UMIST Interim Report, April 91 - May 92, 1992.
11. de Leeuw, G., "Aerosol effects on electro-optical propagation over sea," In: 8th meeting on Optical Engineering in Israel: Optical Engineering and Remote Sensing, M. Oron, I. Shladov and Y. Weissman (Eds.) Proc. SPIE 1971, 2-15, 1993.
12. Paulson, M.R. and H.G. Hughes, "A lidar technique for adjusting aerosol model number densities close to the ocean surface," Naval Ocean Systems Center Technical Report 1388, December 1990.
13. Jensen, D.R., G. de Leeuw and A.M.J. van Eijk, "Work plan for the Marine Aerosol Properties and Thermal Imager Performance trial (MAPTIP)," Naval Command, Control and Ocean Surveillance Center, San Diego, CA, USA, Technical Document 2573, September 1993.
14. Jensen, D.R., EOPACE Workplan, in preparation.

15. Gathman, S.G. and K.L. Davidson, "The Navy Oceanic Vertical Aerosol Model," NCCOSC TR 1634, December 1993.
16. Gathman, S.G., Private communication.
17. Bendal, C., Private Communication.

## DISCUSSION

**K. DAVIDSON**
Would you describe more about the aerosol component of the LOWTRAN model you addressed?

**AUTHOR'S REPLY**
All calculations were made using the Navy Aerosol Model (NAM) in LOWTRAN.

**E. SCHWEICHER**
What were the cooling temperatures for both detectors? Was InSb used for the 3 - 5μ band and MCT used for the 8 - 12μ band? Within each band did you use a single detector or detector arrays with some signal processing like TDI?

**AUTHOR'S REPLY**
The detectors were liquid nitrogen cooled. The InSb is the 3 - 5μm and the MCT is the 8-12μm detector. The sandwiched detector consists of two single detectors (InSb and MCT), they are not arrays.

**A. JUNCHAT**
Pourquoi utilisez-vous pour "calibrer" vos mesures relatives, 3 - 5μm et 8 - 12μm, le modèle LOWTRAN alors que le propos de vos mesures est justement d'analyser le modèle LOWTRAN dans des cas de propagation dans le conduit?

A quel moment et dans quelles conditions faites-vous cette calibration?

*Since the goal of your measurement is to evaluate LOWTRAN for propagation within the duct, why do you use LOWTRAN to calibrate your relative measurements in the bands 3-5μm and 8-12μm? Where and under which conditions was the calibration done?*

**AUTHOR'S REPLY**
The raw 3-5 and 8-12 micron signals cannot be directly compared because the system is not calibrated and the transmission properties of the two wave bands have not been compensated for. Therefore, to allow a relative comparison of the two signals, the first data point for each band was normalized to the fair weather LOWTRAN transmission calculated values. The remaining data points are then relative to this initial normalized value. The LOWTRAN calculations for the remainder of the data period are for the existing meteorological conditions.

# Radiance of the Ocean Horizon

**C. R. Zeisse**
Ocean and Atmospheric Sciences Division
NCCOSC RDTE DIV 543
53170 WOODWARD ROAD
SAN DIEGO, CA 92152-7385
USA

## SUMMARY

In 1954 Cox and Munk [1] used aerial photographs of sun glint to determine the statistical distribution of ocean capillary wave slopes as a function of wind velocity. When their equation connecting the slope distribution with sun glint is used on the horizon, however, an infinite glint is predicted even though it can easily be shown that sun glint should never exceed solar radiance. This paper derives an integral equation which connects the capillary wave slope distribution with ocean radiance. It predicts a finite sun glint on the ocean horizon and the proper value of sun glint in the calm sea limit. Away from the horizon an approximation reduces this integral to the algebraic equation used by Cox and Munk.

## LIST OF SYMBOLS

| | |
|---|---|
| $A$ | Area of pixel footprint. |
| $B$ | Area of ergodic cap projected toward ray. |
| $dA$ | Area of single facet projected on horizon. |
| $dB$ | Area of single facet projected toward ray. |
| $dF$ | Area of single facet. |
| $dS$ | Area of receiver aperture. |
| $H_o$ | Solar irradiance arriving at footprint. |
| $J$ | Jacobian of transformation, slopes to sky. |
| $N_r$ | Reflected radiance. |
| $N_r^{sun}$ | Reflected solar radiance. |
| $N_o$ | Incident solar radiance. |
| $N_s$ | Incident radiance of source (sky or sun). |
| $P$ | Occurrence probability. Beam power. |
| $p$ | Occurrence probability density. |
| $Q$ | Interaction probability. |
| $q$ | Interaction probability density. |
| $R$ | Distance from facet to receiver. |
| $S_x$ | Facet slope in X (upwind) direction. |
| $S_y$ | Facet slope in Y (crosswind) direction. |
| $\mathbf{U}_n$ | Unit vector at origin normal to facet. |
| $\mathbf{U}_r$ | Unit vector pointing from origin to receiver. |
| $\mathbf{U}_s$ | Unit vector pointing from origin to source. |
| $W$ | Wind speed. |
| $X$ | Coordinate axis pointing upwind. |
| $Y$ | Coordinate axis pointing crosswind. |
| $Z$ | Coordinate axis pointing to zenith. |
| $\phi$ | Azimuth of **U**. |
| $\theta$ | Zenith angle of **U**. |
| $\rho$ | Fresnel reflectivity of the sea. |
| $\sigma_c$ | Standard deviation of $S_y$. |
| $\sigma_u$ | Standard deviation of $S_x$. |
| $\omega$ | Angle of incidence. Angle of reflection. |
| $\Omega_o$ | Solid angle subtended by the sun at the earth. |

## 1. INTRODUCTION

Since the wavelength of an ocean capillary wave is on the order of cm while the wavelength of light is on the order of μm, the interaction of light with the ocean surface can be treated from the standpoint of geometrical optics. The ocean surface can be regarded as a collection of flat facets each of which is randomly tilted with respect to the local horizon. As time passes the tilt of a given facet varies under the influence of the wind. When the solar disk is reflected by the ocean these fluctuating facets produce a dancing pattern of highlights known as sun glint.

By photographing solar reflections from an airplane Cox and Munk [1,2] were able to measure the probability

$$P \equiv p(S_x, S_y, W) dS_x dS_y \qquad (1)$$

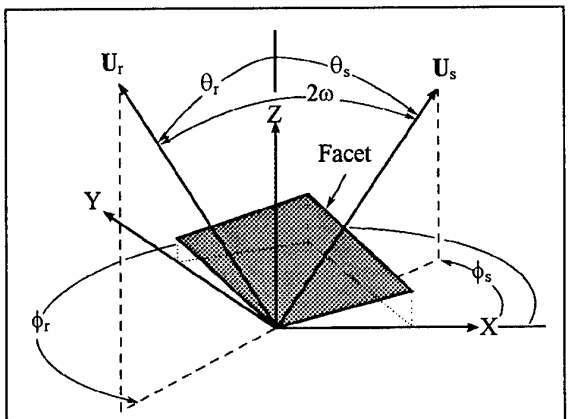


Figure 1. The geometry of facet reflection. The facet normal $\mathbf{U}_n$ has been left out of the figure for clarity. Azimuths are considered positive when measured counterclockwise looking toward the nadir.

*Paper presented at the Sensor and Propagation Panel Symposium on "Propagation Assessment in Coastal Environments" held in Bremerhaven, Germany 19-22 September 1994.*

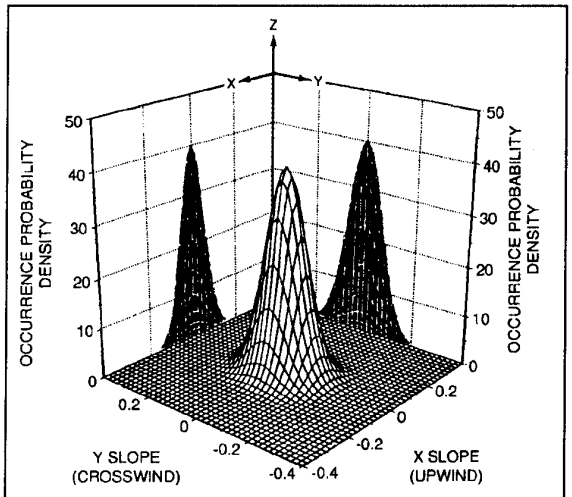


Figure 2. A plot of occurrence probability density as a function of capillary wave slope. The wind speed is 1 m $s^{-1}$. The coordinate system of figure 1 has been inserted at the top to illustrate the relationship between coordinates and slopes. The first quadrant contains negative slopes.

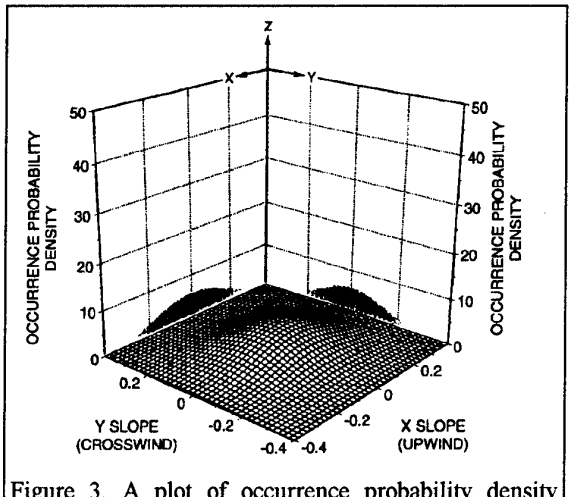


Figure 3. A plot of occurrence probability density throughout slope space for a wind speed of 10 m $s^{-1}$.

that a wave facet would have a slope within $\pm dS_x/2$ of $S_x$ and $\pm dS_y/2$ of $S_y$. Cox and Munk [1] obtained an expression for the capillary wave slope probability density whose lowest order term is

$$p(S_x,S_y,W) \approx \frac{1}{2\pi\sigma_u\sigma_c}\exp\left\{-\frac{1}{2}\left(\frac{S_x^2}{\sigma_u^2}+\frac{S_y^2}{\sigma_c^2}\right)\right\},$$

$$\sigma_u^2 = 0.000 + 3.16\cdot 10^{-3} W, \qquad (2)$$

$$\sigma_c^2 = 0.003 + 1.92\cdot 10^{-3} W.$$

The primary goal of the original Cox-Munk work was to determine the wave slope probability distribution. The wave slope distribution is now well accepted and there is more interest in the inverse situation where, given the value of $p$, the radiance reflected from the sea surface can be predicted. In particular, we are interested in predicting the reflected solar radiance from a low altitude such as the deck of a ship when the sun is anywhere in the sky. This prediction has already been provided by Cox and Munk [1]. In rearranged form and our notation their prediction is

$$\frac{N_r^{sun}}{H_o} = \frac{\rho(\omega)\,\sec^4\theta_n\; p(S_x,S_y,W)}{4\cos\theta_r}. \qquad \text{CM(9)}$$

The geometry implicit in CM(9) is that the incident ray comes from the center of the sun, the reflected ray goes to the receiver, and the facet slope creates a specular reflection between these rays.

There is a problem with equation CM(9) for horizontal views because CM(9) approaches infinity as $\theta_r$ approaches 90°. But an infinite radiance is never observed. A perfectly calm ocean (which can never occur but which serves as a useful limiting case) can be imagined which reflects the rays of the sun into a receiver mounted at the edge of the shore. Then any theory of solar glints should predict a radiance equal to the solar radiance times the reflectivity of sea water because a perfectly calm ocean is like a flat mirror.

This infinity will now be addressed.

## 2. THE GEOMETRY OF REFLECTION

Only single scattering events will be considered. Multiple reflections, the shadowing of one facet by another, transmission losses, and bending as the rays traverse the atmosphere to and from the ocean surface will be ignored. Polarization will be ignored and gravity waves will not be included.

Figure 1 shows the geometry of reflection. The origin of the coordinate system is the point of reflection with the $X$ axis pointing upwind, the $Y$ axis crosswind, and the $Z$ axis toward the zenith such that a right handed system is formed. The X-Y plane lies in the local horizon coincident with mean sea level. The tilted facet passes through the origin.

Three unit vectors are involved in reflection and they are connected by the law of reflection:

$$\mathbf{U}_s + \mathbf{U}_r = 2\cos\omega\,\mathbf{U}_n. \qquad (3)$$

## 3. THE OCCURRENCE PROBABILITY

Because it gives the likelihood that a facet with a given slope will occur in a group of facets with all possible slopes, $p$ is called the occurrence probability density. The shape of $p$ is shown in figures 2 and 3 for wind speeds of 1 and 10 m $s^{-1}$ respectively. The volume of a

column underneath $p$ whose base is $dS_x$ on one side and $dS_y$ on the other is the probability $P$ given by (1).

Using the occurrence probability density an area $A$ of the mean horizon can be used to represent the ocean as a whole. Area $A$ can also be thought of as the footprint of a single pixel in an image of the ocean. Within the footprint a typical facet is shown in figure 4. Now choose a convenient small range of $X$ and $Y$ slopes which will be the same for all facets. Let the horizontal projection of each facet occupy an area $dA$ whose ratio to the total area $A$ is equal to the probability that the facet will occur:

$$\frac{dA}{A} \equiv p\, dS_x dS_y. \tag{4}$$

The collection of all facets similar to the one shown in figure 4 will represent the average condition of the wind driven open ocean for any chosen wind velocity.

## 4. THE INTERACTION PROBABILITY

The occurrence probability we have just described is the same as the probability that a vertical ray will interact with the facet. However, as pointed out by Plass, et al. [3] a slanted ray will interact with the facet according to a different probability. The interaction probability

$$Q \equiv q(\theta, \phi, S_x, S_y, W) dS_x dS_y \tag{5}$$

gives the chance that a ray arriving from the arbitrary direction $\mathbf{U} \equiv (\theta, \phi)$ will interact with a facet whose slope is within $\pm\, dS_x/2$ of $S_x$ and $\pm\, dS_y/2$ of $S_y$ when the wind speed is $W$.

The interaction probability between the ray and the facet will be proportional to the area $dB$ which the facet has when projected normal to direction of the ray. Hence by reasoning similar to that used to arrive at equation (4)

$$\frac{dB}{B} \equiv q\, dS_x dS_y. \tag{6}$$

In equation (6) $B$ is the sum of all other similarly projected facets:

$$B = \int_{\substack{\omega \le \pi/2 \\ \mathbf{U}=const.}} dB. \tag{7}$$

Area $B(\theta, \phi, W)$ has been called the "ergodic cap" or the "ergodic cup" by Gordon [4] and Preisendorfer [5] who studied its shape. The integral in equation (7) is restricted to those facets for which the ray will strike the front rather than the back of the facet, that is, for all slopes such that $\omega \le \pi/2$. Furthermore, the notation "$\mathbf{U}=const.$" has been added under the integral sign to indicate that the ray direction is held constant during integration over the facets.

The interaction probability can be expressed in terms of the occurrence probability because of a geometrical relation between $dB$ and $dA$ evident from figure 4:

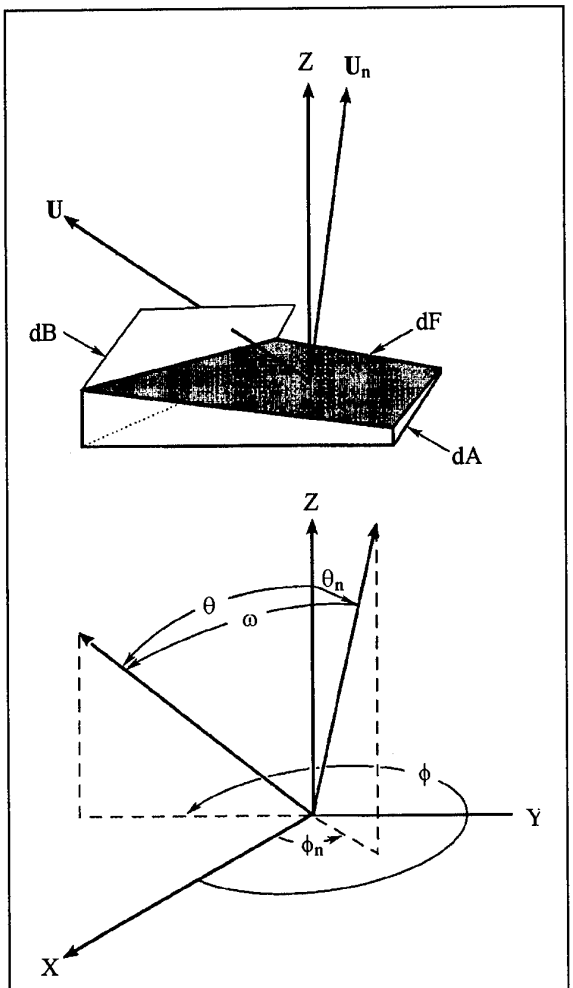


Figure 4. Upper portion: A typical facet. Its area is $dF$, its horizontal projection is $dA$, and its projection toward $\mathbf{U}$ is $dB$. Lower portion: Coordinates.

$$\begin{aligned} dB &= dF \cos\omega, \\ dA &= dF \cos\theta_n, \end{aligned} \tag{8}$$

which implies that

$$q = \frac{A}{B} \frac{\cos\omega}{\cos\theta_n} p. \tag{9}$$

Using equations (6) and (9) in (7) we arrive at the following expression for the area of the ergodic cap in terms of the occurrence probability:

$$\frac{B}{A} = \iint_{\substack{\omega \le \pi/2 \\ \mathbf{U}=const.}} \frac{\cos\omega}{\cos\theta_n} p\, dS_x dS_y. \tag{10}$$

The behavior of $B/A$ for a footprint of unit area is shown in figure 5 for various wind conditions.

Using (10) in (9) the interaction probability density is

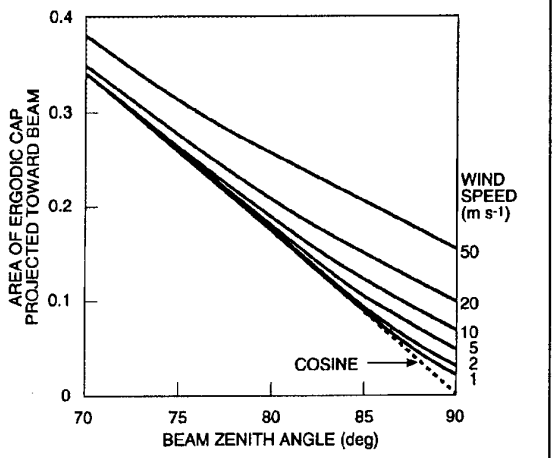


Figure 5. Area of ergodic cap $B$ projected toward a ray (or beam) of a given zenith angle. The ray is upwind and the footprint has a unit area.

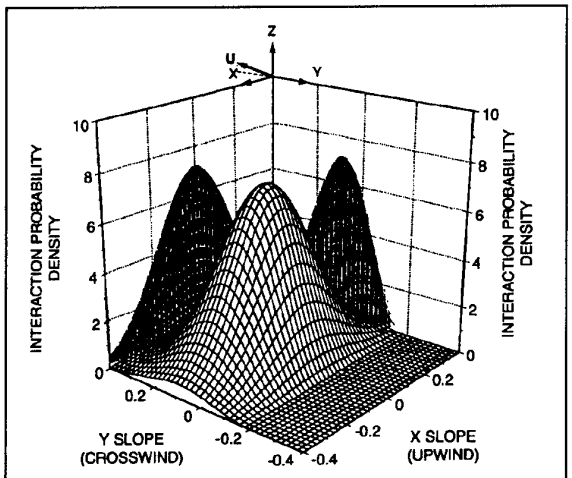


Figure 6. A plot of $q$ versus capillary wave slope for a wind speed of 10 m $s^{-1}$ and a ray pointing toward (80°, 270°). The density is tilted toward the ray.

$$q = \frac{\frac{\cos\omega}{\cos\theta_n} p}{\iint\limits_{\substack{\omega\le\pi/2 \\ \mathbf{U}=const.}} \frac{\cos\omega}{\cos\theta_n} p \, dS_x dS_y}. \qquad (11)$$

Equation (11) is only defined for $\omega \le \pi/2$. In the calm sea limit $p(S_x,S_y,0)$ approaches $\delta(S_x,S_y)$ and $q$ approaches $p$ regardless of ray direction.

Figure 6 shows a plot of $q$ for a ray direction of (80°,270°). Compared to the distribution of $p$ whose peak is at the origin (figures 2 and 3), the distribution of $q$ is tilted so that its peak no longer occurs at the origin. Slopes with positive $Y$ values are by and large responsible for the interaction in this case because they are tilted toward the receiver. Those tilted away from the ray (such as the one shown in figure 4) are less likely to interact with the ray ($dB$ will be smaller) and may even be excluded (as the facet in figure 4 would be for a ray closer to the horizon than shown there).

We have thus far considered the interaction of facets with a ray pointing in an arbitrary direction. From this point on, however, we will most often be considering the situation when the ray points toward the receiver ($\mathbf{U}=\mathbf{U}_r$).

## 5. REFLECTION BY A RUFFLED FOOTPRINT

Having found how a ray interacts with a group of facets, we will next show how those facets reflect radiance into a receiver. Figure 7 shows the instantaneous position of a single facet whose area may be on the order of one $mm^2$. The footprint area, on the other hand, is on the order of 10 $m^2$ after projection normal to the receiver. Therefore figure 7 is drawn so that the facet fails to fill the receiver field of view. We analyze the situation in figure 7 by: (1) converting the radiance incident on a single facet into a power, (2) finding how the facet reflects that power, (3) adding up the reflected power from all facets within the footprint, and (4) converting the resultant sum into a radiance leaving the footprint for the receiver.

(1) The source power arriving at the facet is contained in a beam whose radiance is $N_s$. If this radiance were received directly (without being altered by the facet) it would have an angular divergence of $dB/R^2$ at the receiver aperture. From the definition of radiance as the product of the beam power per unit solid angle per unit area normal to the beam we have

$$dP_s = N_s \frac{dB}{R^2} dS = N_s \frac{dS}{R^2} dB. \qquad (12)$$

(2) The facet reflects source power $dP_s$ from direction $\mathbf{U}_s$ to direction $\mathbf{U}_r$. After leaving the facet this power is multiplied by $\rho$:

$$dP_r = \rho \, dP_s. \qquad (13)$$

The effect of the facet is simply to alter the direction of the power (as indicated by the dashed lines in figure 7) and multiply it by $\rho$.

(3) The footprint as a whole will contain facets of all possible slopes. The power reflected from the entire footprint will be given by integration of (13) over the footprint area $A$:

$$P_r = \int_A dP_r = \int_A \rho N_s \frac{dS}{R^2} dB. \qquad (14)$$

This total reflected power is contained in a solid angle $dS/R^2$ and passes through the area

$B(\theta_r,\phi_r,W)\equiv B_r$, the ergodic cap projected toward the receiver. Hence the received radiance contributing to a single pixel is

$$N_r = \frac{P_r}{B_r \cdot \left(dS / R^2\right)}. \qquad (15)$$

(4) Substituting (14) for $P_r$ into (15) and using (6) the received radiance can be expressed as

$$N_r = \iint_{\substack{\omega\le\pi/2 \\ \mathbf{U}_r=const}} \rho N_s q_r \, dS_x dS_y \qquad (16)$$

where the subscript on $q$ is used as a reminder that the interaction probability density must be applied to a ray projected toward the receiver.

Equation (16) shows that the interaction density $q_r$ plays the mathematical role of a weighting factor attached to the facet position shown in figure 7.

Figure 8 shows how objects in the marine sky contribute to the radiance of a pixel in the ocean. The conditions are meant to be approximately the same as those used to draw figure 6, namely a receiver elevated by 10° and a wind speed of 10 m $s^{-1}$. Facets of various slopes have captured a broad portion of the sky and redirected it toward the receiver where it is sensed as a single undivided radiance. The importance of a particular slope in the capture process is given by its weighting factor $q_r$ shown in figure 6. The full width half maximum contour for the capture (labeled FWHM in the figure) is elliptical rather than circular because the slope variances in the up and crosswind directions are different.

## 6. A TRANSFORMATION: OCEAN TO SKY

Although equation (16) is the easiest way to visualize the geometry of facet reflection throughout the footprint, it is sometimes easier to integrate over objects in the sky (rather than slopes in the ocean) for the purpose of calculating the received radiance. For a fixed receiver position the location of the source radiance in figure 7 is determined by the facet slope. Equations can be derived which give the sky location $(\theta_s,\phi_s)$ reflected into a receiver located at $(\theta_r,\phi_r)$ by a facet whose slope is $(S_x,S_y)$. These equations can be regarded as a transformation from slope coordinates to sky coordinates with the receiver position a parameter of the transformation. Hence in place of equation (16) we can equally well write

$$N_r = \iint_{\mathbf{U}_r=const} \rho N_s q_r \, J d\theta_s d\phi_s \qquad (17)$$

where we have introduced the Jacobian $J$ of the transformation between facet slope and sky location.

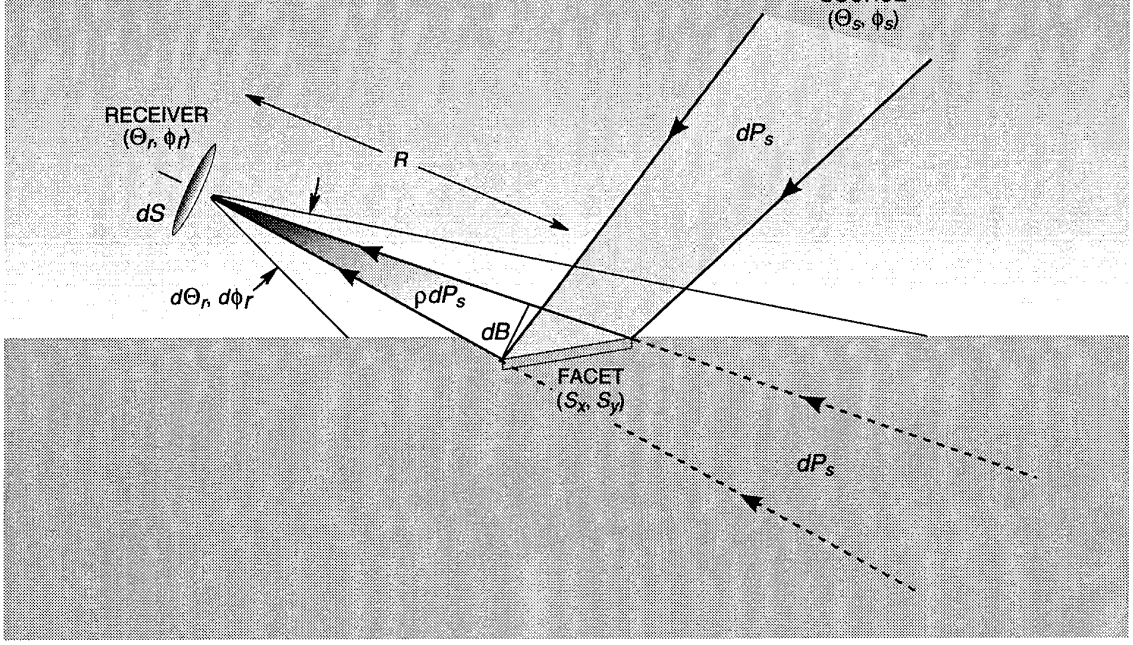


Figure 7. Instantaneous specular reflection by a single facet. The radiance of the marine sky is redirected by the facet into a receiver looking down toward the ocean surface.

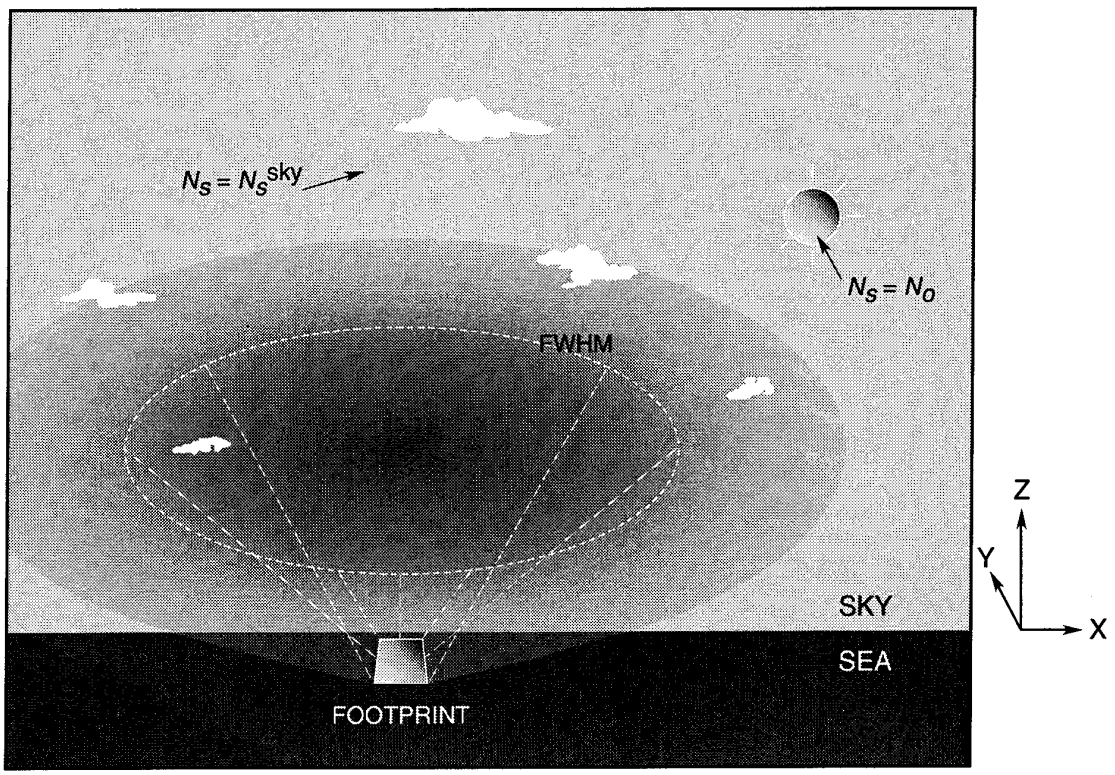


Figure 8. The pixel footprint seen by a receiver looking down on the surface of the ocean.

Starting from equations (28) and (29) it can be shown [6] that

$$J \equiv \frac{\partial(S_x,S_y)}{\partial(\theta_s,\phi_s)} = \frac{\sec\omega \sec^3\theta_n \sin\theta_s}{4} \tag{18}$$

Inserting equation (9) for $q_r$ and equation (18) for $J$ into equation (17) we arrive at the following general expression for the radiance received from the footprint:

$$N_r = \frac{A}{4B_r} \iint_{\mathbf{U}_r=const} \rho(\omega) N_s(\theta_s,\phi_s) \cdot \sec^4\theta_n \, p(S_x,S_y,W) \sin\theta_s d\theta_s d\phi_s. \tag{19}$$

Here $B_r$ is given by (10) with the ray pointing toward the receiver (that is, (10) with $\mathbf{U}=\mathbf{U}_r$) and $p(S_x,S_y,W)$ is given by (2). During integration of equation (19) the radiance is received by specular reflection from the source. The appendix gives expressions for $\omega$, $\theta_n$, $S_x$, and $S_y$ in terms of source and receiver coordinates when there is a specular reflection, and these expressions should be used in equation (19).

Equation (19) is the integral equation for the receiver radiance we have been seeking. It is an exact mathematical consequence of the Cox-Munk-Plass model for the wind ruffled sea surface and can be used to describe reflected sky radiance, thermal black body emission, or sun glint by proper choice of $N_s$ and the domain of integration [6].

## 7. EXACT SUN GLINT

For sun glint, $N_s$ is equal to $N_o$ and the integral is carried out over the solar disk in the sky or the tolerance ellipse in the ocean. (The tolerance ellipse contains all those slopes capable of reflecting a ray from any part of the solar disk into the receiver.) Since solar radiance is constant throughout the solar disk (the sun is a Lambertian source), $N_o$ can be brought outside the integral to give the following expressions for the ratio of glint radiance leaving the footprint to solar radiance arriving at the footprint:

$$\frac{N_r^{sun}}{N_o} = \iint_{\substack{ellipse \\ \mathbf{U}_r=const}} \rho q_r \, dS_x dS_y \tag{20}$$

for integration over the sea, and

$$\frac{N_r^{sun}}{N_o} = \frac{A}{4B_r} \iint_{\substack{disk \\ \mathbf{U}_r=const}} \left\{\rho \sec^4\theta_n \, p\right\} \sin\theta_s d\theta_s d\phi_s \tag{21}$$

for integration over the solar disk.

In the calm sea limit $q$ approaches a delta function selecting zero slope and (20) shows that

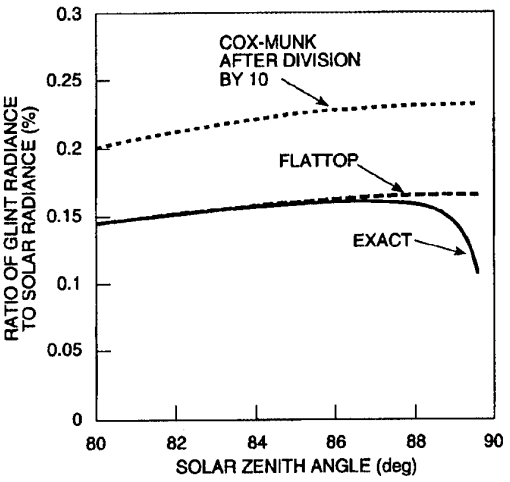


Figure 9. Glint radiance for a horizontal view of a sun setting over a moderate sea (W = 10 m $s^{-1}$). The facet reflectivity is 100%. The location of the receiver is (89.75°, 90°).

$$\frac{N_r^{sun}}{N_o} \approx \rho \le 100\% \qquad (22)$$

for a calm sea as expected.

The behavior of equations (20) and (21) for a receiver looking straight toward a setting sun is given in figures 9 and 10 by the curves labeled "Exact". Note that the vertical scale in these figures never exceeds 1% which may be surprising in view of the 100% calm sea limit set forth in (22). The exact calculations produce a smaller value than 100% because most of the slopes in an ocean footprint deflect solar rays away from the receiver toward other parts of the sky even at very low wind speeds.

## 8. APPROXIMATE SUN GLINT

Since the solar disk occupies such a small part of the sky, the integrand in (21) will remain almost constant during integration over the disk and can be brought outside the integral. Since the integral of $\sin\theta_s$ over the disk is equal to $\Omega_o$ we obtain

$$\frac{N_r^{sun}}{H_o} \approx \frac{A}{4B_r}\left\{ \rho \sec^4\theta_n p \right\}_o \qquad (23)$$

for the approximate ratio of glint radiance leaving the ocean surface to the solar irradiance arriving at the ocean surface. In (23) we have used the fact that $N_o\Omega_o$ is equal to the solar irradiance $H_o$. The subscript on the bracket means that quantities within the bracket should be evaluated for a ray specularly reflected from the center of the sun into the receiver. The curves marked "Flattop" in figures 9 and 10 show the behavior of equation (23).

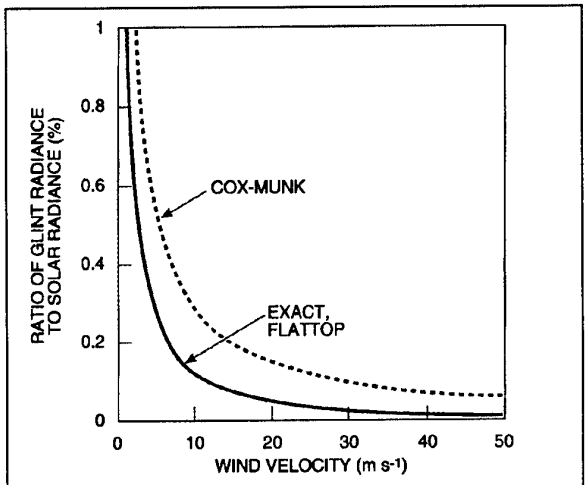


Figure 10. Ocean glint as a function of wind speed. Conditions are $\rho$ = 100%, $(\theta_s,\phi_s)$ = (88°, 270°), $(\theta_r,\phi_r)$ = (88°, 270°).

A second approximation can be introduced by noting that facets tilted by less than the ray elevation will always present their front surface to the ray. If the wind velocity is low enough that area A is almost entirely occupied by such facets the restriction on the angle of incidence in (10) and (11) may be dropped without appreciable error and it can be shown [6] that

$$\frac{B_r}{A} \approx \iint\limits_{U_r=const} \frac{\cos\omega}{\cos\theta_n}\, p\, dS_x dS_y = \cos\theta_r \qquad (24)$$

for a ray pointing toward the receiver.

Combining both approximations by inserting (24) into (23) we obtain

$$\frac{N_r^{sun}}{H_o} \approx \left\{ \frac{\rho \sec^4\theta_n p}{4\cos\theta_r} \right\}_o \qquad (25)$$

which is identical to the equation used by Cox and Munk given in our introduction. The "Cox-Munk" approximation improves as the wind speed decreases: for a receiver ray elevated by 10° or more, the error is less than 10% for wind speeds below 11 m $s^{-1}$ and less than 1% for wind speeds below 3½ m $s^{-1}$.

## 9. DISCUSSION

Equations (20) and (21) show the proper finite behavior for sun glint on the horizon. How has the infinity disappeared? The answer can be found in the distinction between the actual sea surface, which is rough, and the footprint surface, which is flat. In the derivation of section 5, part 3, we have projected the facets (rather than the footprint) toward the receiver. This removes the unphysical infinity mentioned in the introduction because, although the footprint projects toward zero for a horizontal ray, the facets do not. The wind always tilts some facets so they can be seen by the receiver even though the receiver might be looking out in a direction

which grazes mean sea level. In fact the simple observation that the sea horizon can be seen is proof that the sea is rough because "If the sea were absolutely flat, then the radiance of the sea surface just beneath the horizon would equal the radiance of the sky just above it, and there would be no visible horizon."[7].

Saunders [8] pointed out that multiple reflections and shadowing should be included in any theory of solar glints. Multiple reflections occur when the source ray bounces off of several facets before reaching the receiver. Shadowing refers to the fact that slopes on the back sides of the waves and deep in the troughs between waves are hidden from view. Each of these effects becomes more important when the source or receiver approaches the horizon. (Cox and Munk did not include either effect but were careful to take measurements when both source and receiver were near the zenith to minimize the contributions of each effect.) Saunders established upper and lower limits to the observed radiance based on multiple scattering and he included shadowing by introducing a shadowing factor. His shadowing factor multiplies equation CM(9) and clamps the Cox-Munk radiance to a finite value for horizontal observation of solar glints. However, we do not find that the application of Saunders' shadowing factor to equation CM(9) produces the proper radiance in the calm sea limit.

## 10. CONCLUSION

Neglecting multiple scattering and shadowing, an integral expression for ocean radiance has been obtained which is correct for all geometries. The integral produces a finite glint radiance reflected horizontally by the ocean even when the sun is also on the horizon. It also gives the proper radiance in the calm sea limit.

When the reflected ray is elevated by more than about 10° over a moderate sea an approximation may be employed which reduces the exact formulation we have derived to the form used by Cox and Munk.

## ACKNOWLEDGMENT

This work was supported by the office of Naval Research.

## REFERENCES

1. Cox, C. and Munk, W., "Measurement of the Roughness of the Sea Surface from Photographs of the Sun's Glitter," *Journal of the Optical Society of America,* vol. 44, p. 838, 1954.
2. Cox, C. and Munk, W., "Slopes of the Sea Surface Deduced from Photographs of Sun Glitter," *Scripps Institution of Oceanography Bulletin,* vol. 6, p. 401, 1956.
3. Plass, G., Kattawar, G., and Guinn, J.,. "Radiative Transfer in the Earth's Atmosphere and Ocean: Influence of Ocean Waves," *Applied Optics,* vol. 14, p. 1924, 1975.
4. Gordon, J., "Directional Radiance (Luminance) of the Sea Surface," *Scripps Institution of Oceanography Visibility Laboratory,* SIO ref. 69-20, 1969.
5. Preisendorfer, R., *Hydrologic Optics.* Pacific Marine Environmental Laboratory, ERL/NOAA, vol. VI, p. 263 ff., 1976. [Part of a six volume set: vol. I, *Introduction,* PB-259273, 218 pp., vol. II, *Foundations,* PB-259794, 400 pp., vol. III, *Solutions,* PB-259795, 256 pp., vol. IV, *Imbeddings,* PB-259796, 204 pp., vol. V, *Properties,* PB-259797, 296 pp., vol. VI, *Surfaces,* PB-268704, 390 pp.]
6. Zeisse, C. R., "Radiance of the Ocean Horizon," *NCCOSC RDTE DIV Technical Report,* no. 1660, 1994.
7. Cox, C. and Munk, W., "Some Problems in Optical Oceanography," *Journal of Marine Research,* vol. 14, p. 74, 1955.
8. Saunders, P., "Radiance of Sea and Sky in the Infrared Window 800-1200 $cm^{-1}$," *Journal of the Optical Society of America,* vol. 58, p. 645, 1968.

## APPENDIX: SPECULAR REFLECTION

The calculation of the Jacobian in (18) and the general equation for ocean radiance given by (19) require the following expressions for $\omega$, $\theta_n$, $S_x$, and $S_y$ in terms of source and receiver coordinates when there is a specular reflection:

$$2\cos^2\omega = 1+\sin\theta_s\sin\theta_r\cos(\phi_s-\phi_r)+\cos\theta_s\cos\theta_r, \tag{26}$$

$$\tan^2\theta_n = \frac{\sin^2\theta_s+\sin^2\theta_r+2\sin\theta_s\sin\theta_r\cos(\phi_s-\phi_r)}{(\cos\theta_s+\cos\theta_r)^2}, \tag{27}$$

$$S_x = -\frac{(\sin\theta_s\cos\phi_s+\sin\theta_r\cos\phi_r)}{(\cos\theta_s+\cos\theta_r)}, \tag{28}$$

and

$$S_y = -\frac{(\sin\theta_s\sin\phi_s+\sin\theta_r\sin\phi_r)}{(\cos\theta_s+\cos\theta_r)}. \tag{29}$$

## DISCUSSION

**G.S. BROWN**
What about the effects of shadowing in your analysis?

**AUTHOR'S REPLY**
Shadowing (and multiple reflections) are very important effects, especially on the horizon. Indeed, Saunders has already proposed that shadowing will remove the infinity I have alluded to here as a paradox. My point has been that proper account of the capillary wave slope geometry is by itself sufficient to resolve this paradox; the next steps to be taken would be to include shadowing and multiple reflections which I have ignored in this analysis.

**K. DAVIDSON**
Would work now being done on ocean surface radar (C-, Ku-, X-band) backscatter properties be important to this problem?

**AUTHOR'S REPLY**
Yes. The shape of the ocean surface determines the properties of infrared radiance and ocean backscatter. Proper treatment of ocean reflection on the horizon should improve our understanding of infrared and radar effects observed there.

# Summary of the Marine Aerosol Properties and Thermal Imager Performance Trial (MAPTIP)

Organized by

NATO AC/243 PANEL 4/RSG.8 ON
ATMOSPHERIC PROPAGATION EFFECTS ON
ELECTRO-OPTICAL SYSTEMS
OCT 11 - NOV 5, 1993

**D. R. Jensen**
Ocean and Atmospheric Sciences Division
NCCOSC RDTE DIV 543
53170 WOODWARD ROAD
SAN DIEGO, CA 92152-7385
USA

**G. de Leeuw**
**A. M. J. van Eijk**
TNO Physics and Electronics Laboratory
Oude Waalsdorperweg 63
2509 JG The Hague
The Netherlands

## SUMMARY

During the fall of 1993 a field experiment entitled Marine Aerosol Properties and Thermal Imager Performance Trial (MAPTIP) was conducted by NATO AC/243 Panel 04/RSG.8 and 04/RSG.5 in the Dutch coastal waters. The objectives of the trial were:

1. To improve and validate vertical marine aerosol models by providing an extensive set of aerosol and meteorological measurements, within a coastal environment, at different altitudes and for a range of meteorological conditions.

2. To make aerosol and meteorological observations in the first 10 m of the ocean surface with a view to extending existing aerosol models to incorporate near-surface effects.

3. To assess marine boundary layer effects on thermal imaging systems. Calibrated targets at different altitudes were observed to the maximum observable range under a wide variety of conditions in both the 3-5 and 8-12 μm bands. These data will be used for the development and validation of IRST models and IR ship signature models with the view of determining the effects of marine-generated aerosols, turbulence, and meteorological profiles on their performance.

Aerosol and meteorological instruments, as well as thermal imagers and calibrated targets, were utilized on the Dutch Meetpost Noordwijk (MPN) tower, at a Katwijk Beach Station, the Hr. Ms. Tydeman oceanographic vessel, on a Lynx helicopter, on a Dutch P3 Orion, on the NCCOSC RDT&E DIV (NRaD) airborne platform, and on buoy systems. This network of instrumentation has provided a comprehensive data base of aerosol size distribution profiles and relevant meteorological variables throughout the marine atmospheric boundary layer. Thermal imagery was included to provide ground truth for assessing the low-level propagation effects near the ocean surface. Measurements were made of atmospheric turbulence and refractivity effects in the IR and RF bands to assess the marine boundary layer effects on the degradation of thermal images.

Calibrated targets at different altitudes were observed to the maximum observable range under a wide variety of conditions in both the 3-5 and 8-12 μm bands. These data are to be used for the development and validation of IRST models and IR ship signature models for determining the effects of marine-generated aerosols, turbulence and meteorological profiles on their performance.

## 1. INTRODUCTION

Atmospheric aerosol and infrared sea and terrain background models are of special importance for the assessment of the performance of electro-optical (EO) systems. The degradation of the radiance contrast between a target and its natural background, as viewed by an infrared sensor, is determined by the constituents of the intervening atmosphere that absorb and scatter the radiation. The assessment, therefore, depends upon the accuracy of the atmospheric models being used in the propagation prediction codes. The performance of the electro-optical systems is further degraded by turbulence and refractivity effects, causing blurring, scintillation, beam wander, mirages, etc. In thermal imagers, these effects may result in image distortion, contrast reduction, and other detection problems.

Presently, the Atmospheric Transmission/Radiance computer code, LOWTRAN [1,2], is the primary tool used for this assessment. With the inclusion of the Navy Aerosol Model, NAM [3-10], into LOWTRAN 6 [1] and an upgraded version of NAM into LOWTRAN 7 [2], users are now able to determine the effects of aerosols on EO propagation in a maritime environment. This model has proven to be a useful tool in predicting atmospheric transmission in the marine atmosphere along horizontal paths at shipboard levels (above 10 m). Another atmospheric aerosol model, NOVAM [11-19] (The Navy Oceanic Vertical Aerosol Model), is being prepared for inclusion into LOWTRAN/MODTRAN and accounts for the generation, dispersal and removal of the marine aerosols, including transport processes, in the vertical dimension. This model uses NAM as its kernel and is useful for predicting the vertical profiles of extinction from shipboard heights upward through the marine boundary layer. However, to date, the NAM and NOVAM validation has been restricted to a limited range of meteorological situations and geographical locations and must be extended to include coastal regions with substantial continental aerosol inputs. Also, recent studies have shown that NAM/NOVAM in their present forms should not be extrapolated into the region very near the surface (below 10 m) of the ocean for predicting atmospheric properties [20, 21].

It is important to obtain more detailed information on atmospheric characteristics for the 3-5 and 8-12 micron wavelengths in the first few meters above the surface of the ocean. An effort needs to be undertaken to model the first 10 m above the ocean surface and incorporate it in LOWTRAN for prediction performance of EO systems used for detecting low-altitude targets.

In response, the NATO AC/243 (Panel 04/RSG.8), in collaboration from AC/243 (Panel 04/RSG.5), planned and conducted a field experiment to address these very problems. The name of the trial was entitled the Marine Aerosol Properties and Thermal Imager Performance (MAPTIP). The MAPTIP project, in principle, consisted of two parts, i.e., the development and validation of models describing atmospheric effects on electro-optical propagation properties (aerosol extinction, refraction, and turbulence) and the assessment of thermal

*Paper presented at the Sensor and Propagation Panel Symposium on "Propagation Assessment in Coastal Environments" held in Bremerhaven, Germany 19-22 September 1994.*

imager performance in a maritime environment. In this unique effort, these two disciplines were integrated by virtue of a cooperative effort between two NATO study groups by combining their expertise in the fields of atmospheric propagation effects and IR thermal imagers, targets and backgrounds.

The MAPTIP trial was conducted in the North Sea, between October 11 and November 5, 1993. The geographical layout is shown in Figure 1. Aerosol and meteorological instruments, as well as thermal imagers and calibrated targets, were utilized on the Dutch Meetpost Noordwijk (MPN) tower, at a Katwijk Beach Station, on the Hr. Ms. Tydeman oceanographic vessel, on a Lynx helicopter, on a Dutch P3 Orion, on the NRaD airborne platform, and on buoy systems. This network of instrumentation was used for obtaining a comprehensive data base of aerosol size distribution profiles and relevant meteorological variables throughout the marine atmospheric boundary layer. This information is required for the development of the next generation aerosol model ANAM (Advanced Navy Aerosol Model). Emphasis was placed on observations close to the ocean surface (below 10m). Thermal imagery was also included to provide ground truth for assessing the ANAM model development for low-level propagation predictions near the ocean surface. To achieve the second goal, measurements were made of atmospheric turbulence and refractivity effects in the IR and RF bands to assess the marine boundary layer effects on the degradation of thermal images.

The MAPTIP trial was organized by the TNO Physics and Electronics Laboratory and was supervised by a scientific committee consisting of representatives from the atmospheric effects and thermal imaging communities associated with the NATO AC/243 Panel 04/RSG.8 and 04/RSG.5. Altogether, about 50 scientific and engineering personnel participated in MAPTIP from 19 institutes located in 9 countries (Table 1). An extensive description of the MAPTIP trial and instrumentation provided by each participating institution can be found in the work plan [22]. An overview of the MAPTIP experiment for the RSG.8 and RSG.5 participants has been prepared and is available upon request [23].

## 2. SCIENTIFIC OBJECTIVES

The scientific objectives of the MAPTIP trial were: 1) Improve and validate vertical marine aerosol models, 2) Extend existing aerosol models to incorporate near-surface effects, 3) Assess marine boundary layer effects on thermal imager systems, 4) Provide inputs for the development and validation of IRST models, 5) Provide inputs for the development and validation of IR ship signature models, 6) Provide additional data for analysis in areas of interest and importance to IR seeker and IR IRST applications. The latter includes horizon, sea, and coastal clutter, sea and sky background signatures, cloud data, day/night and dawn/sunset variations, turbulence, scintillation, ducting, mirage, and false alarms.

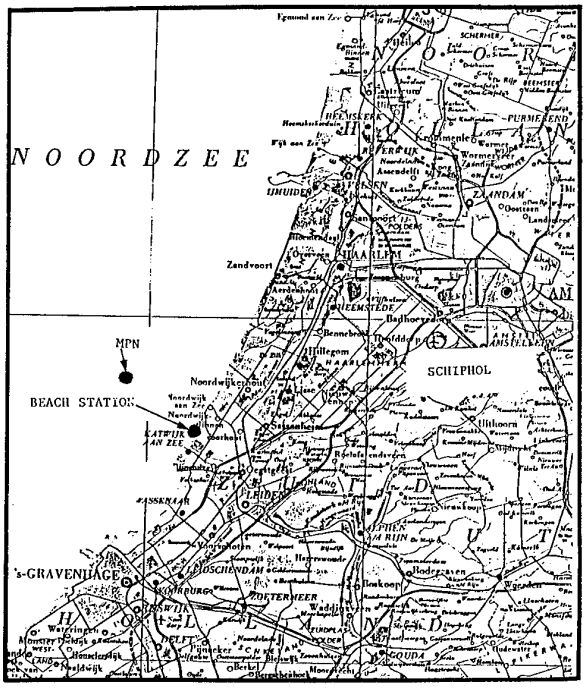


Figure 1. Geographic location for the MAPTIP trial.

| Institute | Institute (Abbreviation) | Country |
|---|---|---|
| TNO Physics and Electronics Laboratory | TNO-FEL | NL |
| Royal Netherlands Navy | KM | NL |
| Ministry of Public Works | RW | NL |
| University of Antwerp | UIA | BE |
| Defence Research Establishment Valcartier | DREV | CA |
| Danish Defence Research Establishment | DDRE | DK |
| CELAR | CELAR | FR |
| DGA/DCN/CESDA | DGA | FR |
| Forschungs Institut für Optik | EfO | GE |
| Fraunhofer Institut für Atmosphärische | IFU | GE |
| Norwegian Defence Research Establishment | NDRE | NO |
| University of Manchester Institute of Science and Technology | UMIST | UK |
| Naval Command Control and Ocean Surveillance Center, RDT&E DIV 543 | NRaD | USA |
| Naval Postgraduate School | NPS | USA |
| Office of Naval Research | ONR | USA |
| Mesa Inc. | MESA | USA |
| Massachusetts Institute of Technology | MIT | USA |
| Naval Surface Warfare Center | NSWC | USA |

Table 1. MAPTIP Participants.

## 3. EXPERIMENTAL PROGRAM

A suite of instrumentation was mounted on the seven MAPTIP operational platforms to characterize the atmosphere and to assess the performance of thermal imagers. Several platforms served a dual purpose as a carrier for instrumentation and as a target for the imagers. The focal platform for the experiment was the Meetpost Noordwijk (MPN) oceanographic tower (owned and operated by the Dutch Ministry of Public Works) located 9 km from the Dutch coast, position 45° 16' 25.9" N, 04° 17' 45.8" E. A land based facility was established at the lifeguard station on the beach at Katwijk. Oceanographic buoys were located near MPN and at a position a few kilometers from the beach along the MPN-Beach Station line of sight. The oceanic research vessel Hr. Ms. Tydeman from the Royal Netherlands (RNL) Navy sailed a pre-described pattern in the vicinity of the MPN tower. Two aircraft and a helicopter completed the MAPTIP scenario. A Lynx helicopter and a P3 Orion patrol aircraft were made available by the RNL Navy. The second aircraft was the NRaD airborne platform [24], a twin-engine Piper Navajo. The operational platforms are shown in Figures 2 and 3.

### 3.1 Meetpost Noordwijk

The MPN tower was used both for comprehensive meteorological characterization and as a platform for thermal imagers and sources (Figure 2). During MAPTIP a 20 m boom was used by TNO-FEL to make air temperature and unperturbed turbulence measurements [25] using a Gill Sonic Anemometer. An Advanet $H_20$ and $C0_2$ fluctuation meter was also installed on the boom to determine the respective fluxes. The boom was further equipped with optical particle counters (PMS CSAS 200 P and OAP) to determine particle size distributions at low levels and to profile the aerosol distributions. Mean relative humidity and air temperature were measured on the boom with a Rotronic Hygrometer. Unfortunately, only few data were collected on the boom due to a structural failure during a storm.

On the helicopter deck located at 18.6 m above mean sea level (MSL), a mast was rigged by UMIST for a sonic anemometer and an OPHIR hygrometer to measure the turbulent air flow components, air temperature, and absolute humidity. UMIST

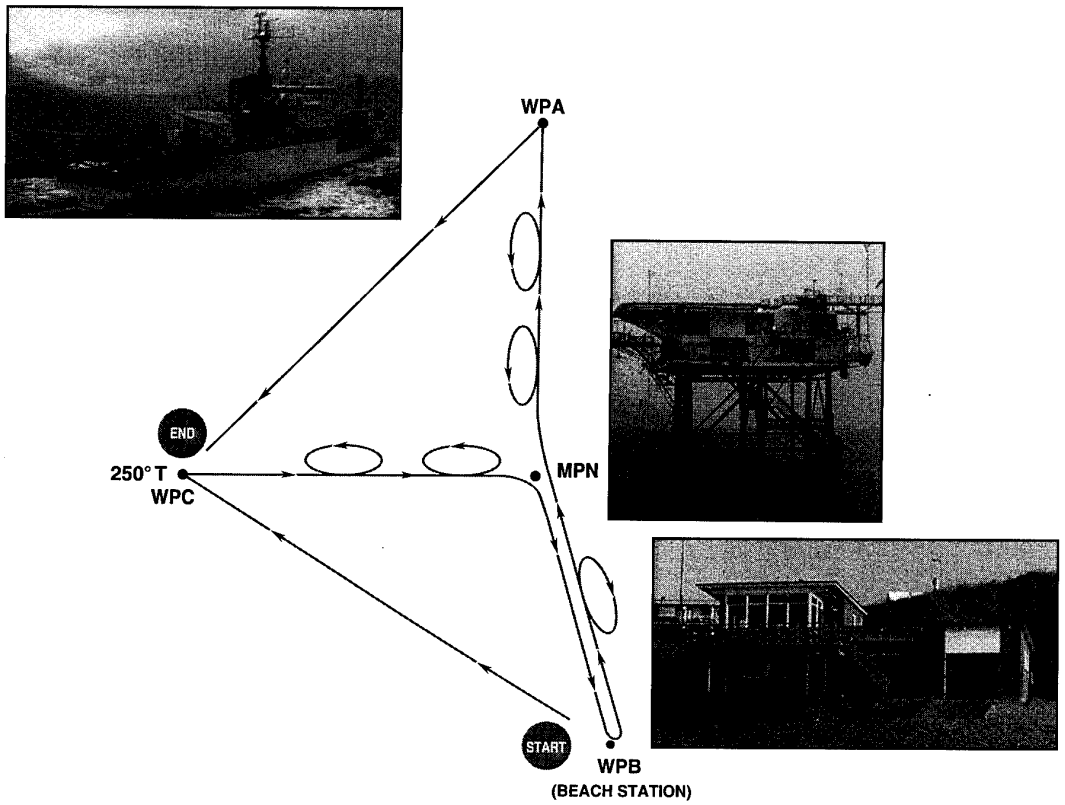


Figure 2. MAPTIP operational sequence (surface).

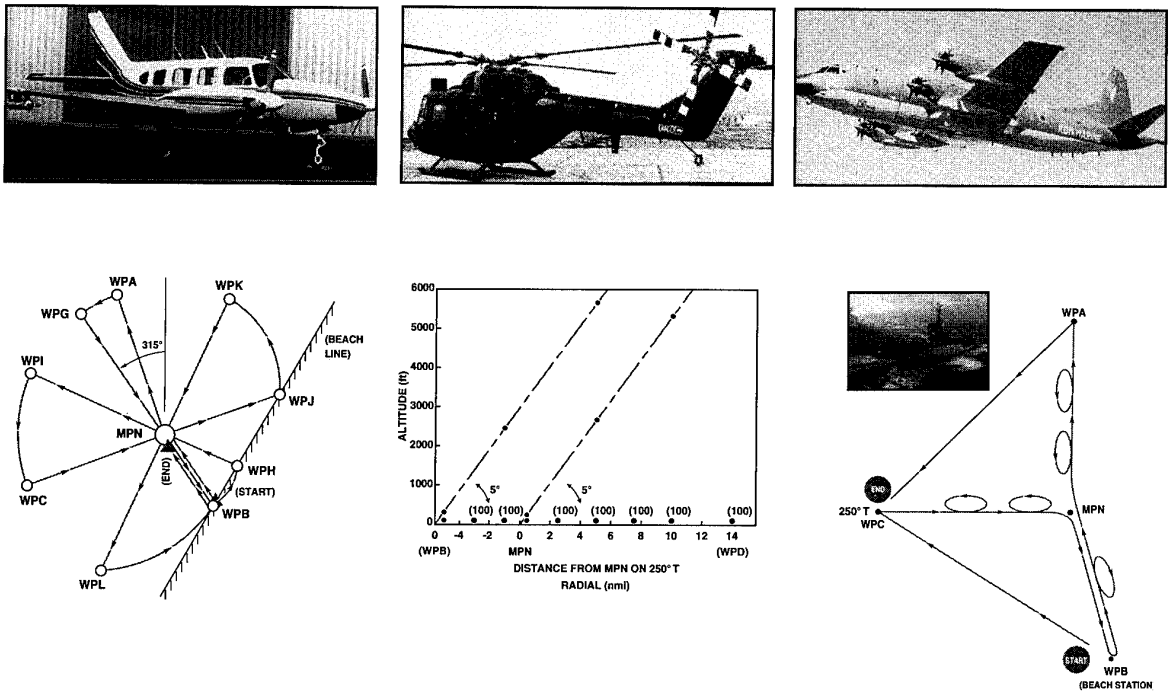


Figure 3. MAPTIP operational sequence (airborne).

also measured aerosols from the 11.6 m deck, where a meteorological station was mounted to determine local wind speeds and direction, air temperature, and relative humidity. The sea spray package consisted of a PMS FSSP-100 and a PMS OAP-230X optical particle counter. Aerosol size-segregated composition was determined with a PMS ASASP-X in combination with a volatility system. Soot carbon loadings were determined with an aetholometer. Weather conditions and sea state were monitored and pictures were recorded with a video camera. A radon counter was used as a back-up for air mass analysis. A second radon counter and a condensation nuclei (CN) counter were operated on the tower by NRaD.

Aerosol particle-size-distribution profiles were measured by NRaD utilizing an optical particle counter (PMS ASSP-100), and by NRaD and TNO-FEL with Rotorod impaction samplers (for particle diameters > 13 μm) [26]. Particle-size-distribution profiles were obtained in the size range from 0.5 to 100 μm diameter. The optical particle counter measurements were performed with the instrument mounted in a box that was hoisted up and down from the 15 m deck. The NRaD Rotorod was also mounted on this box, as well as instrumentation to measure air temperature and relative humidity. The TNO-FEL Rotorod measurements were made with the samplers mounted on a float that was deployed from a 10 m long outrigger mounted on the northwest 11.6 m platform [26]. Figure 4 shows measured aerosol-size-distributions taken near the ocean surface and the 11.6 m deck for low (0.1-2.1 m/s) and high (11-16 m/s) winds.

In support of the interpretation of the aerosol profile measurements, bubble size distributions were measured at fixed depths from 0.5 to 2 m below the sea surface with an optical device deployed on a floating platform. The float was anchored close to the MPN aerosol samplers at a position such that the bubble measurements were free of the MPN platform influences (currents advecting bubbles generated at the platform structure). Bubbles, when protruding the water surface, generate film and jet droplets in addition to spume droplets that are generated by direct tearing in high winds (wind > 9 m/s). These data will be used to formulate a reliable source function for use in aerosol generation models involving sea salt aerosols [27,28]. Figure 5 shows a measured bubble-size-distribution at 1 m and is compared with data from open literature.

Information on the vertical structure of the atmospheric boundary layer near MPN was obtained utilizing lidar systems. The NRaD ANGVS/5 lidar was used for profiling aerosol returns near the ocean surface ( < 10 m), and the TNO-FEL smal lidar system [29] was used for slant path measurements under both negative and positive elevations. The lidar returns will be used for studying the variability of the inversion height and the depth of the transition layer [19]. Ship plume observations were also made.

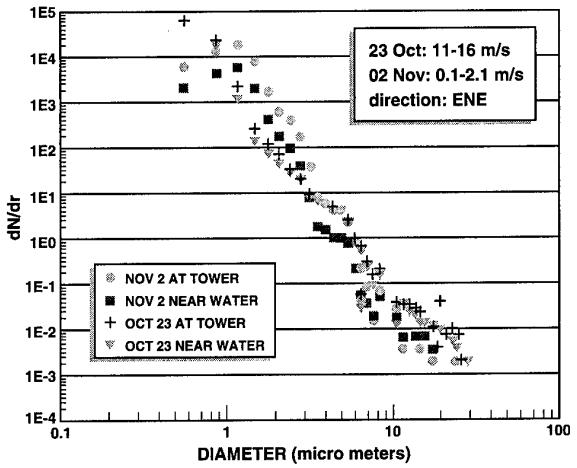


Figure 4. Measured aerosol-size-distributions at MPN.

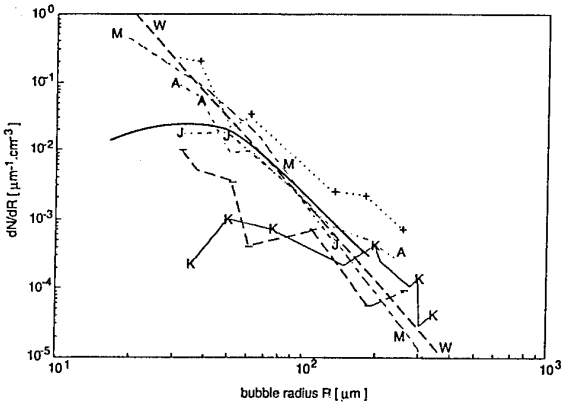


Figure 5. Measured bubble-size-distribution at 1 m (solid line) compared with data from the open literature.

Direct measurements of the extinction in the visible (0.53 μm) and at 10.6 μm were made by DREV using an HSS VR-310 Forward Scatter meter and a PVM-300 Forward Scattering Probe, respectively. The instrumentation was mounted on the 15 m deck. This location is well exposed to the prevailing winds and data should be representative of conditions unperturbed by the tower.

Meteorological data were routinely measured at MPN and is part of the North Sea monitoring network. Data includes wind speed, direction, air and sea temperature, atmospheric pressure, relative humidity, tide (water level land current) and wave observations. In addition to these observations, TNO-FEL mounted Rotronic sensors for air temperature and relative humidity at heights of 5.2, 6.6, 13, and 27 m MSL to monitor the atmospheric surface layer structure in support of optical and IR measurements of atmospheric refraction phenomena. A rain gauge and a pyranometer were added to this suite of instrumentation.

During MAPTIP four thermal imagers were located on MPN [30]. A US Kodak 2-5 μm PtSi radiometric imager was operated by MIT and a TICM II camera (8-12 μm), made available by DRE Funtington (UK), was operated by TNO-FEL. Both cameras were mounted on the 11.6 m deck at the southwest corner of the platform where unobstructed measurements could be made of sun glint, land backgrounds, and ship and airborne targets. On the top deck (18.6 m MSL), the Amber Model AE4128 Thermal Imager (InSb, 3-5 μm) from DDRE and a Philips FLIR (8-12 μm) from TNO-FEL were mounted.

With this instrumentation, both IR wavelength regions, 3-5 and 8-12 μm, were covered at each level. The Hr. Ms. Tydeman, was specially equipped with IR and visible sources, the Lynx helicopter with a source suspended at 20 m below, and the P3 Orion and the Navajo Piper served as targets for IR imaging. All operations utilizing these targets were scheduled around MPN. Figure 6 shows the 3-5 and 8-12 μm IR images of the Hr. Ms. Tydeman (stern view). Figures 7 and 8 show the 3-5 μm image of the Lynx helicopter and the P3 Orion, respectively.

A number of IR and visible sources were mounted on MPN. These included the FfO 300°C fixed temperature calibration source, the TNO-FEL 900°K 1000 Hz modulated source, and a sequence of visible lamps on the South side of MPN. The FfO source was mounted on the top deck as a reference for the FfO imaging systems at the Katwijk Beach Station. The TNO-FEL source was used for transmission measurements between MPN and the Beach Station. The visible lamps were mounted by DREV at differing heights above MSL from about 3.5 to 20 m for the study of refractivity effects.

### 3.2 Katwijk Beach Station

The Katwijk Beach Station consisted of two platforms: 1) the

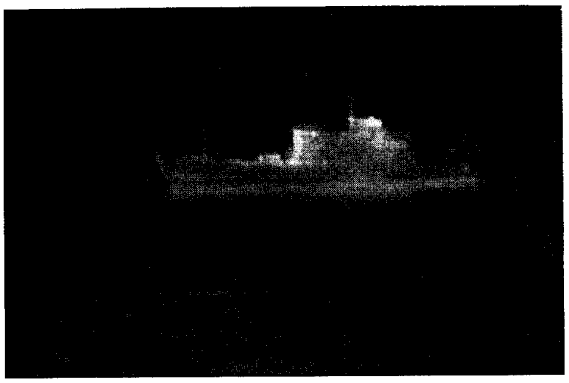

22-10 13.43.52 Z

1,36 km 19-10 18.48.28 Z

Figure 6. Hr. Ms. Tydeman IR images.

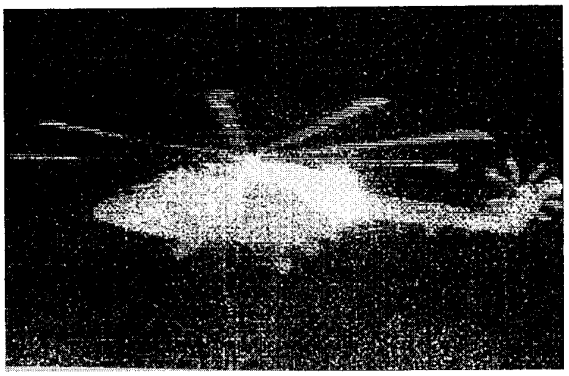

Figure 7. Lynx IR image.

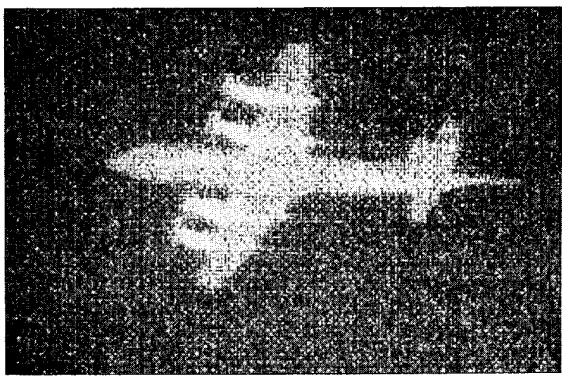

Figure 8. P3 Orion IR image.

lifeguard station at the beach (Figure 2), and 2) the parking lot higher on the boulevard. FfO operated two thermal imaging systems at the parking lot location: 1) a dual waveband DUWIR that simultaneously measures in the 3-5 and 8-12 μm bands, and 2) an IRC-64 steering array camera (InSb 64X64 focal plane array) sensitive in the 4.5 - 4.7 μm wavelength region. Sky backgrounds were measured in the 2.5 - 8 μm wavelength region. Extended black bodies were located close to the camera systems for calibration. Supporting meteorological measurements (wind speed and direction, air temperature, relative humidity, pressure, visibility and up/down welling radiance) were made using a meteorological station.

Also located in the parking lot were two IFU mobile lidar systems: 1) a three-wavelengths aerosol lidar (355, 532, and 1064 nm), and 2) a 1.56 μm eye-safe lidar. The three-wavelength lidar has a range of $>$ 15 km with a resolution of $\leq$ 15 m (532 and 355 nm) and $\leq$ 30 m (1064 nm). The 1.56 μm eye-safe lidar has a range of $>$ 15 km with a resolution of 15 m. With these range capabilities, the atmospheric structure was characterized from the Katwijk Beach Station to ranges extending beyond MPN. Horizontal and vertical variations in the extinction coefficients at these wavelengths were also directly measured.

On the upper deck of the Beach Station IFU made measurements of extinction at 543 nm and 1.56 μm utilizing a two-wavelength White-Cell transmissometer. CESDA also made 0.55 μm extinction measurements on the upper deck utilizing an HSS VR-301-B-120 visibility meter. Aerosol size distribution measurements were made at this location using two optical particle counters (ASASP-X and CSASP-100 HV). A meteorological station recorded wind speed, air temperature, and relative humidity. The TNO-FEL transmissometer receiver for the MPN/Beach Station transmission path (10.44 km) was also on the upper level of the Beach Station. Using the 1000 Hz source on MPN, transmission measurements were made at wavelengths in the visible and 8-12 μm bands.

Also on the upper level of the Beach Station, polarization measurements in the 3-5 and 8-12 μm bands were made by NPS [31] using an AGA 780 Thermovision dual band radiometric imaging system fitted with IR polarization filters. Preliminary results indicate that the use of the polarization filters can suppress the backgrounds and can enhance target detection significantly (Figure 9).

NDRE operated two TICM-II camera systems on the lower deck of the Beach Station, i.e., in the 3-5 μm band and 8-12 μm wavelength bands. For continuous calibration, three sources were mounted a short distance from the cameras on the beach. A laser range finder was used for accurate range determination of the sources and the Hr. Ms. Tydeman and the Lynx helicopter targets. It was also used for determining the maximum target detection ranges.

Refraction studies were made by DREV to test the WWKD model [32] over open seas in the presence of waves. A series of 8 halogen lamps were mounted on the MPN tower between 3.5 and 20 m MSL, and four lamps on the Hr. Ms. Tydeman at 4, 8, 13, and 23.7 m MSL. These lights were monitored with two CCD Sony AVC-D5 visible cameras and one IR Mitsubishi FPA model IR5120A camera (3.3-5.0 μm). All three cameras were equipped with strong telescopes. Continuous monitoring of the light sources yielded important information on the refractivity phenomena as a function of range and weather conditions. Strong refraction was observed with clear mirage effects during large air-sea temperature differences which occurred for off-shore winds when cold air masses were being advected over a relatively warm water surface (Figure 10). Figure 11 shows a sequence of images of the Hr. Ms. Tydeman mast light as the ship was reaching the maximum detection range.

The objective of the CELAR experiment was to study the refractivity effects in the marine boundary layer and to test the refraction model "Bulk-CELAR". Three camera systems were used, a CASTOR (8-12 μm), a Mitsubishi model IR 512 A (3-5 μm) and a Sony (visible) to collect sequences of Hr. Ms.

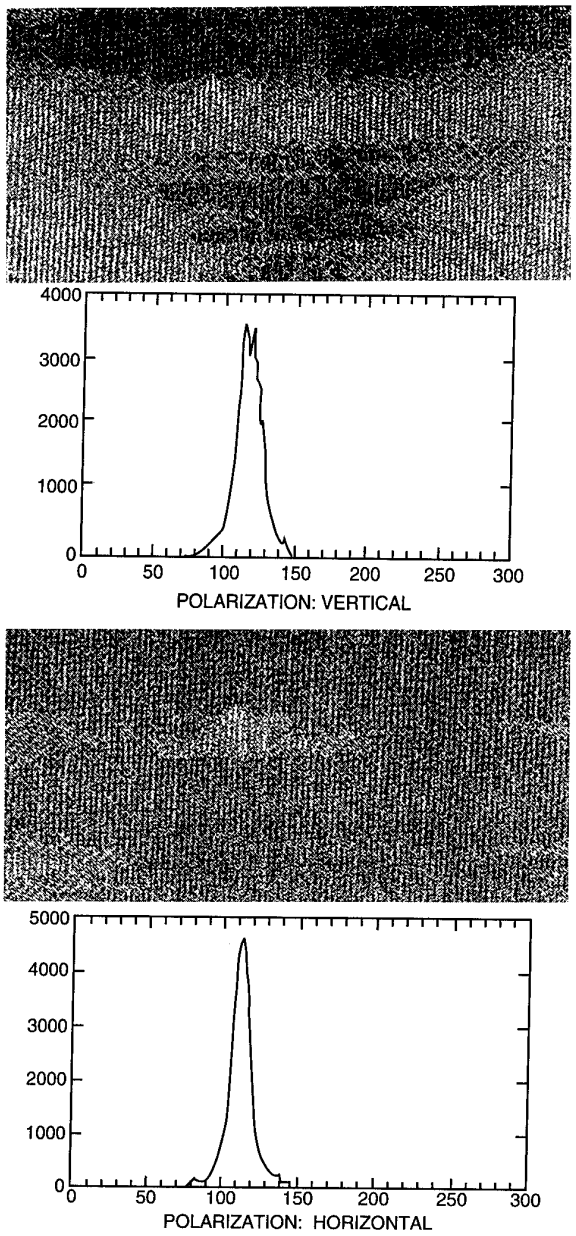


Figure 9. Polarization images of the Hr. Ms. Tydeman.

Tydeman and MPN images. The CELAR experiment was similar to the experiments conducted by DREV. The Beach Station also served as the receiver and monitoring location for the CELAR buoy data.

### 3.3 Hr. Ms. Tydeman

The oceanographic research vessel Hr. Ms. Tydeman (Figure 2), was made available for the MAPTIP trial by the RNL Navy. This platform served as a imaging target for the ship-signature studies (Figure 6), and as a platform for the visible and IR sources (Figure 11). The ship was instrumented with thermocouples and radiometers to monitor the temperatures of the hull, stack and the exhaust plume. A visible/IR 6X3 light source array was mounted on the stern for refractive studies. The upper and lower three sources emitted predominantly in the IR, the middle row emitted only in the visible. The main purpose was to have a low altitude intensive IR source to simulate a point target, i.e., a sea skimming missile that could be observable at variable distances. The ship's operational procedure allowed for the maximum use of this low level IR source. On inbound/outbound radials to MPN and the beach station, the

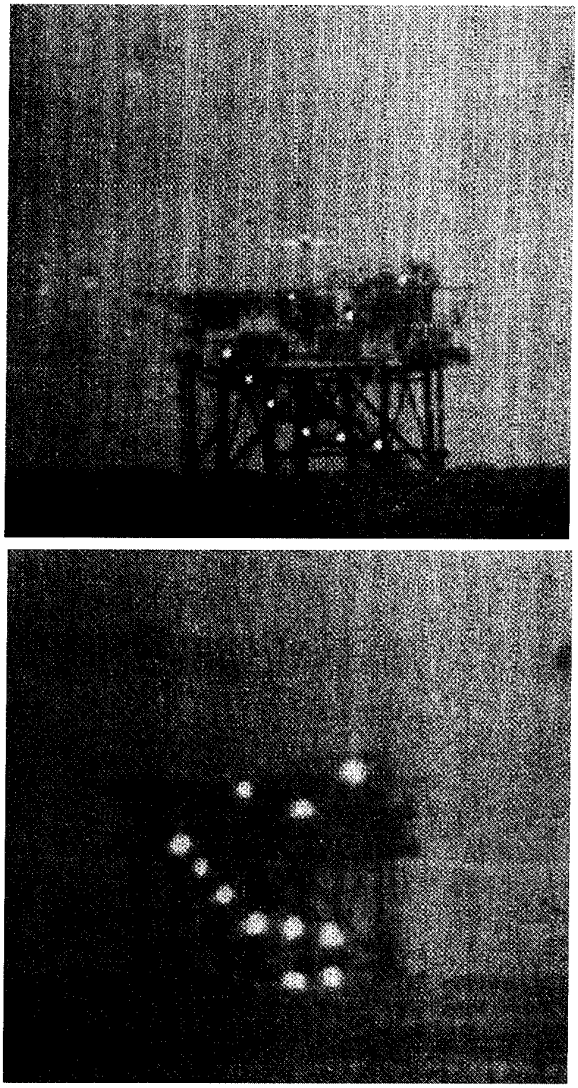

Figure 10. IR images of the MPN oceanographic tower (visible CCD Sony Camera).

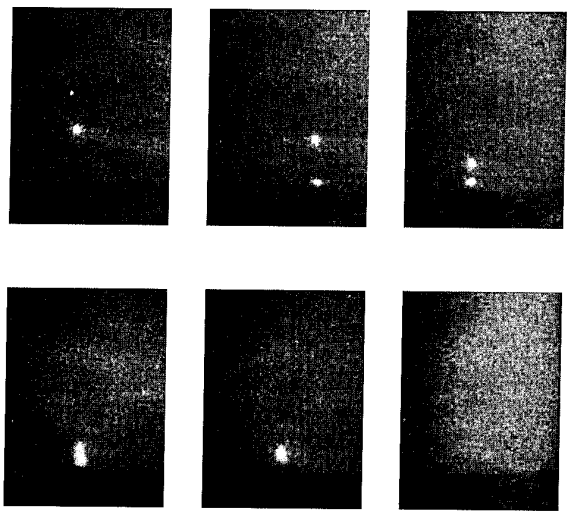

Figure 11. Sequence of images of Tydeman mast light as the ship was reaching the maximum detection range (visible CCD Sony Camera).

ship made elliptical (oval) turns every 2 NMi, staying on a steady course for about two minutes to give the maximum opportunity for good imaging of the IR source, even for those imaging systems with a narrow field of view and accounting for the rolling and pitching of the ship. A typical operational pattern for the MAPTIP trial is shown in Figure 2. The basic cruise pattern of the ship was to sail: 1) between MPN and the Beach Station, 2) along the sun glint radial from MPN to way point C, and 3) on a radial away from the sun between MPN and weight point A. The B-C radial provided over-the-horizon and sun glint imaging for the Beach Station. The A-C radial was intended for detection and identification runs by the P3 Orion. The outlined operational procedures were flexible in response to special requests by the MAPTIP participants to allow for changes in the atmospheric and weather conditions.

In addition to the IR/visible sources, DREV mounted halogen lamps (reference 3.2) on the Hr. Ms. Tydeman to supplement the halogen lamps that were standard equipment on the ship. These halogen lamps were used for studying the refractivity effects as described in Section 3.2. No thermal imagers were mounted on the Hr. Ms. Tydeman.

TNO-FEL operated a scanning radiometer on the port of the ship for elevation measurements of sea and sky horizon backgrounds. Also, TNO-FEL made standard meteorological measurements on the ship, i.e., wind speed and direction, air temperature, relative humidity, pressure, water temperature, and sea states. The wind and temperature sensors were mounted on the mast of the foredeck. Aerosol particle size distribution measurements were made utilizing the PMS aerosol particle counters (ASAS 300 and the CSAS 100 HV). Aerosol chemical composition was determined by UIA from samples collected with a May impactor inserted in a sample tunnel. The aerosol equipment was mounted on the roof of the bridge.

Environmental parameters and particle size distributions were measured continuously. Impactor samples were taken only when the ship was steady on station during an extended period of at least 8 hours. This occurred near MPN and for positions located a day sailing from MPN. The main purpose of the chemical analyses was to acquire data for the extension of aerosol models from the MPN area to a larger part of the North Sea. Some speculation has been made about the relative contributions of aerosol from maritime and continental origin to explain the effect of wind direction on the wind-speed dependence of the aerosol concentrations [33]. Data on the aerosol spatial variability and other environmental parameters, in the direction of and perpendicular to the prevailing winds as a function of distance from the coast, are required for definite conclusions and for quantification of the observed effects. The data collected on the Tydeman, together with that at the fixed locations (MPN and Beach Station) will serve as an indicator for variations due to a change in the meteorological conditions and will be used for the quantification of the spatial variability.

An average of five radiosondes were released daily from the Hr. Ms. Tydeman to characterize the atmospheric vertical structure along the operational path. The timing was such that a good temporal coverage of vertical soundings was obtained during the intensive operational periods by combining the Tydeman radiosonde soundings with the vertical profiles taken by the Piper Navajo. The information on the atmospheric vertical structure is of crucial importance for testing NOVAM.

### 3.4 NRaD Airborne Platform

The NRaD airborne platform (Figure 3) was equipped with aerosol and meteorological instrumentation. The aerosol spectrometer instrumentation included the PMS FSSP-100 and the OAP-200. The meteorological measurements were IR sea surface temperature, air and dew temperatures, and absolute pressure. The Navajo flew a star pattern centered on the MPN tower to monitor the spatial variability of aerosols and meteorological conditions (Figure 3). At the start and end of each star pattern the Navajo profiled the vertical structure by spiralling over MPN to 1524 m. The data are intended to be used for the validation of NOVAM and in the development of ANAM. During the Navajo in- and out-bound radial from the MPN tower and the Beach Station, the Navajo served as a target for the imaging community. On special occasions, when the Hr. Ms. Tydeman made long tracks and there was no need to fly the complete star pattern, in- and out-bound radial were flown to allow for continuous tracking of the aircraft by the thermal imaging community as a function of altitude and distance to the horizon (Figure 12).

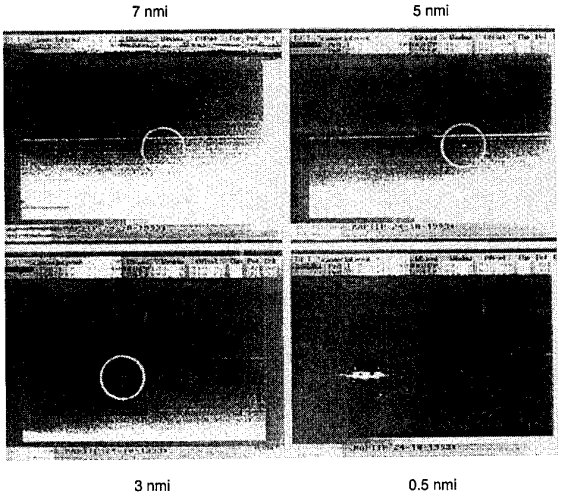


Figure 12. IR images of the inbound Navajo at different ranges.

### 3.5 Lynx Helicopter

A Lynx helicopter (Figure 3) was made available by the RNL Navy. A total of ten dedicated flights were made throughout the MAPTIP trial. The helicopter was equipped with an IR point source that was suspended 20 m below the helicopter. It served as a target by hovering at a number of fixed positions with respect to the Beach Station and MPN. Figure 13 shows the IR image of the Lynx point target as a function of distance. The distances ranged from 0.5 NMi to 20 NMi. The helicopter flew at an altitudes of 24 m (46 and 91 m at the largest distances) to keep the point target above the horizon. The flight profile is

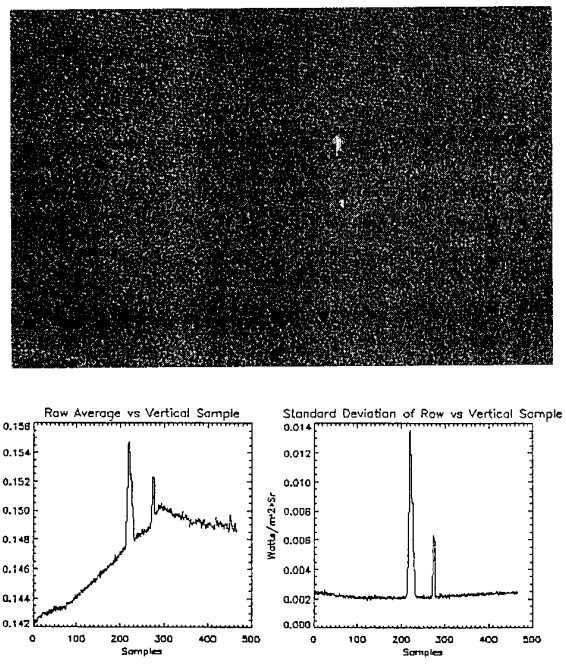


Figure 13. 3.5-4.2 μm thermal images of the Lynx helicopter and infrared source at 2.5 nmi, 26 Oct 93, 1637.

shown in Figure 3. This flight sequence allowed for the determination of the maximum detection range of the point source, transmission measurements, and imaging. The Lynx helicopter was also equipped with a FLIR and imaged the Tydeman during each flight. Two circles were flown around the ship at different distances and heights for all aspect imaging.

### 3.6 P3 Orion

A FLIR-equipped P3 Orion (Figure 3) was provided by the RNL Navy for determing detection and identification ranges on the Hr. Ms. Tydeman (while the ship was stopped). Figure 14 shows the P3 Orion FLIR image of the Hr. Ms. Tydeman. It also served as a target for the imagers at the Katwijk Beach Station and the MPN tower (Figure 3). Both outbound and inbound radials were made (maximum radial distance of 20 NMi). On the outbound runs the Orion was tracked until the IR signal was lost. On the inbound radials the objective was to determine the detection range for the P3.

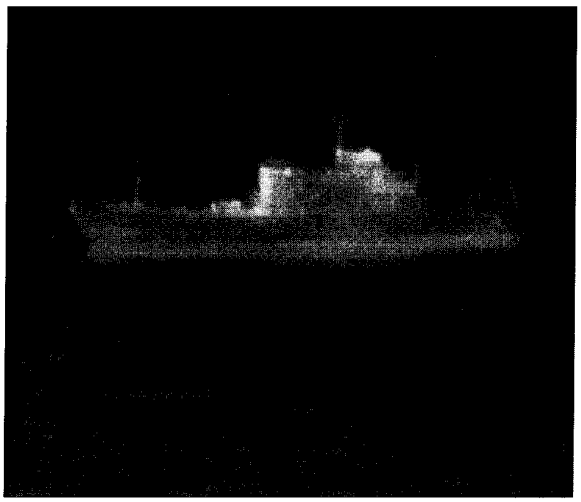

Figure 14. Image of the Hr. Ms. Tydeman in the 8-12 μm band (recorded with the FLIR-2000 for the P3 Orion).

### 3.7 Buoys

Three buoy systems were deployed during MAPTIP. NPS deployed a coastal climate minimet buoy at approximately 0.5 NMi NW from MPN. This buoy was instrumented with a Gill Sonic Anemometer to measure the components of the turbulent air and the air temperature at 5 m. A Rotronic hygrometer was also installed to determine the mean air temperature and relative humidity at a height of 2 m MSL. A 1-D accelerometer provided wave information. CELAR deployed two buoy systems at approximately 4 km from the beach near the Beach Station. One, a Wave Rider, measured instantaneous wave heights, while the other, a meteorological buoy, measured the mean air temperature, relative humidity, solar irradiation, wind speed, wind direction, pressure (all at a height of 3.4 m MSL) and sea surface temperature (0.2 m below the surface).

In addition to the local platform measurements described above, meteorological information was made available from all the meteorological stations located in the North Sea and from satellite observation of sea surface temperatures. Weather maps and air mass trajectories were also made available for the MAPTIP trial period to allow larger-scale interpretation of the MAPTIP data.

## 4. DATA OVERVIEW AND CONCLUDING REMARKS

The MAPTIP trial, intended as a coastal maritime environment experiment for developing and validating marine aerosol models and for determining the effects of the marine atmosphere on thermal imager performance, turned out to be dominated by continental air masses with little maritime influence. The prevailing winds were easterly, in contrast to normal westerly flow. However, the occurrence of off-shore winds (NNE-SSE) is not uncommon in this area [34]. The resulting meteorological situation depends, of course, on the season. During the MAPTIP trial, the atmospheric thermal stratification was very unstable due to a cold air mass being advected over a relatively warm sea. Because such situations can be encountered in other areas, we feel that valuable data were collected for studies of the effects of surface layer turbulence and thermal stratification causing strong refractivity effects on thermal imager performance.

Unfortunately, the weather situation did not allow for an extensive comprehensive study on marine aerosol properties, i.e., the fetch was short and little aerosol was generated from the easterly winds. The aerosol sampled at MPN was predominantly of continental origin. Only a limited data base was obtained for use in extending the existing aerosol models to incorporate near-surface effects. On the other hand, all other measurements were carried out as planned.

A wide variety of weather conditions from clear sunny skies to overcast were encountered. Visibilities ranged from dense fog to very clear. A wide range of thermal stratifications from very unstable (air to sea temperature differences (ASTD) of more than -9°C) to neutral and stable (ASTD of +1°C) occurred. Wind conditions ranged from light to gale force winds (1-20 m/s), causing sea state conditions of 2.2 m waves. As deduced from the lidar data, boundary layer structures were encountered where turbulent mixing occurred as indicated by well-defined eddy structures. On other occasions, convective plumes were observed [19]. Also, quiescent boundary layers were observed with layered structures. Lidar measurements at a negative elevation angle, made to study surface layer phenomena, indicated influences of waves.

All operational scenarios were well documented with the available meteorological data being made available from the various platforms, including the aerosol measurements and the lidar measurements made at MPN and the Beach Station. Information on larger spatial variations is available from the star patterns flown by the Navajo and in particular from the long treks made by Hr. Ms. Tydeman. The MAPTIP data set will be uniquely valuable for the development and validation of models for the assessment of the effects of atmospheric properties on electro-optical systems.

The thermal imager data provides an excellent data set for the evaluation of the atmospheric propagation models. The transmission data that can be deduced from the target measurements as a function of range can be directly compared with those derived from the models. Also, the detection limit, blurring, refraction phenomena, etc., were measured directly. Range predictors [35], IRST and refraction models can be developed and validated. Preliminary tests of the refractive models show an excellent agreement with observed refraction phenomena, e.g., the DREV model that calculates ray bending from atmospheric parameters.

An extensive data set for the analysis of thermal imager performance was taken, e.g., for IR seekers, LR IRST application, and the development and validation of ship signature models. A data base of such data has been collected, e.g. sea, sky and land backgrounds, sea and coastal clutter, horizon clutter, cloud data, etc. The operational period was shifted throughout the day to build a data base spanning from early morning until midnight. Thus day/night variations and dawn/sunset variations are included. Targets were observed in the sun glint during early hours. Data on turbulence, scintillation, and refractive effects (mirage, ducting) are available as explained above.

All the MAPTIP data are in support of the US IRAMMP (Infrared Analysis, Measurements, and Modeling Program) and will be used for the continued development of models describing the performance of thermal imagers. These include ship signature models, IRST models, background models, point source detection models, and clutter characterization models. Combining the respective models for targets, backgrounds, etc. with atmospheric models and an adequate description of the imager system parameters is expected to result in a comprehen-

sive model for the assessment of thermal imagers for a variety of targets as function of atmospheric conditions.

## 5. ACKNOWLEDGEMENTS

MAPTIP was organized by NATO AC/243 PANEL 4/RSG.8, in collaboration with AC/243 (Panel 04/RSG.5), under funding provided by NATO AC/243 grants 6056 and 6092, and from the Office of Naval Research (ONR) grant N00014-91-J-1948. The MAPTIP work plan was written through a cooperative effort between NRaD under ONR sponsorship, and the TNO Physics and Electronics Laboratory in the framework of assignments A92KM615 and A92KM776 of The Royal Netherlands Navy. All institutions from the 9 NATO participating countries provided their own funding. In support of MAPTIP, The Netherlands Royal Navy made available the oceanic research vessel Hr. Ms. Tydeman, a Lynx helicopter, a P3 Orion and the Naval Air Base Valkenburg as well as logistics support for these platforms. The efforts of the crews and personnel of these Royal Navy platforms made MAPTIP a success. We wish to acknowledge the cooperation of the Direktie Noordzee of the Dutch Ministry of Public Works for their cooperation, advice and the use of the Meetpost Noordwijk tower, the Scheveningen harbor facility, the ships Albatros and Smal Agtr, and the dedication of the respective crews. In particular, we wish to express our appreciation to the crew of MPN. KNMI made available the boom at MPN. The MAPTIP Scientific Committee express's it's thanks for all who helped to make the MAPTIP experiment a success. We especially express our thanks to TNO-FEL for their cooperation and dedication in logistically organizing MAPTIP.

## 6. REFERENCES

1. Kneizys, F.X., E.P. Shettle, W.O. Gallery, J.H. Chetwynd, Jr., J.H. Abreu, J.E.A. Selby, S.A. Clough and R.W. Fenn, "Atmospheric Transmittance/Radiance: Computer Code LOWTRAN 6," Air Force Geophysical Laboratory Technical Report No. 83-0187, August 1983.
2. Kneizys, F.X., E.P. Shettle, L.W. Abreu, J.H. Chetwynd, G.P. Anderson, W.O. Gallery, J.E.A. Selby, and S.A. Clough, "Users Guide to LOWTRAN 7," Air Force Geophysical Laboratory Technical Report No. 88-0177, Aug 1988.
3. Gathaman, S.G., "Optical Properties of the Marine Aerosol as Predicted by the Navy Aerosol Model," Opt. Eng. 22, 57-62, 1983.
4. Gathman, S.G., "Optical Properties of the Marine Aerosol as Predicted by a BASIC Version of the Navy Aerosol Model", NRL Memo Report #5157, 1983.
5. Gathman, S.G., "Navy Hygroscopic Aerosol Model" In: Hygroscopic Aerosol, L.H. Ruhnke & A. Deepak, editors, A. Deepak publisher, Hampton, VA., p93, 1984.
6. Hughes, H.G., "Evaluation of the LOWTRAN 6 Navy Maritime Aerosol Model Using 8 to 12 micron Sky Radiances," Opt. Eng., Vol. 26, #11, 1155-1160, 1987.
7. Battalino, T.E. and R.A. Helvey "Air Mass Parameterization in the Navy Aerosol Model," Geophysical Sciences Technical Note # 103, PMTC, Point Mugu, CA, 1985.
8. Gerber, H.E., "Relative-Humidity Parameterization of the Navy Aerosol Model (NAM)," NRL Report #8956, December 1985.
9. Hughes, H.G. and M.R. Paulson, "Lidar Technique for Adjusting Aerosol Model Number Densities to Existing Conditions," NOSC TD #1637, September 1989.
10. Smith, M.H. and D.R. Bates, "Radon Concentrations over the North East Atlantic," UMIST Interim Report, April 91 - May 92, 1992.
11. Gathman, S.G., "A Preliminary Description of NOVA-M, the Navy Oceanic Vertical Aerosol Model," NRL Report #9200, 1989.
12. de Leeuw, G., K.L. Davidson, S.G. Gathman, R.V. Noonkester, "Modeling of Aerosols in the Marine Mixed-Layer," In: Propagation Engineering, SPIE proceedings, vol 1115, p 287-294, 1989.
13. de Leeuw, G., K.L. Davidson, S.G. Gathman and R. V. Noonkester, "Physical Models for Aerosol in the Marine Mixed-Layer," In: Operational decision aids for exploiting or mitigating electromagnetic propagation effects, AGARD-CP 453, pp. 40-1 to 40-8, 1989.
14. Gathman, S.G., G. de Leeuw, K.L. Davidson and D. R. Jensen, "The Navy Oceanic Vertical Aerosol Model: Progress Report," In: Atmospheric propagation in the UV, visible, IR and mm-wave region and related systems aspects, AGARD-CP-454 17-1 to 17-11, October 1989.
15. Davidson, K.L., G. de Leeuw, S.G. Gathman and D. R. Jensen, "Verification of the Naval Oceanic Vertical Aerosol Model During FIRE," In: FIRE Science Results 1989, D.S. McDougal, editor, NASA Conference Report #3079, pp. 191-196, 1990.
16. Gerber, H., S.G. Gathman, J. James, M.H. Smith, I. Consterdine and S. Brandeki, "NRL Tethered Balloon Measurements at San Nicolas Island during FIRE IFO 1987," In: FIRE Science Results 1988, D.S. McDougal and H.S. Wagner, editors, NASA conference publication #3079, 191-196, 1990.
17. Cecere, T.H., "An Evaluation of the Naval Oceanic Vertical Aerosol Model during Key-90," NPS Thesis, June 1991.
18. Gathman, S.G., "Ocean Aerosol Measurements and Models in the Straits of Florida (The Key-90 Experiment)," Atmospheric Propagation and Remote Sensing, A. Kohnle and W.B. Miller, editors, SPIE proceedings Vol. 1688, 2-13, 1992.
19. de Leeuw, G. and G.J. Kunz, "NOVAM Evaluation from Aerosol and Lidar Measurements in a Tropical Marine Environment," Atmospheric Propagation and Remote Sensing, A. Kohnle and W.B. Miller (Eds.), Proc. SPIE 1688, 14-27, 1992.
20. de Leeuw, G., "Aerosol effects on electro-optical propagation over sea," In: 8th meeting on Optical Engineering in Israel: Optical Engineering and Remote Sensing, M. Oron, I. Shladov and Y. Weissman (Eds.) Proc. SPIE 1971, 2-15, 1993.
21. Paulson, M.R. and H.G. Hughes, "A lidar technique for adjusting aerosol model number densities close to the ocean surface," Naval Ocean Systems Center Technical Report 1388, December 1990.
22. Jensen, D.R., G. de Leeuw and A.M.J. van Eijk, "Work plan for the Marine Aerosol Properties and Thermal Imager Performance trial (MAPTIP)," Naval Command, Control and Ocean Surveillance Center, San Diego, CA, USA, Technical Document 2573, September 1993.
23. de Leeuw, G., A.M.J. van Eijk and D.R. Jensen, "MAPTIP Experiment, Marine Aerosol Properties and Thermal Imager Performance: An Overview", TNO-report FEL-94-A140, June 1, 1994.
24. Jensen, D.R., private communication.
25. Wills, J.A.B., "HEXOS models tests on the Noordwijk tower," NMI report R184, 1984.
26. de Leeuw, G., "Profiling of aerosol concentrations, particle size distributions and relative humidity in the atmospheric surface layer over the North Sea," Tellus 42B, 342-354, 1990.
27. de Leeuw, G., "Spray droplet source function: from laboratory to open ocean," In: Modeling the fate and influence of marine spray. P.G. Mestayer, E.C. Monahan and P.A. Beetham, editors, Univ. Connecticut, Avery Point, Groton, CONN, 17-28, 1990.
28. Kunz, G.J., "A high repetition rate lidar," TNO Physics and Electronics Laboratory, report FEL-90-A352, 1990.
29. Katsaros, K.B. and G. de Leeuw, "Comment on "Sea spray and the turbulent air-sea heat fluxes", by E.L. Andreas, J. Geophys. Res. 97, 1992," Accepted for publication in J. Geophys. Res., 1994.
30. Taczak B. (ed.), "MAPTIP quick-look report," prepared by Office of Naval Research, Arlington, VA, USA, 1993.
31. Gregoris, D.J., S. Yu, A.W. Cooper, E.A. Milne (1992). Dual-band infrared polarization measurements of sun glint from the sea surface. In: Characterization, propagation, and simulation of sources and backgrounds II. SPIE Proc. 1687, 381-391, 1992.

32. Beaulieu, A.J., "Atmospheric refraction model and the effects of surface waves," DREV Report 4661/92, 1992.
33. van Eijk, A.M.J. and G. de Leeuw, "Modeling aerosol particle size distributions over the North Sea," J. Geophys. Res. 97, (Vol. C9), 14417-14429, 1992.
34. Korevaar, C.G., North Sea climate. Kluwer, Dordrecht, The Netherlands, 1990.
35. van Eijk, A.M.J. and G. de Leeuw, "Atmospheric effects on IR propagation," In: Infrared Technology XIX, B.F. Andresen, F.D. Sheperd, Editors, Proc. SPIE 2020, 196-206, 1993.

# Characterisation of Atmospheric Properties during MAPTIP

**Alexander M.J. van Eijk, Frank H. Bastin, Filip P. Neele and Gerrit de Leeuw**
Physics and Electronics Laboratory TNO,
P.O.Box 96864, 2509 JG The Hague, The Netherlands

and

**Jasna Injuk**
University of Antwerp (UIA)
Antwerp, Belgium

## SUMMARY

Aerosol particle size distributions were measured during the MAPTIP experiment at Hr.Ms. Tydeman. Extinction coefficients were calculated using a Mie routine. The analysis shows that the TNO local MPN aerosol model accurately predicts the aerosol extinction for data in its range of validity. The applicability of the MPN model decreases outside its limits for geographical region and environmental parameters. The model is compared to the Navy Aerosol Model. The chemical composition of the aerosol during MAPTIP is discussed in terms of geography and environmental parameters.

## 1. INTRODUCTION

The performance of electro-optical systems is affected by suspended aerosol particles that scatter and absorb electromagnetic radiation. In this way, the atmospheric aerosol is in part responsible for the degradation of the radiance contrast between a target and its natural background, as viewed by an infrared sensor. For correct assessment of the effective range of electro-optical systems in a given meteorological scenario it is necessary to understand and to predict the effects of the atmosphere on propagation of electromagnetic radiation. Hence, there is a need for accurate atmospheric models that can be used in propagation prediction codes.

Presently, the Atmospheric Transmission/Radiance computer code LOWTRAN[1] is the primary tool for this assessment. This code uses the Navy Aerosol Model,[2,3,4] NAM, to predict the transmission in the marine atmosphere along horizontal paths at shipboard levels (around 10 m). NAM is based on an extensive data set including a variety of geographical locations and performs well in open-ocean conditions at mid-latitudes in low to moderate wind speeds. Nevertheless, discrepancies have been observed in sub-tropical regions, high wind conditions and in coastal areas with polluted continental air masses.[5,6,7] Apparently, the influence of a variety of nearby local sources is not well handled by NAM.

A local aerosol model has been developed for the polluted North Sea, based on aerosol size distributions as measured during the HEXMAX experiment[8] in October - November 1986 at the Meetpost Noordwijk (MPN), a platform located at 9 km off the Dutch coast. The MPN aerosol model calculates the aerosol extinction in two steps. First, the aerosol size distribution is calculated from meteorological parameters, including wind direction.[9] The wind rose between 110 - 340° is partitioned in various sectors based on industrial, rural continental and predominantly marine influences. Subsequently, an approximated Mie-algorithm is used to calculate the aerosol extinction from the size distribution. The model predicts the aerosol extinction to within a factor of 2.0 (68% confidence limit), which is a factor of 2 better than the generally used NAM model.[5] The effect of wind direction on the aerosol extinction has been ascribed to the relative contribution of aerosol from marine and continental origin.[10] Data on the spatial variability of aerosol and other environmental parameters, at various distances from the coast, are required to validate the MPN aerosol model and to ascertain the geographical limits of its applicability.

The MAPTIP (Marine Aerosol Properties and Thermal Imager Performance) experiment,[11] conducted between October 11 and November 5, 1993, yielded new data sets on aerosol particle size distributions and environmental parameters in the area of Meetpost Noordwijk (MPN). During MAPTIP, the oceanic research vessel Hr.Ms. Tydeman was made available by the RNL Navy. One of the tasks of Hr.Ms. Tydeman was to monitor environmental conditions and their spatial variations. Standard meteorological parameters such as wind speed, wind direction, air temperature, relative humidity, pressure and water temperature were measured continously. In addition, aerosol particle size distributions were recorded and impactor samples were taken at several times to determine the aerosol chemical composition. The operational sequence of MAPTIP was chosen such that Hr.Ms. Tydeman was able to collect data both near MPN and at various locations a day sailing from MPN.[12] Figure 1 presents the composite sailing schedule of Hr.Ms. Tydeman.

The present contribution focusses on the aerosol extinction, calculated from the particle size distributions measured at Hr.Ms. Tydeman. The experimental extinction values are compared to predictions by NAM and the local MPNaerosol model. We show that the local MPN model provides an

*Paper presented at the Sensor and Propagation Panel Symposium on "Propagation Assessment in Coastal Environments" held in Bremerhaven, Germany 19-22 September 1994.*

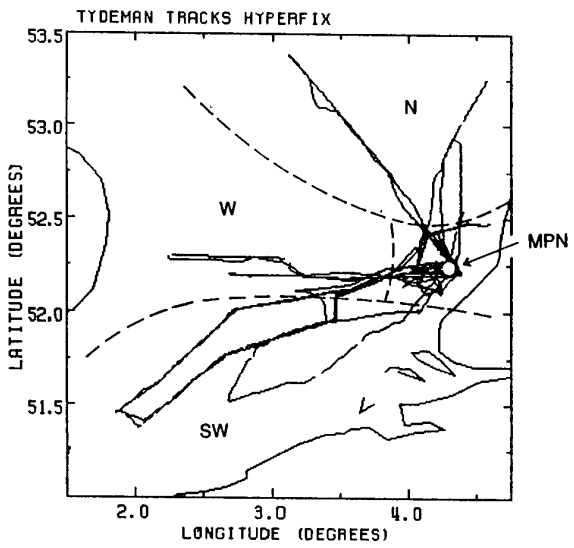


Figure 1: Composite sailing schedule of Hr.Ms. Tydeman. The position of the MPN tower is indicated by the arrow. The dashed lines define the regions used in the assessment of spatial variability of the aerosol extinction.

accurate estimate of the aerosol extinction close to the MPN tower, but that the accuracy is reduced further from the coast. The aerosol extinction and aerosol chemical composition is discussed in terms of environmental parameters.

## 2. EXPERIMENTS

### 2.1 Aerosol sampling

Two Knollenberg optical particle counters (Particle Measuring Systems, Boulder, Colorado) were used to measure particle size distributions in the 0.16 - 32 µm diameter range, that is, an ASAS 300 A active probe and a CSAS 100 HV classical probe. The probes were mounted on the roof of the bridge of Hr.Ms.Tydeman, at a height of approximately 15 m above the mean water level. The aspiration tubes were manually pointed into the wind. The probes were operated unattended and could thus be used 24 hours per day. Down times occurred due to rain, maintainance, data processing and storage, probe failure, etc.

The data were stored and digitized in the data acquisition system and transferred to a personal computer, via an IEEE interface at preset time intervals. Particle size distributions $dN/dD$ ($\mu m^{-1}cm^{-3}$) were calculated and stored together with meteorological parameters obtained from Hr.Ms. Tydeman standard instrumentation and TNO operated sensors. The size distributions were averaged over 10-min periods and polynomials of degree 1 and 5 were fitted to the datapoints in *log (dN/dD)* versus *log (D)* space.

Aerosol samples for elemental analysis were collected in a continuous forced air flow inside a wind tunnel, which directed itself continuously towards the wind. The wind tunnel was mounted next to the PMS-probes, at a height of approximately 16 m above the mean water level. The aerosols were separated by a Batelle cascade impactor (cut off diameters 0.25, 0.5, 1, 2, 4, 8 and 16 µm) and collected on quarz reflector holders. Aerosol collection took place while Hr.Ms. Tydeman was anchored and sample times were typically 11.5 hours. The samples were subsequently analyzed at the University of Antwerp (UIA) by the Total-Reflection Xray Fluorescence (TXRF) Technique[11] to yield the elemental composition in each size bin.

### 2.2 Postprocessing

The experimental aerosol size distributions were used to compute extinction coefficients at 5 wavelengths (10.6, 4.0, 1.064, 0.6943 and 0.55 µm), with an upgraded version of the FEL-TNO Mie code.[13,14] This code yields an exact solution for each size, and uses a Simpson integration method to integrate over the particle size distribution until a specified accuracy (0.01) is obtained. Since extinction was not measured directly at the Hr.Ms. Tydeman, we consider those extinctions to be the best estimate of the actual aerosol extinctions during the experiment.

The NAM model predicts an aerosol extinction based on *u24*, the average wind speed in the previous 24 hours, $u_{10N}$, the wind speed at 10 m height in neutral conditions, the relative humidity and the visibility. The local MPN aerosol model uses $u_{10N}$, the wind direction, the relative humidity and the ASTD (air-sea temperature difference) to calculate the aerosol extinction. To supply the input parameters for the models, the values of the wind speed $u$ measured at 22.6 m above mean sea level were converted to $u_{10N}$. Corrections were made using *Liu et al.*[15] and the shallow-water expression for the drag coefficient $C_{DN}$ that applies to the MPN area.[8,16] Subsequently, *u24* was calculated from the $u_{10N}$ values. Because no direct measurements were made of the visibility at 0.55 µm at Hr.Ms. Tydeman, we have calculated the visibility VIS from the extinction coefficients $\alpha$ at 0.55 µm obtained with the exact Mie code: VIS = 3.915 / $\alpha$.

### 2.3 Validation

The data set of the PMS probes was validated prior to the analysis. In the last week of the experiment, only a partial aerosol spectrum (0.75 - 32 µm) could be recorded during nights due to failure of the ASAS probe. The lack of data on smaller diameters (0.16 - 0.75 µm) gave rise to systematic underestimation of the slope of the Junge fit compared to records which contained the full size range (0.16 - 32 µm). Therefore, the records with partial spectra have been removed from the data set.

A heavy fog developed in the morning of Sunday 31 October. The fog lasted untill the evening of Tuesday 2 November, but was most dense on Sunday. The fog was accompanied by high humidity, which could give rise to a slight supersaturation. Under these conditions the

hygroscopic aerosols may be activated. They grow very rapidly in size and behave as cloud droplets. Consequently, they cannot be described by equations that apply to subsaturated aerosol. We decided to study the fog event on Sunday 31 October as a case study.

Small numbers of data records were removed from the data set because they were polluted by the diesel exhaust from the stack or because Hr.Ms. Tydeman made short port calls to Scheveningen and IJmuiden. Incidentally, records were rejected for other reasons. A total of 1518 data records (76%) was available for the analysis.

The NAM model could be applied to 1254 data records. The remaining records lacked one or more of the environmental input parameters required for the NAM calculation (mostly relative humidity). The local MPN aerosol model could be applied to only 794 data records, because wind direction data of the Hr.Ms. Tydeman were not always available. In the future, the data set will be completed with wind direction data from the MPN tower, for the periods that Hr.Ms. Tydeman was in the vicinity of MPN.

## 3. ANALYSIS

### 3.1 Assessment of the performance of aerosol models

The performances of NAM and the local MPN aerosol model were assessed from logarithmic scatterplots of the extinction predicted by either model, versus the extinction as calculated from the experimental aerosol size distributions. For these plots, the standard deviation $\sigma_{y=x}$ of the data points with respect to the line Y = X (ideal model performance) was calculated. The value of $\sigma_{y=x}$ is a measure for the factor *F* to within the model predicts the experimental aerosol extinction (68% confidence limit): $\sigma_{y=x} = \log F$.

### 3.2 Validation of the local MPN aerosol model

The local MPN aerosol model predicts the aerosol extinction at the MPN tower for wind directions between 110 and 340 °N. [9] Therefore, we decided to use only those data records for the validation that had been collected in the vicinity of the MPN tower, i.e., in a region centered around MPN with a radius of roughly 40 km. This subset was then further reduced by imposing the restriction of a wind direction between 110 and 340 °N during data collection. Unfortunately, during the MAPTIP campaign the prevailing wind direction was east and only a limited amount of data records was recorded in wind directions between 110 and 340 °N. As a consequence, the subset for validation of the MPN model is rather small. Data records are only available for the wind sectors 110-155 °N and 240-310 °N. Table 1 presents the performance of the MPN model and, for comparison, the performance of NAM. In addition, the perfomances of the NAM and MPN models obtained previously for the HEXMAX data set (on which the MPN model is based) are listed.[5]

Table 1: Performance of the local MPN aerosol model and NAM in the vicinity of the MPN tower. The row labelled *N* indicates the number of data records available in each wind sector.

| | *Wdir* | *110-340* | *110-155* | *240-310* |
|---|---|---|---|---|
| | *N* | *72* | *31* | *39* |
| $\lambda$ = 10.6 µm | MPN | 2.2 | 2.8 | 1.7 |
| | NAM | 2.0 | 2.1 | 3.2 |
| $\lambda$ = 4.0 µm | MPN | 1.9 | 2.6 | 1.4 |
| | NAM | 3.9 | 4.3 | 3.5 |
| $\lambda$ = 1.064 µm | MPN | 2.6 | 3.5 | 2.2 |
| | NAM | 3.1 | 1.9 | 4.9 |
| $\Sigma\lambda$ | MPN | 2.2 | 2.9 | 1.7 |
| | NAM | 2.9 | 2.6 | 3.8 |
| $\Sigma\lambda$ | MPN | 2.0 | | |
| HEXMAX | NAM | 4.1 | | |

Table 1 shows that overall the MPN model predicts the aerosol extinction within a factor of 2.2, which is close to the performance of 2.0 reported earlier.[5] Although the present validation is based on a rather small dataset, this is encouraging. It proves that for an arbitrary aerosol sample the MPN model prediction is accurate, within its limits of application. The MPN model predicts the aerosol extinction more accurate than the NAM model, which supports the suggestion that the predictions from general models such as NAM must be carefully interpreted for a polluted coastal area.

The MPN model performs better in the 240-310 °N wind sector. This may reflect that for the original formulation of the model more aerosol data was available for this wind sector (224 hours of sampling) than for the 110-155 °N wind sector (28 hours of sampling),[9] which leads to a reduced accuracy for the latter wind sector. The MAPTIP data set with predominantly easterly winds provides a tool to increase the performance of the MPN model in the 110-155 °N wind sector and to extend the model to wind directions smaller than 110 °N.

### 3.3 Spatial variations

One of the TNO objectives in MAPTIP was to assess the geographical limits of the validity of the local MPN aerosol model for the North Sea. To this end, Hr.Ms. Tydeman made various treks over the North Sea. To assess the spatial variability, the aerosol data set was partitioned into 4

subsets (cf. Figure 1): a) the vicinity of MPN ; b) the region west of MPN; c) the region north of MPN; and d) the region southwest of MPN.

During the treks of Hr.Ms. Tydeman, only a small amount of data was collected while the wind direction was between 110 and 340 °N (37 data records total). However, these data show that the accuracy of the MPN model decreases when Hr.Ms. Tydeman is not in the vicinity of the MPN tower. The decrease is not surprising, since the transport of aerosol from sources on the continent and in the UK is only taken into account for the immediate vicinity of the MPN tower by virtue of its dependence on wind direction and wind speed. The partitioning in wind direction was made in the first place to account for different source regions. Of course also the fetch, and thus aerosol transport, changes with wind direction. The transport mechanism is further affected by wind speed, as explained by *Van Eijk and De Leeuw*.[9] However, to generalize the MPN model, the empirical equations must be extended with physical descriptions of the transport processes. The Hr.Ms. Tydeman data set has been collected for this purpose.

The limited data set offers few possibilities to assess the spatial variability of the aerosol extinction. To increase the data set it is necessary to extend the MPN model to wind directions smaller than 110 °N and larger than 340 °N. As a zero-order approximation, we have extended the wind sector labelled 'North Sea' (310 - 340 °N) to 310 - 030 °N and the sector 'rural region of Holland' (110 - 155 °N) to 030 - 155 °N.[9] In this way, the MPN model covers the full wind rose.

The performances of the extended MPN and the NAM models for the various regions are presented in Table 2. The table shows that the extended MPN model predicts the aerosol extinction in the vicinity of the MPN tower to within a factor of 3.7, compared to a factor of 2.2 for the original MPN model (cf. Table 1). Clearly, the zero-order extension is too crude and must be refined in the future to take explicitly into account the aerosol advected from Amsterdam (and its harbor) and the industrial area near IJmuiden.

Table 2 supports the conclusion mentioned above that the accuracy of the MPN model decreases outside the vicinity of the MPN tower. The prevailing easterly winds prompt the MPN model to include a large amount of aerosol of continental origin and relatively few aerosol of marine origin, due to the limited fetch. Further away from the coast, the contribution of continental aerosol decrease due to removal processes. As a consequence, the aerosol extinction in this region decreases, especially for the visible and near-IR wavelengths. On the other hand, the contribution of marine aerosol will increase with increasing fetch, leading to larger aerosol extinction, especially for the far-IR wavelengths. The net effect depends on their relative importance. We found that the MPN underestimates the aerosol extinction, in particular for the far-IR wavelengths. This suggests that the effect of the increased concentration of marine aerosol dominates the effect of the decrease in concentration of continental aerosol.

The above reasoning explains why the MPN model prediction is less accurate for the region 'west' compared to the region 'MPN'. For the regions 'north' and 'southwest', other factors are of importance too. The average wind speed encountered by Hr.Ms. Tydeman while in the regions 'north' and 'southwest' was some 4 m/s more than in the regions 'MPN' and 'west'. The wind speed in combination with the

Table 2: Performance of the NAM and extended MPN models for various geographical regions and for the total data set. The column labelled *N* gives the number of data records for each model in each region.

| Region | Model | N | 10.6 μm | 4.0 μm | 1.064 μm | Σλ |
|---|---|---|---|---|---|---|
| All | MPN | 794 | 4.1 | 5.6 | 4.5 | 4.7 |
| | NAM | 1254 | 1.9 | 3.2 | 2.2 | 2.4 |
| MPN | MPN | 531 | 3.2 | 4.2 | 3.7 | 3.7 |
| | NAM | 888 | 2.0 | 3.4 | 2.3 | 2.5 |
| West | MPN | 63 | 3.6 | 6.2 | 2.6 | 3.9 |
| | NAM | 103 | 1.9 | 3.7 | 3.1 | 2.8 |
| North | MPN | 81 | 5.6 | 7.8 | 5.5 | 6.2 |
| | NAM | 108 | 1.6 | 2.0 | 1.7 | 1.8 |
| SW | MPN | 119 | 7.8 | 12.5 | 9.5 | 9.8 |
| | NAM | 153 | 1.7 | 3.3 | 1.7 | 2.1 |

larger fetch must have resulted in an increased concentration of marine aerosol in these regions, as compared to the prediction by the MPN model. Hence, the MPN model substantially underestimates the aerosol extinction in the regions 'north' and 'southwest' resulting in a poor performance. The increased contribution of aerosol of marine origin in the regions 'north' and 'southwest' is also reflected in the performance of the NAM model. This model yields better results for the more marine conditions encountered in these regions. This supports our earlier conclusion[9] that in air masses with a large marine component NAM performs well, even in coastal areas.

### 3.4 Atmospheric stability

The MAPTIP experiment was characterized by unstable thermal stratifications, with an average ASTD (air-sea temperature difference) of approximately -4 °C. In very unstable conditions, the values of the ASTD reached -9 °C, whereas values of +1 °C were observed in neutral and stable conditions. The effect of the ASTD on the performance of the NAM and MPN aerosol models is assessed in Table 3.

Table 3: Performance of the NAM and MPN aerosol models for very unstable thermal stratification (ASTD < -4 °C), and other thermal stratifications (ASTD > -4 °C).

| | *ASTD* | *> -4 °C* | *< -4 °C* |
|---|---|---|---|
| | *N* | *415 / 719* | *380 / 536* |
| λ = 10.6 μm | MPN | 3.5 | 4.7 |
| | NAM | 1.7 | 2.3 |
| λ = 4.0 μm | MPN | 5.1 | 6.0 |
| | NAM | 2.5 | 4.3 |
| λ = 1.064 μm | MPN | 3.7 | 5.2 |
| | NAM | 2.0 | 2.5 |
| Σλ | MPN | 4.1 | 5.3 |
| | NAM | 2.1 | 2.9 |

The table shows that the performance of the aerosol models is reduced during very unstable thermal stratification. For the MPN model, this probably reflects that the model is not correctly parameterized for these extreme conditions. The original formulation was based on a data set with ASTD values in the range of -4.5 to +3 °C. The present results show that the ASTD dependence cannot be extrapolated to very unstable conditions.

The reduced performance of the NAM model may be attributed to the meteorological conditions during MAPTIP. In unstable conditions, rising thermals and associated downward motions of colder air parcels cause efficient mixing of the aerosol throughout the boundary layer resulting in a reduced concentration of aerosols at deck level. Opposed to this effect, the whitecap coverage which relates to the aerosol production, becomes larger.[17] During MAPTIP, the production of marine aerosol was low due to the limited fetch in the predominantly easterly winds. Consequently, the NAM model overestimates the amount of aerosol and yields an aerosol extinction that is too high.

### 3.5 Chemical composition

Impactor samples have been collected during MAPTIP to determine the composition of the aerosol as a function of size and geographical location. Table 4 presents dates and locations of the various samples. The aerosol was collected in 7 size bins, and for each size bin the concentrations of 18 elements in the aerosol have been determined. For the analysis, we have selected 4 elements that are characteristic for aerosol from anthropogenic sources (Cu, Zn, Pb, Se) and 3 elements that are characteristic for marine aerosol (Ca, Sr, Cl). Figures 2 and 3 present the mass distributions. The figures show clearly that the smaller aerosol is predomi-

Table 4: date and location of impactor samples. The asterisk denotes a time on the following day.

| Sample | Date | Time | Region |
|---|---|---|---|
| A | 24 Oct | 01.00 - 12.25 | southwest |
| B | 26 Oct | 19.15 - 07.30* | MPN |
| C | 28 Oct | 20.20 - 07.45* | west |
| D | 30 Oct | 07.30 - 19.20 | southwest |
| E | 1 Nov | 18.30 - 06.30* | MPN |

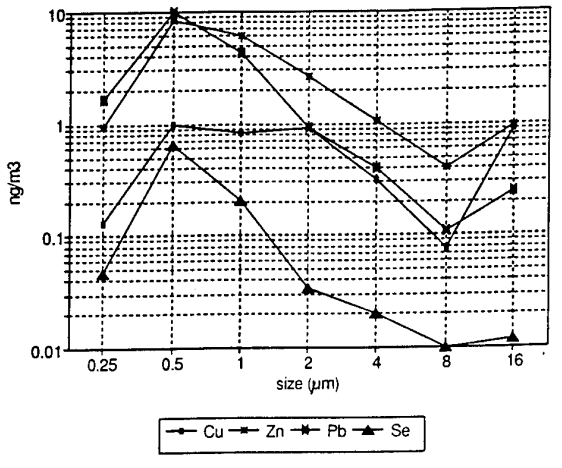


Figure 2: Average mass distribution of elements characteristic for aerosols from anthropogenic sources

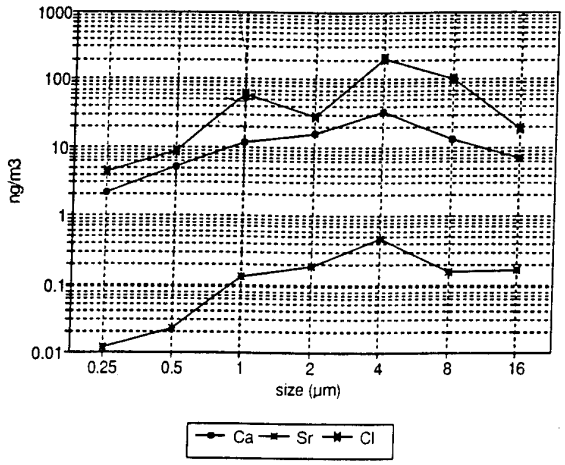


Figure 3: Average mass distribution of elements characteristic for aerosol of marine origin.

Table 5: elemental concentration of aerosol in ng/m$^3$

| | B+E mpn | A+C+D | A+B mpn | C+D+E |
|---|---|---|---|---|
| Cu | 5.1 | 3.6 | 1.0 | 6.3 |
| Zn | 15.9 | 24.7 | 4.0 | 31.0 |
| Pb | 17.4 | 17.3 | 4.7 | 25.8 |
| Se | 0.63 | 1.15 | 0.08 | 1.52 |
| Ca | 52.5 | 114 | 112.5 | 74 |
| Sr | 0.48 | 1.18 | 1.34 | 0.61 |
| Cl | 277.5 | 52.9 | 1023 | 32.3 |

Table 6: elemental concentration of aerosol in ng/m$^3$ for consecutive impactor samples

| | B mpn | A | E mpn | C+D |
|---|---|---|---|---|
| Cu | 0.7 | 1.3 | 9.4 | 4.8 |
| Zn | 3.1 | 4.9 | 26.9 | 33.8 |
| Pb | 7.88 | 1.56 | 27.0 | 25.2 |
| Se | 0.09 | 0.07 | 1.17 | 1.70 |
| Ca | 74 | 151 | 31 | 96 |
| Sr | 0.75 | 1.92 | 0.21 | 0.81 |
| Cl | 531 | 1515 | 24 | 36.5 |

nantly of anthropogenic origin, whereas the larger aerosol is of marine origin. This result justifies our approach in the local MPN aerosol model to treat the aerosol at the North Sea as a mixture of smaller aerosol of continental origin and larger aerosol of marine origin.[9]

Table 5 presents results of the elemental analysis of the aerosol samples. For each impactor sample (A-E) the elemental concentrations have been summed over all size bins to yield total concentration per impactor sample. In table 5, we present the average total element concentration for the impactor samples collected near MPN (B+E) and for the samples collected at some distance of the coast (A+C+D). For the latter samples, the fetch was larger in the easterly winds. This should result in a larger concentration of 'marine' elements (Ca, Sr and Cl) and in a smaller concentration of 'anthropogenic' elements (Cu, Zn, Pb and Se). The table shows that the expected behaviour is only observed for 3 of the 7 elements (Cu, Ca and Sr). This is due to a change in the general conditions, which is explained below. If we compare individual impactor samples that were collected consecutively, the results are better in line with the expectation.

Thus, for the assessment of spatial variability we may compare sample B (near MPN) to sample A (southwest), and sample E (near MPN) to samples C+D (west, southwest). The comparison is shown in table 6. The 'marine' elements (Ca, Sr, Cl) now all show the expected increase in concentration for a location at some distance of the MPN tower. For the 'anthropogenic' elements, the expected decrease in concentration for a location at some distance from MPN is only observed in 50% of the cases. Apparently, more data is needed for a firm conclusion about the spatial variability of 'antropogenic' aerosol.

The aerosol content, both physically and chemically, changed markedly during the MAPTIP experiment. This resulted in a large change in visibility in the afternoon of 28 Oct. Prior to this time the visibility was good (mostly larger than 10 nMi), whereas afterwards the visibility did not exceed 10 nMi and heay fog events occurred. The change in visibility could not be associated with a change in wind direction, i.e. with a change in origin of air masses. The change in visibility was confirmed by independent measurements of the visibility at MPN, and by manual observations at Hr.Ms. Tydeman. As mentioned previously, the prevailing wind direction was east during the whole campaign. However, the event changed the chemical composition of the aerosol drastically. This is shown in table 5, where we compare the impactor samples collected before (A+B) and after (C+D+E) the change in visibility. At this time, any explanation is speculative. It is possible that in haze and fog the deposition rate of aerosol of anthropogenic sources is reduced, because the particles are trapped in the fog droplets and stay aloft. This would result in the observed increase in concentration after 28 Oct. The reduction of aerosols of marine origin may be related to the wind speed and wave height. Before 28 Oct, the wind speed varied between 5 and 20 m/s and the wave heights were in

the range 50-150 cm. Afterwards, the wind speed did not exceed 10 m/s and the wave height was typically 40 cm.

## 4. CONCLUSION

We have presented an analysis of the aerosol extinction, as calculated from aerosol size distributions measured by Hr.Ms. Tydeman during the MAPTIP campaign. The local aerosol model developed previously for the vicinity of the MPN tower was found to yield accurate estimates of the aerosol extinction for data in its range of validity. However, the MPN model in its present form cannot be used for other geographical regions, nor for environmental conditions that are outside the specified range. We intend to use the MAPTIP data set for extension of the MPN model to other environmental conditions (easterly winds, unstable stratification) and other geographical regions (by taking into account the transport of aerosol).

The analysis of the aerosol extinction could not be completed without taking into account the specific conditions of a coastal area, such as limited fetch and contributions of aerosol of continental origin. The development of local models is fruitful, because these models can yield more accurate results than general models, such as NAM. This supports our feeling that there is a need for models, which take into account the physics of aerosol production and transport in the coastal zone.

## 5. ACKNOWLEDGEMENTS

This work was supported by the MOD-NL (assignment A92KM614). MAPTIP was sponsored by NATO AC/243 (Panel 4) (Grants 6056 and 6092) and by the US Office of Naval Research ONR (Grant N00014-91-J-1948) to contribute to the logistic costs. The MAPTIP participation of the TNO Physics and Electronics Laboratory was supported by the MOD-NL (assignments A92KM615 and A92KM776). We thank our colleagues at TNO for their support. The Netherlands Royal Navy made available the oceanic research vessel Hr.Ms. Tydeman. Special thanks to the crew of Hr.Ms. Tydeman for their splendid cooperation and dedication during the experiment.

## 6. REFERENCES

1. Kneizys, F.X., Shettle, E.P., Abreu, L.W., Chetwynd, J.H., Anderson, G.P., Gallery, W.O., Selby, J.E.A., and Clough, S.A., "Users guide to LOWTRAN 7", US Air Force Geophysical Laboratory Technical Report No. 88-0177, August 1988.

2. Gathman, S.G., "Optical properties of the marine aerosol as predicted by the Navy aerosol model", Optical Eng., *22*, 1983, pp 57-62.

3. Gerber, H.E., "Relative humidity parameterization of the Navy Aerosol Model (NAM)", National Research Laboratory Washington DC report 8956, 1985.

4. Gathman, S.G., "A preliminary description of NOVAM, the Navy Oceanic Vertical Aerosol Model", National Research laboratory Washington DC report 9200, 1989.

5. Van Eijk, A.M.J., and De Leeuw, G., "Modeling aerosol extinction in a coastal environment", Proc. SPIE Int.Soc.Opt.Eng., *1688*, 1992, pp 28-36.

6. Tanguy, M., Bonhommet, H., Autric, M., and Vigilano, P., "Correlation between the aerosol profiles measurements, the meteorological conditions and the IR transmission in a mediterranean marine atmosphere", Proc. SPIE Int.Soc.Opt.Eng., *1487*, 1991.

7. De Leeuw, G., "Aerosol effects on electro-optical propagation over sea", Proc. SPIE Int.Soc.Opt.Eng., *1971*, 1992, pp 2-14.

8. Smith, S.D., Katsaros, K.B., Oost, W.A., and Mestayer, P.G., "Two major experiments in the humidity exchange over the sea (HEXOS) program", Bull.Am.Meteorol.Soc., *71*, 1990, pp 161-172.

9. Van Eijk, A.M.J., and De Leeuw, G., "Modeling aerosol particle size distributions over the North Sea", J.Geophys.Res. *97C*, 1992, pp 14417-14429.

10. Van Eijk, A.M.J., and De Leeuw, G., "Atmospheric effects on IR-propagation", Proc. SPIE Int.Soc.Opt.Eng., *2020*, 1993, pp 196-206.

11. De Leeuw, G., Van Eijk, A.M.J., and Jensen, D.R., "MAPTIP experiment, Marine Aerosol Properties and Thermal Imager Performance: An overview", Physics and Electronics Laboratory TNO report FEL-94-A140, June 1994.

12. Jensen, D.R., De Leeuw, G., and Van Eijk, A.M.J., "Work plan for the Marine Aerosol Properties and Thermal Imager Performance Trial (MAPTIP)", US Navy NRaD Technical document 2573, September 1993.

13. Dave, J.V., "Subroutines for computing the parameters of the electromagnetic radiation, scattered by a sphere", IBM, Palo Alto Scientific Center, 1968.

14. Hancock, J.H., and Livingston, P.M., "Program for calculating Mie scattering for spheres, using Kerker's formulation, over a specified particle-size distribution", Naval Research Laboratory Washington DC report 7808, 1974.

15. Liu, W.T., Katsaros, K.B., and Businger, J.A., "Bulk parameterization of air-sea exchanges of heat and water vapor including the molecular constraints at the interface", J.Atmos.Sci, *36*, 1979, pp 1722-1735.

16. Davidson, K.L., Frederickson, P.A., and De Leeuw, G., "Surface layer turbulence and aerosol profiles during MAPTIP", AGARD conference on Propagation Assessment in Coastal Environments, Bremerhaven, Germany, 19-22 September 1994.

17. Monahan, E.C., and O'Muircheartaigh, I.G., "Whitecaps and the passive remote sensing of the ocean surface", Int.J.Remote.Sensing *7*, 1986, pp 627-642.

# Aerosol Profiles Near the Sea Surface During MAPTIP

**Stuart G. Gathman**
Ocean and Atmospheric Sciences Division
NCCOSC RDTE DIV 543
53170 WOODWARD ROAD
SAN DIEGO CA 92152-7385
USA

## SUMMARY

The large sized aerosol which are found just over the sea in high wind conditions affect infrared (IR) propagation in paths that pass very close to the surface. These aerosol are produced by various air and sea interactions. Various processes by which aerosol are formed and injected into the lowest layers of the marine atmosphere have been identified. One of these is the production of film and jet drops by the bursting of air bubbles at the sea surface, a process which is initiated by the entrainment of air into the upper layers of the ocean by the breaking of the waves. An additional mechanism is the formation of spume drops produced through the tearing of wave crests by the wind. Unlike smaller particles, the largest of these droplets will not mix throughout the marine boundary layer because of the overriding effects of gravity on these larger particles. This should result in significantly higher numbers of large aerosol close to the water surface than are found at higher altitudes. The larger particles are more effective at scattering IR radiation from a beam passing close to the tops of the wave crests. Therefore, a knowledge of the aerosol properties in this area is necessary to determine the optical / IR properties of the path. The Marine Aerosol Properties and Thermal Imager Performance (MAPTIP) experiment was designed to determine the profiles of the full size range of aerosol in the first 15 meters above the water surface under differing weather and wave conditions.

Aerosol data taken during MAPTIP by NCCOSC RDT&E Div (NRaD) at the Meetpost Noordwijk (MPN) tower (52.2739° N, 4.2961° E) were used to determine the profile of aerosol during this period. The aerosol size distributions obtained from 1/2 hour averages were all converted to four aerosol extinction values for the wavelengths of 0.55, 1.06, 3.5 and 10.6 microns. The data obtained were shown to be from four different scenarios. First of all, during one period of very high relative humidity values, fog conditions were encountered which gave very high extinction values. There were also times when the data was apparently contaminated by eddies from the tower which contained the exhaust from the power generator. However, most of the data came from two other regimes which could be easily separated in the data set. The times when the wind was from the north, the aerosol were more truly marine in nature. The rest of the time there was a strong continental component of the aerosol coming to the tower from the towns and factories to the east. This paper shows the profile of extinction from 12 meters to the water's surface for the oceanic type of aerosol as it is affected by the wind and other factors. Profiles of relative humidity from measurements and models are used to determine the extent to which extinction profiles would be modified by the growth of hygroscopic particles. A log curve is fitted to the open ocean data from MAPTIP to describe the variation in extinction from shipboard levels to the tips of the surface waves.

## 1. INTRODUCTION

Atmospheric aerosol can both scatter and absorb electromagnetic radiation. Thus they have a potential adverse effect on the operation of optical and IR systems. Aerosol models have been developed to describe the size distribution and chemical properties that clouds of aerosol might have in the real atmosphere under certain meteorological conditions. Once the size distribution and the index of refraction of the aerosol are known, then with the assumption that the aerosol have spherical shapes, Mie theory is invoked to provide the scattering, extinction, and other electro optical properties of the aerosol cloud.

The need for a model to accurately describe the atmosphere's optical and IR properties in terms of its meteorological state has been an important driving force for the development of the Navy Aerosol Model (NAM) and its extension, the Navy Oceanic Vertical Aerosol Model (NOVAM). Ideally, this model should describe the optical and/or IR properties of the atmosphere by only using easily obtained meteorological data as input. Several atmospheric "windows" exist in which the molecular absorption of the electromagnetic energy is relatively small and through which IR transmission and communication can take place. In these windows, the natural atmospheric aerosol plays an important part in degrading the transmission of radiation from point A to point B. This is done when the aerosol both scatters and absorbs electromagnetic energy. Of particular interest to the Navy is the role natural marine aerosols

*Paper presented at the Sensor and Propagation Panel Symposium on "Propagation Assessment in Coastal Environments" held in Bremerhaven, Germany 19-22 September 1994.*

play within the marine boundary layer (MBL) in causing extinction at visible and infrared wavelengths.

IR extinction over the oceans is known to be a function of various meteorological parameters such as absolute humidity , relative humidity (RH), and wind speed. The optical and IR properties of the MBL are related by NAM to the meteorological quantities that are measurable from a shipboard environment. NAM has certain limitations, however, because it was developed from a limited data base containing only measurements made at or near the shipboard level. It is essentially a non-dimensional model that contains no real vertical structure.

The aerosol size distribution may be represented by any number of different functional forms based on the intuition of the individual investigator. The lognormal type functions have been used by this author because there is a close relationship between statistical quantities and these functions. The NAM and NOVAM use a form of lognormal which differs somewhat from other published forms of the function. The NAM [1] was developed from a set of field data taken largely from deck height observations from ships and other special type of measurement platforms. While this model seems to describe the physical characteristics of the aerosol at the shipboard levels for which it was designed, the NOVAM [2,3] model has been developed to extend the useful range of NAM to above the marine boundary layer so that changes in the aerosol properties could be determined as a function of altitude.

There is evidence [4] that the extension of the region of validity of the model from deck height to the sea surface may also be important during high wind conditions when large aerosol are produced by mechanisms such as spume production [5]. This region is very important to naval applications since a line-of-sight path between two separated points near the sea surface may graze this region. This is a difficult area in which to obtain measurements when wind is high because of wave action and other problems associated with storms at sea. It is the purpose of this paper to test the aerosol size distribution data obtained from MAPTIP to see if variations in extinction exist between deck height observations and the sea surface.

## 2. THE AEROSOL PROFILE EXPERIMENT

One of the main objectives of the MAPTIP experiment was to make profiles of aerosol size distributions and appropriate meteorological observations within 10 m of the ocean surface [6]. To accomplish this goal, a simple wooden instrument box was constructed which could house the working parts of several instruments. The devices installed in the box were a Particle Measurement Systems, Inc., ASSP-100 aerosol spectrometer, four remotely activated rotorod motors, and a Rotronic Relative Humidity probe (Model MP-100 ). The aerosol spectrometer counts and sizes aerosol from 0.5 to 30 μm diameter. The air flow through the instrument was maintained by a fan which ventilated the apparatus with a wind speed of 26.45 m/s. The data from the rotorod devices have not yet been completely analyzed at the time of this writing but will be reported on later.

The box could be raised and lowered by means of a steel cable from a motorized winch installed on the tower. The box was lowered until the tips of the highest waves just missed the bottom of the box. Each profile was accomplished by setting the box at a particular level and letting the ASSP obtain a half hour sample of aerosol at that level. The length of the marked cable between the box and the winch, the height of the winch above mean water level and the height of the tide was used to determine the height of the box above the mean tide level. Because the box could not go lower than the tops of the highest waves, the measurement could be several meters in height above the mean tide level during heavy seas. This is a limit of this technique and precludes getting data right at the surface of the sea in areas between waves.

In addition to the data obtained by the instruments on the aerosol box, other meteorological measurements were taken by colleagues of MAPTIP and are used in part for the analysis in this paper. A considerable amount of supporting meteorological data is available from MAPTIP. These data came from radiosonde and surface reports from UK and Continental cities, from the research ship Hr.Ms. TYDEMAN, from the measurements made by MAPTIP colleagues at the beach station, from French and American MAPTIP buoys, from the MPN tower and from other North Sea observatories. From these data , a set of consensus meteorological data were obtained for the major weather elements and used in this analysis.

### 2.1 The Relative Humidity Profile

Relative humidity variations within the vertical range of the aerosol box motion will have an effect on the aerosol size distributions that are measured. If there are real variations in the relative humidity in the profile range, these will cause individual aerosol to swell or shrink and cause apparent changes in the size distribution which are not related to the dry size number concentrations in the atmosphere. Therefore, the profiles of relative humidity must be made during the profiles so that these hygroscopic growth effects will not interfere with the conclusions of the

experiment. Therefore, a series of relative humidity measurements made at different levels and the plotted results from a relative humidity profile model were done with each experimental aerosol profile. These relative humidity profile measurements consist of data from the Rotronic relative humidity device located on the aerosol box, the consensus relative humidity at 10 meters, the relative humidity from the French Meteorological Buoy close to the sea surface, and two relative humidity sensors fixed at 4 and 12 meters on the MPN tower. In addition, a theoretical plot of the relative humidity profile using the Liu, Katsaros and Businger, LKB, model [7] was superimposed on the plots of measured data.

The relative humidity profile measurement data (an example of which is shown in figure 1) had the usual spread of data values associated with relative humidity measurements. The error bars of a plus or minus a few percent is typical and is not too much of a problem so long as the relative humidity is 90% or less. However, at the higher relative humidities, there is more uncertainty in the accuracy of the measurement.

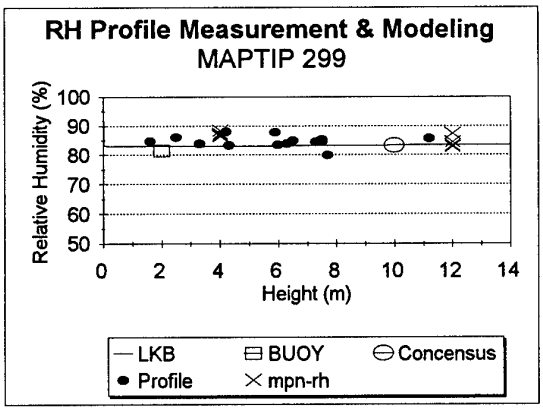


**Figure 1:** A typical profile of relative humidity is shown above for Julian Day 299. In this plot are shown the French Buoy measurement, the consensus relative humidity measurement, the relative humidity values at 4 and 12 meters from the TNO instrumentation on MPN and the NRaD measurements from the ASSP box during which time the measurements were made. The line in the measurement is relative humidity profile model based on the LKB model of Liu & Blanc, [7]. This plot shows that under the conditions of MAPTIP, there are essentially constant relative humidity values until we approach very close to the surface. Here there must be a large gradient in relative humidity since we know that the value must be 98% at the water's surface.

In order to determine the overall growth of the particles with respect to the ambient relative humidity, the simplified formulation of Fitzgerald [8] shown in equation 1 can be used for illustration.

$$f = \left[ \frac{2 - \frac{RH}{100}}{6\left(1 - \frac{RH}{100}\right)} \right]^{\frac{1}{3}} \qquad (1)$$

In this equation the growth of the hygroscopic aerosol is expressed by the factor "f" which is the ratio of the diameter of a particle at the current relative humidity (RH) with respect to the diameter of that same particle if it were exposed to a ambient RH of 80%. The factor "f" is 1 at RH = 80% and grows when RH increases towards 100%. A plot of the swelling factor "f" shown as a function of relative humidity is shown in figure 2.

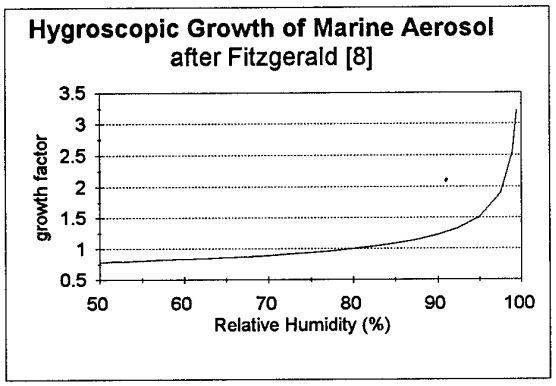


**Figure 2:** The swelling factor or growth factor for a typical marine aerosol as given by Fitzgerald is plotted in this figure. Here we see that the higher the relative humidity, the more sensitive is the size of a typical particle to changes in the relative humidity.

It is concluded, with one possible exception, that within the height ranges used during MAPTIP, the hygroscopic growth of aerosols due to changes in the relative humidity along the vertical profile is not a major contributor to changes in aerosol size distribution. On Julian day 304, October 31, fog was encountered. During the profile of this day the consensus relative humidity was over 95%, thus the accuracy of the relative humidity instruments decreases, and the sensitivity of the aerosol growth factor to changes in relative humidity increases. The coupling of these two factors makes it difficult to determine if and how much change in the size distribution with respect to height is due only to relative humidity growth on this day.

## 2.2 Aerosol Size Distributions

The ASSP device provides 60 different sized aerosol counter bins. These counts, together with the known width and mid size of these bins, the time the counters are active, the size of the active region, and the air flow through this region are required to obtain to an aerosol size distribution. The 60 channels are divided into four ranges which have some overlap with each other, but when taken together cover the full range of 0.5 to 30 micron diameter. All of the data obtained in 1/2 hour of recording for all 60 channels were used in this analysis. The data was fitted to a 6th order polynomial for each observation. An example of one of these polynomial fits is seen in figure 3. In the very largest diameter channels, there are sometimes no counts found even over the half hour sample. In these cases with zero counts, the data was eliminated from the fitting process. In addition to the parameters needed to describe the polynomial, a correlation coefficient to indicate a measure of the scatter in the experimental points for that sample and the size of the largest sample with data in it were recorded. Obviously, the closer the correlation coefficient is to 1 the more self consistency there is in the experimental sample.

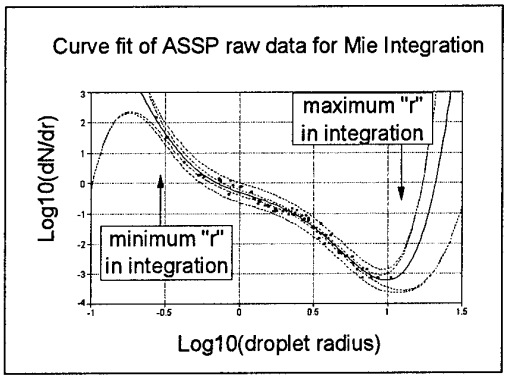


**Figure 3:** This is a plot of the fitting of the ASSP data from experiment 4b on Julian Day 291 to a 6th order polynomial. The center curve is the fit while the outside two curves represent envelopes of two sizes into which the data will fit. The data here are plotted on a log-log plot and the polynomial represents the log-log equivalent of the size distribution dN/dr for the observation. Note that the approximation is only good for the region between the smallest measured size of aerosol and the largest measured size of aerosol. The portion of the polynomial between these two end points is used as the dN/dr value for the Mie integration.

Several initial comparisons have been made of the aerosol size distributions measured with the various aerosol spectrometers mounted on MPN. The NRaD instrument was compared with the UMIST and TNO fixed point aerosol spectrometers, when all instruments were located at approximately the same height but at different locations about the tower. A non-regular inconsistency was observed where at times all three of the size distributions matched each other to a reasonable degree, other times only 2 of the 3 matched, while at other times, there was a significant disagreement among all of the instruments. The actual cause of this inconsistency is not really known at this time, but it was obvious that a few of the NRaD ASSP spectra were very noisy and inconsistent. These cases can be distinguished by relatively low values of the correlation coefficient between the points and the polynomial fitted to the data. In an effort to eliminate instrumental differences, the profiles discussed in this paper were made with the same instrument mounted at different heights. Because at some times a single ASSP channel might seem to be particularly noisy, it is felt that the best way to represent the overall characteristics of the aerosol spectra as it affects the transmission of optical and IR signals is to use the fitting program which combines all 60 channels into a more manageable number of parameters which represent the main size distribution. In the end, however, what is important is the effect of the total aerosol spectrum on the extinction to optical and IR radiation. To this end, the aerosol size distribution represented by the 6th order polynomial was again integrated into four numbers using Mie Theory which represent extinction of the aerosol to radiation at four wavelengths which represent the practical windows in the atmosphere.

## 2.3 Extinction Data

The extinction coefficients for the wavelengths of 0.55, 1.06, 3.5 and 10.6 micron were calculated from the 6th order polynomial which represented the dN/dr of the aerosol size distribution. The polynomial was integrated between the limits of the smallest and largest radii which had non-zero dN/dr. In this calculation, the Mie coefficient was obtained from [9], and a population of droplets with sea salt type of index of refraction was assumed for the integration. Extinctions for all four wavelengths were obtained for all NRaD observations taken during MAPTIP. In an effort to investigate the disagreement among instruments located on the tower, a box-and-whisker plot of all of the NRaD data was made for the four extinction values at the four wavelengths. This plot, shown in figure 4, is used to look for anomalies in the data. The line in the middle of the box represents the median or 50th percentile of the data. The box extends from the 25th percentile to the 75th percentile, the so-called interquartile range. The lines emerging from the box are called the whiskers and they extend to the upper and lower adjacent values. The adjacent

values are formally defined as three-halves the interquartile range rolled back to where there is data. Observed points more extreme than the adjacent values are referred to as outside values and are individually plotted. It is interesting to note that eliminating the observations which give the outside points to the 0.55 micron plot also eliminates the outside points of all of the others. There is a strong correlation between wavelengths for values in each of the outside points indicating that they probably belong to a set of observations in which either there is contamination of the samples from the generators on the tower, or perhaps these are indications of fog formation processes taking place where all of the aerosol grow to large sizes.

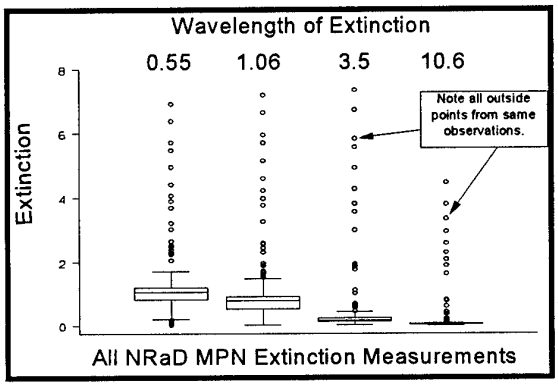


**Figure 4:** Box and Whisker plots of all NRaD's MPN extinction measurements shown for the four wavelengths of interest.

Some of these points do occur during a fog event which occurred on the tower on Julian day 304. Indeed when we exclude these data, most but not all of these outside points disappear. In the analysis which is to follow, I will eliminate these observations and concentrate on the more natural processes taking place. I will now refer to the data remaining after we eliminate these abnormally high extinction points as "selected data".

Using the selected data set, we now show a histogram of the extinction values. In figure 5 we see a plot for the visible wavelength (0.55 microns). Here there is a clear indication of a double hump indicating two classes of extinction data. If we look at the times that the first hump data were taken we see that this group contains all of the selected data in the time range of Julian Day 291 through 297. This group contains no data taken later than day 297. Just the opposite is true for the data in the second hump which contains no selected data taken during the first period but only in the second period. Clearly, during the first period, the prevailing wind was coming from a northerly direction and was essentially uncontaminated by the various coastal sources. On the other hand, during the second part of the experiment the air mass trajectory swung around and came mainly from the European Continent. These data are those represented in the second hump.

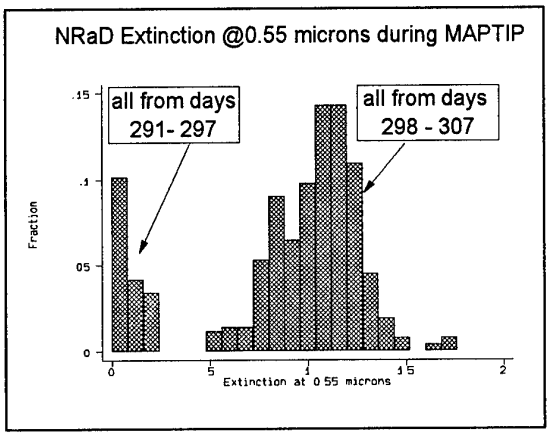


**Figure 5:** This is a histogram of the 0.55 micron data after all of the outside points shown in figure 4 have been eliminated. This graph shows a curious double hump which can be explained by when the data were taken. It is related to the direction from which our sample was coming. There are two species of aerosol here and they have different physical characteristics.

If we look at some of the properties of the aerosol in these two groups, we will see that there is indeed quite a difference in them. In particular, if we look at the correlation values for each of the extinction wavelengths with respect to a parameter like wind speed, we see that there is a very marked difference in these populations. Table I shows the correlation coefficients between the extinction at the four wavelengths and the wind speed at their time of measurement. A very significant positive correlation exists for all of the extinctions of part I whereas in part II of the experiment, there is a negative correlation coefficient, indicating that the aerosol was not being generated by wind ruffled waves but rather the aerosol were being mixed throughout a deeper mixing layer for these times of high wind.

## Table I
## Correlation coefficients between extinction values and wind speed for all selected data with relative humidity < 94%

| wavelength | λ=0.55 μ | λ=1.06 μ | λ=3.5 μ | λ=10.6 μ | # of obs. |
|---|---|---|---|---|---|
| part I of exp. | 0.8266 | 0.8277 | 0.7710 | 0.7151 | 47 |
| part II of exp. | -0.2957 | -0.4391 | -0.4780 | -0.3007 | 188 |

This mixing process is illustrated in figure 6 where the consensus wind speed for the MAPTIP experiment is plotted along with the inversion height at the MPN tower as measured by the temperature profiles made with the NRaD aircraft. The figure shows a strong correlation between the wind speed and the inversion height. The interpretation here is that with the stronger wind speed there was more volume in the MBL and the continental sources of aerosol were more diluted.

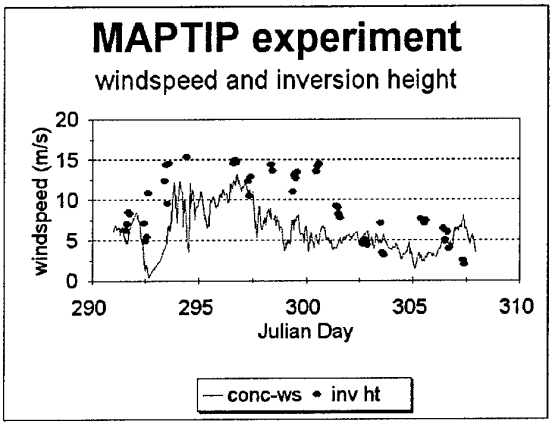


**Figure 6:** A time series of the measured inversion height above the MPN tower as obtained from the NRaD aircraft soundings and the consensus wind speed measurements for MAPTIP. The time is plotted as Julian Day, where day 290 is 17 Oct. 1993.

There were some high wind times in the later period, where the wind was coming from the shore. But in order to look at what is really happening with respect to the possible production of aerosol at the sea surface and how this will effect the aerosol profiles, it is apparent that the data from the last part of the experiment must be eliminated from the data set. This is necessary because even though the processes may have existed during this time, they were completely masked by the continental aerosol in the area. This cuts down the available data we had from MAPTIP, but there is sufficient data in the few profiles we collected to make some general comments on the behavior of the aerosol profile.

### 2.4 Extinction Profiles

In the following series of plots, the extinction profiles are shown for all four wavelengths. In order to accomplish this on the same graph, ratios of extinctions are plotted with respect to the height of the instrumented box above the tide levels. These ratios are defined as the ratio of the extinction at a height z with respect to the extinction at the lowest level made during the profile. Thus all of the profiles will start at a value of 1 and either increase or decrease with altitude. A decrease in the ratio indicates that there are more aerosol at the lower levels than there are at the higher levels. Also shown in the plot is a rectangle which represents the measured height of the waves during the profile measurement. On figure 8, note that a very low wind speed was measured and the apparatus was able to be dropped quite close to the surface. In contrast, the sea state in figure 12 was quite high and because the box had to be above the highest wave that might come along, the measurements were made quite high during those periods.

In the series of figures which follow (figures 7 through 14) are shown the extinction ratio plots for the four wavelengths of interest for the profiles in which we know that the contamination by shore based aerosol is at a minimum.

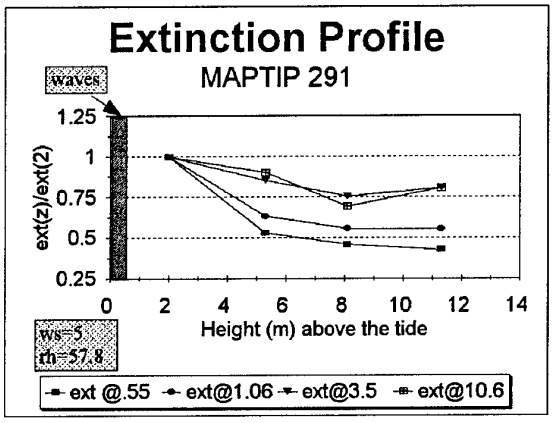


**Figure 7:** Extinction Profiles for 18 Oct. 1993.

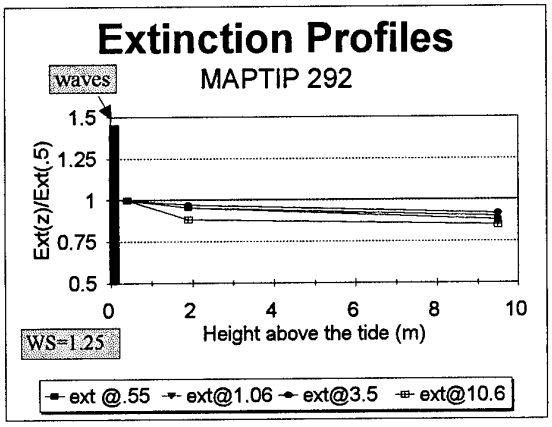


**Figure 8:** Extinction Profiles for 19 Oct. 1993.

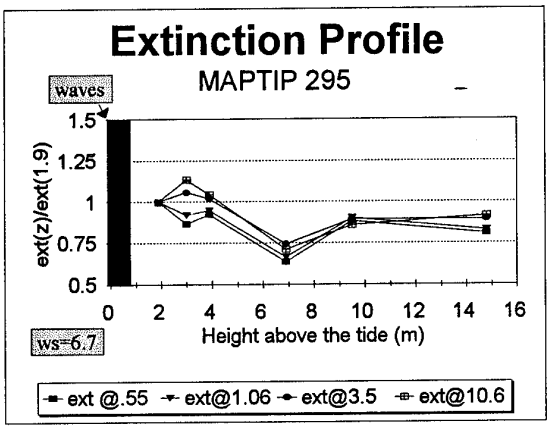


**Figure 11:** Extinction profiles for 22 Oct. 1993.

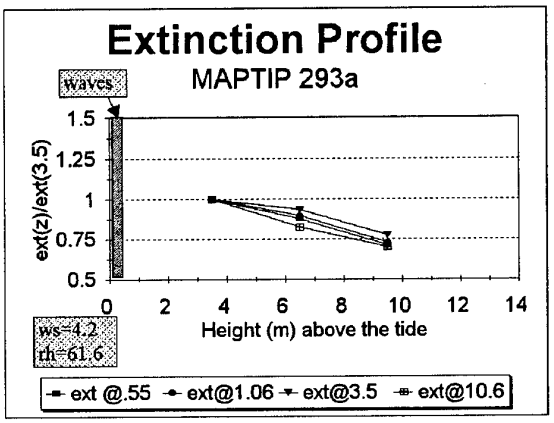


**Figure 9:** Extinction profiles for first experiment of 20 Oct. 1993.

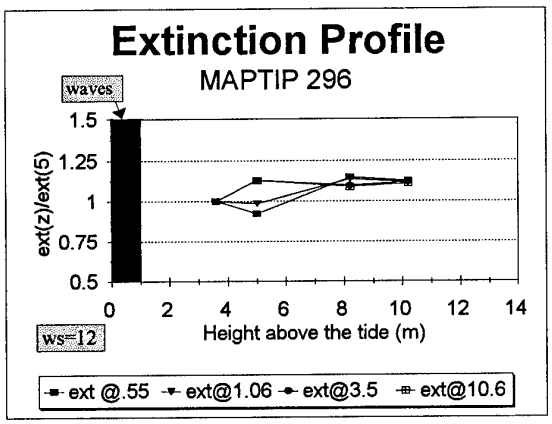


**Figure 12:** Extinction profiles for 23 Oct. 1993.

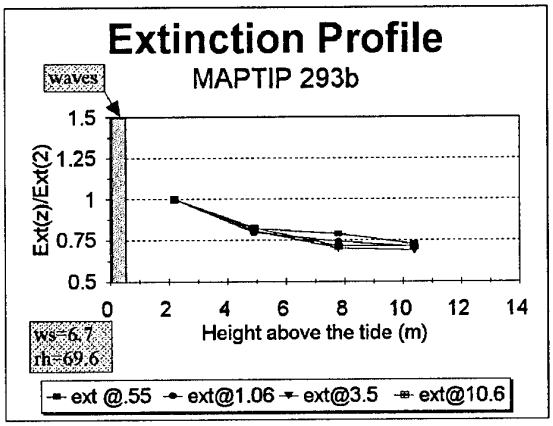


**Figure 10:** Extinction profiles for the second experiment of 20 Oct. 1993.

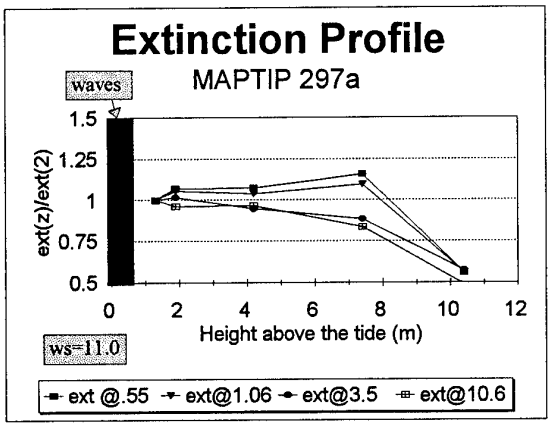


**Figure 13:** Extinction profiles for the first experiment of 24 Oct. 1993.

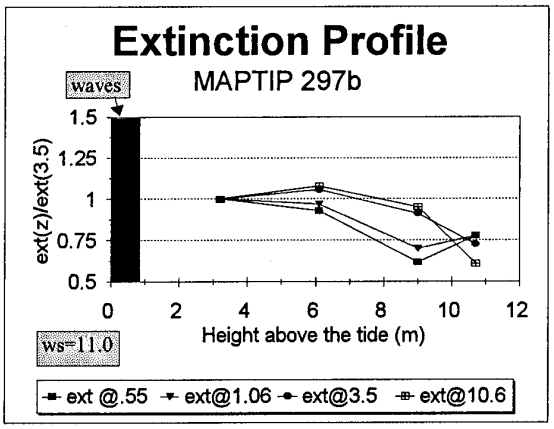


**Figure 14:** Extinction profiles for the second experiment of 24 Oct. 1993.

In the plots shown above, there is of course, a certain characteristic of the shapes when compared with the consensus wind speeds that are listed for each plot. As one would expect, the lowest wind speed case, shown in figure 8, has almost no gradients that were observed. It appears that as the wind speed increases, the general profile picture shows a sort of log decrease with altitude until the times when the high wind speeds were encountered, i.e. days 296 and 297. On these days, the profiles again seem to be almost vertical in extent which might indicate that the scale height of the distribution increases with increasing wind speed. Indeed, in looking at the 11 m/s data on day 297, both profiles show that there is a decrease at altitudes over 10 meters but that the aerosol below 10 meters appears to be well mixed. The highest wind speed experiment shown in figure 12 does not indicate any drop off at higher altitudes but this could still happen if the scale height had risen above that which we could measure.

There really isn't enough data available to make a solid statement as to the behavior of the aerosol profile curve. However, certain features of the profile of the size distribution can be made by looking at some first order approximations.

### 2.5 Linear Approximation to the Profile

The first approximation that can be made is a linear regression of the profile data. We can use the extinction ratio and height data and fit it with a straight line. In this approach the data is fitted to the form

$$Ratio = offset + slope \cdot height \qquad (2)$$

where we wish to see if the slope of this fitted line is related to the wind speed parameter. This relationship is plotted in figure 15. The data shows a general decrease in the slope with increased wind speed but a reversal at the highest wind speed value of 12 m/s. There is too little data here to uncover a statistically significant relationship. Indeed, one could also say that there was no apparent wind speed relationship with the slope parameter.

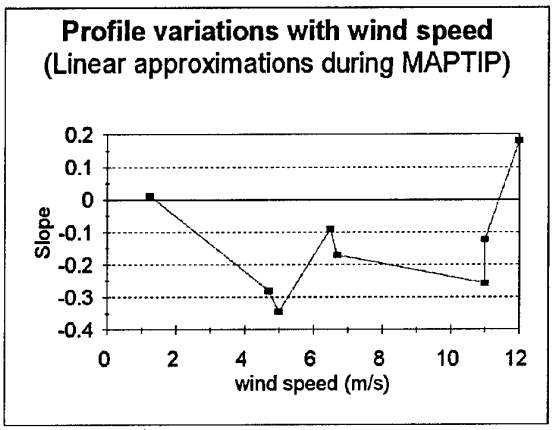


**Figure 15:** The measured relationship between the linear slope of the profile data and the consensus wind speed .

### 2.6 The Logarithm Fit to the Profile Data.

A second process that can be used is to fit a logarithmic profile to the data points and then investigate the behavior of the fitting parameters with respect to wind speed variations. This seems to be a more reasonable approach since most of the profiles have a logarithmic type shape. In this case, the ratio is represented by a formula of the form

$$Ratio = a + b \cdot \ln(height) \qquad (3)$$

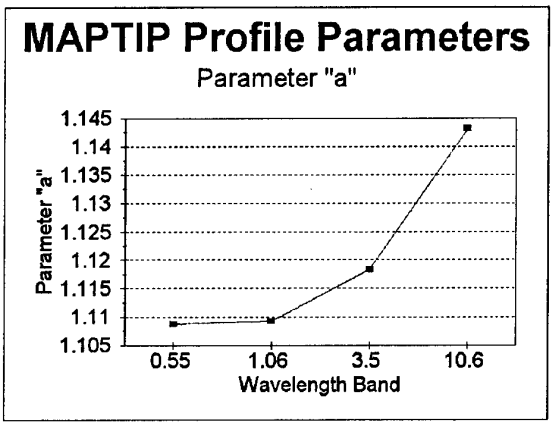


**Figure 16:** The dependence of the parameter "a" with wavelength.

Again, the profile data were fit to this equation form with the parameters "a" and "b" being functions of measurable weather elements. No relationship could be determined for these parameters with wind speed. However the parameter "a" did have a wavelength sensitivity as seen in figure 16.

The parameter "b" showed no strong correlations with either wind speed or wavelength. It had both negative and positive values indicating the surface values were higher or lower than the ratios at higher heights. The mean values of "a" and "b" are shown in table II.

**Table II**
Profile parameters for fitted ratio profile of the form:
*ratio=a+b*ln(z)*

| | "a" | "b" |
|---|---|---|
| 0.55 | 1.11 | N/A. |
| 1.06 | 1.11 | N/A. |
| 3.5 | 1.12 | N/A. |
| 10.6 | 1.14 | N/A. |
| average value | 1.12 | -0.13 |

After this analysis it is possible to reconstruct an average profile for the four wavelengths used. The curve for 3.5 microns will fit for an overall average curve, but slight differences in the "a" parameter with respect to wavelength allow us to plot the different curves on a graph as shown in figure 17.

## 3. DISCUSSION

The Aerosol profile measurements taken during MAPTIP provide a glimpse of the mechanisms affecting the distribution of aerosol in the vicinity of the MPN tower. A series of only 8 "good" aerosol profiles were obtained where data were not contaminated with continental aerosol. During this part of the experiment, a variety of winds speeds from a high of 12 meters per second to a low of 1.7 meters per second were measured. Although this doesn't provide the very high wind speed data necessary to fully characterize the spume drop distribution from a thoroughly aroused sea, it does give a picture of the conditions leading up to the final high wind picture.

The major question that must be asked is: Is there enough data to make a determination as to the structure of the aerosol/extinction profile ? The answer, of course, is no. There are only 3 days of profiles in which the average wind speed during the profiles exceeded 10 m/s. While there is real evidence that there is increased production of large sized aerosol at the sea surface during high wind conditions, the data from the MAPTIP experiment is insufficient to base the final parameter formulation of the very large aerosol in the models. The data does allow us, however, to make an overall determination in the variation of extinction values with respect to height for the various wavelengths based on the average set of log parameters obtained from the measurements.

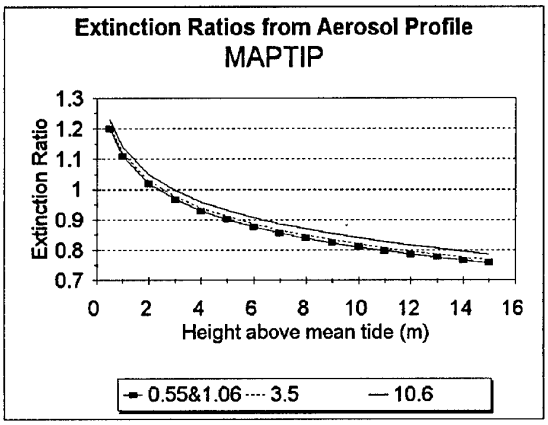


**Figure 17**: This is a plot of the log form of the aerosol profile obtained from the selected set of MAPTIP data. There is no strong wind speed dependence in this limited data set but there is a wavelength dependence showing that the extinction due to the largest aerosol do not mix throughout the boundary layer as well as do the smaller aerosol.

There was, unfortunately, a considerable amount of continental aerosol brought to the tower from the various land sources in the area during the later part of the MAPTIP experiment. When large amounts of these aerosol, produced at land sources, are brought to the tower, the details of the mechanisms from the smaller sources of wind wave production of sea salt aerosol are overwhelmed. This resulted in a more limited set of data with which to work.

## 4. CONCLUSIONS

The aerosol profile experiment of MAPTIP was able to determine real non-constant profiles of aerosol in the marine boundary layer close to the sea surface during a limited number of near marine air mass conditions. For the most part, these experiments indicate that extinction at all of the wavelengths were essentially constant with respect to altitude for the very calm situation but that as the wind speed increased, the values of extinction at the surface were shown to be larger than the extinction measured at higher levels above the mean tide height. Many of the profiles exhibited a logarithmic profile and when all of the marine air mass data were fitted to a logarithmic

equation, an average set of profile parameters was obtained.

The use of the "a" and "b" profile parameters can be used to determine the extinction ratio between the measured extinction and the extinction at the average lowest level of 2 meters.

**ACKNOWLEDGMENTS**

I wish to thank Mrs. K.M. Littfin for her excellent help in preparing the instrumentation and software for doing this experiment and for helping in handling the equipment throughout the MAPTIP experiment. I wish also to thank the MAPTIP scientific committee and especially our Dutch colleagues for their provisions in making this experiment possible. I also wish to thank Dr. Juergen Richter of NRaD who has provided both moral and financial support to carry out this research. I wish to thank ONR code 322 for the support of this project.

**REFERENCES**

1. Gathman, S.G., "Optical properties of the marine aerosol as predicted by the Navy aerosol model", Opt. Eng., 22, 1, pp. 057.
2. Gathman, S.G., Jensen, D.R., Hooper, W.P., James, J.E., Gerber, H.E., Davidson, K., Smith, M.H., Consterdine, I.E., de Leeuw, G., Kunz, G.J., Moerman, M.M., "NOVAM Evaluation Utilizing Electro-Optics and Meteorological Data from KEY-90", NCCOSC, RDT&E div. Technical Report 1608, September 1993.
3. Gathman, S.G., Davidson, K.L.,"The Navy Oceanic Vertical Aerosol Model", NCCOSC, RDT&E div. Technical Report 1634, Dec. 1993.
4. de Leeuw, G., "Aerosols near the air-sea interface", Trends in Geophys. Res. 2, 1993, pp55..
5. Monahan, E.C., D.E .Spiel, and K.L. Davidson, "A Model of Marine Aerosol Generation Via Whitecaps and Wave Disruption", in E.C. Monahan and G. Mac Niocaill (eds), "Oceanic Whitecaps", D. Reidel Publishing Company, 1986, (ISBN 90-277-2251-X), pp 167-174.
6. Jensen, D.R., and de Leeuw, G., "Work Plan for the Marine Aerosol Properties and Thermal Imager Performance Trial (MAPTIP)", NCCOSC, RDT&E div, Technical Report 2573, September 1993.
7. Liu, W.T. and Blanc, T.V., "The Liu, Katsaros, and Businger (1979) bulk atmospheric flux computation iteration program in FORTRAN and BASIC" NRL Memo Report 5291, May 1984..
8. Fitzgerald, J.W., "On the Growth of Aerosol Particles with Relative Humidity," NRL Memorandum Report 3846, 1978.
9. Dave, J.V.,"Subroutines for Computing the Parameters of Electromagnetic Radiation Scattered by a sphere", IBM Palo Alto Scientific Center Report #320-3237, 1968

## DISCUSSION

**S.D. BURK**
Several papers in this conference suggest a need for improving aerosol models in the surface layer (e.g., models such as NAM). You show a significant correlation between extinction, wind speed, and boundary layer depth. The implication is that aerosol, being mixed throughout the full depth of the marine boundary layer $Z_i$, is affecting the value in the surface layer. Thus, do you think it is feasible to develop a surface layer aerosol model that doesn't account for the physics/dynamics throughout the full depth of the boundary layer, i.e., do we need to include prediction of $Z_i$? In surface layer similarity theory for parameters such as temperature and moisture, account must be taken for boundary layer depth ($Z_i$) as so-called free convection conditions are approached because large eddies that extend through the depth of the boundary layer have a substantial impact on the surface layer. This type of $Z_i$ - dependence may impact the aerosol in the surface layer a great deal of the time, not just under free-convective conditions. This would make it very difficult to develop a surface-layer aerosol model that doesn't deal with the full dynamics of the entire boundary layer.

**AUTHOR'S REPLY**
Your comments are certainly right, in that the more information we know about a particular situation, the better off we are in trying to describe it. In the MAPTIP data shown for "the open ocean" conditions, the generator process was dominant. When the aerosol is advected to the site, as in the coastal aerosol condition, the concentration more clearly depends on the $Z_i$. The more advanced NOVAM model takes $Z_i$ into account in its predictions.

**K. DAVIDSON**
How did the length of time required to obtain an aerosol profile affect your results?

**AUTHOR'S REPLY**
The profile time is somewhat of a compromise in that ½ hour of sampling is needed to get a solid size distribution resulting in a total profile time of more than two hours. Conditions could possibly change during this time period, however the two plots for Julian day 293 are not too different. The same can be said for the double profile on Julian day 297.

**D. DION**
In the measured extinction profile graphics shown during the presentation, what can be concluded from the noted differences between profiles as a function of the wavelength?

**AUTHOR'S REPLY**
The wavelength dependence of the profiles is not as apparent as I would have expected. I don't know if this is because there is no dependence or if we don't have enough data for it to be statistically significant.

# Aerosol Maps Made During MAPTIP

**Stuart G. Gathman**
**Douglas R. Jensen**
Ocean and Atmospheric Sciences Division
NCCOSC RDTE DIV 543
53170 WOODWARD ROAD
SAN DIEGO CA 92152-7385
USA

## SUMMARY

In coastal areas, the simplifying assumptions of horizontal homogeneity used in open ocean analysis are not always useable. Various human-generated aerosol sources such as towns and industrial centers can provide a complex portrait of merging plumes of non-natural aerosols which are advected out to the littoral zones. The extensive meteorological and aerosol measurements made during the Marine Aerosol Properties and Thermal Imager Performance (MAPTIP) experiment [1] provided an ideal opportunity to view how these aerosol were advected from their sources to the littoral zone of the North Sea. MAPTIP was conducted along the Dutch coast in October/November 1993. The NCCOSC, RDT&E DIV (NRaD) instrumented Navajo aircraft flew two star pattern flights a day during the experiment at altitudes below 500 feet. During these flights, aerosol size distribution measurements along the flight path were being continuously recorded. These measurements were utilized for making aerosol concentration maps of the various sized aerosol groups. This paper shows the mesoscale effects of aerosol advection making the marine boundary layer in a littoral zone much more complicated than that of an open ocean.

## 1. INTRODUCTION

The Naval Aerosol Model, (NAM) [2] and the Naval Oceanic Vertical Aerosol Model, (NOVAM) [3,4] (which uses NAM as its kernel) have not been shown to represent the coastal areas as accurately as marine or open ocean applications. This is because the data on which NAM was based came largely from the open ocean area.

It is known that in a coastal area where aerosol from industrial sources are advected out to a specific location, these aerosol may well overwhelm the numbers of the oceanic aerosol which are represented in the models. For this reason a coastal aerosol model needs to be developed. MAPTIP produced a good data base for this analysis since the operational period was divided into two distinct parts: an open ocean type of air mass and a continental air mass situation in which the air had been advected from over Europe.

## 2. COASTAL AND OCEANIC AEROSOL

The MAPTIP experiment offered an excellent set of measurements in which to investigate the differences between the coastal and the open ocean aerosol regimes. Gathman [5] has shown that during the experiment times of 18 October and 3 November 1993, both types of aerosol situations were experienced at the Meetpost Noordwijk (MPN), and occurred during different sub-periods of the experiment times.

The NAM/NOVAM set of models were developed for open ocean environments from open ocean data. Extension of these models to coastal regimes with very high air mass parameters has shown from time to time to cause excessive error in the models extinction predictions [6].

The NAM model is a three/four component log normal representation of the aerosol size distribution. It represents the dN/dr of the aerosol distribution by the expression in equation 1.

$$\frac{dN}{dr} = \sum_{i=0}^{3} k_i \cdot \frac{A_i}{f_i} \cdot \exp\left\{-1 \cdot \left[\log\left(\frac{r}{(r_{0i} \cdot f_i)}\right)\right]^2\right\} \quad 1)$$

where the "$f_i$" parameters are the Gerber [7] growth factors which are functions of the ambient relative humidity, and the "k" parameters are normally unity but can be used for calibration and correction purposes. The mode radii parameters $r_{oi}$ are: .03, 0.24 and 2.0 μm. Amplitudes $A_i$ are determined by various meteorological parameters. Of particular interest is the parameterization of the $A_0$ and $A_1$ terms which are related to the air mass parameter. The original models were developed for the open ocean regime where the air mass parameters were of the order of 2 to 3. Provision was made for the model to represent the aerosol in a more continental air mass by allowing the air mass parameter to increase to larger values. This process works fairly well where the air mass is not totally "continental" in nature. In a truely continental region, the model is very sensitive to the air mass parameter as is shown in table I.

*Paper presented at the Sensor and Propagation Panel Symposium on "Propagation Assessment in Coastal Environments" held in Bremerhaven, Germany 19-22 September 1994.*

## Table I

Sensitivity of NAM extinction predictions to 10% errors in the airmass parameter (a.m.p) for two wind speeds and two wave lengths.

| | % error: 0.55 ext. | | %error: 10.6 ext. | |
|---|---|---|---|---|
| a.m.p. | ws=5 | ws=10 | ws=5 | ws=10 |
| *2* | 7 | 3 | 1 | 0 |
| *8* | 17 | 12 | 6 | 3 |
| *16* | 19 | 18 | 13 | 9 |
| *32* | 33 | 20 | 20 | 17 |

Here several cases were calculated using NAM in which a 10 percent error in the determination of the air mass parameter was assumed. The table shows the percentage error in the visible and far infrared (IR) aerosol extinctions from a 10% uncertainty in the air mass parameter. In the open ocean conditions, when the a.m.p. term is small, the IR determination of aerosol extinction is not really affected by the errors in the a.m.p. Even errors in the visible wavelengths are of the same order of magnitude as the errors in the a.m.p. for low wind regimes. However, when we approach the situations which occur near the coast areas, the aerosol extinction errors increase considerably for the assumed 10% error in the determination of the a.m.p. It is for this and other reasons a coastal aerosol model needs to be developed which will specifically address the description of coastal aerosols.

Determination of the coastal and open ocean regimes during MAPTIP was determined following the technique of Gathman [5]. The extinction data shown in figures 1 and 2 were obtained using the measured aerosol size distribution from a Particle Measurement Systems (PMS) ASSP-100 device located on the MPN. The histogram for the visible wavelength extinction showed two distinct modes with the means separated by an order of magnitude (figure 1).

A time series of this set of data (figure 2) shows clearly how the extinction values at 0.55 μm transition rapidly from the low "open ocean" values during the first part of MAPTIP to an order of magnitude higher during the second period, when air was continental in origin.

It is informative to see if other measurements of visual extinction show the same sort of two mode behavior. The data shown in figures 3 and 4 were obtained from the Canadian participants in MAPTIP [1], the Defense Research Establishment Valcartier (DREV). They operated an HSS Model VF-500-110 Visibility Sensor located near the NRaD ASSP aerosol spectrometer during the experiment. The data in these two figures are expressed in terms of extinction for easy comparison with the extinction calculation obtained from the aerosol measurements. Figure 3 is a histogram of the extinction data showing the same two modes as does the NRaD data. Although the figure here shows relatively more data in the "open" ocean regime than in the "coastal" regime, this can be explained by the amount of times the two different instruments were in operation. The ASSP device was used sparingly during the first half of MAPTIP because of a need to time-share power with other investigators. During the last half of the MAPTIP, however, the instrument was allowed to operate in a more or less continuous mode. The means of the two groups are very close, however.

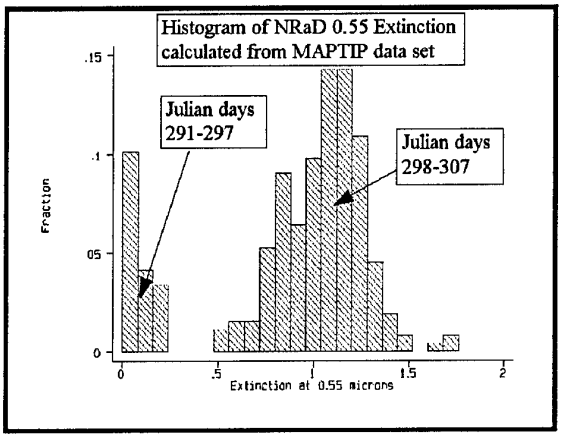


**Figure 1:** Reproduction of the histogram plot obtained by Gathman [5] from the 0.55 micron extinction calculations made from the ASSP data on the MPN tower by NRaD. This plot shows two distinct groups of aerosols which differ by at least an order of magnitude from each other.

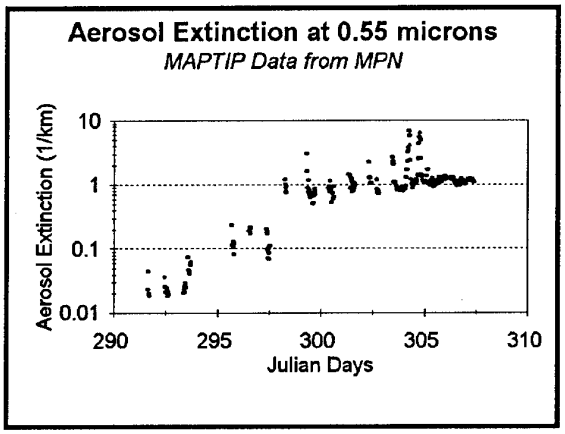


**Figure 2:** Time series of the calculated 0.55 micron extinction made from the 1/2 hour averages of the aerosol size distribution made by the PMS ASSP aerosol spectrometer on the MPN tower during MAPTIP 1993.

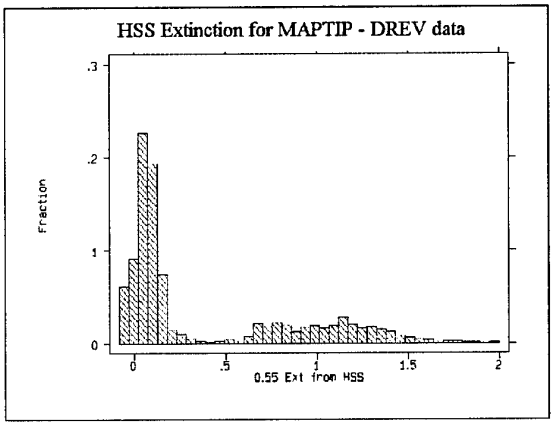


**Figure 3:** There are two distinct groups in the HSS data as well as in the ASSP extinction data.

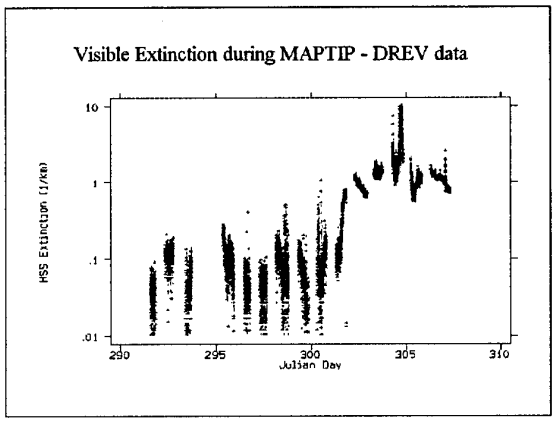


**Figure 4:** A time series plot of the 0.55 micron extinction as measured by DREV's HSS visiometer during MAPTIP 1993.

Figure 4 shows a time series of the Canadian HSS data taken during MAPTIP. It show the same general shape as did the NRaD data except there is a discrepancy between the two data sets as to when the actual transition between "open" ocean to "coastal" regime took place. There is a time difference of about 1 day for this transition. In order to be on the safe side, we will we will define the earliest time for the end of the "open" ocean regime and the latest time for the start of the "continental" regime.

## 3. OTHER INDICATORS OF AIR MASS

### 3.1 Radon

One of the measurable parameters used in the calculation of the a.m.p. in NAM is the radon concentration. The technique of using radon as a tracer of how long an air mass was over water was originally suggested by Larson and Bressan [8]. The reasoning is that radon 222 is only produced over land areas and has a half life of several days. Thus if the air is relatively free from this trace gas, then we know that the air mass has been at sea for several days. It can then be assumed that the various processes in operation to "clean" the air from its original "continental" aerosol state to a more pure "marine" state would be related to the radon concentration. This technique has been hampered by a lack of off - the - shelf reliable measurement systems. (The sensitivity of these devices is about 3 orders of magnitude higher than that needed for routine radon measurements in homes.) Littfin [9] has assembled a reliable automatic radon monitoring device for this purpose. This device was mounted on MPN and produced data throughout the MAPTIP experiment. Shown in figure 5 is a time series of the radon concentration. Here we see that the radon counts change over time from a low during Julian day 301 to a rather rapidly increasing high toward the end of the experiment.

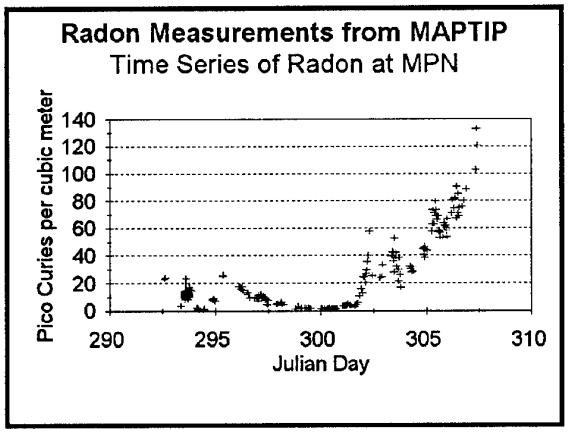


**Figure 5:** A time series plot of measured Radon concentration at MPN during the MAPTIP experiment. Radon gas is used as a tracer of continental air in NAM and NOVAM.

The radon measurements during MAPTIP thus show the two regimes of the air mass as suggested by the aerosol and visibility measurements. The transition time between the regimes agrees with the visibility measurements.

### 3.2 Wind Direction

The wind direction at the tower is an indicator of where the air mass is coming from. Wind direction in and of itself, however, is not a good indicator because of the non-linear nature of the wind direction. For short term indicators it is helpful in determining that the air mass is coming from a certain sector, but slight curvature to the streamlines of wind cause larger

uncertainties as distances increase. Wind direction is thus only a short term indicator of the history of the air mass.

MPN is only 9 km off the Dutch coast. When the wind is from the east, European aerosol should be evident. When the wind is from the general north northeast directions, it should be more representative of an open sea situation. This is evident in the data shown in figure 6.

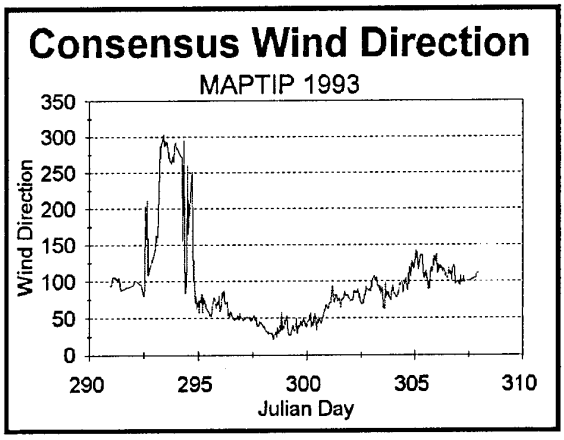


**Figure 6:** A time series plot of the consensus wind direction measurements made during the MAPTIP experiment. Note the "pulse" on day 293 and 294 showing directions from 250 to 300 degrees, which is really from the northwest.

### 3.3 Air Mass Trajectories

Air mass trajectories are very important in understanding the history of the air mass and its changes as it traverses the earth. The Meteorological Office at de Bilt, the Netherlands, produced a series of air trajectories during the MAPTIP experiment. Shown in figure 7 are the trajectories at the lowest altitudes for the experiment.

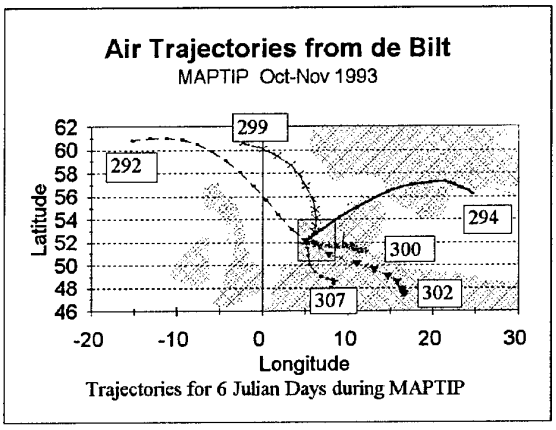


**Figure 7:** A plot of six air trajectories as calculated by the Met Office at de Bilt for the period of MAPTIP superimposed on a sketch of the land masses in the area.

The square at the hub of the spokes is the MAPTIP operational area of interest. The plot shows again the twofold nature of the air masses during MAPTIP, i.e., air coming from the North Sea at the beginning of the measurements and from the central continent of Europe toward the end of the experiment.

Some of the changes in the radon concentration can be related to how long the air mass has been over land. For instance, on Julian day 300, it is indicated that the air has come almost directly from the east. Even though directly east from MPN is industrial Europe, the air spent time over the Baltic Sea and did not pick up additional radon gas. This is confirmed in the time series of radon gas measurements on MPN. Contrast this to the air on Julian Days 302 and 307 where the air was from over central Europe. The radon concentration for this case is very high. This is of course also confirmed by radon 222 measurements (figure 5). This shows the shortcoming of the assumptions made in relating the "continental" aspects of the air mass with its radon content.

## 4. DISCUSSION

The various indicators as to the origin of the air mass during MAPTIP, as determined by the various methods available to the MAPTIP experiment, all agree as to an "open" sea and a "continental " type of air mass being advected into the area by meso scale mechanisms. The techniques discussed above all determine to some degree the type of aerosol at a point. This type of information is essential for determining the air mass type at a point. It is interesting to note the comparison of the radon measurements at MPN to the airmass trajectories. The highest radon concentrations come from the air that had been over the central parts of the continent for a long period of time and the lowest where the air came toward the tower directly over the North Sea.

In summary, the plot shows again the twofold nature of the air masses coming to the MAPTIP area. Air came from the North Sea at the beginning of the measurements and from the central continent of Europe toward the end of the experiment.

## 5. AEROSOL MAPS

In the coastal areas, many sources of aerosol exist. During times when offshore winds are blowing, one would expect that the aerosol content just off shore would not be particularly well mixed in the horizontal directions and various structures would no doubt exist. For instance, there might be plumes of aerosol from several different factories, which, as they are advected offshore would be distinct from each other for several kilometers before they blended together into a single continental air mass. This complex

structure can best be viewed by mapping the coastal aerosol. Several techniques might potentially be used for this purpose. For instance, there were aerosol measurements made aboard H.M.S. Tydeman as it traversed the area throughout the experiment. The speed of the ship, however, limits its usefulness as the structure of the atmosphere can change rapidly with time. Continuous measurements of aerosol were made on the MPN tower and at the shore station as well as on the ship, but this is, at best, only three points on which to base the map. The NRaD aircraft, however, does offer an opportunity to produce such a map because of its speed and the flight path used during MAPTIP.

### 5.1 Aircraft Measurements during MAPTIP

The NRaD aircraft was used for multiple applications, from being an IR target to providing profiles of aerosol and sea surface temperature measurements throughout the experimental region. There were two different flight patterns used during the experiment. One was a vertical spiral made over the MPN tower to make a sounding of the aerosol and the meteorological parameters at the site. The other mode of operation was to fly in a starlike pattern at a relatively low altitude (below 500 feet) ( figure 8).

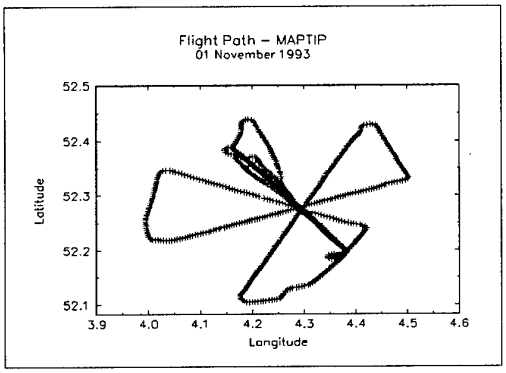


**Figure 8:** The flight path of the NRaD aircraft during the constant altitude phase of the 01 November 1993 MAPTIP experiment. The total flight takes about two hours, so parts of the structure that might change in this time scale would be lost in this technique. The hub of the wheel shape is the MPN tower at 52.2739 degrees North and 4.2961 degrees East.

The position of the aircraft was accurately recorded by a GPS satellite system from Trimble Navigation (model TNL-2000 GPS). It also contained an FSSP_100 (0.5-47μm) and an OAP_200 (30-300 μm) aerosol spectrometer both from Particle Measurement Systems Inc.. These instruments allow us to make some inference as to the aerosol structure in the MAPTIP area of interest.

The speed of the aircraft has both a good and a bad aspect for getting an accurate aerosol map of the area. First of all, the speed is absolutely necessary if the sampling area is to be of reasonable size. A slow moving sensor would take many hours to cover the same area as the aircraft, and the structure of the aerosol may well change during this period of time. However, it is difficult to make statistically significant samples of the larger aerosol when the sample time is on the order of 1 second. Of course, longer sample times would no longer be a point sample. Some sort of compromise must be made in using the aircraft measurements to map the aerosol structure. In this paper we chose to look at the aerosol concentration in the smallest size bin of the PMS system (mean size of 0.375 microns diameter and a width of 0.25 microns). This size range usually has counts of 100 or more every second so that we feel that the counts used in our mapping procedure will be statistically significant. It does not however address the more interesting geographical structure of the larger aerosol, which will affect IR transmission the most. However, these small particles will provide a map by which we can see something of the structure of the aerosol during the various phases of MAPTIP.

### 5.2 Aerosol Maps

In the process of carrying out the MAPTIP experiment, the NRaD aircraft made a number of "star" pattern flights each day. These flights were carried out at a relatively low altitude and were interspersed with vertical spirals. These low constant altitude flights obtained a considerable amount of information on the concentration of aerosol in a widely diverse spatial array.

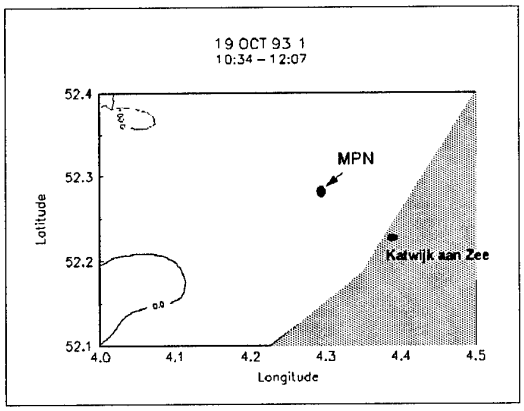


**Figure 9:** An aerosol concentration map made during 19 Oct. in which measurements at the MPN tower indicated an essentially "open" ocean aerosol environment. The pockets of aerosol seen here may or may not be from ships traversing the region but it is felt that they could indeed be from noise sources either in the data itself or from the interpolation needed in the contouring of irregular data.

The profile data was processed using only the constant altitude data. Latitude, longitude and aerosol concentration from range 1 were used as an input to an irregular data contour plotting package called *Axum*, from TriMetrix, Inc. The flight pattern was not ideal for use in a contour plot but by increasing the grid sizes for the irregular data, a reasonable plot could be obtained. Figure 9 shows a typical "open" ocean situation in which our point measurements at MPN indicated a non coastal aerosol regime. We see that there are few aerosol and there is no indication of plumes leaving the shore. On the other hand, the data shown in figure 10 is for the period where our platform measurement indicated that we were indeed in a coastal aerosol regime. This plot shows the evidence of aerosol plumes leaving the coast and overtaking the tower.

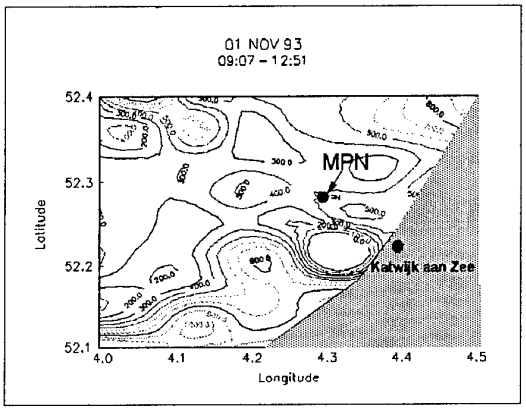


**Figure 10:** This is a map of the MAPTIP area during the period when the measurements at MPN indicated that there were indeed coastal aerosols in the region.

## 6. CONCLUSIONS

The maps shown in figures 9 and 10 indicate that there is considerable structure in the concentration of the smallest measured sizes of coastal aerosol during MAPTIP. Differences in the plumes from various land based sources can well cause differences in identical measurements made at the same time but in physically separated places. The maps show that trying to model the coastal aerosol will be a difficult job if detailed structures are to be included.

Although the flight path shown in figure 8 was not designed for contouring purposes, an adequate map could be produced which shows the main structures in the experiment area. However, by carefully adjusting the flight path to improve the contouring effort, more detailed structures could be obtained.

The complex nature of the coastal aerosol and its non-uniform horizontal distributions show why a simple model such as NAM, designed for the "open" ocean environment where horizontal homogeneity is the norm, can not be adequately applied to coastal aerosol. Because of the importance of these waters to the modern Navy, an extensive effort should be expended to provide a meso scale coastal aerosol model which can adequately take into account the complex structures of a coastal environment.

## ACKNOWLEDGMENTS

We wish to thank the MAPTIP scientific committee and especially our Dutch colleagues for their provisions in making this experiment possible. We also wish to thank Dr. Juergen Richter of NRaD who has provided both moral and financial support to carry out this research. We wish to thank ONR code 322 for the support of this project.

## REFERENCES

1. Jensen, D.R., and de Leeuw, G., "Work Plan for the Marine Aerosol Properties and Thermal Imager Performance Trial (MAPTIP)", NCCOSC, RDT&E div, Technical Report 2573, September 1993.
2. Gathman, S.G., "Optical properties of the marine aerosol as predicted by the Navy aerosol model", Opt. Eng., 22, 1, pp. 057.
3. Gathman, S.G., Jensen, D.R., Hooper, W.P., James, J.E., Gerber, H.E., Davidson, K., Smith, M.H., Consterdine, I.E., de Leeuw, G., Kunz, G.J., Moerman, M.M., "NOVAM Evaluation Utilizing Electro-Optics and Meteorological Data from KEY-90", NCCOSC, RDT&E div. Technical Report 1608, September 1993.
4. Gathman, S.G., Davidson, K.L.,"The Navy Oceanic Vertical Aerosol Model", NCCOSC, RDT&E div. Technical Report 1634, December 1993.
5. Gathman, S.G., "Aerosol Profiles Near the Sea Surface During MAPTIP", AGARD CP 567, pp 20.1-20.10, 1994.
6. de Leeuw, G., "Aerosols near the air-sea interface", Trends in Geophys. Res. 2, 1993, pp55..
7. Gerber, H.E., "Relative-Humidity Parameterization of the Navy Aerosol Model (NAM)", NRL Report 8956, December 1985.
8. Larson, R.E. and B.J. Bressan, "Air Mass Characteristics Over Coastal Areas as Determined by Radon Measurements", preprint volume: 2nd Conference on Coastal Meteorology, Jan. 30-Feb. 1, 1980, Los Angeles, published by A.M.S., Boston.
9. Littfin, K.M.,"Technical Manual, Redesigned ARC-2A Automatic Radon Counter", Technical Document 2395, September 1992.

## DISCUSSION

**J. ROSENTHAL**

In tracing, mapping, and explaining the source of aerosols, we have found during air pollution studies in Southern California that one must use winds at levels above the surface (e.g. near 500 m). The surface wind may be unrepresentative of the air source because it may be a local (westerly) sea breeze within an overall easterly polluted flow.

**AUTHOR'S REPLY**

The air mass trajectories shown were done for a constant pressure of 800 mb, or for the lowest level. The trajectories for pressure levels 500 mb and less show generally the same path so I think this doesn't matter too much for the MAPTIP experiment. Additional experiments should take several levels into account in this analysis.

# UMIST OBSERVATIONS OF ACCUMULATION MODE AEROSOL CONCENTRATIONS AND COMPOSITION DURING MAPTIP

**Michael H Smith**
Pure and Applied Physics Department
UMIST
P O Box 88
Sackville Street
MANCHESTER M60 1QD
United Kingdom

## 1. SUMMARY

The primary contribution of the UMIST Group to the MAPTIP campaign consisted of measurements of the concentration and composition of the accumulation mode aerosol ($0.05 < r < 1.0\mu m$). Direct measurements of soot carbon concentrations, by means of an aethalometer, demonstrated its ubiquitous presence throughout most of the trial. A thermal analytical technique was employed to determine the size-differentiated composition of the aerosol and confirmed that these soot carbon particles dominated the aerosol spectrum below about $0.1\mu m$ in radius, with substantial particulate sulphate contributions for radii from 0.1 to $0.5\mu m$. The light winds and short fetches during most of the campaign meant that the sea salt contribution to this small aerosol was generally slight. However, a brief period of northerly winds during the measurement period gave significant sea salt loadings for radii from 0.2 to $0.5\mu m$.

## 2. INTRODUCTION

The UMIST Group contributed to the MAPTIP trial in three distinct areas involving measurements of: a) the concentration and composition of the accumulation mode aerosol with particle radii around $0.1\mu m$; b) the concentrations of larger sea spray aerosol particles ($0.25 \leq r \leq 150\mu m$); and c) detailed micrometeorological observations to study momentum, moisture and heat fluxes.

The accumulation mode aerosol is generally dominated by gas-to-particle production processes and the relevant precursor gases are predominantly associated with continental (often anthropogenic) sources, although the contribution of oceanic sources remains a current subject of scientific debate. Thus, the concentration of accumulation mode particles is often regarded as an indicator of the contribution of continental sources to the particulate loading within a given air mass. Indeed, part of the rationale behind the use of the Dutch MPN platform for the MAPTIP trial was that it provided a good opportunity to extend the validation of existing maritime aerosol models to a coastal area subject to strong continental aerosol and meteorological inputs. The size of these particles is such that their influence upon atmospheric extinction is strongest at visible and near infra-red wavelengths.

This paper deals with the measurement of the accumulation mode aerosol by means of a thermal analytical method which has been used effectively by the UMIST Group in a NE Atlantic cruise during 1989 (*O'Dowd et al, 1993a*) and in recent aircraft studies. This volatility technique involves the heating of continuous-flow aerosol samples prior to recording their sizes and concentrations by means of a Particle Measuring Systems ASASP-X optical particle counter.

One significant optically-active component of this accumulation mode aerosol comprises soot carbon from high temperature combustion sources such as oil-fired power stations and internal combustion (especially diesel) engines. Whilst it is possible to derive estimates of this component from the volatility technique, its importance in the atmospheric extinction of continental air masses prompted the deployment of a Magee Scientific aethalometer in order to measure directly the overall mass loading of this material. The aethalometer operates by measuring the absorption of light passing through a filter sample and the instrument is computer-controlled so that successive samples may be obtained, with automatic corrections for changes in lamp brightness and the build-up of material upon the filter.

The volatility technique relies upon the fact that various aerosol species, such as sulphuric acid, ammonium sulphate and sea salt, dissociate at characteristic temperatures and, from observations of particle size, concentration and temperature, the size-differentiated composition of the aerosol may be determined. The instrumentation deployed during MAPTIP comprised the ASASP-X, a heated quartz tube assembly and a small computer for control of the system, as well as the recording and processing of the aerosol and temperature observations. Although longer sampling periods are desirable, especially for the larger aerosol particles, statistically-significant aerosol composition and concentration information can be provided with undisturbed sampling times of about one hour.

Observations from several previous field projects are presented in Figure 1 in order to demonstrate the volatility technique and are shown as particle concentrations within

*Paper presented at the Sensor and Propagation Panel Symposium on "Propagation Assessment in Coastal Environments" held in Bremerhaven, Germany 19-22 September 1994.*

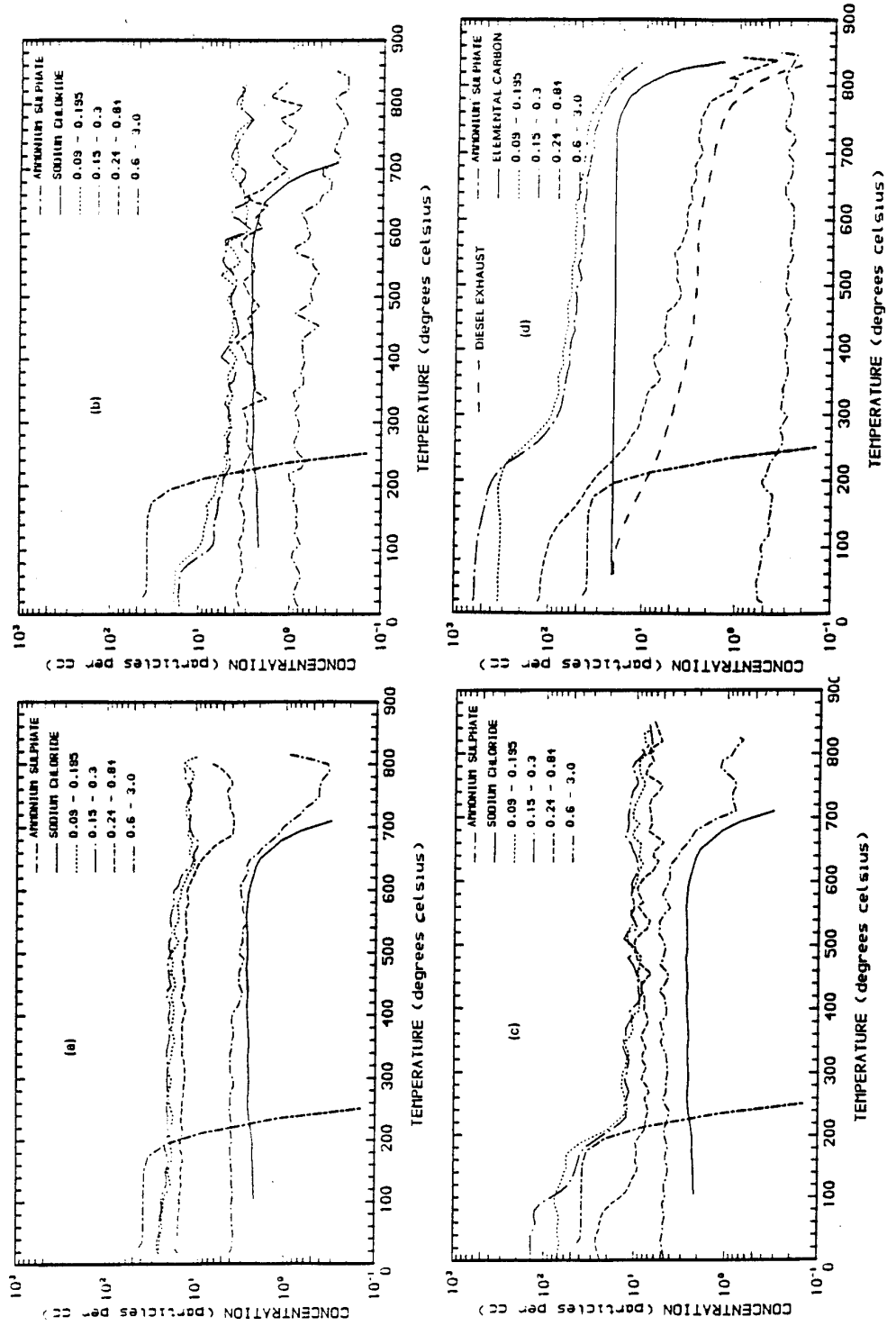


**Fig. 1:** Volatility temperature fractionation curves for (a) maritime (high wind), (b) Arctic, (c) modified Arctic, and (d) continental aerosol. Sizes given are diameters ($\mu$m).

four size bands plotted against temperaure. For comparison purposes, lines showing the response of the system to laboratory-generated ammonium sulphate, sodium chloride, elemental carbon and diesel exhaust aerosols are included in the figures, as appropriate. Figures 1(a) - (c) were obtained during a cruise in the NE Atlantic (*O'Dowd & Smith, 1993b*), whereas Figure 1(d) resulted from a cruise off the west coast of Ireland (*O'Dowd et al, 1992*).

Figure 1(a) displays the thermal response of the aerosol during maritime high wind conditions and clearly shows the dominance of the sea salt particles for these sizes, with little or no sulphate aerosol present within the sample. During the Arctic conditions illustrated in Figure 1(b), the concentration of sea salt was much reduced in these lighter wind conditions whereas there is evidence of a much more volatile component, identified as sulphuric acid aerosol, dominating the smaller particle sizes. An unusual case, classified as modified Arctic, is shown in Figure 1(c) where the smallest aerosol particles consisted of ammonium sulphate whereas sulphuric acid aerosol dominated the intermediate aerosol sizes, suggesting a strong source of sulphate aerosol (possibly volcanic) in the region. The presence of sea salt in the largest size band is consistent with the prevailing wind speeds at the time of the sample. Finally, the continental air presented in 1(d) demonstrates the characteristic volatilization of elemental carbon at temperatures around 800°C for all but the largest particle size band. However, in contrast with the clear signatures given by this technique for most aerosol species, diesel exhaust fumes show a much more gradual, though characteristic response to heating. It is suggested, following *Cachier et al (1989)*, that the component of the aerosol giving a gradual response to heating comprises a highly polymerised organic fraction arising from the combustion process.

## 3. MEASUREMENTS

The accumulation mode sampling equipment was initially mounted on the lower deck at the south side of the Meetpost Noordwijk (MPN) platform. However, the persistent northerly and easterly winds resulted in the equipment being generally in the shadow of the platform and, frequently, the measurements were influenced by exhaust fumes from the electricity generators situated on the northeast corner of the platform. In an attempt to improve the quality of these data, the instruments were mounted at the head of the interior stairwell with the aerosol intakes fixed below the platform.

### 3.1 Soot Carbon Observations

Observations from the aethalometer for the duration of the MAPTIP trial, shown in Figure 2, confirm the strong continental influences, as might be expected for the prevalent light easterly winds which dominated almost the whole of the campaign. Earlier observations in the NE Atlantic and the Outer Hebrides indicated that roughly 10% of the accumulation mode aerosol comprised soot carbon and that typical background loadings for these relatively remote regions amounted to around 20 - 40ng $m^{-3}$. Thus, it may be noted that the aerosol sampled at the MAPTIP platform is strongly influenced by continental sources throughout most of the trial period, with only a brief period of relatively unpolluted air from about 25 to 27 October, during which the prevailing wind was more northerly.

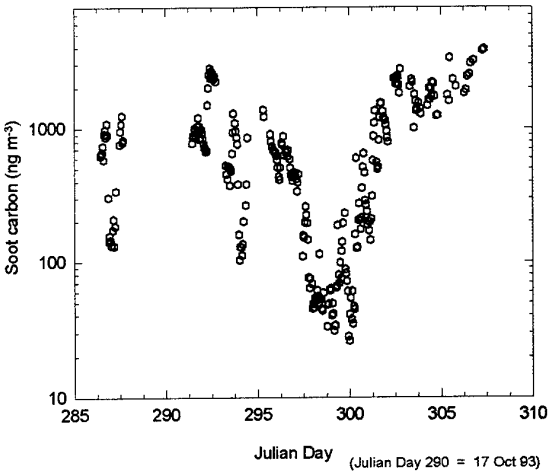


Figure 2. MAPTIP aethalometer soot carbon loadings

The association between wind direction and soot carbon loadings is clearly indicated in Figure 3 where the only loadings below about 100ng $m^{-3}$ occurred for the sector from 0 to 45°. Most of the observations for wind directions outside this narrow range possessed soot carbon loadings approaching, and often exceeding, 1000ng $m^{-3}$.

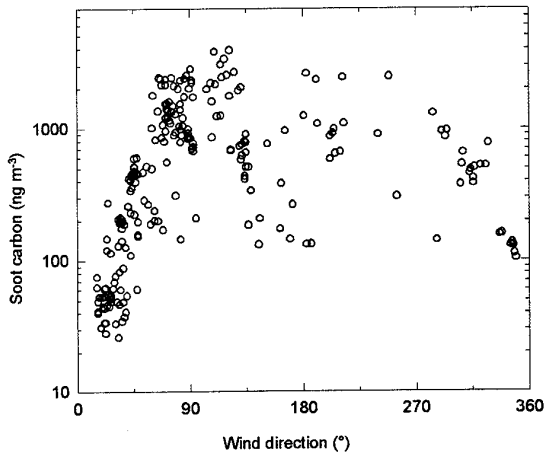


Figure 3. Variation of soot carbon loading with wind direction during the MAPTIP trial.

### 3.2 Accumulation Mode Aerosol Observations

Observations from two distinct periods of the MAPTIP trial are presented to demonstrate the ability of the volatility technique to determine the size-differentiated composition of the accumulation mode aerosol. The first of these intervals, the morning hours of 25 October 1993, was selected as being representative of the brief episode of maritime conditions encountered during the project, while the second period, over the night of 30 October 1993, was regarded as characteristic of the polluted continental conditions experienced throughout the majority of the time on MPN. Also, these intervals were chosen because they permitted long integration periods to be used in order to smooth the statistical variations present in the aerosol sampling statistics. On several occasions during the trial, the passage of ships close by the platform, or more especially the berth of supply vessels at the platform, led to localised contamination (sometimes severe) of the aerosol record by their diesel exhausts.

A further limitation of the data set arose because power supply limitations meant that the quartz tube could not be heated to the levels in excess of 800°C required to volatilize the elemental carbon particles. Thus, an unambiguous signal regarding this component could not be established. However, previous trials have indicated that, in continental regions with little sea salt input, the residual aerosol remaining at temperatures above 350°C is dominated by soot carbon particles. Therefore, it is suggested that, for this trial, the aerosol particles remaining at temperatures above 680°C (beyond the volatilization temperature of sea salt) may be regarded as elemental carbon with little loss of accuracy. The validity of this assumption will be explored subsequently.

The variation in aerosol number concentration with temperature for the first period on 25 October 1993 is shown in Figure 4. The clear signature of ammonium sulphate at around 200°C may be noted for the three smaller size bands, with a contribution from sulphuric acid indicated in the largest (and perhaps the next largest) size category. The two largest size bands show the presence of sea salt which is volatile at around 650°C. The slight increase at this temperature in the particle concentrations within the two smaller size classes is often found under these conditions and is believed to result from the thermally-induced shattering of the larger sea salt crystals into numerous smaller fractions. The general decrease in particle concentrations for the three smallest size ranges at temperatures above 240°C is consistent with the presence of polymerised organic carbon components.

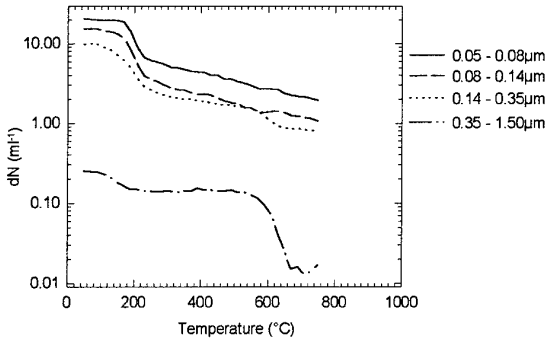


Figure 4. Variation in particle concentration dN with temperature for 25 October 1993 from 03:00 - 09:00 GMT

By extracting particle spectra within specific temperature bands from the data set, the response of the aerosol to heating may be determined and used to indicate its fractional composition. Thus, changes in the aerosol spectrum between 65°C and 145°C may be associated with sulphuric acid, those between 145°C and 270°C with ammonium sulphate, and so on. Aerosol spectra derived in this fashion for the 25 October 1993 samples are presented in Figure 5.

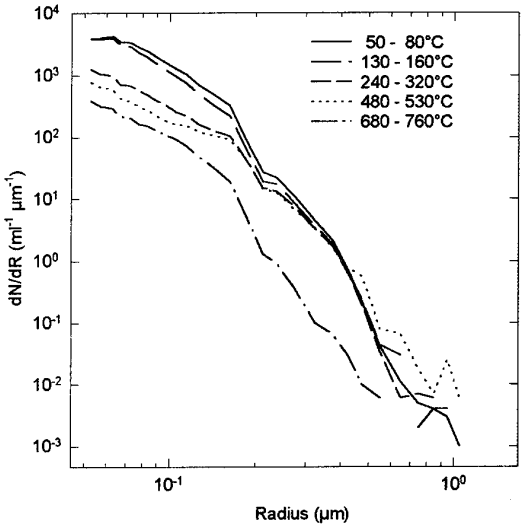


Figure 5. Particle spectra at specific temperatures for 25 October 1993

From this figure, it may be noted that the contribution of the sulphate components is substantial for radii below about 0.2μm, whereas the sea salt component extends down to 0.1μm or less. The organic carbon component, most of which is volatile at temperatures between about 300° and 500°C, is only present in significant quantities for aerosol sizes below about 0.2μm in radius, while the residual elemental carbon provides a very small fraction of the total aerosol loading..

The relative proportions of the various chemical species within the aerosol may be determined by taking the difference between the relevant spectra shown in Figure 5

and these components are presented in Figure 6 as fractions of the total aerosol loading. However, the particle counts for radii beyond about 0.5μm remain very low, despite the extended sample periods employed, and useful composition information cannot readily be derived for these larger sizes.

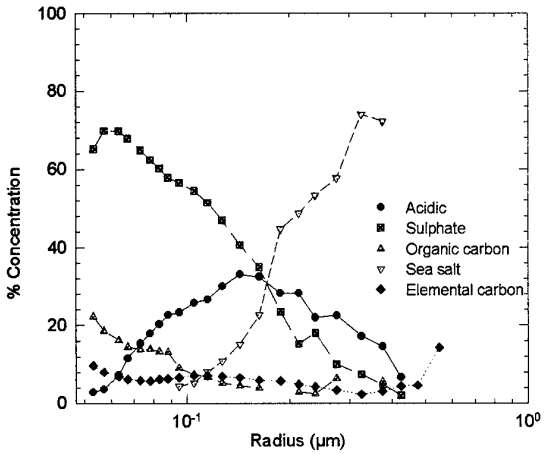


Figure 6. Fractional composition of the aerosol sampled on 25 October 1993.

From this figure, the contributions of ammonium sulphate and sea salt to the smaller and larger aerosol fractions, respectively, may be readily noted. The contribution of sulphuric acid to the intermediate particle sizes is also apparent and may represent the capture of new sulphur gas species as these sizes probably dominate the total particulate surface area. This point illustrates a limitation of presenting the aerosol composition information in the manner employed in Figure 6, namely, that an externally-mixed aerosol is assumed. An internally-mixed aerosol (i.e. one where some particles contained two or more chemical species) would tend to respond to heating by a shift to smaller aerosol sizes, as individual chemical compounds became dissociated, while retaining its overall spectral shape. With the possible exception of sulphuric acid, there is little evidence for such a shift in the spectra illustrated in Figure 5 and, therefore, Figure 6 almost certainly provides a realistic, and visually illuminating, representation of the various aerosol components.

In this relatively unpolluted air mass, the soot carbon aerosol contributes about 30% of the total for radii below about 0.1μm and it may be noted that the proportions of one-third elemental to two-thirds organic carbon are reasonably typical of anthropogenic sources.

For the more heavily polluted case overnight on 30 October 1993, the variation in aerosol concentration with temperature is shown in Figure 7 for the same size categories as in Figure 4. In this case study, the ammonium sulphate component is present in only the larger two size bands, with just a slight indication of sulphuric acid in the largest size category. The lack of a sea salt component is consistent with the light winds of less than 4m $s^{-1}$ prevalent during this period.

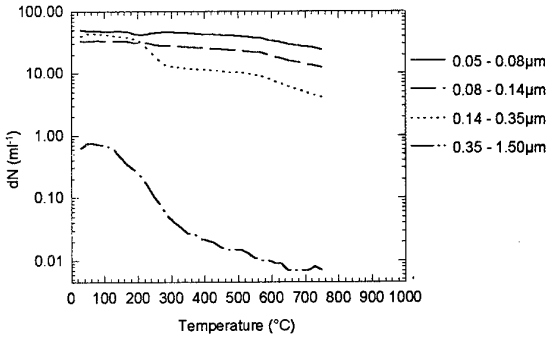


Figure 7. Variation in particle concentration dN with temperature for the period from 19:00 GMT on 30 October to 08:00 GMT on 31 October 1993.

The particle spectra within the temperature bands, selected as for Figure 5, are illustrated in Figure 8, from which it may be noted that the contribution of the sulphate components is relatively modest for particle radii below about 0.1μm, but is substantial from this radius up to about 0.6μm. The transition from the 480-530°C temperature band to that of 680-760°C, which is normally associated with sea salt, exhibits a bimodal structure. More detailed consideration of the thermal response of the aerosol suggests that only the spectral changes for radii above about 0.25μm are associated with sea salt, whereas those at lower temperatures correspond to the dissociation of organic carbon components.

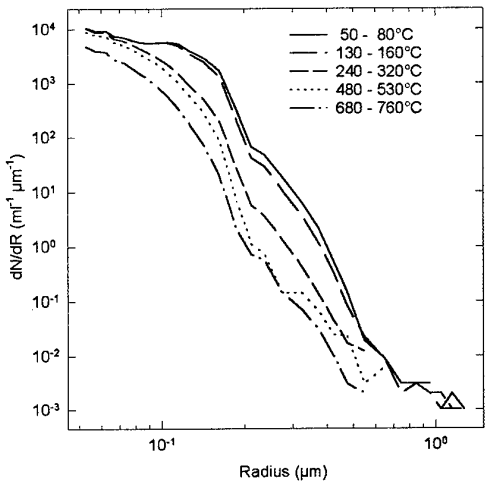


Figure 8. Particle spectra within specific temperature bands for 30 October 1993

The fractional composition of the aerosol under these

polluted conditions is shown in Figure 9 and differs markedly from that in the previous case study.

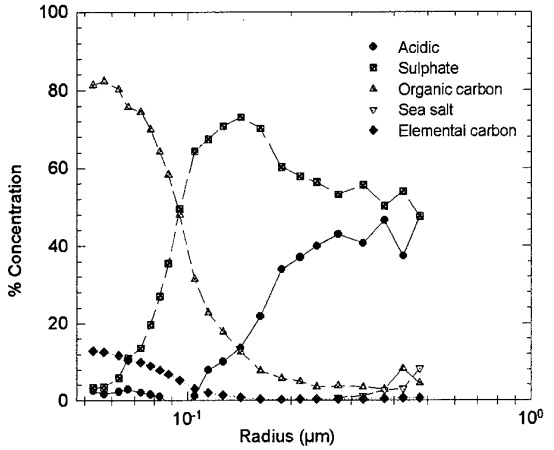


Figure 9. Fractional composition of the aerosol sampled on 30 October 1993.

For this situation, the strong dominance of the soot aerosol is obvious - the two carbon components constitute almost 100% of the particles with radii around 0.05 to 0.07μm. However, the soot carbon has a very narrow size distribution and the larger aerosol sizes are dominated by the sulphate components. The very small sea salt fraction is only evident at sizes above 0.4μm. Once again, the sulphuric acid material appears concentrated around the middle size categories.

One further point regarding these aerosol spectra is that, even at the lowest point in the heating cycle, the aerosol is significantly warmer than the prevailing environmental temperature. Thus, if aerosol particle spectra pertinent to the ambient environmental conditions are required, the particle size distributions measured by the volatility technique must be grown to their equilibrium sizes at the prevailing relative humidity. Experience has shown that the relatively simple algorithms developed by *Gerber (1988)* may be employed for this purpose, up to relative humidities of 100%. A typical example of a particle size distribution from the MAPTIP campaign adjusted in this manner is shown in Figure 10, where observations from the volatility equipment are combined with sea spray measurements produced from other Particle Measuring Systems instruments operating under ambient conditions.

Agreement between the spectra from the various optical particle counters is generally good apart from the region above 0.5μm for the ASASP-X volatility measurements. Separate extensive tests have confirmed that this discrepancy arises from particle losses, at these larger sizes, within the piping associated with the heated quartz tube but that losses of the smaller particles are almost negligible. Thus, the volatility system significantly undercounts particles with radii above 0.5μm although the relative composition of these larger particles remains valid.

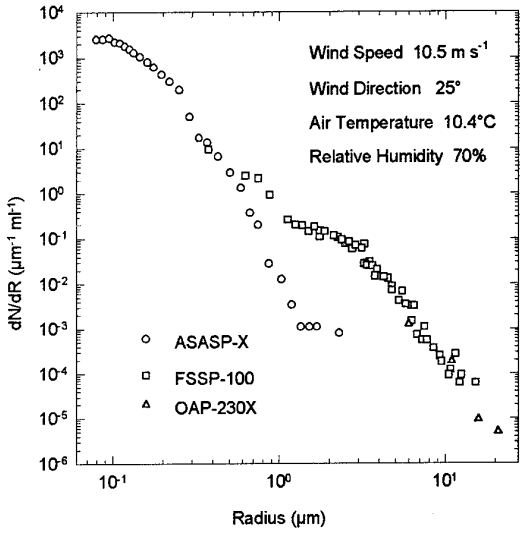


Figure 10. Aerosol particle spectrum for the period 07:00 - 08:00 GMT on 25 October 1993.

### 3.3 Comparisons of Soot Carbon Estimates

The validity of the volatility method for deriving soot carbon loadings may be tested simply by comparing the results from the two methods. Since the production processes for the polymerised organic and elemental carbon components are usually closely related, the correlations between each of these components and the integrated aethalometer measurements should be similar, as is the case for these data shown in Figures 11(a) and (b). From these figures, which include data from the whole of the MAPTIP campaign, it may be noted that the organic carbon component dominates the soot carbon loading, with levels approximately three times larger than those for elemental carbon.

As may be seen from the figures, there is generally a good correlation between the two methods although a significant amount of scatter in the individual observations is apparent. Investigation of the aethalometer performance at a number of sites under a range of conditions demonstrates that it does exhibit a substantial degree of variability even for ostensibly steady states. As the instrument operates by measuring the absorption of a light beam before and after a known volume of air is drawn through the filter, these fluctuations may arise from slight uncorrected variations in lamp brightness giving a higher variability in the signal, which is the difference between the two much larger readings.

Variations will also appear in the volatility measurements due to fluctuations in ambient aerosol concentrations and this problem will be especially acute when the aerosol sources are relatively close to the measurement point, as

was the case for much of the MAPTIP trial with industrial sources in close proximity to the Dutch coast.

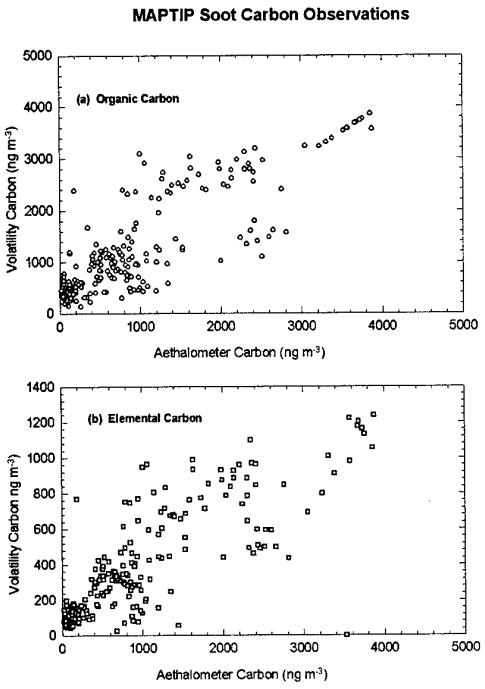


Figure 11. Comparison of volatility and aethalometer carbon loadings measurements.

Comparisons of the total soot carbon aerosol loadings provided by the two techniques, shown in Figure 12, indicate surprisingly good absolute agreement, although the levels derived from the volatility method are somewhat higher than those from the aethalometer. Discrepancies between the two data sets may be covered by experimental errors, though it is worth noting that the volatility estimates were calculated assuming a specific gravity for carbon of 2.0, which may not be accurate for these carbon combustion products. Also, soot carbon particles possess refractive indices with real and imaginary components somewhat different from those of particles for which the ASASP-X optical particle counter is calibrated, and may result in some mis-sizing of these carbon particles. Finally, whether the slight offset on the y-axis of Figure 12 indicates a small non-carbon aerosol residue which could not be detected at the temperatures below 800°C used in this project is open to debate.

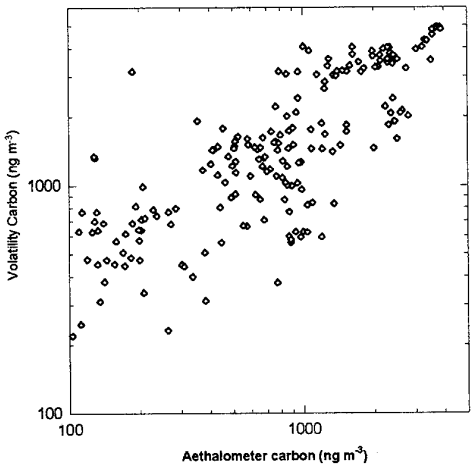


Figure 12. Comparison of total soot carbon loadings from the volatility and aethalometer measurements.

## 4. DISCUSSION

This paper has attempted to demonstrate the effectiveness of the volatility technique for determining aerosol particle composition and concentrations over the radius range from 0.05 to around 1μm. The lack of precision available from this technique, when compared with more conventional chemical analysis methods, is more than compensated by its ability to provide information on size-differentiated particle composition which could not readily be achieved by other means. Also, this composition information can be provided on an almost real-time basis. Extending the procedure to higher temperatures permits its use for measuring the important contribution of optically-active soot carbon particles to the aerosol present in polluted air masses.

Throughout the majority of the MAPTIP campaign, the aerosol loadings were dominated by the contributions from continental sources, clearly demonstrating their significance in coastal or polluted environments. Even at the small sizes characteristic of the accumulation mode, these particles are pertinent to the problems of atmospheric propagation at visible and near infra-red wavelengths, and will be of even greater significance at ultra-violet and near ultra-violet wavelengths.

This thermal analytical technique has been adapted for airborne operation by employing a series of pre-heated quartz tubes at selected temperatures, in order to bring the required sampling times down to durations appropriate for aircraft use. By switching the optical particle counter intake between the pre-heated tubes, estimates of the contributions of specific aerosol species to the particulate spectrum may be determined with sample times of a few minutes.

Finally, a revised volatility system is being developed for installation on a recently-purchased TSI Scanning Mobility Particle Sizer instrument. It is proposed to utilise this system to extend the volatility method down to particle radii of $10^{-8}$m or less, in order to investigate the composition of aerosol particles during the early stages of their formation.

**5. REFERENCES**

Cachier H, Bremond M-P and P Buat-Ménard, "Determination of atmospheric soot carbon with a simple thermal method", Tellus, 41B, 379-390, 1989.

Gerber H, "Relative humidity parameterization of the lognormal size distribution of ambient aerosols", Lecture Notes in Physics, 309, (edited by P E Wagner and G Vali), 241-244, Springer Verlag, Berlin, 1988.

O'Dowd C D, S G Jennings, M H Smith and W Cooke, "A high temperature volatility technique for determination of atmospheric aerosol composition", J Aerosol Sci, **23**, Supp 1, S905-908, 1992.

O'Dowd C D, M H Smith and S G Jennings, "Submicron particle, radon and soot carbon characteristics over the Northeast Atlantic", J Geophys Res, **98**, 1123-1135, 1993a.

O'Dowd C D and M H Smith, "Physico-chemical properties of aerosols over the Northeast Atlantic: Evidence for wind-speed-related submicron sea-salt aerosol production", J Geophys Res, **98**, 1137-1149, 1993b.

**6. ACKNOWLEDGEMENTS**

This work has been conducted with the support of the UK Defence Research Agency, Funtington, who funded UMIST involvement in the MAPTIP project under Agreement No 2044/189/CSM. Also, the assistance of NRaD (Code 543) in providing travel funds and other means to facilitate the data analysis is gratefully acknowledged. Finally, many thanks are due to the scientists and staff, too numerous to mention, who assisted with the planning and logistics for the MAPTIP campaign.

## DISCUSSION

### D. DION

Concerning the North Atlantic measurements where continental aerosols were detected away from the coast, did you identify the meteorological process that was responsible for that? Was this condition usual?

### AUTHOR'S REPLY

We have air mass trajectory analyses which show paths of anthropogenic aerosols from central Europe and the UK. Although much of the 5-week period in Oct/Nov 1989 was in polluted conditions, other trajectories brought cleaner maritime or Arctic air to the ship. One interesting case (fig 1c) indicated a strong sulphur source which was believed to result from air passage over the Icelandic volcanic region, and which had a high radon, though low soot carbon content; thus, no 'indicator' is ideal to define the air mass.

# Impact of Coastal Environment on Point Target Detection

K. Stein, A. Kohnle, W. Schuberth, R. Jantzen
FGAN-Forschungsinstitut für Optik (FGAN-FfO), Doc. 1994/74
Schloss Kressbach, D-72072 Tübingen, Germany

**Summery**

It is still difficult for a sensor system to detect low flying anti-ship missiles over long distances with high detection probability and low false alarm rates. In continuation of the work in this subject area concerning infrared (IR) sensor systems the FGAN-FfO participated in the MAPTIP trial of NATO AC/243 (Panel 04/RSG.08) with two infrared (IR) / visible (VIS) camera systems set-up on the Katwijk coast in The Netherlands. Two main types of measurements were performed. Observations of a fixed target mounted on a mast on the Meetpost Noordwijk platform 5.6 miles off the Katwijk coast, and tracks of planes, especially of the inbound flights of a Piper Navajo, chartered by the US-NCCOSC.

Initial analysis results of the temporal and spatial behaviour of the fixed and moving targets, especially the two engines of the Piper Navajo, are given. In addition, experimentally determined signal-to-noise ratios from IR imagery are compared with calculations using the FGAN-FfO thermal range model for point target detection (TRP). The correspondence is quite good.

It was possible to track the Piper Navajo up to 13 nautical miles (nmi) in the 8 - 12 µm waveband, less far in the 3 - 5 µm wavelength region. This was partially due to the lower sensitivity of the used sensor in this waveband. The two engines of the approaching plane were resolved at 8 nmi.

Steps have been undertaken to analyze the handle of extremely close multiple targets (as the two Navajo engines seen at long distance) by different image processing algorithms. One example is given where bispectrum analysis is used to clearly resolve the two Navajo engines at long distances.

Forschungsinstitut für Optik (FfO, Research Institute for Optics) presents first results from their participation in the MAPTIP measurement campaign.

---

## 1. Introduction

The detection of low flying anti-ship missiles (sea skimmers) with high detection probability and low false alarm rates is still a challenge. The FGAN research institutes FfO and FIM have been working in this subject area for several years (see [SPIE]). Both sensor radiometric and algorithm considerations are treated equally. The participation in a NATO experiment designed to obtain a more in-depth understanding of the interrelation between propagation and background effects and sensor performance was therefore a unique opportunity.

The main objectives of the MAPTIP trial (Marine Aerosol Properties and Thermal Imager Performance) of NATO AC/243 (Panel 04/RSG.08) were to characterize the marine boundary layer, to asses boundary layer effects on thermal imaging systems and to provide data for the improvement and validation of IRST algorithms and in the analysis of design criteria for Infrared Search and Track (IRST) systems.

For this purpose several thermal imaging systems were set-up by member nations of the NATO Research Study Groups 08 and 05 on the beach site in Katwijk, The Netherlands, the Meetpost Noordwijk platform (MPN) 5.6 miles off the Katwijk coast, in a Lynx helicopter and in a P3-Orion Marine Patrol Aircraft of The Netherlands Navy. Calibrated IR sources were installed on board the Netherlands Oceanographic ship Hr. Ms. Tydeman, on the MPN platform, and hanging underneath the Lynx helicopter. Moreover the P3-Orion and a Piper Navajo chartered by the US-NCCOSC acted as moving targets.

All this provided a great variety of imaging data in the 3 - 5 µm and the 8 - 12 µm wavelength bands near the sea surface which are appropriate for the prediction analysis of low-level target detection ranges above sea.

## 2. Experimental Set-up

The FGAN-FfO imaging systems were installed inside a shelter placed on the parking lot near Katwijk beach station at approximately 17 meters above sea level.

In addition a FGAN-FfO designed infrared source was mounted on a mast at the MPN at a height of approximately 22 meters above mean sea level. This point-like target of 0.22 m diameter was temperature stabilized and calibrated at 300°C. From the beach station it was possible to detect the point target against the sky background.

The FGAN-FfO used two infrared camera systems mounted on a fixed and tracking platform, respectively. Each system consisted of a thermal imager and a video camera. One video camera was used to record the general visibility conditions, e.g. by taking images of the MPN platform. Both IR- and video cameras had the same optical axis and had nearly the same field of view.

*Paper presented at the Sensor and Propagation Panel Symposium on "Propagation Assessment in Coastal Environments" held in Bremerhaven, Germany 19-22 September 1994.*

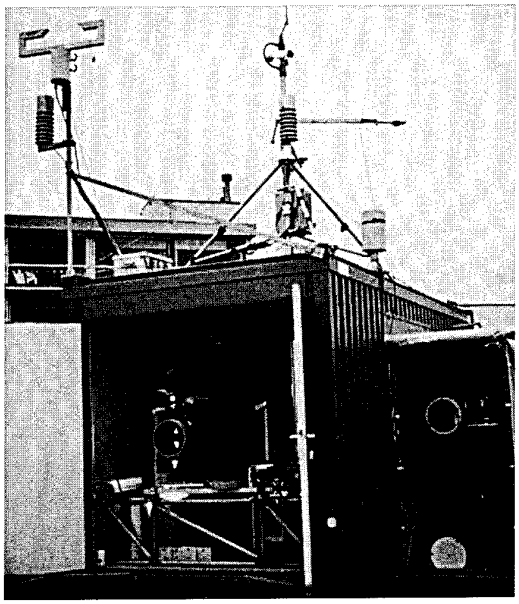

**Figure 2.1:** Experimental set-up during the MAPTIP campaign: in the shelter the DUWIR-system, in the tent next to it the IRC-64-system. Mounted on the shelter is a meteorological station.

The first camera system was a dual waveband thermal imager (DUWIR, GEC) working simultaneously in the 3 - 5 µm (MWIR) and 8 - 12 µm (LWIR) wavelength region. It is a scanning system with a frame rate of 25 Hz and a field of view of 53 x 35 mrad. The DUWIR system was set-up inside the shelter and mounted on a tracking platform which was controlled by a computer. The DUWIR imagery together with the imagery of the co-aligned video camera were recorded on S-VHS tapes.

The second camera system was located in a tent next to the shelter. The IR imaging system was a focal plane array camera (IRC-64, Cincinnati Electronics), equipped with a 64 x 64 element Indium Antimonide (InSb) detector. Due to a narrow filter the camera is sensitive in the 4.2 to 4.8 µm region. The focus length of the mirror telescope of the camera is 1.2 m which results in a camera field of view of 5.71 x 5.71 mrad. By tilting the secondary mirror of the telescope by 90 degrees the instrument could take images either in the IR or in the visible. The system "IRC-64/VIS" was primarily aligned to take pictures of MPN.

The IRC-64 camera images were recorded either by direct digitization (12 bits) and storing on a PC disc or by analog on S-VHS tapes depending on the length of the scene.

Supporting meteorological measurements were made with a meteorological station mounted on the shelter.

Two types of observations were performed during MAPTIP: observations of the MPN-structure and the fixed point target against various sky backgrounds, and tracks of the two planes and the Lynx helicopter with the tethered point target in different flight profiles.

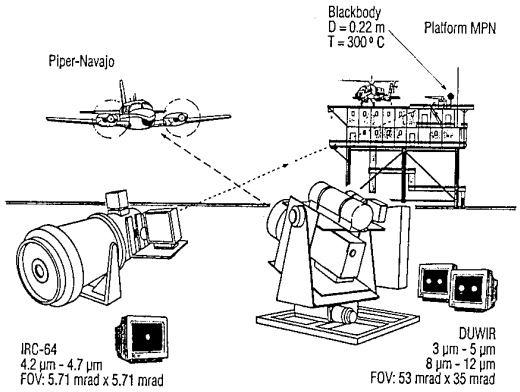


**Figure 2.2**: Schematic of the FGAN-FfO experiment: two camera sets located on the boulevard of Katwijk, taking IR images of the MPN tower and an approaching aircraft.

### 3. Fixed Target

One goal of the experiment was the detection of a fixed point target against various sky backgrounds at different extinction profiles along the propagation path and how that "behaviour" changes in each wavelength region of the DUWIR camera.

A point source at a long distance shows special characteristics in the image sequence of an IR sensor. Generally, temporal and spatial fluctuations are seen in the digitized imagery.

Images of the FfO-blackbody on MPN were taken simultaneously in both wavebands. To analyze the fluctuations several sequences were digitized.

All images presented in this paper were processed using the IDL programme [IDL]. IDL is an array oriented programming language specifically suitable for analysis and graphical display of images.

A rectangular dark spot is apparent in the centre of all DUWIR pictures. This is the detector narcissus due to reflection. Moreover, the images of the 8 - 12 µm waveband show an additional undesirable effect: one defective horizontal line in the middle of the picture.

The images taken in the 3 - 5 µm waveband are of inferior quality than those taken in the 8 - 12 µm region. This is due to the less sensitivity of the HgCdTe detector in the MWIR.

The following pictures compare data obtained during two different weather conditions: a very clear day and a day of dense fog. Figures 3.1a and 3.2a show the situations in both wavebands. The grey value distribution of an area of 11 by 11 pixels laid around the point target is shown next to them (Figures 3.1b and 3.2b).

Imagery #1 was taken in the morning of October 24, at 8:00 GMT, a very clear day. The visibility range

measured on MPN platform by the Defence Research Establishment Valcartier, Canada [DREV] was better than 20 km. The French participants [CELAR] operated a buoy system which measured the mean air temperature to be 7.7 °C and the sea surface temperature (0.2 m below the surface) to be 11.7 °C. The second scene was taken on October 30, at 13:00 GMT. Visibility during that day was around 2 km [DREV]. The mean air temperature was 5.5 °C [CELAR] and the IR sea surface sensor on board of the NCCOSC chartered aircraft measured a temperature of 8°C [NCCOSC].

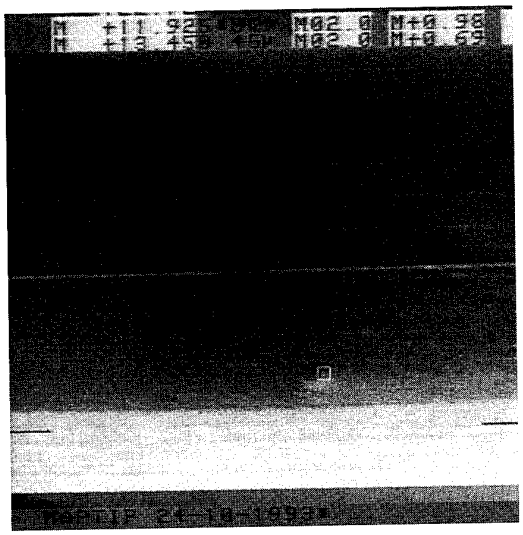

a)

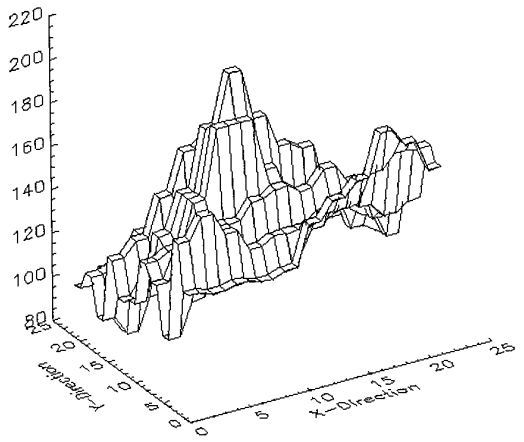


b)

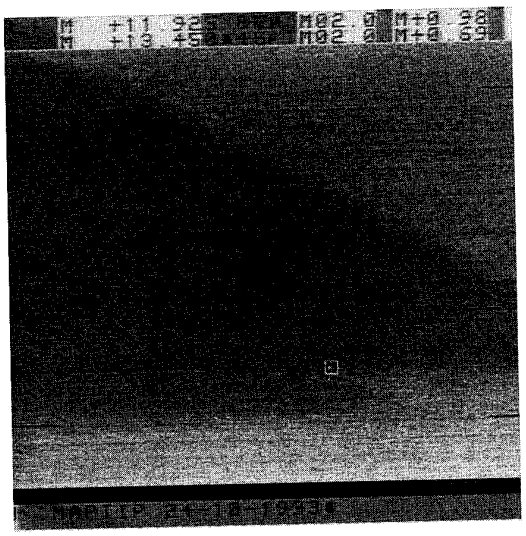

a)

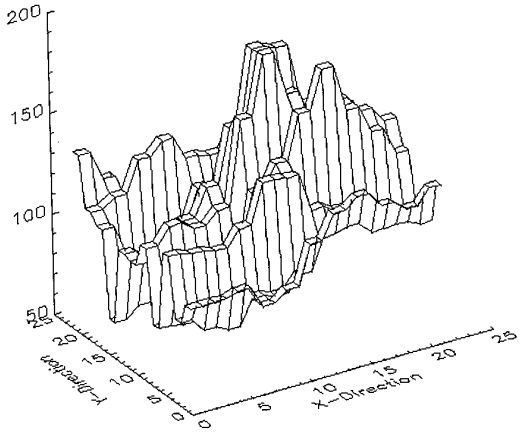


b)

**Figure 3.1**: Images of the point target on MPN taken on October 24, 8:00 GMT(a) and the grey value distribution of the marked area (b). Above: 8 to 12 µm waveband, below 3 to 5 µm waveband.

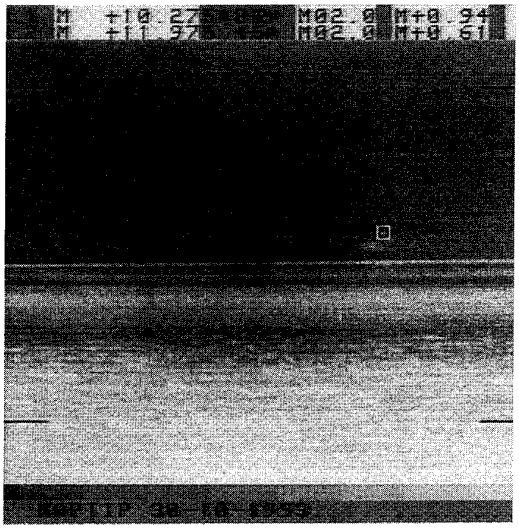

a)

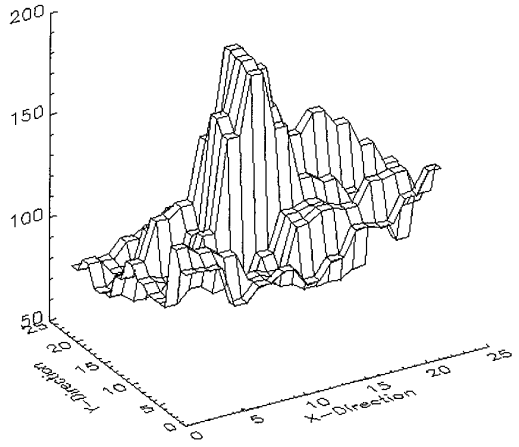


b)

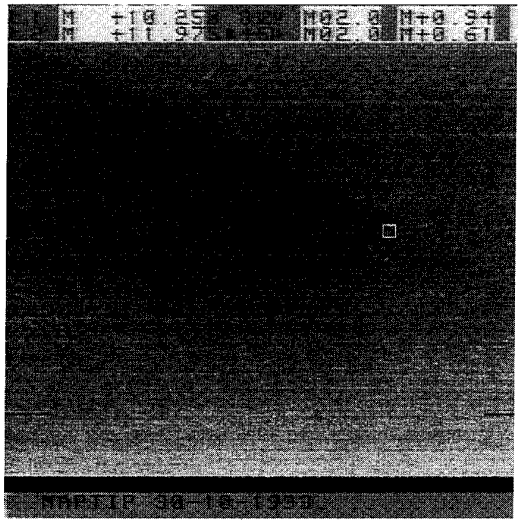

a)

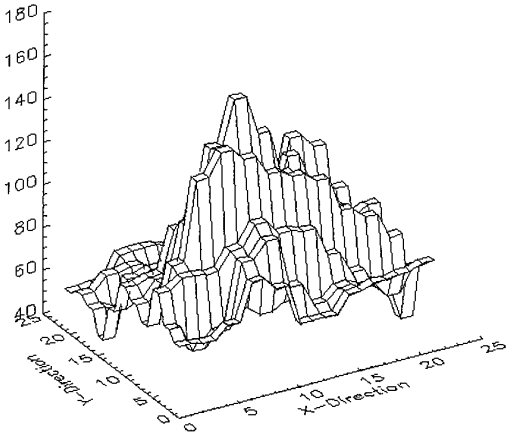


b)

**Figure 3.2**: Images of the point target on MPN taken on October 30, 13:00 GMT(a) and the grey value distribution of the marked area(b). Above: 8 to 12 µm waveband, below 3 to 5 µm waveband.

The distribution in the 8 - 12 µm waveband shows a "sharp" peak which clearly exceeds the discrimination level. Whereas in the 3 - 5 µm wavelength region the signal is more distributed. For the pictures taken on October 30, the images in the IR show quite a good signal even though the visibility was low.

For a more detailed analysis we looked at a sequence of 10 s time periods. The grey values of the 11 x 11 matrix are analyzed. The following diagrams show the variations of the peak signal of the grey value distribution. The values are plotted against the image number (250 images span a sequence of 10 seconds).

The spatial variation of the fixed point target signal is analyzed for October 24, 8:00 GMT for both wavebands.

The following diagrams (3.3a and 3.3b) show the positions of the maximum signal within the 11 x 11 matrix. The dashed line marks the y-position, the straight line marks the position in the x direction. As can be seen in the left diagram (8 - 12 µm) the y-position varies by one pixel. Whereas the spatial fluctuations in x direction have a difference up to 3 pixel.

The smaller variation in y direction is due to the scanning technique of the system.

In the LWIR the maximum can be located quite clearly. This is not the case for the MWIR as can be seen from figure 3.3b. The position of the peak varies a lot more and the signal is more broadened than in the far infrared. This is consistent with our observations concerning figures 3.1b and 3.2b.

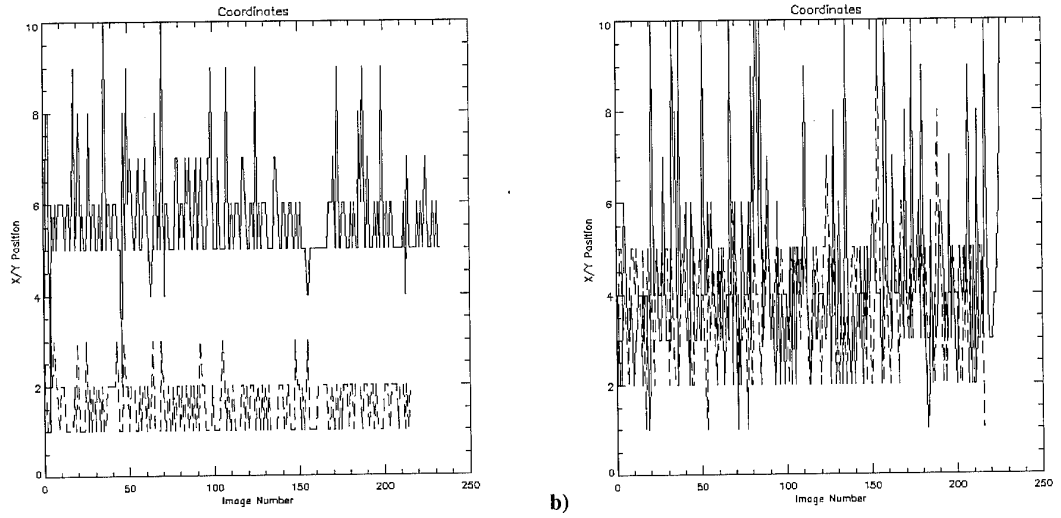


a) b)

**Figure 3.3:** X-(straight line) and y-(dashed line) positions of the peak signal on October 24, 8:00 GMT:
a) in the LWIR,
b) in the MWIR.

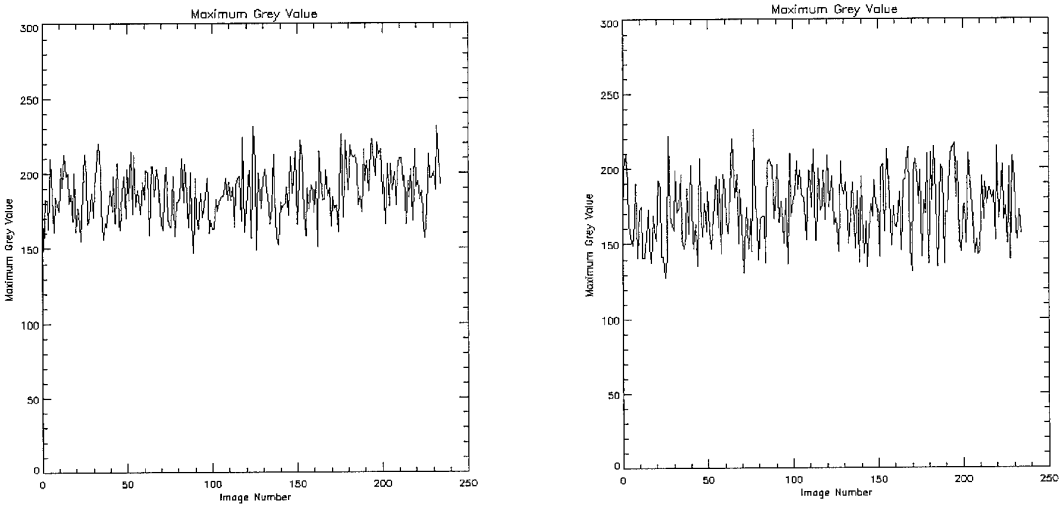


a) b)

**Figure 3.4**: Peak signal variation on October 24, 8:00 GMT(a) and October 30, 13:00 GMT(b), for the 8 - 12 µm wavebands.

The temporal fluctuations of the signal are shown in figure 3.4. We chose the signal in the 8 - 12 µm waveband on October 24, 8:00 GMT (a) and October 30, 13:00 GMT (b).

Plotted is the maximum grey value against the image number. For the clear weather situation on October 24, the maximum signal is higher than on October 30. But we find greater fluctuations of the signal during bad visibility conditions.

The same conclusions can be drawn from the analysis of the MWIR-images: sea fog leads to a slightly lower signal in the infrared compared to good visibility conditions, but the signal is more exposed to temporal fluctuations.

## 4. Aircraft Target

The NCCOSC operated an airborne platform: the Piper Navajo aircraft carrying equipment to measure the horizontal and vertical variation of the aerosol particle size distribution and the meteorological parameters.

This twin engined Piper Navajo was the primary target of interest for IR imaging. The aircraft manoeuvred in a star pattern around MPN tower to provide a moving target at low altitude. We directed our attention to tracking the plane on its inbound run to the beach and in particular we were interested in resolving its engines.

Simultaneous pairs of images in the MWIR and LWIR bands were taken by the DUWIR camera.

On October 24, a day with very stable, clear conditions the Piper Navajo flew at different altitudes at a constant speed of 120 mph. We selected two inbound runs: (1) 7:55 - 8:04 GMT at 200 feet and (2) 8:18 - 8:27 GMT at 500 feet.

The approaching plane becomes discernible on the telescreen in the LWIR at 11 nautical miles and 10 nmi in the MWIR at an altitude of 200 feet. Due to the decreasing extinction coefficient with increasing altitude, with an altitude of 500 feet the aircraft can even be tracked at 13 nautical miles in the LWIR.

Note that on a telescreen the motion of the target can be detected easier because of the extraordinary integration capacity of the human eye. In a single picture it is often hard to spot the signal. The following pictures show an example of the approaching Piper Navajo at a distance of 5 nmi in the morning of October 24. Marked is an area of 21 by 21 pixels around the two engines (Figure 4.1).

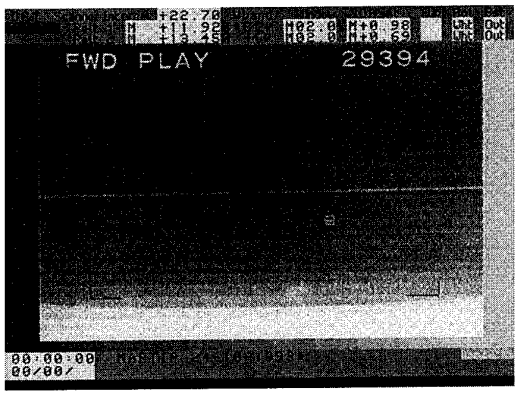


**Figure 4.1**: Inbound flight at an altitude of 200 feet in the 8 - 12 µm waveband region. The example shows a single picture of the aircraft at a distance of 5 nmi.

Figure 4.2 gives an enlargement of the marked area (a) and the grey value distribution of this matrix (b). It clearly shows the two engines.

A method which allows a clear extraction of the two engines and a suppression of the background is shown in chapter 6.

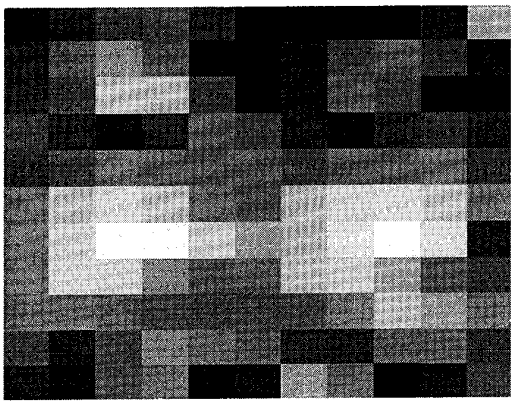

a)

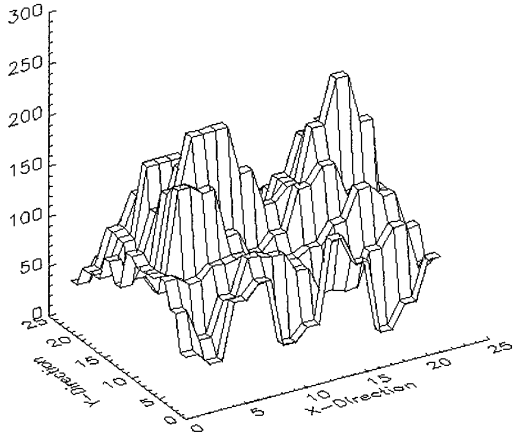


b)

**Figure 4.2:** Enlargement of the marked area of the Figure 4.1 and grey value distribution of this area (21 x 21 pixels).

The second series of situations we chose were on October 30, a day characterized by dense fog. The Piper Navajo flew at three different altitudes: 12:50 - 12:56 GMT 100 feet, 13:04 - 13:10 GMT 200 feet and 13:18 - 13:23 GMT 300 feet. Again, its speed was held constant at 120 mph.

Although the visibility was rather low, we got some good images in the infrared, especially in the LWIR. In the 8 - 12 µm region it was possible to track the plane visually from 7 nmi at an altitude of 100 feet and from 8.5 nmi at an altitude of 300 feet.

In the 3 - 5 µm region the aircraft was detected at 6 nmi irrespective of its altitude.

## 5. The Thermal Range Model for Point Target Detection (TRP)

The FGAN institutes FfO and FIM performed a feasibility study for long range IRST systems, called POSEIDON. This study was initiated by the German Ministry of Defence.

In the context of the POSEIDON study an analytical model (TRP) was developed to estimate first detection ranges of point target detection systems working in the infrared [TRP]. TRP assumes homogeneous backgrounds, which is approximately true for sea horizon applications. Sub-models of TRP consider the different contributions of the electro- optical transfer function from the source (point target) to the sensor output:

- the target-background model computes the radiance difference between target and background,
- the transmitting medium model considers atmospheric extinction and angle of arrival fluctuations due to optical turbulence,
- the sensor model takes into account the optical parameters of the sensor, the scanning mechanism, detector sensitivity and size and the jitter of the platform.

If the spectral radiance of the target is not known, the model assumes an equivalent blackbody target. One of the results from TRP is the signal-to-noise ratio S/N as a function of range and the spatial distribution of the target signal at the sensor output.

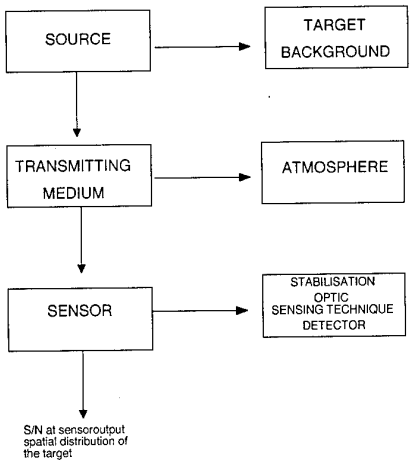


**Figure 5.1**: Structure of the Thermal Range Model for Point Target Detection (TRP).

Input data for the target - background sub-model of TRP are the size and temperature of the target and the background temperature. To compute the transmitting medium model it is usually possible to calculate the spectral atmospheric transmission by using LOWTRAN 7 [LOWTRAN].

However, there is no LOWTRAN 7 standard model appropriate to describe a coastal marine atmosphere suitable for the MAPTIP trial. Thus, it is necessary to make some assumptions concerning the necessary atmospheric transmission calculations.

We calculate the spectral molecular transmission $\tau(\lambda)_{mol}$ by using LOWTRAN 7 without taking into account aerosols. For the aerosol part of the transmission the 10.6 µm extinction data are used, which had been measured by the Canadian group [DREV] on the MPN platform.

We assume that $\tau_{aer}$ is constant in the LWIR. Thus, a rough formulation for the spectral transmission $\tau(\lambda)$ for a range R is:

$$\tau(R,\lambda) = \tau_{mol}(R,\lambda) \cdot \tau_{aer}(R), \qquad (5.1)$$

with $$\tau_{aer}(R) = e^{-\sigma_{aer}(\tau=10.6\mu m)\cdot c \cdot R}. \qquad (5.2)$$

$\sigma$: extinction coefficient.

The constant c in Eq. (5.2) is a correction factor which accounts for the transfer of the 10.6 µm aerosol extinction to the mean aerosol extinction in the 8 - 12 µm waveband. It has been shown previously [Clement] that this transfer factor is about 0.8 for a marine type aerosol.

From the DREV data we find that on October 24, both the visible and the far infrared extinction coefficients are very small which is consistent with a high visibility. On October 30, the visibility extinction is fairly high while the far infrared sensor gives a small value: i.e. the sea fog is thick for the visible but not for the infrared. This verifies the rather good quality of our images taken on October 30.

The mean effective atmospheric transmission for the used DUWIR camera is given by:

$$\tau_{eff}(R) = \int_{\Delta\lambda} S_n(\lambda)\, \tau(R,\lambda)\, d\lambda \,, \qquad (5.3)$$

with $S_n(\lambda)$ being the normalized DUWIR spectral sensitivity.

TRP uses a first order approximation of $\tau_{eff}(R)$ given by:

$$\tau_{eff}(R) = \tau_o\, e^{-\sigma_{eff}\cdot R}, \qquad (5.4)$$

with $\tau_o$ and $\sigma_{eff}$ being determined from a set of $\tau_{eff}(R)$ calculations according to Eq. (5.3) for ranges R between 3 and 30 km by linear regression.

The error of this simplification for a blackbody target has been determined for the 8 - 12 µm spectral sensitivity of the DUWIR camera to be 2 - 5 % for a relevant set of meteorological data.

For an initial test we modelled the S/N ratio of the fixed target on MPN tower (T = 300 °C, Ø = 0.22 m) on October 24. In addition, the S/N ratio is determined from a digitized IR picture by dividing the maximum grey

value by the rms-noise of the background. Both S/N values supply a good agreement. Thus, the same approximations were chosen for the calculation of the S/N ratio for the approaching Piper Navajo.

Figures 5.2 and 5.3 show S/N-values calculated by TRP for a DUWIR detector in the LWIR band. Again, the situations of October 24, and October 30, were chosen. The values of a division of the grey values and the rms-noise of the background which can be extracted from an IR-image of the scene in the 8 - 12 µm wavelength region are marked.

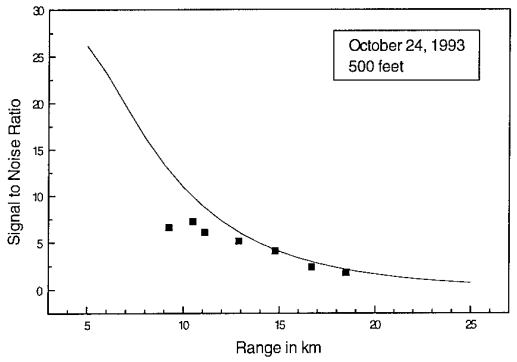


**Figure 5.2**: S/N ratio of the inbound flight of the Piper Navajo versus range for the LWIR. Date: October 24. The S/N values extracted from the digitized images are marked.

The temperature of the aircraft engines has been calculated to be 100°C. This temperature can be evaluated from a grey value analysis using the blackbody on MPN as a calibration source.

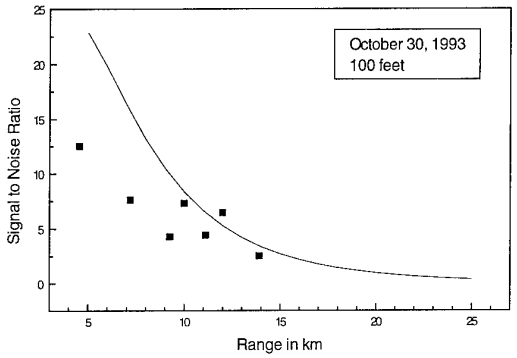


**Figure 5.3:** S/N ratio of the inbound flight of the Piper Navajo versus range for the LWIR. Date: October 30. The S/N values extracted from the digitized images are marked.

The TRP model calculates the signal to noise ratio for a point target. This basic requirement is certainly not fulfilled for short distances. Therefore, at small ranges there are deviations between the modelled curve and the dotted values calculated from the digitized IR images in figures 5.2 and 5.3.

The distances where the approaching aircraft becomes discernible (see chapter 4) result in a S/N of 0.9 for October 24, (altitude: 500 feet) and 2.4 for October 30, (altitude: 300 feet).

## 6. Signal Recovery from Bispectra

An IR image of a moving target is often very noisy due to a structured background or a turbulent atmosphere. It is sometimes nearly impossible to extract the target from the background.

An averaging of images leads to a reduction of the signal to noise ratio. This is a useful method if the target is fixed, but the image of a moving target will become a blurred picture or, in the worst case, disappear in the background.

Figure 6.1 shows the enlarged first and the last images of a sequence of 6 seconds duration. It shows the Piper Navajo in the morning of October 24, at an altitude of 200 feet and a distance of 7.5 nautical miles. According to the results of the previous chapter the signal to noise ratio at that distance is about 4.5.

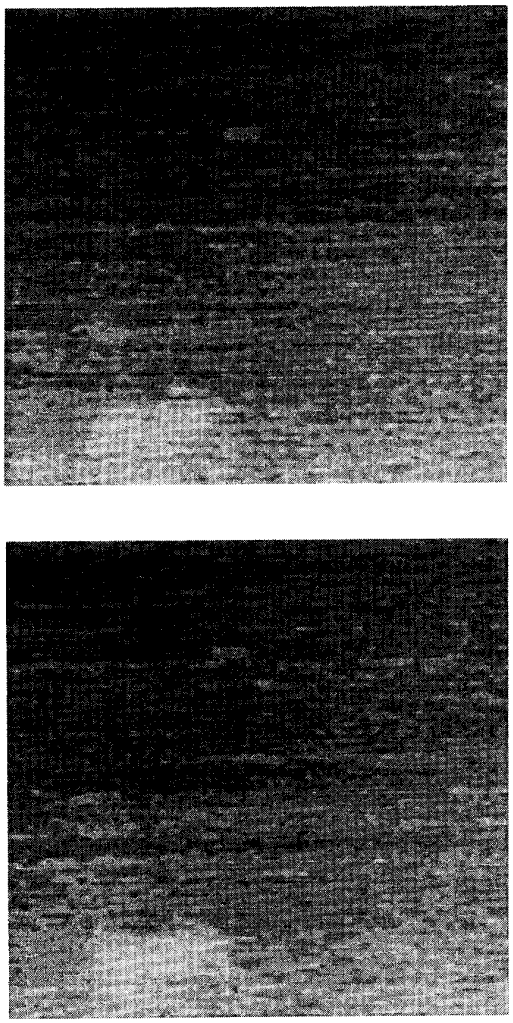

**Figure 6.1**: Enlarged images of the approaching aircraft on October 24, altitude: 200 feet, distance: 7.5 nmi. The time interval between the pictures is 6 s.

Figure 6.2 gives an example of an averaging of the scene. Each third picture was taken; in doing so, 49 images were added. The results is a poorly defined object.

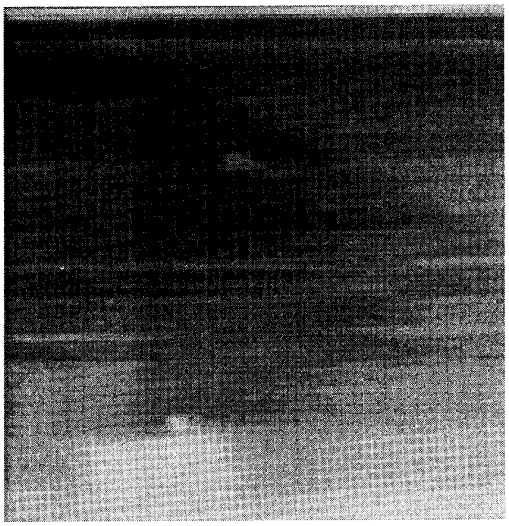

**Figure 6.2:** Temporal averaging of the scene (see text)

An averaging scheme that takes into account the movement of the target fails because the image of the object changes its shape.

To detect the target, independent of its movement, an algorithm has been developed at FGAN-FfO [Jantz] which uses bispectrum analysis.

The bispectrum is the Fourier transform of the triple correlation, sometimes also referred to as triple product integral. Bispectrum analysis has the advantage that information about both, modulus and phase of the Fourier transform of the signal is retained.

The autotriple correlation $T^{(3)}(x_1,x_2)$ of a function $T(x)$ can be interpreted as a higher dimensional generalization of the common correlation operation.:

$$T^{(3)}(x_1,x_2)=\int T(x)T(x+x_1)T(x+x_2)dx. \qquad (6.1)$$

Its Fourier transform is called the bispectrum $T'^{(3)}(u_1,u_2)$:

$$T'^{(3)}=T'(u_1,u_2)T'(u_1)T'(-u_1,-u_2). \qquad (6.2)$$

Our method for recovery from bispectra is based on a technique by Bartelt et al. [Bart]. But whereas they used one-dimensional (1-D) signals, our algorithm includes 2-D signals ( note that the triple correlation and the bispectrum of a 2-D function are 4-D functions).

Figure 6.3 shows the signal recovered from bispectrum data. The bispectra of each third picture of the scene mentioned above were taken. These 49 bispetra were then averaged. Now both engines of the aircraft can be clearly separated.

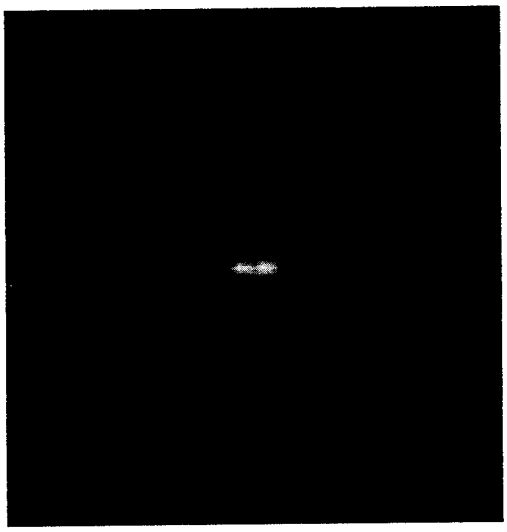

**Figure 6.3:** Averaging of bispectra (see text)

The algorithm includes a filtering method taking into account atmospherical noise.

In the near future this algorithm will be modified by including meteorological data and performance parameters from the thermal imager.

## 7. Conclusions and Recommendations for Future Work

In this paper we presented the initial results of the analysis performed by the FGAN-FfO with respect to point target characterization in a coastal environment. IR-images taken in the two wavebands (3 - 5 µm and 8 - 12 µm) of a DUWIR camera were examined.

Two weather situations were selected: clear weather and heavy sea fog. Even though the visibility was sometimes very low, the transmission in both IR-wavebands was quite good. The LWIR provided higher target-to-background contrast than the MWIR band.

Most of the results reported here were drawn from the images in the 8 - 12 µm waveband. Future work will concentrate on a comparison of both wavebands.

In addition, we will treat a greater variety of weather situations. The influence of meteorological parameters and aerosol size distribution profiles on the spatial and temporal behaviour of fixed and moving targets will be analyzed.

The problem of resolving multiple targets at long distances will also be further analyzed by using different IRST algorithms. Of particular interest to this analysis is the point where a single target can be resolved into two targets.

**Acknowledgement**

The authors thank Engelbert Wolf for his active assistance during the experiment.

**References**

[Bart] Bartelt, H., Lohmann, A.W., Wirnitzer, W., "Phase and amplitude recovery from bispectra", Applied Optics Vol. 23, No.18, 1984.

[CELAR] Hurtaud, Y., Centre D'Electronique de L'Armement, Division ASRE, Bruz, France, Private Communications.

[Clement] Clement, D., Höhn, D.H., Jessen, W., Kohnle A., "Atmospheric Performance Statistics for IR Broad-Band and Laser Systems based upon OPAQUE Data (N.U.)", AGARD Conference Proceedings No. 454, 1989.

[DREV] Bissonette, L. R., Defence Research Establishment Valcartier, Quebec, Canada, Private Communications.

[IDL] Interactive Data Language Version 3.5; Research Systems, Inc., November 1993 Edition.

[Jantz] Jantzen, R., FGAN-FfO, Tübingen, Germany, to be published.

[LOWTRAN] Low Resolution Atmospheric Transmittance and Emission, Computer Code US AFGL.

[NCCOSC] Jensen, D. R., Naval Research and Development (NRaD), Code 543, San Diego, USA, Private Communications.

[SPIE] Kohnle, A., Stein, K., et al., "Evaluation of Essential Design Criteria for IRST Systems", SPIE Vol. 2020 Infrared Technology XIX, San Diego 1993.

[TRP] Schuberth, W., "Thermisches Reichweitenmodell zur Punktzielauffassung (TRP)", FGAN-FfO, Tübingen, Germany, Report 1992/20.

# MAPTIP: Canada's Measurements of Refraction Effects

**J.L. Forand, D. Dion and J. Beaulieu**
Defence Research Establishment Valcartier
2459 Pie XI Blvd., North (P.O. Box 8800)
Courcelette, Québec
Canada GOA 1R0

## 1. SUMMARY

This paper presents some results obtained by Canada's Defence Research Establishment Valcartier (DREV) during the Marine Aerosol Properties and Thermal Imager Performance (MAPTIP) trial off the North Sea coast of The Netherlands during October 1993. Our study of refraction effects in the Marine Boundary Layer (MBL) in both the visible and infrared (IR) wavelength bands produced a large quantity of excellent experimental data. Along with data obtained from previous campaigns[1,2] in both Canada and Germany, this data set is being used to test the validity of the WKD[3] and the Wavy WKD (WWKD)[4] models developed by DREV. These early results from the recent MAPTIP trial have shown that in general the predictions of the WWKD model agree remarkably well with the experimental data.

## 2. INTRODUCTION

Due to the electromagnetic nature of many sensors and probes used by today's military, the propagation of electromagnetic radiation through the atmosphere is a question of extreme importance and relevance. A non-refractive atmosphere is one in which the refractive index is invariant with position or in which all radiation follows straight lines. However, the refractive index of the atmosphere depends upon position dependent quantities such as pressure, temperature and water vapour content and as a result radiation will generally follow a curved path. In other words, the apparent elevation angle of an object to an observer will not be that defined by the straight line between them but by the tangent, at the observer, of the curved path between them (see Fig. 1). Close to the earth, this leads to two important atmospheric phenomena (Fig. 2 & 3). The first is called

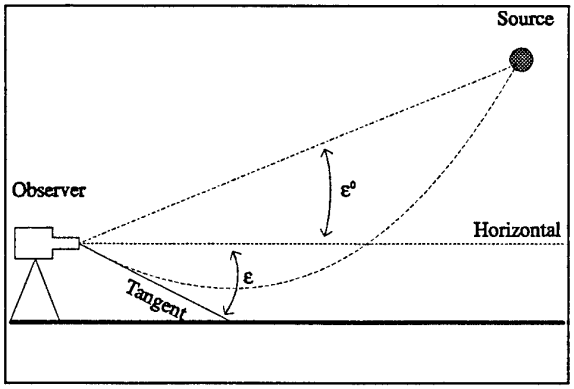


**Figure 1** - The dashed lines show rays for a non-refractive and refractive atmosphere. $\varepsilon^0$ and $\varepsilon$ are their respective elevation angles.

sub-refraction and in certain cases leads to the creation of a mirage. This occurs when electromagnetic radiation from an object appears to an observer as if it is coming from two different objects at different elevations (Fig. 2). The second is commonly called ducting (super-refraction) and occurs when electromagnetic radiation from an object, which would not be observable in a non-refractive atmosphere, is nevertheless detectable by an observer (Fig. 3). The amount and direction (towards or away from the earth) by which radiation is deviated from a straight line depends

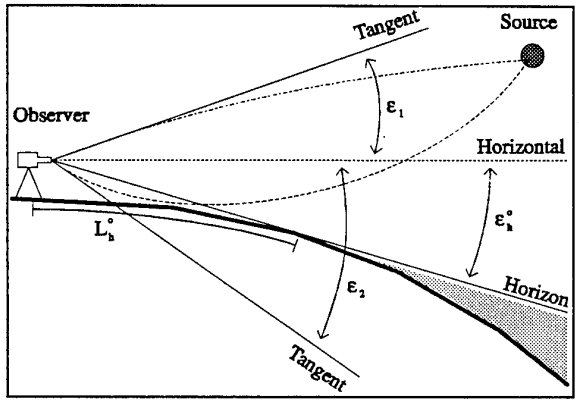


**Figure 2** - Two images of the source are seen at two elevation angles. $L_h^0$ and $\varepsilon_h^0$ are the horizon distance and angle.

upon both the meteorological conditions of the atmosphere and the wavelength of the radiation. In the marine environment, where the only obstructions are due to the waves, this leads to the fact that under some conditions the distance to the horizon may be shortened while under other conditions it may be lengthened. In either case, the maximum detection range (MDR) at which an object can be observed and its measured elevation angle are different from what one would expect if the atmosphere was non-refractive. The maximum intervisibility range (MIVR) can be determined under sub-refractive or near neutral conditions if the range is not limited by the visibility conditions of the atmosphere.

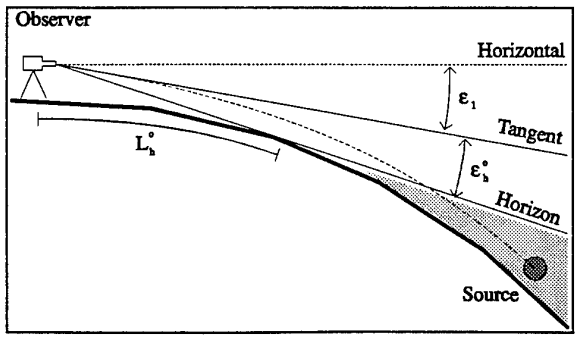


**Figure 3** - An image of the source is seen when it is below the normal horizon. $\varepsilon_1$ is the elevation angle.

*Paper presented at the Sensor and Propagation Panel Symposium on "Propagation Assessment in Coastal Environments" held in Bremerhaven, Germany 19-22 September 1994.*

## 3. ATMOSPHERIC REFRACTION

The bending of electromagnetic waves by the atmosphere is due to vertical and horizontal gradients in the atmosphere's refractive index. These gradients are caused by variations in atmospheric parameters such as the total atmospheric pressure, the air temperature, and the partial pressure of the atmosphere's various gases. The most important of these gases is water vapour due to its often substantial variation with height. In fact, as all these parameters vary principally with height, the atmosphere's index of refraction, to first order, can be expressed as a function of height. Available information[5] on the refractive index of air for the dry air contribution and the water vapour contribution to the index of refraction, allows the index of refraction, n, as a function of both height (h) and wavelength ($\lambda$) to be expressed by:

$$n(\lambda,h) = 1 + R(\lambda,h) \times 10^{-6} \quad (1a)$$

where

$$R(\lambda,h) = A(\lambda)[P(h)-V_p(h)]/T(h) + B(\lambda,T)V_p(h)/T(h) \quad (1b)$$

and R is the refractivity. The atmospheric pressure, P (millibars), the air temperature, T ($^0$K), and the water vapour pressure, $V_p$ (millibars), are all functions of the height. $A(\lambda)$ is a coefficient given by Edlén[6] for the dry air contribution and $B(\lambda,T)$ is the coefficient for the water vapour contribution[5]. As discussed by Beaulieu[4], the coefficients A and B for the 3 to 5 μm band (mid-infrared) and the 8 to 12 μm band (far-infrared) can be approximated with constants. Using the same arguments for the visible band (0.5 to 1.0 μm) and the near-infrared band (1 to 3 μm), the following coefficients (see Table 1) can be obtained for the four bands.

**Table I**: Coefficients

| Wavelength Band | Range (μm) | A | B |
|---|---|---|---|
| Visible | .5 - 1 | 78.5 | 67.0 |
| Near-Infrared | 1 - 3 | 77.7 | 65.5 |
| Mid-Infrared | 3 - 5 | 77.5 | 65.0 |
| Far-Infrared | 8 - 12 | 77.5 | 40.0 |

The gradient of Equation 1 with respect to height is given by:

$$n'(\lambda,h) = dn/dh = R'(\lambda,h) \times 10^{-6} \quad (2a)$$

where

$$R'(\lambda,h) = [AP'(h) + (B - A)V'_p(h) - R(\lambda,h)T'(h)]/T(h). \quad (2b)$$

As a typical value for R in both the visible and infrared bands is about 300, Equation 2b implies that in order for the terms involving the atmospheric pressure gradient and the water vapour pressure gradient to be the same order of magnitude as the term containing the temperature gradient, their gradients must be approximately 4 and 15 times greater, respectively. From the hydrostatic equation[6], the atmospheric pressure gradient and the water vapour pressure gradient are approximately equal to -1 mbar/10 m. Thus, depending on the value of the temperature gradient, one of the two following approximations can often be made.

$$R'(\lambda,h) \approx -R(\lambda,h)T'(h)/T(h) \quad ;P' << T' \ \& \ P' \approx V_p' \quad (3a)$$

$$\approx BP'(h)/T(h) \quad ; T' << P' \ \& \ P' \approx V_p' \quad (3b)$$

From these relationships, a very good indication as to whether a given weather situation will produce sub-refractive or super-refractive effects can be made simply by measuring the air-sea temperature difference (ASTD). An ASTD greater than zero ($T'(h) > 0$) implying that the atmosphere is super-refractive (ducting) and an ASTD less than zero ($T'(h) < 0$) implying that the atmosphere is sub-refractive (mirage) atmosphere. For an ASTD close to zero, for which the conditions in Equation 3a are not satisfied, Equation 3b implies that the atmosphere should be slightly super-refractive since both $P'(h)$ and $V_p'(h)$ are normally negative.

To model refractivity effects in the atmosphere using Equation 1, a method is required to determine the vertical profiles of air temperature, water vapour pressure and total air pressure. The first two are particularly important. As it is not generally practical to measure these parameters at a large number of points for the first tens of meters of the atmosphere (boundary layer), profiles generated using similarity theory[7,8] are often used. At DREV we have been using our own WKD Marine Boundary Layer model (MBL)[3,4] which requires measurements of the water temperature, the wind speed, the air temperature, water vapour pressure (or relative humidity) and total air pressure. The last three should be measured at the same height above the water level. Once these profiles are generated, they can be used in Equation 1 to determine the refractivity profile which can be used by a ray tracing program to generate theoretical predictions.

## 4. EXPERIMENTAL METHODS

The experimental methods that were used during the MAPTIP trial were variations of two simple techniques that we have previously used[1,2] (Fig. 4). At one end of a range, henceforth to be called the BASE, several observation devices, for example

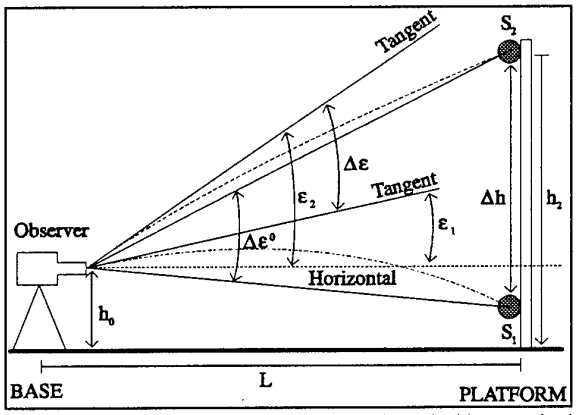


**Figure 4** - Two radiation sources are placed with a vertical separation, Δh, at a distance, L, from the observer. The observer measures the angle Δε.

camera systems in the IR and visible, are placed at known heights above the mean water level (MWL). At the other end of the range, henceforth to be called the PLATFORM, several radiation sources are placed at different known heights above the MWL. One of the sources should be placed as high as possible to serve as a reference. In this way, refractive effects can be studied using one of two previously discussed techniques[2]. If the range is kept constant, one can study the effect of varying the height of the observers or the sources (Height Scan). This technique is excellent for comparing the measured angular separation ($\Delta\varepsilon$) between images and the angular separations expected for a non-refractive atmosphere ($\Delta\varepsilon^0$) or the angular separations predicted by theory. On the other hand, the elevations of the sources and observers can be kept fixed while the range between the BASE and the PLATFORM is continuously varied (Range Scan). This technique is an excellent method for measuring the maximum intervisibility range (MIVR), as the range at which a source at a given height disappears below the horizon can easily be compared with that expected for a

non-refractive atmosphere or that predicted by a theoretical model.

### 4.1 Non-refractive Atmosphere

For a non-refractive atmosphere, $\Delta\varepsilon^0$ depends on the range, the height of the observer at the BASE ($h_0$) and the heights of the two sources at the PLATFORM ($h_1$, $h_2$) above the MWL such that:

$$\Delta\varepsilon^0 = \varepsilon^0_1 - \varepsilon^0_2 \approx \Delta h/L \quad \text{if } L, h_0, h_1 \,\&\, h_2 << R_e \qquad (4a)$$

where

$$\varepsilon^0_n = \tan^{-1}[(R_n\cos(L/R_e) - R_0)/(R_n\sin(L/R_e))] \approx (h_n - h_0)/L, \qquad (4b)$$

and

$$R_n = R_e + h_n \ (n = 0,1,2) \qquad (4c)$$

where $R_e$ is the earth's radius. Two other quantities of interest, are the distance to the horizon in a non-refractive atmosphere ($L_h^0$) and its elevation angle ($\varepsilon_h^0$). They are given by

$$\varepsilon_h^0 = \cos^{-1}[(R_e + h_w)/R_0] \approx [2(h_0 - h_w)/R_e]^{1/2} \ ; \ h_w<h_0<<R_e \qquad (5a)$$

and

$$L_h^0 = R_e \times \varepsilon_h^0 \approx [2(h_0 - h_w) \times R_e]^{1/2} \ ; \ h_w<h_0<<R_e, \qquad (5b)$$

respectively with $h_w$ being the amplitude of the waves. This means that for a non-refractive atmosphere the minimum observable height, $h^0_{min}$, for an object at a range, $L > L_h^0$ is

$$h^0_{min} = \frac{h_0\cos(\varepsilon_h^0)+R_e[\cos(\varepsilon_h^0)-\cos((L-L_h^0)/R_e)]}{\cos((L-L_h^0)/R_e)} \qquad (6a)$$

$$\approx h_0 + L(L - 2L_h)/2R_e \ ; \ L << R_e \qquad (6b)$$

Thus the MIVR for a source at a height, h, in a non-refractive atmosphere can be approximated by

$$MIVR = L \approx L_h^0 + [2R_e(h - h_w)]^{1/2}. \qquad (7)$$

## 5. EXPERIMENTAL SETUP

The work plan for the MAPTIP trial[9] mentions in great detail the general setup of the experiment. Consequently, only the setup used by Canada at the beach station (WPB), on the meteorological station (MPN), and on the Hr. Ms. Tydeman will be discussed. Figure 5 shows the principal waypoints and the positions of the MPN and the beach station. The MPN is about 10.4 km from the beach station and the principal tracks of the Tydeman are marked by the solid lines. These lines join waypoints WPB and WPG and waypoints MPN and WPC. Most of our measurements were taken during the WPB to WPG track.

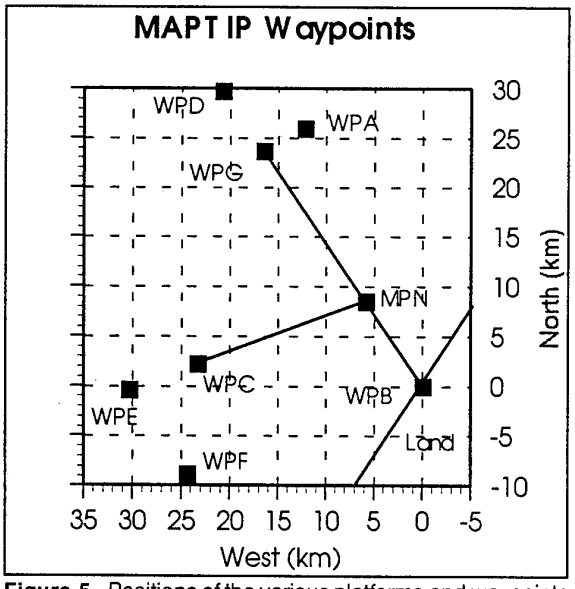


**Figure 5** - Positions of the various platforms and waypoints used during the MAPTIP trial.

### 5.1 Katwijk Beach Station

A schematic of our setup at the beach station is shown in Fig. 6. Three camera systems, two working in the visible band and the other in the 3 to 5 micron IR band were used. Table 2 summarizes the operating characteristics of each. The VIS 1 camera system

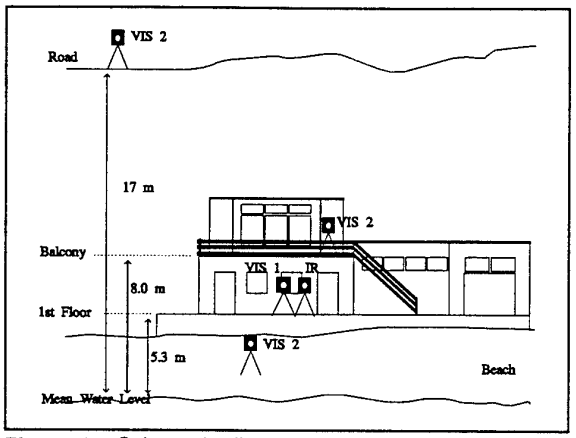


**Figure 6** - Schematic diagram of the setup at the beach station.

consisted of a CCD camera with a cuton filter at 850 nm and a 2.0 m f/10 telescope with a resolving power of 6 μrad at 1 μ. The VIS 2 camera system used an identical camera with a cuton filter at 715 nm and a 1.3 m f/14 telescope with a resolving power of 13 μrad at 1 μ. The IR camera system consisted of a PtSi detector sensitive to the mid-IR band (3-5 μ) and a 2.0 m f/10 telescope with a resolving power of 24 μrad at 4 μ. To use the Celestron telescope in the mid-IR, its corrector plate was removed. As the VIS 2 system was very portable, it was operated from a position on the beach and occasionally from both the balcony and the road. The less portable (VIS 1) and IR cameras were always operated from the first floor and almost always at the same height above the MWL.

The video outputs of the three camera systems had time-codes added to their signals and they were recorded for later study onto SVHS tape in NTSC format. Further analysis is done using a 640(H) x 480(V) square pixel framegrabber using software developed at DREV. The pixel resolution for each of the camera systems is given in Table 2.

**Table 2:** Camera System Specifications

| | VIS 1 | VIS 2 | IR |
|---|---|---|---|
| **Camera** | | | |
| Make | Sony | Sony | Mitsubishi |
| Model | AVC-D5 | AVC-D5 | 5120A |
| Detector(HxV) | CCD 510X492 | CCD 510x492 | PtSi 512x512 |
| Wavelength(μm) | > 0.850 | >0.715 | 3.3 - 5.0 |
| **Telescope** | | | |
| Make | Celestron | Questar | Celestron* |
| Focal Length(m) | 2.032 | 1.300 | 2.032 |
| f number | f/10 | f/14 | f/10 |
| Res. power(μrad) | 6 @ 1μ | 13 @ 1μ | 24 @ 4μ |
| **Framegrabber** | | | |
| Resolution(μrad/pix) | 6.66 | 9.19 | 7.1 |

* Corrector plate removed.

### 5.2 Hr. Ms. Tydeman

The Hr. Ms. Tydeman (Fig. 7) is a Dutch navy research vessel that has a length of 90 m long and a width of 14.5 m and has a top cruising speed of 15 knots (28 km/hr). Figure 7 shows a rear view of the Tydeman with the measured locations of seven lamps. Of the two lamps close together in the middle, only one of them was used at a time. The lamp to the right was a 500 W halogen lamp provided by DREV while the lamp on the left was a small white navigation light. It was used during the morning of Oct. 27 while our light, which had bumt out, was being replaced. The remaining lights were all 500 W halogen provided by the Tydeman. Of these lights, the four lowest lights were simply reoriented so that they were horizontally level and facing straight off the ship's stem. The remaining light was specially mounted, with the Captain's permission, in the crow's nest. With this setup, we were able to track the ship on its outward legs and determine the MIVR of each lamp for each of the three camera systems.

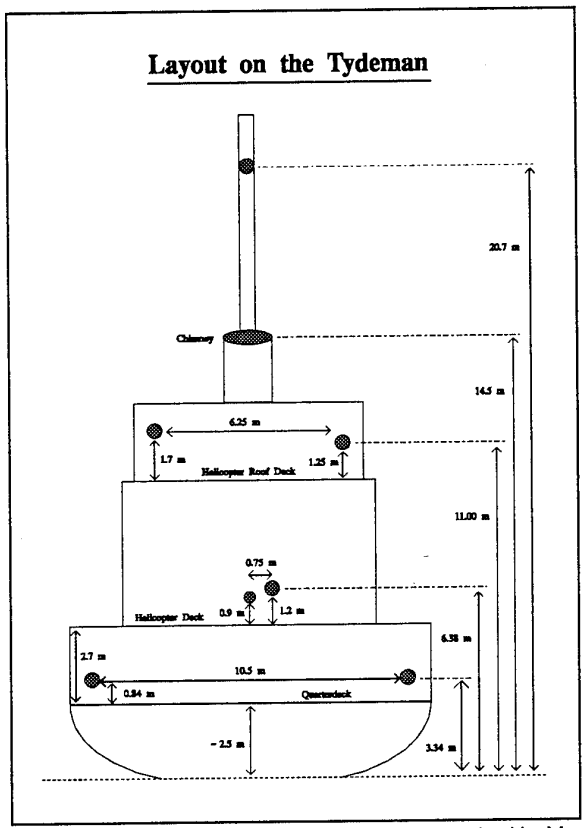


**Figure 7** - Schematic diagram of the setup on the Hr. Ms. Tydeman.

### 5.3 Meetpost Noordwijk (MPN)

The MPN (Fig. 8) is a platform sitting in about 20 m of water about 8 km off the Dutch coast near the town of Noordwijk and about 10.4 km from the beach station. Its steel superstructure is 25x16x7 m and sits about 12 m above the MWL. Figure 8 is a schematic of the platform's south side and shows the locations of the eight 500 W 110 V halogen lamps that we mounted to its structure. To use the 220 V power supplied by the platform, the lamps were run in four matched sets of two and were positioned from 3.5 m to 20 m above the MWL. They were horizontally spaced about 1 m apart so as to minimize any possible overlap of the images when seen by the three camera systems and to facilitate later image analysis. At the beginning of the trial (Oct. 18) only four of the lamps were in operation. The highest two lamps were brought into service on Oct. 19 and the two lowest lamps by 1300 GMT on the same day. All eight lamps remained in operation until Oct. 29 when Canada ended its participation in the MAPTIP trials.

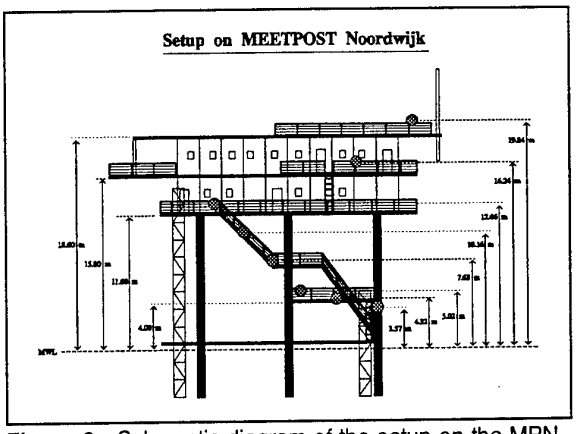


**Figure 8** - Schematic diagram of the setup on the MPN.

## 6. RESULTS

The following section shows several examples of some early results that we have investigated. Two examples are shown for the observations obtained while tracking the ship and a single case for observations obtained while watching the MPN. For the WWKD model calculations, the largest uncertainty involved the air temperature, as readings from different sites and sensors were not always consistent. As a result a somewhat best guess has been used.

### 6.1 Measurements of the Tydeman

Figures 9 and 10 show both the measurements and the WWKD model prediction for two different ship tracking sessions. The figures show the geometrical horizon limit (dashed line), the WWKD model calculated horizon limit (thick solid line), and the WWKD model predicted range at which mirages should first form (solid line). For figure 9, this means that for a target at a height of 10 m that is moving away from an observer, the observer will suddenly see two images of the target (a mirage) at a distance of about 10.6 km. As the range increases, these two images will gradually approach one another, fuse together, and finally disappear from view at a refraction-shortened horizon of 16.1 km. This is 5 km closer than the calculated distance to the geometrical horizon of 21 km.

Figure 9 corresponds to the morning track on Oct. 19. During the track, the ASTD was relatively large (~-7°C) and the wind was from the east and relatively light at ~3 m/s. The wave heights were about 30 cm, the sky was clear, and the relative humidity was about 80%. The plotted data was obtained for both the IR and VIS 1 sensors at a nominal height of 7.5 m above the MWL. As can be seen the measured data for both sensors (IR: ▲ and VIS 1: ■) compares very well to the model predicted distance to the horizon limit. The model prediction for the earliest formation of a mirage is also quite good for the VIS 1 camera, but there is a definite problem with the IR camera results. This may be

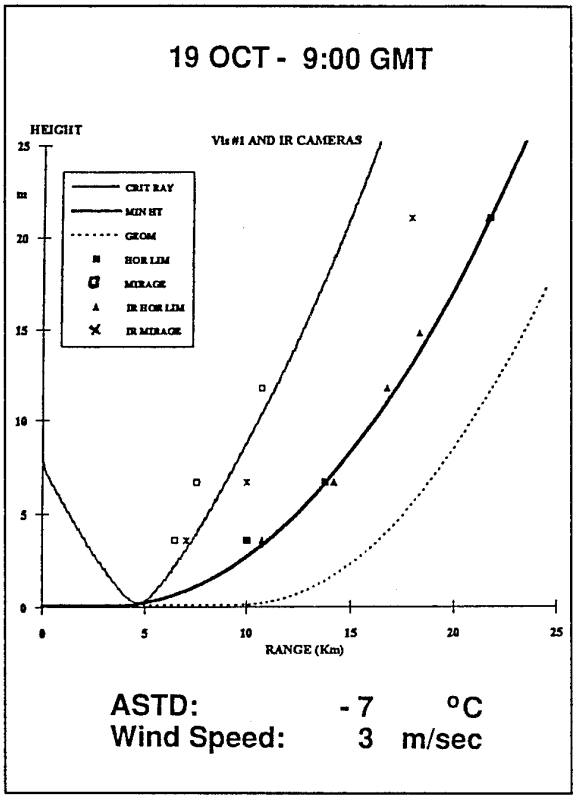


**Figure 9** - Results from the tracking of the Tydeman on Oct. 19, 1993.

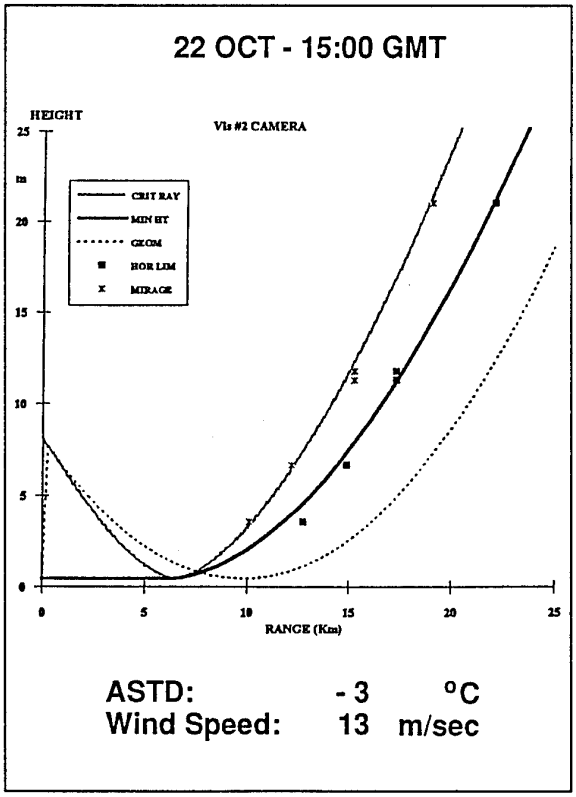


**Figure 10** - Results from the tracking of the Tydeman on Oct. 22, 1993.

due to the reduced sensitivity of the IR system compared to the visible systems such that the onset of the initially weak mirage was not observed until the ship was at a greater range and the mirage was more intense.

Figure 10 corresponds to the afternoon track on Oct. 22. During the track, the ASTD was ~-3°C and the wind was from the northeast and relatively strong at ~13 m/s. The wave heights were about 100 cm, the sky was partly clear, and the relative humidity was about 72%. The plotted data shows results obtained with the VIS 2 sensor at a nominal height of 8.0 m above the MWL. As can be seen, the measured data (■ and x) agree quite well with the two range limits predicted by the model.

The good agreements between the MIVR measurements and the WWKD model calculations are quite representative of all the results obtained from tracks of the ship during MAPTIP. In most cases, the difference is less than 500 m. This is quite reasonable as the uncertainty in the measured range is about 200 m. This uncertainty is largely due to the subjective nature of determining at what time (and range) one has begun to see a mirage or has lost sight of an image because it has gone beyond the horizon. The difficulty lies in the fact that the ship was often bouncing up and down in the waves by several meters such that for a source at a height of 10 m, Fig. 9 shows that a variation in height of 1 m could leadto a variation in the predicted horizon limit of 600 m.

### 6.2 Measurements of MPN

In most cases studied, the measurements taken are in rather good agreement with the WWKD model predictions. In fact the variation between the two is often less than 10 μrad which corresponds closely to the resolution power of the camera systems (see Table 2). Figure 11 is an example of one of the exceptions. It shows the results of a measurement taken with the VIS 1 camera at 11:06 GMT on Oct. 28, 1993. On this day the wave heights were 50 cm, the ASTD was ~-3°C, the wind was from the east (~80°) at about 6 m/s, the relative humidity was ~77%, and the sky was partly cloudy. The graph plots the relative observation angle of each recorded image with respect to the topmost light (light #8) against the relative height of each light source with respect to light #8. The graph shows the measured values (■) along with three curves generated using the WWKD model with three different ASTDs. From the graph it is obvious that the best fits are given for an ASTD of -3.5°C or -4°C and that the fit is not very good for an ASTD of -2.5°C. These discrepancies are thought to be principally due to horizontal inhomogeneities in the marine

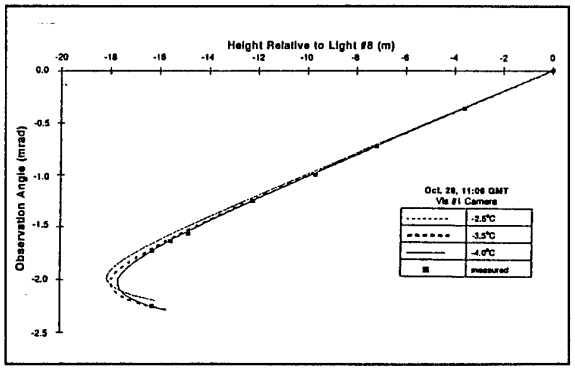


**Figure 11** - Results from an observation of the MPN platform at 11:06 GMT on Oct. 28, 1993.

boundary layer of the atmosphere along the direction of observation.

## 7. CONCLUSIONS

The MAPTIP trials, which were held in The Netherlands during Oct. of 1993, were very successful and have provided us with a large quantity of excellent data about refraction effects. Significant refraction effects were observed under conditions with ASTDs from $0^0$C to $-7^0$C along with wind speeds ranging from 3 to 15 m/s. The results taken from the measurements obtained from both the Hr Ms. Tydeman and the MPN platform are very encouraging and give results are in satisfactory agreement with the predictions of the WWKD model in both the mid-infrared and visible. The discrepancies between the model predictions and the measurements are thought, in large part, to be due to inhomogeneities in the marine boundary layer because of coastal effects. This is particularly true when the wind comes from the land as is the case with the data given in both Fig. 9 and Fig. 11.

In the following year we need to produce a more refined weather summary for the relevant experimental time periods. This is required so that the reasons put forward for the differences between the model predictions and the results can be more rigorously investigated and so that the degree of agreement can be more quantitatively measured.

## 8. ACKNOWLEDGEMENTS

MAPTIP was sponsored by NATO AC/243 (Panel 4) (Grants 6056 and 6092) and ONR (Grant N00014-91-J-1948) to cover logistic costs. Canada's refractive studies were sponsored by DMCS-4 (Task #121). Canada would like to personally thank all the Dutch personnel who were involved in the trial, both civil and military, for their excellent work and assistance before, during, and after the trial. This is particularly true for the installation and orientation of our light sources on both the Tydeman and the MPN. Lastly, but certainly not least we would like to thank the members of our technical staff. Thanks to J. Oman for his fine work and stamina on the MPN, to C. Grenier and M. Hale for their work installing our equipment, positioning and repositioning it and helping to take the data. Special thanks go to M. Hale who organized the transport of all our equipment.

## 9. REFERENCES

1. Dion, D., Forand, J.L., Fournier, G.R. and Pace, P, "Experimental Data on Near-Surface Refraction Effects at Optical Wavelengths", Proceedings of SPIE's Int. Symposium on Optical Applied Science and Engineering, San Diego, 1992.

2. Forand, J.L., Fournier, G.R., Dion, D., Pace, P. and Beaulieu, J., "Details of the "MIRAGE" Trials: Atmospheric Refraction in the Maritime Boundary Layer", DREV-TM-9407, May 1994, UNCLASSIFIED.

3. Low, T.B. and Hudak, D.R., "Final Report on the Development and Testing of a Marine Boundary Layer Model", KelResearch Corp. Report under DSS contract #W7701-8-2419/01-XSK, September 1990.

4. Beaulieu, A.J., "Atmospheric Refraction Model and the Effects of Surface Waves", DREV R-4661/92, May 1992, UNCLASSIFIED.

5. Dion, D. and Leclerc, B., "Investigation of the Air Refractivity Effects on IR Sensors in the Marine Boundary Layer", DREV R-4570/90, August 1990, UNCLASSIFIED.

6. Edlén, B., "The Dispersion of Standard Air", J. Opt. Soc. Am., Vol. 43, No. 5, pp. 339-343, May 1953.

7. Lumley, J.L. and Panofsky, H.A. "The Structure of Atmospheric Turbulence", Interscience Monographs and Texts in Physics and Astronomy, Vol. XII, John Wiley & Sons, 1964.

8. Hornstein, J.S., Prifst, R.G., Takken, E.H. and Baukman, D., "Models of Refraction in the Marine Atmospheric Surface Layer", Naval Research Laboratory, NRL/FR/7227--93-9547, September 1993.

9. Jensen, D.R., de Leeuw, G. and van Eijk, A.M.J., "Work plan for the Marine Aerosol Properties and Thermal Imager Performance trial (MAPTIP)", Technical Document 2573, Naval Command, Control and Ocean Surveillance Center, San Diego, CA, U.S.A., September 1993.

## DISCUSSION

**J. CLAVERIE**

Vous montrez une situation où ASTD = -2,5°C avec un vent de terre ce qui conduit à un désaccord avec les observations, que vous expliquez par des inhomogénéités horizontales. De telles valeurs d'ASTD avec d'autres conditions de vent ont-elles été observeés et ont-elles conduit à une meilleure adéquation entre la modélisation et les mesures?

*You showed a case for ASTD=-2.5 °C with wind from the land leading to a disagreement between observations and predictions that you explained as due to horizontal inhomogeneities. Were similar ASTDs observed under different wind conditions and did these conditions lead to better agreements between observations and model predictions?*

**AUTHOR'S REPLY**

De bonnes prédictions (i.e. de l'ordre de la résolution des mesures) ont été obtenues pour une grande gamme d'ASTD et de vitesse de vent lorsque le vent ne venait pas directement de la terre.

*Very good agreements were obtained (i.e. discrepancies within measurement resolution) under a large diversity of ASTD and wind speed conditions when the wind did not blow directly from land.*

**R. PAULUS**

The ray trace diagram that you showed did not trace rays reflected off the sea surface. If these rays were traced, they would indicate that you would observe a reflected image at ranges shorter than the mirage range. Have you observed a reflected image?

**AUTHOR'S REPLY**

No clear and persistent reflections have been observed in our data set so far at mirage ranges or at closer ranges. To my knowledge, reflections of such sources are unlikely against a non-flat mirror sea surface.

# Surface Layer Turbulence and Aerosol Profiles During MAPTIP

**K. L. Davidson**
**P. A. Frederickson**
Department of Meteorology
Naval Postgraduate School
589 Dyer Rd., Room 254
Monterey, CA 93943-5114
USA
Tel: 408.656.2309 Fax: 408.656.3061 EMail: davidson@osprey.nps.navy.mil

**Gerrit de Leeuw**
TNO Physics and Electronics Laboratory
Oude Waalsdorperweg 63
2597 AK The Hague
The Netherlands

## SUMMARY

The Naval Postgraduate School (NPS) and the TNO Physics and Electronics Laboratory (TNO-FEL) deployed in situ sensors near and on Meetpost Noordwijk (MPN) during MAPTIP to describe the surface layer processes and also to evaluate models for near-surface aerosol profiles. Vertical profiles of aerosol counts were measured on the MPN tower by TNO-FEL with Rotorod impaction samplers. The aerosol distribution measurements were made for 10 radius bins, with centered radii ranging from 6.5 to 75 μm. Atmospheric surface-layer turbulence and stratification were measured by NPS from an instrumented buoy that was located a short distance from MPN. Existing models relate aerosol profiles to source, sink, and turbulent transport processes. The assumed source process is bursting air bubbles at the surface. The removal processes are turbulent deposition and gravitational fallout. Turbulent transport is described by the friction velocity and the near-surface stratification. The combined buoy and MPN data sets are shown to provide valuable descriptions of surface layer properties during the variable period from 26 October through 3 November. Results from eleven profile sampling periods were compared with model predictions for which buoy measured parameters and aerosol sizes were inputs. The predicted concentration often decreased more with height than observed. This is believed due to the coastal input to the aerosol source since advected aerosol would reduce influences on gradient of bubble production at the surface.

## 1. INTRODUCTION

Describing height variations of aerosol size spectra in the surface layer is important to both understanding thermal imaging results from MAPTIP and to understanding processes important in modeling of aerosol, in general. Surface layer aerosol properties described by existing equilibrium models, i.e. NOVAM [1], are based on empirical data and can be assumed to apply to a level some distance above the surface, around 10 meters. For imaging of targets near the horizon, some knowledge of vertical gradients are necessary to take into account a path that traverses layers extending from the surface and up. Models for aerosol in the marine boundary layer are based on source/sink, transport (mixing), and chemistry characteristics. Processes affecting aerosol are expected to increase/decrease from the boundary, i.e. in the vertical. Relative humidity will decrease from the ocean surface which is also the source of bubble produced sea-salt aerosol. It is also the sink if removal is by gravitational fall-out and turbulent deposition. Turbulent mixing would diminish the strengths of the gradients produced by the surface's dominant role in the processes. However, accurate measurement of aerosol profiles (gradients) are as appropriate for evaluation of model performances as are aerosol concentrations themselves. For this to be true, the turbulent processes (mixing and deposition) have to be accounted for.

We will describe the results from examinations of near-surface aerosol profiles measured during MAPTIP relative to transport and removal processes, available through measurement or calculated from the data. We will also present atmospheric surface layer properties, as measured from MPN and the NPS buoy, during MAPTIP. The latter show the wide range of wind forcing and stability conditions affecting MAPTIP and important to all interpretations of the collaborative obtained data bases.

An expression for given aerosol radius concentrations, $X_i$, at two different heights, $Z_i$, where i = 1 and 2, is [2,3]

$$\mathrm{Ln}(X_2/X_1) = -[V_d/ku*]\,[\mathrm{Ln}(Z_2/Z_1) - \Psi(Z_2/L) + \Psi(Z_1/L)] \quad (1)$$

$u*$ is the surface-layer friction velocity, $\Psi(Z_i/L)$ is an empirically formulated scaling expression, e.g. Businger et al. [4], L is the Monin-Obukhov stability length, and $V_d$ is a removal velocity that depends on turbulent deposition and gravitational settling [5]. By convention, $V_d$ is positive if the aerosol is falling. This expression was formulated by Toba [6] with the assumption of a balance between surface production and removal, no horizontal advection, and constant turbulent vertical transport. Eqn (1) extends Toba's formulation to include non-neutral stratification but neglects the relative humidity influence on aerosol size. The latter could be important if the very near-surface, Z < 2 meters, gradients are being considered or if relative humidity is close to 100%.

The Eqn (1) predicted gradient depends on aerosol size because of $V_d$ which is the sum of gravitational settling and turbulent deposition velocities, [5]. Gravitational settling depends on aerosol density and the radius squared, $r^2$, and turbulent deposition depends on $u*$ as well as the radius.

*Paper presented at the Sensor and Propagation Panel Symposium on "Propagation Assessment in Coastal Environments" held in Bremerhaven, Germany 19-22 September 1994.*

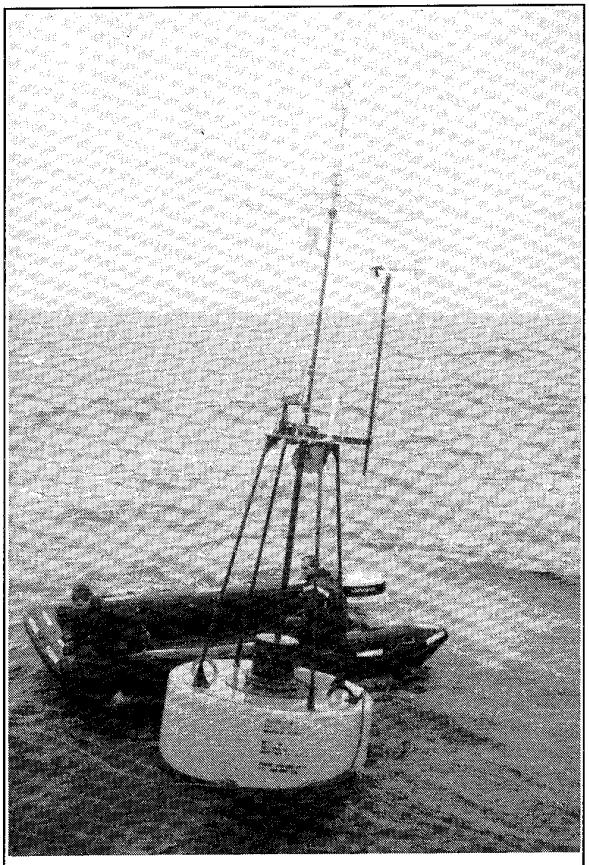

Figure 1.
NPS surface-flux buoy being deployed NW of MPN, top of mast is 5 m above water line

## 2. NPS BUOY AND SURFACE LAYER CONDITIONS DURING MAPTIP

### 2.1. Buoy Deployment and Turbulence Calculations

The NPS buoy, Figure 1, was deployed at fixed location approximately 560 meters northwest of MPN, Figure 2. Its first deployment was at 1500 UT on 11 October. At that time, continuous mean and turbulent wind and virtual temperature measurements were made with a sonic anemometer (Solent) mounted atop a mast 5 meters above the water surface. Mean wind speed and direction measurements were also made with a propeller and vane (R. M. Young) located on the mast 4 meters above the water surface. Sea temperature was measured with a thermistor located approximately 0.5 meters below the water surface but yielded unexplained variations from the MPN measured values. Also, relative humidity and atmospheric pressure measurements could not be recorded, even at the time of initial deployment, due to a computer board failure.

At about 1130 UT on 12 October, less than 24 hours after initial deployment, a severe storm occurred and combined wave and wind effects cased the buoy sensors and inboard computer system to be damaged. Even though it was a short period, and not within the MAPTIP intensive observation period (MAPTIP-IOP), examination of data collected during the period was important to understanding the buoy's usefulness.

The buoy was redeployed near 1300 UT, 26 October with the sonic but no other systems working. Data not available from the operating buoy systems but necessary for estimating Z/L, i.e. humidity and sea temperature, were available from MPN. The buoy operated successfully until recovered at 1000 UT on 4 November, and provided data for 12 of 18 of the aerosol profile sampling periods.

The two boundary layer parameters necessary to describe the aerosol profile, according to Eqn (1), are the friction velocity $u_*$ and L. Variance spectra, $S_u(f)$, were calculated from sonic anemometer turbulent wind records and used to calculate $u_*$ values on the basis of the inertial-dissipation method. The method's value for shipboard or buoy application is that it is based on the high frequency portion of the spectrum which is not affected by wave-induced platform motion. The method was that used previously with the buoy system, Skupniewicz and Davidson [7]. The Monin-Obukhov stability length, L, necessary for the inertial dissipation method as well as in Eqn. (1), was calculated with mean wind, temperature and humidity values.

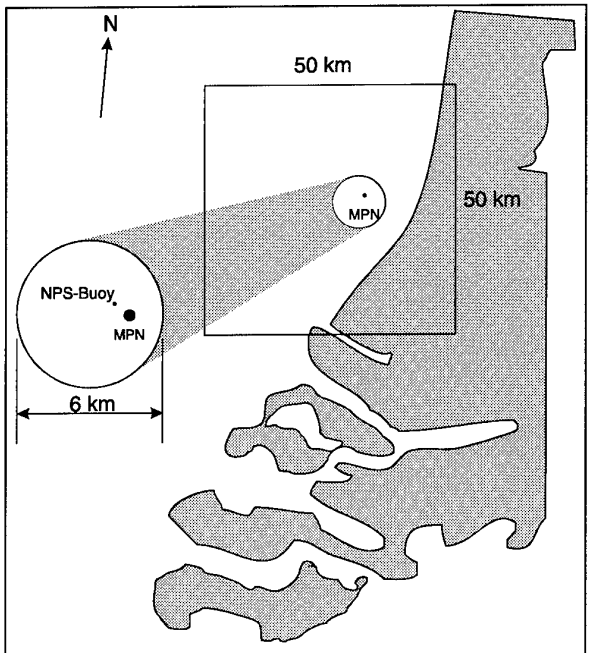


Figure 2.
Relative locations of MPN to The Netherlands coast and NPS buoy to MPN.

These were those from MPN mounted sensors since, as mentioned previously, buoy relative humidities and eventually both air and sea temperatures were not available during the MAPTIP-IOP.

Applications of surface layer similarity flux-profile relationships yield [8] the following inertial-dissipation based relation between $u_*$, Z, Z/L, $S_u(f)$, f and U.

$$u_* = [S_u(f) f^{5/3} / (\alpha U^{2/3})]\ [kZ/\Phi_\varepsilon(Z/L)]^{1/3} \qquad (2)$$

U was the sonic measured mean wind speed. $\Phi_\varepsilon$ is a dimensionless stability function, and $\alpha$ is an empirical constant. Our selections for the function and constant were those described by Edson et al [9] and formulated on the basis of MPN tower data. Also Z/L, based on mean MPN data with a bulk method, was calculated using the drag coefficient and turbulent heat (sensible and latent) exchange coefficients described by Smith et al [10] which also were formulated from an earlier experiment at MPN.

Wind speeds from MPN and the buoy, scaled to 10 meter height, and bulk and inertial-dissipation $u_*$'s for the period 11-12 October period are shown in Figure 3. The quality of the sonic measured wind speed from the wave-influenced buoy platform is an important consideration in the evaluation of its performance. The range of wind speed encountered during the initial deployment period allowed an excellent evaluation of the buoy systems, including mooring procedures, for estimating $u_*$ via the inertial dissipation method.

The MPN (solid lines) wind speeds and NPS buoy wind speeds measured by a propeller anemometer (dashed) and the sonic anemometer (dotted) are in good agreement until storm winds occurred after 0600 UT on 12 October.

The NPS (buoy) sonic anemometer failed at approximately 1020 UT on 12 October, when the winds reached a speed of 15 m/s. Also, at that time the NPS propeller winds become lower than the MPN winds, by as much as 5 m/s, until the storm subsided at about 1800 UT 12 October. This may have been caused by the buoy leaning at a large angle because of high storm winds which resulted in the propeller not measuring the full horizontal wind speed. A conclusion reached from this was the that sonic anemometer would provide accurate mean and turbulent wind values over the wide speed ranges expected.

Traces in Figure 3b indicate that during this initial deployment period the buoy (sonic anemometer) measured air temperature had a bias, near 1 °C lower than the MPN air temperature, after both were scaled to the 10-meter height. However, the buoy air temperature tracked the MPN temperature extremely well. Since the buoy bias was viewed to be correctable to MPN with further analyses of the sonic transmitter/receiver spacing, we believe the MPN values can be applied to the buoy location. Examination of Figure 3b reveals that the MPN-buoy sea temperature difference was variable, with the buoy sea temperature contributing most to the variability and being between 1-1.5 °C lower.

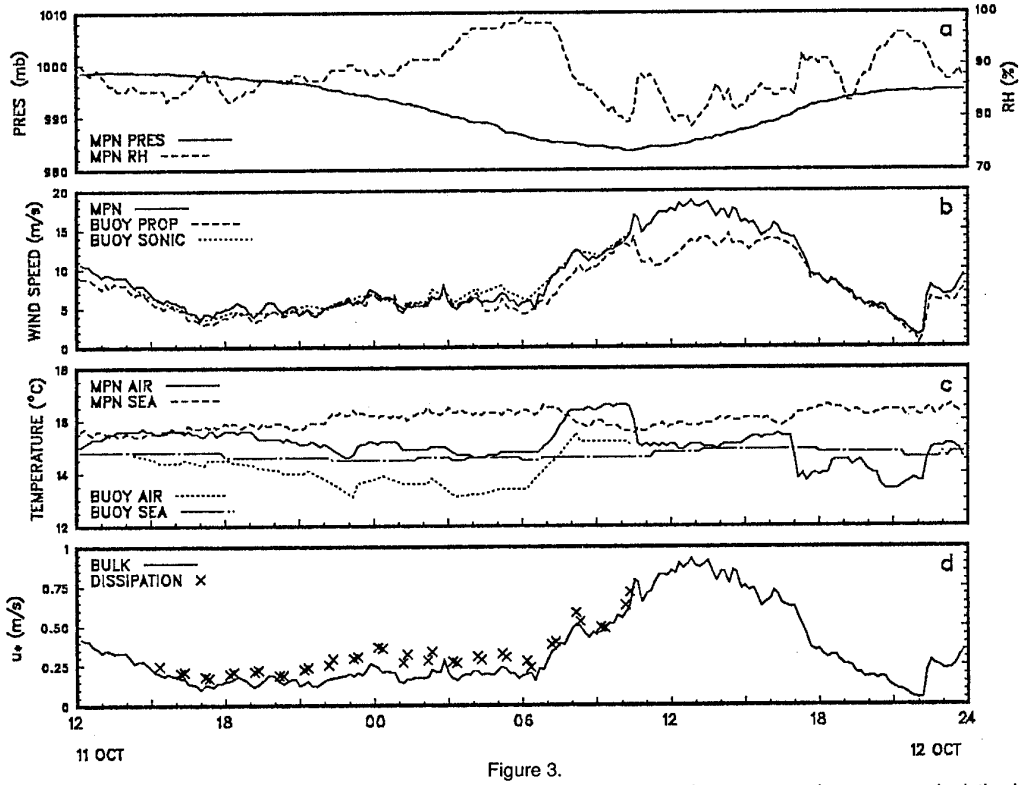


Figure 3.
Time series (10/11/00 - 10/13/00 UT, 1993) of buoy and MPN measured and calculated parameters, a) pressure and relative humidity, b) 10-meter wind speed, c) air and sea temperature, d) bulk [10] and dissipation $u_*$

So again, it was decided to use the MPN values to represent the buoy location. A conclusion reached on the basis of comparisons between these buoy and MPN data was that MPN mean wind, humidity, and air and sea temperature values were sufficient in determining stability, Z/L, for the buoy location.

The x's in Figure 3c are $u_*$'s calculated with the inertial-dissipation method and, of course, end with the failure of the sonic anemometer at 1020 on 12 October. The solid line in Figure 3c was drawn to $u_*$'s calculated with mean MPN data using the bulk formulations based on previous MPN data [10]. For 9 hours (11/21 to 12/06 UT), buoy inertial-dissipation $u_*$ values are 10-20% higher than the bulk friction values based on MPN data. However, the NPS friction velocity values are in excellent agreement with the bulk values during the storm which arrived shortly after 0600 UT 12 October, until the NPS sonic anemometer failed at 1020 UT 12 October. Further, the error during the preceding 9-hour period is not considered serious since the bulk formulation used does not take into account wave-age influences which should cause $u_*$ to be larger during a increasing wind speed.

## 2.2 MAPTIP-IOP Surface-Layer conditions

The collaborative MAPTIP measurement period began on 19 October. Significant personnel and ship efforts were made to have the buoy recovered, to have repairs/replacements made, and to have it redeployed. This was because the turbulence data were considered key parameters for descriptions of the surface layer processes. Post-storm evaluations of the buoy revealed that the system could be repaired to collect mean and turbulent wind and temperature from the sonic anemometer, without having to wait for parts to arrive. Hence, to avoid further delay, the buoy was redeployed near 0000 UT, 26 October with the sonic but no other sensor systems working. Data not available from the buoy but necessary for Z/L calculations were available from MPN. They were shown to be representative for the buoy location in above discussions.

The buoy operated successfully until recovered near 1000 UT on 4 November. It provided data for 7 of 12 of the aerosol profile sampling periods with acceptable wind directions, listed in Table 1.

There were a total of 18 aerosol profile sampling periods but 6 of these occurred with wind directions that were determined to be too influenced by MPN's structure. The Table 1 profile period list is sorted according to wind direction. Occurrences of positive slopes, $X_i$ in Eqn (1) increasing with height, are marked for purposes of later discussions.

Time series measured at both buoy and MPN for the 26 October - 4 November period appear in Figure 4. Symbols along the bottom of Figure 4 d mark times with aerosol profiles, listed in Table 1. Mean parameters from both platforms are shown in the time series because Z/L was estimated from MPN winds, temperatures and humidity and because $u_*$ was estimated from buoy (sonic) mean and turbulent winds.

MPN and buoy wind speeds and air temperatures in Figure 4 were all scaled to a 10-meter reference height. The scaled buoy wind speeds are generally within (always higher than) 1 m/s of MPN wind speeds. The two platforms are in good agreement during the period of winds less than 5 m/s, from about 10/30/1800 UT to about 11/03/1200 UT. The buoy air temperatures are generally within 1 °C (always lower) than MPN's until about 10/28/1800 UT, after which they agree very well. We believe differences between the two locations, in both air temperature and wind speed, become more important at lower wind speeds because then the differences have more influence on Z/L, an important parameter in the tested model. Fortunately, the platforms were in good agreement during the time of lower wind speeds.

As was the case for the first deployment, the buoy obtained inertial-dissipation $u_*$ values are often higher than the bulk $u_*$ values, calculated with MPN-based exchange coefficients. This is not always the case however, the buoy values have the appearance of being always higher because they are indicated with x's and the bulk values being are with a thin line. There are no times when the two differ by factors of two which occurs when storms fronts move through. One of the reasons the bulk values are in such apparent agreement is that the applied $C_{D10N}$ formulation was from MPN, [10]. Such agreement in these results will lead us to confidently use MPN bulk $u_*$ values when aerosol profiles are available but not buoy $u_*$'s.

Table 1. MAPTIP Profile Periods

| date/time | Wdir | U | RH | Tair | Tsea | Radius (μm) | | | | | | | | | 8-21 | 28-62 |
|---|---|---|---|---|---|---|---|---|---|---|---|---|---|---|---|---|
| mo/day/UT | (°P) | m/s | % | C | C | 8 | 12 | 16 | 21 | 28 | 38 | 50 | 63 | Tot | μm | μm |
| 10/25/0705 | 28 | 9.3 | 74 | 10.6 | 11.5 | x | x | | | | | | | 2 | 2 | 0 |
| 10/26/1712 | 31 | 5.9 | 81 | 9.8 | 11.5 | | x | x | x | | | | | 3 | 2 | 1 |
| 10/26/0848 | 37 | 7.8 | 81 | 12.1 | 11.3 | x | x | | | | | x | | 2 | 2 | 0 |
| 10/19/1346 | 48 | 2.1 | 55 | 7.4 | 13.5 | x | x | x | x | x | x | x | | 7 | 4 | 3 |
| 10/27/1030 | 52 | 5.5 | 86 | 9.5 | 11.6 | | | | | | | | | 0 | 0 | 0 |
| 10/24/0834 | 53 | 11.9 | 65 | 6.9 | 11.7 | x | x | x | x | | x | | | 5 | 4 | 1 |
| 10/24/1310 | 54 | 10.7 | 65 | 8.8 | 11.7 | x | x | | | | | x | | 3 | 2 | 1 |
| 10/22/1039 | 61 | 8.6 | 76 | 8.4 | 12.4 | x | x | x | x | x | | | | 5 | 4 | 1 |
| 10/30/1600 | 65 | 6.6 | 95 | 5.2 | 11.3 | | | x | x | x | | | | 3 | 2 | 1 |
| 10/28/1611 | 72 | 5.5 | 82 | 8.7 | 11.7 | | x | x | x | x | x | | | 5 | 3 | 2 |
| 10/29/1328 | 74 | 6.5 | 87 | 7.7 | 11.5 | | | x | x | x | x | x | | 5 | 2 | 3 |
| 10/28/1121 | 85 | 6.2 | 78 | 9.4 | 11.7 | x | | x | x | x | | x | | 5 | 3 | 2 |
| | | | | | Total Positive | 7 | 8 | 8 | 8 | 6 | 4 | 5 | 0 | 46 | 31 | 15 |
| | | | | | Total Profiles | 12 | 12 | 12 | 12 | 12 | 12 | 9 | 2 | 83 | | |
| | | | | | | | | | | | | Percent Positive | | 55% | | |

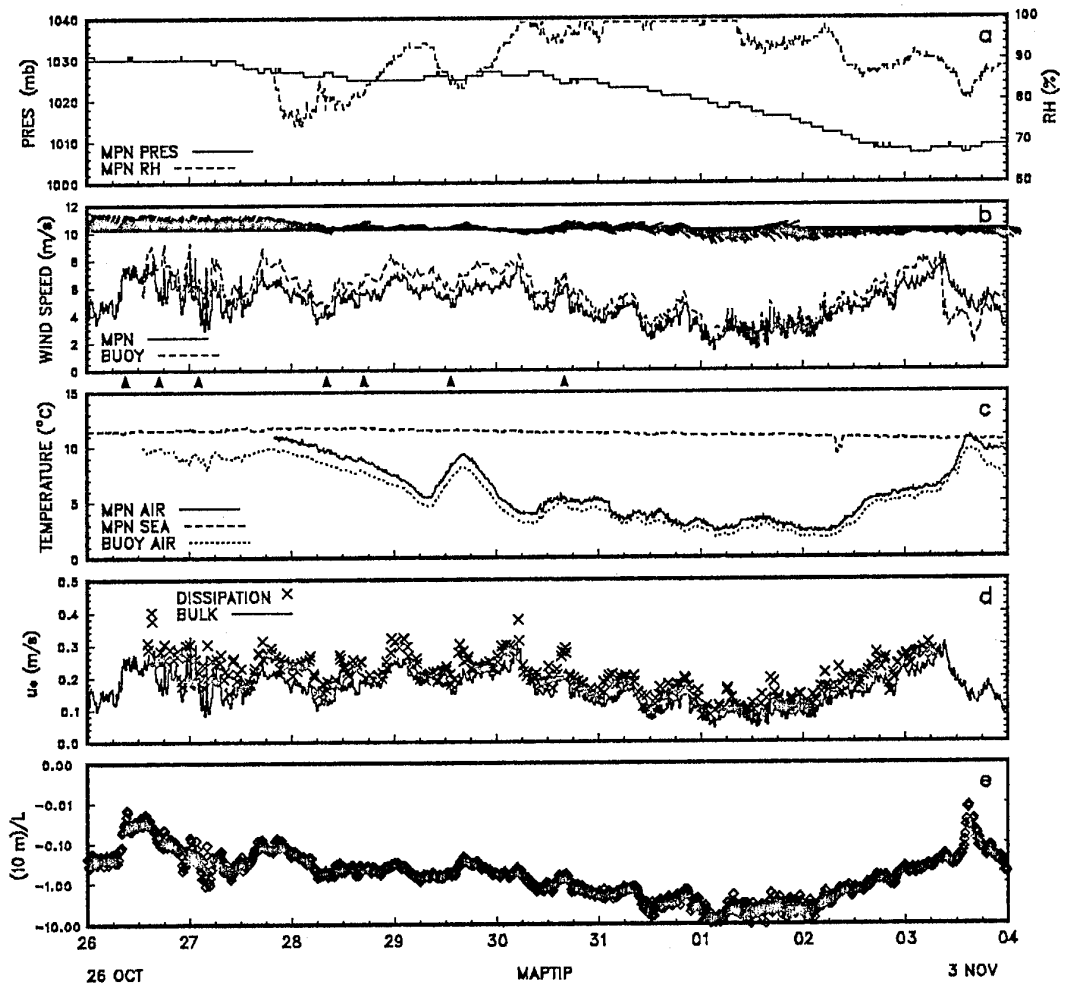


Figure 4.
Time series (10/26/00 - 10/04/00 UT, 1993) of buoy and MPN measured and calculated parameters, a) pressure and relative humidity, b) vector wind where barbs are from MPN, c) air and sea temperature, d) bulk [10] and dissipation $u_*$, e) Z/L where Z = 10 m. Symbols between panels b) and c) mark valid aerosol profile sampling periods.

Time series in Figure 4 show the wide range of wind and thermal stratification that occurred over the time when the buoy data were available. This range was cause by a synoptic-scale cyclone (low pressure center) approaching MPN most of the period with passage on 3 November, Figure 4 a..

Relative humidity, Figure 4a, was near 100% for two days, 30-31 October, and could affect our neglect on relative humidity's role on aerosol gradient. As the low approached, winds generally decreased through 1 November when they increased as the low center passed south of the MPN North Sea location. Also with the low's passage, winds turned clockwise from NE through SE. The evolving wind direction caused the airflow to be partially from the North Sea for 26 October, from off-shore but still not through MPN for 27-30 October, and through MPN for 31 October - 3 November.

The wind direction being through MPN led to no post-30 October aerosol profiles being examined, Table 1. Therefore, aerosol profiles were examined for a period (10/26/1200 -10/30/1600) when winds speeds were high enough to expect active surface production. Aerosol profiles were also examined for the times in the preceding week (19-25 October) when winds were E-NE and except for 10/19 high enough for surface production, Table 1. Air and sea temperatures and 10/L time series in Figures 4c and 4b reveal the thermal stratification to certainly have been unstable. With 10/L approaching -1, convective mixing will have an influence on aerosol profiles.

We also use the neutral drag coefficient, $C_{DN}$, in our evaluation of the $u_*$ measurements. $C_{DN}$ is $u_*$ normalized for both wind speed U and stratification, z/L. according to the following expression,

$$C_{DN}(z)=[(u_*/U) +\psi(z/L)/k]^{-2}, \quad (3)$$

where $\psi(z/L)$ is a flux-profile related function.

Since $C_{DN}$ depends on height, the calculated neutral drag coefficients were extrapolated to a reference level of 10 meters and are denoted as $C_{D10N}$.

Figure 5 has a comparison of buoy inertial-dissipation and MPN bulk derived $C_{D10N}$'s , Figure 5b, relative MPN water-level departures from mean tide, and Figure 5a. The water (tide) height and $C_{D10N}$ variation are correlated because wind speed was not adjusted for the tide-influenced surface current. These results provide evidence on the accuracy of the $u_*$ estimates since $C_{D10N}$'s calculated from them reflect the non-removed surface current

## 3. TNO-FEL AEROSOL PROFILES

Size distributions of particles larger than 5 μm in radius were measured with a Rotorod inertial impactor. The sampler consists of two polished stainless steel rods, mounted in a retracting collector head on a motor which rotates at a nominal speed of 2400 rpm. The linear velocity of the rods is 10 m/s. Particles impacted on the rods are retained by a sticky coating (silicone).

Microscope images of the rods are digitized to determine the particle size distribution by computer, [11]. Impaction and magnification limits determine the 5 μm radii and larger sizes range. Concentrations were estimated for up to 10 radii bins; centered at 6.5, 8.5, 12, 16, 21, 28, 37.5, 50, 62.5, and 75 μm.

Profiles were defined on the basis of up to 7 fixed-heights (1, 2, 3, 5, 7, 9, 11 meters) above mean tide height and of up to 7 levels (from .5 to 2.0 meters) above a wave follower. We consider profiles from the "fixed" levels only because Eqn. (1) is not based on wave-following scaling. Profiles were possible for up to 9 different radii but numbers were often too small to be statistically significant to define them for largest sizes.

A typical set of MAPTIP profiles, corresponding to 13:28 UT on 29 October, is shown in Figure 6a, with linear regression lines to the Ln versus Ln distribution. The Ln(DN/dD, i.e. $X_i$) versus Ln($Z_i$) display and regression are based on the Eqn. (1) prediction. DN/dD is the number of aerosol per diameter interval per volume. A typical set of profiles, corresponding to 1510 UT on 24 September, from the MPN based (September 1993) Air-Sea Gas Exchange (ASGASEX) experiment [12] is shown in Figure 6b. ASGASEX results enter into the final discussions of MAPTIP results. Table 2 lists ASGASEX profile sampling periods for periods when the wind direction was determined to be acceptable, counter-clockwise from 090 - 180 deg. Table 2 is similar to Table 1 for MAPTIP in that it includes measured mean parameters and indicators of positive slope occurrence according to radii. It differs in that the Table 2 profile list is sorted according to wind speed.

Figure 6 profiles are nearly linear in the Ln-Ln display and some of the measured have unexpected positive slopes. Tables 1 and 2 list MAPTIP and ASGASEX profiles, according to size, that had positive slopes. The fraction with positive slopes is given on the bottom row of each experiment's listing, i.e. 7/8 for MAPTIP's and 3/4 for

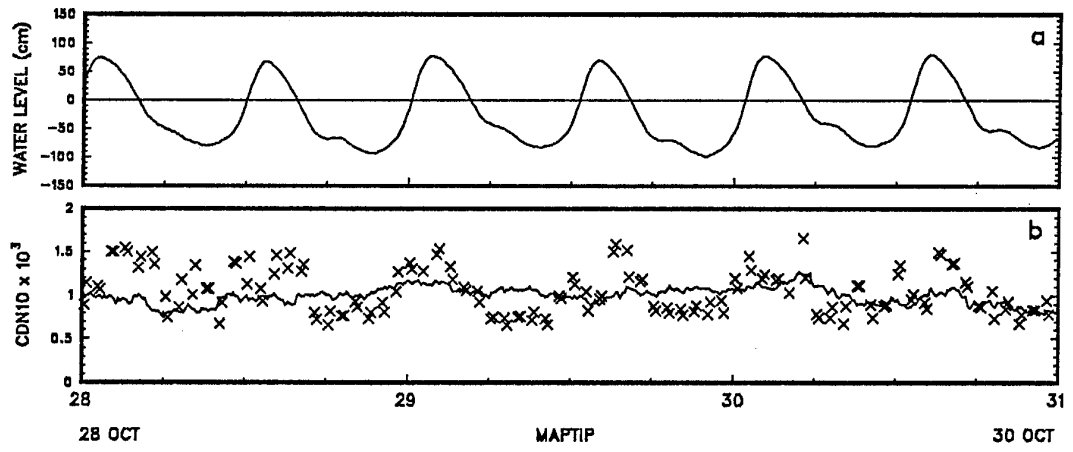


Figure 5.
Time series of a) water level measured at MPN and b) Buoy obtained neutral 10-meter drag coefficient, $C_{D10N}$.

Table 2 ASGASEX Profile Periods

| date/time | Wdir | U | RH | Tair | Tsea | Radius (μm) | | | | | | | | | 8-21 | 28-62 |
|---|---|---|---|---|---|---|---|---|---|---|---|---|---|---|---|---|
| mo/day/UT | (°) | m/s | % | C | C | 8 | 12 | 16 | 21 | 28 | 38 | 50 | 63 | Tot | μm | μm |
| 9/23/1445 | 355 | 4.3 | 84 | 15.8 | 16.7 | x | | x | x | x | x | | | 5 | 3 | 2 |
| 9/24/0919 | 66 | 5.2 | 89 | 13.1 | 16.4 | | | | | | | | | 0 | 0 | 0 |
| 9/24/1540 | 18 | 9.1 | 81 | 15.1 | 16.5 | x | | | | | | | | 1 | 1 | 0 |
| 9/15/1110 | 250 | 9.4 | 77 | 14.7 | 16.2 | x | | | | | | | | 1 | 1 | 0 |
| | | | Total Positive | | | 3 | 0 | 1 | 1 | 1 | 1 | 0 | 0 | 7 | 5 | 2 |
| | | | Total Profiles | | | 4 | 3 | 4 | 4 | 4 | 2 | 0 | 0 | 21 | | |
| | | | | | | | | | | | Percent Positive | | | | 33% | |

ASGASEX's 8 μm size bins. Equilibrium profiles for situations with a surface source, assumed in Eqn (1)/, should have negative slopes. Minimal slopes are expected for smaller aerosol sizes which have smaller $V_d$'s and are more likely advected from a distance. Causes for positive slopes could be due to no surface production or advected aerosol, more likely at small sizes, or a non-equilibrium situation where upward transport exceeds downward transport plus gravitational settling, causing a maximum above the surface.

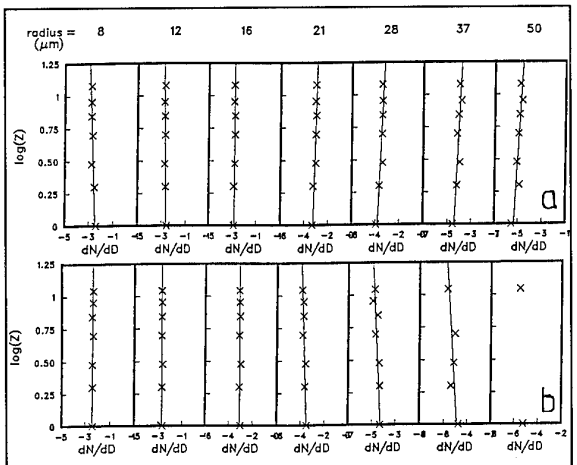


Figure 6.
Profiles and best fit regression lines of/for Ln(dN/dD) versus Ln(Z) for a) MAPTIP (10/20/13:28 UT) and b) ASGASEX (09/24/15:10). Profile nominal radii ( m) is listed on top.

The MAPTIP (Table 1) fraction of positive slopes decreases as radii increases, as expected. However, MAPTIP's fraction with positive slopes is quite large, 46 out of 83 or 55% of the profiles. A possible reason for this MAPTIP result is that the influence of the surface production is diminished by advection from land; the airflow was always from the NE-E quadrant. Positive slope distributions in Table 1, MAPTIP periods sorted according to wind direction, seem to show an increase in positive slopes, particularly for larger sizes, when the wind direction is clockwise from 50 deg. The 13:46 UT 19 October, with a wind direction of 35 deg, is a definite exception to this rule since all 7 radii had positive slopes. However, that period also had the lowest wind speed, 2.1 m/s, so surface production was unlikely. Although the ASGASEX sample size is small, the ASGASEX fraction of positive profile slopes was significantly smaller, 33% versus 55%, Table 2. The most apparent aspect of ASGASEX positive slopes is that a light wind, 4.2 m/s, period was the only one that had them at radii greater than 8.5 μm.

## 4. RESULTS ON MODELING SURFACE-LAYER AEROSOL GRADIENTS

The Eqn (1) prediction for the profile gradients rather than concentrations at a given height is the feature being examined in the combined data set. Further, gradient is evaluated on the basis of the apparent deposition velocity, $V_d$, i.e.

$$V_d = \frac{[ku_*]\,[\mathrm{Ln}(X_2)-\mathrm{Ln}(X_1)]}{[\mathrm{Ln}(Z_2/Z_1) - \Psi(Z_2/L) + \Psi(Z_1/L)]} \qquad (4)$$

where $\mathrm{Ln}(X_i)$'s were determined on the basis of regression-obtained coefficients and $Z_i$'s values were 30 and 15 meters.

The appropriateness of Eqn (1) for describing near-surface aerosol profiles was evaluated on the basis of comparing $V_d$'s calculated with Eqn ( 4) and available data with the gravitational settling rate, $V_g$,

$$\text{i.e. } V_g = 2\,\rho\,g\,r^2/(9\gamma) \qquad (5)$$

where $\gamma$ is viscosity of air and $\rho$ is density of aerosol

With Eqn (5), the aerosol is assumed to be in equilibrium with the local relative humidity. Further, we are neglecting the turbulent deposition rate which increases the $V_d$. The difference becomes less with increasing radius so that $V_d$ is essentially determined by $V_g$ for radii greater than 10 μm, [5]. In this analysis, 8.5 μm was the smallest size for which profiles were determined.

Comparisons of $V_d$'s calculated with Eqn (4) with $V_g$'s are shown in Figures 7a and 7b, for MAPTIP and ASGASEX respectively. The $V_d$'s are based on both buoy inertial-dissipation determined $u_*$'s in Eqn (4) and on $u_*$'s determined with a bulk method [10] and MPN data. $V_g$ dependence on the radii leads to vertical columns of data points, corresponding to the radii bins. There are 8 such columns for MAPTIP corresponding to radii from 8.5 to 62.5 μm and 6 for ASGASEX corresponding to radii from 8.5 to 37.5 μm. Pairs of $V_d$'s from the two methods are also apparent since the dissipation datum point is slightly above (usually) the bulk data point in the column. Of course, an unpaired bulk data point means there was no buoy data. We include $V_g$'s calculated with bulk $u_*$'s in this comparison because aerosol profiles were available for 6 periods listed in Table 1 before buoy data became available, from 10/19 through 10/25. Also, we want to examine the importance of the method for specifying $u_*$'s.

MAPTIP comparisons in Figure 7a show that $V_d$'s are both greater and less than $V_g$. The spread around the identity line is within a factor of 3. There is a tendency for $V_g$ to be less than $V_d$ for larger radii, $V_g$>9 cm/s or r>20 μm. Additional examinations were done to explain the scatter. They showed that correcting $V_g$ for turbulent deposition does not improve comparison agreement nor does restricting the comparison to MPN wind directions that are more northeasterly than easterly. With respect to the wind direction, the local wind direction may not be the best indicator of the trajectory. Trajectory analyses is being performed as a continuing step with this data.

ASGASEX comparisons in Figure 7b show $V_d$ in agreement with $V_g$, with less scatter than for MAPTIP. The ASGASEX non-bulk $u_*$ values were obtained from calculating the <u'w'> covariance from turbulent wind from MPN. This is normally referred to as the "direct" method. As for MAPTIP, $V_d$ is generally less than $V_g$ for $V_g$>9 cm/s or r>20 μm. We do not believe it is the different method, direct versus dissipation, that causes the apparent better agreement in the ASGASEX comparison because the bulk also has better agreement. ASGASEX definitely had the higher percentage of North Sea winds,

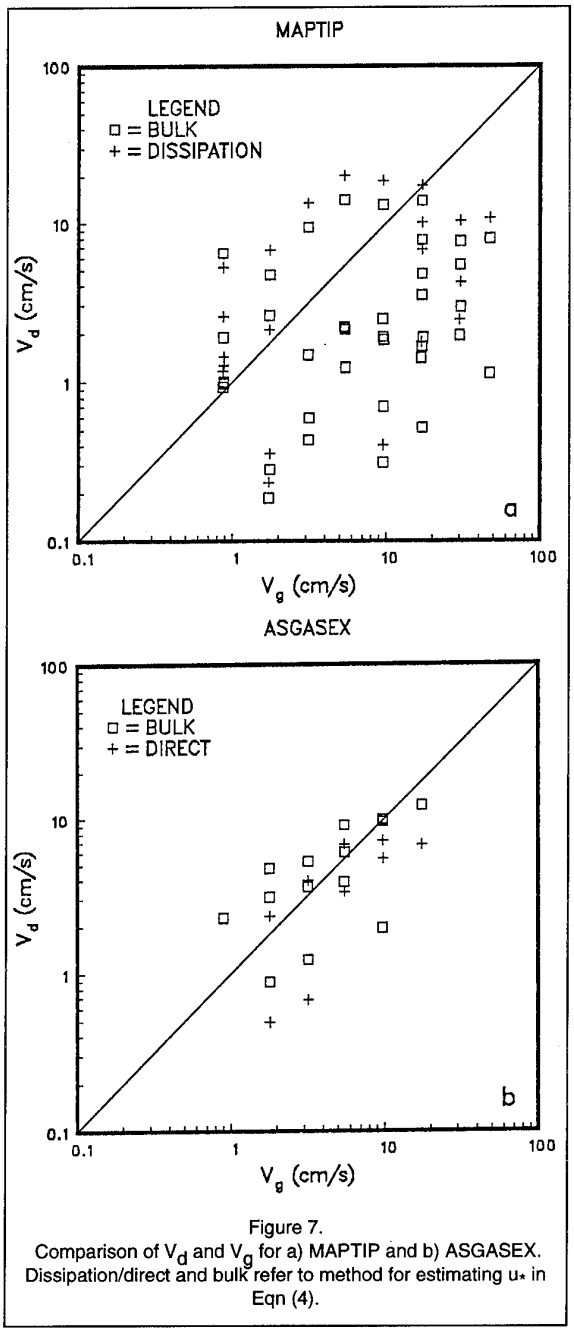


Figure 7.
Comparison of $V_d$ and $V_g$ for a) MAPTIP and b) ASGASEX. Dissipation/direct and bulk refer to method for estimating $u_*$ in Eqn (4).

only one was more clockwise than 50 deg, Table 2. Of course the one with the lowest wind speed, 1445 UT on 23 September, had 5 of the 7 positive slopes in ASGASEX. Because the sample size is small, trajectory analyses results have to be available before further interpretations can be made.

Although both MAPTIP and ASGASEX comparisons yielded reasonable agreement between the aerosol profile gradient calculated $V_d$'s and the $V_g$'s, we have to note the large fraction not included in Figure 7 due to positive slopes. Not included in Figure 7a (MAPTIP) were results from 46 of 83 profiles, or 55%, and in Figure 7b (ASGASEX) from 7 of 21 profiles, or 33%. We believe the positive slope profiles in MAPTIP were closely associated with the local wind direction, i.e. advection while the most apparent one in the small ASGASEX sample was definitely associated with low wind speed, i.e. no production. However, we can say that when the graduate is negative a simple model seems to exist.

These results are from a much more thorough examination on the representativeness and use of Eqn (1) than performed previously, by Davidson and Schutz [13]. The latter did not have the important aerosol profile data but inferred the correctness of Eqn (1) from single level data relying on varying L and $u_*$ instead of different Z values .

## 5. DISCUSSION

Combined surface layer turbulence and aerosol profile data sets were successfully obtained during a portion of the MAPTIP-IOP. Comparisons of the inertial-dissipation derived $u_*$ at the buoy with bulk values derived from the MPN data leads to the conclusion that MPN data are sufficient for characterizing MAPTIP-IOP periods when buoy data were not available. The characterization is required by a model for surface-layer aerosol profiles that is based on gravitational settling rate, $V_g$, turbulent transport, $u_*$, and thermal stratification, Z/L.

An objective of this study has been to provide other MAPTIP-IOP participants an approach for estimating multi-radius profile gradients when MPN aerosol measurements were not made or not valid because of flow through the platform. In this regard, model prediction will always yield negative concentration gradients even though the actual gradients may be positive. The positive gradients will be more likely for smaller sizes, for light wind conditions, and for more easterly wind, clockwise from 45 deg.

Further studies will be useful with the combined data sets. These would lead to better understandings of the following influences,

a) air-mass trajectory,

b) relative humidity gradient, and

c) turbulent deposition.

## 6. ACKNOWLEDGEMENTS

Data collection and analyses in this work was funded under NRaD program element 62435N, RL3C Project RO35W82/01, Marine EO Effects, and by the MOD-NL (assignment A92KM615). Grants were obtained from NATO AC/243 (Panel 4) (Grants 6056 and 6092) and the US Office of Naval Research ONR (Grant N00014-91-J-1948) as contributions to the MAPTIP logistics costs. We thank staff persons at NPS and TNO-FEL who were involved in collection and analyses of the data; K. Jones, T. Neta, Leo Cohen, Lex van Eijk, F. Bastin. We also thank CDR L. van der Poel and his crew of the Tydeman who were instrumental in recovering and repairing the buoy. Rijkswaterstaat Directorate North Sea is gratefully acknowledged for making available MPN and the platform manager for their cooperation. This paper was written while KLD was a visiting Scientist at TNO-FEL.

## 7. REFERENCES


1. Gathman, S. G. and K. L. Davidson, "The Navy Oceanic Vertical Aerosol Model", NRaD TR-1634, December 1993, 107 pp.

2. Goroch, A. K., S. K. Burk, and K. L.. Davidson, "Stability Effects on Aerosol Size and Height Distributions", Tellus, 32, 1980, pp 245-250.

3. Fairall, C. W., and K. L. Davidson, "Dynamics and Modeling of Aerosols in the Marine Atmospheric Boundary Layer", in "Oceanic Whitecaps", D. Reidel Publishing Company, E. C. Monahan and G. Mac Niocaill (eds), 1986, pp 195-208.

4. Businger, J. A., J. C. Wyngaard, Y. Izumi, . E. F.. Bradely, "Flux-profile Relationships in the Atmospheric Surface Layer", J. of Atmos. Sci., 28, 1971, pp 181-189.

5. Fairall, C. W.. and S.E. Larsen, "Dry Deposition, Surface Production and Dynamics of Aerosols in the Marine Boundary Layer", Atmos. Envir., 18, pp 69-77, 1983.

6. Toba, Y., "On the Giant Sea-salt Particles in the Atmosphere, II. Theory of the Vertical Distribution in the 10 m over the Ocean", Tellus, 17, 1965, pp 365-382.

7. Skupniewicz, C. E. and K. L. Davidson, "Hot-film measurements from a small buoy: Surface stress estimates using the inertial-dissipation method", J. of Atmos. and Ocean. Tech., 8, 1991, pp 309-322.

8. Panofsky, H. A. and J. A. Dutton, "Atmospheric Turbulence", Wiley-Interscience, New York, N. Y., 1984, 397 pp.

9. Edson, J. B., C. W. Fairall, S. E. Larsen, and P. G. Metsasyer, "An Experimental and Theoretical Investigation of the Inertial-Dissipation Method for Computing Air-Sea Fluxes", J. of Geophys. Res., 96, 1991, pp 10689-10711.

10. Smith, S. D., R. Anderson, W. A.. Oost, C. Kraan, N. Maat, J. DeCosmo, K. B.. Katsaros, K. L. Davidson, K. Bumke, L. Hasse, and H. M. Chadwick , "Sea Surface Wind Stress and Drag Coefficients: The HEXOS Results", Boundary-Layer Meteorology, 60, 1992, pp 109-142.

11. De Leeuw, G., "Profiles of Aerosol Concentrations, Particle Size Distributions and Relative Humidity in the Atmospheric Surface Layer Over the Sea", Tellus, 42B, 1990, pp 342-354.

12. Oost, W. B., "The ASGASEX experiment", KNMI Technical Report, TR-161, 1994, 29 pp.

13. Davidson, K. L., and L. Schutz, "Observational Results on the Influence of Surface Layer and Inversion Entrainment on Surface Layer Marine Aerosol Number Density (1 μm)", Opt. Eng., 23, 1983, pp 45-49.

# POLARIZATION ENHANCEMENT OF CONTRAST IN INFRARED SHIP/BACKGROUND IMAGING.

**A. W. Cooper**
**W. J. Lentz**
**P. L. Walker**
**P. M. Chan[+]**
**Naval Academic Center for Infrared Technology**
**Physics Department, Naval Postgraduate School**
**833 Dyer Road, Room 105, Monterey, CA 93943-5117 USA.**

## 1.SUMMARY

During the MAPTIP experiment series in Dutch coastal waters in October 1993 shore-based polarized infrared images were recorded of air (fixed wing and helicopter) and sea targets in sea and air backgrounds, including a number of vertically and horizontally polarized image pairs of the Dutch oceanographic research vessel Hr Ms Tydeman. Complete characterization of the environmental conditions in the measurement area will be available through other MAPTIP participants. These images show no significant polarization features in ship images ( < 5%) or in sky background, but a considerable degree of vertical ("p") polarization in the sea background radiance at low emission (near grazing ) angles, which is ascribed to surface emission polarization. This phenomenon for all observed times of day and sun positions, and more strongly in the LWIR than in the MWIR. A horizontal polarization filter provided 10 to 20% ship-to-sea contrast improvement due to suppression of sea background, and enhances horizon sea/sky contrast by up to 15 % . These results are consistent with our previous measurements of polarization in the sun glint channel.

## 2. INTRODUCTION.

We have previously reported observations of a significant degree of linear polarization in both the Mid and Far Infrared across the near-horizon sun-glint channel and in the adjacent sea background radiance[1]. The measured degree of linear polarization showed a strong horizontal ("s" ) polarization peaked in the center of the channel with near-exponential decrease and sign reversal to vertical ("p") polarization in the wings of the glint and the surrounding sea background. The magnitude of degree of polarization was found to be much greater in the 3 - 5 micrometer (MWIR) band than in the 8 - 12 micrometer (LWIR) band, and showed good correspondence to computer calculations[2] based on Fresnel reflection from a Cox-Munk wave slope distribution. The MAPTIP experiment series in the Dutch coastal region in October 1993 provided an opportunity to record polarized images of various air and sea targets against sea and air backgrounds, including a number of vertically and horizontally polarized image pairs of the Dutch oceanographic research vessel Hr Ms Tydeman, with environmental characterization by the participants in MAPTIP. Image pairs recorded with target stationary allowed comparison to determine degree of polarization of targets and background, and the contrast improvement factor achieved with a polarization filter.

The Marine Aerosol Properties and Thermal Imager Performance Trial (MAPTIP) is a multinational field experiment organized by NATO AC/243 PANEL 4/RSG.8 on atmospheric propagation effects on electro-optical systems with participation by Panel 04/RSG.5 on thermal imaging[3,4]. Measurements were made by the eight participating countries during the period October 11 to November 5, 1993. The trial was conducted in Dutch coastal waters at Katwijk, near The Hague. A variety of sea, land and air platforms were used as measurement locations and targets for imaging and measurement. The objectives and achievements of the MAPTIP experiment are available elsewhere; this paper deals with polarized image data obtained from the Beach Station at Katwijk.Supporting environmental data are available from concurrent aerosol, visibility, and radiometer measurements made from an oceanographic tower (MPN) 4.9 nmi from the beach, from the Beach Station at Katwijk, from the Oceanographic ship Hr.Mr. Tydeman, and the NCCOSC Piper Navajo aircraft and listed in the MAPTIP Consensus Environmental Data package. Sea surface measurements recorded on two buoys are also included in the consensus package. The objectives of the NPS measurements are to extend background polarization measurements to regions remote from the sun glint, to investigate polarization features in ship targets, and to evaluate influence of polarization on target discrimination against background.

---

**Present address: Code C29 A4, Naval Air Warfare Center, China Lake, CA 93555-6001.**

*Paper presented at the Sensor and Propagation Panel Symposium on "Propagation Assessment in Coastal Environments" held in Bremerhaven, Germany 19-22 September 1994.*

## 3. POLARIZATION IN SEA AND TARGET RADIANCE.

The infrared radiance from the sea can be expressed as the sum of the thermal emission from the water and the sky radiance reflected specularly from the surface [5,6]. Sun glint in the direction close to the sun is caused by specular reflection of direct sunlight from the wave facets. The total sea radiance can be described by the expression;

$$N_{tot} = N_{sky}\rho(\theta) + N_{sea}\epsilon(\theta) + N_{sol}\rho(\theta) \qquad (1)$$

Each term in Equation 1 is a function of the spectral reflectivity or emissivity ($\rho_\lambda, \epsilon_\lambda$) of sea water averaged
over the orientations of the sea wave facets relative to the reflected sources and the observer; for low sensor elevation the reflectance does not approach unity as for a smooth surface but becomes highly dependent on sea state. In regions remote from the sun direction the third direct sunlight contribution may be ignored. An immediately analogous expression can be written for the radiance from a man-made object, for example a ship target, embedded in the sea background.

### 3.1 Polarization in Reflection

Polarization of the reflected radiation occurs in accordance with the Fresnel Equations applied relative to each facet normal and resolved into the vertical and horizontal directions. The individual effective reflectivities for the horizontal and vertical

$$\rho^h_{eff} = \rho_\perp(\theta)\cos^2(\alpha) + \rho_\parallel(\theta)\sin^2(\alpha) \qquad (2)$$
$$\rho^v_{eff} = \rho_\perp(\theta)\sin^2(\alpha) + \rho_\parallel(\theta)\cos^2(\alpha)$$

polarizations can be expressed;
Here the terms $\rho_\perp$ and $\rho_\parallel$ are the spectral reflectivities of the sea water determined by the angle of incidence (reflection) or emission, $\underline{\theta}$, through the Fresnel equations and $\alpha$ represents orientation of the electric vector relative to the wave facet normal. The degree of polarization of the reflected radiance is defined [7] relative to the plane of incidence as shown in Equation (3).

$$P = \frac{\rho_\perp - \rho_\parallel}{\rho_\perp + \rho_\parallel} \qquad (3)$$

$\rho_h$ and $\rho_v$ are then the averaged values relative to a flat sea surface.

### 3.2 Emission Polarization.

The radiance term $N_{sea}\epsilon(\theta)$ due to thermal emission also shows polarization, with electric vector predominantly parallel to the plane of emission (ie vertical). The process of emission polarization is less intuitive than that of reflection; it has been well reviewed by Sandus [8] for solid materials and applied to the sea surface by Basener and McCoyd [5] and Sidran[7].
Polarization in emission at angle $\theta$ is described by the relations of Equation (4)

$$\epsilon_\perp(\theta) = 1-\rho_\perp(\theta)\,;\ \epsilon_\parallel(\theta) = 1-\rho_\parallel(\theta) \qquad (4)$$

where each emissivity is related to the reflectance at the same angle $\theta$. This emittance can be interpreted as the sea surface transmittance from below. The effective surface values $\epsilon_h$ and $\epsilon_v$ are then obtained analogously to Equation (3), averaged over the wave slope distribution. The degree of emission polarization can then be written[7] as

$$Q = \frac{\epsilon_\parallel - \epsilon_\perp}{\epsilon_\parallel + \epsilon_\perp} \qquad (5)$$

applied to the facet, or equivalently for the effective sea surface. Sidran[7] shows Q rising to 40 % at 3 $\mu$m and 30% at 10 $\mu$m as $\theta$ approaches 90°. With both the reflection and emission processes inducing polarization, the observed degree of polarization of the radiance can be written in the form

$$POL = \frac{\langle N_v \rangle - \langle N_h \rangle}{\langle N_v \rangle + \langle N_h \rangle} \qquad (6)$$

where $\langle N_v \rangle$ and $\langle N_h \rangle$ are the mean apparent radiance recorded by the AGA 780 imager with polarizing filter in the vertical and horizontal direction, respectively. A negative value of the percent polarization corresponds to net horizontal polarization.

Previous measurements[1,2] of sun glint from the sea surface showed that the polarization within the glint corridor is predominantly horizontal, while outside the corridor the polarization is frequently vertical. It was concluded that for the glint region, the reflective components dominate the radiance in the MWIR band while in the LWIR the emission components dominate all but the glint center.

Target radiance must be considered in the same fashion as sea radiance. Since both emission and reflection polarization are strongly dependent on direction relative to the surface normal, targets such as ships may show significant differences from sea background.

## 4. CONTRAST AND CONTRAST IMPROVEMENT.

The contrast signature of a target in background for either polarization or for an unpolarized image is defined by

$$C = \frac{< N_{target} > - < N_{Bkgd} >}{< N_{Bkgd} >} \qquad (7)$$

where $< N_{target} >$ and $< N_{Bkgd} >$ are the average apparent radiances of the target and its immediate surroundings. Differences in polarizations of target and background may result in significant differences in contrast. Defining the vertically and horizontally polarized averaged apparent radiances of target and background as $N_{VT}$, $N_{HT}$, $N_{VB}$, and $N_{HB}$ , and the equivalent unfiltered values as $N_{UT}$ and $N_{UB}$ we can further define the contrast functions relevant to this paper as $C_V$, $C_H$, and $C_U$ in the same form as Equation (7); for example

Contrast without polarization filter;

$$C_U = \frac{N_{UT} - N_{UB}}{N_{UB}} \qquad (8)$$

The Contrast Improvement Factor can then be defined as a simple ratio representing the ratio of contrast with filter to contrast without.

$$F = \frac{C_H}{C_U} \qquad (9)$$

Since unpolarized images were not obtainable in the MAPTIP data, an "Equivalent unpolarized" image was generated by array addition of the vertical and horizontal polarizations. These functions have the advantage of being independent of the temperature calibration of the instrument.

## 5. METHOD OF MEASUREMENT.

The polarized images reported here were recorded during the MAPTIP experiment using an AGA 780 Thermovision dual band radiometric imaging system with pass bands in the 3 to 5 $\mu$m and 8 to 12 $\mu$m windows. Each channel is fitted with a 71 mm diameter Cambridge Physical Sciences Model IGP-228-71 Infrared polarization filter in the form of a grid of 0.12 micrometer aluminum strips at pitch of .25 micrometers deposited on a barium fluoride substrate. The filters are mounted external to the lenses and can be rotated manually about the optical axis. The filter assembly can be used only with the 7° x7° system field of view. Performance specifications of the polarizer over the spectral range of 1-12 $\mu$m are: 85% transmission efficiency and 98% polarization effectiveness at 3.9 $\mu$m. Each channel is a single detector (InSb and HgCdTe respectively) scanning imager generating four 140 x 70 pixel fields per frame at a field rate of 25 per second. The digital image storage and display system (AGEMA Corp CATS 2.01 software) allows the option of recording either one or two fields per frame in single-frame (snapshot) or multiframe (integrated) mode, displayed in false color equivalent temperature representation or extracted for off-line processing. All images reported here were recorded under CATS and transferred as Isotherm Value files for processing under Interactive Data Language (IDL) software to provide degree of polarization and image contrast. The image pairs were recorded in snap-shot mode with an average time delay of 10 seconds between polarizations.

The AGA 780 scanner was recalibrated in the laboratory by comparison of thermal value with and without the polarizers against reference source temperature. The curve shape shows long term stability with adequate correction for local conditions provided by optimization of an Offset Correction (OC). With the polarizer in place the AGA shows an increased Offset Correction at low temperatures and the dynamic range is decreased. For computer data acquisition and processing, calibration data in terms of digital signal are stored as computer files. During experimentation the Offset Correction was checked and adjusted occasionally against a local thermal reference. The Degree of Polarization and the Contrast Improvement Factor are in any event independent of the temperature calibration.

## 6. DATA COLLECTION

The NPS thermal imaging equipment was located in the upper level of the Katwijk Beach Station, the scanner viewing a clear field through an open transom window at ten meters elevation above mean sea level. The imaging path traversed a broad beach and surf line. An expanded description of the experimentation with further image samples can be found in Chan et al[9].

### 6.1 Infrared Polarization Images

A total of 3236 image files were recorded within a twelve-day period of air and sea targets, including many in matched vertical and horizontal polarization pairs. The image files are summarized by target type and waveband in Reference (9). For the purposes of this paper only the ship polarized image pairs will be considered, with emphasis on those for which the target remained stationary. This facilitates the registration of pixels which is required for the determination of degree of contrast improvement. A

selection from the 666 MWIR (3-5 $\mu$m) and 718 LWIR (8-12 $\mu$m) of the Hr. Ms. Tydeman will be treated. This ship is a Dutch oceanographic vessel, of length 90 meters and beam 14.5 meters. An array of high intensity lamps (operated on a published schedule) and the exhaust stack formed a further strong local infrared source visible as a hot spot in the ship images. The ship operated on a prearranged path which included stations on the direct path between the Beach Station and the MPN Tower, and also provided suitable stationary imaging periods close to the Beach Station. Images of the Tydeman holding positions at distances of 1085 m to 1737 m were recorded. Additional information on the Tydeman (dimensions, equipment, etc.,) and details of its cruise path can be found in the MAPTIP work plan.[4]

### 6.2 Environmental Data

The complete meteorological history during the entire measurement period was recorded at each principal site (i.e., MPN and WPB). Additionally, measurements of air temperature, relative humidity, winds, visibility, sea state, etc. were taken manually and recorded in the daily data log.

## 7. IMAGE DATA AND ANALYSIS

The images presented in this paper were processed using IDL programs. The recorded CATS files of thermal values in eight-bit binary form are read by the IDL program and rescaled linearly into 256 steps. This provides finer scale resolution for display and advanced image processing. Degree of polarization can however be estimated from the polarization image pairs with the filter axis vertical and horizontal, using Equation (6).

Figure (1) shows as an example a perspective display of an image of the HrMs Tydeman. The lowest level is a gray scale radiance image; the middle level shows a three dimensional representation of the same scene, and the top shows a contour plot. The Three Dimensional plot is useful as an intermediate step in processing. The narcissus spot formed by reflection from the external polarizer and its influence on the image can easily be seen. These plots are indicative of the data quality. Care was taken in analysis to minimize effects of this artifact.

Figure 2 is a comparison of polarization image pairs recorded simultaneously in the MWIR ( 3-5 $\mu$m ) and LWIR (8-12 $\mu$m ) bands. Each pair contains horizontally and vertically polarized images. In these pictures the ship image is located well clear of the narcissus region. The MWIR images show less definite contrast improvement with horizontal filter ( see Table 2). Qualitative conclusions can be drawn from these images by inspection: 1) Sea background is reduced in both wavebands with a horizontal polarization filter, relative to vertical 2) Apparent contrast of ship versus sea is improved with horizontal filtering , to a greater degree in the LWIR; 3 ) contrast of ship versus sky is not noticeably improved; 4) ship and sky show little change with filter orientation. Since the effects are larger in the LWIR, the discussion will emphasize that band.

### 7.1 Evaluation of Contrast Improvement Factor

Only horizontally or vertically polarized images were recorded in the MAPTIP measurements. From these image pairs the degree of polarization for targets and backgrounds and the contrast differences obtained vertical and horizontal polarizers can be extracted. Samples are shown in Tables I and II, and will be discussed later. Evaluation of the effectiveness of polarization filtering requires evaluation of the Contrast Improvement Factor achievable compared to observation of the unfiltered scene. For this purpose equivalent unpolarized scenes were constructed by superposition and matrix addition of the horizontally and vertically polarized radiance images. An example is shown in Figure 3. The quality of the composite image indicates the high degree of pixel registration achieved. This procedure has been shown in the past to represent a good approximation to the unfiltered scene due to the high efficiency of the polarizers. From the composite image files the Contrast Improvement Factor was evaluated for a large number of cases. The value obtained for target/background contrast depends on the method of data analysis; in this paper the ship image outline is defined by the clearer image ( horizontally polarized) and the average thermal value evaluated within this outline for each image. The outline is defined by a selected temperature threshold ( 0.1 °C or less above background). This procedure maintains image size in the comparison.

Two sets of images were selected to provide quantitative illustration. The data of Table 1 represent nine image pairs extracted from a two hour record with the Tydeman stationary at a range of 1085 meters.from the Beach Station. The eight image pairs shown in Table 2 form a set obtained within a two minute period, and show the short term fluctuations in the data. For these images the degree of polarization of the target or background is calculated from Equation 6 where $N_v$ and $N_h$ are the apparent radiances recorded by the AGA 780 imager for vertical and horizontal polarizations respectively. The average values $<N_v>$ and $<N_h>$ for the target (or background) were computed using selected target and background areas matched for the paired and the composite images. The contrast signature of target-to-background for each case is calculated by Equation (7). The data exemplify the general conclusion that

target degree of polarization is small and variable, having both positive and negative values. Negative degree of polarization means electric vector predominantly horizontal. The background shows relatively large positive values indicating vertical polarization. The target-to-background contrast is also shown in Table 1 for the horizontal and vertical polarizations, and also ($C_U$) for the composite image. The numbers indicate that a contrast improvement in the range of 10 to 25 % may be expected through use of a horizontal polarizer filter.

Table 2 compares the sea/sky contrast for vertical, horizontal and composite ( unpolarized) polarization images obtained over a two minute period. While fluctuations are obvious The $C_V$ and $C_H$ values calculated from Equation (7) for selected regions of background above and below the horizon, the Unpolarized Contrast $C_U$ from Eq. (8) and the corresponding Contrast Improvement Factor CIF from Equation (9) show qualitative consistency, with lower values for the MWIR images. The contrast of ship to sea background similarly shows relatively consistent behavior and significant value of contrast improvement.

### 7.3 Long Term Stability of Polarization of Target-to-background Contrast Improvement

Figure 4 shows as examples four pairs of images recorded at widely varying local times ( 9 a.m., 12:51 p.m., 3 p.m., and 9 p.m.) as representing varied sun locations, selected from stationary imaging series on different days. The sea radiance is seen to show vertical polarization in all cases, including one image recorded several hours after sunset. The more obvious polarization target-to-background contrast improvement is shown in the morning periods. The image pairs are shown with vertical and horizontal polarization; the contrast improvement factor relative to unpolarized viewing is shown in the caption, and in all cases is in the range 11% to 33%. The effect of direct sun reflection in the contrast figures is not noticeable. All images were taken well away from the sun direction.

## 8. DISCUSSION OF RESULTS

In the polarized images obtained in the MAPTIP experiment,the man-made objects observed did not show any large degree of polarization or significant polarization preference. Sky radiance similarly appeared unpolarized. The sea background, however, showed a considerable degree of emission polarization with electric vector vertical. In these circumstances s-polarization (horizontal) filters produce improved contrast between target and sea-background. These results were consistently obtained under varying sky light levels, including night conditions. No opportunities occurred to observe the effects of grazing incidence solar illumination which might be expected to show polarization features. Observations were clearer in the LWIR than the MWIR, as might be expected with less interference from solar illumination. Since sun or sky light reflected from the sea tends to be horizontally polarized and emitted radiance tends to be vertically polarized, the balance between the two will depend on the ratio of sky radiation to thermal emission. This ratio is much smaller in the 8-12 $\mu$m band than the 3-5 $\mu$m band. No noticable polarization was observed in sky radiance.These observations are consistent with previous measurements in sun glint [1,2] . The quantification of the contrast and contrast improvement factor is based on specific definitions of these quantities, recognizing that the target area (the ship area presented to the receiver is the same for the two polarizations. This preserves the spatial aspects of the discrimination. An alternative target definition based on gradient or on fixed threshold will lead to comparison of targets of different area, which might lead to different conclusions.

## 9. FUTURE PLANS

These considerations have been restricted to those image pairs obtained while the target was stationary, since any target movement between images in a polarization pair prevents adequate registration of the images. The time delay of ten seconds between exposures is sufficient to cause inaccuracies with even slower-moving platforms, and to make measurement impossible with fixed-wing aircraft. Improved instrumentation is under development to allow simultaneous imaging at both polarizations. Previous tests have indicated that the unpolarized radiance can be well estimated by summation of the two polarization components. Nonetheless, in order to establish that polarization filters have significant advantages it is desirable to be able simultaneously (or nearly simultaneously) to acquire the image in both polarization components and also without polarization. All results presented here are of directly observed contrast at the receiver; for complete understanding and application to modeling or prediction it is necessary to validate the expected range dependence of the contrast improvement factor. This should be addressed in future studies with the MAPTIP data and further experimentation with the upgraded instrumentation.

## 10. ACKNOWLEDGEMENTS

It is a pleasure to acknowledge support of Naval Command, Control and Ocean Surveillance Center, RDT&E Division under Document 93WR0086 (JO#MP95543725) and Johns Hopkins University APL (Surface Combat Systems) under contract 605976-0. Support of the polarization measurement program by Naval Sea Systems Command, PEO-TAD

is also appreciated.

## 11. REFERENCES


1. Cooper, A.W., Crittenden, E. C., Milne, E. A., Walker, P. L., Moss, E. and Gregoris, D. J., "Mid and Far Infrared Measurements of Sun Glint From the Sea Surface", SPIE Proceedings, Vol 1749, 1992, pp 176-203.

2. Gregoris, D. J., Yu, S., Cooper, A. W. and Milne, E. A., "Dual Band Infrared Polarization Measurements of Sun Glint from the Sea Surface", SPIE Proceedings, Vol 1687, 1992, pp 381-393.

3. de Leeuw, G., Van Eijk, A. M. J. and Jensen, D. R., "MAPTIP Experiment. Marine Aerosol Properties and Thermal Imager Performance, An Overview", TNO Defence Research Report FEL-94-A140, June 1994.

4. Jensen, D. R. and de Leeuw, G., "Work Plan for Three Marine Aerosol Properties and Thermal Imager Performance Trial (MAPTIP)", NCCOSC RDT&E Division, Technical Document 2573, September 1993.

5. Basener, R. F. and McCoyd, G. C., "Polarization of Infrared Light Emitted by the Sea", Grumman Research Department Memorandum RM-360, 1976.

6. Beard, J. L., "Reduction of Solar Glints from the Sea with a Linear Polarizer", ERIM Technical Report 120500-9-T, 1976.

7. Sidran, M., "Broadband Reflectance and Emissivity of Specular and Rough Water Surfaces", Applied Optics, Vol 20, No 18, 15 September 1981, pp 3176-3183.

8. Sandus, Oscar, "A Review of Emission Polarization", Applied Optics, Vol 4, No 12, 1965, pp 1634-1642.

9. Chan, P. M., Cooper, A. W. and Lentz, W. J., "Infrared Polarized Image Measurements in the NATO MAPTIP Exercise", NPS Technical Report NPS-PH-94-011, June 1994.

10. Cooper, A. W., Lentz, W. J., Walker, P. L. and Chan, P. M., "Infrared Polarization Measurements of Ship Signatures and Background Contrast", *in* Characterization and Propagation of Sources and Backgrounds, Proceedings, SPIE Vol 2223, 1994, pp 300-307.

| Image Pair | File Name | Pol | Tgt <N> | Bkgd <N> | $C_V$, $C_H$ | $Pol_T$ (%) | $Pol_B$ (%) | $C_U$ | $C_H / C_U$ |
|---|---|---|---|---|---|---|---|---|---|
| 1 | OC19L087 | V | 157 | 33 | 5.76 | -4.56 | 83.3 | 7.3 | 7.7 |
| | OC19L088 | H | 172 | 3 | 56.3 | | | | |
| 2 | OC19L103 | V | 208 | 58 | 2.59 | -0.95 | 61 | 4.83 | 2.8 |
| | OC19L104 | H | 212 | 14 | 14 | | | | |
| 3 | OC19L105 | V | 159 | 82 | .94 | -1.24 | 14.7 | 1.25 | 1.33 |
| | OC19L106 | H | 163 | 61 | 1.67 | | | | |
| 4 | OC19L107 | V | 181 | 130 | .39 | 1.12 | 7.89 | .48 | 1.24 |
| | OC19L108 | H | 177 | 111 | .59 | | | | |
| 5 | OC19L109 | V | 186 | 141 | .32 | 1.6 | 7.63 | .397 | 1.22 |
| | OC19L110 | H | 180 | 121 | .487 | | | | |
| 6 | OC19L111 | V | 188 | 141 | .33 | 2.45 | 8.04 | .406 | 1.21 |
| | OC19L112 | H | 179 | 120 | .491 | | | | |
| 7 | OC19L122 | V | 184 | 136 | .35 | 3.08 | 9.68 | .439 | 1.24 |
| | OC19L123 | H | 173 | 112 | .545 | | | | |
| 8 | OC19L124 | V | 188 | 140 | .34 | 4.73 | 11.11 | .425 | 1.24 |
| | OC19L125 | H | 171 | 112 | .527 | | | | |
| 9 | OC19L147 | V | 188 | 96 | .96 | -0.79 | 27.15 | 1.51 | 1.64 |
| | OC19L148 | H | 191 | 55 | 2.47 | | | | |

TABLE 1 Degree of Polarization of Target and Background: Contrast Ratios and Contrast Improvement Factor

Tgt <N> : Target Average Radiance
Bkgd <N> : Background Average Radiance
$C_V$ : Vertical Polarization Contrast
$C_H$ : Horizontal Polarization Contrast
$Pol_T$ : Target Degree of Polarization
$Pol_B$ : Background Degree of Polarization
$C_U$ : Unpolarized Image Contrast
$C_H/C_U$: Contrast Improvement Factor, CIF.

HORIZON AND SHIP CONTRAST; SHORT TERM VARIATION.
Two Minute Period 0913-0915, 26 Oct 93

| | | Sea to Sky Contrast | | | Ship to Sea Contrast | | |
|---|---|---|---|---|---|---|---|
| File Name | Pol | Horizon Contrast | Unpol. Contrast | Contrst Imp Fac | Ship Contrast | Ship Unpol Ctst | Ship CIF |
| | | $C_V$,$C_H$ | $C_U$ | CIF | $C_H$ | $C_U$ | CIF |
| | | | | | | | |
| OC26L022 | V | 0.28 | 0.48 | | | | |
| OC26L023 | H | 0.76 | | 1.59 | 0.72 | 0.5 | 1.41 |
| OC26L024 | V | 0.05 | 0.1 | | | | |
| OC26L025 | H | 0.15 | | 1.5 | 0.23 | 0.195 | 1.19 |
| OC26L026 | V | 0.16 | 0.49 | | | | |
| OC26L027 | H | 1.09 | | 2.24 | 0.52 | 0.4 | 1.3 |
| OC26L028 | V | 0.15 | 0.29 | | | | |
| OC26L029 | H | 0.47 | | 1.6 | 0.22 | 0.17 | 1.29 |
| OC26S022 | V | 0.28 | 0.3 | | | | |
| OC26S023 | H | 0.31 | | 1.05 | 0.53 | 0.64 | 0.82 |
| OC26S024 | V | 0.04 | 0.05 | | | | |
| OC26S025 | H | 0.06 | | 1.24 | 0.18 | 0.17 | 1.04 |
| OC26S026 | V | 0.21 | 0.23 | | | | |
| OC26S027 | H | 0.24 | | 1.07 | 0.63 | 0.36 | 1.2 |
| OC26S028 | V | 0.1 | 0.11 | | | | |
| OC26S029 | H | 0.12 | | 1.08 | 0.17 | 0.05 | 3.36 |
| | | | | | | | |
| | MEAN | 0.279 | 0.256 | 1.421 | 0.4 | 0.310 | 1.451 |
| | St Dev | 0.28 | 0.167 | 0.404 | 23351 | 0.198 | 0.79 |

TABLE 2. Short Term Variability of Horizon and Ship Contrast and Improvement Factor.

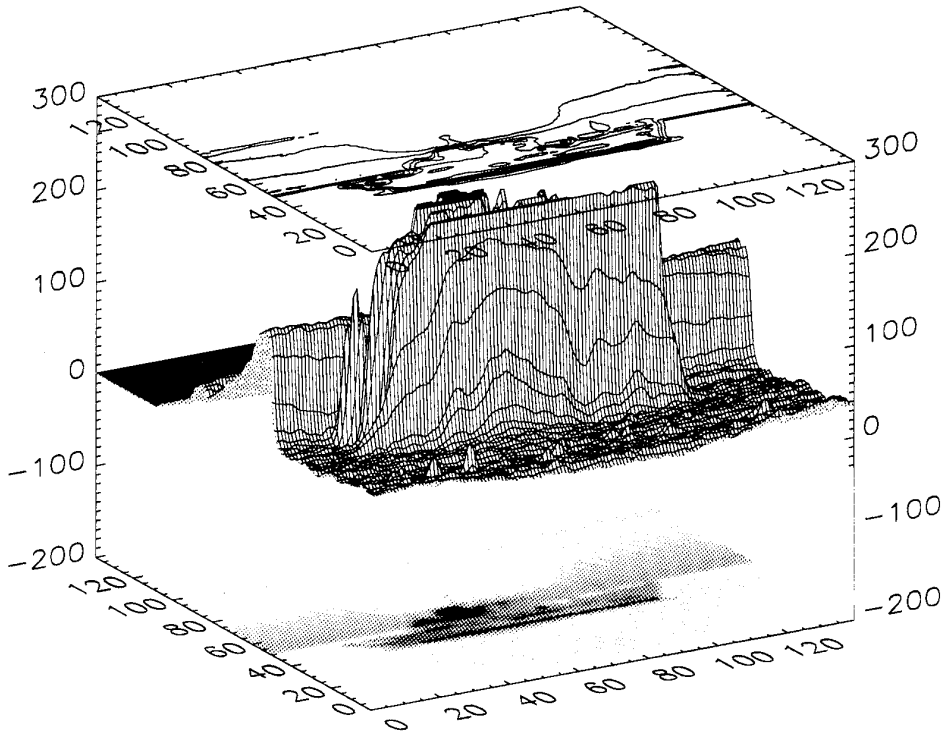


Figure 1. OC19L104 Vertical Polarization Hr. MS. Tydeman in LWIR

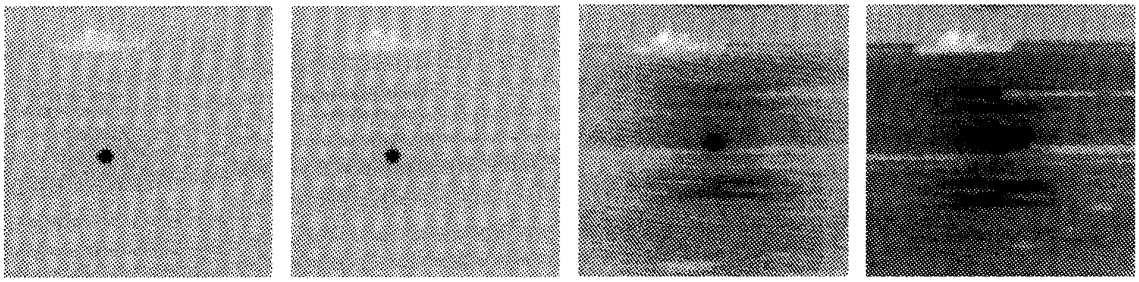

Contrast = 0.107779
Contrast/Unpolarized
Contrast = 0.831417
OC26S024: (0.6 deg)
Polarization: Vertical
IR Band: 3-5 um

Contrast = 0.149864
Contrast/Unpolarized
Contrast = 1.156057
OC26S025:
Polarization: Horizontal
IR Band: 3-5 um

Contrast =0.284245
Contrast/Unpolarized
Contrast = 0.943793
OC26L022:
Polarization: Vertical
IR Band: 8-12 um

Contrast =0.319080
Contrast/Unpolarized
Contrast = 1.059459
OC26L023:
Polarization: Horizontal
IR Band: 8-12 um

DATE & TIME: 26 OCT 93, 9:13 am
Position: 1900 yds to WPB
Air temp=11.2C, Water temp=11.5C, RH=85%

Figure 2. 3-5 um and 8-12 um Comparison with Mostly Sea Background

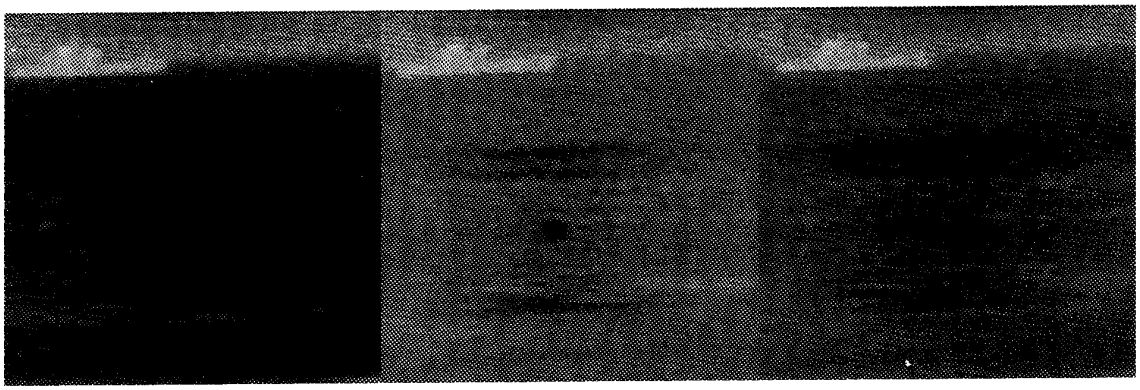

Polarization: Horizontal.
Contrast = 0.404994
Contrast/Unpolarized
Contrast = 1.107376

Polarization: Vertical.
Contrast = 0.333597
Contrast/Unpolarized
Contrast = 0.912156

Polarization: Unpolarized
Contrast = 0.365724

Figure 3. Comparison of Horizontally and Vertically Polarized Images of Hr. MS. Tydeman in LWIR Band OC29L028/029 29 Oct 93, 15:04 hr, IR Band: 8-12 um

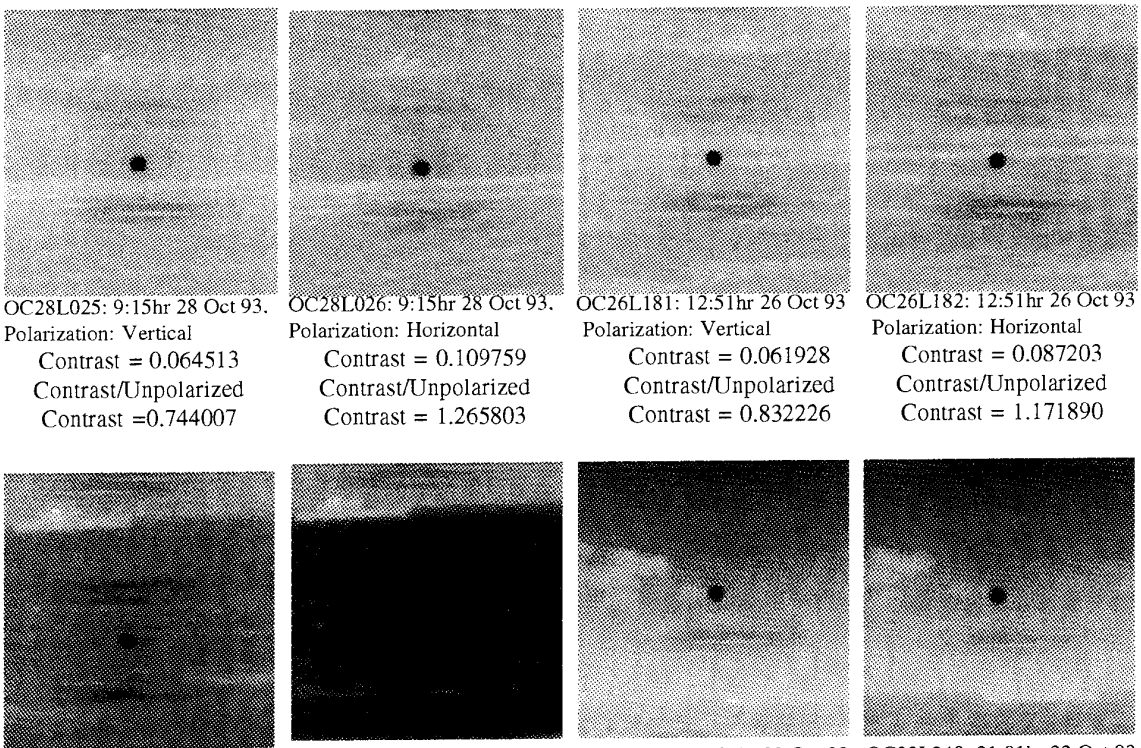

OC28L025: 9:15hr 28 Oct 93.
Polarization: Vertical
Contrast = 0.064513
Contrast/Unpolarized
Contrast =0.744007

OC28L026: 9:15hr 28 Oct 93.
Polarization: Horizontal
Contrast = 0.109759
Contrast/Unpolarized
Contrast = 1.265803

OC26L181: 12:51hr 26 Oct 93
Polarization: Vertical
Contrast = 0.061928
Contrast/Unpolarized
Contrast = 0.832226

OC26L182: 12:51hr 26 Oct 93
Polarization: Horizontal
Contrast = 0.087203
Contrast/Unpolarized
Contrast = 1.171890

OC29L028: 15:04hr 29 Oct 93
Polarization: Vertical
Contrast = 0.333597
Contrast/Unpolarized
Contrast = 0.912156

OC29L029: 15:04hr 29 Oct 93
Polarization: Horizontal
Contrast = 0.404994
Contrast/Unpolarized
Contrast = 1.107376

OC22L239: 21:01hr 22 Oct 93.
Polarization: Vertical
Contrast = 0.046078
Contrast/Unpolarized
Contrast = 0.684281

OC22L240: 21:01hr 22 Oct 93.
Polarization: Horizontal
Contrast = 0.089696
Contrast/Unpolarized
Contrast = 1.332037

Figure 4. LWIR Horizontally and Vertically Polarized images of Hr. MS. Tydeman at 0915; 1251; 1504 and 2101.

# OVERVIEW OF NATO/AC 243/PANEL 3 ACTIVITIES CONCERNING RADIOWAVE PROPAGATION IN COASTAL ENVIRONMENTS

(Tour d'horizon des activités de l'OTAN/AC243/Com.3 concernant la propagation radioélectrique en zone côtière)

*F.Christophe, N.Douchin CERT-ONERA; Y.Hurtaud CELAR, FR
D.Dion, CRDV, CA; R.Makaruschka FGAN-FHP, GE
H.Heemskerk FEL-TNO, NL; K.Anderson NCCOSC, US

*CERT-ONERA, DERMO
2, avenue Ed. Belin
B.P. 4025
31055 TOULOUSE Cedex (FRANCE)

**Résumé** Les campagnes de mesure conduites en collaboration internationale au voisinage de Lorient en 1989, Toulon en 1990 et Lorient en 1993 ont permis l'acquisition de nombreuses données simultanées de propagation à des fréquences de 3 à 94 GHz et de caractérisation du milieu. Les deux premières campagnes, sur des trajets transhorizon, ont donné lieu à une exploitation statistique des amplitudes reçues avec recherche de corrélation aux modèles de propagation dans la couche limite océanique. La dernière, sur un trajet plus court, est axée sur la caractérisation des distorsions de front d'onde créées par les effets de réflexion et de réfraction.

## I - INTRODUCTION

The performances of most systems operating at RF and millimeter waves can be seriously affected by propagation effects. That is the reason why NATO established the Research Study Group No.8 (RSG8) within Panel 3 (physics and electronics) of Defense Research Group (AC 243), with its Propagation Subgroup (PSG) responsible for the propagation aspects. Comparison of mm and other wavelengths was to be considered. In maritime and coastal environments, the use of such wavelengths for various military applications like anti-ship seekers, fire control radars, ship to ship communications or Electronic Support Measurements (ESM) led to the setting up of specific measurement campaigns; the last three are reported hereafter.

The first two experiments used facilities close to Lorient, on the Atlantic coast, and Toulon, on the Mediterranean coast of France, with the purpose of documenting the refractive effects for medium range over the horizon paths **[11]**. These experiments, which are referred to as Lorient 89 and Toulon 90 campaigns, are described in this paper, and some typical results are presented.

The latest cooperative work of RSG8/PSG took place recently (fall 1993) near Lorient, on a line-of-sight 10 km path over seawater. This experiment, referred to as Lorient 93 campaign, was devoted to the analysis of phase-front distortions due to multipath along with refractive effects, and to the assessment of performances for naval systems like short range tracking radars. Analysis of the data, either on a statistical base or as specific case studies, is being performed presently, but some early typical results will be given in this paper after a detailed description of the experiment. Further reports about the last Lorient experiment will be available from the recently established RSG21 of Panel 3, in charge of assessing propagation and signatures effects on naval systems.

The nations (and institutions) contributing to those common activities of RSG8/PSG were France (CELAR and CERT-ONERA), Canada (DREV), Germany (FGAN-FHP), the Netherlands (FEL-TNO) and USA (NRL and NCCOSC-RDTE Div.).

## II - STATE OF THE ART KNOWLEDGE OF REFRACTIVE EFFECTS

### 1. Refractivity in the Marine Boundary Layer (MBL)

Refraction effects are related to the gradients of the refractive index, n, especially in the vertical direction, but sometimes also in the horizontal direction. n and its usual forms N and M are easily calculated for an air parcel if the pressure, temperature, and vapor pressure are known.

Over the ocean, air adjacent to the surface is saturated with water vapor, and the relative humidity is nearly 100 %. Within a few meters above the surface, the air rapidly dries out and reaches an ambient value that depends on the meteorological conditions.

This rapid decrease of the air moisture creates a strong negative M gradient, which decreases in magnitude with increasing height. The few meters where the M gradient is negative are referred to as the evaporation duct, and the height where the M gradient is zero, is defined as the evaporation duct height, which has been shown to be a good measure of the strength of the evaporation duct **[1]**, **[2]**.

The evaporation duct is a nearly permanent propagation phenomenon over the ocean that can strongly affect the performances of EM sensors operating close to the sea surface. Directions of cm and mm wavelength propagation within 1° of horizontal are concerned with the evaporation duct effects which lead principally to a modification of the position and shape of the interference lobes due to multipath propagation in the line-of-sight region. Also the steep refractivity gradients encountered in the evaporation duct can cause ducting with detection ranges well beyond the radio horizon, accompanied by holes in the upper radar coverage. Thus, the use of sophisticated EM sensors close to the sea surface requires good characterisation of the propagation medium and accurate propagation models for the evaluation of coverage.

### 2. Modelling of the vertical refractive index profile

Several atmospheric models allows one to describe the vertical structure of the air in the Marine Boundary Layer (MBL) from a limited set of standard meteorological parameters. They all are based on the physics of the turbulent transport processes at the sea surface. The variation of the influential atmospheric parameters is described by a logarithmic formulation but with an air stability dependent correction. The various existing models differ in the formulation of this correction factor and in the method to calculate the main profile parameters (stability length, roughness lengths, etc).

So far, for the analysis of the experimental data, two MBL models have been used by the members of RSG8/PSG :

- the PAULUS model **[3]** based on an earlier model developed by JESKE **[4]** which uses an empirical stability correction function ;
- a second MBL model, developped at CELAR, referred to as the BULK - CELAR model, which relies on new advances in the understanding of turbulent transport processes to estimate the stability correction function **[5]**.

The major limitation appears to be in adequate meteorological measurements. For example, in stable cases (i.e., $T_{air} > T_{sea}$), small changes in the air-sea temperature difference can result in significant differences in the calculated evaporation

*Paper presented at the Sensor and Propagation Panel Symposium on "Propagation Assessment in Coastal Environments" held in Bremerhaven, Germany 19-22 September 1994.*

duct height and then can change the predicted radar detection range by many kilometers. The proximity of the coast can cause particular phenomenon to appear such as the stable cases [6]. Thus, the performances of both MBL models had to be assessed by measurements.

3. Modelling of radiowave propagation

Once the vertical modified refractivity profile has been determined, it is possible to model EM propagation by solving the wave equation either through a modal analysis [7] or through a technique known as the Parabolic Equation (PE) [8]. Propagation models based on a modal analysis are difficult to use, especially in case of range varying refractivity profiles. In coastal regions such horizontally non homogeneous conditions can be encountered if dry and warm air coming from land slides over a moist and cooler air mass at the sea surface.

In contrast, PE solvers can handle range varying atmospheric conditions and also accomodate sea surface roughness although it is much more time consuming to compute the results then.

For the analysis of the data, members of the RSG8/PSG used PE models above all.

## III - DESCRIPTION OF THE EXPERIMENTS

1. LORIENT 89 and TOULON 90 campaigns

a) Description of the sites

Since refractive effects, which both campaigns were devoted to, are known to be driven by meteorological conditions, opposite conditions were selected for the two experiments : LORIENT 89 took place in fall and winter on the North Atlantic coast, and TOULON 90 in summer on the Mediterranean coast in conditions close to those over warmer seas. Figures 1 and 2 show the geographical locations of both campaigns. The propagation path, indicated by a straight line, lied in the vicinity of the coast so that propagation conditions sometimes varied significantly along the path, especialy when low wind speed or advection movements prevailed. On the other hand, when the wind was blowing relatively strongly at a right angle to the propagation path, the conditions were thought to be homogeneous. Finally, both geographical locations are representative for coastal conditions.

In both experiments, the geometry of the path was representative of over the horizon propagation conditions, with changes of the antenna heights due to the tide in case of LORIENT 89 (tidal effects are negligible in the Mediterranean). During TOULON 90 campaign, the over-the-horizon links were completed by some LOS measurements at 36 GHz (see Figure 2).

b) RF equipments

The propagation measurements were performed using seven propagation sets operating at 3.0, 5.6, 10.5, 16.0, 35.0, 36.0 and 94.0 GHz. In addition, Germany (FGAN) performed measurements with a 95 GHz monopulse radar. During both experiments, the radiolinks were operated continously during several months, allowing analysis of the data on a statistical (long-term) base.

c) Meteorological sensors

Various meteorological sensors were used during the two campaigns :

- two meteorological stations were set up, one at each end of the path, to supply the standard meteorological parameters needed by MBL models (ie : $T_{air}$, pressure, relative humidity and wind speed) except the sea temperature (they also included some other parameters).
- a meteorological buoy was moored near the middle point of the path. It measured the same set of meteorological parameters as the weather stations, along with the sea temperature and the wind direction, the latter being important for horizontal homogeneity considerations.
- data on sea surface temperature were acquired, as given by the infrared radiometer on the transiting satellite NOAA11.

In addition, some specific meteorological sensors were used during the TOULON campaign like a digital thermometer and a psychrometer to check the reliability of the other measurements. Finally, direct measurement of the air refractivity was performed using a refractometer.

Table 1 gives the differences between reference data (those delivered by the psychrometer) and the data collected by the weather stations. Significant discrepancies are noticed in the humidity measurements, which prove the difficulty to get reliable data on humidity.

2. LORIENT 93 campaign

a) Description of the site

Measurements were made over a line-of-sight 10 km path between ILE DE GROIX and GAVRES, on the Atlantic coast (see Figure 1 for a description of the geographical location of the experimental site). Again some coastal influence can be expected, especially when the wind was blowing from the North, or from the North West.

b) Description of the RF equipments

The purpose of this latest experiment differed from that of LORIENT 89 and TOULON 90 campaigns. In fact, the previous experimental work of PSG focussed on amplitude effects and LORIENT 93 was devoted to the analysis of the distortions of the phase-front, due essentially to multipath which can be accompanied by ducting. Thus, RF equipments used during LORIENT 93 are specific sensors dedicated to angle-of-arrival (AOA) assessment, like arrays or monopulse radars. In addition, the previously used 36 GHz RF link was used for propagation path loss assessment.

Table 2 gives a brief description of the various RF equipments used almost continuously during the four weeks of LORIENT 93 campaign. During the campaign, observations of refraction effects in the IR and the visible were also performed, which could be interesting for comparison between radiowaves and IR ( refractive effects are not the same in both cases). A GPS receiving set was also provided for the analysis of propagation effects on its signal at grazing angles.

| REFERENCE | TEMPERATURE | HUMIDITY | PRESSURE |
|---|---|---|---|
| SIMOUN STATION | + 1.4° C (average) | between + 3 and + 15 % | - 3 HPa (average) |
| NATO STATION | + 1° C (average) | between - 2 and + 25 % | + 5 HPa (average) |
| BUOY | between - 0.6 and - 1.5° C | between - 2 and 23 % | $\lvert\delta P\rvert$<1 HPa |

**Table 1: Difference between reference data (psychrometer) and data collected by the weather stations**

| SYSTEMS | PROVIDED BY |
|---|---|
| LOLETTA: 8 + 1 elements receive array at 10.5 GHz and transmitter; 2 elements interferometer at 16 GHz and transmitter ; IR camera and recorder | FEL-TNO (NL) |
| Monopulse receiver at 35 GHz and transmitter<br>Monopulse receiver at 94 GHz and transmitter | FGAN (GE) |
| 4 elements receive array at 35GHz and transmitter<br>GPS receiver for grazing angle analysis | CERT-ONERA (FR) |
| Line-of-sight system at 36 GHz | CELAR (FR) |

**Table 2: Radiofrequency equipments**

c) Description of the meteorological sensors (cf. Table 3)

The two weather stations and the meteorological buoy, used in the previous campaigns, were used again durinf LORIENT 93. But additional sensors have been used during this latest campaign : among them, an upper-air measurement system consisting of radiosondes launched by balloons filled with helium along with the transmitting/receiving and storage package has to be noticed. In fact, after the analysis of the data measured during LORIENT 89 and TOULON 90, the inclusion of a more detailed upper air structure in prediction models was recommended.

One has to notice also the use of another buoy, during LORIENT 93, dedicated to the measurement of the instataneous wave height; since phase front distorsions are strongly related to multipath effects, knowledge of the sea state is in fact of great importance.

*Evaporation duct height statistics*

Concerning LORIENT 89, histograms of evaporation duct height calculated by BULK-CELAR and PAULUS methods are presented in Figure 3. They differ radically from predictions derived from the Engineer' s Refractive Effects Prediction System (EREPS) Surface Duct Summary (SDS) computer program. In the latter the distribution of evaporation duct height is derived from 15 years of surface meteorological observations made by ships at sea for 10 degrees-by-10-degrees areas of the world known as Marsden Squares (MS). Using BULK - CELAR, the mean duct height is 6.1 m, while it is 8.2 m according to the SDS. The atypical form of the measured distributions is due to the unusually fine weather encountered during the test period and the short timescale of the trial that is not representative of conditions met in an "average" year.

| EQUIPMENTS | PROVIDED BY |
|---|---|
| . NATO weather station with rain gauge and computer storage<br>. Refractive index "profiler" : 3 altitudes measurement system | FEL-TNO (NL) |
| . Pulsonic weather station<br>. Riding buoy<br>. Spectropluviometer | CELAR (FR) |
| . Upper-air measurement system : radiosondes launched by balloons filled with helium | NCCOSC(US)<br>DREV(CA) |

**Table 3: Meteorological equipments**

## IV - SOME TYPICAL RESULTS

1. LORIENT 89 and TOULON 90 campaigns

a) Meteorological data

*Occurence frequency of events*

Table 4 gives the occurrence frequency of nine criteria related to air stability, refractivity gradients, horizontal homogeneity and presence of hydrometeors.

*Analysis of stability*

Based on the statistics of the air-sea temperature difference, conditions (in terms of stability) were different during the two campaigns : LORIENT 89 showed a majority of stable cases ($T_{air} < T_{sea}$ for 75 % of the time), while during the three months measurement of TOULON 90 about 40 % of the time stable conditions were observed. The vicinity of the land can be the reason why such high percentage of stable cases are observed, when conditions are often unstable in open sea regions.

*Occurrence of surface-based duct*

Later analysis of all the meteorological and radio data enables us to make an estimate of the periods when a surface-based duct could be prevailed. These periods represent 3 % of the total time of the experiment for LORIENT 89, and 14 % for TOULON 90. These percentages agree quite well with the known statistics **[9]**. However, the need of specific equipment for a more detailed description of upper-air structure has also been demonstrated during both experiments.

*Subrefraction*

In general, subrefraction is likely to occur under very stable atmospheric conditions associated with high humidity and often low visibility. This was the case during the LORIENT 89 campaign and situations where dM/dz was greater than 118 M units/km represent 25 % of the total time, and where it was greater than 157 M units/km 12 % of the time. During TOULON 90 campaign, subrefraction was much more frequent and dM/dz was greater than 118 M units/km only 0.4 % of the time.

| CRITERION | LORIENT CAMPAIGN Occurrence frequency of events (in % of the total dura- tion of the experiments) | TOULON CAMPAIGN Occurrence frequency of events (in % of the total dura- tion of the experiments) |
|---|---|---|
| **estimated surface-based ducts** | 3 | 14 |
| **measured subrefraction** (path loss greater than diffraction loss) | 25 at 3 GHz<br>13 at 10.5 GHz<br>11.5 at 36 GHz | 8 at 3 GHz<br>0.4 at 10.5 GHz<br>0.15 at 36 GHz |
| **dN/dz>118 N/km** (calculated by bulk-CELAR model) | 25 | 0.4 |
| **dN/dz>157 N/km** (calculated by bulk-CELAR model) | 12 | 0.04 |
| **neutral conditions (\|ASTD\|<0.5°)** | 13 | 33 |
| **unstable conditions (ASTD<0)** | 24 | 60 |
| **very unstable conditions (ASTD<-2° C)** | 4 | 6 |
| **homogeneous situation** | 29 | 9 |
| **rain or fog situation** | 30 | 0.8 |

**Table 4: Occurrence frequency of events for the two campaigns**

campaign and situations where dM/dz was greater than 118 M units/km represent 25 % of the total time, and where it was greater than 157 M units/km 12 % of the time. During TOULON 90 campaign, subrefraction was much more frequent and dM/dz was greater than 118 M units/km only 0.4 % of the time.

*Presence of horizontal homogeneity*

Essentially because of the proximity of the shore, the propagation conditions sometimes vary significantly along the link. An "homogeneous situation" criterion was therefore considered based principally on the wind speed and the wind direction. According to it, the percentage of time where the situation is homogeneous is very low, as given in Table 4. This means that most of the time the conditions were nonhomogeneous along the path, which is typical of coastal regions.

b) Radio propagation data

*Cumulative probability*

Concerning the LORIENT 89 campaign, a study of enhancement factors ( measured path loss relative to diffraction loss ) shows that 50 % of the time, the enhancement at 3 GHz was more than 5 dB, and 10, 10 and 6 dB at 5.6, 35.0 and 94.0 GHz respectively. Enhancements larger than 10 dB are observed 19 %, 48 %, 70 %, 70 %, 50 % and 21 % of the time at 3.0, 5.6, 10.5, 16.0, 35.0 and 94.0 GHz respectively. An explanation for the distinct behaviour at the different frequencies can be given with the PC-PEM predictions (using PE method) of Figure 5. Maximum enhancement factors of 18-20 dB and 16-18 dB for 10.5 and 16.0 GHz respectively indicates the presence of duct heights of about 6m. At the higher frequencies (35 and 94 GHz) the maximum overall enhancement at such duct heights is smaller and the signal fluctuation as a function of the duct height and tide becomes significant. Indeed, the analysis of the 36 GHz data reveals that the path loss varied by more than 40 dB, while the maximum received signal reached the free space level.

Moreover, when ducting effects are observed at the lower frequencies, large fluctuations in the 94 GHz signal level are observed around the level obtained without ducting. It appears that turbulence in the low troposphere diminishes the duct effects at this frequency.

Concerning TOULON 90 campaign, the cumulative distribution of enhancement factor was analysed for all frequencies. For lower frequencies, the enhancement ranges between 0 and 40 dB, with more than 10 dB enhancement measured during 58 %, 75 %, 93 %, 95 %, 97 % and 18 % of the time, respectively. This suggests large duct heights, which indeed have been observed.

Once again, an inspection of the received signal strength versus time shows a very strongly fluctuating signal at 94 GHz, most of the time. Also at 35 GHz there are fluctuations but much less.

Finally, a comparison of the data related to the French 36 GHz link with those related to the German 35 GHz link shows directly the influence of the 1 m higher position of the 36 GHz receiver. Obviously, the path loss measured by the latter are less on average than those for the 35 GHz link.

*Comparison of predictions and measurements*

Long-term predictions

MLAYER (based on a modal approach ) has been used with a neutral evaporation-duct profile (which is log-linear) weighted by the annual evaporation duct height-percent-occurrence distribution to give the accumulated frequency distributions of absorption-free path loss, which are then compared to the measured distributions. Figure 6 shows the results at 16 and 94 GHz, for the LORIENT 89 campaign. The comparisons between predictions and measurements are excellent up to and including 16 GHz. Thus, a system designer could use such long-term theoretical predictions to assess possible interference effects on existing systems, for example.

At 35 and 94 GHz, the predictions generally underestimate the path loss by 5 to 7 dB. However, the shape of the predicted and measured curve are similar, which may indicate that gaseous absorption is underestimated in models. Other possible explanations for the differences at the highest frequencies may be :

- surface roughness effects, which are likely to increase the predicted path loss ;
- horizontal homogeneity of the meteorology along the path affecting absorption ;
- the shape of the evaporation duct M profile near the surface which has a stronger effect as the frequency increases ;
- more probably a combination of all these factors.

Generally speaking, the conclusions are the same for the TOULON 90 campaign. Good long-term predictions up to 16 GHz, and poorer results for the millimeter waves. However, for the 3 and 5.6 GHz cases, the predictions generally overestimate the measured path loss, particularly near free-space levels. This might be attributed to the presence of elevated layers. So, once again the need of a detailed description of upper air structure is recommanded.

Short-term predictions

For every 10 minutes, the path loss predictions were calculated using the meteorological data of the buoy, the PAULUS model and PC-PEM.

In the case of LORIENT 89, the calculated overall rms deviations are 6.3, 6.8, 6.5, 6.6, 7.5 and 6 dB respectively for the frequencies in ascending order. Then, we can conclude that the short-term predictions are not as good as long-term predictions.

In the case of TOULON 90, the short-term predictions are even poorer, since the calculated overall rms deviations are respectively 11.8, 11.2, 8.8, 9.1, 7.6 and 10.4 dB. Larger differences were observed at the lower frequencies (3.0 and 5.6 GHz). The presence of other types of ducts (elevated layers) than the evaporation duct is thought to be the cause.Indications are that there was surface duct during about 26 % of the time.

Generally speaking, it can be concluded that, when calculating the refractivity profile based upon a single point measurements, good predictions are possible if we consider long-term statistics. For short-term analysis, the refractivity profile should be measured at several ranges.

Another way to proceed, when data at various frequencies are available, consists in deducing the duct height from path loss measured at a frequency and then predicting path loss at the other frequencies using this duct height. In the context of the LORIENT campaign, the use of the 3 GHz data to estimate the duct height reduced discrepancies significantly. But this was not the case for the TOULON 90 campaign : other atmospheric structures than the evaporation duct were likely to prevail.

It is obvious that in general short-term predictions are not as accurate as the long term predictions. However, it must be noted that the measurements ranged only over a part of the year and that the geographical location of both sites may have caused specific land-induced effects.

*Spectral analysis*

The fine structure of the refractivity of the atmosphere varies both temporally and spatially, causing amplitude fluctuations referred to as scintillations. However, over-the-horizon propagation of millimeter waves at low altitude above the sea is also closely linked to the conditions of the sea surface (i.e., the sea state).

Main conclusions about power spectra of scintillations are:

- the general shape of the fading spectra at 35 GHz on a over-the-horizon path and at 36 GHz on a line-of-sight path is essentially the same for the higher frequency spectra range (f>1Hz) ;
- the reflection from the sea does not seem to affect the fading densities at higher spectral frequencies (f>1 Hz) ;
- the power spectra are pronounced at the low-frequency end and power spectra densities are consistently higher at shorter wavelength ;
- at all measured frequencies (10.5 GHz, 35.0 GHz, 36.0 GHz and 94.0 GHz) the spectra follow the $f^{-8/3}$ power law showing excellent agreement with the theoretical model given by Tatarski **[10]** ;
-the power spectra of signal fading in the lower frequency range (F<1Hz) are closely linked to the conditions of the sea surface. When the sea is calm, the shape of the power spectrum shows a more or less marked spectral density peak in the lower frequency range (around 0.1 Hz). Due to signal reflection against the sea surface, these frequency peaks can be associated with the periodicity of the swell. When the sea is rough, the peaks are smoothed out (except at 10.5 GHz) because the reflections from the sea surface at shorter wavelength are more random.

2. LORIENT 93 campaign

Either on a long-term statistical base or related to case studies, the analysis of LORIENT 93 data concentrates on AOA determinations in order to assess the phase-front distortions effects due to multipath and ducting essentially, and also to the atmospheric turbulence in the case of the millimeter waves.

Overall data analysis has not yet been completed, statistical results are not yet available, and so we present here only a case study corresponding to 28 September, a day of smooth sea conditions. Figure 7 gives the path loss and AOA measured by the Ku-band interferometer provided by TNO.

Obviously both the path loss and the AOA highly depend on the tide height, which indicates that multipath is the dominant mechanism with regard to phase-front distortions and also to path loss. Also a strong correlation between AOA and path loss is noticed, which confirms the main role played by multipath effects. In contrast, there is no evidence of a strong correlation between the measured duct height and either the AOA or the path loss. The calculation of the interference pattern (due to multipath) at 5 h 00 UT and 17 h 00 UT shows that the X-band array was situated in a null (destructive interferences) at these times. Figure 7 shows that the measured AOA is completely erroneous, at these moments Thus, difficulties encountered by tracking systems operating at low altitude above the sea surface due to reflection are well illustrated here.

## V - CONCLUSION

This paper has emphasized the availability of radiowave propagation and meteorological data provided by extensive experimental cooperative work conducted by RSG8/PSG. This material has allowed an assessment of refractive and multipath effects on systems operating in a maritime environment, near the coast, either in centimeter or in millimeter wavelengths.

Main conclusions that can be derived from 3 main campaigns are :

- with regard to predictions, obtaining meteorological profiles is more critical than using them in propagation models ;
- for cm-wave systems, use of existing models provides sufficient prediction performance for global sensors performance study, while short term data is not as accurate but can be operationally useful ;
- at mm-waves, poorer prediction performances were obtained even for global sensor performance study. It is thought to be due to the increasing sensitivity of the refractive profiles and duct height on the path loss computation as the frequency increases and also to the insufficient characterization of sea-state effects.

Also the work performed by RSG8/PSG allows one to analyse the implications on military systems:

-multipath and refractivity gradients permanently affect the operations of cm- and mm-wave naval sensor against low-flying targets ;

-for naval radar systems, ducting leads to over-the-horizon detection of low-flying targets. However, for short and medium ranges the probability of detection may be degraded at ranges depending on the geometry of the path ;

-refractive effects can modify the target acquisition range of missile seekers and affect the ship's ECM effectiveness ;

-under ducting conditions active systems can be detected at longer ranges (OTH) by Electronic Warfare Support Systems (ESM) ;

-better performance of radar or communication systems should be obtained through frequency agility or diversity, antenna height diversity and applying advanced processing array antennas and adaptative signal processing.

## REFERENCES

**[1]** S. ROTHERAM, "Radiowave propagation in the evaporation duct", The Marconi Review, vol. XXXVII, pp. 18-40, 1974

**[2]** W.L. PATTERSON, "Comparison of evaporation duct and path loss models", Radio Science, vol. 20, No 5, Sept-Oct 85

**[3]** R.A. PAULUS, "Specification for environmental measurements to assess radar sensors", NOSC TD. 1685, Nov 1985

**[4]** H. JESKE, "State and limits of prediction methods of radar wave propagation conditions over sea", in "Modern Topics in Microwave Propagation and Air-Sea Interactions", A. ZANCLA, Reidel Pub., 1973

**[5]** J. CLAVERIE, "Détermination des profils météorologiques dans le conduit d'évaporation", Centre d'ELectronique de l'ARmement (CELAR), fiche technique n° ASRE/180/ASRE.16457, 28 pages, octobre 1990

[6] J. CLAVERIE, Y. HURTAUD, "Propagation transhorizon en atmosphère marine : modélisation et nouveaux résultats expérimentaux", AGARD-CP 502, pp. 4-1.4-14, CESME (TURKEY), septembre-octobre 1991

[7] H.V. HITNEY, J.H. RICHTER, R.A. PAPPERT, K.D. ANDERSON and G.B. BAUMGARTNE Jr, "Tropospheric radio wave propagation", Proc. IEEE, vol. 73, No 2, Feb. 1985

[8] K.H. CRAIG, M.F. LEVY, "Parabolic equation modelling of the effects of multipath and ducting on radar systems", IEE Proceedings-F, vol. 138, No 2, April 1991

[9] W.L. PATTERSON, "Climatology of marine atmospheric refractivity effects : a compedium of the Integrated Refractive Effects Prediction System (IREPS) historical summaries", NOSC TD.573, December 1982

[10] V.I. TATARSKI, "Wave propagation in a turbulent medium", Mc Graw-Hill, New-York, 1961

[11] NATO/AC243/Panel3/RSG8(PSG), "Radiowave Propagation at 3 to 100 GHz near the Horizon above the Sea", Technical Report AC/243(PANEL 3)TR/10, 28 Sept. 1994.

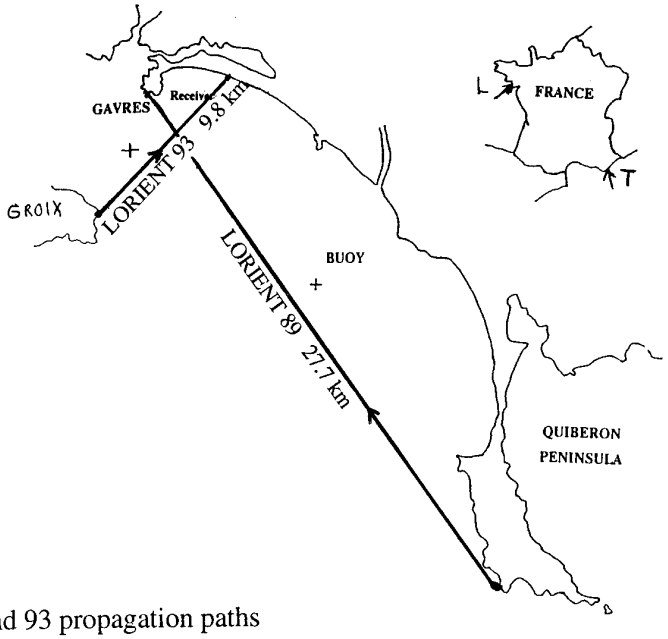


Figure 1 : Lorient 89 and 93 propagation paths

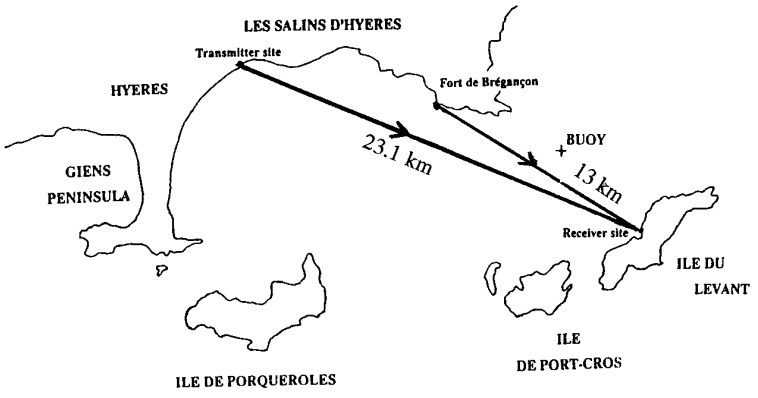


Figure 2 : Toulon 90 propagation path

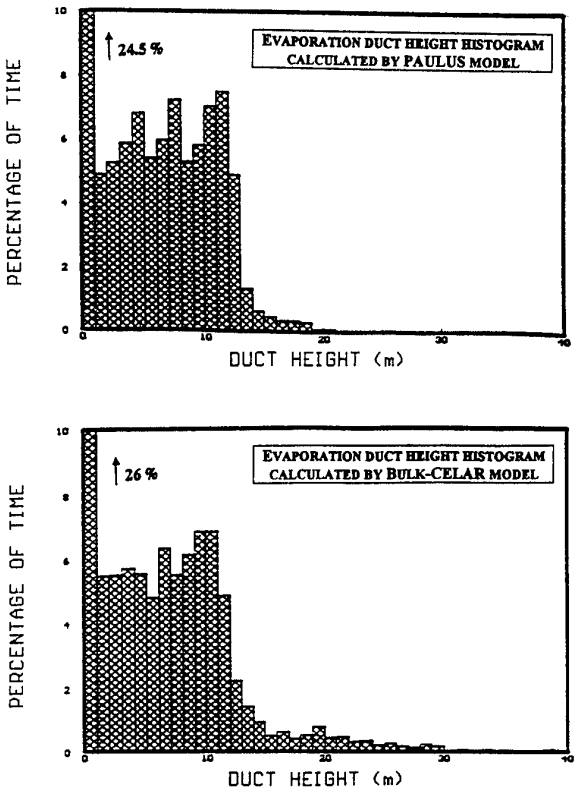


Figure 3 : Duct-height histograms for Lorient 89 ; different MBL modelling

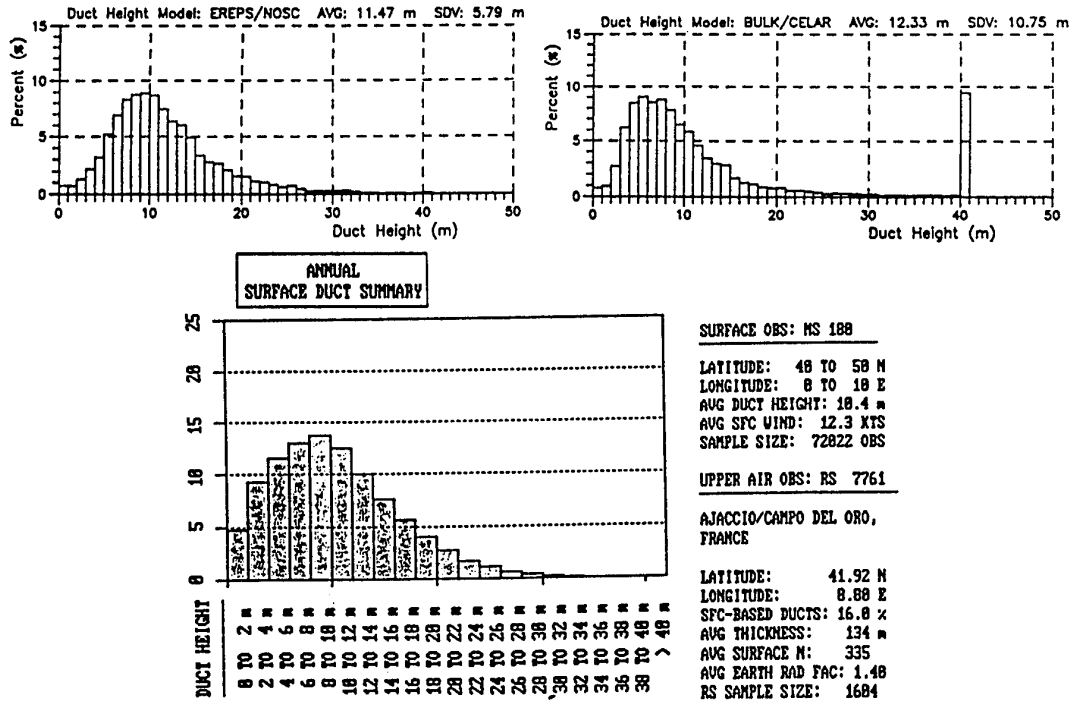


Figure 4 : Duct-height histograms for Toulon 90 and long term data base

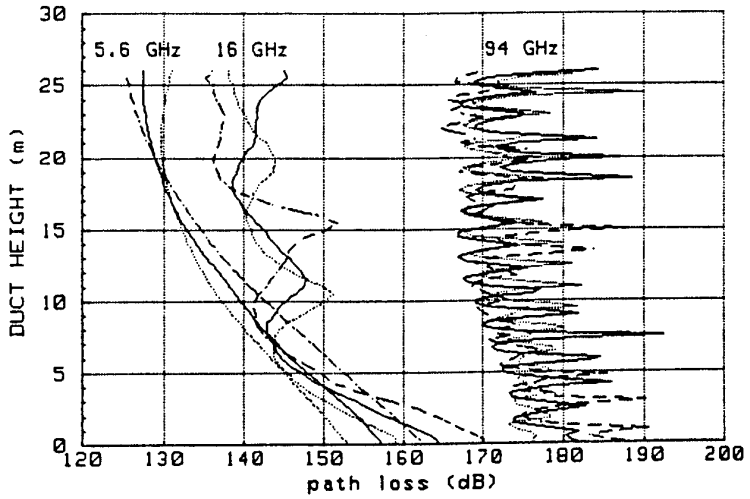


Figure 5 : Path loss dependence with receiver height and tidal effects
( PC-PEM calculations )

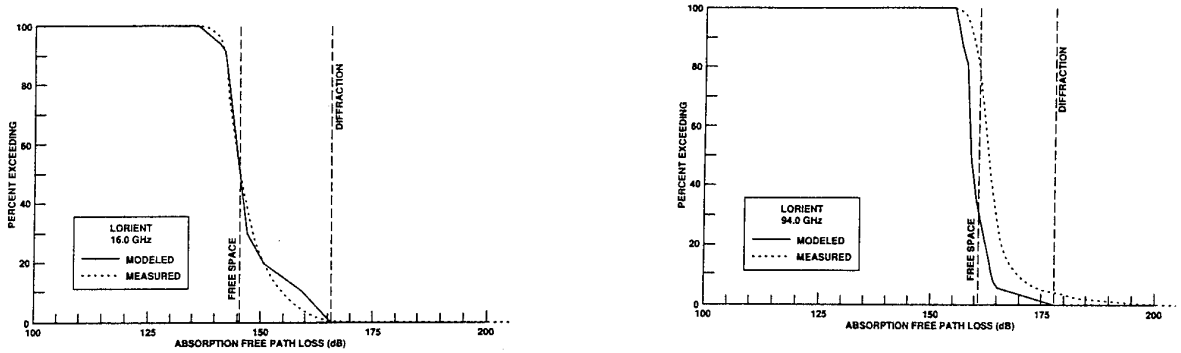


Figure 6 : Comparison, at 16 and 94 GHz, of observed path loss
with predicted values

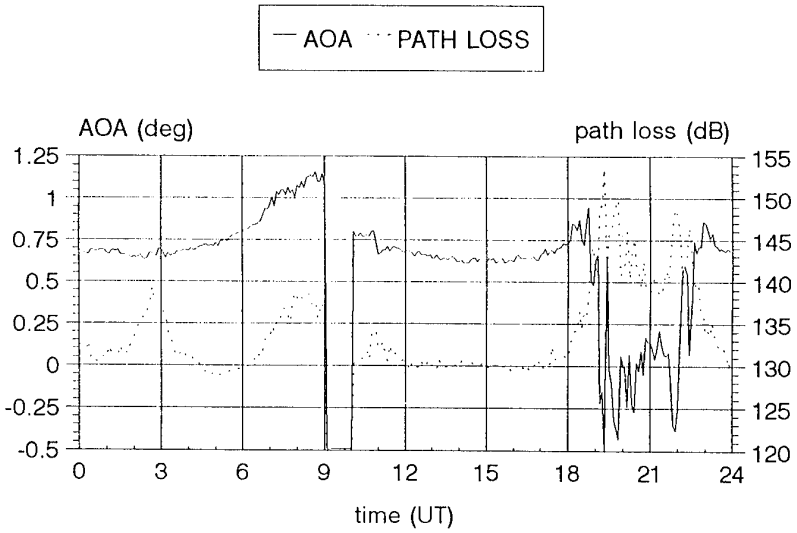


Figure 7 : Lorient 93: Measured path loss and angle of arrival at 16 GHz for september 28 th. : tidal effect with smooth sea

# LORIENT CAMPAIGN 1993
# The Dutch contribution

**R.B. Boekema**
TNO Physics and Electronics Laboratory
P.O. Box 96864
2509 JG The Hague
The Netherlands

## SUMMARY

The performance of radar and infrared systems in a maritime environment is strongly dependent on the conditions of the atmosphere and the sea surface. In the autumn of 1993 an experiment was set up by the NATO Research Study Group AC/243 Panel3/RSG21 to collect propagation data at a line-of-sight propagation path. Purpose of the experiment was to gain knowledge about the behaviour of the path loss and angle of arrival of the signals.

This paper presents the results of the Dutch contribution to the experiment and a comparison of the measurements with model predictions. For radar in the line-of-sight situation the propagation is dominated by the multipath interference and influenced by ducting. Predictions performed with the propagation model PCPEMC [1] and the Bulk-CELAR [2] duct model show satisfying results for the position of the nulls, if wind speed and wave height are taken into account.

Using the data of this experiment, a synergism between radar and IR angle of arrival could not be proven.

## 1 INTRODUCTION

The performance of radar and infrared systems in a maritime environment is strongly dependent on the conditions of the atmosphere and the sea surface. The NATO Research Study Group AC/243 Panel3/RSG21 has conducted a measurement campaign near Lorient, France in the autumn of 1993. Purpose of this measurement campaign was to gain knowledge about the microwave and infrared propagation low above the sea at a line-of-sight propagation path. This is of great importance for the defence of ships against attacks by sea-skimming missiles. Special attention was paid to the behaviour of the angle of arrival for radar and infrared (IR) signals under the influence of ducting. The measurements at the radar frequencies are used to validate propagation model predictions.

This paper is based on the propagation data measured by the Dutch equipment and the meteorological data measured by a buoy halfway the propagation path. The microwave equipment consisted of an interferometer system at 16 GHz and an antenna array system at 10.5 GHz. The IR measurements were recorded with a line scanner in the 3-5 and 8-12 μm infrared bands.

For radar applications several models are available to predict the propagation under the influence of evaporation ducting. The PCPEMC model, based on the parabolic equation method is able to calculate the phase and amplitude components of the electromagnetic wave propagation. Input to this model is the duct height calculated by a bulk measurement model from the meteorological data measurements at the propagation path. These models and the expected propagation behaviour of the radar signals over the propagation path are presented in section 2.

The experiment is described in section 3. There, the microwave and the IR equipment are explained briefly. Also the location at the Atlantic ocean coast with the specific meteorological conditions encountered during the experiment is described.

The experimental results are given in section 4. This includes a comparison between microwave measurements and performed model predictions. The IR angle of arrival measurement results are also studied in this section.

In section 5 some conclusions are drawn about the angle of arrival behaviour for both radar and IR.

## 2 RADAR PROPAGATION

### 2.1 Theory

At the line-of-sight measurement configuration used, the propagation conditions are mainly determined by multipath. At the receiver location, the phase difference between direct waves from the transmitter and waves reflected at the sea surface creates a regular vertical lobing pattern of the electromagnetic field. If the direct and reflected waves have about the same phase, the values add up; if the direct and reflected waves have opposite phases, this results in cancellation of the electromagnetic fields. As a consequence, high path losses at certain altitudes occur. The locations of these high path losses are called interference nulls.

This field pattern caused by multipath is altered by a change in the structure of the atmosphere. Above sea the propagation is nearly permanently determined by the presence of an evaporation duct. This is a trapping layer caused by the characteristic refractivity profile in the lower atmosphere due to the evaporation of the sea water. The evaporation duct is characterised by its duct height. Under influence of the evaporation duct, the entire lobing pattern is bent downwards. This means that the height of an interference null decreases with increasing duct height.

For the used land-based measurement system also the tide has influence on the propagation between transmitter and receiver because their effective heights above the sea level change. From the point of view of the receiver, the interference pattern is lifted with increasing tide level.

*Paper presented at the Sensor and Propagation Panel Symposium on "Propagation Assessment in Coastal Environments" held in Bremerhaven, Germany 19-22 September 1994.*

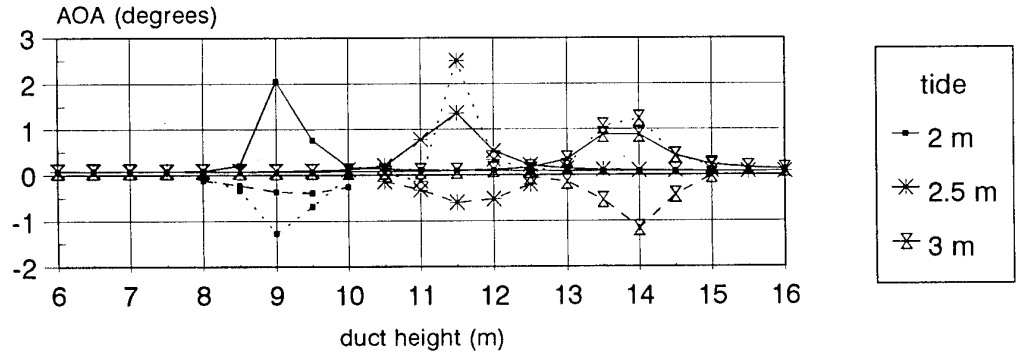


Fig. 1 PCPEMC angle of arrival predictions for Ku-band situation.

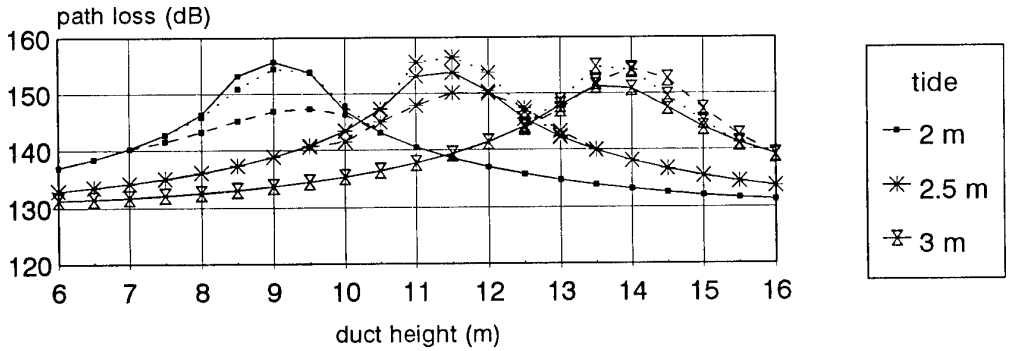


Fig. 2 PCPEMC path loss predictions for Ku-band situation.

### 2.2 Modelling

The modelling of the propagation is performed in two steps, as depicted in the next scheme.

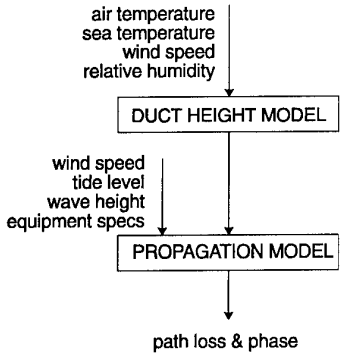


First the duct height model determines the refraction profile of the lower atmosphere based on the temperature of the sea and the parameters describing the condition of the air at one altitude ("bulk" measurement) above the sea level. This results in a duct height value. There are a number of models calculating the duct height using the "bulk" measurement method. They are all based on the Monin-Obukhof [3] boundary layer theory. In an unstable atmosphere (air temperature lower than sea temperature) they all give similar results.

The second step of the modelling, the theoretical predictions of path loss and angle of arrival is performed with a propagation model. There are a number of propagation models available as described in [4]. For the Lorient experiment the PCPEMC propagation model is used. This model based on the parabolic equation calculation is a version of PCPEM, adapted to produce the phase information apart from the path loss information. Input to the model are the variable values of duct height, the wind speed, the tide level, the wave height and the equipment specifications.

The tide level and wave height are used as a correction on the transmitter and receiver height.

The figures 1 and 2 show some results of the angle of arrival and path loss calculated for the Ku-band situation using the PCPEMC predictions. For three tide levels at the used measurement configuration the predictions are calculated over a duct height range from 6 to 16 metres. In the figures three wind speed situations are marked by the different line types. The solid line for a 5 m/s wind speed, the dotted line for 7.5 m/s and the dashed line for 10 m/s.

Extreme values of the angle of arrival only occur when the receiver is in an interference null, which can be correlated with the high path loss value. In all three tide cases this is the same null which occurs at the receiver at a different duct height, according to the tide and duct height theory in 2.1. In a null the direction and magnitude of the angle of arrival is strongly dependent on the wind speed. The wind speed influences the reflection coefficient at the sea surface. If the receiver is not in a null the angle of arrival is slightly positive (which means propagation slightly downwards) and nearly constant in value. At the 6 to 16 metre duct height range a small decrease in angle of about .02 degree was observed.
In the path loss figure one can see that the wind speed changes the depth of the nulls.

## 3 DESCRIPTION OF THE EXPERIMENT

The experiment is performed to investigate situations for the defence of warships against attacks by sea-skimming

missiles at a line-of-sight distance. For this purpose the location near Lorient was ideal with an island at about 10 kilometres from a peninsula at the Atlantic ocean coast.

The measurements have been performed at 10.5 GHz and 16 GHz.
The equipment consisted of separate transmitter and receiver combinations instead of radars. This has the advantage of a large cost reduction and a more reliable non-stop performance.

Both transmitters, consisting of a continuous wave (CW) source and a large parabolic reflector antenna mounted on a steady frame, were located on the island Ile the Croix, at a height of about 15 metre above average sea level.

The receivers were positioned at the beach of the peninsula of Gâvres separated from the transmitters by 9.7 kilometres of open sea. They were mounted on top of a cabin containing the registration equipment at a height of about 10 metres above average sea level. Both receivers, specially build to derive power and phase information from the received signal, worked with different techniques.

The 16 GHz interferometer consisted of a 2 element vertical array. The array elements were pyramidal horns with a 24 cm aperture connected to the receiver with a 90° hybrid component. From the output signals of the hybrid the amplitude and phase information of the signals received by the two antennas can be derived.
The output signals of the hybrid were registered by a computer with an AD-converter, and processed afterwards.

The 10.5 GHz signal was received by a vertical array of 10 horizontally polarised microstrip antenna elements. The centre 8 elements were used for the actual signal measurements. The receiver is coherent, with the phases of the received signals of each of the eight elements determined with respect to the phase of the top element. The eight antenna elements can be sequentially linked with a common receiver channel through a multiplex PIN diode switch. A measurement scan of the eight antenna elements is executed in 1 millisecond, fast enough to consider it as an instantaneous measurement. The eight antenna signals are processed and stored in memory in a 12 bits I and Q format.

The angle of arrival (AOA) is calculated from the phase data by

$$\mathrm{AOA}=\mathrm{ARCSIN}\ \frac{d\Phi\,\lambda}{2\pi D},$$

in which $d\Phi$ is the phase difference between the antenna signals, D the distance between the antennas and $\lambda$ the wavelength of the received signal. The maximum unambiguous angle of arrival range for the 16 GHz interferometer is ± 2.4° and for 10.5 GHz ± 7.2° if the antenna is configured as two arrays of four adjacent antennas.

The radar propagation measurements at both frequencies are performed every 5 minutes. To eliminate small disturbing effects like those from small waves, every measurement consist of a sequence of samples.
At 16 GHz eight samples of the two channels are taken with an interval of 10 μseconds to get one record. Ten of these are taken at an 1 second interval. This data is averaged to get one measurement.
At 10.5 GHz sixteen scans of the eight antennas are taken directly after each other to get one record in 16 mseconds. Ten of these records, taken with an 1 second interval are averaged.

IR measurements were performed simultaneously with the radar measurements over the same 9.7 kilometre path. The measurements were recorded with the TNO-FEL WBS-3 line scanner in the 3-5 and 8-12 μm infrared bands. This instrument was positioned next to the receivers on the mainland. The IR sources were placed at two heights on the island, one next to the radar transmitters at about 15 metres and one higher on the cliff at about 38 metres above average sea level. The positional accuracy of the instrument was 0.35 mrad. IR-measurements were performed only over short periods of the day for several reasons: the line scanner needs regular maintenance during measurements, it cannot operate during rain and the data processing has to be performed manually.

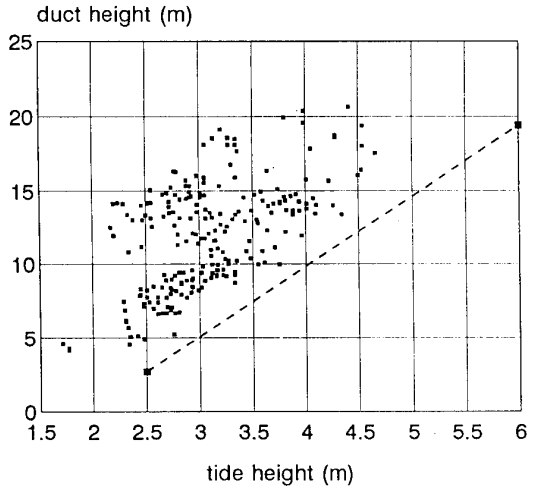


Fig.3 Occurrence of the nulls at X-band with Paulus duct height and no tide correction.

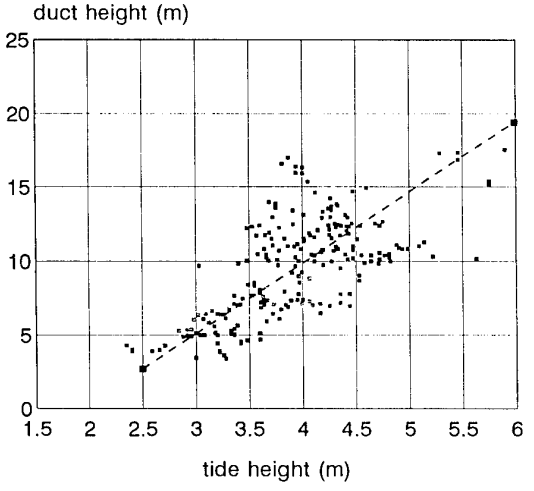


Fig.4 Occurrence of the nulls at X-band with Bulk-CELAR duct height and wave height correction on tide.

Halfway the propagation path, two French buoys were anchored: a waverider buoy to measure the wave spectrum of the sea, and a meteorological buoy to collect the data necessary for the duct modelling. The meteorological buoy recorded the air and sea temperature, wind speed, air humidity, and also the solar flux and wind direction as supplementary information.
At this part of the Atlantic Ocean the tidal variation is large. It can reach values of up to 5 meters. This information is registered at a local weather station at the coast.

## 4 EXPERIMENTAL RESULTS

The weather conditions during the experiment were rough for the time of the year. There were periods with storms and the amount of rainfall was twice the normal amount at the end of September and even three times the normal amount for October. The conditions along the path were representative for open sea conditions because the wind direction was mainly from the sea. Therefore the atmosphere was most of the time unstable, indicating an air temperature lower than the sea temperature, and securing a reliable prediction of the duct height. More than 90 percent of the duct heights were between 6 and 16 meters.

A way to validate the model predictions with the measurements is to consider the nulls. As indicated by the figure 1 and 2, the nulls are characterised by high path loss values and an extreme angle of arrival behaviour. For these predictions it appears that, when there is a null at the receiver for specific duct and tide combinations, the duct heights and tides seem to have a nearly linear relation.

Figures 3 and 4 show the relation between the measurements and predictions for the nulls at X-band. For these figures, situations with high path losses and extreme angles of arrival have been selected from the measurement data. The duct and tide heights at these conditions are presented by points in the figure. The line in the figure indicates the PCPEMC prediction.
In figure 3 the actual tide height and the duct height calculated with the Paulus formulation [5] is presented. The correlation with the model prediction in the figure is very poor, in all cases the Paulus duct height is at least four metre to high. This corresponds with the experiences at former propagation experiments on over-the-horizon paths [6].

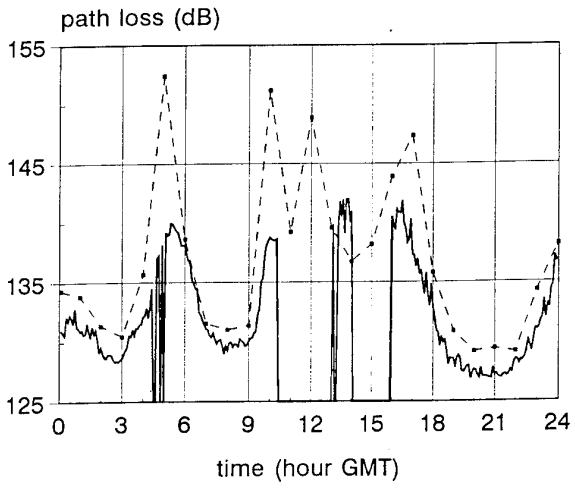


Fig.5 X-band path loss of 28 September.

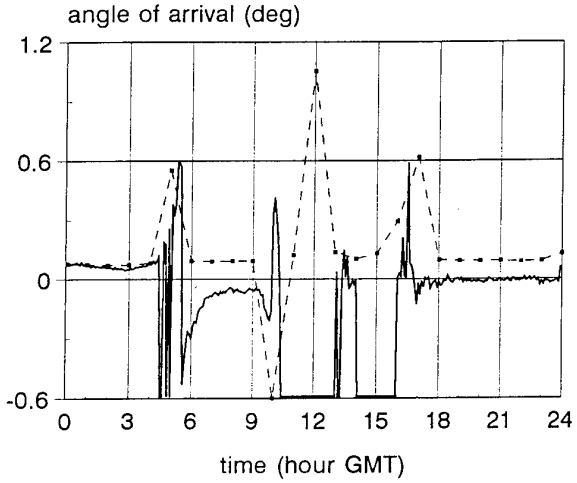


Fig.6 X-band angle of arrival of 28 September.

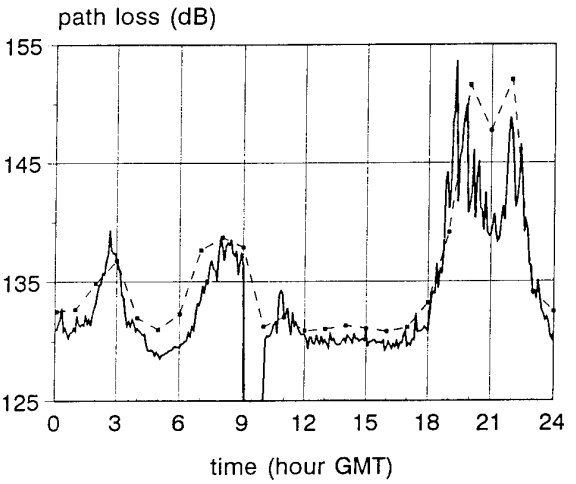


Fig.7 Ku-band path loss of 28 September.

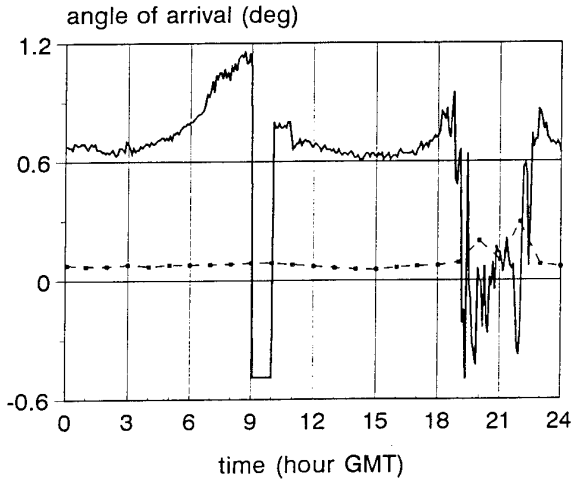


Fig.8 Ku-band angle of arrival of 28 September.

In figure 4 the duct height calculated with the Bulk-CELAR model is used, this results in smaller duct heights. The tide height in this figure is corrected with the H1/3 (significant) wave height value measured by the waverider buoy. This shifts the points measured under rough sea conditions to the right.
The correlation between these measurements and the predictions is good.

To get a good impression of the overall model performance, the results of the model must be compared with the path loss and angle of arrival for a wide variety of tides and meteorological situations. In this section the results of one representative day are presented in detail. The PCPEMC predictions at X and Ku band of 28 September 1993 are calculated for every hour and compared with the measurement data. Although only one day is presented, the conclusions are based on the general behaviour, encountered during the entire measurement campaign.

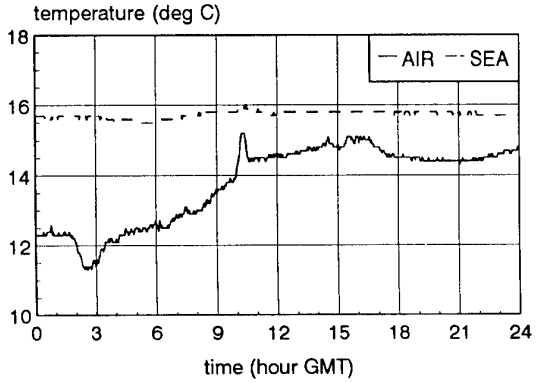


Fig.9 Air and sea temperature at 28 September.

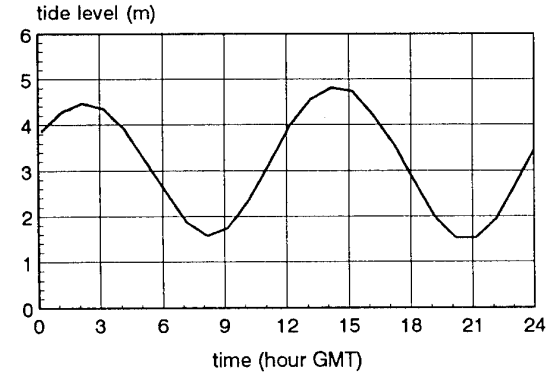


Fig.10 Tide variation at 28 September.

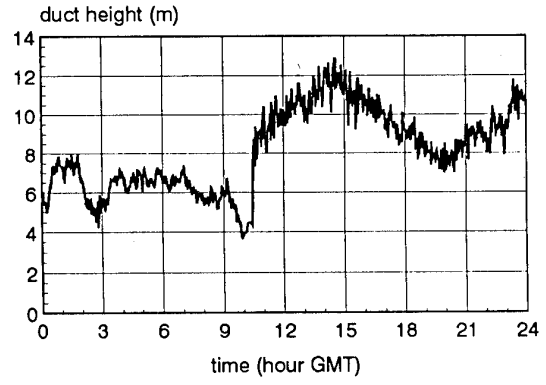


Fig.11 Bulk-CELAR duct height at 28 September.

### 4.1 X-band sample day

Figures 5 and 6 present the path loss and angle of arrival (AOA) at X-band. The measurements are presented by the solid line, and the PCPEMC predictions by the points connected by the dotted line. Unfortunately there is some loss of measurement data due to calibration and back-up activities, like around 12:00 and 15:00 hour, and due to locking problems like at 5:00 hour. The PCPEMC predictions are performed with the Bulk-CELAR duct height and with the sea level corrected with the H1/3 wave height.
Comparing the measured and predicted path loss one observes that they agree well, though the predicted path loss is generally a few dB higher than the measured one. The measured nulls are predicted at the right time, but they are not as deep (high path loss value) as predicted.

Looking at the measured and predicted AOA, one also observes a prediction of the nulls (high angles of arrival) at the right time.
For the measurement configuration used, an error occurs at low tide situations because the individual antenna elements have picked up reflections from the beach. This effect is minimised by configuring the eight antenna elements as two arrays of four antennas, thereby limiting their field of view, but it still results in a negative offset at low tide. This is visible between 7:00 and 9:00, and between 18:00 and 24:00 hour.

### 4.2 Ku-band sample day

Figures 7 and 8 present measured and PCPEMC predicted path loss and AOA at Ku-band. Due to back-up activities some measurement data is missing between 9:00 and 10:00 hour. The PCPEMC predictions, presented by the points connected with the dotted line, are also calculated with the Bulk-CELAR duct height and the sea level corrected with the H1/3 wave height.
Comparing the measured and predicted path loss one again observes that the predicted path loss is generally only a few dB higher than the measured one, apart from the times when nulls occur. The measured nulls are predicted at the right time, but they are not as deep (high path loss value) as predicted.
The measured and predicted AOA show a large difference. Although showing the same trends, the measured AOA is much larger than the predicted one. If not in the null, the deviation is about a factor ten, but in the null it is much smaller. The reason for this large AOA deviation is still unknown. It is probably a result of a wrong system calibration, but it will be point of further research.

Figures 9, 10 and 11 show some of the parameters used for the modelling at 28 September. Figure 9 presents the air and sea temperature, the tidal variation is presented in figure 10 and the calculated Bulk-CELAR duct height in figure 11.

If the X and Ku band figures are compared one sees very different shapes. For this day the nulls at the two frequencies manifest at different moments, but that is no general rule. With this measurement configuration the

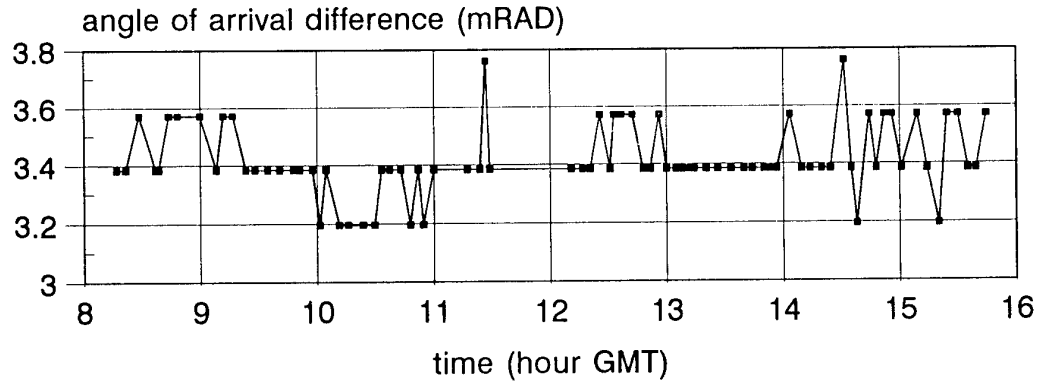


Fig.12 IR angle of arrival difference measured in the 4μ band at 28 September.

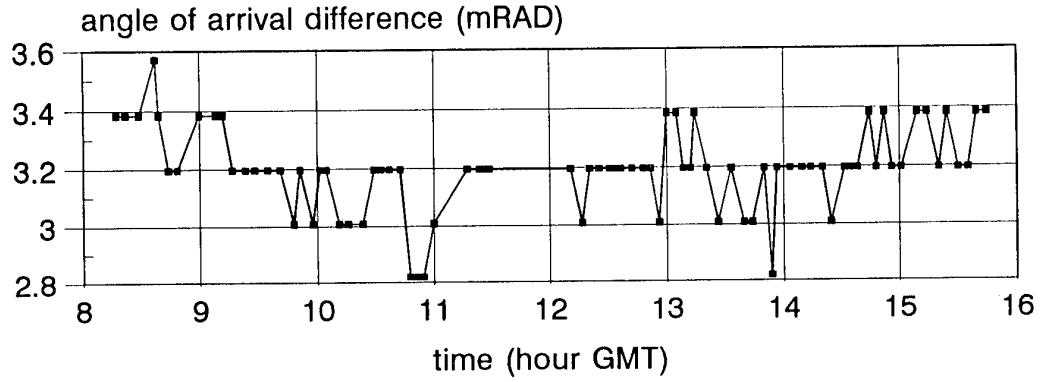


Fig.13 IR angle of arrival difference measured in the 10μ band at 28 September.

model predicts no simultaneous nulls at the two bands for the duct range from 6 to 16 meters, but this is dependent on the heights of the equipment above the sea level. In general we can conclude that the model performance concerning the prediction of the nulls is satisfying. In an operational situation, a radar performance prediction program can be used as a decision tool to select the radar frequency which gives optimum performance under the actual circumstances.

### 4.3 Infrared data

At the same day the IR data in the 4μ and 10μ bands has been measured between eight and sixteen hour. Although very small, the IR AOA variation at this day was more than on average. The figures 12 and 13 present the AOA difference between the two sources (ΔAOA). At both bands one can see a clear decrease in ΔAOA between eight and eleven, followed by a recovery and a small increase. Between eight and nine an IR subrefraction case is present. This correlates with the large negative air and sea temperature difference early in the day (fig.9).
A direct correlation with the CELAR duct height can not be found, and also not with the radar AOA. The total measured ΔAOA variation is .8 mRAD ( 0.046 deg).

## 5 CONCLUSIONS

At the X and Ku-band radar line-of-sight situation the propagation is dominated by the multipath interference and influenced by ducting.

The path loss shows a large variation due to the lobing structure of the interference pattern. The angle of arrival is slightly positive except for the short periods when the receiver is located in an interference null. The angle of arrival then increases very fast, to values of up to more than 2 degrees. Dependent on the wind speed this angle can be positive or negative.

Predictions have been performed using the propagation model PCPEMC and the Bulk-CELAR duct model.
These model predictions based on simple one spot meteorological measurements show satisfying results for the position of the nulls.
Important for the model predictions is the correction of the sea level with the wave height.
In general the measured path losses in the nulls are not as high as predicted. Accurate prediction of the angle of arrival in the null is not possible while the angle of arrival behaviour is very critical.

Angle of arrival measurements in the IR band are also influenced by the meteorological conditions, but show no extremities as in the radar band. The behaviour can not be correlated with the radar duct height. The small IR data set and the nearly constant stability of the atmosphere does not allow further comparison.

In an operational situation, a radar performance prediction program can be used to predict the occurrence of interference nulls in the actual environment. The occurrence of these nulls can then be remedied by either

switching to another radar frequency or by relying more heavily on the infrared equipment.

## ACKNOWLEDGEMENTS

We would like to acknowledge our collegues from CELAR, CERT, DREV, FGAN and NCCOSC for their cooperation in this campaign.

## REFERENCES

[1] Craig, K.H. and Levy, M., "PCPEM software program.", Signal Science Limited, Abingdon, Oxon, UK, 1990.

[2] Claverie, J., "Determination des profils meteorologiques dans le conduit d'evaporation", ASRE/16 437, CELAR, Bruz, France, 1990.

[3] Monin, A.S. and Obukhof, A.M., "Basic laws of turbulent mixing in the ground layer of the atmosphere", Akad. Nauk. USSR, Geofiz. Inst. Tr., 1954.

[4] Vogel, M.H., "A comparison between several computer codes for calculations on microwave propagation.", FEL-29-A435, FEL-TNO, The Hague, The Netherland, 1992.

[5] Paulus, R.A., "Specification for environmental measurements to assess radar sensors.", TD-1685, NCCOSC, San Diego, California, USA, 1989.

[6] Boekema, R.B., "Comparison of the results from the propagation experiments at the Atlantic Ocean and Mediterranean Sea coast.", FEL-93-B150, FEL-TNO, The Hague, The Netherlands, 1993.

## DISCUSSION

**D. DOCKERY**

1. Were wavelength corrections to the modelled data made by adjusting antenna heights or by using a rough surface in the PCPEM model?

2. When correcting modelled data to agree with measurements, which factor was more important: incorporation of sea height (roughness and tide) or changing to the Bulk-Celar duct model?

**AUTHOR'S REPLY**

1. The wave height corrections were made by adjusting the transmitter and receiver antenna heights.

2. Changing to the Bulk-Celar model resulted in a lower duct height of about 3-4 m. The correction for significant wave height was somewhat less than about 1 meter. It is hard to say which factor is more important. One has to do both.

**N. DOUCHIN**

You told us that you made a correction for wave height. Could you specify how? Did you a find a systematical correction factor as a function of the significant wave height ($H_{1/3}$)? (Some people are taking 0.5 $H_{1/3}$ as "correction factor").

**AUTHOR'S REPLY**

We corrected for H1/3. Calculations for 0.5 $H_{1/3}$ did not improve the predictions in this case. There seems to be no consensus, and further studies are needed.

# MODELISATION DES PROFILS VERTICAUX D'INDICE DE REFRACTION ET DE $C_n^2$ EN ATMOSPHERE MARINE.

Jacques **CLAVERIE***, Yvonick **HURTAUD****, Yannick **DE FROMONT***, Alain **JUNCHAT****

* Centre de Recherches des Ecoles de Coëtquidan
56381 GUER CEDEX - FRANCE

** Centre d'Electronique de l'Armement
35170 BRUZ - FRANCE

## RESUME

La détermination des conditions de propagation, pour des systèmes évoluant dans la CLSO (Couche Limite de Surface Océanique), nécessite la connaissance du profil vertical d'indice de réfraction. A partir de mesures météorologiques simples, le modèle PIRAM (Profils d'Indice de Réfraction en Atmosphère Marine) permet de calculer ce profil à partir des profils verticaux de température et d'humidité.
PIRAM reprend, moyennant quelques modifications, la démarche suivie dans le modèle Bulk-CELAR conçu initialement pour les radiofréquences. Les calculs ont été désormais étendus au domaine optique. PIRAM permet également la modélisation du profil vertical du paramètre de structure de l'indice de réfraction de l'air (Cn2). Cette nouvelle modélisation devra être validée par des données expérimentales.
A proximité des côtes, la connaissance des profils verticaux n'est cependant pas toujours suffisante, en raison notamment des inhomogénéités horizontales du canal de propagation.

## I. INTRODUCTION

Les performances des systèmes de télécommunications navales et de détection des cibles évoluant à basse altitude au-dessus de la mer, dépendent très étroitement de la structure de la Couche Limite de Surface Océanique (CLSO), et plus particulièrement du profil vertical d'indice de réfraction de l'air.

La détermination du profil vertical d'indice de réfraction aux fréquences radioélectriques et de l'ensemble des profils météorologiques verticaux à partir de la connaissance locale des températures de l'eau et de l'air, de l'humidité de l'air et de la vitesse du vent a fait l'objet de la modélisation "Bulk-CELAR" ([1]). La détermination des profils verticaux de température et d'humidité, en plus du classique calcul de la hauteur du conduit d'évaporation, est importante pour obtenir une estimation précise de l'absorption atmosphérique aux longueurs d'onde millimétriques.

Aucune mesure directe des profils météorologiques verticaux n'a, à ce jour, été entreprise de façon précise dans le but de tester la validité du modèle Bulk-CELAR. Néanmoins les hauteurs de conduit d'évaporation déduites de ce modèle ont permis une interprétation globalement satisfaisante des résultats des campagnes de propagation transhorizon LORIENT 89 et TOULON 90 ([2], [3]).
Par ailleurs, la paramétrisation choisie rendait envisageable l'extension du modèle dans deux directions :

- calcul du profil d'indice de réfraction dans le domaine des fréquences optiques,
- calcul du profil vertical du paramètre de structure de l'indice de réfraction, $C_n^2$,

pour aboutir finalement au modèle global baptisé PIRAM (Profils d'Indice de Réfraction en Atmosphère Marine).

De plus, et dans le but d'une meilleure prise en compte des spécificités des zones côtières, notamment en matière de stabilité atmosphérique, nous avons, par rapport au modèle Bulk-CELAR initial, modifié le calcul des longueurs de rugosité, sans pour autant accroître le nombre et la nature des paramètres d'entrée du modèle, ce qui aurait nui à sa simplicité d'utilisation opérationnelle.

Dans la suite de cet article, nous commencerons tout d'abord par rappeler les équations de base des méthodes de type "bulk" (partie II). Nous insisterons ensuite sur le choix des fonctions de stabilité retenues dans le modèle PIRAM (partie III) et sur le délicat problème du calcul des longueurs de rugosité (partie IV). Dans la partie V, nous montrerons comment le modèle, initialement conçu pour les fréquences radioélectriques, s'adapte très facilement au domaine optique. Puis, dans la partie VI, nous exposerons les différentes étapes et les hypothèses nécessaires à la détermination de la valeur de $C_n^2$. Enfin (partie VII), nous aborderons les difficultés de modélisation du canal de propagation dans les régions côtières, notamment l'existence d'inhomogénéités horizontales qui rend souvent délicate l'extension des profils verticaux déterminés à partir de mesures effectuées en un point, à l'ensemble d'une liaison d'au plus quelques dizaines de kilomètres.

## II. PRINCIPE DE LA METHODE BULK

### II-1 Position du problème

En utilisant les hypothèses de la théorie de Monin-Obukhov, les méthodes de type bulk permettent de caractériser complètement la structure des basses couches de la

*Paper presented at the Sensor and Propagation Panel Symposium on "Propagation Assessment in Coastal Environments" held in Bremerhaven, Germany 19-22 September 1994.*

troposphère marine à partir de la seule connaissance des paramètres suivants (appelés paramètres bulk) :

- température de surface de la mer ($t_0$)
- température de l'air ($t_1$), humidité relative ($H_1$), pression atmosphérique ($p_1$) et vitesse du vent ($v_1$), mesurées à une altitude $z_1$ de l'ordre de quelques mètres.

Dans la plupart des applications concernant la propagation des ondes radioélectriques en atmosphère marine, ces méthodes sont utilisées pour déterminer la hauteur du conduit d'évaporation qui existe de façon quasi continuelle au-dessus de la mer. Le modèle PIRAM, tout comme son prédécesseur Bulk-CELAR, est plus complet car il calcule l'ensemble des profils verticaux de température (T), d'humidité relative (H), de vitesse du vent (u) et de coindice de réfraction (N). La connaissance de ces profils verticaux caractérise complètement la CLSO tant du point de vue des effets de la réfraction que de l'absorption atmosphérique, non négligeable dans le domaine millimétrique ([4]).

**II-2 Calcul du profil vertical d'indice de réfraction aux radiofréquences**

Le coindice de réfraction de l'air est, aux fréquences considérées ici, fonction de la pression atmosphérique p (en HPa), de la température T (en K) et de la pression partielle de vapeur d'eau e (en HPa) :

$$N = \frac{77,6}{T}\left(p + 4810\frac{e}{T}\right) \qquad (1)$$

Dans la basse troposphère, la pression atmosphérique décroît linéairement en fonction de l'altitude (notée z par la suite), avec une pente de -0,12 HPa/m. Le profil vertical d'indice de réfraction pourra donc être calculé si on connaît les profils verticaux de température et d'humidité.

Dans la CLSO, supposée horizontalement homogène, la théorie de Monin-Obukhov se traduit par les équations suivantes :

$$\frac{du}{dz} = \left(\frac{u_*}{kz}\right).\Phi_m\left(\frac{z}{L}\right) \qquad (2\text{-a})$$

$$\frac{d\theta}{dz} = \left(\frac{\theta_*}{kz}\right).\Phi_h\left(\frac{z}{L}\right) \qquad (2\text{-b})$$

$$\frac{dq}{dz} = \left(\frac{q_*}{kz}\right).\Phi_h\left(\frac{z}{L}\right) \qquad (2\text{-c})$$

avec :

$\theta$ température potentielle ($\theta = T + 9,86.z$),

q humidité spécifique ($q = 0,622\frac{e}{p}$),

k est la constante de Von Karman pour laquelle la valeur 0,4 semble maintenant unanimement admise,

$u_*$, $\theta_*$ et $q_*$ constituent les échelles de vent, température et humidité ($u_*$ est aussi appelée vitesse de frottement),

L est une échelle de longueur appelée longueur de Monin-Obukhov,

$\Phi_m$ et $\Phi_h$ sont des fonctions universelles pour lesquelles de nombreuses formulations déduites d'études expérimentales ont été proposées (voir partie III).

La longueur de Monin-Obukhov est donnée par :

$$L = \frac{\overline{\theta_v} u_*^2}{kg\theta_{v*}} \qquad (3),$$

où l'on a :

g accélération de la pesanteur,

$\theta_v$ température potentielle virtuelle définie par :

$$\theta_v = T_v + 9,86.10^{-3} z \text{ avec } T_v = T.(1 + 0,608q),$$

ce qui conduit à :

$$\theta_{v*} \approx \theta_* + 0,608\bar{\theta}q_*$$

la notation $\overline{\theta_v}$ (resp. $\bar{\theta}$) désigne la valeur moyenne sur l'épaisseur de la CLSO; en pratique, on détermine $\overline{\theta_v}$ (resp. $\bar{\theta}$) en assimilant ces moyennes aux valeurs obtenues à l'altitude $z_1$.

L est en outre un indicateur de stabilité. Sa valeur est positive (resp. négative) pour une atmosphère stable (resp. instable), et infinie pour une atmosphère neutre[1]. Dans ce dernier cas, les fonctions $\Phi_m$ et $\Phi_h$ valent simplement 1 et l'intégration des équations (2) conduit à des profils logarithmiques.

D'une façon générale, l'intégration des équations (2) ne commence pas à z = 0, mais à des altitudes notées respectivement $z_{0u}$, $z_{0t}$ et $z_{0q}$, appelées longueurs de rugosité. Compte tenu de l'état de surface de la mer, ces longueurs de rugosité correspondent aux altitudes à partir desquelles les différents paramètres cessent d'être égaux aux valeurs relevées à l'interface air-mer. En supposant les rugosités connues (voir partie IV), l'intégration de (2) conduit, pour les profils verticaux, aux expressions suivantes :

$$u(z) = \frac{u_*}{k}\left[\mathrm{Ln}\left(\frac{z}{z_{0u}}\right) - \Psi_m\left(\frac{z}{L}\right)\right] \qquad (4\text{-a})$$

$$\theta(z) = \theta_0 + \frac{\theta_*}{k}\left[\mathrm{Ln}\left(\frac{z}{z_{0t}}\right) - \Psi_h\left(\frac{z}{L}\right)\right] \qquad (4\text{-b})$$

$$q(z) = q_0 + \frac{q_*}{k}\left[\mathrm{Ln}\left(\frac{z}{z_{0q}}\right) - \Psi_h\left(\frac{z}{L}\right)\right] \qquad (4\text{-c})$$

avec, par définition, et en posant $\xi = \frac{z}{L}$ :

$$\Psi_m(\xi) = \int_0^{\xi} \frac{(1 - \Phi_m(\xi'))}{\xi'} d\xi' \qquad (5\text{-a})$$

$$\Psi_h(\xi) = \int_0^{\xi} \frac{(1 - \Phi_h(\xi'))}{\xi'} d\xi' \qquad (5\text{-b})$$

$\theta_0$ et $q_0$ sont calculés connaissant $T_0$ et en supposant une humidité relative de 100% à l'interface air-mer. Au voisinage de cet interface on a de plus supposé que le vent est nul (voir partie IV). Les équations (4), appliquées à l'altitude $z_1$ où sont mesurés les paramètres bulk, et combinées avec (3) conduisent à un système de quatre équations à

[1] En première approximation, on peut considérer que l'atmosphère est stable si la température de l'air est supérieure à la température de l'eau, et instable dans le cas contraire.

quatre inconnues : les paramètres d'échelle $u_*, \theta_*, q_*$, L. Ce système doit être résolu de façon itérative. Une solution élégante et rapide consiste à introduire différentes expressions du nombre de Richardson ([5]). Une fois les paramètres d'échelle déterminés, l'équation (1) associée aux équations (4) permet le calcul du profil vertical d'indice.

**II-3 Calcul de la hauteur du conduit d'évaporation aux radiofréquences**

En dérivant (1), on obtient une expression du gradient vertical d'indice de la forme :

$$\frac{dN}{dz} = a\frac{dp}{dz} + b\frac{d\theta}{dz} + c\frac{dq}{dz} \qquad (6)$$

où a, b, c sont des fonctions de ($p, \theta$ , q) auxquelles on peut attribuer des valeurs constantes déterminées par la connaissance des paramètres bulk.

La très forte décroissance de l'humidité dans les premiers mètres de la CLSO suffit à elle seule à expliquer l'existence de gradients d'indice inférieurs à -0,157 N/m, valeur limite d'existence d'un conduit de guidage des ondes électromagnétiques qui correspond ici au conduit d'évaporation. La hauteur $z_c$ de ce conduit, si celui-ci existe, est solution de :

$$\frac{dN}{dz} = -0{,}157 \text{ N/m} \qquad (7)$$

Au-dessus de l'altitude $z_c$, le gradient vertical d'indice augmente et tend en général (voir partie VII) vers une valeur voisine de -0,039 N/m qui correspond à l'atmosphère dite standard.

La valeur constante de $\frac{dp}{dz}$ ainsi que les expressions (2-b) et (2-c) de $\frac{d\theta}{dz}$ et $\frac{dq}{dz}$ conduisent pour $z_c$ à une équation qui, pour les fonctions universelles $\Phi_m$ et $\Phi_h$ les plus couramment usitées, est du 3ème, voire du 2ème degré, donc soluble analytiquement. Lorsque l'équation (7) n'admet pas de solution, on conclut à l'absence de conduit; le profil d'indice calculé peut être alors caractéristique de situations d'infraréfraction ou de proche infraréfraction. Dans les cas stables, on peut parfois obtenir des valeurs très élevées pour la hauteur de conduit qui est alors fixée arbitrairement à 40 m (voir partie suivante).

## III. CHOIX DES FONCTIONS DE STABILITE

De nombreuses formulations semi-empiriques des fonctions $\Phi_m$ et $\Phi_h$ ont été publiées depuis la fin des années 60. Elles peuvent conduire à des hauteurs de conduit d'évaporation sensiblement différentes, notamment dans les cas stables.

**III-1 Cas instables**

Il y a désormais un quasi consensus dans la littérature pour affirmer que $\Phi_m$ et $\Phi_h$ doivent avoir la forme suivante :

$$\Phi_m(\xi) = (1 - M\xi)^{-1/4} \qquad (8\text{-a})$$

$$\Phi_h(\xi) = (1 - M'\xi)^{-1/2} \qquad (8\text{-b})$$

Récemment EDSON et al ([6]) ont comparé plusieurs formulations de ce type, dont celles de DYER et HICKS ([7]) retenues dans le modèle Bulk-CELAR, à des observations expérimentales , notamment des mesures de flux turbulents. Elles conduisent toutes à des résultats très voisins et en bon accord avec les mesures. La pertinence de notre choix initial est donc à posteriori renforcée, et, dans le modèle PIRAM, nous conserverons donc :

$$\Phi_m(\xi) = (1 - 16\xi)^{-1/4} \qquad (9\text{-a})$$

$$\Phi_h(\xi) = (1 - 16\xi)^{-1/2} \qquad (9\text{-b})$$

**III-2 Cas stables**

En plein océan, les situations atmosphériques stables sont assez peu probables. Néanmoins, elles peuvent être rencontrées pendant un pourcentage non négligeable du temps, dans les mers chaudes ou à proximité des côtes (voir partie VII). Leur modélisation est cependant délicate car l'épaisseur de la CLSO, au sein de laquelle sont valides toutes les relations écrites au §II, peut ne pas excéder quelques mètres. C'est donc d'une façon totalement arbitraire et abusive - faute de mieux - que l'on a coutume d'appliquer les méthodes bulk pour décrire la structure atmosphérique dans les quarante premiers mètres d'altitude.

Dans la mesure où la théorie de Monin-Obukhov reste applicable, EDSON et al ([6]) préconisent les relations suivantes :

$$\Phi_m(\xi) = \Phi_h(\xi) = 1 + M\xi \text{ avec } 5 < M < 9 \qquad (10)$$

Dans ces conditions, l'équation (2-b) conduit à un gradient de température toujours strictement positif, quelque soit l'altitude. Or, si pour les cas stables , la température croît dans les premiers mètres, on s'attend intuitivement à ce qu'elle redevienne à peu près constante par la suite; on a alors $\frac{d\theta}{dz} \approx 0$ dès que l'altitude atteint quelques dizaines de mètres. Ceci est possible en choisissant pour $\Phi_m$ et $\Phi_h$ des expressions proposées par KONDO ([8]) :

$$\Phi_m(\xi) = \Phi_h(\xi) = 1 + \frac{6\xi}{1+\xi} \qquad (11)$$

Aux altitudes les plus basses, ces relations sont bien compatibles avec la forme donnée par (10). L'utilisation de ces fonctions de stabilité a permis d'interpréter les données des campagnes de LORIENT 89 et TOULON 90, même en présence de situations très stables.

## IV CALCUL DES LONGUEURS DE RUGOSITE

**IV-1 Méthode utilisée dans le modèle Bulk-CELAR**

Dans le cas d'une atmosphère neutre, le coefficient de transfert en vent, $C_{DN}$, aussi appelé coefficient de traînée, est défini à l'altitude de 10 m par :

$$C_{DN}^{1/2} = \frac{k}{Ln(\frac{10}{z_{0u}})} \qquad (12\text{-a})$$

De nombreuses formulations empiriques ont permis d'exprimer simplement $C_{DN}$ en fonction de la vitesse du vent mesurée à l'altitude de 10 m. BLANC ([9]) a montré que ces formulations pouvaient conduire à des écarts sur les valeurs de la rugosité $z_{0u}$ atteignant 100 %. Les relations proposées par KONDO ([8]) semblent cependant constituer un compromis acceptable pour le calcul de $C_{DN}$ et par suite de $z_{0u}$. Une difficulté supplémentaire est introduite par le fait qu'en général la vitesse du vent n'est pas connue à 10 m, mais à une altitude $z_1$ différente. En supposant un profil de vent simplement logarithmique, une résolution itérative est nécessaire pour obtenir la valeur de $z_{0u}$.

De façon similaire, des coefficients de transfert en température et en humidité (à 10 m), notés $C_{HN}$ et $C_{EN}$ sont reliés aux rugosités $z_{0t}$ et $z_{0q}$ par :

$$C_{HN} = \frac{k^2}{Ln(\frac{10}{z_{0u}}).Ln(\frac{10}{z_{0t}})} \qquad (12\text{-b})$$

$$C_{EN} = \frac{k^2}{Ln(\frac{10}{z_{0u}}).Ln(\frac{10}{z_{0q}})} \qquad (12\text{-c})$$

et reliés empiriquement à la vitesse du vent à 10 m.

**IV-2 Méthode utilisée dans le modèle PIRAM**

Les relations (12) ne constituent des définitions des coefficients de transfert que dans le cas d'une atmosphère neutre. Dans le cas d'une stratification quelconque, la définition de ces coefficients, que nous noterons alors $C_D$, $C_H$ et $C_E$ fait intervenir les fonctions de stabilité $\Psi_m$ et $\Psi_h$ définies au II, ce qui alourdit considérablement la résolution. KONDO ([8]) suggère une démarche simplifiée et empirique décrite ci-après :

1) $C_{DN}$, $C_{HN}$, $C_{EN}$ sont calculés à partir du vent mesuré (Cf. IV-1)

2) $C_D$, $C_H$, $C_E$ sont donnés par :

- <u>cas stables</u> ($S < 0$ et on suppose $S > -3,3$)

$$\frac{C_D}{C_{DN}} \approx \frac{C_H}{C_{HN}} \approx \frac{C_E}{C_{EN}} \approx 0,1 + 0,03S + \exp(4,8S) \qquad (13)$$

- <u>cas instables</u> ($S > 0$)

$$\frac{C_D}{C_{DN}} \approx 1 + 0,47\sqrt{S}; \quad \frac{C_H}{C_{HN}} \approx \frac{C_E}{C_{EN}} \approx 1 + 0,63\sqrt{S} \qquad (14)$$

où S est un paramètre de stabilité calculable à partir des paramètres bulk :

$$S = \frac{|S_0|}{|S_0| + 0,01} \text{ avec } S_0 = \frac{\theta_{v0} - \theta_{v1}}{u_1^2 . \left[1 + \log_{10}(\frac{10}{z_1})\right]^2} \qquad (15)$$

3) Les rugosités $z_{0u}$, $z_{0t}$ et $z_{0q}$ sont calculées par les relations (12) en remplaçant $C_{DN}$, $C_{HN}$ et $C_{EN}$ par $C_D$, $C_H$ et $C_E$.

Cette correction liée à la stabilité atmosphérique a été testée sur les données de la campagne de LORIENT 89. Pour des situations instables ou modérément stables (vent supérieur à 5 m/s), les valeurs des hauteurs de conduit d'évaporation ne sont quasiment pas modifiées. Par contre, pour des cas stables caractérisés par un vent inférieur à 5 m/s, les hauteurs de conduit estimées se rapprochent sensiblement des valeurs déduites des données de propagation mesurées.

Appliquée aux données de la campagne de TOULON 90, cette nouvelle méthode n'apporte aucun changement d'ensemble significatif. Il est vrai que pour cette campagne, la présence de fortes inhomogénéités horizontales rend toute interprétation assez délicate.

**IV-3 Perspectives - Discussion**

De nombreuses publications ([10], [11] par exemple) indiquent clairement que le coefficient de traînée $C_D$ ne dépend pas seulement de la vitesse du vent et de la stabilité atmosphérique, mais aussi d'autres paramètres comme "l'âge de la vague" ou le fetch, particulièrement importants dans les régions côtières. Dans ces conditions, le calcul de la rugosité $z_{0u}$ n'est pas immédiat; il s'appuie notamment, dans l'hypothèse restrictive d'une mer levée par le vent, sur la connaissance du spectre hydrodynamique des vagues.

L'hypothèse d'un vent nul à l'interface air-mer, n'est d'autre part pas exacte. Une valeur approchée de $u_0 = u(z = 0)$ pourrait être $u_*$. Certains modèles tiennent compte également des effets de marée pour calculer $u_0$.

Par ailleurs, la signification physique exacte, et par suite la modélisation, des rugosités $z_{0t}$ et $z_{0q}$ est encore assez discutée. Or ces deux paramètres ont une influence sensible sur la détermination des profils verticaux et notamment sur la hauteur du conduit d'évaporation ([5]).

Il est donc, à notre avis, prématuré de compliquer le modèle PIRAM, notamment en augmentant le nombre de paramètres d'entrée. Si les études expérimentales et théoriques récentes constituent des avancées significatives vers une meilleure compréhension des interactions entre l'atmosphère et la mer, il reste encore bien des hypothèses à vérifier et beaucoup de questions sans réponses.

## V. CALCUL DU PROFIL D'INDICE DANS LE DOMAINE OPTIQUE

Dans le domaine des longueurs d'onde optiques, du visible à l'infrarouge, le coindice de réfraction N dépend, comme aux radiofréquences, des grandeurs météorologiques p (en HPa), T (en K), e (en Hpa), mais aussi de la longueur

d'onde $\lambda$ (en $\mu$m). HILL et al. ([12]) ont proposé l'expression suivante :

$$N = 0{,}284 N_0 \frac{p}{T} - 12{,}79 \frac{e}{T} \text{ , avec :}$$
$$N_0 = 64{,}328 + \frac{29498{,}1}{146 - \lambda^{-2}} + \frac{255{,}4}{41 - \lambda^{-2}} \qquad (16)$$

Contrairement au cas des radiofréquences, on constate que la dépendance de N vis à vis de l'humidité est très faible. N est également faiblement dépendant de la longueur d'onde, et même quasiment indépendant dans l'infrarouge[2].

Le modèle PIRAM se basant sur la modélisation des profils météorologiques verticaux (Cf. II), l'obtention du profil vertical d'indice par l'application de (16) est immédiate.

D'autre part, en dérivant (16) on peut obtenir une expression du gradient vertical d'indice similaire à (6). On montre alors que pour une atmosphère instable, il ne saurait exister de conduit de guidage des ondes; au contraire il peut même y avoir infraréfraction. L'existence d'un conduit, qu'il serait alors impropre d'appeler conduit d'évaporation, n'est possible que pour une atmosphère stable. La hauteur de ce conduit est une fonction croissante de l'écart de température entre l'air et l'eau et dépasse rarement 5 m. Le guidage des ondes, si guidage il y a, s'effectue donc au ras de la surface de la mer. Dans ces conditions il serait important de savoir prendre en compte l'état de surface de la mer car les vagues constituent un obstacle pour la propagation.

Plus généralement, des efforts doivent être entrepris pour déterminer quelle est l'altitude zéro des profils modélisés :

- sommet de la vague ?
- creux de la vague ?
- hauteur moyenne des vagues ?
- faut-il moyenner la partie basse des profils sur une vague complète ?

Les données de la campagne MAPTIP 93 qui s'est déroulée aux Pays-Bas devraient nous apporter des éléments de réponse, et, plus globalement, permettre de valider le modèle PIRAM dans le domaine optique.

## VI. MODELISATION DU PARAMETRE $C_n^2$

L'ensemble des profils verticaux est nécessaire aux calculs des pertes de propagation moyennes, c'est à dire sur des durées de l'ordre de la dizaine de minutes, sur une liaison donnée. Les amplitudes des signaux se propageant dans la CLSO présentent également des fluctuations rapides ( plusieurs dB sur quelques secondes dans la domaine millimétrique) qui ont essentiellement deux origines :

- l'agitation de la mer (non traitée ici),
- la turbulence atmosphérique.

Du point de vue de la propagation, la turbulence atmosphérique peut être caractérisée par le paramètre de structure de l'indice de réfraction, $C_n^2$. La détermination du profil vertical de $C_n^2$, à partir des seuls paramètres bulk, constitue donc une première étape vers une modélisation plus complète des fluctuations rapides de signal.

Soit une grandeur X (température, humidité, indice de réfraction), X(d) et X(d+z) ses valeurs aux altitudes d et d+z; en supposant l'atmosphère horizontalement homogène et isotrope, on définit le paramètre de structure de la variable X, noté $C_X^2$, par :

$$\left\langle [X(d) - X(d+z)]^2 \right\rangle_{moy} = \left\langle \Delta X^2 \right\rangle_{moy} = C_X^2 . z^{2/3} \qquad (17)$$

Compte tenu des expressions (1) et (16) reliant le coindice de réfraction aux paramètres météorologiques, on peut obtenir pour $C_n^2$ une expression de la forme :

$$C_n^2 = \alpha_1 . \left( \alpha_2 C_T^2 + \alpha_3 C_{TQ} + \alpha_4 C_Q^2 \right) \qquad (18)$$

avec :

Q humidité absolue (Q = 1,3.q),

$C_{TQ} = \langle 2 \Delta T \Delta Q \rangle_{moy}$,

$\alpha_i$ fonctions des paramètres météorologiques et de la longueur d'onde dans le domaine optique.

Dans la CLSO les paramètres de structure $C_T^2$, $C_Q^2$ et $C_{TQ}$ suivent la paramétrisation de Monin-Obukhov. On a :

$$C_T^2 = T_*^2 . z^{-2/3} . f_1(\frac{z}{L}) \qquad (18\text{-a})$$

$$C_Q^2 = Q_*^2 . z^{-2/3} . f_2(\frac{z}{L}) \qquad (18\text{-b})$$

$$C_{TQ} = r_{TQ} . T_* . Q_* . z^{-2/3} . f_3(\frac{z}{L}) \qquad (18\text{-c})$$

avec :

$T_*$ et $Q_*$, échelles de température et d'humidité que l'on peut exprimer simplement à partir de $\theta_*$ et $q_*$ et donc calculer par une méthode de type bulk,

$f_i$, fonctions à déterminer expérimentalement,

$r_{TQ}$, coefficient de corrélation température-humidité qui est positif (resp. négatif) si l'atmosphère est instable (resp. stable). On admet généralement que la valeur absolue de ce paramètre est comprise entre 0,6 et 1. Pour notre part nous l'avons fixée à 0,8 en remarquant que la valeur exacte a peu d'influence sur le résultat.

Dans le domaine optique, $C_n^2$ dépend presque exclusivement de $C_T^2$. Comme les effets de la turbulence sont très sensibles aux fréquences optiques, la détermination de la fonction $f_1$ a fait l'objet de soins particuliers. Plusieurs groupes d'expressions ont été proposées, notamment par EDSON et al. ([6]) qui apportent une correction aux relations de WYNGAARD et al. ([13]), ou par des chercheurs du F.F.O.[3] (voir [14]).

[2] En réalité, l'indice de réfraction complexe de l'air, dans l'infrarouge, dépend de la longueur d'onde. L'expression (16) correspond à la partie réelle de cet indice et, de ce fait, n'est utilisable que dans les fenêtres de transmission.

[3] Forschunginstitut Für Optik (Allemagne).

cas stables :

$$f_1(\frac{z}{L}) = 5{,}8.\left[1+2{,}4(\frac{z}{L})^{2/3}\right] \text{ (EDSON)} \qquad (19\text{-a})$$

$$f_1(\frac{z}{L}) = 6{,}3.\left[1+7(\frac{z}{L})+20(\frac{z}{L})^{2}\right]^{1/3} \text{ (F.F.O.)} \quad (19\text{-b})$$

cas instables :

$$f_1(\frac{z}{L}) = 5{,}8.\left[1-7(\frac{z}{L})\right]^{-2/3} \text{ (EDSON)} \qquad (20\text{-a})$$

$$f_1(\frac{z}{L}) = 6{,}3.\left[1-7(\frac{z}{L})+75(\frac{z}{L})^{2}\right]^{-1/3} \text{ (F.F.O.)} \quad (20\text{-b})$$

La fonction $f_2$ étant très difficile à déterminer, une hypothèse souvent rencontrée est la relation de proportionnalité :

$$\frac{C_Q{}^2}{C_T{}^2} = a.\frac{Q_*{}^2}{T_*{}^2} \qquad (21)$$

où le paramètre a peut varier de 1 jusqu'à $10^4$ dans le cas de fortes fluctuations d'humidité ([15]). Nous lui avons, pour l'instant, attribué la valeur 1, mais comme son influence sur l'ordre de grandeur du $C_n{}^2$ est importante, des mesures seront nécessaires pour trouver une valeur sans doute plus réaliste.

La fonction $f_3$, quant à elle, a été supposée identique à $f_1$.

La figure n°1, à titre d'illustration, montre les variations de $C_n{}^2$ aux radiofréquences (calculé avec les formules du F.F.O. pour $f_1$) en fonction de la différence de température entre l'air et l'eau (ASTD), pour un vent de 5m/s, et pour des valeurs d'humidité relative allant de 50 à 100%.

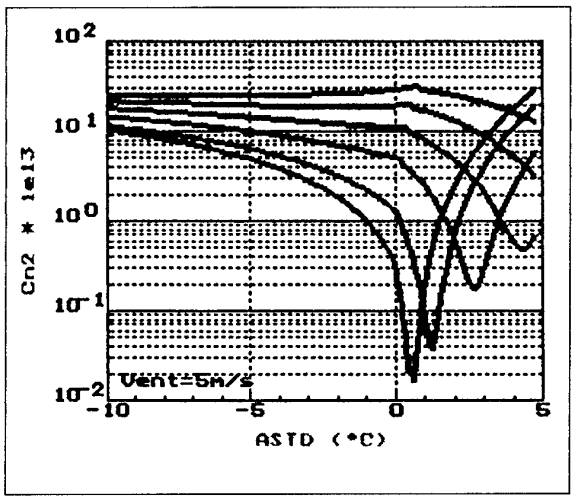


***Figure n° 1***
*Variations de $C_n{}^2$ aux radiofréquences en fonction de la différence de température entre l'air et l'eau (ASTD), pour un vent de 5m/s, et pour une humidité relative variant de 50 à 100%.*

On peut constater sur cette figue que la gamme de valeurs possibles pour $C_n{}^2$ augmente avec l'humidité et qu'un minimum est observé pour des situations neutres ou modérément stables.

Dans le domaine optique, l'influence de l'humidité, comme nous l'avons déjà dit, est négligeable. De plus, un minimum très prononcé dans la valeur de $C_n{}^2$ apparaît toujours au voisinage de la neutralité. L'existence d'un tel minimum peut surprendre, mais est à rapprocher des observations expérimentales de BATAILLE ([14]) qui a enregistré des minima similaires au moment des transitions jour-nuit.

En ce qui concerne les profils verticaux de $C_n{}^2$, excepté au voisinage immédiat de l'interface air-mer, on trouve des valeurs de $C_n{}^2$ quasiment indépendantes de l'altitude. Par ailleurs les deux groupes d'expression mentionnés plus haut pour la fonction $f_1$ conduisent à des profils très voisins.

Une autre approche concernant le calcul de $C_n{}^2$, basée sur les travaux de GOSSARD ([16]), a été étudiée. Elle ne s'applique que dans les cas stables et peut conduire à des valeurs faibles, voire nulles, lorsqu'existent dans le domaine radio, des situations de proche infraréfraction.

Quant à la méthode retenue et décrite plus haut, nous espérons pouvoir la valider prochainement par des mesures directes, mais aussi en terme de calcul des propriétés statistiques des fluctuations de courte durée des signaux se propageant dans la CLSO.

## VII. INFLUENCE DE LA PROXIMITE CÔTIERE SUR LA MODELISATION DU CANAL DE PROPAGATION

Le calcul des pertes de propagation sur une distance donnée nécessite la connaissance des profils d'indice de réfraction sur l'ensemble du trajet. A partir de mesures ponctuelles effectuées à l'aide de bouées, de stations météorologiques ou de radiosondages, le maillage bidimentionnel de l'indice de réfraction est généré, moyennant:

- des approximations, pour le calcul des profils verticaux
- des hypothèses d'homogénéité, pour réaliser l'extension horizontale.

La proximité des côtes rend l'ensemble de cette modélisation plus délicate.

### VII-1 Modélisation verticale dans la CLSO

Les modélisations proposées dans les parties précédentes permettent d'évaluer, sur le lieu de mesure des paramètres météorologiques, les variations verticales de l'indice de réfraction. Indépendamment de la validité des modèles semi-empiriques utilisés, cette évaluation est bien sûr sujette à des incertitudes liées :

- à la précision des mesures météorologiques,
- à la stabilité de la CLSO,

- à l'existence ou non de structures atmosphériques supérieures (inversions de température, conduits de surface)
- à l'agitation de la mer, dans sa partie la plus basse.

L'influence de la précision des mesures sera traitée dans le paragraphe concernant la stabilité.

Stabilité de la CLSO

Le profil d'indice de réfraction dépend fortement, dans les cas stables, de la différence de température entre l'air et l'eau (ASTD). Ainsi, la hauteur du conduit calculée par PIRAM varie t'elle de 10 m pour une variation d'ASTD de +2 °C, soit une pente de 5 m /°C, ceci pour $T_0$ = 15 °C, $H_1$ = 70%, $v_1$ = 5 m/s. De faibles variations locales sur la température ou des incertitudes liées à la mesure peuvent donc entraîner des biais sur l'estimation de la hauteur du conduit.

L'occurrence des cas stables à proximité des côtes est fortement dépendant des zones climatiques et des saisons. Le tableau n° 1 fournit, à titre d'exemple, les pourcentage de temps pendant lesquels des cas stables (nombre de Richardson positif) ont été relevés durant 4 campagnes de mesures.

| Campagne de mesures | Saison | Nbre de jours de mesures | Pourcentage de cas stables (RiB>0) |
|---|---|---|---|
| **LORIENT 89 (Bretagne)** | Automne | 52 | 63 |
| **TOULON 90 (Côte d'Azur)** | Eté | 89 | 24 |
| **LORIENT 93** | Automne | 19 | 8 |
| **MAPTIP 93 (Hollande)** | Automne | 13 | 0 |

***Tableau n° 1***
*occurrence des cas stables pour différentes campagnes de mesures.*

Par ailleurs, une très forte stabilité (associée à une humidité supérieure à 95 %) conduit à des situations de proche infraréfraction. L'analyse des résultats de la campagne de LORIENT 89 montre que la modélisation globale rend compte de ce phénomène sans toutefois reproduire de façon fidèle les pertes de propagation mesurées ([1]). Les écarts obtenus peuvent être dus à plusieurs causes telles que :

- la mesure imprécise de l'humidité
- la forte sensibilité du modèle de CLSO
- la présence éventuelle d'inhomogénéités horizontales

Raccordement avec les structures supérieures

Le profil d'indice de réfraction issu de la modélisation PIRAM tend aux altitudes supérieures vers celui correspondant à l'atmosphère standard. Or, les radiosondages effectués lors de la campagne de LORIENT 93 montre que cette hypothèse n'est pas toujours vérifiée ([17]) :

- inversion de température dès les plus basses couches de la CLSO ( ex: le 28/09 vers 12 h)
- gradient d'indice de réfraction fortement positif (ex : le 24/09, G = 260 M/km sur les 40 premiers mètres)

Agitation de la mer

La modélisation globale des profils de température, d'humidité et des aérosols au-dessus et au niveau des vagues est actuellement en cours d'établissement à l'Ecole Centre de Nantes. Elle s'appuie sur les lois régissant la mécanique des fluides et devrait déboucher dans les prochaines années sur une représentation globale des différents phénomènes impliqués.

L'influence de l'agitation de la mer se manifeste principalement dans les bandes millimétrique et optique.

**VII-2 Inhomogénéités horizontales**

L'évaluation des pertes de propagation sur des distances de plusieurs dizaines de kilomètres à proximité des côtes suppose une hypothèse d'homogénéité si l'on ne dispose que de mesures ponctuelles. Or, cette hypothèse se heurte fréquemment à la réalité des divers phénomènes physiques intervenants. On peut citer :

- les variations locales de température de l'eau

La température de la mer présente, dans certaines mers du monde, de fortes variations spatiales. Ainsi, en Méditerranée ([18]), il n'est pas rare de rencontrer de fronts thermiques de 1 à 2 °C sur 5 km à proximité des côtes, mais aussi en pleine mer (ex: Sud-Est de la Sicile). Ces fronts peuvent atteindre 4 °C sur 5 km dans certaines zones, avec des occurrences de 30 % certains mois de l'année. De même, en Atlantique, lors de la campagne de LORIENT 89, des variations de 4 °C sur 30 km ont été observées en Décembre.

- les variations locales des paramètres aérologiques

Du fait de la différence de constantes thermiques entre la terre et la mer, des homogénéités de température de l'air sont fréquemment relevées, particulièrement, par temps calme, lors de belles journées ensoleillées. Ainsi, des écarts de température d'environ 10 °C ont-ils été relevés de part et d'autre de la liaison de 23 km lors de la campagne TOULON 90. De même, des variations de 5°C/5km ont été notées lors de la campagne de LORIENT 93.

Ces variations conjuguées avec celles du vent et de l'humidité rendent difficile l'évaluation de la hauteur de conduit sur l'ensemble du trajet. Durant ces périodes, on observe en mer une variation constante du conduit, qui marque l'aspect non-stationnaire du canal de propagation.

La complexité de la modélisation est accrue quand la liaison se place à proximité de zones montagneuses comme cela était le cas pour l'expérimentation de TOULON 90. Il peut alors se produire des inversions de température dans les basse couches, engendrant des conduits de surface ou des conditions d'infraréfraction.

- les mouvements d'advection

L'arrivée de fronts thermiques sur la liaison entraîne de fortes variations de l'ensemble des paramètres météorologiques et donc de la structure du conduit. La durée de passage du front peut-être réduite à quelques heures. Ainsi, à Lorient, le passage d'un front chaud et humide venant de l'océan a modifié la température de l'air de 7°C en 3 heures et a doublé l'humidité absolue ([19], p. 121].

- la dépendance de l'agitation de la mer avec le fetch

En bandes millimétrique ou optique, la connaissance de la rugosité de la mer est nécessaire. Cette rugosité n'est pas homogène sur la liaison si le vent souffle de la côte . En effet, la distance sur laquelle la mer se forme (fetch) est alors limitée.

La non-stationnarité du canal de propagation se traduit :

- en visibilité directe, par une déformation des figures d'interférence. Il vient s'ajouter au déphasage nominal entre signal direct et signal réfléchi, un déphasage supplémentaire du à l'effet de réfraction atmosphérique. A titre d'illustration, la figure n° 2 montre à 36 GHz, les fortes fluctuations de signal consécutives au changement progressif de la hauteur du conduit d'évaporation entre 10 h et 14 h.
- en liaison transhorizon, par une variation temporelle des pertes moyennes de propagation d'autant plus grande que la fréquence est basse.

## CONCLUSION

Le modèle PIRAM décrit dans cet article permet la détermination des profils verticaux de température, d'humidité, d'indice de réfraction et de $C_n^2$ dans la Couche Limite de Surface Océanique. Pour les études de propagation, il s'applique aussi bien dans le domaine des fréquences radioélectriques que dans celui des fréquences optiques. PIRAM ne requiert qu'un nombre limité de paramètres d'entrée correspondant à des mesures météorologiques courantes. Aux longueurs d'onde centimétriques et millimétriques, ce modèle a permis une interprétation satisfaisante , au plan statistique notamment, des données enregistrées lors des campagnes de mesure de LORIENT 89 et TOULON 90.

Une validation plus complète du modèle reste cependant à effectuer. Les points suivants mériteraient notamment d'être étudiés :

- l'influence du champ de vagues sur la partie basse des profils verticaux,
- l'estimation, à partir de données expérimentales, d'un certain nombre de paramètres mal connus et nécessaires au calcul de $C_n^2$,
- l'apport éventuel d'une modélisation plus complexe des longueurs de rugosité, ce qui nécessiterait d'augmenter le nombre de paramètres d'entrée, sans pour autant lever toutes les ambiguïtés.
- la recherche de lois empiriques concernant les gradients horizontaux dont l'influence est non négligeable à proximité des côtes.

Néanmoins, quels que soient les progrès envisageables dans les modélisations, seules des mesures bidimentionnelles du milieu de propagation, utilisant notamment des moyens de télédétection, permettraient une prédiction en temps réel fiable des performances des systèmes évoluant dans la CLSO.

## REMERCIEMENTS

Les auteurs remercient chaleureusement le Dr P.G. MESTAYER de l'Ecole Centrale de Nantes pour ses avis et conseils précieux concernant les fonctions de stabilité et le calcul des rugosités.

## REFERENCES

[1] **CLAVERIE (J.), HURTAUD (Y.)**. Propagation transhorizon en atmosphère marine. Modélisation et nouveaux résultats expérimentaux, 49th AGARD-EPP Symposium, Izmir, Octobre 1991, pp 4-1, 4-14.

[2] **CLAVERIE (J.), HURTAUD (Y.)**. Validation de modèles de propagation des ondes centimétriques et millimétriques au-dessus de la mer, L'Onde Electrique, Vol 72, n°3, Mai-Juin 1992, pp 42-46.

[3] **HURTAUD (Y.), CLAVERIE (J.), LELIEVRE (S.)**. Statistical analysis of two over-the-horizon centimetre and millimetre propagation campaigns in the marine boundary layer, NATO/AC243/PANEL03/RS-G8 Workshop, Toulouse, Mai 1992, 19p.

[4] **LEVY (M.).** Propagation troposphérique en air clair, Journées d'etudes SEE "Propagation électromagnétique du décamétrique à l'angström", Rennes (France) 9-10 Oct. 1991.

[5] **CLAVERIE (J.)**. Détermination des profils météorologiques dans le conduit d'évaporation, Note Technique du Centre d'Electronique de l'Armement n° ASRE/180/ASRE/16437, Octobre 1990.

[6] **EDSON (J.B.), FAIRALL (C.W.), MESTAYER (P.G.), LARSEN (S.E.).** A study of the inertial-dissipation method for computing air-sea fluxes, J. of Geoph. Res., Vol 96, N° C6, Juin 1991, pp 10.689-10.711.

[7] **DYER (A.J.), HICKS (B.B.).** Flux-gradient relationships in the constant flux layer, Quart. J. Roy. Meteorol. Soc., 96, 1970, pp 715-721.

[8] **KONDO (J.),** Air-sea bulk transfert coefficients in diabatic conditions, Bound. Layer Meteo., 9, 1975, pp 91-112.

[9] **BLANC (T.V.),** An error analysis of profile flux, stability and roughness length measurements made in the atmospheric surface layer, Bound. Layer Meteo., 26, 1983, pp 243-267.

[10] **GEERNAERT (G.L.), KATSAROS (K.B.), RICHTER (K.),** Variation of the drag coefficient and its dependance on sea state, J. of Geoph. Res., Vol 91, N° C6, Juin 1986, pp 7667-7679.

[11] **NORDENG (T.E.),** On the wave age dependant drag coefficient and roughness length at sea, J. of Geoph. Res., Vol 96, N° C4, Avril 1991, pp 7167-7174.

[12] **HILL (R.J.) et al.,** Refractive index and absorption fluctuations in the infra-red caused by temperature, humidity and pressure fluctuations, J. Opt. Soc. Am., Vol 70, N°10, Oct. 1980, pp 1192-1205.

[13] **WYNGAARD (J.C.), IZUMI (Y.), COLLINS (S.A.),** Behavior of the refractive index structure parameter near the ground, J. Opt. Soc. Am., Vol 61, N°12, Déc. 1971, pp 1646-1650.

[14] **BATAILLE (P.),** Analyse du comportement d'un système de télécommunication optique fonctionnant à 0,83 µm dans la basse troposphère, Thèse de Doctorat de l'Université de Rennes 1, Nov. 1992.

[15] **McMILLAN (R.W.)** et al., Millimeter wave atmospheric turbulence measurements : preliminary results, SPIE, Vol 337 Millimeter Wave Technology, 1982, pp 88-95.

[16] **GOSSARD (E.E.),** Clear weather meteorological effects on propagation at frequencies above 1 GHz, Radio Science, Vol 16, N° 5, Sept-Oct 1981, pp 589-608.

[17] **DION (D),** communication privée

[18] **LE VOURCH (J.) et al**., Atlas of thermal fronts of the Mediterranean Sea derived from satellite imagery", Mémoires de l'Institut océanographique de Monaco, n°16, VI, 1992, 152 p., 184 fig., ISSN 0304-5714.

[19] **SNIEDER (J.),** Millimetre Wave propagation joint data analysis of the measurement campaigns", Document Technique OTAN n° AC/243 (Panel 3) TR/4, Mars 1991, 216 p.

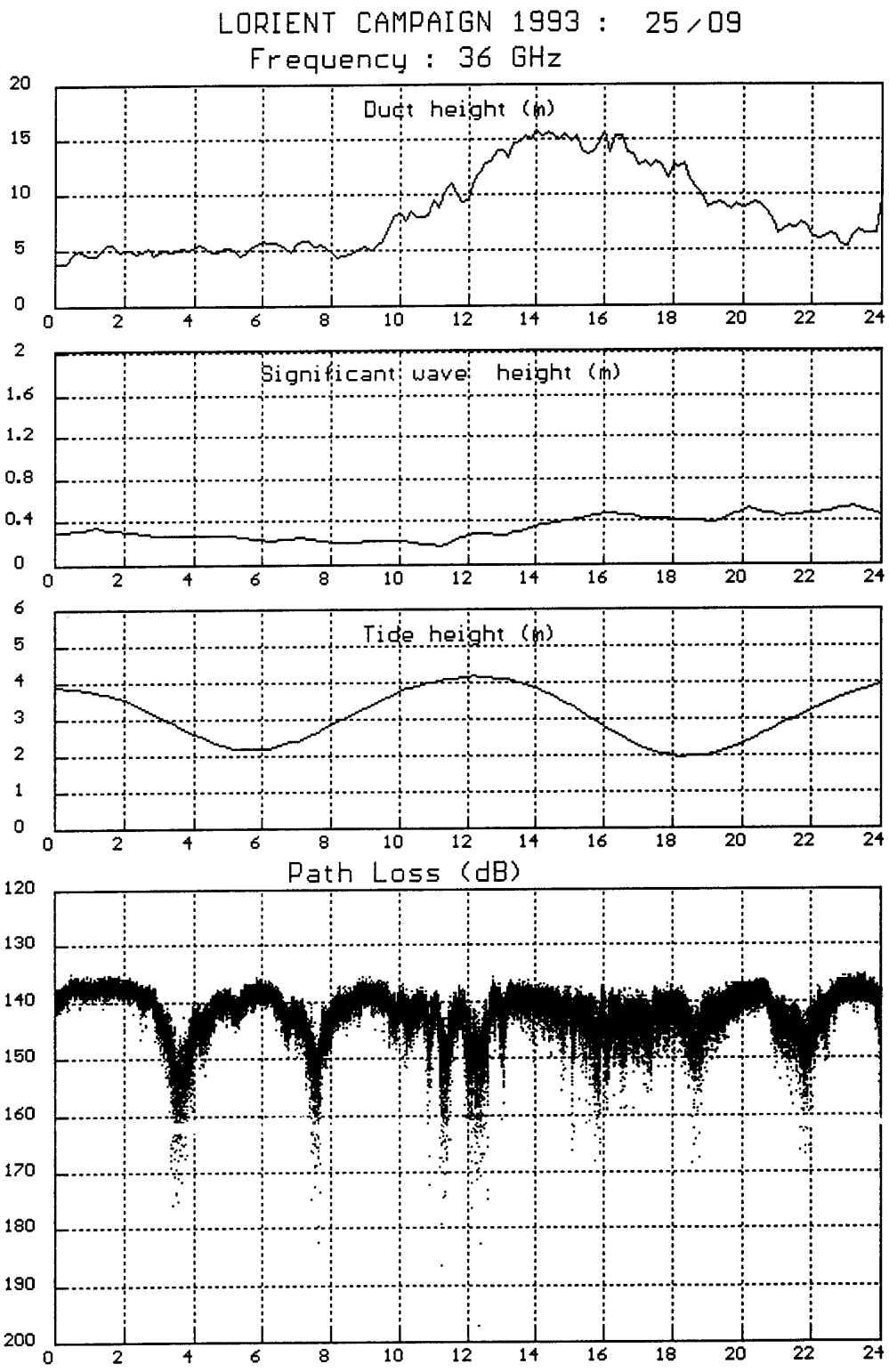


***Figure n° 2***

*Effet de la non-stationnarité du canal de propagation sur le signal reçu.*

*(Campagne de LORIENT 93 , fréquence : 36 Ghz, altitude emetteur : 15,4 m, altitude récepteur : 8,05 m, longueur de la liaison : 9,7 km)*

## DISCUSSION

**K. DAVIDSON**
Will the use of exchange coefficients from coastal campaigns, e.g. HEXMAX, change the results from the models?

**AUTHOR'S REPLY**
There are actually many exchange coefficient formulations for calculating different roughness lengths ($Z_0$, $Z_{0T}$, $Z_{0q}$). The use of the equation published by KONDO has lead to a profile model enabling a globally very satisfactory explanation of the observations during the LORIENT 89 and TOULON 90 campaigns which took place in a coastal environment.

We also simulated the influence of roughness on evaporation duct height as estimated by the model. This influence is particularly sensitive in the stable cases and to the roughness $Z_{0T}$ and $Z_{0q}$.

Unfortunately those two last roughnesses are the less well known and even their definition is not clear. Therefore, the discussion is not closed.

# An Overview of an Intensive Observation Period on Variability of Coastal Atmospheric Refractivity

**Richard A. Paulus**
Ocean and Atmospheric Sciences Division
NCCOSC RDTE DIV 543
53170 WOODWARD ROAD
SAN DIEGO CA 92152-7385
USA

## SUMMARY

This paper is an overview of an experiment called Variability of Coastal Atmospheric Refractivity (VOCAR). VOCAR was designed to be conducted under a larger program called Coastal Variability Analysis, Measurements, and Prediction and is a multi-year experimental effort to investigate the variability of atmospheric refractivity with emphasis on the coastal zone. The experiment is being conducted jointly with the Naval Air Warfare Center Weapons Division, Point Mugu, CA, the Naval Research Laboratory, and the Naval Postgraduate School. In addition, the National Oceanic and Atmospheric Administration Environmental Technology Laboratory and Penn State University/Applied Research Laboratory are participating in the measurement phase of VOCAR.

The propagation measurements being made during VOCAR consist of monitoring signal strength variations of VHF/UHF transmitters in the southern California coastal region. Corresponding meteorological measurements are made during routine, special, and intensive observation periods. During an intensive measurement period from 23 August to 3 September 1993, radio data were collected at two receiver sites and meteorological data were collected from three profiler sites, eight radiosonde sites, three aircraft, and numerous surface weather sites. Samples of the data will be shown.

## 1. INTRODUCTION

In 1944, the U.S. Navy Radio and Sound Laboratory began a radio-meteorological experiment along the coast of southern California [1-2]. Transmitter and receiver terminals were located on the coast at San Pedro (south of Los Angeles) and San Diego at altitudes of 30 m above mean sea level. The propagation path between the terminals was entirely over water, a distance of 148 km, and transmission frequencies of 52, 100, and 547 MHz were used. Signal levels were recorded for extended periods between June 1944 and July 1945. Plots of the data revealed a striking negative correlation between the height of the base of the temperature inversion and radio signal levels. A statistical analysis of sixty concurrent observations of signal strength and inversion base height made in the period July 15 to September 14, 1945 yielded a correlation coefficient of -0.68 [3]. However, the height of the base of the temperature inversion alone was found to be inadequate for predicting the peak values of maximum signal levels. It is noted that refractivity is also a function of moisture and variations in the vertical gradients of temperature and moisture result in vertical variations of the gradient of refractivity. If the gradients are strong enough, superrefraction or trapping occurs. Although the existence of a temperature inversion is neither a necessary nor sufficient condition for the existence of a trapping layer, temperature inversions are generally associated with a decrease in moisture and the result is often a trapping layer, particularly over the ocean in the southern California area.

Utilizing a recently developed hybrid propagation model called the Radio Physical Optics (RPO) model and taking advantage of the observed correlation, Hitney [4] demonstrated a capability to assess the height of the base of the trapping layer from observations of the radio signal strength. His method involved using median values of the modified refractivity difference across and thickness of the inversion along with refractivity gradients below and above the inversion. These statistics were derived from a set of radiosonde soundings taken in the years from 1969 to 1976 from Point Loma in San Diego, CA. The comparison between predictions of trapping layer height, determined from the 1944 radio signals, and observed base of the temperature inversion was quite good. A proposal was made to pursue this technique further, resulting in the establishment of an experimental program designated VOCAR.

## 2. EXPERIMENTAL APPROACH

The objectives of VOCAR are to provide an assessment capability for horizontally varying refractivity conditions in a coastal environment and develop a radio remote sensing capability. Hitney's technique provided the foundation for possible radio remote sensing of refractive structure. Since there are numerous radio sources in coastal areas worldwide, radio remote sensing is potentially a very powerful tool. Among the

*Paper presented at the Sensor and Propagation Panel Symposium on "Propagation Assessment in Coastal Environments" held in Bremerhaven, Germany 19-22 September 1994.*

disadvantages of this technique is that the inferred refractive structure pertains only to the given path and no data exist to indicate how representative this structure would be for different paths. Methods to characterize the horizontal variability of the refractive structure include satellite remote sensing, numerical weather models, and meteorological data assimilation systems. To attack this problem, the Naval Command, Control and Ocean Surveillance Center RDT&E Division (NRaD) conducted an experiment jointly with the Naval Air Warfare Center Weapons Division, Point Mugu, CA (NAWCWPNS), the Naval Research Laboratory (NRL), and the Naval Postgraduate School (NPS). The National Oceanic and Atmospheric Administration Environmental Technology Laboratory (ETL) and Penn State University Applied Research Laboratory (PSU/ARL) made supporting measurements.

The experiment was planned for the southern California bight [5]. Ducting is present in this area more than 70% of the time on an annual basis, the coastline geometry is well suited for overwater propagation paths, and there are numerous transmitters already operating along the coast. In particular, the Automatic Terminal Information Service (ATIS) transmitters, located at many airports, provide convenient signals in the VHF/UHF band. Figure 1 shows a number of these transmitters and their transmission frequency in MHz. However, all of these transmitters have partial overland paths to one or both of the receiver sites: Point Loma in San Diego and Point Mugu near Oxnard. To ensure a clear overwater path to both receivers, additional transmitters were installed on San Clemente Island. These paths are very nearly equal in length (127 km to Point Loma and 132 km to Point Mugu) and are of primary interest in the experiment. Differences in signals over these two paths, separated by approximately 120 degrees in azimuth, provide data on the inhomogeneity of the refractive structure. Secondarily, paths to ATIS transmitters along the southern California coast provide information on signal propagation intersecting a coastline. Radio-meteorological data were planned in three categories: routine, special, and intensive observation periods. A routine observation period (ROP) consists of the radio measurements at two receiver sites and the meteorological data that is routinely available from the existing observing network. A special observation period (SOP) is a period of a few days time for which propagation conditions are particularly interesting and a few additional meteorological observations are taken to supplement the routine data. An intensive observation period (IOP) is an interval during which the VOCAR participants take meteorological observations at a number of sites with a number of sensors in order to characterize the refractive conditions and related atmospheric properties in as much detail as feasible. The Johns

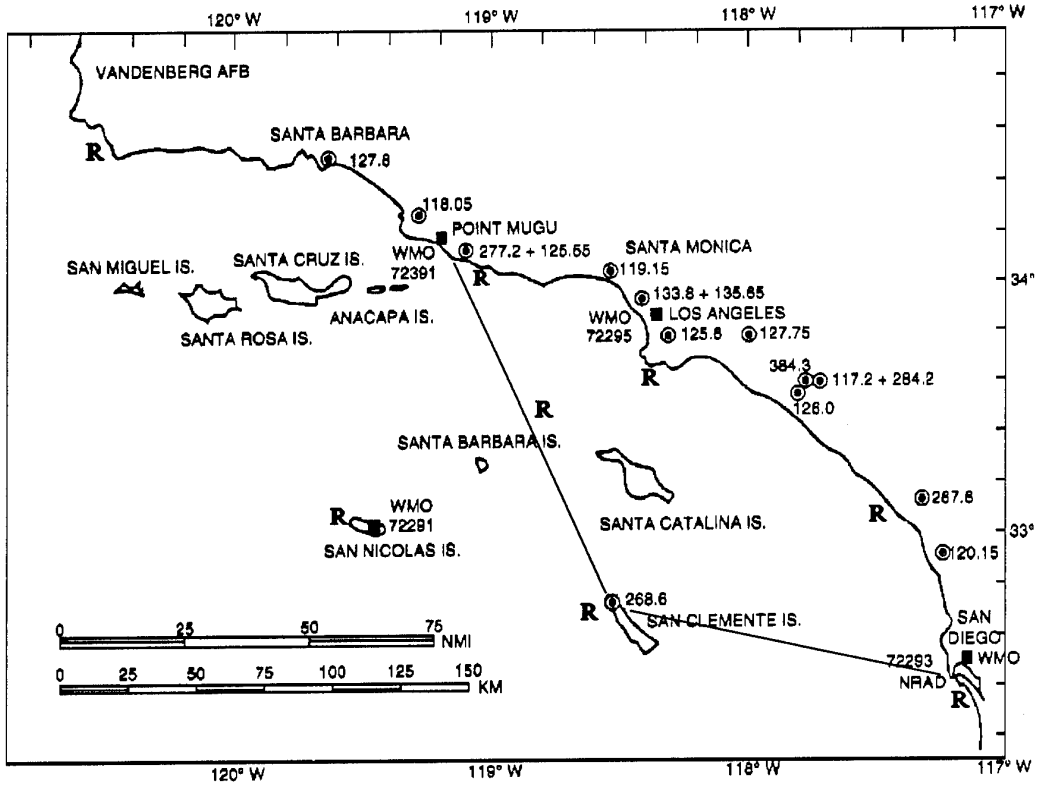


**Figure 1.** Selected ATIS transmitters (circled dots) and primary propagation paths for the VOCAR experiment. Numbers by transmitter sites are frequencies in MHz. "R" indicates radiosonde launch site.

Hopkins University Applied Physics Laboratory and San Diego State University made collaborative measurements during the IOP.

## 3. INTENSIVE OBSERVATION PERIOD

One such intensive observation period was conducted 24 August to 3 September 1993 during which meteorological data were collected by three boundary layer profiler sites, three aircraft, eight radiosonde sites, and numerous surface weather stations. Radio data were measured at Point Mugu and Point Loma with nearly identical receiver systems in 15 minute cycles [6]. With this data set, propagation predictions using RPO and observed or forecast refractive structure can be compared to observed signals to provide insight to a number of questions, such as the temporal and spatial resolution of meteorological data required to characterize the propagation conditions and the capabilities of different types of sensors to provide such resolution.

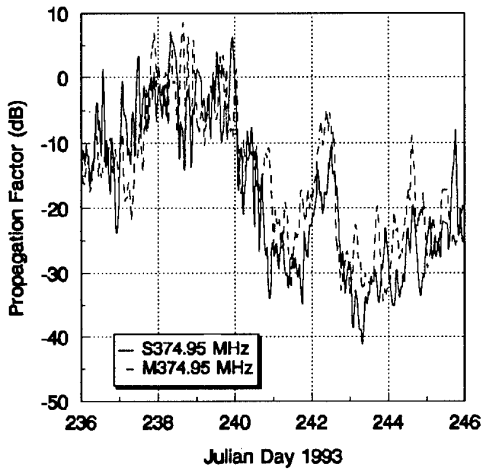


**Figure 2.** Weighted average propagation factor for 374.95 MHz links measured at Point Loma (solid line) and Point Mugu (dashed line) from 24 August to 03 September. Troposcatter level is approximately -49 dB.

### 3.1 Radio Data

Figure 2 is a sample of the radio data for the IOP. These data have been smoothed with a 2-hour wide triangular window which has removed 5 to 10 dB fluctuations that are common on time scales of an hour or two. Over the 10 day period, the smoothed signals on the two links varied by approximately 45 dB and tend to follow each other; however, neither signal consistently exceeded the other. Signal levels early in the period are associated with low-elevated and surface-based ducts. This situation changed abruptly on day 240 when received signals fell to levels consistent with elevated ducts; however, signals never did fall to the troposcatter levels expected with standard atmosphere propagation conditions (approximately -49 dB). On shorter time periods, the signals fluctuate 15 to 25 dB over periods of a few hours to a day. Figure 3 shows the cumulative frequency distribution for the data shown in figure 2; the medians of the observed signals are almost 35 dB above the level expected for standard atmosphere propagation.

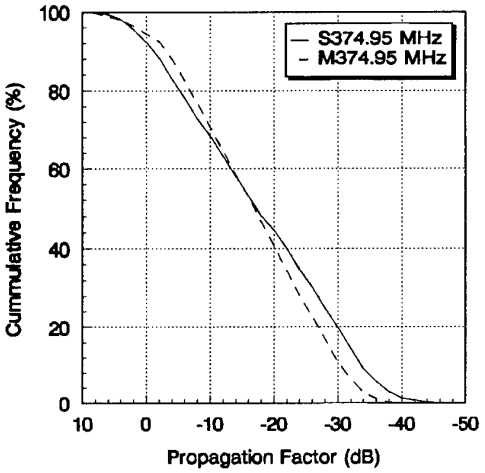


**Figure 3.** Cumulative frequency distribution of the data in Figure 2.

Figure 4 is a scatter diagram of propagation factors measured at the two receiver sites. In contrast to the data used to plot Figure 2, the data in Figure 4 have not been smoothed. The correlation coefficient is .71; the correlation coefficient for the smoothed data is .79 [6]. The measured propagation factor on one link is within 10 dB of the propagation factor on the other link 72% of the time.

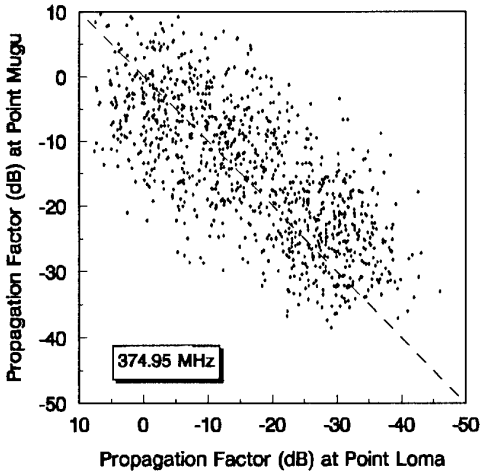


**Figure 4.** 374.95 MHz propagation factor measured at Point Loma versus propagation factor measured at Point Mugu.

Figure 5 is a scatter diagram of the 262.85 MHz propagation factor measured at Point Loma versus the 374.95 propagation factor. The correlation coefficient is

.90 and the propagation factor at 262.85 MHz is within 10 dB of the 374.95 MHz propagation factor 88% of the time. Again, this is unsmoothed data. Another interesting feature in Figure 5 is that the scatter in propagation factor decreases as the propagation factor increases. Longer term data, such as discussed in [4], do not show this feature consistently. One can speculate that this may be due to the meteorological regime creating the ducting conditions. In the southern California offshore area, elevated refractive layers are usually the result of large-scale subsidence in the eastern sectors of subtropical high pressure systems. Additionally, an offshore foehn wind (often referred to as a Santa Ana in southern California) can create similar elevated layers. And these two conditions may exist simultaneously [7]. Since the VOCAR IOP was dominated by large-scale subsidence, Santa Ana conditions may be the factor than increases signal fluctuations at higher signal levels. That is, subsidence induced surface-based ducts may tend to be homogeneous in range while Santa Ana induced ducts may tend to be inhomogeneous in range.

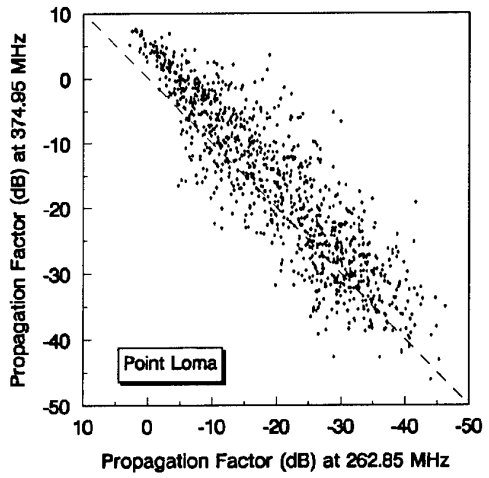


**Figure 5.** 262.85 MHz propagation factor versus 374.95 MHz propagation factor measured at Point Loma.

### 3.2 Meteorological Data

The Environmental Technology Laboratory (ETL, formerly the Wave Propagation Laboratory) of the National Oceanic and Atmospheric Administration established a network 915 MHz wind profilers equipped with Radio Acoustic Sounder Systems at 3 sites in support of VOCAR. These sites, at Point Loma, San Clemente Island, and Point Mugu, operated October 1992 through October 1993 and were in operation during the IOP. This network provided 55 minute averages of wind speed, direction, and reflectivity and 5 minute averages of virtual temperature profiles. Typical heights realized with the profilers were 2 to 3 km with virtual temperature profiles nominally to 1 to 1.5 km. Collocated at each site was a surface meteorological station that provided 1 minute averages of pressure, temperature, relative humidity, wind speed and direction, and solar and net radiation. These data have been compiled, reduced, and delivered by ETL (C. King, C. Russell, L. Lewis, and A. White, "Summary and Data from the NOAA Environmental Technology Laboratory Measurement Program During the 1992/93 VOCAR Study").

For the IOP, the participants established a special radiosonde observation network at 7 coastal/island sites and 1 shipboard site as indicated by an "R" in Figure 1. Soundings, with emphasis on the lowest 3 km, were taken 5 times daily, every 4 hours, with the land sites omitting the 08Z launch. Figure 6 is an overplot of soundings taken on 26 and 27 August (Julian days 238 and 239) at the San Diego site when radio signals (Figure 2) were high and fluctuating. This figure shows the boundary layer variability in San Diego on these two days. Figure 6 also shows atypical moisture (30 to 80% relative humidity) above the boundary layer; relative humidities of less than 30% are the norm.

To augment the radiosondes, two instrumented aircraft from NCCOSC RDT&E Division and NAWCWPNS collected data on the range variation of the inversion throughout the bight. These aircraft flew sawtooth profiles along the primary propagation paths, and on the periphery, varying in altitude from approximately 150 m below the inversion to 300 m above the inversion. A third aircraft with a downward looking lidar was utilized by NRL Washington to map boundary layer height variations over a larger area.

## 5. REMARKS

A concept for passively determining refractive structure by monitoring VHF/UHF signal strength variations was discussed and an overview of a cooperative experiment to test this concept was presented. This experiment, VOCAR, is a multiyear experiment combining the efforts of several research groups and the results of the first investigations are just beginning to be reported, many in these proceedings. An Intensive Observation Period was conducted 23 August to 3 September 1993 and consisted of 15 minute cycles of radio measurements, eight radiosonde sites, three aircraft, three profiler sites, a lidar profiler, satellite data collection, numerical meteorological models, and numerical meteorological data assimilation systems. Additional measurements are being considered as Special Observation Periods, including measurements in conjunction with a project to infer refractive profiles from Global Positioning System signals [8].

## ACKNOWLEDGEMENT

The VOCAR experiment and this paper were supported by the Office of Naval Research, Code 322.

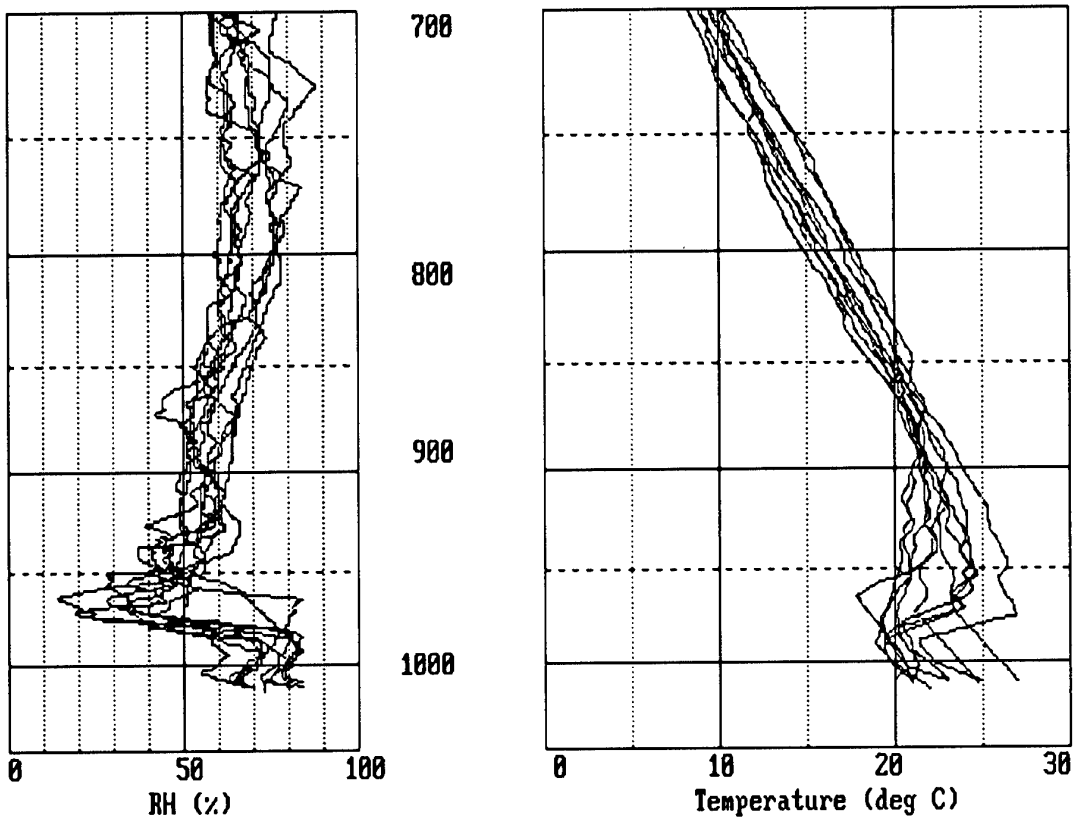


**Figure 6.** Overplot of temperature and relative humidity versus pressure (hPa) for Julian days 238 and 239.

## REFERENCES


1. Anderson, L.J. *et al.*, "Atmospheric Refraction - A Preliminary Quantitative Investigation." NRSL Report No. WP-17, 1944.
2. Kerr, D.E., "Propagation of Short Radio Waves," New York:McGraw-Hill Book Co., Inc., 1951, pp. 328-335.
3. Hoffman, W.C. and E.E.Gossard, "A Guide to Multiple Regression and Covariance Analysis," Special Report, Cooperative Institute for Research in Environmental Sciences, University of Colorado, 1992.
4. Hitney, H.V., "Remote Sensing of Refractivity Structure by Direct Radio Measurements at UHF," in "Remote Sensing of the Propagation Environment," AGARD CP-502 February 1992, Paper 1.
5. Paulus, R.A., "VOCAR: An Experiment in Variability of Coastal Atmospheric Refractivity," in "1994 International Geoscience and Remote Sensing Symposium (IGARSS'94) Digest," pp. 386-388, August 8-12, 1994, Pasadena, CA.
6. Rogers, L.T., "Statistical Assessment of the Variability of Atmospheric Propagation Effects in the Southern California Coastal Area," in "1994 International Geoscience and Remote Sensing Symposium (IGARSS'94) Digest," pp. 389-393, August 8-12, 1994, Pasadena, CA.
7. Gossard, E.E. and Strauch, R.G., "Radar Observation of Clear Air and Clouds," Amsterdam, Elsevier Science Publishers, 1983 (ISBN 0-444-42182-3), pp 33-41.
8. Anderson, K.D.,"Tropospheric Refractivity Profiles Inferred from Low Elevation Angle Measurements of GPS Signals," in "Propagation Assessment in Coastal Environments," AGARD CP-567 1994, Paper 2.

## DISCUSSION

**G.S. BROWN**
Are you planning to look at the propagation path data using transmitters located on the main-land but near the coast, e.g. "transmitters of opportunity?"

**AUTHOR'S REPLY**
Molly Barrios has already utilized some of these data for predicting signal levels as affected by terrain (paper 9); otherwise, we have not yet looked at these data. Our plan is to use the data from the "transmitters of opportunity" in the evaluation of radio remote sensing techniques as proposed by Hitney [4].

# Effects of Spatial and Temporal Variability of Atmospheric Refractivity on the Accuracy of Propagation Assessments

**L. Ted Rogers**
Ocean and Atmospheric Sciences Division
NCCOSC RDTE DIV 543
53170 WOODWARD ROAD
SAN DIEGO CA 92152-7385
USA

## SUMMARY

Meteorological measurements indicating range dependent refractive structures have been documented by several observers (Goldhirsh and Dockery, 1991, Anderson, 1991, Levy and Craig, 1991.) A central concern arising from these observations is the effect the assumption of horizontal homogeneity has on the accuracy of propagation assessments, where accuracy is defined as the difference between estimated and measured propagation loss. Complicating the discussion of variability are conflicting goals for propagation model performance versus propagation assessment system performance. With the former, the goal is to minimize error at the time of environmental observation used for the model inputs. With the latter, the goal is to minimize error over the time of use of propagation estimates, a period of time that is often measured in hours with the current level of environmental sensing technology. With these considerations in mind, the effect of spatial and temporal variability of the atmospheric refractive structure on real-time or nearly real-time radio frequency (RF) propagation assessment system performance is examined.

## 1. INTRODUCTION

The Variability Of Coastal Atmospheric Refractivity (VOCAR) experiment assessed the effects that spatial and temporal variability of the atmospheric refractive structure in the southern California coastal area have on RF propagation. Propagation loss measurements were made for three months on two ~ 130 km over-water, over-the-horizon paths having a common endpoint but on radials separated by 120 degrees. Propagation loss values calculated from endpoint atmospheric soundings which were made over a ten day period, are compared to measured propagation loss values to examine the errors arising from that method of performing environmental measurement and its implicit assumption of horizontal homogeneity.

## 2. EXPERIMENTAL SETUP

Figure 1 illustrates the geographical layout of the VOCAR experiment. Three continous wave (CW) transmitting systems at 143.09, 262.85, and 374.95 MHz are installed at the northwest end of San Clemente Island (SCI, 33°- 01.4′ N, 118°- 33.8′ W). Receiving systems are located at the Naval Air Warfare Center Weapons Division (NAWCWPNS), Point Mugu (34°- 07.2′ N, 119°- 9.4′ W) and at the Naval Command Control and Ocean Surveillance Center RDT&E Division, San Diego (32°- 41.8′ N, 117°- 15.9′ W). Path "A" in Figure 1 is from the transmitting site on SCI to the receiving site at Point Mugu. Path "B" is from the same transmitting site to the receiving site in San Diego.

The CW links provide detectable signal levels at the receiver sites under standard atmosphere conditions. Each transmitting system consists of a transmitter, cables, a power divider, and two Yagi-Uda antennas, one aligned with the azimuth for path A and the other aligned with the azimuth for path B. Each receiving system consists of a log periodic antenna, a spectrum analyzer used as a receiver and a personal computer used for control and data recording. Path geometry parameters are listed in the first four rows of Table 1.

| Path | A | B |
|---|---|---|
| Transmitting antenna height (m) | 18.4 | 16.6 |
| Receiving antenna height (m) | 30.5 | 30.5 |
| Path length (km) | 132.6 | 127.2 |
| Azimuth to receiver (deg.) | 337 | 106 |
| 143.09 MHz std. prop. factor (dB) | -50.4 | -50.4 |
| 262.85 MHz std. prop. factor (dB) | -49.1 | -49.0 |
| 374.95 MHz std. prop. factor (dB) | -49.4 | -49.4 |

**Table 1.** Geometry and standard atmosphere propagation factors for VOCAR CW links.

The next three rows of Table 1 are the standard atmosphere propagation factors (propagation loss referenced to free space propagation loss) computed using the geometry parameters and frequency as input to the Engineers Refractive Effects Prediction System (EREPS) program (Patterson, et al., 1990.) It should be noted that under standard atmosphere conditions for the described geometry, at all three frequencies, troposcatter

*Paper presented at the Sensor and Propagation Panel Symposium on "Propagation Assessment in Coastal Environments" held in Bremerhaven, Germany 19-22 September 1994.*

levels are above diffraction field levels, so troposcatter levels correspond to standard propagation.

Receiving systems are operated in 15 minute cycles. Within each 15 minute cycle, five sampling cycles are run. During each sampling cycle, at each of the 3 CW frequencies, instantaneous measurements of peak amplitude, peak amplitude frequency and noise level were measured and stored. After the fifth sampling cycle, the measurements were averaged and recorded to disk.

## 3. LONG TERM OBSERVATIONS

Figure 2 is a time series of the received signal level (RSL) at 262.85 MHz on both path A and path B for the period June 1, 1993 through September 7, 1993. The abscissa is days of the year and the ordinate is the propagation factor in dB. The most striking feature of the plot is the large portion of time that signals are above troposcatter levels. It is observed that the gross features are largely homogeneous, that is, when there are elevated signal levels on path A there are also elevated signal levels on path B. Short term deviations from the mean value over fractions of a day do not appear to be correlated between the two paths. Plots of the signals at 143.09 MHz and 374.95 MHz (not included in this paper) are similar in appearance.

The linear auto correlations and the cross correlation for the 262.85 MHz signals on both paths A and B are plotted in Figure 3. The abscissa is from -384 to 384 lag hours, i. e. hours that the signal on path B lags the signal on path A. The solid line is the autocorrelation of the path A signal and the dashed line is the auto correlation of the path B signal. Differences between the two are slight. The dot-dashed line is the cross correlation between the path A and path B signals. The cross correlation appears very close to the auto correlations except in the immediate vicinity of zero lags, where it reaches a maximum value of 0.68.

A reduced abscissa scale is used in Figure 4 to provide better detail of the 262.85 MHz correlation functions in the vicinity of zero lags. The peak cross correlation occurs at approximately 1.5 hours of lag and the cross correlation function is nearly symmetric about its peak. This could be explained as a large component of the signal level amplitude on path B appearing as a time shifted function of the signal amplitude on path A.

For validation of models and assessment systems, it is the error of the estimates that is directly of interest, rather than the correlation, even though the error is a function of the correlation. The emphasis will now be shifted to the analysis of effects of spatial and temporal variability upon the error of propagation loss estimates.

## 4. ESTIMATION ACCURACY LIMITATIONS

When, how, and where to sense the environment are among the principal questions still to be answered in propagation assessment (Richter, 1994.) Use of the estimates of propagation effects tends to be uniformly distributed over time (i.e. detection ranges are of as much interest at 1400 as at 1230.) Environmental inputs for calculating propagation estimates in many cases though, are obtained at discrete times; e.g., atmospheric soundings are taken at 1200, 1600, etc. The selection and use of sensors is an optimization problem and the form of that problem is to minimize estimation error while constrained by cost and operations or to minimize cost within error and operational constraints. In either case, it is essential to know the error of propagation estimates over the period of time that they are used as estimates.

### Example

An example of such an optimization problem would be choosing the best estimator for the propagation effects on a path of interest using either 1) range dependent refractivity profiles obtained at four hour intervals taken on the path of interest, or 2) continuously available, remotely sensed, refractive profiles from a different path. Figure 5 is a time series of the received signal level at 262.85 MHz that illustrates the trade-off of determining optimal sensor usage. The measured signal level on path A (the value that is to be estimated) is plotted using a thin solid line. The potential performance of the two regimes (defined here as the systems and methodologies employed for developing propagation loss estimates) are now illustrated using measured data.

The thick solid line in figure 5 is representative of the optimal performance for a method of propagation estimation where model inputs are from high resolution range dependent refractivity profiles taken at four hour intervals and where the estimate created from the last environmental sampling is used as the current estimate (i.e. no averaging.) Its performance is simulated by four-hour sample-and-hold values of the measured loss on path A.

Justification for stating that the sample-and-hold values optimize (i.e. minimize the error of ) this method of estimation is as follows: Neglecting computational considerations, a perfect radio propagation model's calculations of propagation loss should asymptotically approach the actual values of the propagation loss as the spatial resolution of the environmental inputs is increased and the range step size is decreased. Decreasing spatial resolution of the environmental inputs while holding range step size constant should result in errors in estimating current actual values that are uncorrelated with difference between the current and future actual values, as information about current and future events are *not* being added to the estimates. If it is assumed that the actual and estimated values are identically distributed, and that the differences between current estimates and current actual values are uncorrelated with differences between current and future actual values, it can be shown that the minimum error will occur when the current estimate is equal to the current actual value.

Remote sensing techniques such as the GPS sounder (Anderson, 1994) are currently under development for inferring effective refractivity from the integrated refractive effects along the entire transmission path (Richter, 1994.) These techniques hold promise for real-time or nearly real-time retrievals of profiles of integrated refractive effects. The high frequency of updates means the estimates are amenable to filtering for error reduction. The path on which the effects are sensed though, is not necessarily on the path of interest.

The performance of using remotely sensed refractivity data on another path as an estimate is illustrated using the recursively filtered signal level on path B to estimate the signal level on path A. Let $y[i]$ be the actual signal level on path A and $x[i]$ be the actual signal level on path B. A recursive estimate of the signal level on path A ($\hat{y}[i]$) is calculated from equations 1 and 2. In this case the coefficient $a$ has been arbitrarily set to 0.2. The filter output is shown using the dotted line in figure 5.

$$\hat{y}[0] = x[0] \tag{1}$$

$$\hat{y}[i] = a \cdot x[i] + (1-a) \cdot \hat{y}[i-1] \tag{2}$$

An important visual impression from figure 5 is that the path A sample-and-hold values often take on the extreme values of the data. There is no reason for estimates developed from high spatial resolution atmospheric refractivity profiles not to take on local extreme values seen in the data; they should be distributed exactly as are the data. The insight to be gained from this observation is that without employing temporal or spatial averaging of estimates, the variance of the estimates should not be expected to be less than that of the instantaneous values. Another important observation is that it is not altogether clear which of the two illustrated methods of estimation is superior. It is only by computing accuracy statistics that judgment can be made.

**Accuracy Criteria**

Correlation is routinely thought of in terms of lag time but estimation error is not. When the use of estimates occurs more frequently than the observations used to create estimates, the estimation error, as a function of the time interval since an observation, is as important as the instantaneous error. Equation 3 is the general form for the root-mean-squared error (RMSE) of estimating $x[i+k]$ using $\hat{x}[i]$, where $k$ is the number of time intervals between the creation and the use of the estimate. The instantaneous error at the time of an observation is with $k$ equal to zero. In equation 4, the expected value of the RMSE is related to the standard deviation ($\sigma$) and mean ($\mu$) of the actual values and those of the estimator, as well as the cross correlation ($\rho$) of the actual value and the estimator. The difference in the means ($\mu_X - \mu_{\hat{X}}$) is referred to as the bias.

$$RMSE[k] = \left( \frac{1}{N} \sum_{i=1}^{i=N} (x[i+k] - \hat{x}[i])^2 \right)^{1/2} \tag{3}$$

$$E(RMSE[k]) = (\sigma_X^2 + \sigma_{\hat{X}}^2 - 2 \cdot \sigma_X \sigma_{\hat{X}} \rho_{X,\hat{X}}[k] + (\mu_X - \mu_{\hat{X}})^2)^{1/2} \tag{4}$$

Insight into the criteria for judging the goodness of estimators in propagation assessment is provided by closer examination of equation 4. It is quite common in propagation model validation to use comparisons of the distributions of estimated and predicted values or to use their correlation. For the purpose of validating assessment systems, use of either one of these measures, by itself, does not adequately describe the accuracy of estimators. It is seen in equation 4 that having RMSE equal to zero implies that $x[i+k]$ equals $\hat{x}[i]$ and thus they are identically distributed and their correlation is equal to 1.0. Having the correlation between $x[i+k]$ and $\hat{x}[i]$ equal to zero though, does not by itself imply that RMSE is equal to zero. Although $x[i+k]$ and $\hat{x}[i]$ being identically distributed implies that their means and standard deviations are equal, it does not imply that RMSE is equal to zero. The point is that neither the correlation nor comparisons of distributions alone sufficiently describe the accuracy of estimates.

Use of a statistic other than the RMSE as the primary statistic for the validation of propagation assessment systems should be the exception rather than the rule. An instance of such an exception is when using a possibly biased experimental data set to find the potential accuracy of such an estimator where the value of the expected bias is zero. Under such conditions it is appropriate to use the standard error (SE), which is the standard deviation of the error of estimating $x[i+k]$ using $\hat{x}[i]$. It is found using equation 5 and its expected value is found by equation 6. Comparing equations 5 and 6 to equations 3 and 4 respectively, it is seen that the SE is the RMSE with the bias term removed.

$$SE[k] = \left( \frac{1}{N} \sum_{i=1}^{i=N} (x[i+k] - \hat{x}[i] - \bar{x} + \bar{y})^2 \right)^{1/2} \tag{5}$$

$$E(SE[k]) = (\sigma_X^2 + \sigma_{\hat{X}}^2 - 2 \cdot \sigma_X \sigma_{\hat{X}} \rho_{X,\hat{X}}[k])^{1/2} \tag{6}$$

When using the previously measured received signal levels on path A to estimate the received level on path A, the estimator is inherently unbiased. This is not the case when using the loss on path B to estimate the loss on path A. To provide for level comparisons, the SE will be used to determine the *potential* accuracy of estimators of the received signal on path A based upon

received signal level measurements on both path A and path B.

**Potential estimator performance**

In Figure 6, the SE of the exact estimator of the current RSL on path A (solid line) is plotted as a function of the time lag (or delay) since the ideal estimator was current using a solid line. When the estimate is current (lag hours equal to zero) there is no error, however measurements 15 minutes later show greater than 4 dB SE, and four hours later the SE is over 7 dB. The SE of using the RSL on path B as the estimator of the RSL on path A is shown using the "long dashes" line. At zero lags the error is slightly greater than 8 dB; yet the increase in the error over the next four hours is only 0.5 dB. A roughly 1 dB improvement in accuracy of the estimates is found when the path B RSL measurements are processed using the filter described in equations 1 and 2.

Therefore, temporal resolution must be increased at the same time that spatial resolution is increased in order to realize substantial gains in the accuracy of propagation loss estimation. Realizing the best accuracy obtainable by including range dependent refractivity profiles in the estimation process may be difficult though. For example, the statistics plotted in figure 6 are based upon averages of five instantaneous measurements taken within a fifteen minute period. The variance of each of the instantaneous values is greater than or equal to the variance of the averages, therefore the slope of the path A curve would be as steep or steeper if the data were obtained using a higher sampling frequency. Another difficulty is timing; obtaining even a modest number of evenly spaced vertical refractivity profiles along a transmission path, all within seconds of each other, is a clearly difficult task.

## 5. ESTIMATION ERROR USING RADIOSONDES

From August 23, 1993 to September 2, 1993, personnel from NAWCWPNS, Point Mugu launched 43 radiosondes from SCI, the seaward endpoint for both paths A and B. The radiosondes were launched at roughly four hour intervals. The modified refractivity profiles (M-profiles) calculated from these soundings along with the path geometries (Table 1) were used as inputs to the Radio Physical Optics program (Hitney, 1992) to calculate propagation loss values for path A in a 10 km by 5 m (range by height) window centered about the location of the receiving antenna. The M-profiles were used as-is except in the first 100 meters where the measured profile was replaced with the M-profile of a standard atmosphere to negate the effects of localized heating on the atmosphere close to the ground. Propagation loss values used for this analysis were averages of the approximately 800 propagation loss values in the described window. Measurements of the accuracy of the propagation estimates for path A based upon measured values on path A, measured values on path B (note that these are unfiltered,) and the SCI radiosondes are now examined.

The error curves for the Path A estimator, the Path B estimator, and the SCI radiosondes as functions of the time since an observation are shown in figure 7. The performance of path A and path B estimators differ only slightly from that seen in figure 6. The primary difference is the better performance of path B estimates. With respect to these statistics, the period of August 23, 1993 to September 2, 1993 is fairly representative of the three month observation period for the whole VOCAR data set. The error using the SCI radiosondes (dot-dashed line) is not as smooth as the other two. This is because there are only 43 radiosondes compared to approximately 1000 measured propagation factor values; each SE calculation in figure 7 for the SCI radiosonde based estimates is based on just 43 error values. Each path A and path B SE value is based on 1000 error values. The jaggedness of the line notwithstanding, it is clear that the estimates based upon the SCI radiosondes are slightly better estimators of the propagation factor on path A than are the estimates derived from the propagation factors on path B. Furthermore, these estimates are only marginally worse than using the previously measured propagation factor on path A when the lag exceeds two hours.

The foregoing error analysis confirms the following: 1) There is an uncorrelated error component in the signal of roughly 5 dB that is difficult to predict; 2) propagation loss calculations based on seaward radiosondes (where horizontal homogeneity is implicitly assumed) can provide propagation factor estimates as good as having the actual propagation loss on the path of interest an hour previously; and 3) the potential exists for propagation loss calculations based on remotely sensed integrated path refractivity from paths other than the path of interest to provide accuracy on a par with calculations based on the best radiosondes.

## 6. CONCLUSIONS

1. The development and the operation of a real or near real-time propagation assessment system should be viewed as an optimization problem, either minimizing error subject to constraints on cost, etc. or minimizing cost subject to constraints on accuracy, availability, etc.

2. The error over the period of time that estimates are used is of important, not just the error at the time of the observations used to make a propagation estimate.

3. Comparisons of distributions of measured propagation effects and model estimates is, by itself, not sufficient to describe the accuracy of the model estimates. The same may be said for the correlation. The rule for judging the accuracy of estimates should be to use the root-mean-squared error.

4. The accuracy of propagation loss estimates is as much a function of temporal resolution as it is of spatial resolution. Temporal resolution must be increased at the same time as spatial resolution to achieve substantial improvements estimation accuracy.

**ACKNOWLEDGMENT**
This work is sponsored by the Office of Naval Research.

**REFERENCES**

1. Anderson, K.D., "Remote sensing of the evaporation duct using an X-band radar," AGARD CP 502, pp. 3.1 - 3.9, 1991

2. Anderson, K.D., "An evaluation of three GPS receivers for use in the GPS sounder," NRaD Tech. Rep. 1637, April, 1994

3. Goldhirsh, J. and G.D. Dockery, "Propagation measurements and modeling at C band for over-the-water, line-of-sight propagation links in the Mid-Atlantic coast," Radio Science, Volume 26, No. 2, pp. 671-690, May - June, 1991

4. Hitney, H.V., "Hybrid ray optics and parabolic equation methods for radar propagation modeling," IEE Radar 92 Conference Proceedings No. 365, pp. 58 - 61, 1992

5. Levy, M.F. and K.H. Craig, "Use of mesoscale models for refractivity forecasting," AGARD CP 502, pp. 7.1 - 7.12, 1991

6. Patterson, W. L. , C.P. Hattan, H.V. Hitney, R.A. Paulus, A.E. Barrios, G.E. Lindem, K.D. Anderson, "Engineers refractive effects prediction system (EREPS) 2.0," NOSC Tech. Doc. 1342, Revision 2.0, 1990

7. Richter, J.H. , "Sensing of radio refractivity and aerosol extinction," AGARD CP 567, paper no. 1, 1994

FIGURE 1. Layout of VOCAR CW links.

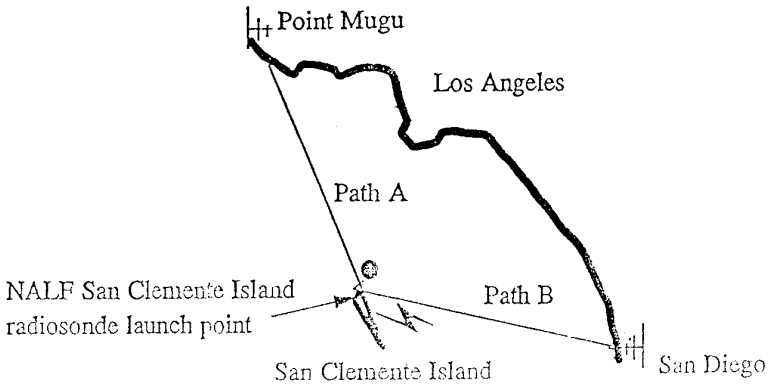


FIGURE 2. Time series of 262.85 MHz propagation factors for path A and path B.

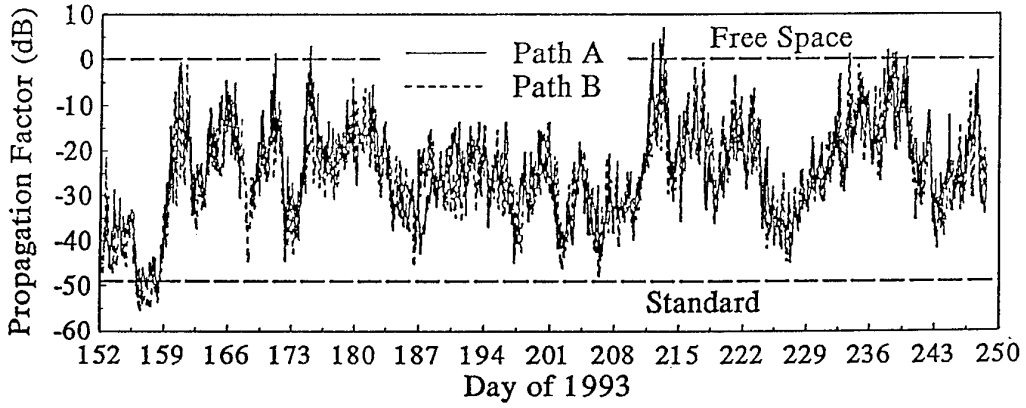


FIGURE 3. Correlation at 262.85 MHz
(full abscissa.)

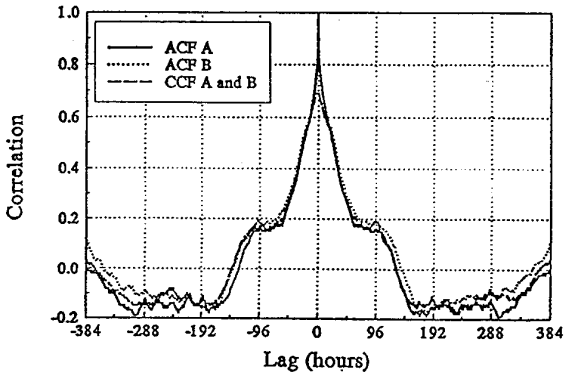


FIGURE 4. Correlation at 262.85 MHz
(reduced abscissa.)

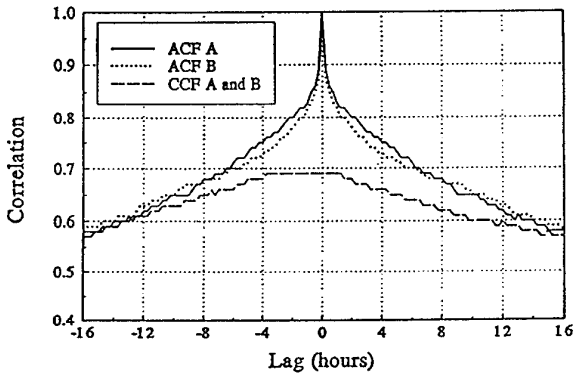

Figure 5. Time series from July 30, 1993 to August 2, 1993.

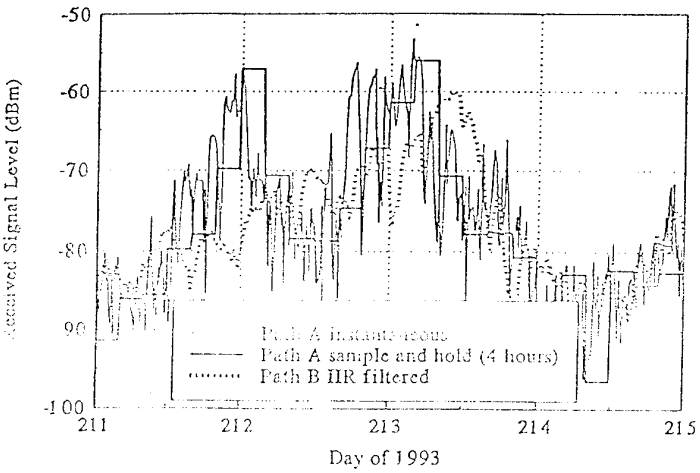


Figure 6. Estimation error from June 1, 1993 to September 5, 1993.

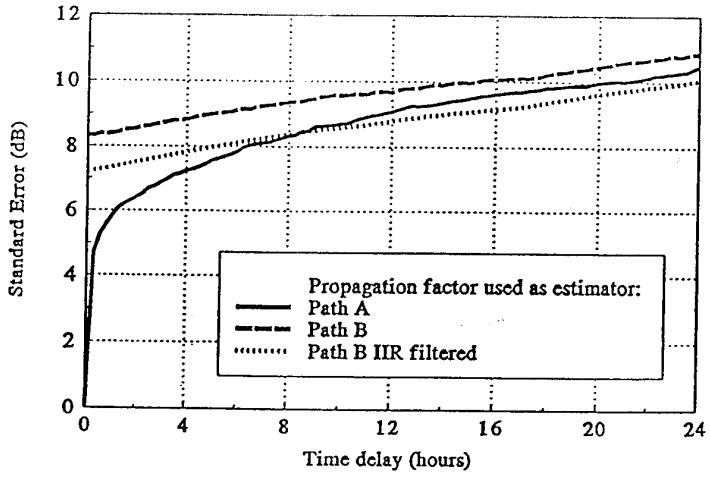


Figure 7. Estimation error from August 23, 1993 to September 2, 1993.

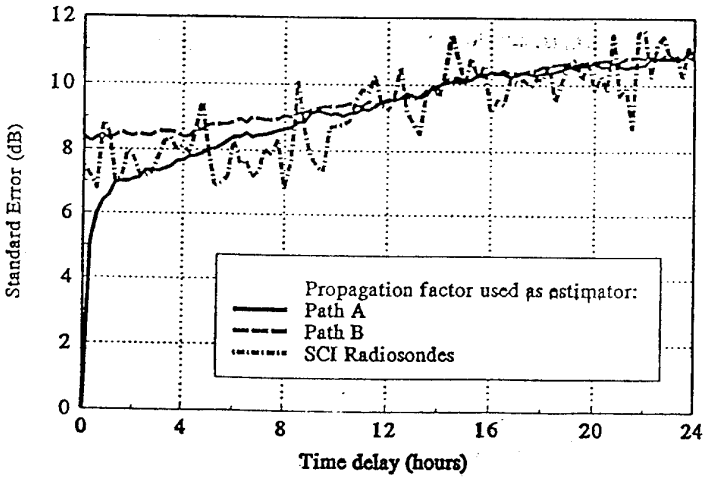

## DISCUSSION

**D. DION**
Do you think that the time variability and the width of the notch in the autocorrelation function can be reliably predicted from the prevailing atmospheric conditions?

**AUTHOR'S REPLY**
The width of the autocorrelation function of the propagation factor, itself a measure of temporal variability, is a non-linear function of frequency, path geometry, and the state of the propagation environment including its rate of change. Predicting the shape of the autocorrelation from prevailing atmospheric conditions is probably a difficult problem.

**J. CLAVERIE**
You have shown that using propagation data from a path A to explain propagation on path B, you had quite better results than using meteorological data. We had "similar" conclusions from our LORIENT 89 campaign: for 2 identical geometrical paths, 3 GHz data gave better results to explain 36 GHz data than using meteorological measurements. In fact, the question is: can we expect to make good propagation predictions without using meteorological data?

**AUTHOR'S REPLY**
Propagation estimates calculated from over-water meteorology provided roughly the same accuracy for estimating propagation on path A as did radio measurements from path B. Only propagation calculations based upon shore meteorology performed substantially worse than the radio measurements for estimating propagation on path A. Radio measurements do accurately measure a path's integrated refractive effects in real time but suitable emitters are not always available. Just how accurate measurements of integrated refractive effects at one frequency are at estimating the integrated refractive effects at another frequency has yet to be determined. Meteorological modeling and measurements may give you horizontal structure and, if forecast, a predictive capability. Combining meteorological and radio data should provide better propagation assessments than either used alone.

**K. DAVIDSON**
Would a merging of remote MLD estimates, as frequent as overpass, and end-point radiosondes, at 6-12 hours, be a good idea?

**AUTHOR'S REPLY**
One important use of such data is for indication of which areas are representative, and which are not. Your images of the VOCAR area indicated that meteorological conditions along the shoreline were not representative of the over water areas for portions of time during the VOCAR experiment. This was verified by the greater error of propagation calculations based upon shoreline path end-point radiosondes (Pt. Mugu) as compared to propagation calculations based upon mid path (R.V. Point Sur) and seaward end point (San Clemente Island) sounding.

**K.H. CRAIG**
Your autocorrelation function showed no evidence of diurnal effects. In NW Europe surface and elevated layers due to subsidence and/or advection often show such effects. Can you comment please?

**AUTHOR'S REPLY**
Significant diurnal effects have not been observed in the over water VOCAR links, however other researchers have identified diurnal effects in the VOCAR links running along the shore line.

It should be noted that the evaporation duct, a phenomenon which is often observed to be diurnal in coastal areas, has little effect on propagation as VHF/UHF frequencies.

**J. TURTON**
Referring to fig 4 (as in the paper). If there was only one ship out in the bay making radiosonde measurements for propagation predictions along a variety of different paths, does the data shown in the figure suggest that, because of the variability of the atmosphere (temporally and spatially), there would be no point in making sounding at intervals of less than 6 hours (because of the flatness of the CCF A&B curve)?

**AUTHOR'S REPLY**
Your interpretation is correct for propagation estimates where no temporal averaging of propagation model calculations is employed. Figure 7 is better for answering the question as it plots RMS error as a function of lag time for propagation calculations based upon radiosondes.

**J.H. RICHTER** (Comment)
Regarding Dr. Craig's question concerning the lack of evidence of diurnal changes: we have looked at thousands of hours of FM-CW radar (mentioned in paper 1) observations that continuously and accurately measure height changes of refractive layers with the intent of identifying diurnal changes. We found no clear evidence of diurnal changes.

# Refractive Variability during VOCAR 23 August to 03 September 1993

**Roger A. Helvey**
Geophysics Division, Code 521420E (P3542)
Naval Air Warfare Center Weapons Division (NAWCWPNS)
Point Mugu, CA 93042-5001
USA

## SUMMARY
Measurements of the lower atmosphere from the southern California coastal area were obtained from a number of sources during the 23 Aug - 03 Sep 1993 VOCAR Intensive Observation Period (IOP). Data from high-resolution radiosondes, surface stations, aircraft and weather satellite have been collected for use in identifying mesoscale atmospheric phenomena and related refractive features. Spatial and temporal variations in the height of the elevated duct associated with these phenomena are a major factor in determining refractive conditions in this region. An automated isentropic cross-section analysis tool is being applied to the upper-air data, to facilitate correlation with analyses of data from satellite imagery and the other sources.

## 1. INTRODUCTION
Ocean areas are typically covered by a mixed boundary layer up to one or two kilometers deep, with relatively homogenous properties throughout. A strong superrefractive layer or elevated duct is often found at the quasi-horizontal interface between this moist marine air mass and an overlying warmer, drier air mass. The altitude of this interface and the optimum coupling height within the elevated duct are usually coincident. This condition is especially common over areas such as the eastern Pacific Ocean in temperate latitudes, where high pressure and subsidence cause warming aloft which intensifies the vertical contrast between the lower and upper air masses.

Influence of the elevated duct on low level radar/radio propagation is greatly affected by the duct height, so a knowledge of the factors governing the topography of the interface is needed for understanding and anticipating changes in the operational propagation environment. Range dependent propagation effects are specially sensitive to spatial changes over mesoscale distances (roughly 10 to 100 kilometers). Over the open ocean there are no long-term geographically stationary processes on this scale, except in the vicinity of strong sea surface temperature gradients. In coastal regions, however, the dominant factors tend to be terrain-related so that certain characteristic patterns relative to the fixed terrain features will be observed, for similar atmospheric conditions. Terrain-induced variations in refractive layering should be both more robust and more predictable than variations over the open sea. Although in any coastal zone atmospheric processes generic to that type of environment will occur, significant differences at different localities can be expected related to local climate, and orientation and shape of coastline and terrain features.

A large number of different kinds of measurements were made during the VOCAR IOP to determine the refractive variability during concurrent propagation measurements made by the NCCOSC RDT&E Division San Diego (NRaD), and the meteorological factors responsible for those variations. At NAWCWPNS Point Mugu compilation and analysis of several sets of data are being carried out, including radiosonde profiles, aircraft soundings, weather satellite imagery and surface observations. A basic goal is to combine the different types of information to identify and follow the evolution of the coastal meteorological phenomena and associated refractive conditions, with emphasis on behavior of the elevated duct. Various analysis tools are being used which may have operational utility for Fleet applications. Described below is some preliminary information resulting from this effort.

## 2. DATA SOURCES AND APPLICATION

### 2.1 Radiosondes
The existing upper-air stations in coastal southern California were not adequate for the purposes of the VOCAR IOP. Two of these stations, at Vandenberg Air Force Base and at Montgomery Airfield (San Diego), provide data only at the two synoptic times 00Z and 12Z. Furthermore, they are located a few miles inland at altitudes over 100 meters, so often are not representative of the lower marine atmosphere containing the elevated duct. Two other stations, at Point Mugu and San Nicolas Island, are acceptably located but data are not normally obtained at night or on weekends. Therefore, special measurements were taken at the seven island and coastal sites shown in Figure 1, distributed to provide better coverage of the area of interest. These sites were in operation from 23 August to 03 September 1994, comprising Point Arguello (PGU), Point Mugu (NTD), Point Vicente (PVL), Camp Pendleton (CPN), and North Island (NZY) along the coast, and San Clemente (NUC) and San Nicolas (NSI) Islands offshore. An eighth site was provided by a Naval Postgraduate School (NPS) ship, which from 25 to 30 August was near a location centered in the region between Point Mugu, San Clemente Island, Point Vicente, and San Nicolas Island. The ship also made soundings while enroute to and from this location, along the coast to the north. A four-hour release schedule was attempted at the eight sites, although midnight soundings were omitted except at the ship. Vaisala MARWIN systems or the Navy MRS version were employed, with data mostly recorded at two-second intervals, although some sites changed to a five or ten second interval at five or ten minutes after release. The raw data were edited to remove occasional bad points or periods. Over 425 radiosonde releases were made during the IOP, which after editing and compression required 26 Mb (million bytes) of disk storage space.

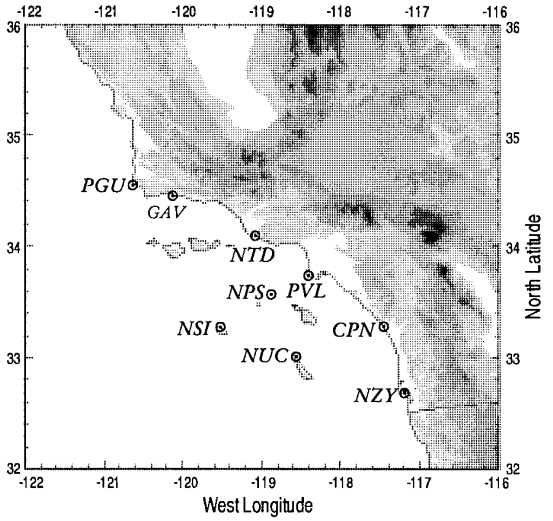


Figure 1. VOCAR radiosonde sites during IOP: PGU=Point Arguello, NTD=Point Mugu, PVL=Point Vicente Lighthouse,CMP=Camp Pendleton, NZY=North Island, NSI=San Nicolas Island, NUC=San Clemente Island, NPS=Naval Postgraduate School; also GAV=Tethersonde at Gaviota. Highest terrain inland (darkest shade) is about 3000 meters altitude.

*Paper presented at the Sensor and Propagation Panel Symposium on "Propagation Assessment in Coastal Environments" held in Bremerhaven, Germany 19-22 September 1994.*

**2.11** *UpDown Soundings*
At four sites (PGU, NSI, NPS and NUC) a large percentage of the soundings were tracked during both ascent and descent. The upward progress of the radiosonde during these "UpDown" soundings was terminated using a method devised by the author, with subsequent descent by parachute from roughly 3 to 6 km altitude to yield an additional nearby sounding through the lower atmosphere. The descent and ascent rates were similar, roughly 2 to 4 meters per second. Although the horizontal location of the descent was not controllable, due to site locations and prevailing winds the final impact point generally occurred overwater within about 10 to 20 km from the release point. Most were tracked re-entering the elevated trapping layer and many were followed to the surface. In addition to doubling the amount of data obtained from the altitudes of particular refractive interest, the UpDown soundings are valuable for investigating radiosonde sensor characteristics, and spatial-temporal variability in atmospheric properties. Figure 2 is a plot of temperature and dewpoint for one such pair of soundings. A substantial difference in altitude of the inversion base is apparent, for a separation of about 20 minutes and 10 km. Also, in a number of cases such as that shown, the humidity transition at the top of the marine layer is less abrupt during descent than ascent. This may indicate a hysteresis in humidity response due to sensor lag, or be due in part to mixing down of drier air in the lee of the island or coastal site where the radiosonde was released. Surface conditions shown for the ascent from the island release site are not representative of the environment indicated during the subsequent descent to the water surface offshore.

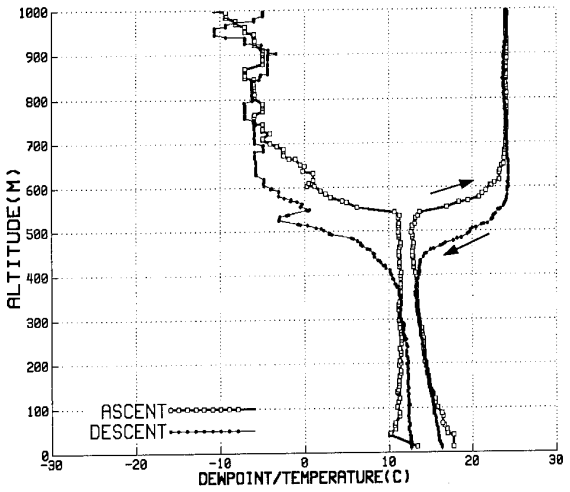


Figure 2. NSI UpDown sounding for 25 August 1993, 20Z (1200PST local time). Temperature (right) and dewpoint (left); ascent thick lines with open squares, descent thin lines with filled circles. Difference in altitude of features indicates changes over about 20 minutes and 10 km. Note difference in first few hundred meters between land (ascent) and ocean (descent) environments.

**2.12** *Automated Cross-Section Analysis*
When investigating variability in atmospheric structure in temporal or spatial sequences of radiosonde profiles, construction of vertical cross-sections is a helpful analytical procedure. The use of potential temperature as a vertical coordinate is advantageous for this purpose, usually as a tool in analysis of synoptic weather features, but also recognized as valuable for refractive analysis (Levy and Craig, 1992). An automated process for generating time or space cross-sections of refractive layering using potential temperature (isentropic) vertical coordinates has been developed (Helvey, 1994).

The scheme is presently implemented in HiSoft BASIC on an Amiga desktop computer. It has provisions for estimating missing sections of profiles, and ensuring that the analyzed atmospheric layers are always of finite, positive thickness. Some smoothing of the raw 2-second data is performed. Superadiabatic layers are eliminated since potential temperature is required to increase monotonically upwards to serve as the vertical coordinate. More precisely, virtual potential temperature is used; it is believed preferable to equivalent potential temperature since the latter is unduly sensitive to moisture variations along the profile. The altitudes of an upper and lower bounding isentrope are interpolated for reference, which encompass the maximum and minimum overall potential temperatures reported; for mathematical expedience they are not confined to the vertical limits of the analysis domain (the lower reference can be partly at negative altitudes). The interpolation is done using a cubic spline under tension, which tends to reduce unsupported waviness between the reported profile points. Thicknesses of intermediate isentropic layers are similarly interpolated laterally(a transformation to and from the logarithm of thickness is performed to preclude the possibility of layers with negative thickness). These thicknesses are integrated vertically to obtain relative altitudes at each horizontal interpolation point, then scaled to fit within the original upper and lower reference isentropes. Observed pressure, temperature and mixing ratio values are then interpolated along the isentropes, and corresponding refractivities computed.

When applied to a series of radiosonde profiles located along or near a horizontal line, the procedure results in a height versus distance grid of refractivity values suitable for range-dependent propagation model input. When applied to a series of soundings for a single site, the results depict the temporal variability in refractive layering at that location. An example of the latter is given in Figure 3, which shows a time cross-section at NSI, during the VOCAR IOP 23 August through 02 September 1993. The wavy lines running across the plot show variations in the atmospheric layering, for selected isentropes (potential temperatures). Troughs in the isentropes indicate comparitively warm periods, ridges indicate cold. Refractive gradients are shown by shading; light shading for superrefractive, dark for trapping, and solid black for strong trapping. The strongest and most persistent layering is at the top of the marine layer, which moves up and down between about 100 to 600 meters altitude through the period, lowest around 27 August, highest 29-30 August.

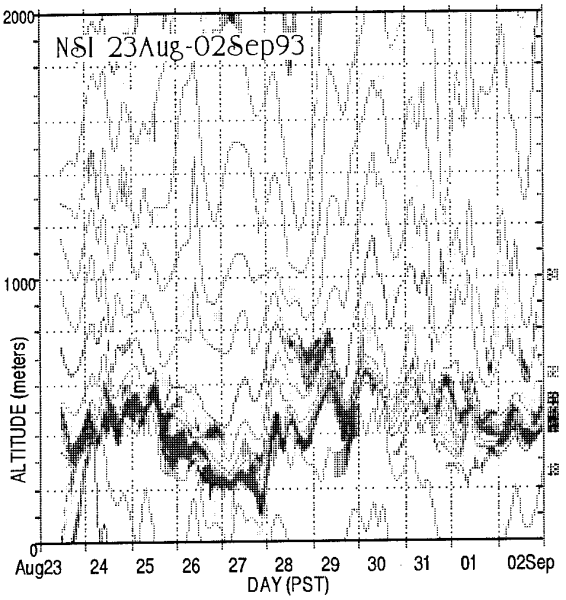


Figure 3. 11-day isentropic time cross-section for NSI, 23 Aug to 02 Sep 93. Vertical lines separate days (PST). Wavy lines are isopleths of potential temperature. Refractive gradients shown by shading, light for superrefractive, dark for trapping. The main elevated duct moves up and down with the top of the marine layer.

Another cross-section for NSI is given in Figure 4, for a single 24-hour period, 28 Aug 1993. Even some of the less significant layers aloft apparently persist over several sounding intervals.

Since the soundings were not always simultaneous at all sites, and were occasionally missing, another application of the time-sections will be to estimate synchronous conditions for use in constructing space cross-sections.

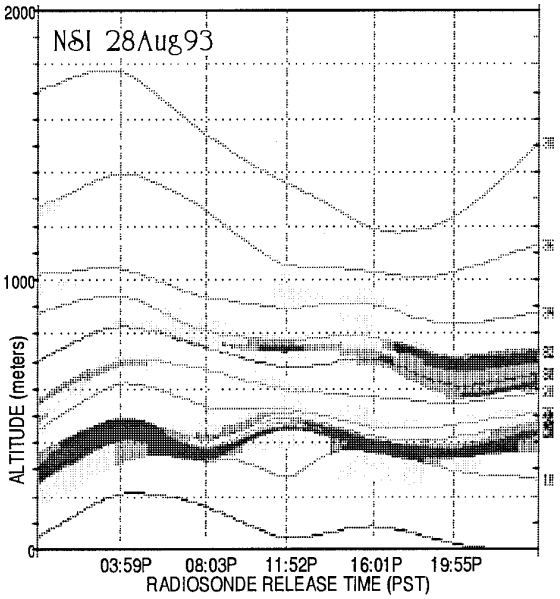


Figure 4. Same as Figure 3, but for one day, 28 Aug 93. The amplitude of the undulations in the main elevated duct layer altitude is about 100 meters. The ridge in height near midday (11:52PST) appears to be related to a moving cloud feature (see text, section 3.)

## 2.2 Aircraft

Three fixed-wing aircraft were used during the IOP. One was operated by the Naval Research Laboratory, Washington at altitudes well above the marine layer, using a downward-pointing LIDAR to remotely sense the underlying atmosphere, including the apparent depth of the marine boundary layer and altitudes of clouds and haze. The other two were light aircraft operated by NAWCWPNS Point Mugu and NRaD. These were flown at relatively low altitudes to measure temperature, humidity and associated refractive structure in the region of the elevated duct atop the marine layer. The horizontal flight plan shown in Figure 5 was used during the first half of the IOP when both low-level aircraft were present; during the second half another NAWCWPNS leg was added since the NRaD aircraft was then unavailable.. The end-points of each flight leg were placed near radiosonde sites to provide complementary information, with a crossing near the NPS ship location. Because of flight restrictions due to the amount of air traffic near the coast and inland, it was not feasible to traverse the overland communication paths sampled by NRaD, but the overwater links between San Clemente Island to San Diego and Point Mugu were covered. To enable detection of short-term changes, two tracks were immediately repeated in the reverse direction (between NSI-PVL and NUC-Palomar). Also, to determine changes accompanying the daily development of the sea breeze circulation, the morning flight plan was repeated in the afternoon. Figure 6 depicts a flight by the Mugu aircraft during the morning of 28 August. The vertical sawtooth pattern shown schematically was typical. The series of connected slant ascents and descents usually ranged in altitude from about 150 meters below to 350 meters above the local top of the marine layer to provide multiple penetrations of the strong refractive layer responsible for the main elevated duct. Processing of the meteorological data by NAWCWPNS is still underway; a version of the automated cross-section analysis scheme is being developed for that purpose.

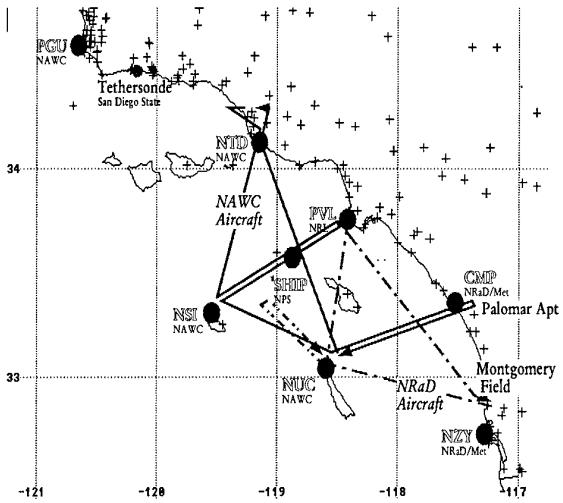


Figure 5. Flight plan for NAWCWPNS and NRaD aircraft, first half of IOP, round trips morning and afternoon. During second half of IOP the NAWCWPNS aircraft flew an additional leg from NUC to Montgomery field, southward in the morning and return in the afternoon, to compensate for absence of the NRaD aircraft..The endpoints of each leg were near radiosonde sites.

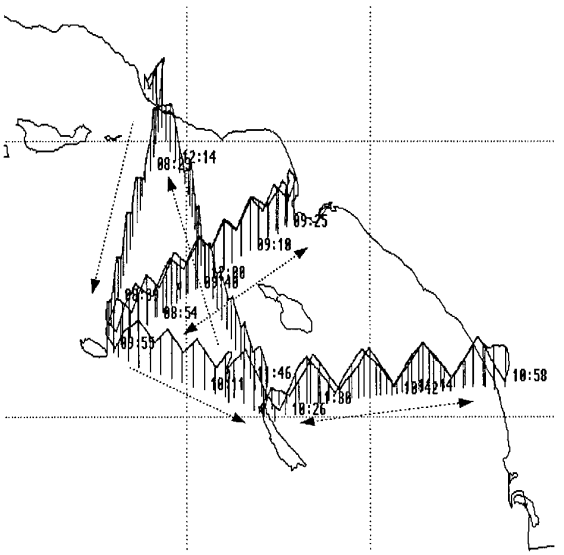


Figure 6. A depiction of the NAWCWPNS aircraft morning flight, 28 Aug 93, total time 4 hours.. Aircraft airspeed was about 110 knots (55 mps), with ascent and descent at 500 fpm (3 mps), so the true slope of the sawtooth profiles was approximately 1:20. Horizontal spacing between successive profiles was roughly 5 nmi (10 km.) The vertical lines are one minute apart. Vertical scale exaggerated.

## 2.3 Surface Stations

Surface meteorological data were collected from numerous sources throughout the southern California area, from Federal, State, County and local government agencies, and

VOCAR participants. The parameters, observation times and reliability varied, but a concerted effort was made to obtain as complete a set of hourly data as possible, especially during the IOP. About 100 stations normally reported through conventional weather circuits, and another 250 or so were acquired by special arrangement. Extensive editing was carried out in an attempt to improve the quality of the data. This included time series plots and contoured analyses to detect and replace obviously aberrant data. As an example of these plots, Figure 7 shows the locations of the surface sites, including buoys, with wind vectors plotted where observed at 1600PST (late afternoon) 01 September. For comparison, contours of marine layer depth from radiosonde measurements near that time are superimposed (corresponding to the base of the elevated trapping layer); this is a preliminary analysis performed for data quality control purposes and probably not accurate over inland or offshore areas distant from the upper-air sounding sites. With additional data from a tethered sonde operated by Dr. Clive Dorman of San Diego State University, the existence of a pronounced depression in the inversion topography was revealed over the coast around 20km east of Point Arguello. This feature is common when moderately strong north/northwest winds at low levels curve around the coastal headlands in that region to create a cyclonic eddy, as suggested by the turning evident in the wind vectors.

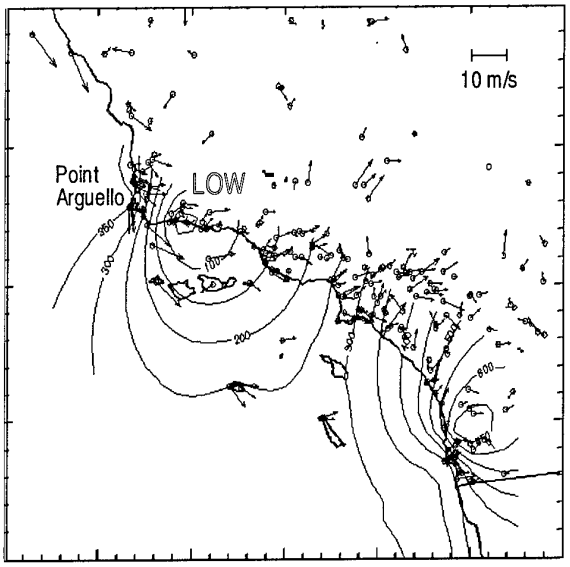


Figure 7. Surface wind vectors and marine layer depth, for 1600PST 01 Sep 93. The contours are drawn at 100 meter intervals based on radiosonde and tethered sonde data, and give a rough indication of elevated duct topography. The depression is believed dynamically caused by eddying due to flow around the headland to the west.

### 2.4 Weather Satellite

Another paper presented at this conference (Helvey et al, 1994) discusses use of satellite imagery for diagnosis of large-scale refractive conditions. The satellite information is also valuable for understanding refractive variations on a smaller scale. Collection of satellite data at NAWCWPNS was limited to that from GOES-7, consisting mainly of 4km visual (VIS) and infrared (IR), and 1km VIS data. The GOES is a geostationary platform which routinely provides half-hourly images of selected areas; this enables detection and tracking of cloud features at a joint spatial and temporal resolution otherwise unattainable. For a 12 day period including the IOP, 688 individual images constituting 220 Mb (million bytes) of data were acquired. Inspection of image sequences reveals numerous mesoscale phenomena in the marine atmosphere. some stationary or slowly evolving, some translatory or short-lived. Computer time-lapse displays of the IOP imagery have been prepared which vividly demonstrate the evolution of the marine clouds associated with these phenomena. Figure 8 contains three selected 1km VIS images from 28 August. Some of the salient features indicated are:

(A) Small-scale stratocumulus cloud structures (dimensions of a few km) which are imbedded in and carried by the marine layer winds.

(B) Larger regions containing enhanced stratocumulus (dimensions tens of km) which move with the marine flow.

(C) Small vortices generated by horizontal flow around terrain obstacles, and which often subsequently detach and are carried downstream by the marine layer winds.

(D) Vortices or lateral waves similar to the above but occurring in offset pairs as symmetric oscillations to the lee of islands (Karman vortex street). These have been recognized as a frequent occurrence in other locales, for instance downwind of the Canary Islands (offshore northwest Africa) or Guadalupe Island (in the Pacific just west of Mexico).

(E) Diffuse parallel bands of alternately enhanced and decreased marine cloud amounts, not moving with the marine layer flow but apparently related to winds aloft. The wavelengths of these features are on the order of 200km.

(F) Lines which project seaward from prominent mainland or island coastal terrain features, transverse to the marine layer flow. These features are quasistationary, and so must be propagating upstream at about the same speed as the low level winds; gradual adjustments in position occur, apparently in response to changes in low level conditions.

(G) "V"-shaped clear zones attached to some islands (especially common at San Nicolas as in the images shown). These are often very prominent, forming an arrow which appears to point into the marine airflow. They have been explained (Edinger and Wurtele, 1972) as atmospheric internal gravity waves at the top of the marine boundary layer around an island, similar to ocean bow waves formed by a moving ship.

(H) Clouds moving in a "jet" along the coast.

(I) Cloud surges associated with changes in wind direction and speed.

(J) Daytime clearing in the marine cloudiness in the coastal zone, propagating seaward during the day; this is largely a result of lowering of the marine layer depth due to subsidence as the sea breeze circulation develops (Lee,1979).

(K) General tendency for clearing over the entire region, due to gradual rising of the condensation level as the atmosphere warms during the day.

(L) A tendency for a more westerly orientation to the flow as the sea breeze develops.

## 3. DISCUSSION

Several vortices of roughly 20 kilometers in diameter were observed in the satellite imagery, moving with the general flow. The small, relatively clear area near their centers suggests locally lower marine layer depths there. A rough estimate assuming cyclostrophic flow (balance between pressure gradient and centrifugal forces) within the marine layer indicates that the optimum coupling height could be depressed by about 100 meters at their centers. The presence of these and several other features indicates significant variability in low level winds and clouds at scales less than the spatial and temporal spacing of the radiosonde profiles. The horizontal spacing of successive aircraft ascents and descents is sufficient to help determine if associated deformation of the elevated duct is substantial enough to noticeably affect propagation. The aircraft data and satellite imagery will be carefully coordinated to determine when and where such features may have been sampled.

Apparent correlation in marine layer depth and some larger scale features can be found. For example, the patch of brighter stratocumulus indicated as (B) in Figure 8 moves over San Nicolas Island during midday, roughly coincident with a temporary increase in marine layer depth of about 100 meters between 0800 and 1200 PST (Figure 4).Another example is the increase in layer height at NTD apparently coincident with the time of arrival of a surge of cloudiness (I) from the west through the Santa Barbara channel.

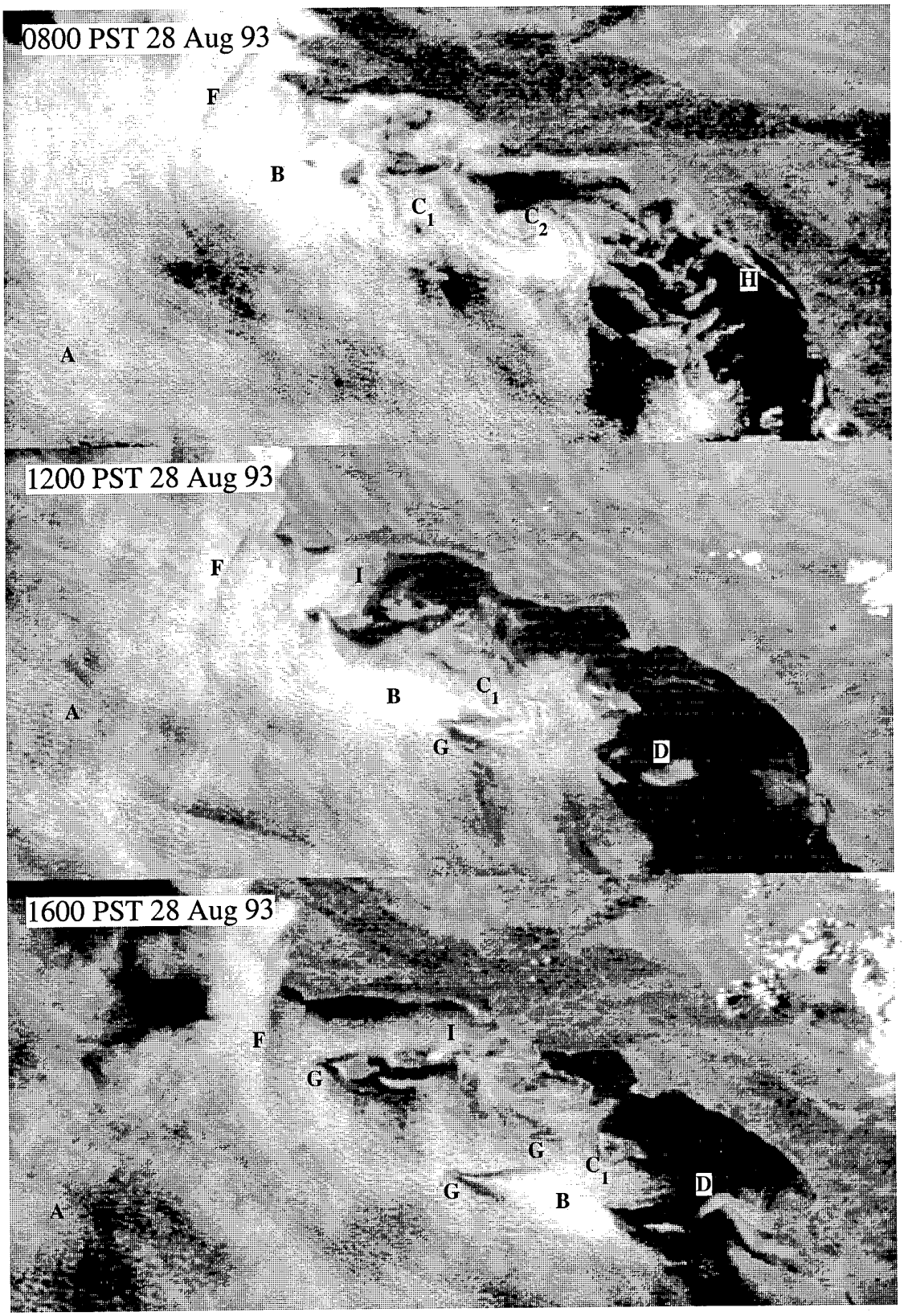


Figure 8. Selected GOES 1km VIS images for 28 Aug 93, showing evolution of marine stratocumulus cloud features. Upper is for 0800PST, middle is 1200PST, lower 1600PST. Examples of specific structures: (A) Stratocumulus cells, (B) Region of enhanced cover, (C) Small cyclonic vortices, (D) Lateral vortices or oscillations in wake of islands, (E) Diffuse bands moving with upper flow (only visible in animation), (F) Lines in cloud structure extending seaward from terrain, (G) "V"-shaped clear zones like bow waves attached to islands, (H) Cloud "jet" along coast, (I) Afternoon westerly surge in Santa Barbara Channel. See text (sections 2.4 and 3) for more comments.

Other data, not shown here, can shed light on the characteristics and effects of the mesoscale phenomena. For instance, surface winds reported by the NPS ship vary in a manner consistent with the passage of the vortex labeled (C2) in Figure 8. Data from remote sounders are also available for NTD, NUC and near NZY; the vertical resolution from these is much less than from the radiosondes, but samples averaged over one hour or shorter intervals were obtained through the IOP.

The significance of these phenomena lies in their relevance to the refractive structure in the lower atmosphere, especially with regards to implied perturbation of the elevated duct topography. There is a dynamic connection between topography of the elevated duct and eddying and wave motions in the marine layer due to terrain interactions and other causes, similar to the waves and vortices which disturb a water surface flowing around obstacles in a channel. Mesoscale effects on duct height are also identifiable at somewhat greater dimensions, including horizontal circulations involving the entire coastal region of southern California (such as the well-known Catalina Eddy), and vertical motions associated with the daily coastal seabreeze/landbreeze cycle. Also, although temperature and humidity conditions within the marine air are generally rather uniform, some variation in refractivity can be expected for different low-level air trajectories which will affect the strength of the elevated duct. The appearance of the marine stratocumulus clouds often provides a means of recognizing and following disturbances of the marine atmosphere, furnishing a valuable aid for integration of the various information available to explain variations in the coastal refractive environment.

## 4. ACKNOWLEDGEMENTS

A number of NAWCWPNS Geophysics Division personnel contributed to the VOCAR data collection effort. Lee Eddington and Robert Nagy arranged for and performed acquisition of surface weather reports from many agencies, and together with Matt McGovern, Bernie Cohenour, and members of the RAWIN Section carried out the radiosonde soundings at four sites. Paul Greiman operated the MIDDS system to collect satellite, gridded and surface meteorological data. The Instrumentation Branch provided logistical support. Terry Eggleston of the Data Processing Systems Division contributed to development of the aircraft data acquisition system and software. Other participants supplying data described here include NRaD, NPS, the Naval Research Laboratory at Monterey (NRL-MRY), and Dr. C. Dorman (San Diego State University). Support of the Project sponsor at NRaD, Dr. J. Richter, and the VOCAR coordinator, Rich Paulus under the U.S. Navy's EM/EO Propagation Assessment Program is gratefully acknowledged.

## 5. REFERENCES

Edinger, J.G. and M. Wurtele, Interpretation of some phenomena observed in southern California stratus, Mon. Wea. Rev., Vol. 100, No. 5, pp 389-398, 1972

Helvey, R., Refractive variability using automated isentropic cross-section analysis, Proc. IGARSS '94, 1994

Helvey, R. et al, Use of satellite imagery and other indicators to assess variability and climatology of oceanic elevated ducts, AGARD-CP-567, No. 33, 1994

Lee, T.F., Diurnal variations of coastal stratus, Pacific Missile Test Center, Point Mugu, CA, Geophysical Sciences TP-80-02, 1979

Levy, M. F. and K. H. Craig, Use of mesoscale models for refractivity forecasting, AGARD-CP-502, pp 7.1-7.12, 1992

## DISCUSSION

**T. ROGERS**
To what extent do you see travelling versus standing waves in the marine boundary layer?

**AUTHOR'S REPLY**
Both present - no opinion as to proportion at this stage in the analysis. Stationary bow wave features attached to San Nicolas Island are a frequent occurrence.

**S. BURK**
This is more of a comment than a question. Previous papers in this conference have noted a lack of diurnal signal in the VOCAR propagation measurements, whereas you note, there is often considerable diurnal variation in the marine stratus layer, even off of the coast. Typically the stratus clears out over the water during the day in association with sea-breeze forced subsidence. Evidently, however, this variation in boundary layer thermodynamic structure, which is sufficient to eliminate the stratus, does not result in a simultaneous diurnal impact on propagation conditions. That is, the boundary layer structure is changing diurnally over the water near the coast sufficiently to move the lifting condensation level above and below the inversion, but the conditions may remain surface-based ducting throughout the full 24 hour day. This is interesting because often the gradients in temperature and moisture at the top of the marine layer are sharper, if a stratus layer is present than in clear conditions.

**AUTHOR'S REPLY**
The supposed diurnal variation in marine layer depth is not the only explanation for coastal daytime clearing. There is a long-term tendency for a trough in layer depth along the coast, so that even in the absence of diurnal lowering in that zone, daytime warming due to solar heating would raise the condensation level so that clearing over water would first occur along the coast where the marine layer was most shallow, and gradually expand seaward. Other factors may also be involved, whose net effect will have to be considered to explain behavior of the refractive profiles and propagation conditions. The comment on sharpness of gradients depending on marine cloud conditions is an important point (and may explain an apparent diurnal variation in oceanic elevated ducting incidence).

# Use of Satellite Imagery and Other Indicators to Assess Variability and Climatology of Oceanic Elevated Ducts

Roger Helvey, Jay Rosenthal, Lee Eddington, Paul Greiman and Charles Fisk
Geophysics Division, Code P354
Naval Air Warfare Center Weapons Division
(805)989-8383/7893
Point Mugu, Ca 93042-5001
USA

## ABSTRACT

Much of the world's ocean area is overlain by persistent elevated ducting due to a strong super-refractive gradient at the top of the marine layer. Several techniques are used to describe characteristics of the elevated duct on climatological, synoptic and local scales. In addition to statistical analysis of radiosonde databases, these techniques include subjective and objective applications of satellite imagery, computation of a duct height index from surface and upper level numerical analyses or forecasts, and various other indirect meteorological indicators of ducting. Refractive statistics from worldwide coastal, island and ship radiosonde profiles reveal a widespread diurnal variation in duct occurrence believed related to day-night changes in marine stratus/stratocumulus cloud amounts. Incorporation of this diurnal behavior, together with relationships found between elevated duct characteristics and conventional parameters suggest a basis for generation of improved worldwide oceanic elevated duct climatology from historical gridded surface upper-air analyses. The climatology world be in a gridded format, calibrated against climatological summaries from radiosondes to enable estimates of conditions for arbitrary locations, dates and times. Techniques for synoptic and mesoscale inference of elevated duct behavior are demonstrated using satellite imagery and synoptic indicators. Geostationary satellite imagery obtained during VOCAR in 1993-4 revealed synoptic and mesoscale cloud features depicting space/time variability over the eastern Pacific Ocean and adjacent coastal areas. The variability was related to large-scale air mass changes and weather systems; the development, dissipation and translation of coastal eddies in the marine layer; and diurnal land/ sea breeze influences in the coastal zone.

## 1. INTRODUCTION

An important operational need of the Navy is the ability to anticipate and exploit radar propagation conditions over ocean and coastal regions where ducting and radio 'hole' phenomena are most prominent. These phenomena, caused by elevated refractive layers resulting from 'inversion conditions' in which warm, dry air overlays cooler, moist air, are strongly influenced by both large scale air mass conditions as well as mesoscale features induced by coastlines, mountains and islands. Any attempt to assess or forecast radio propagation conditions must therefore necessarily take into account the synoptic and mesoscale variability of the lower atmosphere. Over the open ocean, it is believed that the assumption of horizontal homogeneity is valid about 80 percent of the time for typical radio path lengths of importance to the Navy (Glevy, 1976). However, near fronts (air and sea), and in the vicinity of islands and coastal terrain, horizontal and temporal variations can be much more prominent.

Under the Navy's electromagnetic EM/EO Propagation Assessment Program, several approaches are being explored to obtain an assessment or prediction of atmospheric conditions in sufficient detail to estimate the occurrence, height and intensity of elevated ducts (Richter, 1994). One method (Burk et al, 1994), underway at the Naval Research Laboratory (NRL) in Monterey involves development of a high resolution numerical forecast model and data assimilation system in which all available observations are incorporated into a model forecast for use in range-dependent assessments of refractive structure. Another approach is represented by the Naval Air Warfare Center Weapons Division, Point Mugu, Geophysics Division's attempts to relate refractive structure to synoptic, mesoscale and satellite data parameters by application of statistical relationships established during work under the EM/EO Program. This effort is focused on the (generally) elevated ducts due to refractive (trapping) layers aloft; the behavior of the evaporative duct attached to the ocean surface is not considered. Implicit is a conceptual model of an elevated trapping layer associated with an inversion-dominated weather regime with low stratus or stratocumulus clouds that are lowest and flattest in the south-eastern parts of the sub-tropical oceans, closely associated with anticyclones (high pressure regions) where the overlying inversion is lowest and strongest. This general trend in both cloud and inversion characteristics correlates well with the occurrence, height and intensity of elevated ducts as observed in extensive radiosonde data sets from the eastern and central north Pacific Ocean. An initial effort to apply these weather-refractive relationships were described in a Refractive Effects Guidebook or "REG" (Rosenthal, 1976). This guide attempted to assign specific refractive (N-Profile) types to locations within various sectors of the sub-tropical oceanic high pressure belt and peripheral regions of disturbed weather using characteristic seasonal maps for different regions of the world. This initial REG was

*Paper presented at the Sensor and Propagation Panel Symposium on "Propagation Assessment in Coastal Environments" held in Bremerhaven, Germany 19-22 September 1994.*

found, however, to be overly ambitious in specifying detailed refractive profiles based on the guidance available. Subsequently, additional studies were performed (Helvey, 1981; Helvey and Rosenthal, 1983) to improve and determine additional relationships providing a more objective framework for the approach. Also, methods for inferring elevated ducting from weather satellite imagery were explored (Rosenthal et al, 1989; Rosenthal and Helvey, 1991). The improved guidelines were adapted by the Naval Pacific Meteorology and Oceanography Center at Pearl Harbor, Hawaii into a Horizontal Refractivity Depiction (HRD) procedure. In that form, an Independent Verification and Validation (IV&V) was performed (Vogel, 1992) under tasking from the Commander, Naval Oceanography Command, and the guidelines found to be statistically valid and useful. Accordingly, the (now) Commander, Naval Oceanography and Meteorology Command) CNMOC) declared the HRD techniques operational for the eastern Pacific Ocean. Since it was recognized that the full implementation of the updated REG techniques requires a level of skill or experience in satellite and synoptic/mesoscale interpretation that may at times exceed the skills of the anticipated user on a ship or ashore center, and also that a less manual-intensive approach is desirable, the Geophysics Division began preparing a version for incorporation into an automated, "expert" system. Conversion into a computer implementation which will eventually reside on TESS(3) is being carried out at NRL-Monterey with the technical coordination of NAWCWPNS and sponsorship of the Navy's Environmental Systems Program Office at the Space and Naval Warfare Systems Command. Termed Experduct (Peak, 1992), this system combines information entered by the operator from a variety of sources to furnish either current estimates or short-term predictions (to 72 hours) of elevated ducting conditions.

## 2. THE ELEVATED DUCT AND OCEANIC ATMOSPHERE

The elevated duct is a phenomenon arising from presence of a near-horizontal layer, generally at some altitude aloft, separating air of dissimilar refractive properties. Although it or the meteorological layer causing it may lie on the surface, it is more commonly found at the top of a more or less uniformly mixed depth of atmosphere known as the boundary layer, as opposed to the evaporative duct which always forms in direct contact with the ocean surface. The elevated duct can exert an important influence on propagation of radio/radar energy through the lower atmosphere, especially over oceanic or coastal locations where meteorological conditions are often propitious. Effects include major deviations in apparent target altitudes for height finder or tracking radars, anomalous propagation in the form of extended detection ranges for distant targets to transmitters, enhancements of surface clutter, and degradation of digital data transmissions due to multipath interference. Its presence is easily detectable in M-unit refractive profiles, generally derived from radiosonde measurements of pressure, temperature and humidity with altitude. Figure 1 shows an idealized representation of an elevated duct, shown both as N- and M-unit profiles, together with corresponding vertical distributions of temperature and dewpoint. A lower cool, moist layer with imbedded stratus/stratocumulus clouds is commonly capped by a temperature inversion and overlying warm, dry air mass. The altitude of the interface between the two is usually coincident with the so-called optimum coupling height (OCH), found at the base of the trapping layer, a zone of rapid vertical decrease in refractivity due mostly to the change from moist to drier air. Even when the vertical contrast in humidity and temperature is not sufficient to cause ducting, a super refractive layer is often present.

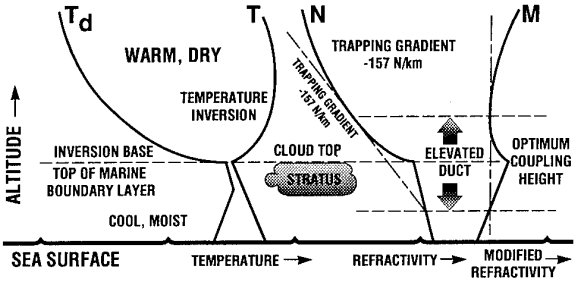


Figure 1. Idealized temperature and dewpoint profiles with elevated duct. Note that the top of the marine atmospheric boundary layer, the tops of marine stratus/ statocumulus clouds, and the base of the overlying temperature inversion are all at the same altitude.

### 2.1 Climatology

An elevated duct (or at least a super-refractive layer) is a widespread and relatively frequent occurrence over most of the world's ocean areas. Figure 2 illustrates global incidence for this condition, based on a 5-year set of worldwide radiosonde data compiled by GTE Sylvania (Ortenburger, 1978). Year-round geographical distribution varies markedly with both latitude and longitude. The general features of this distribution can be understood in terms of climatological patterns in sea surface and air temperature and hence potential moisture content and refractivity in the marine atmospheric boundary layer, and in relation to the general atmospheric circulation which is marked in temperate latitudes by a belt of higher pressure and warming aloft due to subsidence. The climatology for elevated ducting is particularly favorable over the eastern portions of the major ocean areas, where prevailing winds cause upwelling of colder water in the ocean along the continental margin, cooling the marine atmosphere from below and strengthening the vertical contrast in atmospheric properties. The Pacific Ocean offshore southern California and Peru experiences annual occurrences exceeding 60-70 percent due to these factors.

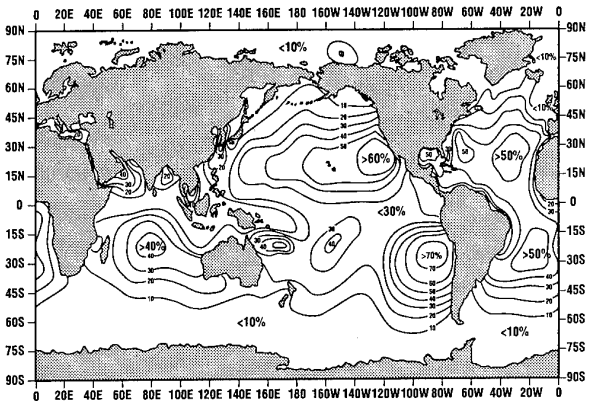


Figure 2. Global occurence of oceanic elevated ducts, annual incidence in percent (adapted from GTE Sylvania 5-year Radiosonde Data Analysis III, Ortenburger et al, 1978)

**2.2 Diurnal Variations**

In addition to this overall geographic variation in elevated ducting there is also strong evidence of diurnal and seasonal variability as well. Some of the apparent diurnal variation is instrumental or procedural in nature and is spurious. Other diurnal variability that has also been discovered by Helvey in 1994, is believed real, and is global in nature.

**2.3 Spurious Indications**

Evidence for systematic variations in elevated ducting characteristics can be found in radiosonde records. As with any compilation of data from meteorological or other instrumentation sensing the natural environment, it is important to be aware of idiosyncrasies in the measurements which may distort or invalidate the information obtained. Of particular interest in this regard is an apparent daytime maximum occurrence of ducts due to surface-based trapping layers computed from radiosonde data, but found to be an artifact caused by sensor errors exacerbated by routine measurement procedures (Helvey, 1983). Such a surplus of surface ducts is contrary to meteorological experience, which instead indicates that subrefractive conditions should commonly occur in daytime due to the strong vertical decrease in temperature normal at that time over land or even over the heated deck of a ship. Over the ocean it is more reasonable to expect very little or no discernible diurnal variation in any ducts due to surface-based trapping layers, because of the negligible variation in sea-surface temperatures over that short a time period.

**2.4 Evidence For Elevated Duct Diurnal Variations**

During analysis of radiosonde data for signs of correlation with various weather parameters useful for refractive diagnosis or forecasting over oceans, indications of a diurnal signal in elevated duct records were initially ignored as a statistical aberration, there seeming to be no artificial or natural mechanism to produce such a variation in refractive gradient in the free atmosphere. But it was eventually realized that there was nevertheless strong evidence for a widespread, systematic fluctuation in elevated ducting between night and day. Figure 3 presents summaries of data for various radiosonde sites from the GTE Sylvania (Ortenburger, 1978), 5-year data base (1966-69 and 73-74), selected to illustrate some interesting characteristics of this diurnal and seasonal behavior. The individual graphs are arranged approximately by relative geographical position, with name and location at the top. Average 3-monthly overlapping percent frequencies are plotted in pairs for each synoptic observation time, with 12Z on the left and 00Z to the right. The bars are shaded according to local time, dark to indicate nighttime (nominally 1800 to 0600) and daytime (0600-1800). Thus it will be noted that the dark bars denoting night are at 12Z, on the left for the dateline hemisphere sites (3a, c, d, e) and at 00Z on the right (3b, f) for the Greenwich meridian hemisphere sites. Figure 3a (SHIP4YP) represents the low occurrence of elevated ducting, with little diurnal variation, found at high latitudes. Figure 3b (Heraklion, Greece) shows a substantial seasonal variation with nighttime occurrences in late summer exceeding daytime by about 10% on the average. The general summertime maximum in occurrence is expected because low-level refractivity will increase as the sea surface warms, and heating of the surrounding land area and retreat northward of frontal storminess will result in prolonged fair weather with warm, subsiding air and small values of refractivity aloft. In Figure 3c (Eniwetok Atoll) the seasonal cycle is reversed, with the greatest occurrence and day-night deviations in winter. This can be explained by the site's near-equatorial location; in the northern hemisphere the proximity of the intertropical convergence zone and deep convective activity tend to lift, weaken, and frequently eradicate the elevated duct. Conversely, the equatorial site depicted in Figure 3e (Pago Pago) is in the southern hemisphere, so that the summer minimum occurs between November- April. Figure 3d (SHIP4YN) exhibits a seasonal variation with two maxima and minima, typical of intermediate latitudes with composite patterns; for these regions a general tendency for greater ducting occurrences in summer (as the sea warms and frontal activity retreats) is partially counteracted in mid-summer by weakening or elimination of the elevated duct due to occasional weather disturbances of tropical origin, Finally Figure 3f (Ascension Island) is one of a few sites where the diurnal bias is often in a sense opposite to most of the other locations; at present the reason for this is not known.

**2.5 Effect Of Overall Incidence On Diurnal Changes**

Although with few exceptions a fairly consistent day-night bias is apparent, the magnitude of the change is not comparable between many of the various sites, obviously because of geographical differences in overall incidence. Data for sites with synoptic observations at local time between 0800-1500LT and 2000-0300LT were examined, eliminating stations with probable ambiguous behavior because of local 00Z/12Z synoptic times too near sunrise or sunset. Figure 4 is a plot of 12-hour change in occurrence (all seasons) for the former sites,

against the corresponding 00Z + 12Z averages. There is considerable scatter, but the tendency for greater day-night change for sites with greater daily average incidence is clear.

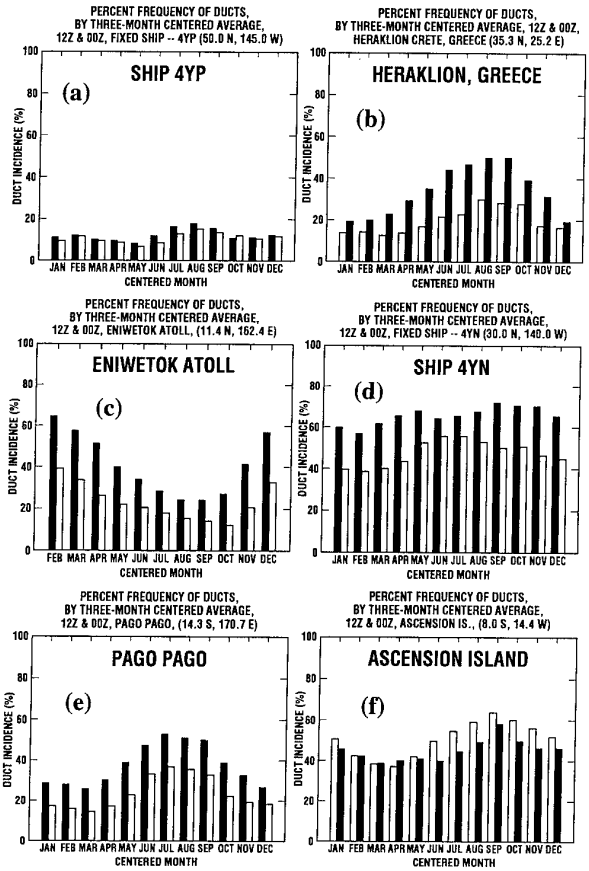


Figure 3. Percent incidence of elevated ducts for selected radiosonde sites, by month and time (00Z, 12Z). Local daytime observations are light bars, nighttime are dark bars. From GTE Sylvania 5-year data base (Ortenbuger, 1978). Station names and locations are indicated on each graph.

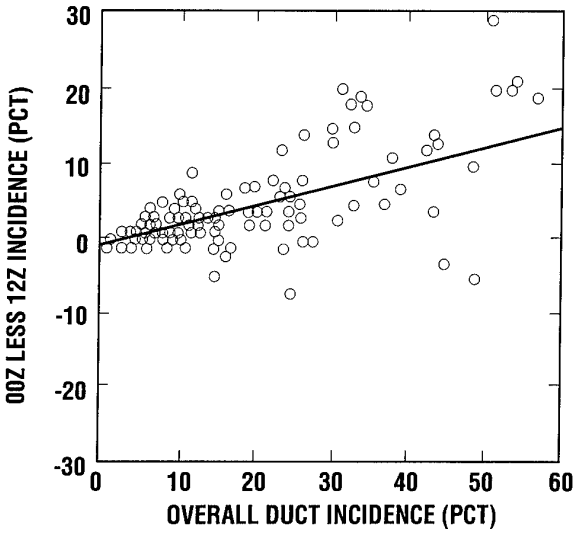


Figure 4. 12-hour changes in elevated duct occurence, versus average occurence (00Z+12Z). Sites with synoptic times 08-15 and 20-03LT

## 2.6 Dependance Of Change On Local Synoptic Time

The trend in the above data suggested normalizing the diurnal changes, dividing the daily average to obtain the relative change. figure 5 shows the relative night-day contrast for sites with average occurrences greater than 30 percent, plotted against local time of the 00Z and 12Z observations. Because of symmetry each data point is plotted twice; the 00Z-12Z change for a site also appears 12 hours later (earlier) with opposite sign. There is some indication that the phase may lag by an hour or so past noon/midnight, but the data which has so far been analyzed can be approximated by a simple cosine relationship. For any arbitrary local time, the deviation from the daily norm can be estimated as follows:

$$dF_{LT}=0.21*Fbar*Cos[LT-LT_{00Z}]*2pi/24$$

$dF_{LT}$=diurnal bias for local time LT

*Fbar*=average of 00Z and 12Z incidences

*LT*=local time for which estimate is desired, and

$LT_{00Z}$= local (standard) time of 00Z observation

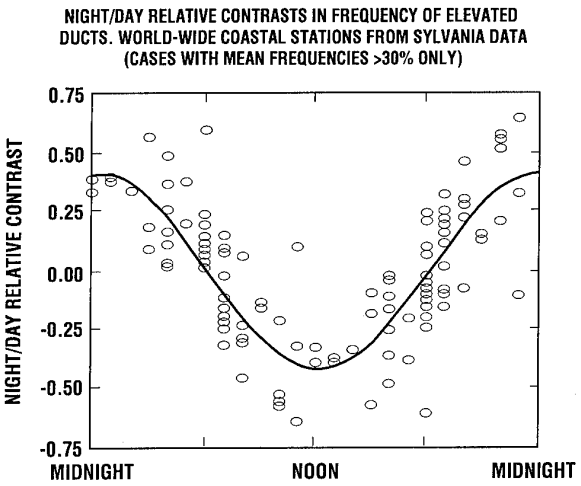


Figure 5. Relative night/day changes in elevated duct occurence, versus local time of synoptic observation (00Z, 12Z).

## 3. INTEGRATION INTO AUTOMATED TECHNIQUES

During the development of Experduct, a knowledge-based computer system that integrates the results of synoptic, satellite and statistical relationships into an expert system for predicting and assessing refractive conditions, it was determined that climatology should also be integrated as a fall-back parameter. As the input data used gets older and older, or the forecast gets further and further ahead in time their reliability becomes more subject to uncertainty and prone to the influence of small scale features. Thus, in such cases climatology should be given more weight. As described by Helvey and Rosenthal (1994), climatology was therefore included as

an additional objective element to improve the Experduct approach. Figure 6 shows one of the output windows in which climatology is included as a factor.

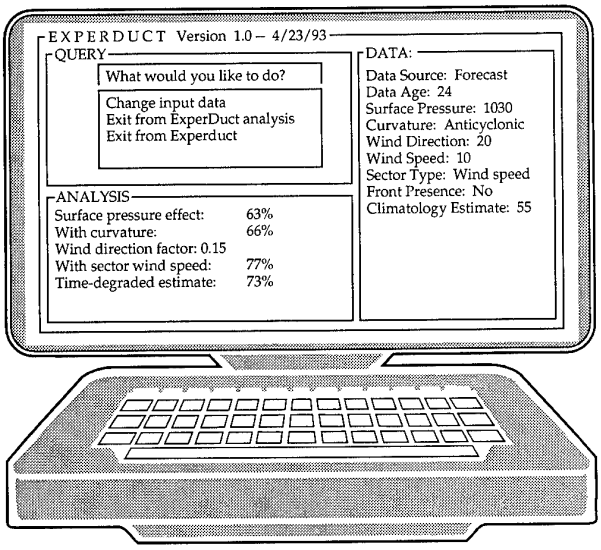


Figure 6. Sample Experduct screen showing duct forecasts with climatology built in.

also being explored as the basis for a first guess estimate for extrapolating climatological elevated duct statistics over data-sparse ocean regions.

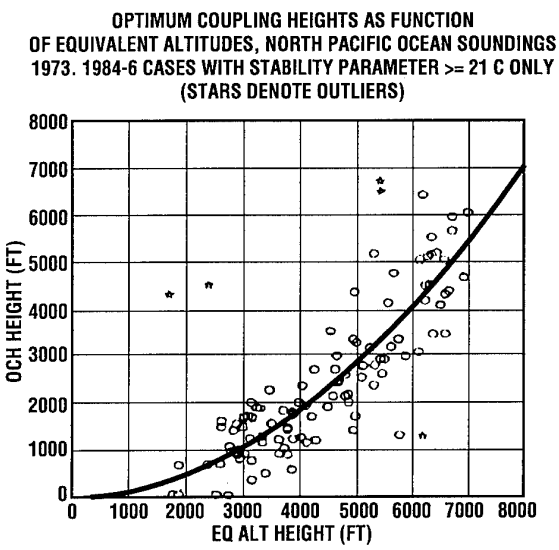


Figure 7. Optimum coupling height versus equivalent altitude.

The other factors are principally synoptic or satellite features which relate the incidence, height and strength of ducts to air mass and frontal features. As described in previous studies, one of the strongest parameters in this category to correlate with ducting was surface pressure. With the introduction of a weighting scheme in Experduct, pressure was one of several parameters blended together to result in a cumulative duct probability estimate. At ship "N" (30°N, 140°W) for surface pressure by 5 mb classes, almost no duct occurrences were noted for pressures below 1005 mb, and the smooth increase in occurrence rate levels off after about 1022 mb.

## 4. EQUIVALENT ALTITUDE TECHNIQUE

In addition to Experduct, another automated technique in which duct occurrence and height is linked to synoptic parameters is termed equivalent altitude. Using the hydrostatic assumption and a single two-layer representation of the lower atmosphere, it is possible to calculate the altitude of the interface between the layers, if temperature and pressure/height at reference levels above and below the region of interest are known (Helvey, 1979). Given 700 mb and 1000 mb data this equivalent altitude so obtained can be used to estimate the height of the inversion base and accompanying duct optimum coupling height. Statistical analysis of historical data sets provides the basis for determining optimum coupling height, given Equivalent Altitude, as illustrated in Figure 7. The likelihood of a duct aloft can be estimated from climatology, reinforced by consideration of the overall stability of the 1000 mb-700 mb layer; ducting is favored by large stabilities (temperature increase with height). This technique is

## 5. CONNECTION OF DUCTING TO LOW CLOUD BEHAVIOR

The tendency for nighttime formation and daytime dissipation of marine layer cloudiness is well known in southern California or other regions with similar climate. Figure 8 is a visual image obtained from a GOES weather satellite. It shows a portion of the typical stratus/stratocumulus cloud regime overlying the eastern Pacific Ocean. The widespread, flat-topped low cloudiness give visual evidence of the high humidity and refractivity conditions pervading the marine layer, while the lack of higher clouds suggests the apparent stability, dryness and low refractivity of the overlying air mass.

The cyclic diurnal variation of this cloudiness is especially manifest in the coastal zone, because of daytime subsidence related to the sea breeze circulation, and inland due to eradication of the marine layer over the heated land surface (Lee, 1979). It is also quite significant over the open ocean as radiational heat absorbed by the low clouds effectively raises the condensation level and reduces the area covered by clouds. Simon (1977) described the mean change in cloudiness in percent offshore southern California from morning to afternoon during the summer of 1975. Over a large portion of the area decreases of 10 percent or more were indicated, and would presumably be greater if the times of maximum and minimum cloudiness were represented.

The regular changes in temperature and humidity which accompany, or cause this variation in cloudiness imply concurrent variations in refractivity. Nighttime radiational cooling of the clouds tends to strengthen the

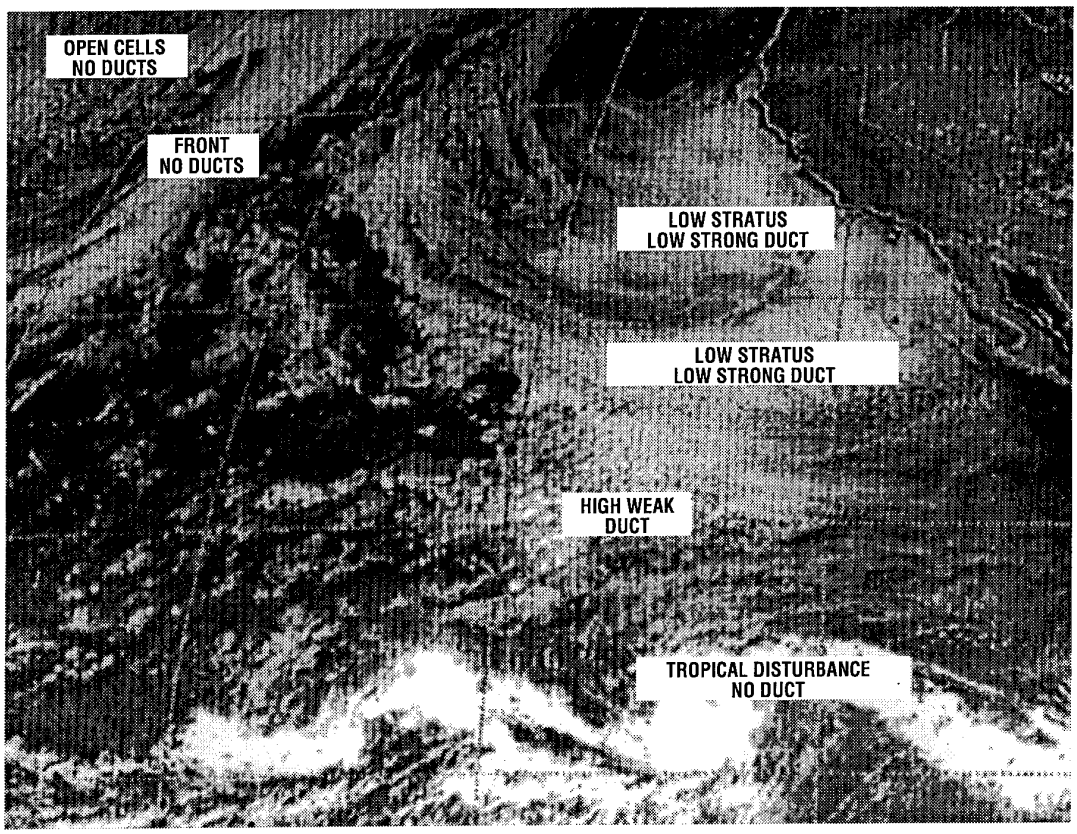


Figure 8. GOES visual image over Northeastern Pacific, for 20:15Z 29 Sep 1975. Clouds appearance correlates to duct characteristics.

vertical refractive contrast; daytime dissipation tends to reduce it. Statistics for several atmospheric and elevated duct parameters derived from an on-going study of worldwide ship radiosonde data support this idea. For a region of the northeastern Pacific Ocean bounded by 30-40N and 140-150W, where the 00Z observations are during the day (1400-1440LT) and 12Z at night (0200-0240LT), the modified refractivity at the top of the duct and trapping layer, and at the OCH or bottom of the trapping layer, both increase from day to night. The change is greater for the OCH which is also at the top of the marine layer. This would increase the likelihood and strength of the elevated duct in the sense discussed previously. Increases in the height of the duct top and OCH are also indicated from day to night, presumably reflecting growth in depth of the marine layer during the reformation of marine clouds. Nighttime cooling occurred at both levels, and mixing ratios (a measure of water vapor content) increased. The nighttime increase of 17 percent in relative humidity is in qualitative agreement with the cloud observations.

## 6. SATELLITE INFERENCES

Since the availability of meteorological satellite data in the 1960's, scientists and operational personnel have been able to view atmospheric circulations remotely in a way that allow the total spatial extent of systems to be defined including details of structure, circulation, and very importantly, an understanding of the relationship between neighboring cloud features.

Satellite imagery also promotes an understanding of the influences that large scale (synoptic) and mesoscale and topographic features exert in shaping cloud patterns. Through use of multi-spectral data quantitative information can also be extracted. One of the operationally important features that satellite data can help diagnose and predict is the elevated duct.

Previous work by Helvey, Rosenthal and Lyons established the feasibility of relating parameters from routine weather charts (both analyses and forecasts), and meteorological satellite data to the occurrence, height and intensity of refractive layers responsible for ducting and anomalous radar propagation.

In general, large regions of stratus that form in the marine layer beneath the subtropical inversion are a signature for regions of elevated ducting. As from Figure 1, the OCH, cloud top and inversion base/marine layer top are co-located. While the existence of stratus is an indication of highly probable duct occurrence, the appearance of the stratus/stratocumulus reveals information on both the height and intensity of these elevated ducts as established by Rosenthal, Westerman and Helvey (1985).

A general synoptic refractive model was developed by

Rosenthal and Helvey, which has been in operational use by the Navy at Pearl Harbor. This is shown in Figure 9 which relates refractive conditions under both elevated duct height (ZD) and uniform 'standard' conditions to the relative positions, sections and proximities of sub-tropical anticyclones, fronts and low-pressure areas. This model is useful for making real-time estimates or forecasts of duct conditions from either synoptic analyses or progs.

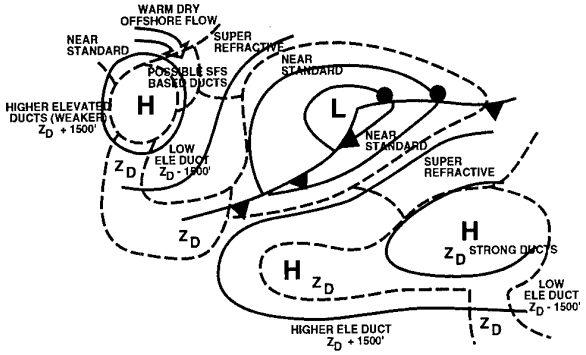


Figure 9. Schematic model relating duct height ($Z_D$) and refractive structure to synoptic air mass conditions.

Satellite data can be even more useful for 'real-time' diagnosis because the details of the cloud patterns are readily discernible, particularly on the visible imagery. The relationship between cloud features and estimated elevated ducting is revealed in Figure 8 which shows the impact of synoptic scale variability.

## 7. APPLICATION OF SATELLITE AND OTHER TECHNIQUES TO ASSESS DUCT VARIABILITY DURING VOCAR

During VOCAR in the spring, summer, and fall of 1993 geostationary satellite data was particularly useful in identifying and describing most of the large and small scale airmass influences and features which resulted in the variation of refractive structures that were observed during these periods. For instance, there were several passages of cold fronts which replaced stratified inversion conditions which favor ducting with deeper, more mixed, marine layers. These situations were revealed on satellite imagery by the sequential changes in the brightness, character and size of the cloud elements within the stratus layer.

However, there were also changes of a more subtle nature synoptically, which had a large influence on the distribution of stratus. These were marked by little height change at specific stations. However, changes in the distribution and relative position of highs and lows resulted in changed wind flow, and these in turn were responsible for altering the stratus distribution.

Since specific data on cloud and duct height was largely unavailable over the open ocean, the IR duct height techniques developed by Lyons (1985) and Helvey (see Rosenthal and Helvey, 1991) was used as a diagnostic analysis tool. The basis of the IR duct technique is the conversion of cloud-top temperature observed by satellite, to estimated duct height based on statistical relationships between inversion base altitude and relative temperature as derived from radiosonde data (see Figure 10). The IR duct technique was used to estimate the duct heights during the VOCAR period, and reveal the low-level changes induced by changes in the upper level patterns.

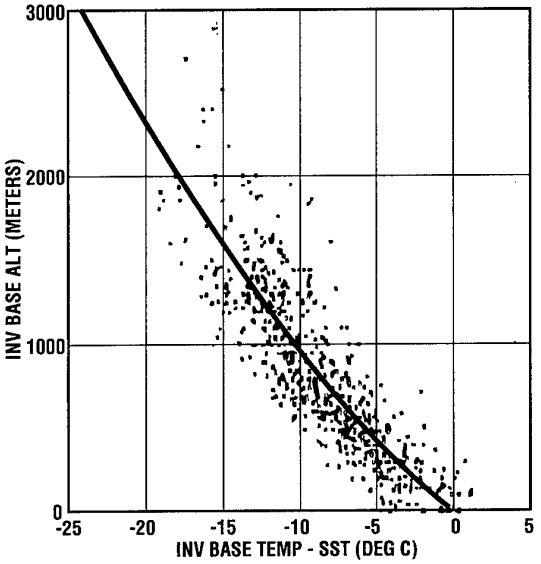


Figure 10. Inversion base altitude versus temperature relative to surface (SST).

One of the interesting days during this period was August 24, 1993. As seen in the surface analysis prepared by the National Meteorological Center (NMC) for 00Z 25 August (Figure 11), the strong Pacific sub-tropical anticyclone was ridging into the Pacific NW states of the U.S. behind a stationary front which stretched from south-central Canada to western Nevada.

Corresponding NMC 500 mb analyses at 00Z on 25 August (Figure 12) revealed high pressure holding over the eastern Pacific and U.S. southwest but with a sharp trough north of 40N with coldest air near the Washington/Idaho border with Canada. The analyzed surface front lay under moderate west to southwest flow around the trough. However, satellite data shows a much more complete and definitive picture. Visual GOES satellite imagery (Figure 13) revealed a much larger NE-SW oriented band of higher clouds corresponding to the upper level remains of the front, with the band stretching across the western U.S. and approximately 500 miles out to sea as compared to NMC analyses which ended the front at the California border with Nevada.

Near simultaneous IR imagery (Figure 14) at 0230Z on the 25th shows the same band of clouds as a bright white (cold cloud top) feature. To the south of the front, from the coast and extending south and westward is a large mass of stratus and stratocumulus. In accordance with

the previous studies, the stratus is lowest near the coast on the eastern side of the Pacific sub-tropical anticyclone, and increases in height as the marine layer deepens over warmer and warmer waters. As previously described by Rosenthal, Westerman and Helvey (1985), the increase in height of the low clouds accompanying the deeper marine layer and higher inversion is also revealed by an increased closed cellular structure with elements getting larger and larger as the clouds get higher and higher. Estimates of duct (OCH) height variability derived from using the IR duct technique are shown superimposed on the clouds in Figure 14.

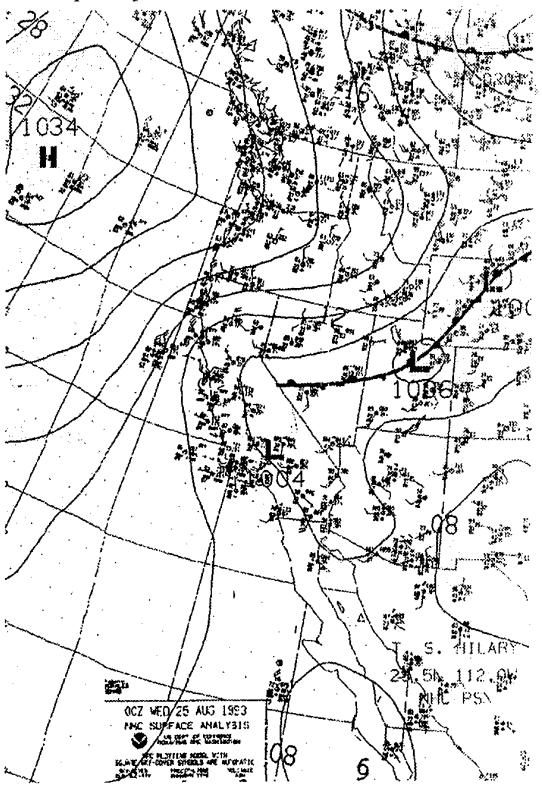


Figure 11. NMC surface analysis for 0000Z 25 August 1993 showing high pressure cell over eastern Pacific Ocean and stationary front across Nevada in U.S.

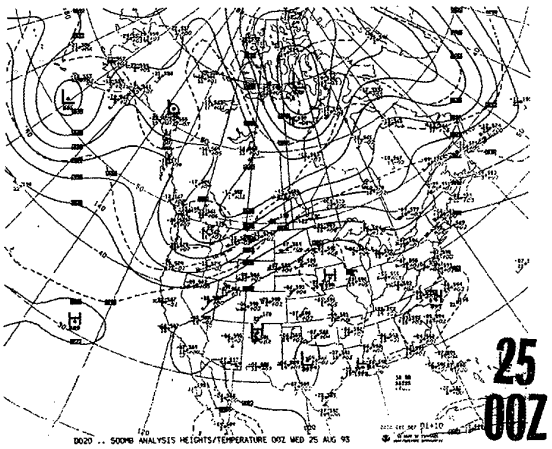


Figure 12. NMC 500mb analysis for 0000Z 25 August 1993 showing sharp trough north of 40N over U.S. Pacific northwest.

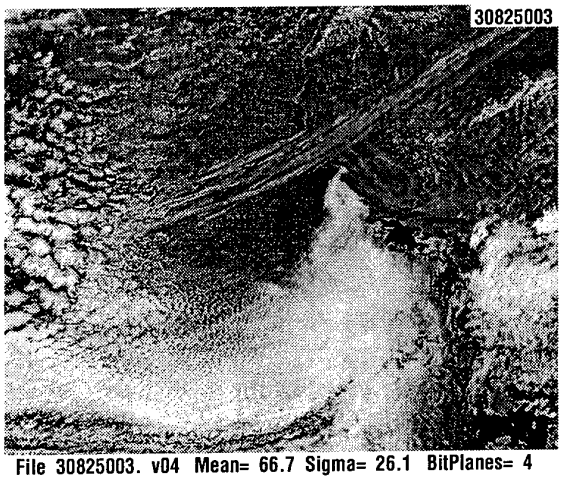


Figure 13. Visual GOES satellite image at 0030Z 25 August 1993 showing much longer frontal remnant across the western U.S. and out into the Pacific with stratus covering lower latitudes

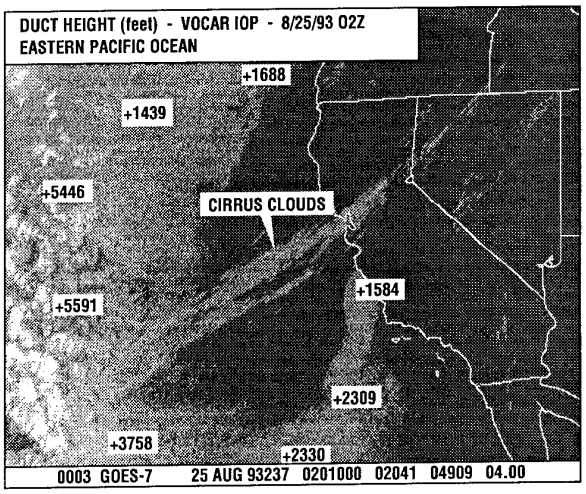


Figure 14. Infrared image at 0230Z 25 August 1993 showing frontal remnants. Superimposed on stratus and stratocumulus over Eastern Pacific Ocean are duct heights calculated by the IR duct technique.

Heights near the coast are around 1600 feet. These increase to over 2300 feet near longitude 130 west and then increase to neat 3800 feet to the west and to 5600 feet where the cells become bright. Behind the front is a clear region with duct heights of only 1400 to 1700 feet under the next upstream anticyclone. The IR duct technique becomes a convenient way to convert the clearly defined cloud patterns on satellite data to estimated but quantitative results.

On the subsequent day near 00Z of 26 August much of the sharp delineation between stratus and mostly clear conditions resumed, even though the frontal clouds had already moved east and dissipated. Thus the impact on stratus and ducting often remains, after the synoptic upper level features which influenced it changed.

Satellite data was also instrumental in revealing an interesting period of change in which a weak low pressure area formed, moved contrary to the normal west

to east flow, and resulted in major changes in stratus and duct conditions along the U.S. west coast and eastern Pacific Ocean. As before, it appears that the impetus for the surface features began with an upper level influence. Figure 15 shows the NMC 500 mb analyses for 00Z 29 August 1993. A strong high enveloped much of the northeastern Pacific Ocean with high heights and anticyclonic conditions prevailing over most of California. However, a sharp short wave trough centered over northern Idaho was eroding the eastern part of the ridge. By the following day (Figure 16), the ridge had sharpened into the Gulf of Alaska, heights fell slightly over California and a region of troughing or more cyclonic conditions began to form from California westward. The tendency for the more cyclonic conditions continued over the next several days with a weak surface low forming near the coast which retrograded westward to the south of the Gulf of Alaska high. This series of events then resulted in the wind flow becoming stronger and more southerly along the coast (Figure 17) and could be expected to result in low-level convergence with a deepening of the marine layer at low levels.

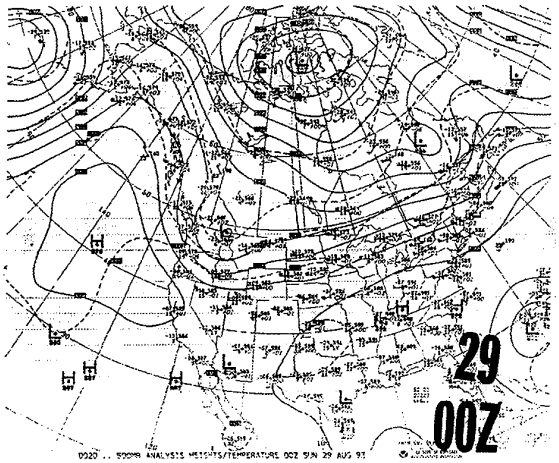


Figure 15. NMC 500 mb analysis for 0000Z on 29 August 1993 showing ridging in the Gulf of Alaska and trough over Pacific Northwest.

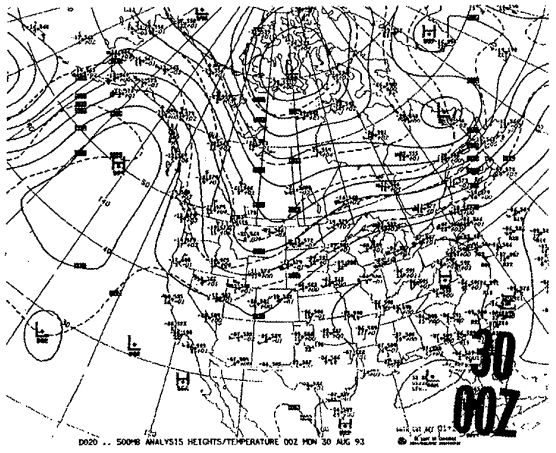


Figure 16. NMC 500 mb analysis for 0000Z on 30 August 1993 showing a sharper ridge in the Gulf of Alaska, and more cyclonic conditions over the U.S. west.

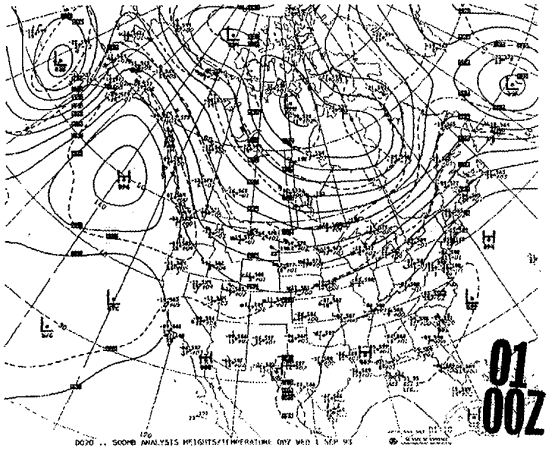


Figure 17. NMC 500 mb analysis for 0000Z on 1 September 1993 showing southerly flow and increased cyclonic conditions over the eastern Pacific Ocean.

Figure 18 shows the surface low pressure region at 00Z on 01 September 1993 that formed in response to the increased cyclonic conditions, after it had moved westward from the coast. The presence of the low at the surface could be expected to raise and deepen the stratus and thereby further elevate ducting conditions.

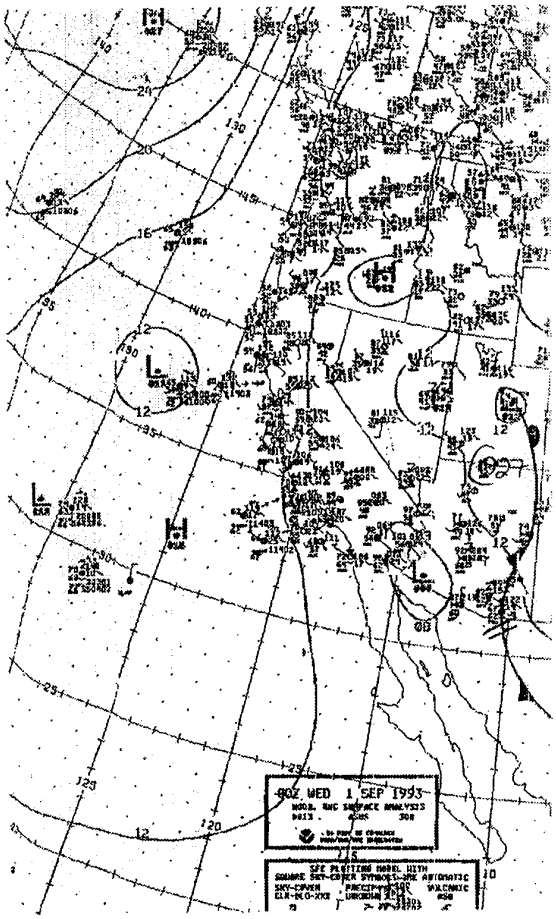


Figure 18. NMC surface analysis for 0000Z on 1 September 1993 showing surface low pressure region off Northern California that formed in response to cyclonic conditions aloft

Figure 19 (a through g) shows a sequence of visual GOES images approximately 24 hours apart which shows the changes in the stratus during this event. At 0030Z on 28 August (Figure 19a), relatively open conditions prevailed along most of the California and Baja coast with large stratus sheets mainly several hundred miles to sea. At 0030Z on the 29th (Figure 19b) when conditions aloft began to get more cyclonic, there was a marked increase in stratus offshore of southern California, and a narrow strip of stratus had formed along the coast up to Monterey Bay. By 24-hours later at 0030Z on the 30th (figure 19c), the increase in stratus coverage and density was dramatic all the way up to northern California, and cyclonic curvature at the edge of the cloud mass off northern California revealed the early formation of the low at the surface. Another day later (2330z on the 30th, Figure 19d), and the low was further defined as revealed in the sense of curvature of the thicker stratus/stratocumulus elements, and the feature had moved significantly westward. As it did, afternoon stratus became less prevalent along the coast in the drier more unstable air.

By 0030Z on 1 September (Figure 19e), the surface low had enlarged and stratus masses were characteristically large and dense within the circulation, while drier, clearer conditions prevailed along nearly all of the California coast and considerably to sea.

A day later at 0030Z on 2 September (Figure 19f), showed the remains of the low well out to sea with stratus broken up into large, fairly high, dense pieces but with clear conditions prevailing along southern and central California and well out to sea. Off Baja, far removed from the effects of the low pressure influence, a much lower and more uniform sheet of stratus began to spread northward as anticyclonic conditions aloft again took over.

Finally in the sequence nearly a day later at 2330Z on 2 September (Figure 19g), with the remains of the low evident by blotches of high, dense stratocumulus far out at sea, most of the coastal and Eastern Pacific area was re-enveloped by a uniform, low stratus sheet as anticyclonic conditions and increased subsidence returned.

To illustrate the effect of these changes on duct height, several areas of cloud were selected for analysis on IR data using the IR duct technique. These are shown in Figure 20 a through g. The IR duct heights were derived from concurrent GOES IR imagery with OCH height values rounded off to the nearest hundred feet, and plotted atop the visual images. Appreciable changes in duct elevation were revealed which coincided with the changes observed aloft and in the satellite imagery.

For instance, at 0000Z on 28 August, derived duct heights in the stratus region several hundred miles west of central California, were near 2600 feet, while in the region west of southern California, duct heights increased from 2500 feet to 3400 as one goes southwestward towards bigger cloud cell sizes and warmer ocean waters (deeper mixing). A region of stratus off Baja California with much smoother structure and smaller cells is lower and duct height estimates there are only 1100 feet, consistent with typical duct heights on the southeast side of the sub-tropical anticyclone near the southern California/Baja coast.

At 0000Z on 30 August, the development of the low pressure area off northern California and the greater, denser stratus clouds in the deeper marine layer are reflected in duct heights there of around 2000 feet increasing again to around 3500 feet with proximity to bigger cloud cells and warmer waters towards the southwest. Also, off Baja and southern California within smoother looking smaller celled stratus clouds, duct heights were estimated by the IR duct technique to be around 1600 to 1700 feet.

At 2300Z on 30 August, as the low continued to develop as it moved westward, estimated duct heights increased near the low to 3100 to 3600 feet, and in the warmer waters of the Pacific to 4300 feet. Meanwhile close to the Southern California coast, they were near 1700 feet.

A day later at 0000Z on 01 September 1993, continued retrogression, deepening and expansion of the low resulted in duct height near the low center of 4300 feet with lower heights to the west (3700 feet) and southeast (3100 feet). Duct heights in the stratocumulus region in warm waters marked by large cell sizes were estimated to be 5300 feet. In the smoother, lower stratus just off Baja California, duct heights were only 1800 feet. By 0000Z on 02 September 1993, low clouds in the vicinity of the low had risen to over 6000 feet, while closer to the coast, low stratus had expanded in the subsiding air there. At 0000Z on 03 September, a low-level streamline analysis prepared by Eddington, Figure 21 shows the return of the divergent flow near the surface which is so typical of stratus conditions there.

In this sequence, the IR duct height provided reasonable estimates of duct OCH throughout the region of study with results that were consistent with prior studies showing duct height increasing with increasing stratus/stratocumulus cell size and 'denser' clouds, and with development of low pressure centers which tend to deepen marine layers. Moreover, the results for this period were also consistent with seasonal and climatological considerations.

Based on the limited data examined here, and prior studies, it appears that the IR duct technique is an excellent assessment tool in mapping out duct height variability over stratus covered ocean areas and is

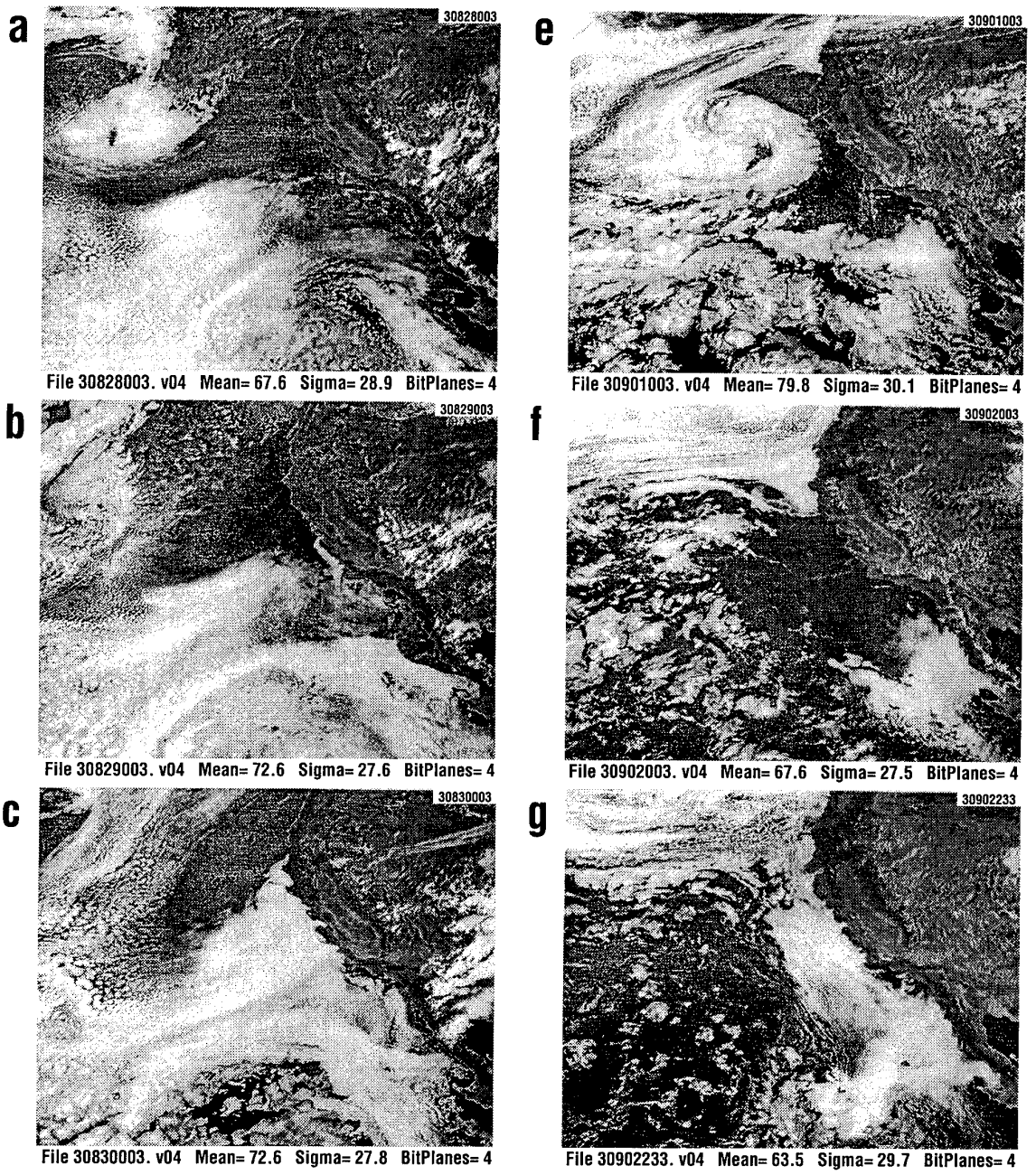


Figure 19. Sequence of GOES visual satellite images approximately 24 hours apart from 0030Z 28 August through 2330Z on 2 September showing the deepening of the marine layer associated with the low formation and westward movement off Northern California, and the subsequent re-formation of low stratus along the coast at the end of the period.

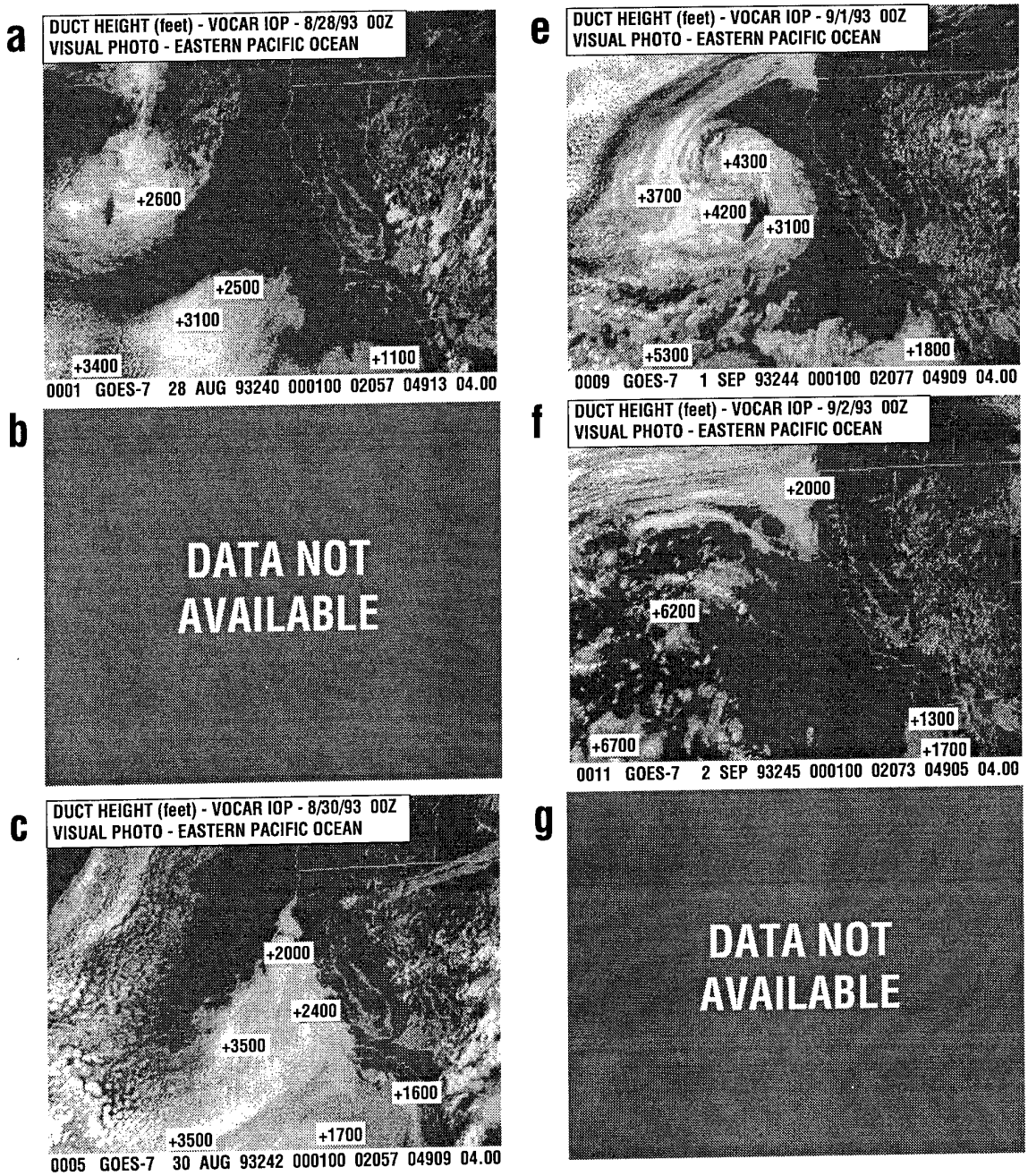


Figure 20. Same GOES images as figure 19 with duct heights estimated using the IR duct technique derived from corresponding infrared data (when available) superimposed on the visual imagery. The changing duct heights are a result of the synoptic and mesoscale changes which occurred over the Eastern Pacific Ocean.

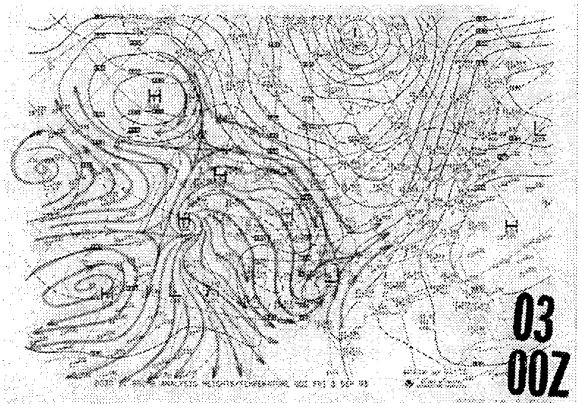


Figure 21. Low-level streamline analysis by Eddington for 0000Z 1 September 1993 superimposed on NMC 850 mb analysis. The streamlines reveal the return of the divergent flow near the surface typical of stratus conditions there.

extremely valuable in demonstrating the influence of synoptic and mesoscale change on duct height.

## 8. SUMMARY

A variety of climatological, statistical, satellite and automated techniques have been developed which describe the variability of elevated ducting in historical, synoptic and mesoscale time and space scales. Most of these are being incorporated into Experduct, an automated knowledge-based predictive and assessment system. One of the most promising of these tools is the IR duct technique which produced realistic duct heights over open ocean areas when applied to several periods of synoptic and mesoscale change during VOCAR. For forecasts beyond 48 hours, climatological statistics have been increasingly blended in to keep predictions realistic. The climatological statistics include a global diurnal variability of duct occurrence recently discovered by Helvey.

## 9. REFERENCES

Burk, S., Thompson, W., Cook, J., and Love, G., "Mesoscale Modeling of Refractive Conditions during the VOACR Experiment", IGARSS 1994.

Glevy, D.F., An assessment of radio propagation affected by horizontal changes, Naval Electronics Lab Center TN 3153, May 1976.

Helvey, R.A., Diagnosis of elevated ducts by means of equivalent altitude, Proceeding of Conference Atmospheric Effects Assessment, 23-25 January 1979, NOSC Technical Document 260, 15 June 1979.

Helvey, R.A., Effect of surface parameters on elevated duct occurrence and altitude, Pacific Missile Test Center, CA, Tech. Pub. TP-81-26,1981.

Helvey, R.A., Radiosonde errors and spurious surface-based ducts, Proc. IEE, Vol. 130, Part F, No. 7, pp 643-648, 1983.

Helvey, R.A. and Rosenthal, J.S., Guide for inferring refractive conditions from synoptic parameters, Pacific Missile Test Center, Tech. Pub. TP-5, 1983.

Helvey, R.A., Diurnal Variation in Oceanic Elevated Ducting, BLOS Conference, 1994.

Helvey, R.A. and Rosenthal, J.S., Guidance for Expert System Approach to Elevated Ducts Assessment over the Northeastern Pacific Ocean", Proc. IGARSS'94, 1994.

Lee, Thomas, F., Diurnal variations of coastal stratus, Pacific Missile Test Center, Point Mugu, CA TP-80-02, 1979.

Lyons, S.W., Satellite derived refractive duct height estimates, Pacific Missile Test Center, Geophysical Sciences TN 98, 1984a.

Lyons, S.W., SPADS automated duct height statistics, Pacific Missile Test Center, Geophysical Sciences TN100, 1985.

Ortenburger, L.N., et al, Radiosonde data analysis III, Contract MDA-904-78-C-0511, GTE Sylvania, Mountain View, CA, 1979.

Peak, J.E., Experduct: a prototype expert system for analysis and short term prediction of atmospheric electromagnetic ducting conditions, Computer Sciences Corporation, Naval Oceanographic and Atmospheric Research Laboratory, TN258, May 1992.

Richter, J.H., Structure, Variability and Sensing of the Coastal Environment, AGARD, CP567, pp. 1.1 - 1.13, 1994.

Rosenthal, J., "Refractive Effects Guidebook REG", Pacific Missile Test Center, Point Mugu, California, published by Naval Environmental Prediction Research Facility, Monterey, California, promulgated as COMTHIRDFLEET TACMEMO 280-1-76, 1976 (canceled in August 1985).

Rosenthal, J., Westerman, S., and Helvey, R.A., Inferring refractivity conditions from satellite imagery, Pacific Missile Test Center, Geophysical Sciences TN96, 1985.

Rosenthal, J., Helvey, R.A, Lyons, S.W., Fox, A.D., Szymber, R., and Eddington, L., Weather Satellite and Computer Modeling Approaches to Assessing Propagation over Marine Environments, AGARD CP-453, pp 47.1-47.15, 1989.

Rosenthal, J. and Helvey, R.A., Refractive assessments from satellite observations, AGARD CP-502, pp 8.1-8.9, 1991.

Simon, Richard, L., The summertime stratus over offshore waters of California, Monthly Weather Review, Vol. 105, No. 10, pp 1310-1314.

Vogel, G.N., A Horizontal Refractivity Depiction Product: An Evaluation, Naval Oceanographic and Atmospheric Research Laboratory, Monterey, CA, TN284, 1992.

## DISCUSSION

**W. OLSEN**

I was fortunate to be in the right place at the right time to have the opportunity to lead a group of Navy operational forecasters in applying and testing the forecast guidelines Jay Rosenthal and his associates at NAWC Point Mugu and NRaD San Diego have developed. For about a two year period, Naval Pacific Meteorology and Oceanography Center at Pearl Harbor produced a daily analysis and 36 hour forecast graphic for the Eastern Pacific Ocean, named Horizontal Refractive Depiction or "HRD". As a result of several on my boss' staff being pessimistic that refractivity forecasting is possible, we were required to undergo a rigorous independent verification and validation (IV & V). I am happy to report that the results were positive and our forecast accuracy was better than climatology, and thus considered to be tactically useful. Do you believe your techniques are applicable to other areas of the world and not just the Eastern Pacific? And secondly, when do you expect EXPERDUCT to be available for use by the operational forces?

**AUTHOR'S REPLY**

The basic meteorological processes must be the same from region to region; in fact that allows us to generalize the techniques. Data from the North and South Pacific, North and South Atlantic, Mediterranean and Indian Ocean all went into the development of the refractive-synoptic parameters. However, while the basic meteorological processes are similar, there are major differences from region to region on how topography and local wind patterns influence refractive structure, and govern the sequences of events. So it is essential that EXPERDUCT be developed regionally. We expect the first regional EXPERDUCT to be available in 1996 with new regions added approximately each year. Thank you again for your support, interest and valuable inputs.

**D. DOCKERY**

Please comment on the possibility of determining when elevated ducts become surface-based ducts, since surface-based ducts have much stronger impacts on ship systems.

**AUTHOR'S REPLY**

When ducting is surface or near-surface-based, stratus appears much more uniform and smooth, and according to the subjective/objective model, can indicate these very low ducts from pattern recognition. The IR-duct technique similarly can assign a very low or near-surface value because as the inversion and associated duct become very low, the cloud top temperature becomes warmer than at higher attitude. The IR-duct technique estimates duct height from the cloud top temperature. Both techniques require the presence of stratus or stratocumulus clouds.

# A FLIR Case Study Using the Electro-Optical Tactical Decision Aid (EOTDA) Mark III

**Charles P. McGrath**
Ocean and Atmospheric Sciences Division
NCCOSC RDTE DIV 543
53170 Woodward Road
San Diego, CA 92152-7385
USA

## SUMMARY

This report compares measured forward-looking infrared (FLIR) system detection ranges of a target ship, the Research Vessel *Point Sur*, with predictions from the Electro-Optical Tactical Decision Aid (EOTDA) version 3.0. The EOTDA was primarily developed by the Air Force, with only minimal attention applied to the complexities of the marine environment. The objective of this case study was to evaluate the infrared EOTDA performance for a target in an open ocean background.

Surface meteorological and navigation data were recorded aboard the *Point Sur*. Eight FLIR missions were flown making 57 detection range measurements. The meteorological and navigation data were input to the EOTDA, and the prediction ranges were tabulated and compared with the reported FLIR data. Results showed reasonable accuracy during the clear-weather portion of the tests, but the EOTDA grossly overpredicted detection ranges when a stratus cloud ceiling prevailed. Attempts to determine integrated target temperature from thermistors mounted on the surface of the ship structure were unsuccessful. Since calibrated target and background temperatures were unavailable at the times of the FLIR detection range measurements, it was not possible to isolate the portion of the EOTDA most responsible for the overpredictions. However, the transmission model, LOWTRAN 7, has been thoroughly exercised and is well accepted. The target model (TCM2) of the EOTDA performed well in another case study [1] during the same field tests. This would make the water background model of the EOTDA most suspect. Further investigation of the water, sky, and cloud radiance models of the EOTDA is recommended, especially in the marine environment.

## 1. BACKGROUND

### 1.1 EOTDA OVERVIEW

Strike warfare planning and vulnerability assessment relies on software-driven tactical decision aids (TDAs). The EOTDA Mark III [2] is a microcomputer code that was developed through the coordinated effort of several contractors and agencies as a strike warfare planning tool. Hughes STX Corporation, under the direction of the Air Force Phillips Laboratory, brought the final product together. The EOTDA has been adapted to a workstation platform for inclusion into the Tactical Environmental Support System version 3.0 (TESS(3)) and the Tactical Aircraft Mission Planning System (TAMPS) version 6.0, under the direction of Naval Research Laboratory (NRL), Monterey, California. The EOTDA is also being marketed globally by Hughes STX Corporation.

The EOTDA predicts the performance of a variety of electrooptical sensors against a variety of user-defined targets and backgrounds. The EOTDA supports three optical regions, the long-wave infrared (8-12-μm), visible (0.4-0.9-μm), and laser (1.06-μm). The sensors include long-wave IR, television, laser, and night-vision goggles (NVGs). The Navy, under the direction of NRL Monterey, leveraged upon the Air Force effort by adding Navy and Marine Corps sensors and targets to the already developed software. Sensors were added for several naval air platforms (e.g., A-6E, FA-18, P-3C, and F-14). Two ship targets (a frigate and a gunboat) have been added, and a user-definable generic ship model developed by Georgia Technology Research Institute (GTRI) is currently being implemented.

IR sensor performance is greatly influenced by environmental conditions. The meteorological input parameters drive the calculations of target and background radiance and atmospheric transmittance. The calculations are computationally intensive. Compromises were necessary to afford reasonable computer run-times and to accommodate the intended operating platform, which was a personal computer with an 80286 microprocessor running under MS DOS. Therefore, a simplified two-layer version of LOWTRAN 7 [3] determines the atmospheric transmittance, and the EOTDA target and background model employs the intermediate grade of TCM2 [4] instead of the more refined research grade software.

*Paper presented at the Sensor and Propagation Panel Symposium on "Propagation Assessment in Coastal Environments" held in Bremerhaven, Germany 19-22 September 1994.*

The target and background thermal contrast model, TCM2, was developed by Georgia Technology Research Institute. TCM2 is a first-principles model. It treats the target and background as a series of three-dimensional isothermal spatial nodes with specific material properties. After a steady-state initialization process, an energy balance solution using the laws of heat transfer are applied to the thermal network to determine the nodal heat transfers. Finally, the radiance values are calculated in the desired wave band for each node. The radiance values of the node facets that are visible in the field-of-view of the sensor are integrated to determine the overall target radiance. The intermediate grade TCM2 uses a one-dimensional solution and allows fewer nodes, thus limiting target resolution compared with the research grade TCM2. The background is modeled as a single homogeneous node resembling an isothermal plate surrounding the target, and the sky is considered a uniform hemisphere covering the target. The complexities of the background and sky, such as clutter, sea-surface wave-slope reflections, and diffuse scattering and cloud effects are ultimately combined into a homogenized background solution. The difference between the uniform background radiance and the integrated target radiance determines the zero-range thermal contrast. Whether this thermal contrast is representative of the real-world scene depends on many conditions, such as scene complexity, human perception, and cueing factors.

User inputs to the EOTDA are entered through a combination of menu selections, keyboard entries, and graphical positioning with a mouse. Temperatures are entered by pointing a mouse at the desired position on a graph. The wind, rain, cloud, visibility, and other meteorological inputs are entered as text in Terminal Aerodrome Forecast (TAF) code format. The aerosol model is selected from a menu of 17 choices. Relative humidity values are calculated. Menus also provide six backgrounds, 18 specific targets, several user-definable generic targets, and many sensors to choose from.

A seemingly unnecessary limitation of the EOTDA is that it calculates the value of some parameters, such as relative humidity and sea surface temperature, even if the user could provide a more accurate value based on measurements. It is likely that future implementations of the EOTDA will automate the meteorological inputs. Automation will decrease the possibility of human error and will restore input data precision that was sacrificed for ease of use.

The run times range from a few seconds to several minutes, depending on the type of computer (for example, an 80486 versus an 80286), the target complexity, and the number of output times selected. Besides the numeric and graphical outputs, a visualization display is available that portrays the radiance values of the background and each target node pictorially.

### 1.2 FLEET USE OF THE EOTDA

Infrared technology was employed extensively in the Persian Gulf during Operation Desert Storm, but the EOTDA was not widely used [5]. When the EOTDA was used, it favorably influenced mission planning decisions. The desert background model proved inaccurate early in the war, but this problem was corrected with a software fix. While some forecasts were found to be incorrect, the overall predictions were considered adequate. However, there was little feedback on the accuracy of the predictions, because the Desert Storm pilots and planners only required general (good, marginal, or poor) forecasts. The most difficult problem reported by meteorologists operating the EOTDA was not with the EOTDA itself, but getting accurate battlefield weather conditions and forecasts to input into the model.

Havener and Funk [5] offer suggestions based on Desert Storm for improving the utility of the EOTDA. One was to tailor the output to the needs of the user. The level of detail required from the EOTDA varied with the type of mission. For example, an aircraft looking for targets of opportunity only needs general information on the IR conditions for various times of the day. For an aircraft striking a specific target, more detailed information on detection and lock-on ranges would help determine the best weaponry and strategies to minimize vulnerability. Version 3 of the EOTDA addresses this suggestion by allowing the user to specify the contents of the output. Other suggestions included: provide more training and awareness, automate the inputs, and provide a capability to correct and redefine the backgrounds and a capability to define new targets.

The EOTDA is more sophisticated and contains more capabilities than the UFLR model [6] residing in the current shipboard Tactical Environmental Support System. It is also much easier to use and has wider distribution than previous versions. Transitioning the EOTDA into TESS(3) will further increase the availability to the fleet. It is reasonable to assume that the fleet's use of the EOTDA will increase dramatically in the coming years. Therefore, it is crucial that the EOTDA be properly evaluated to determine the validity of its output and to identify any problem areas.

### 1.3 VALIDATION OF THE EOTDA

Ideally, the limitations and accuracies of a TDA should be quantified so that the user can properly apply the information it provides. However, the complex modeling requirements and the numerous possibilities of environmental and physical parameters that define an optical scene make calibrating a TDA a formidable task for even a single sensor and target. The best that can be done in most cases is to verify the basic physics involved

for each subroutine and then perform a variety of validation tests under whatever limited conditions naturally occur during the testing period. Much of the physics of the EOTDA is from well-accepted methodology, but little has been done to quantitatively validate the overall performance.

Sensitivity tests have been performed [7]. However, sensitivity tests do not validate the model. Sensitivity tests vary the input parameters for a given base case to show how much each parameter affects the results for a given scenario. For example, small amounts of rain or battlefield-induced contaminants were shown to have a large effect on detection range [8]. In general, clouds were shown to reduce temperature contrast which tends to reduce detection range. However, Shapiro [7] showed that the presence of clouds can actually improve detection range in some cases by delaying or preventing a temperature contrast reversal of the target against the background. While sensitivity tests are important for understanding the behavior of the model, they do not indicate absolute accuracy, and they only apply to the base case conditions.

Real-world validation tests cannot fully determine accuracy and variability either. However, it is important to measure TDA performance from an end-user perspective. A TDA that performs well in theory but cannot be trusted in battle is dangerous. The result will be either poor mission planning or a TDA that will be ignored. End-to-end evaluations typically compare reports of detection ranges from air crews with the EOTDA predictions. Tests controlled by researchers are costly and large data samples over a wide range of conditions are usually unobtainable. Also, it is difficult to quantify the performance differences among different air crews and different aircraft. In spite of the difficulties, this type of evaluation is crucial in defining the usefulness and limitations of the TDA in real-world situations, and often identifies problems that go unnoticed in modular and theoretical testing.

NRL Monterey has conducted several evaluations in the past using measurements from aircraft out of naval air stations at Whidbey Island, Moffett Field, and Lemoore. Data from these measurements have led to TDA improvements and were used to compare various TDAs. These comparisons were instrumental in deciding to include the EOTDA Mark III into TESS(3). The aircraft measurements presented in this report advance the validation process and also illuminate some concerns that need to be investigated.

## 2. MEASUREMENTS

### 2.1 OVERVIEW OF FIELD TESTS

The primary data for this report stem from an open ocean field experiment conducted 29 July to 4 August 1992 off the coast of Monterey, California by Naval Command, Control and Ocean Surveillance Center (NCCOSC), Research, Development, Test and Evaluation Division (NRaD) in cooperation with the Naval Postgraduate School. The purpose of the experiment was to collect a comprehensive set of meteorological and ship temperature data, infrared (IR) images, and airborne FLIR detection range data in support of ongoing research. This included validation of the Performance and Range of Electrooptical Systems (PREOS) detection range algorithm [9] and the SHIPSIG thermal model for combatant ships [10] [11]. The initial results of the PREOS validation were documented in a thesis for the Naval Postgraduate School [12]. The SHIPSIG evaluation was combined with a comparison of TCM2 and presented in another NRaD report [13]. The field data are further utilized in this report to evaluate the EOTDA Mark III.

The Research Vessel *Point Sur* was the primary measurement platform. *Point Sur* is a 135-foot ship that is owned by the National Science Foundation. It served as a platform for meteorological and surface measurements and as an IR target for the airborne FLIR and imaging systems. Scientists from the Naval Postgraduate School, NRaD, and Naval Surface Warfare Center (NSWC) were aboard the *Point Sur* to conduct the onboard measurements. Figure 1 shows the ship track for the five-day cruise as recorded by the Global Positioning System (GPS) receiver.

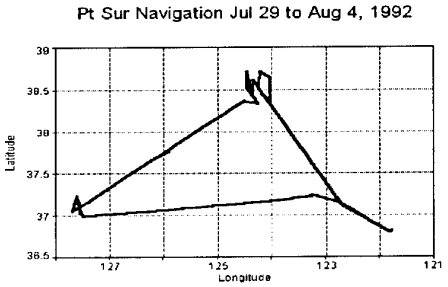


**Figure 1.** GPS track of the Research Vessel *Point Sur*.

Air temperatures ranged from 11.5 to 17.8 °C during the cruise. Sea temperatures were from 11.0 to 18.1 °C, with a warmer sea than air temperature most of the time. Wind speeds ranged from 3 to 26 knots, and were predominately from the Northwest. Stratus clouds dominated until the last day of the test when clear skies prevailed. The stratus base ranged from 500 to 1300 feet according to the aircrew reports. Cloud tops as determined from radiosonde relative humidity gradients ranged from 1200 to 2100 feet.

## 2.2 SHIPBOARD MEASUREMENTS

Ground-truth measurements of the skin temperatures of the ship were collected from 15 thermistors attached to the ship, and a hand-held radiometer. The thermistors were mounted on the large-area surfaces of the ship and were continuously recorded. Spot measurements of IR skin temperature were made several times daily with a hand-held radiometer that operated in the 8-12 micron band.

Meteorological data were collected by the Naval Postgraduate School from a variety of shipboard sensors. The surface parameters measured included: air temperature, sea temperature, dewpoint temperature, wind speed, wind direction, relative humidity, pressure, and solar irradiance. Vertical profiles of meteorological parameters were obtained from a VAISALA RS80 rawinsonde system. The calibrated accuracies of this system are within 0.5 mb pressure, 0.2 °C temperature, 2% relative humidity, and 2% altitude. Atmospheric radon concentrations were also recorded as an aid to identifying continental versus marine air masses. Among the ship navigation data recorded were latitude, longitude, gyro heading, and ship speed.

## 2.3 AIRBORNE MEASUREMENTS

The NRaD airborne platform is a Piper Navajo aircraft that is outfitted with navigation, meteorological, aerosol and thermal image recording systems. The aircraft flew 11 missions. Meteorological and aerosol data were collected as a function of altitude in 13 spiral ascents, each beginning at 200 feet and climbing to 5000 feet. A total of 2603 image frames of the *Point Sur* were collected with the AGA-780 Radiometric Thermal Imaging System, which was operated in the 8-12 μm band. Additional meteorological and aerosol data were collected at 200-foot and 500-foot altitudes during the image collections. Meteorological and navigational parameters were recorded at 5-second intervals. These included date, time, GPS latitude and longitude, altitude, air temperature, dewpoint temperature, relative humidity, and atmospheric pressure.

## 2.4 FLIR MEASUREMENTS

Besides being the primary meteorological measurement platform, the Research Vessel *Point Sur* was also used as the target for the FLIR and IR imaging systems. Seven aircraft employing an 8-12 μm FLIR system with a mercury-cadmium-telluride (HgCdTe) sensor detector flew range detection missions during the tests. Eight missions were flown, four at night (at about 2300 PDT) and four during mid-morning (at about 1000 PDT), making a total of 57 passes at the target. The results from these overflights provide the primary foundation for this report.

A representative from the Naval Postgraduate School instructed flight crews in a preflight briefing before each mission. The aircrews had voice and visual contact with the *Point Sur* before making detection runs. Runs were made from two altitudes: 500 and 1000 feet. For consistency, all detection ranges were determined using the wide field of view lens. Target classification and identification ranges were determined using the narrow field of view lens. Detection was defined as when the operator first notices a dot on the display. The aircrew operator recorded the detection ranges and requested supplemental information on data sheets provided for the tests. Display images were preserved on video tape, which is now archived at the Naval Postgraduate School.

## 2.5 EOTDA OPERATION

The input values required to operate the EOTDA include meteorology, navigation, and operational parameters. Entering the operational parameters, such as type of sensor, aircraft altitude, and ship heading, is a straightforward transfer of measured values. In contrast, the meteorological parameters are more difficult to input because they require some interpretation. Visibility, for example, significantly affects detection range calculations, but is difficult to measure accurately. Wind direction and speed were measured continuously, but the precise values must be translated to TAF code to operate the EOTDA, which tends to degrade the precision.

Comparison tests at NRL Monterey noted discrepancies in the output between versions 2.0 and 3.0. When the meteorological input format was changed from the tabular format in version 2.0 to TAF code format in version 3.0, some software errors resulted. It is possible that some of the detection range error in this data set could be from program errors rather than model performance. However, this is unlikely. The TAF code input was checked for proper format, and the binary input files created by the EOTDA were spot checked to verify that the cloud and other meteorological data were actually getting into the program. Furthermore, the input values were from carefully monitored in-situ measurements, rather than imprecise forecasts. It is therefore reasonable to assume that the output results are primarily from model performance.

# 3. RESULTS

## 3.1 DETECTION RANGES

Figure 2 is a scatter plot of the detection ranges predicted by the EOTDA compared with the detection ranges observed by the aircrews. The data show a tendency of the EOTDA to overpredict the detection ranges. There was no significant difference between the results of the morning flights compared with the night. An overcast stratus layer prevailed throughout the testing period, except on 4 August, the final night of the field tests. The EOTDA predictions agree more closely with the observed detection ranges on the clear weather day, 4 August, but grossly overpredict the detection

range during the stratus cloud conditions. At first glance, the EOTDA cloud model appears to need some refinements, but the problem is not that simple. A multitude of interrelated factors is involved. Sensitivity tests [7] show that clouds can greatly affect detection range, but the effects are maximum during the daylight hours and minimal at night. The field data show the error difference between the clear day and stratus days is large regardless of whether the overflight was night or morning. This suggests that there is more than simply cloud effects causing the overprediction of ranges.

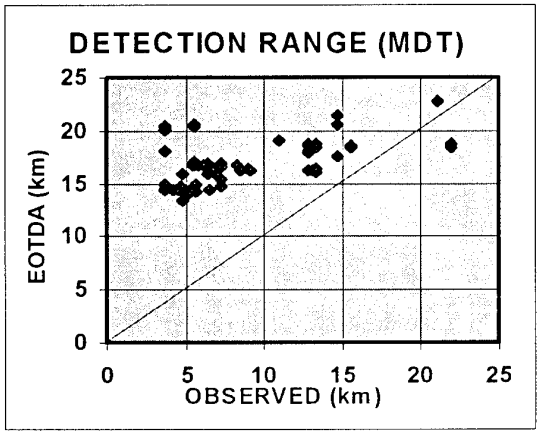


**Figure 2.** Observed detection ranges compared with EOTDA MDT range predictions.

### 3.2 BACKGROUND TEMPERATURES

Figures 3 and 4 compare the measured sea surface temperature with the calculated water background temperatures for each overflight. Figure 3 is a scatter plot of the temperature values. Figure 4 shows the magnitudes of the temperature differences for each set of flights (with zero being perfect agreement).

The calculated values of the physical sea temperature are taken directly from the EOTDA output file FACET.TMP. The measured sea temperatures were taken aboard the *Point Sur* during the cruise from a thermistor submerged in the water. The thermistor measurement depth ranged from about 3 to 12 inches, depending on the ship speed. Radiometric sea temperatures were also measured from onboard the *Point Sur*. The radiometric values were taken with a hand-held 8-12 μm Everest radiometer. Figure 5 shows that the onboard thermistor and radiometric temperatures are in close agreement. The onboard radiometric and thermistor sea temperatures ranged from 11.0 to 18.1 °C over the entire test period, with an average agreement of 0.1 °C and standard deviation of 0.3.

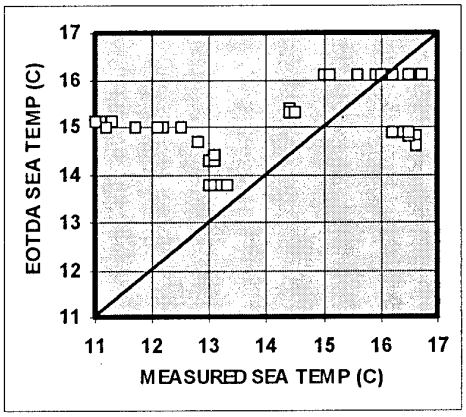


**Figure 3.** EOTDA calculated sea temperature compared with measured values.

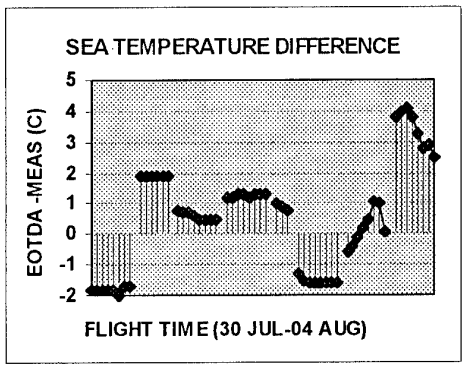


**Figure 4.** Background temperature differences over the test period (57 overflights): *Point Sur* thermistor values minus the EOTDA predicted values.

Figure 4 shows that the TDA calculations of the physical sea temperatures are within ±2.0 °C on the stratus weather days. On the clear sky day, the TDA overpredicted the physical sea temperature an average of 3.4 °C. While the background temperature predictions showed the largest errors with the clear weather data, the range predictions were most accurate for this same data set. Part of the reason for this apparent contradiction is that the contribution of water emissivity to total background radiance is minimized at large angles of incidence, as shown by Fresnel's equation plotted in figure 6 (Shapiro, 1987). The incidence angles for this data set ranged from 85.8 to 89.6 degrees, assuming a smooth ocean surface and isotropic radiation. Although the real-world sea surface is never perfectly smooth and some diffuse radiation is always present, the angles are such that reflected sky radiance makes a major background contribution.

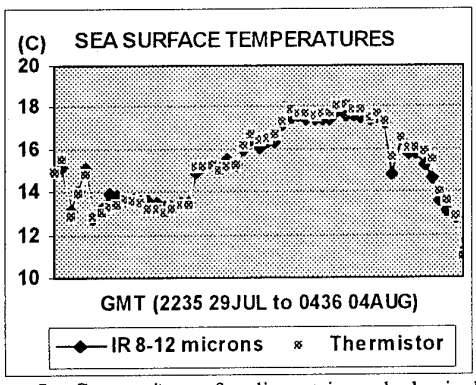


**Figure 5.** Comparison of radiometric and physical sea temperatures.

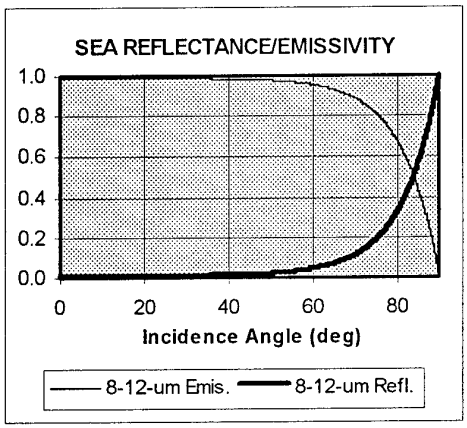


**Figure 6.** Emissivity and reflectance of sea water as a function of incidence angle.

The measurements indicate that the most significant errors in the background temperature predictions probably stem from the integrated sky radiance and ocean surface reflectance calculations. Unfortunately, validation of the sky contribution is not possible for this data set. The data did not include sky radiance measurements or simultaneous radiometric imaging of the target and background.

### 3.3 TARGET TEMPERATURES

The target temperatures predicted by the EOTDA are believed to be reasonably accurate for the data set presented here. Calibrated thermal images of the target were analyzed and the path effects were removed (Hughes and McGrath, 1993). These corrected values were compared to the Georgia Technology Research Institute program TCM2 and the NSWC program SHIPSIG [1]. The model and target temperatures agreed within ±2.0 °C. Table 1 shows a set of the corrected AGA-780 thermal imager temperatures and the TDA target temperatures for the starboard and port views of the target. The overall average temperature of the TDA was 15.3 °C, and the AGA-780 image temperature average was 17.5 °C. This temperature difference is easily explained by time difference between the airborne AGA measurements and the aircraft FLIR measurements. All of the AGA measurements were made in the afternoon, when a hotter target is likely. The TDA validation measurements using the FLIR system were made late at night and at mid-morning when a cooler target temperature is expected. Thus, the 2.2 degree average temperature difference is not unreasonable. No simultaneous measurements were taken with operational FLIR and the AGA imager, so a direct correlation of measured and predicted temperatures is not possible. Attempts to correlate the FLIR and AGA with thermistor recordings of the target also proved unsuccessful. Twelve thermistors were attached to the target during the field experiment, but none of the individual thermistors adequately tracked the average target temperatures. No scheme of combining the thermistor values has yet been devised that represents the composite ship temperature. Until a better data set is available, the target model cannot be properly validated. Meanwhile, it appears that the target model is functioning with an accuracy of ±2.0 °C.

| Date | Time | Meas | TDA | Meas | TDA |
|---|---|---|---|---|---|
| | GMT | Stbd | Stbd | Port | Port |
| 7/29 | 2230 | 17.5 | | 18.1 | |
| 7/30 | 0115 | 15.3 | | 16.0 | |
| 7/30 | 0610 | | 14.8 | | 14.8 |
| 7/30 | 1715 | | 14.5 | | 13.9 |
| 7/30 | 2045 | 18.3 | | 18.5 | |
| 7/31 | 0700 | | 15.2 | | 15.1 |
| 7/31 | 1715 | | 17.5 | | 17.1 |
| 7/31 | 2115 | 19.1 | | 19.0 | |
| 8/01 | 0510 | | 15.2 | | 15.2 |
| 8/01 | 1745 | | 16.8 | | 17.2 |
| 8/01 | 2030 | 18.9 | | 19.6 | |
| 8/03 | 1745 | | 17.1 | | 16.6 |
| 8/03 | 1930 | 18.3 | | 17.0 | |
| 8/03 | 2230 | 16.8 | | 16.7 | |
| 8/04 | 0145 | 16.1 | | 15.2 | |
| 8/04 | 0500 | | 12.2 | | 11.9 |

**Table 1.** Comparison of target temperatures from the AGA-780 imager and the EOTDA predictions for the starboard and port sides.

### 4. CONCLUSIONS

Since the EOTDA program development was primarily directed toward Air Force applications, little has been done to test and validate the marine environment. The results presented here clearly show the need to further investigate and improve the EOTDA. The TDA performed well on the clear sky day of the tests and performed poorly on the stratus days. Tests should especially focus on the transmission, sky radiance, cloud, and water background models.

It is hoped the EOTDA operation can be fully automated in the future. By interfacing the EOTDA to a weather forecasting system, input reliability and consistency are attainable, and the program will be easier to use. It appears, however, that the TDA predictions are unreliable in some situations regardless of the quality of the input data. Therefore, an experienced human operator is still required to interpret the results and adjust the predictions based on feedback from similar scenarios. For example, an operator who knows that the model overpredicts detection ranges in an open ocean background when there is a prevailing stratus cloud ceiling could introduce a correction factor (e.g., divide by 2.5) that would make the results more accurate. It is hoped that further validation and testing will provide solutions that do not require intervention.

The current EOTDA is a vast improvement over the UFLR program that is currently in TESS. The upgraded user-interface makes the program much easier to use, and the models push the limit of the original intended platform, a PC with a 80286 processor. The fleet use of the TDA should greatly increase now that the program is easier to use and has a wider distribution. Inclusion into TESS(3) should further increase the usage of the EOTDA. It is therefore, critical that the model be more fully validated and any problems be annotated and corrected as quickly as possible.

## ACKNOWLEDGMENTS

This work is funded by the Office of Naval Research, code 322. Thanks to Dr. Andreas K. Goroch and Steven B. Dreksler of the Naval Research Laboratory, Monterey, CA. for providing comparative data, technical assistance and reference materials. Thanks to Dr. Douglas Jensen of NRaD and Professor Alfred F. Cooper of the Naval Postgraduate School for organizing the field tests that provided data for this report, and to Lt. Jon C. Kreitz of the Naval Postgraduate School for coordinating the aircraft overflights. Thanks also to Paul Hilton, Chan Touart, and Daniel DeBenedictis of Hughes STX Corporation, Lexington MA., and Paul Tattleman of the Phillips Laboratory, Hanscom Air Force Base, MA. for providing literature and technical assistance pertaining to the EOTDA.

## REFERENCES

1. Hughes, H. G. and C. P. McGrath, "Surface Ship Infrared Signatures Determined Using an Airborne Imaging System," Science and Technology Corporation Technical Report 2727 (September 1993).

2. Freni, J. M. L., M. J. Gouveia, D. A. DeBenedictis, I. M. Halberstam, D. J. Hamann, P. F. Hilton, D. B. Hodges, D. M. Hoppes, J. J. Oberlatz, M. S. Odle, C. N. Touart, and S-L Tung, "Electro-Optical Tactical Decision Aid (EOTDA) User's Manual, Version 3," Phillips Laboratory Technical Report PL-TR-93-2002 Vol. I & II (11 January 1993).

3. Kneizys, F. X., E. P. Shettle, L. W. Abreu, J. H. Chetwynd, Jr., G. P. Anderson, W. O. Gallery, J. E. A. Selby and S. A. Clough, "Users Guide to LOWTRAN 7," Air Force Geophysical Laboratory Technical Report No. 88-0177 (1988).

4. Blakeslee, L. and L.J. Rodriguez, "User's Manual for TCM2," Georgia Institute of Technology, Interim report for period Jan-June 1993 under Wright-Patterson AFB Contract F33615-88-1865 (July 1993).

5. Havener, K. and S. Funk, "The Utility of Electro-Optical Tactical Decision Aids (EOTDAs)," USAF Air Weather Service Report No. AWS/XTA 91-1 (10 September 1991).

6. Computer Sciences Corporation, "Forward Looking Infrared Performance Function Program Performance Specification (PPS) for the Tactical Environmental Support System (TESS), Naval Ocean Systems Center Technical Document TD-1000 (December 1986).

7. Shapiro, R., "Mark III Infrared Operational Tactical Decision Aids for Navy Operations: A Sensitivity Analysis," Naval Research Center Monterey California Contractor Report No. CR-89-12 (September 1989).

8. Keegan, T. J., "EOTDA Sensitivity Analysis," Air Force Geophysics Laboratory Technical Report No. GL-TR-90-0251 (II), (27 September 1990).

9. McGrath, C. P., "PREOS Program for Determining Detection Ranges of Airborne FLIR Systems," NRaD Technical Report 1488 (January 1992).

10. Ostrowski, P. P. and D. M. Wilson, "A Simplified Computer Code for Predicting Ship Infrared Signatures," Naval Surface Warfare Center Technical Report 84-540 (1985).

11. Ostrowski, P. P., "A Simple Thermal Model for FLIR Detection Range Applications," meeting of IRIS Specialty Group on Targets, Backgrounds, and Discrimination, Vol II, pp 177-190 (July 1993).

12. Kreitz, J. C., "Preliminary Evaluation of the PREOS Program for Determining Detection Ranges of Airborne FLIR Systems," Naval Postgraduate School Thesis (December 1992).

13. McGrath, C. P., D. R. Jensen, and P. P. Ostrowski, "Surface Ship Infrared Signature Model Evaluation," NRaD Technical Report 1647 (April 1994).

14. Shapiro, R., "Water Backgrounds in the Infrared (IR) and Visible (TV) Tactical Decision Aids," Air Force Geophysics Laboratory Report AFGL-TR-87-0254 (August 1987).

# MESOSCALE MODELING OF REFRACTIVE CONDITIONS IN A COMPLEX COASTAL ENVIRONMENT

Stephen D. Burk and William T. Thompson
Naval Research Laboratory
Marine Meteorology Division
Monterey, CA 93943-5502 USA

## SUMMARY

A mesoscale model was run in a data assimilation cycle throughout the 12-day period of the Variability of Coastal Atmospheric Refractivity (VOCAR) experiments's Intensive Observing Period (IOP). A developing synoptic low, a mesoscale eddy, sea-land breezes, mountain-valley winds, and coastal low-level jets (LLJ's) are some of the phenomena modeled, and to some extent, observed during VOCAR. Impacts of these processes on the marine atmospheric boundary layer (ABL) and microwave refractivity are highlighted in this paper.

From August 23 to September 3,1993 the IOP of the VOCAR experiment was conducted in the Southern California bight from Point Conception to San Diego. This experiment was designed to observe the mesoscale structure of the ABL in the bight so as to accurately characterize the temporal and spatial variability of the microwave refractivity field. Analyses or forecasts of propagation conditions (e.g., surface-based or elevated trapping layers; extent of over-the-horizon propagation, etc.) require accurate depiction of the depth and structure of the ABL (particularly vertical gradients in temperature and moisture at the ABL top). Numerous special observations were made during the IOP and are used to evaluate model performance.

## 1. INTRODUCTION

In this paper we discuss results from a mesoscale model which was run over the VOCAR domain (shown in Fig.1) with 20 km grid spacing and 30 vertical levels spaced so as to provide high ABL resolution.

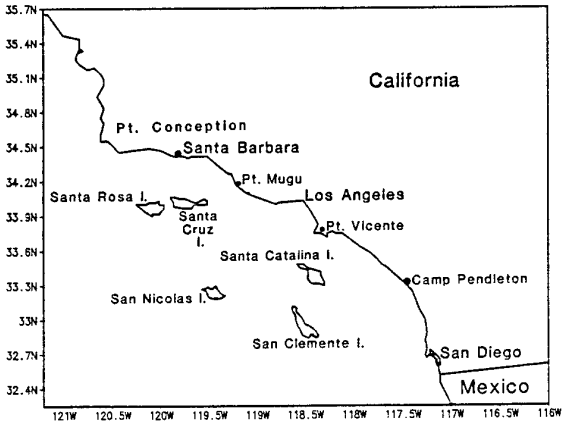


Figure 1. Map of key locations in VOCAR domain. The mesoscale model was run over the much larger domain shown in Fig.2.

Twice daily forecasts to 24 h were made using a continuous 12 h data assimilation cycle. The model computes the modified refractive index, M, which is primarily a function of water vapor and temperature. A layer with negative DM/DZ is, under certain conditions, capable of permitting greatly extended propagation ranges, and such a layer is often called a "trapping layer".

The mesoscale model we use is a version of the Navy Operational Regional Atmospheric Prediction System (NORAPS) which is described in Refs 1 and 2. It is a hydrostatic primitive equation model with a split explicit time integration scheme and uses a sigma (p/ps) coordinate in the vertical. We use a data assimilation cycle in which a previous 12 h forecast is combined with observational data in an optimum interpolation analysis. In this manner much of the mesoscale detail that is produced by the model is maintained throughout the analysis and initialization process. This is important because the observations are much too sparse to adequately define the 3D mesoscale structure of the model domain.

This model contains a second-order closure turbulence parameterization based on the Mellor and Yamada level-3 formulation (Ref 3). A diagnostic expression for cloud liquid water and cloud fraction is used that is based on an assumed joint-normal probability distribution using variances and covariances of temperature and moisture. Model physical parameterizations also include a two-stream radiation scheme which interacts with the predicted clouds by use of the liquid water path length in formulating transmission functions. Over land, prognostic budget equations are used to compute the diurnal cycle of temperature and ground wetness, while at ocean points the sea surface temperature (SST) distribution is fixed during any given model forecast (although updated every 24 h) and similarity expressions are used to compute surface fluxes.

The reader interested in further model description and the parameterizations used in the model is referred to Ref 2.

## 2. SYNOPTIC AND MESOSCALE SETTING DURING VOCAR

The overall synoptic pattern during the first few days of the VOCAR experiment beginning 23 Aug 93 was rather typical for the summertime California coast, with an inverted thermal surface trough of low pressure along the Colorado river between Arizona and California, and the eastern Pacific high established well to the west off the coast. The resulting pressure gradient caused predominantly northerly flow along the coast; however, near 850 mb the flow near Point Conception was somewhat more northeasterly and a substantial eddy is evident in the model's forecast wind field at this level

*Paper presented at the Sensor and Propagation Panel Symposium on "Propagation Assessment in Coastal Environments" held in Bremerhaven, Germany 19-22 September 1994.*

during the first several days of the VOCAR IOP. The eddy is less evident at the surface, although many coastal stations in the bight observed southerly wind components. Orographically-forced eddies are relatively common in this region due to the predominantly E-W Santa Ynez and San Rafael mountains.

During the middle period of the VOCAR IOP (27-31 Aug 93) the 850 mb flow along the California-Oregon border turned from northerly to more northeasterly. At 1200 UTC 29 August the model shows the development of a mesoscale eddy on the Northern California coast in the lee of the Siskiyou and Klamath mountain ranges. This eddy couples with an upper level trough and amplifies into a mesoscale low that drifts southwestward and by 31 August it significantly impacts the flow pattern of the Southern California bight. Figure 2 shows the model's 24 h forecast flow valid 1200 UTC 31 Aug at a height of 1 km, where the model's sigma level data has been interpolated to a constant height surface. Wind vectors do not appear where the model's terrain exceeds 1 km. This low continues to drift westward and eventually leaves the western boundary of the mesoscale model and more typical north-westerly flow is established along the Northern California coast toward the end of the VOCAR IOP.

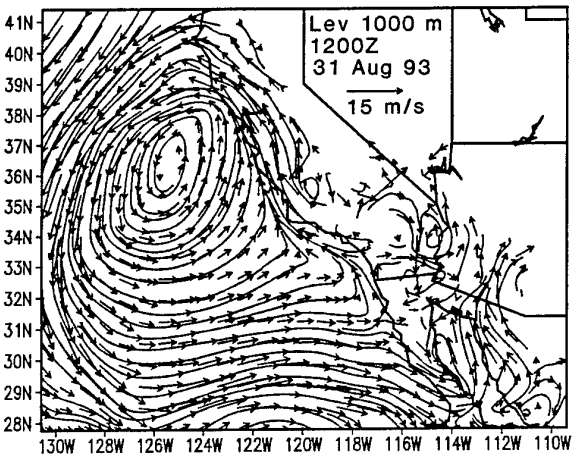


Figure 2. 24-h forecast wind vectors and streamlines.

## 3. MESOSCALE FORECASTS: ABL STRUCTURE AND REFRACTIVITY FEATURES

### 3.1 Sea-Land Breeze Impacts

Although the horizontal resolution is coarser than desirable for the purpose, the model does resolve the sea-land breeze and generally is in agreement with coastal station observations. The sea-land breeze not only modifies the weather experienced by coastal land stations, but it also alters the marine ABL adjacent to the coast. The low-level divergence associated, through continuity, with an accelerating sea breeze can cause subsidence and a lowering of the marine ABL in a strip along the coast during daytime. We also propose that coastal orography can, in some instances, enhance this process when mountains, acting as elevated heat sources, cause additional acceleration and divergence above the ABL. These diurnal changes in the coastal marine ABL can, in turn, alter the propagation conditions within the ABL by, for example, causing an elevated trapping layer to lower into a surface-based duct.

During the first week of VOCAR, the model forecast significant diurnal variations in the marine ABL along the central coastal portion of the bight. Figure 3 is a time-height plot showing the model's trapping layer and contours of potential temperature at an ocean point just west of Huntington Beach (south of Los Angeles). From 24-28 August the trapping layer is shown to be very low at midday and then elevates and generally weakens at night. This is less pronounced on the 26th and by the 29th the trapping layer is somewhat elevated even at noon. Also shown in Fig. 3 is the model forecast base of the duct (heavy dots), which is the height where M equals the minimum value of M in the trapping layer. There is surface-based ducting near local noon (2000 UTC) and elevated ducting near sunrise during this period.

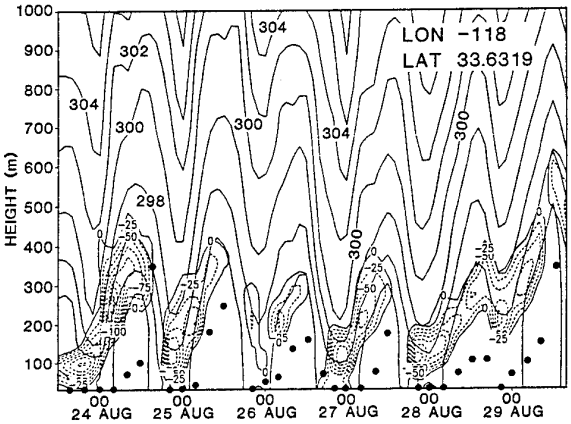


Figure 3. Solid lines, potential temperature (K); dashed lines, negative DM/DZ (trapping layer); and heavy dots, base of the duct location at 4 hour intervals.

This marine ABL diurnal behavior of the trapping layer diminishes rapidly as one moves west away from the coast. At a point 0.8 deg longitude west of the point in Fig. 3 (close to where the research ship, Pt. Sur, operated during VOCAR), the model still shows a tendency towards midday surface-based ducting and slightly elevated ducting at night, but the trend is neither so clear nor so pronounced as in Fig. 3.

### 3.2 Development and Impact of Synoptic Low

As the low shown in Fig.2 moved off the coast, the model forecast development of a deep stratus layer extending over the entire region of cyclonic flow. The marine ABL reaches its greatest depth of about 1 km in the southeast quadrant of the low and its cloud deck is especially thick there, indicating that cloud top cooling is promoting enhanced entrainment in that location.

Satellite observations show the presence of this cyclonic circulation in the position forecast by the model; and the satellite-measured cloud top temperatures are particularly cold in this quadrant, indicating a deep ABL. The model indicates considerable trapping in the inversion just above the stratus deck.

Figure 2 also shows evidence of a mountain-parallel barrier wind flow in the Southern California bight region as the wind abruptly shifts from southwesterly upon entering the bight to southeasterly along the coast. This southerly LLJ, which is just outside the ABL, accelerates as it rounds Pt. Conception. The divergence associated with this acceleration causes subsidence and a thinning of the ABL depth in a narrow strip

adjacent to the coast, while the remainder of the bight has a rather deep ABL.

During the period 28 through 31 August the ABL deepens over most of the bight. The refractive structure changes from a rather strong, shallow trapping layer to a higher and weaker or nonexistent trapping layer. Figure 4 shows an E-W vertical cross section of relative humidity greater than 90% and trapping at 1200 UTC 28 Aug, while Fig.5 shows the situation at 1200 UTC 31 Aug. Figures 4 and 5 are both 24-h model forecasts. The cross sections are taken at a latitude of 33.5N.

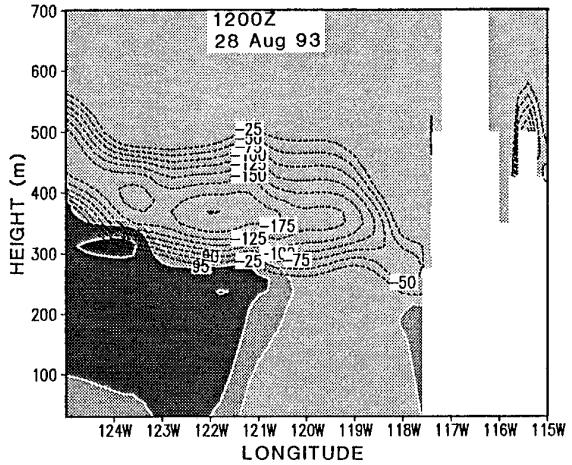


Figure 4. Cloud (shaded) and trapping (dashed) layers in E-W cross section.

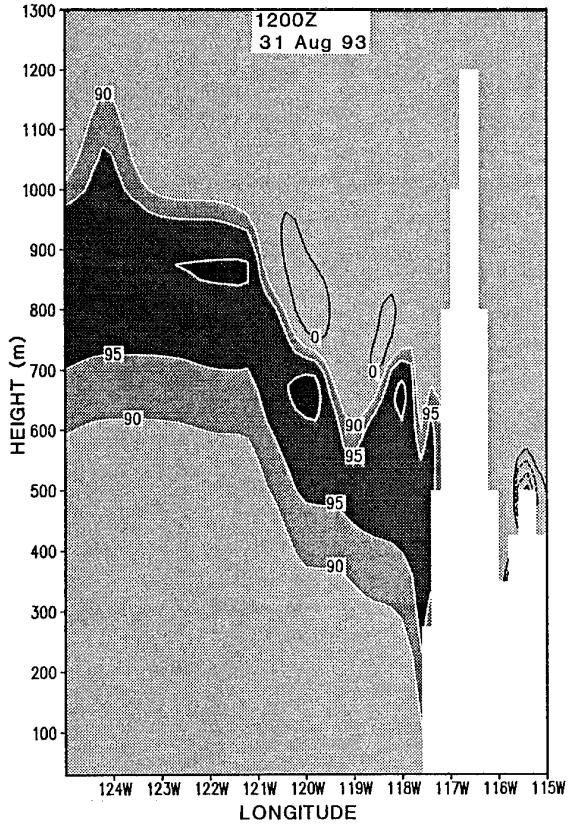


Figure 5. As in Fig.4, except 3 days later. Vertical spacing same as Fig.4, but extends higher.

Figure 4 shows a trapping layer at the ABL top that gently rises from about 400 m near the coast to 500 m at the western extreme of the figure. Clouds are forecast to exist well away from the coast, with the region of the bight between 118 and 120W in this figure being cloud free (we consider regions with relative humidity greater than 95% to be cloudy). By 31 Aug the entire region is forecast to be stratus covered (Fig.5), with the ABL deepening to near 1 km in the west, and the elevated trapping is nearly gone. (Note: the contour interval for trapping is the same in Fig.4 and 5, but Fig.5 only has two small areas of negative DM/DZ). The minimum in ABL depth near 119W in Fig.5 is associated with the LLJ's divergence discussed above.

Generally stratiform clouds promote the development of a trapping layer at their top. Cloud-top cooling, mixing within the cloud layer that abruptly ceases in the inversion immediately above, and subsidence all favor the development of the sharp vertical gradients required for trapping. When the synoptic low influences the bight, however, the subsidence is reduced or eliminated, permitting the marine ABL to grow and, furthermore, southerly flow above the ABL advects in moisture aloft. These processes reduce the gradient at the top of the ABL and weaken or eradicate the trapping layer.

### 3.3 Trends in Model Forecast Trapping Layers Versus Verifying Observations

Routine and special VOCAR radiosondes taken along the coast, on islands, and from a ship confirm this general model trend for ABL deepening and weakening of the trapping layer during the middle portion of the IOP. From the model's forecast fields we computed the base of the trapping layer (where DM/DZ first goes negative) at all of the sites where radiosondes were launched within the VOCAR domain. And we found the base of the trapping layer from the verifying radiosondes. Figures 6a-f show the model forecast trapping layer height along with the radiosonde-determined values for several stations in the Southern California bight region.

Figures 6a-c show the behavior of the trapping layer at three offshore locations -- San Nicolas Island, San Clemente Island and at the location where the Naval Postgraduate School research ship was on station. Each heavy dot in these figures represents a value of trapping layer base as determined from a radiosonde, while the solid line represents the model's forecast of this quantity. Each of these figures show a similar trend, with a minimum in trapping layer height on 27 or 28 Aug. 93 and then lifting to a maximum on about 31 August. This represents the effect of synoptic forcing over the entire Southern California bight. The substantial lifting begins first with the development of cyclonic flow over the bight and then is substantially enhanced when the meso-low discussed earlier begins to affect the region.

The trend in the height of the trapping layer is similar at the coastal stations shown in Figs.6d-f. At Camp Pendleton and Point Vicente (near Long Beach), Figs.6d and 6e show that the model has forecast the trend in trapping quite well during the middle portion of the VOCAR IOP, but it has significantly underforecast the depth early and late in the IOP. While this discrepancy was present in the island stations (Fig. 6a-b) at the end of the period, the model tended to do a better job at those stations early in the IOP.

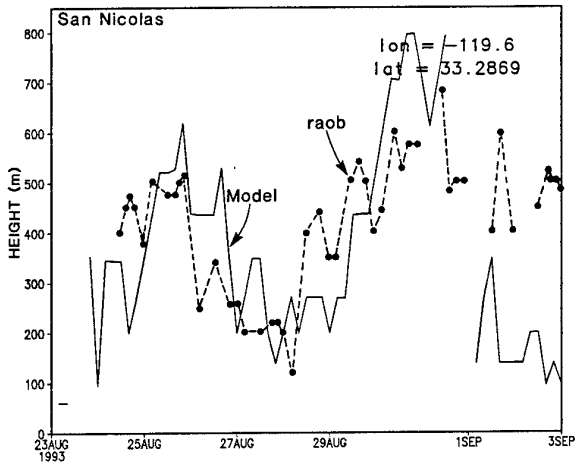


Figure 6a. Base of the trapping layer at San Nicolas Island during the VOCAR IOP as forecast by the model (solid line) and determined from radiosondes (dashed-dotted).

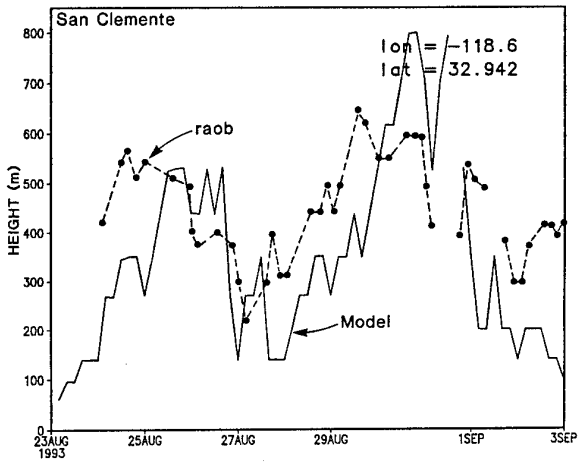


Figure 6b. As in Figure 6a except for San Clemente Island.

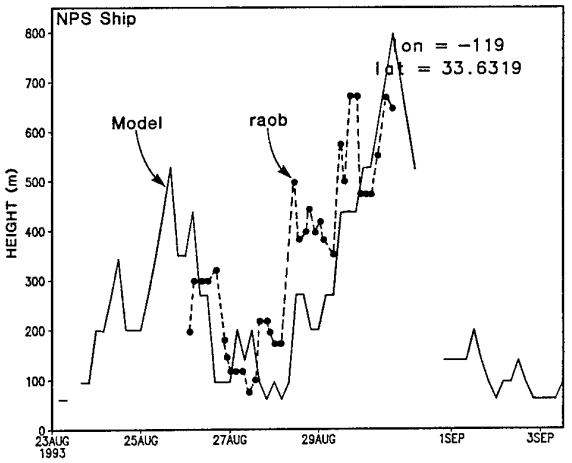


Figure 6c. As in Figure 6a except for the location of the Naval Postgraduate School ship.

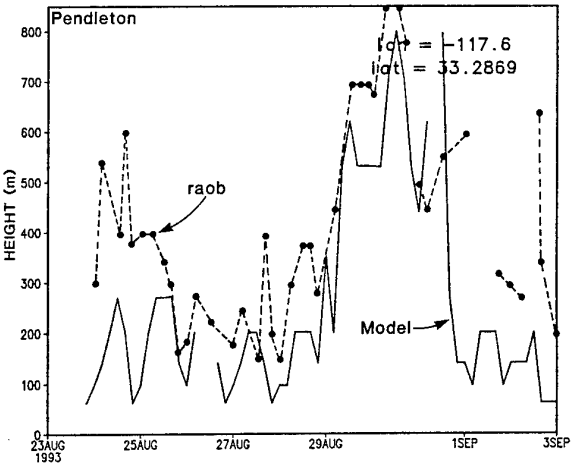


Figure 6d. As in Figure 6a except for Camp Pendleton.

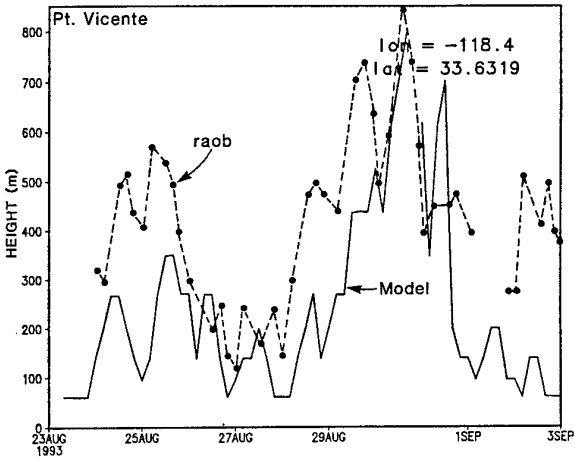


Figure 6e. As in Figure 6a except for Point Vicente.

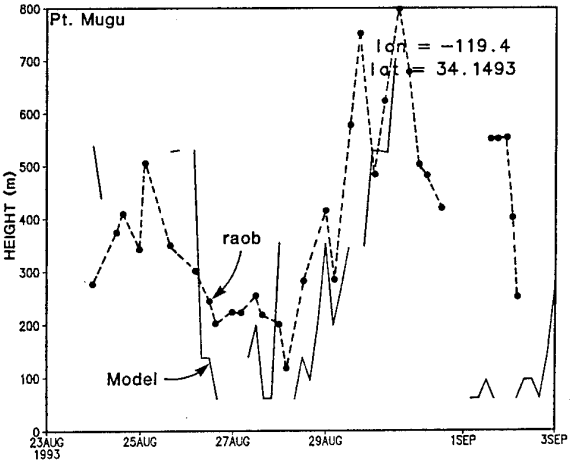


Figure 6f. As in Figure 6a except for Pt. Mugu.

We are still investigating the causes for these poor forecast periods. The symptom is for the marine ABL to be too warm and too shallow, and some of this may be caused by the initialization procedure. During the analysis/initialization the model's first guess field is adjusted based on the errors between the observations and the first guess field. This adjustment can, in some circumstances, result in the mixed layer temperature of the marine ABL being adjusted to a temperature warmer than the SST. When this happens the mixed layer can no longer be maintained by upward fluxes and the model loses the marine ABL structure at such locations. It can take up to a day or so of forecast time for the model to reestablish a marine ABL.

The model forecasts were particularly poor at Pt. Mugu (Fig.6f). This was puzzling because Pt. Mugu and Pt. Vicente are both coastal stations that are only about 100 km apart. At Pt. Mugu we noted a model tendency to develop a strong trapping layer at the surface nearly every afternoon; its character being that of a very strong and deep surface evaporation duct. While initially we suspected the cause to be somehow related to the mountainous terrain just inland from Pt. Mugu, eventually we discovered the true source of difficulty was something quite different and unexpected.

To the west-southwest of Pt. Mugu lie the islands of Santa Cruz and Santa Rosa -- at their closest point being only about 35 km from Pt. Mugu. Due to its 20 km grid spacing, these islands are only crudely represented in the model by three land points that are surrounded by water points. Only one water point separates the island points from the mainland near Pt. Mugu. The island points, like the mainland, undergo a strong diurnal cycle in surface temperature and ABL properties. In the afternoon, when the islands are considerably warmer than the surrounding SST, the wind is generally on shore due to the sea breeze. This carries the warm "heat island" ABL towards Pt. Mugu. This daytime advection of warm, dry air from the island causes the development of a stable surface layer with a strong moisture gradient over the water (air warmer than the SST) which gives rise to strong ducting in the surface layer. Conditions similar to this have been more commonly observed with offshore flow from a heated continent (e.g., Ref.4, Fig.1). The model, however, because of its lack of sufficient resolution, may be tending to spread this process over too broad a region away from the islands.

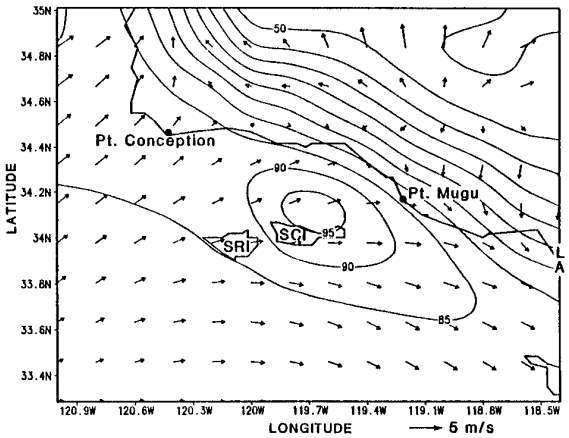


Figure 7. Model 24 h forecast of relative humidity at the lowest model level near 10 m in VOCAR subdomain. Verify time of this forecast is 1200 UTC 26 Aug (0400 LT).

Figure 7 shows an example of the model's night time relative humidity field at the lowest model grid point. Near Santa Cruz and Santa Rosa islands there is a maximum in relative humidity associated with the cooling of the islands below the surrounding SST. Thus, the model is forecasting conditions conducive to fog in the vicinity of the islands at night. During the following afternoon, Fig.8 shows a plume of low relative humidity air being carried from the islands to the mainland near Pt. Mugu. This plume represents the internal boundary layer from the island that creates the surface layer ducting.

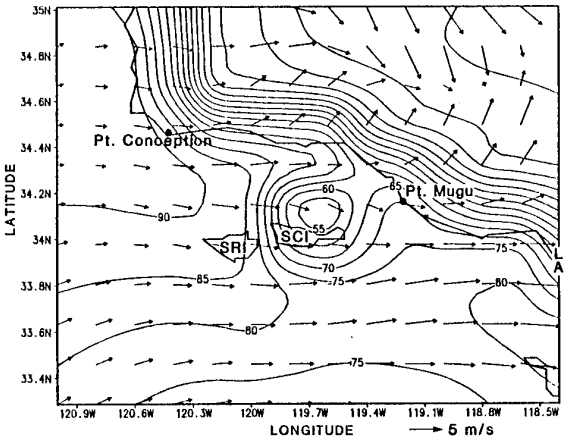


Figure 8. As in Figure 7 except at 00 UTC 27 Aug (1600 LT).

In Figures 9 and 10 we show model 24h forecast profiles of potential temperature ($\theta_v$), specific humidity (Q), and modified refractivity (M) at a water point just off the coast of Point Mugu. Figure 9 is valid at the same time as Fig.7 (0400 LT). It shows an unstable lapse of potential temperature immediately adjacent to the surface, with sharp gradients in Q and M in the surface layer as well. Above the surface layer there is a well-mixed layer to a depth of about 150 m, and then stable stratification above this height. Although the ABL is quite shallow, this is a rather typical marine sounding otherwise.

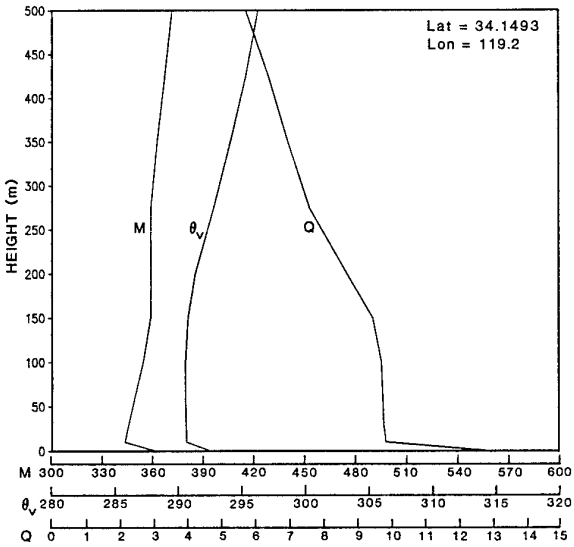


Figure 9. Model 24 h model forecast of virtual potential temperature (K), specific humidity (g/kg), and modified refractivity at an ocean point near Pt. Mugu. Forecast verify time is 1200 UTC 26 Aug. 93 (0400 LT).

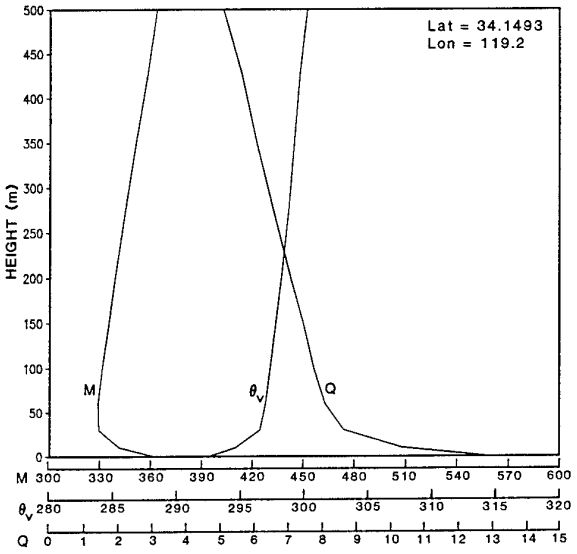


Figure 10. As in Fig. 9 except at 00 UTC 27 Aug. 93 (1600 LT), that is, the same time as Figure 8.

The profiles shown in Fig.9 undergo some significant diurnal changes (even though they are over water with a constant SST) as seen by the midafternoon values in Fig.10. The virtual potential temperature profile is stable near the surface (air temperature greater than SST), and the gradients in Q and M are not so tightly confined to the surface. Thus, a substantially stronger and deeper surface duct exists at this time (1600 LT) as the warm, dry air from the nearby heated islands overruns the cooler SST.

## 4. CONCLUDING REMARKS

Mesoscale processes in the Southern California bight are capable of significantly altering the refractivity conditions. Divergence associated with the sea-land breeze can modulate marine ABL depth, and concurrently, the height of the trapping layer. Orographically-forced circulations above the marine ABL also impact refractivity conditions. Such flows are driven by pressure gradients at levels above the marine ABL that are forced by mountainous elevated heat sources.

A synoptic low during the VOCAR IOP was forecast to aid in deepening the ABL and to lift and weaken the elevated trapping layer. This process is well verified by the VOCAR data base. The impacts of a mesoscale eddy in the bight and a coastal low-level jet upon the refractivity field are further explored in Ref 5.

Numerical weather prediction has only recently matured to the point where it is feasible to consider forecasting refractive variability on the mesoscale. The VOCAR experiment provided an important opportunity to evaluate the strengths and weaknesses of our mesoscale model in a complex coastal environment containing substantial gradients in SST, pronounced orography extending to the coast, strong overland diurnal forcing, and a marine PBL stratus layer which is highly variable. The model seems to have performed well in describing the general trends in the refractivity field during VOCAR and some of the diurnally forced features. We are still investigating, however, whether the model can attain a sufficient skill level to provide useful forecast fields to a radio propagation code. Early results indicate that the greatest difficulty to be overcome will be proper treatment of instances when surface-based ducting is very marginal. Under these circumstances the model may forecast a slightly elevated trapping layer while the verifying observations indicate surface-based ducting (or vice-versa) and this difference, while small in terms of meteorological variables, can have a substantial impact on the propagation.

**ACKNOWLEDGMENTS.** The editorial support of Steve Bishop and Winona Carlisle is greatly appreciated. Graphics and visualization tools developed by John Cook and Gary Love were very helpful. The support of the sponsor, Office of Naval Research, under program element 0602435N, is gratefully acknowledged.

## REFERENCES

1. Hodur, R.M., "Evaluation of a regional model with an update cycle", Mon. Wea. Rev., 115, 1987, pp 2707-2718.

2. Burk, S.D., and W.T. Thompson, "A vertically-nested regional numerical weather prediction model with second order closure physics", Mon. Wea. Rev., 117, 1989,pp 2305-2324.

3. Mellor, G.L., and T. Yamada, "A hierarchy of turbulence closure models for planetary boundary layers", J. Atmos. Sci., 31, 1974, pp 1791-1806.

4. Gossard, E.E., "Formation of elevated refractive layers in the oceanic boundary layer by modification of land air flowing offshore", Radio Sci., 17, 1982, pp 385-398.

5. Thompson, W.T., S.D. Burk, J. Cook, and G.G. Love, "Variations in coastal atmospheric refractivity induced by mesoscale processes", Proc. IGARSS '94, 1994.

## DISCUSSION

**J. TURTON**
You mentioned that one of the problems in the model was the representation of the inversion capping the boundary, and that you had made some progress in improving its representation in the model. What way have you done this?

**AUTHOR'S REPLY**
Yes, the model in general tends to "smear" or diffuse the gradients at the top of the boundary layer. There are many processes in such a complex model than can act to spread out such a gradient, and very few that tend to tighten the gradient. Recently we have tested slight alterations to the model's turbulent length scale formulation. The goal is to enhance mixing within the boundary layer, and to decrease the turbulence in the stable air above the boundary layer. This abrupt change in turbulence in the transition from the boundary layer to the stable air above seems to aid in maintaining the desired sharp gradient.

# High Resolution Meteorological Grid for Clear Air Propagation Modeling in Northern Coastal Regions

Sofus Lystad[1] and Terje Tjelta[2]

[1] Norwegian Meteorological Institute, P.O. Box 43 Blindern, N-0313 Oslo, Norway
Tel: + 47 22 96 31 73, Fax: + 47 22 96 30 50

[2] Norwegian Telecom Research, P.O. Box 83, N-2007 Kjeller, Norway
Tel: + 47 63 80 92 03, Fax: + 47 63 81 00 76

## SUMMARY

Coastal area propagation and meteorological measurements have been studied along with atmospheric mesoscale modeling. Simultaneous propagation data from three consecutive links have been compared with measured and modeled meteorological data from a part of the Norwegian coast at about 65$^0$ latitude. The results show a close relationship between refractivity gradient, obtained by meteorological data, and multipath activity on the links. The mesoscale model does also give valuable information on the spatial and diurnal time dependency of refractivity gradients at the vicinity of ground as well as at various height above the ground.

## 1. INTRODUCTION

On coastal paths multipath propagation is known to usually be more severe than compared with similar inland paths. The difference may be quite large. This fact has also been taken into account in the latest proposed version of Recommendation 530 of the International Telecommunication Union (ITU) that provides prediction methods for multipath fading and enhancement distribution [1]. The methods predict 10 dB more fading on paths over large bodies of water. The maritime climate clearly produces more often a layered atmosphere resulting in anomalous radio wave propagation. Therefore, it is of interest to more precisely know how to plan radio systems in the coastal zone, and go from a maritime to an inland climate.

This paper focuses on a particular coastal area in the northern Norway at latitude of 65$^o$N. High mountains occur right out to the coast in some places and there is also a fairly large glacier not far from the coastline. A mesoscale high reolution model has been used along with meteorological and radio wave propagation measurements for analyzing and interpreting the propagation results.

Previous measurements indicated quite a large fading activity [2] for an over water path in this region. The period analyzed in this paper shows somewhat less fading, but provides simultaneous results from three consecutive links in a network. It has therefore been of particular interest to study the propagation and the meteorological measurements from the same period for an area that is larger than that covered by only one link.

First the paper presents first some general properties of the coastal zone. It presents further the high resolution meteorological grid used by the Norwegian Meteorological Institute and how this has been employed. The next section presents the propagation and meteorological measurements and modeling. These are discussed and explanations sought for anomalous propagation events. Some comparison of atmospheric modeling results and direct measurements is also given.

## 2. COASTAL ZONE PROPERTIES

The atmospheric structures can be classified according to the magnitude of their cause, as given in Table I [3]. In coastal areas causes of the macro scale are the wandering cyclones and anticyclones where the depression and descending air following the anticyclonic high pressures are the most serious. Phenomena on the meso- and the local scale are typically the sea-land breeze mechanism and also the cold air drainage from the elevated plains down and outwards to the sea. Another advective effect on the local and micro scale is the "leading-edge or fetch effect" caused by a moving air mass passing over the borderline between two areas of contrasting surface properties, say the shoreline. As air passes from one surface type to a new and different surface, it must adjust to a new set of boundary conditions. The adjustment is not immediate throughout the depth of the air layer; it is generated at the surface and diffuses upward, thus creating an internal boundary layer with a depth increasing with increasing distance downwind from the border. It is only in the lower 10% of this layer that the conditions are fully adjusted to the properties of the new surface. The remainder of the layer is a transition zone wherein the air is modified by the new surface but not fully adjusted to it. The properties of the air above the internal boundary layer remain determined by upwind influences and not those of the surface immediately beneath. The constitution of the coastal atmosphere is thus a product of various processes, each with characteristic time and length scales.

*Paper presented at the Sensor and Propagation Panel Symposium on "Propagation Assessment in Coastal Environments" held in Bremerhaven, Germany 19-22 September 1994.*

## 3. THE MESOSCALE GRID MODEL

The model used here is a specialized version of the operational weather forecasting model run by the Norwegian Meteorological Institute at the Cray computer of the University of Trondheim.

The operational model is a mesoscale limited area model (LAM) with a grid size of 50x50 km. The analysis scheme is based on a successive correction method proposed by Bratseth [4] and the main features of the model are described in for instance Grønås and Hellevik [5], Grønås and Midtbø [6] and Nordeng [7].

The model used in this paper is also a LAM model but with a 5x5 km grid size and a topographical resolution of 1x1 km. Both models have 31 "layers" in height extending up to 100 hPa, here restricted to the lowest 14 layers, thus approximately reaching about 10 km above the surface. The height of the individual layers will vary from time to time to ensure that the hydrostatic balance in the model results are maintained. In the monthly summaries the monthly mean height is used and it is seen that the variation is typical about 2% of the height in concern.

The use of a model of the LAM type has the advantage that it can be a running operational model with possible prognostic capabilities also for radio-meteorological purposes. The disadvantage, however, is that the integration scheme tends to smoothen out the most pronounced discontinuities in the various meteorological fields; thus hiding the events that can be most interesting from a radiometeorological point of view. Another drawback is the vertical resolution; discontinuity layers of only a few meters can be of critical importance for the propagation of the electromagnetic waves and thus the field strength in space. Such layers will not be "detected" by a LAM model; to discover such phenomena a pure boundary layer model should be used. It is expected that the pressure and temperature fields are reasonably well modelled, but that a certain amount of uncertainty in the humidity values exists.

However, the expectation of using a LAM model is to detect some sort of spatial distribution of the atmospheric refractivity, and also a point variation in time. The time variation is of special interest since most of the observations of the vertical structure of the atmosphere are only done twice a day by radio sondes at hour 00 and 12 GMT. It is to be expected that the weather in transition from a nightly regime to a day regime, or vice versa, could create complex profiles in the various meteorological parameters both in the vertical and the horizontal scale. The improved horizontal resolution in the model will also be an advantage from this point of view.

## 4. PROPAGATION AND METEOROLOGICAL MEASUREMENTS

### 4.1 Meteorological stations

There are several synoptic weather stations in the area under consideration observing the parameters required for computation of the surface refractivity. Radiosondes are launched twice a day from two stations in the area. A list of these stations including geographical coordinates is given in table III

### 4.2 Propagation experiment

Norwegian Telecom has performed some measurements at the coast of Helgeland over the last few years. The links are part of the trunk network to provide 140 Mbit/s. The links operates in the 6 GHz band and the equipment uses 16 QAM modulation, resulting in a radio bandwidth of approximately 35 MHz. Information about these links is summarized in Table IV. It should be noted that space diversity protection is used for the two longest links, and frequency diversity for the shortest one. The terrain profiles with the main path are shown in Fig. 1 on a flat earth model (k-factor=$\infty$). All links have large path inclination angles. They are designed with enough clearance to meet standard recommendations given by ITU, and reflections from the surface of the sea are not visible. However, the specular reflection point on the sea is seen from one of the terminals on the two longest links, and the blocked reflection from the sea could be part of the multipath propagation mechanisms. All paths go over a considerable amount of water, and the longest path in the middle is almost entirely over water.

Measured data from the link Gulsvågfjell-Munken (Transmitter-Receiver) are available for several years, and from parts of the years 1993 and 1994. Only 1993 summer months were covered for the link Åsen-Gulsvågfjell. The measured distributions are based on measurements taken with a sampling interval of 0.033 s. The diversity distribution is based on a "hypothetical" combiner selecting the strongest signal of the two input.

## 5. MEASURED AND MODELED RESULTS

### 5.1 Meteorological synoptic results

This results is compiled in a set of time series for 3 hours of the day, 06,12 and 18 GMT where the single points are a mean of the results from all stations given in table II. The major part of the stations are situated at the coast or even at lighthouses, only 2 stations are "inland". A small variation in the values is to be expected as a consequence of the maritime climate, particularly at 06 GMT, as shown in figure 3. The greater variation in the day is mainly caused by the inland sta-

tions. Mean values for the month are in accordance with long term values given by Lystad [8].

### 5.2 Radiosonde results

Data from the two radiosonde stations are interpolated in vertical 100 m step and fig 4 show the cumulative distribution of the refractivity gradient between selected heights. Clearly the special layered lower atmosphere at Bodø is pointed out. The results of both stations are comparable with curves and figures given by Lystad [8] where for Ørland the long-term gradient 0/100, and for 1993, month as July is -93.9 and -104.5 (N/km) respectively. The same figures for Bodø are -127.0 and -158.1 (N/km) indicating a little more severe layering in 1993 as in the mean for the period of 1982-1991.

### 5.3 LAM results

The LAM 5x5 km grid size model is initialized by values given by the LAM of 50x50 km grid sizes. For the area under consideration a main set of grid values extending from approximately Trondheim in the south to the Lofoten archipelago in the north thus also covering an area with two radiosonde stations were chosen: Ørland in the south and Bodø in the north. Each 5x5 km cell in this area was computed. Interpolated values were calculated for the geographical coordinates of the various terminals of the links. In addition the grid values were computed for Ørland and Bodø to make a comparison with values from the radio sondes.

Fig. 5 shows as an example a horizontal contour plot of the refractivity in the first gridlayer or approximately at the ground. The contouring takes the fine mesh topography into account. Rapid variations of refractivity normal to the coastline are seen as a combined effect of the topography and the variation in the meteorological fields.

To study the horizontal variability the refractivity was computed for points about 7 km west of the radio link terminals as well as for points 7 km east, to ensure that the border of neighboring gridcells are passed. In addition a line of 110 km east of the terminals (about 2 deg. longitude) was chosen to cover conditions further from the coast in the interior of the land. There are therefore 16 points in a sort of a matrix. The points according to this scheme are denoted as (i,j) where (1,1) is the point or "station" leftmost in the upper row (northwest) and (4,4) the rightmost point in the lower row (southeast), see Table III. The line of the link will then be (2,j), where j=1,4. The model was initialized at hour 00 GMT every day in the period of July 1993 and ran with prognostic values for every 3 hours in a period of 24 hours. The statistics were thus based on a total of 62566 single values for the point grid and 1736 values for the radio sonde stations.

Fig. 6 shows a cross section of the atmosphere in the vertical plane between Munken and Gulsvågfjell. Isolines of refractivity are given in N-units together with the heights of the various gridlayers in hPa. It shows clearly certain structures in the vertical refractivity field near by Gulsvågfjell. In Figs. 7 and 8 are shown the mean daily course of the refractivity gradients in the defined subgrid around the links for the two lowest grid layers. In the first layer it is a marked daily course especially in the minimum values. In the second layer this course is more or less inverted. Since the atmosphere is heated from below this seems reasonable. The variation inland (column 4) is generally less than the variation in the coastal district.

### 5.4 Propagation results

Almost one year of the measurements from 1993 on the link Guls_Munk were presented in [9]. The summer months showed most fading and enhancement. Measurements from 1993 are available for Gjel_Munk from June to September, and for Åsen-Guls from July to September. From this period data also exist on a link from Munken to Gulsvågfjell, i.e. in the opposite direction to the first link.

Data show May to be the worst month on the link Guls_Munk_Main [9]. No data are available, however, for May from the two other links. Since the fade depth difference for July is less than 2 dB for the major part of the distribution compared with May, it is considered that July may represent quite closely the worst month this year for all the links. The other months show less fading than July, and this is the case for enhancement as well.

Time series for July are given in Fig. 9 for the three links Gjelt-Munk, Guls-Munk and Åsen-Guls. It is noted that data do not exist from the beginning of July. Because of radio equipment failure the last few days could not be considered in the analyses leaving the period under investigation to about 22 days, including 5th (4th from Åsen) to 27th July. The the time series plot points out the days with most activity, as well as quiet periods. It is noted that there was multipath activity on the 16th for the two most southern links, but not so for the northern link (Åsen-Guls). On the 23rd, for example, the two most northern links were affected, but not the most southern.

The July fading and enhancement distributions are shown in Fig. 10. In total 8 distributions are presented, covering all main and diversity protection channels. All distributions are referred to their median values, i.e. 0 dB for 50% of the period investigated. Note the difference from the northern link to the two others, where the northern and shortest link shows very little activity and the two others show both large fading and fairly large enhancements. Note also the two distributions Guls_Munk_Main and Munk_Guls_Main. These are measured on exactly the same link, but in the two oppo-

site directions (one measured at Munken and the other at Gulsvågfjell).

Measured improvement on the "theoretical combined" signal is shown as distributions in Fig. 11. The improvement I is obtained by taking the percentage at a certain level of the main distribution and divide it by the percentage obtained for the combined distribution I=P/Pd. All space diversity systems show large improvement; for example a 10 times reduction in fading occurrence is obtained at 20.5, 16.0, and 12.5 dB for the links Guls_Munk, Munk_Guls, and Gjel_Munk, respectively.

## 6. DISCUSSION

### 6.1 Multipath and duct statistics

During 1993, both Bodø and Ørland radiosonde data show most surface based ducts in July [9]. At Bodø the duct intensity is largest in July, with a mean of -9 M-units and a standard deviation of 5. The picture is not as clear at Ørland, where the mean shows a somewhat larger intensity during summer months compared with the rest of the year. The duct height shows similarities with the intensity; for example Bodø shows a clearer difference in height from summer to winter than does Ørland. In July at Bodø some of the most extreme duct height values are above 200 m with a mean height of 78 m above the station (20 m above sea), see fig. 12. This month also produces most ducts and ducts with largest intensity, in fact almost every ascent show a duct. Elevated duct heights are generally above 1 km during the summer period.

The link terminal heights are given in Table I. It is noted that Åsen has the lowest height of 79.5 m above sea level, Munken has receivers at 130, 155 and 166 m, Gjeltheia at 590 m, and finally Gulsvågfjell at 758.8 and 788.8 m. This puts the Åsen transmitter close to the mean duct height and transmitters and receiver at Munken are also within the mean plus two standard deviations. At Gulsvågfjell the transmitters and receivers are all well above the ground-based ducts, and the elevated ducts are well above the terminals. The large path elevation angles results in a large negative angle between the direction of the wave transmitted and received at Gulsvågfjell and the horizontal. The elevated ducts probably do not take much part in the propagation mechanisms. It is a similar case for Gjeltheia. On the other hand, at the lower terminals at Munken and Åsen the transmitted and received wave front propagates more or less in parallel with the horizontal surface, in particular at Munken. Therefore, it is likely that the surface ducts play a role on these links, and the parts where the radio wave interact with the duct are near the lowest terminals.

Reflection from the surface of the sea probably play some active role in creating deep multipath events. On the link Guls_Munk_Main, the sea reflection is blocked only by some meters. That means that the level seen from sea could be only 10 dB down from the direct signal. However, the antenna pattern of the combined vertical offset receiver antennas discriminates against this point of reflection with something close to 20 dB. The diversity antenna 10 m below the main has about 10 m extra blockage. The single antenna, however, has a wider beam and therefore discriminates less than for the main against reflections, such that the effect of reflection may be comparable on the two receivers.

On the link Gjel_Munk, it is mountains between the transmitter and sea that blocks for sea reflections. The possible reflection area on the sea is seen from both receiver sites, and has, if any, a comparable influence.

### 6.2 The LAM results versus soundings

To make a comparison of the refractivity values (it seems more reasonable to compare the refractivity values directly than make a comparison between the pressure, temperature or humidity since there is no linear dependence between the refractivity and these parameters) the heights in the LAM-model are determined. The interpolated values of pressure, temperature and dew point temperature are then derived from the radiosondes for the same heights. Since the sounding can report values from a lot more levels, it seems safer to interpolate the ascent from the sonde than for the LAM profile with only 14 levels up to 10 km. By such a procedure two sets of data are obtained at the same height level, one set from the model and one interpolated set from the radio sondes. The two sets of data can now be compared. Soundings from the stations Bodø and Ørland are made twice a day, at 00 and 12 GMT, and therefore there is a possibility to evaluate the prognostic capability of LAM by comparing model data from hours 12 and 24 GMT with the soundings from 12 and 00 GMT, respectively. Looking at the sonde values as the "real" description of the vertical structure of the atmosphere Fig. 13 shows that for monthly mean conditions (July) LAM models quite well the refractivity.

Ten year means for the total refractivity (Nunits) from soundings at Bodø and Ørland, show the following values, Lystad [8]:

| Stat/h | 0 | 100 | 300 | 500 | 700 | 1000 | 1300 | 1600 | 1900 |
|---|---|---|---|---|---|---|---|---|---|
| Ørland | 331.7 | 319.0 | 309.9 | 302.5 | 295.4 | 284.8 | 274.0 | 262.9 | 252.7 |
| Bodø | 332.6 | 323.2 | 314.3 | 305.9 | 297.9 | 286.1 | 275.0 | 264.1 | 253.4 |

The refractivity depending on pressure, temperature and humidity is modeled within 3% of the long-term value for the most active height, the suface level for

the hour 00 GMT; that is when the model is initialized. For prediction 12 hours ahead it is reasonable that the model gives poorer results but still the deviations are within a few percent of the long-term value.It is a little surprising that +24 hour prediction give better results. A possible explanation may be that this is midnight, and since the variation in the night weather regime is less than during the day in coastal areas, it can be possible to get better results than for the +12 hour prediction. Note also that Ørland has better model results than Bodø, the explanation being the rather special local atmospheric structure at Bodø (Lystad [8]).

As expected the dry term of the refractivity, depending on pressure and temperature, is better modelled (rather smooth meteorological fields) than the wet term depending on the humidity. The dry term is slightly underestimated, the wet term overestimated by an order of magnitude. It is therefore tempting to look for a direct relation between the refractivity values from the radio sonde and from LAM. In Fig. 14 is shown an example of a scatter-plot of the N-values by the interpolated values from the sonde and from the LAM model at the height 70 m. This indicates some sort of a linear relationship and a simple linear regression gives the correlation coefficients as a function of height for the two radiosonde stations sites, see Fig. 15.

As expected, the more well-mixed structure at Ørland gives better results in modelling than for the layered structures above Bodø. Here the correlation is almost nil in the lowest layer at hour 00 GMT, but improves as the height increases. For the prediction 12 hours ahead, the correlation is still almost nil and even slightly negative up to about 2500 m above ground. This could be evidence of the mentioned special atmospheric layering at Bodø. while more reasonable correlations for Ørland point to more "standard" atmospheric conditions.

### 6.3 Fade depth distributions

Looking at the fade depth distributions given in Fig. 10 there are several points to discuss. The distributions deviate systematically from a Rayleigh slope of 10 dB per decade at large fade depths. This is probably due the bandwidth of the system, with frequency selective fading averaging over the receiver frequency band. This may at least be the case for relatively long delays, for example 10 ns or longer, which is to be expected from blocked and diffracted sea reflections. However, between 15 and 25 dB the process seems to follow a Rayleigh distribution and it this part of the distributions that should be studied in the context of multipath occurrence.

The Åsen_Guls path show considerably less fading than the two others, and less that expected. There are, however, some points that may give reduced multipath activity on this path. It is the shortest link and have the largest elevation angle. This will normally result in less activity, but perhaps not as much as given by Fig. 10. A third reason for less activity is reduced influence of a possible sea reflection, since the blockage between Åsen and point on see for a specular reflection is much larger than for the two other links.

The links Gul_Mun_Main and Mun_Guls_Main employ the same antennas at both ends and the radio wave should propagate through the same part of the atmosphere, obeying the reciprocity principle. However, the fade depth statistics do show a significant difference at least at large fade depths. It is unlikely that incorrect calibration of the equipment is the cause. One source of differences are antenna alignments and radiation patterns. In this particular case two antennas are combined at each of the ends. At Munken these antennas are mounted such that there is a vertical offset of 2.2 m; at Gulsvågfjell there is no vertical offset. A vertical separation would cause the combined pattern to be narrower in elevation angle than for one single antenna or if the combination is with no vertical separation. Furthermore, the surface-reflected signal would arrive at a larger offset angle at the lowest terminal, i.e. Munken. The antennas at Munken have a narrower beam and sea reflection arrive at a larger angle than at Gulsvågfjell. Both of these will independently reduce fading due to sea reflections, and consequently the amount of fading at Munken if sea reflection is a major cause.

A third explanation has to be sought, such as propagation through an atmospheric layer from above and from below. Ray tracing calculations through the atmosphere using only measured refractivity over Bodø on the 16/7 at 12 hours, and assuming no horizontal gradients in N, show 11 dB fade depth at Munken and 7 dB at Gulsvågfjell. With another position of the layer it would be possible to get larger differences. Considering only the atmospheric part, a duct may result in a larger fade depth at Munken than at Gulsvågfjell. If see reflections of comparable amplitudes are present the result could be deep fading which would occur more often at Munken.

Space diversity are employed at both Munken and Gulsvågfjell. All space diversity path show generally more fading than the main paths. The space diversity antennas are lower than the main antennas. Since the occurrence of ducts is higher at a lower point at Munken it might be expected that the space diversity path show more activity. Since these paths employ only a single antenna, they have consequently a larger antenna beam that the main links, and more of sea reflection effects would be seen. At Gulsvågfjell the space protection antenna has got little clearance and may be obstructed under sub-refractive conditions.

The results from diversity improvement on the longest links follow what is to be expected from analog links, i.e. the larger the spacing the larger the improvement. In one direction the spacing is 10 m, and in the other it is 30 m. However, the shorter 73.3 km link of Gjel-Munk shows significantly larger improvement factor that the 93.8 km links. This is also, to some extent, predicted by the ITU-R method [10].

### 6.3 LAM versus propagation

Propagation conditions on the links are recorded as time series at the link terminals, see Fig 9. Recognizing gradient values of the refractivity less than -100 N/km as an indication of possible propagation problems, a computation of the gradients as time series in the three lowest layers of the LAM "ascent" for all the points (2,j) can be compared to the above mentioned time series. In Fig. 16 are shown the gradients obtained between the first two grid heights. The behavior of the curves shows a striking similarity with Fig. 9, the days 15, 16 standing out clearly and also the period around the 21th. This shows a certain capability of the LAM model to predict periods of bad propagation conditions in spite of the smoothing effect that is included in this type of model.

## 7. CONCLUSIONS

Results from simulation of the atmospheric refractivity conditions by means of a LAM model is in good agreement with the "reality" represented by the radiosondes. The use of a high horizontal resolution of 5 km combined with a topographical resolution of 1 km gives a fairly good description of space variability of the refractivity. The variation in time seems also rather well taken into account by the 3 hour integration span in time. However by a full data assimilation and initializing the model as often as possible (not only pr 24 hour) it could be expected even better results. The results show also that the daily course of the refractivity computed by the model varies reasonably both in vertical and horizontal scale and that the model has a certain capability even to predict anomalous propagation conditions. The computation of the refractivity gradient by means of the model values explains also observed multipath conditions. The possible interpolation in space and time by means of the grid values from the model seems then to be a useful tool in describing radiometeorological conditions even in such a complex atmosphere as that belonging to coastal areas.

## 8. REFERENCES

[1] ITU-R, "Draft revision of recommendation ITU-R PN. 530-4: Propagation data and prediction methods required for the design of terrestrial line-of-sight systems", Doc. 5/68, Geneva, Switzerland, 26 October 1993.

[2] Tjelta, T., Tanem, T., and Lind, K., "New prediction methods for the amount of multipath fading on radio links in Norway", Research Document 70/91, Kjeller, Norwegian Telecom Research, 1991. (In Norwegian)

[3] Lowry, W., "Compendium of lecture notes in climatology for class IV meteorological personal", WMO publication 327, Geneva, 1972.

[4] Bratseth, A.M., "Statistical interpolation by means of successive corrections", Tellus 38A. 1986, pp. 439-447.

[5] Grønås, S. and Hellevik, O.E., "A limited area prediction model at the Norwegian Meteorological Institute", Techn. rep. 61. The Norwegian Meteorological institute, Oslo, Norway, 1982.

[6] Grønås, S. and Midtbø, K.H., "Four dimmensional data assimilation at the Norwegian Meteorological Institute", Techn. rep. 66 Research department, The Norwegian Meteorological institute, Oslo, Norway, 1986.

[7] Nordeng, T.E., "Parameterization of physical processes in the three dimensional numerical weather prediction model", Techn. rep. 65 Research department. The Norwegian Meteorological institute, Oslo, Norway, 1986.

[8] Lystad, S.L., "Surface refractivity and refractive gradients in lower atmosphere of Norway", DNMI klima rapport nr 04/94 klima The Norwegian Meteorological institute Oslo, Norway, 1993.

[9] Tjelta, T. and Lystad. S. "Line-of-sight microwave propagation and clear air climatic conditions for coastal regions under the northern polar circle", in conf. proc. of Climatic Parameters in Radio Wave Propagation Prediction, Moscow, 31 May-3 June, 1993. Paper 8.2

[10] ITU-R, "Recommendations. RPN-series. Propagation in non-ionized media", Geneva, Switzerland, 1992.

## ACKNOWLEDGMENTS

We would like to thank L. Sidselrud and A. Foss from the research division of NMI for invaluable help in transforming the operational LAM models to compute the necessary refractivity values and also P. Vidal from the climate division for running the programs at the Cray computer and local computer systems. Helpful discussions with T. Tanem, A. Nordbotten, and Roderic L. Olsen are also gratefully acknowledged.

Table I: Atmospheric structures

| type | length scale (m) horizontal and vertical | | time scale |
|---|---|---|---|
| micro | $10^{-2}$ - $10^{3}$ | $10^{-3}$ - 10 | min/h |
| local | $10^{2}$ - $5 \cdot 10^{4}$ | 10 - $10^{3}$ | h/day |
| meso | $10^{4}$ - $2 \cdot 10^{5}$ | 10 - $2 \cdot 10^{3}$ | week |
| macro | $10^{5}$ - $10^{8}$ | $2 \cdot 10^{3}$ - $10^{5}$ | week -> |

Table II: Synoptic surface and radiosonde stations, with int.(international number) and nat. (national number) with latitude, longitude and height above mean sea level

| Int. no | Nat no. | Name | Lat. | Lon. | H |
|---|---|---|---|---|---|
| Synoptic stations | | | | | |
| 1228 | 6594 | Sula | 63.85 | 8.467 | 13 |
| 1241 | 7155 | Ørland III | 63.7 | 9.6 | 9 |
| 1240 | 7155 | Halten | 64.167 | 9.417 | 16 |
| 1134 | 7199 | Majavatn III | 65.183 | 13.417 | 339 |
| 1280 | 7210 | Namdalseid | 64.25 | 11.2 | 86 |
| 1295 | 7362 | Harran | 64.583 | 12.533 | 118 |
| 1102 | 7555 | Sklinna fyr | 65.2 | 11.0 | 23 |
| 1149 | 7953 | Rana-Båsmoen | 66.333 | 14.1 | 40 |
| 1115 | 8061 | Myken | 66.75 | 12.483 | 17 |
| 1115 | 8061 | Bodø VI | 67.267 | 14.367 | 11 |
| Radiosonde stations | | | | | |
| 1241 | 7155 | Ørland III | 63.7 | 9.6 | 10 |
| 1152 | 8229 | Bodø VI | 67.267 | 14.7 | 8 |

Table III: Matrix for study of LAM results (Matrix position-(i,j), link stations (for i=2), geographical latitude and longitude, station height (m) (for i=2), and model height (m))

| | | | |
|---|---|---|---|
| (1,1)<br>.....<br>66.017<br>12.5<br>.....<br>164 | (2,1)<br>Åsen<br>66.017<br>12.617<br>60<br>208 | (3,1)<br>.....<br>66.017<br>12.733<br>.....<br>232 | (4,1)<br>.....<br>66.017<br>14.617<br>.....<br>970 |
| (1,2)<br>.....<br>65.65<br>11.717<br>.....<br>117 | (2,2)<br>Gulsvågfjell<br>65.65<br>11.833<br>728<br>207 | (3,2)<br>.....<br>65.65<br>11.95<br>.....<br>136 | (4,2)<br>.....<br>65.65<br>13.833<br>.....<br>633 |
| (1,3)<br>.....<br>64.85<br>11.083<br>.....<br>22 | (2,3)<br>Munken<br>64.85<br>11.2<br>91<br>79 | (3,3)<br>.....<br>64.85<br>11.317<br>.....<br>357 | (4,3)<br>.....<br>64.85<br>13.2<br>.....<br>626 |
| (1,4)<br>.....<br>64.267<br>10.417<br>.....<br>232 | (2,4)<br>Gjeltheia<br>64.267<br>10.533<br>519<br>319 | (3,4)<br>.....<br>64.267<br>10.65<br>.....<br>356 | (4,4)<br>.....<br>64.267<br>12.533<br>.....<br>349 |

Table IV: Radio link characteristics

| | Gjeltheia | Munken | | Gulsvågfjell | | Åsen |
|---|---|---|---|---|---|---|
| Geographical coordinates | 10.5328 E<br>64.2611 N | 11.2078 E<br>64.8539 N | | 11.8300 E<br>65.6572 N | | 12.6281 E<br>66.0186 N |
| Transmitter (T) or Receiver (R) | T | R | R/T | T/R | R | T |
| Path length (km) | 73.3 | | 93.8 | | 54.1 | |
| Frequency (GHz) and polarization, main/freq | 6.80 V | | 6.54 V/6.80 V | | 6.54 H/ 6.7 H | |
| Approximate bandwidth (MHz) | 35 | | 35 | | 35 | |
| Height (m) of terminal groundlevel above sea | 519 | 91 | | 728 | | 60 |
| Antenna height (m) above ground, main/space | 71.0 | 75.0/39.0 | 75.0/65.0 | 60.8/30.8 | 41.6 | 19.5 |
| Antenna diameter (m) | 3.7[1)] | 3.7[1)] | 3.7[1)] | 3.7[1)] | 3.7 | 3.7 |

[1)] Two of these antennas are connected in parallel (beside each other) to achieve larger margin

Fig. 1. The area of northern Norway used for LAM

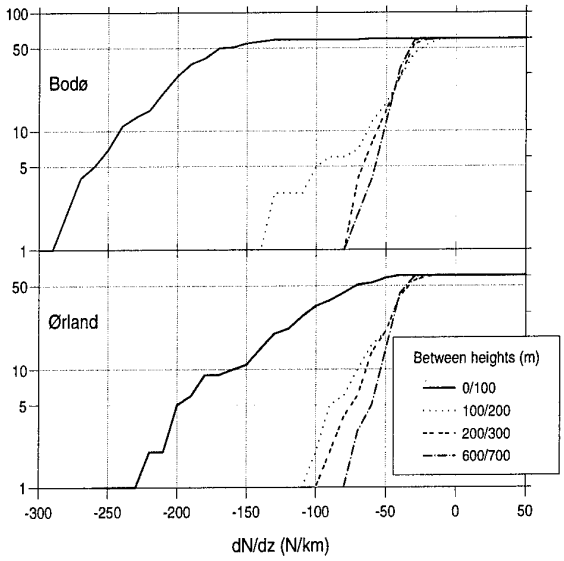


Fig. 4. July 1993 cumulative distributions of dN/dz measured by the radiosondes

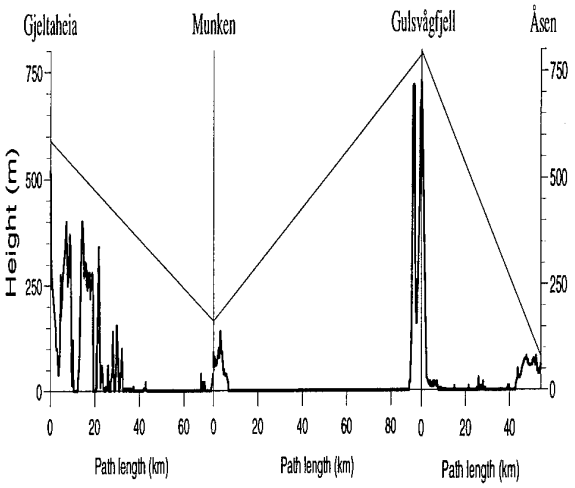


Fig. 2. Path profiles

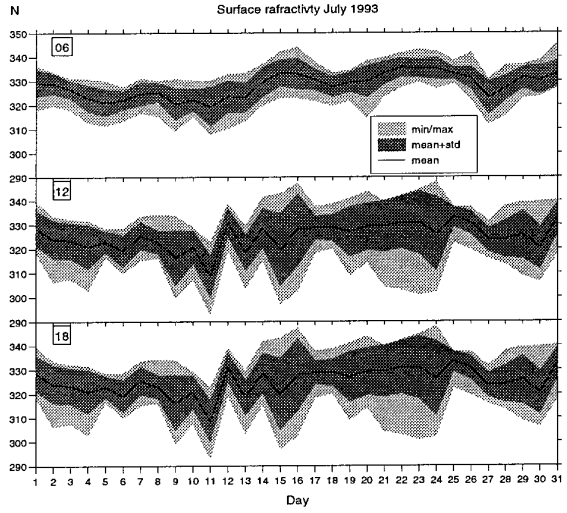


Fig. 3. Synoptic station results

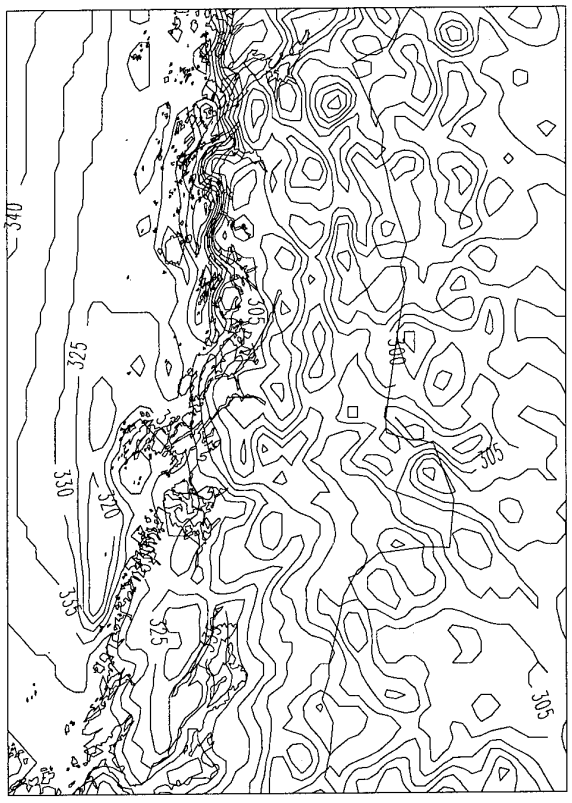

Fig. 5 Mapping of refractivity at approximately ground level (first grid height) at 16/7 06 GMT

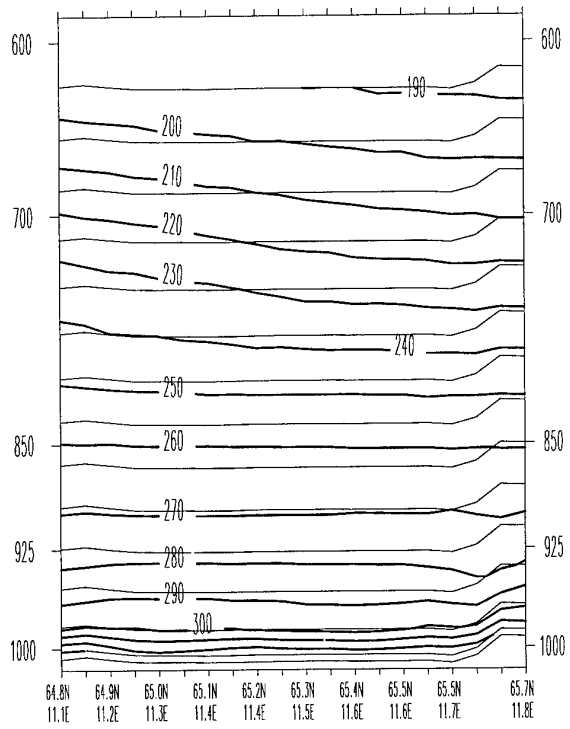


Fig. 6. Refractivity in a vertical plane from Munken to Gulsvågfjell 16/7 06 GMT (height scale in HPa).

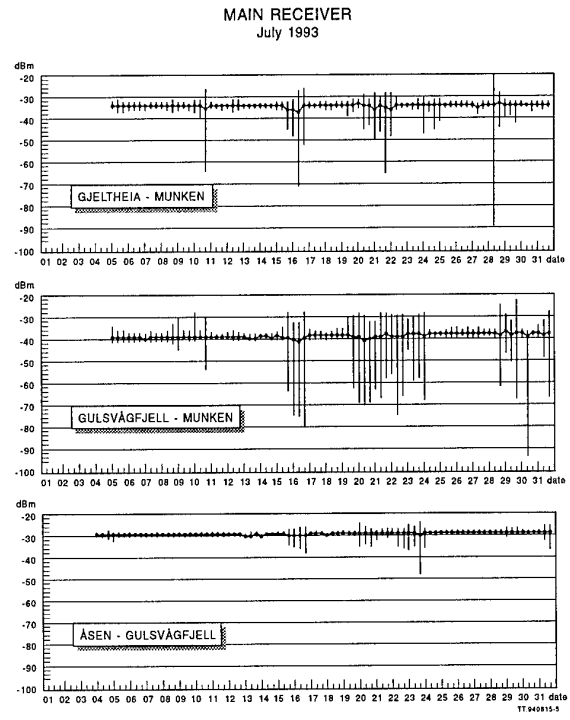


Fix. 9. Time series for the three main links

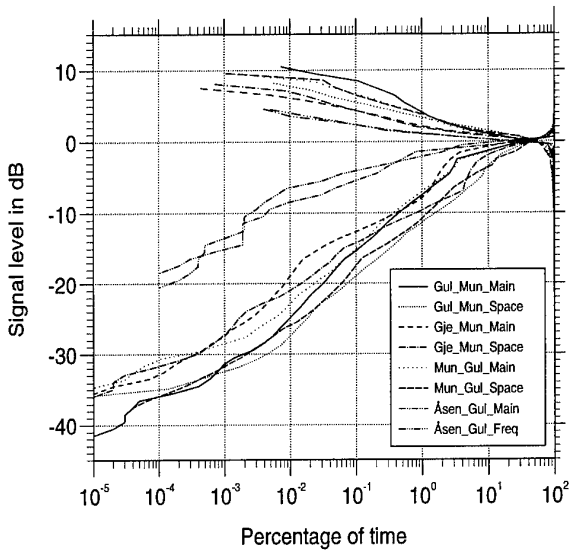


Fig. 10. Cumulative fade depth and enhancement distributions for the 8 links July 1993

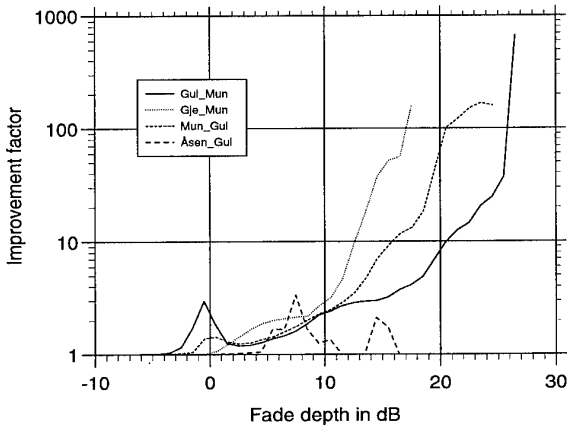


Fig 11. Measured diversity improvement

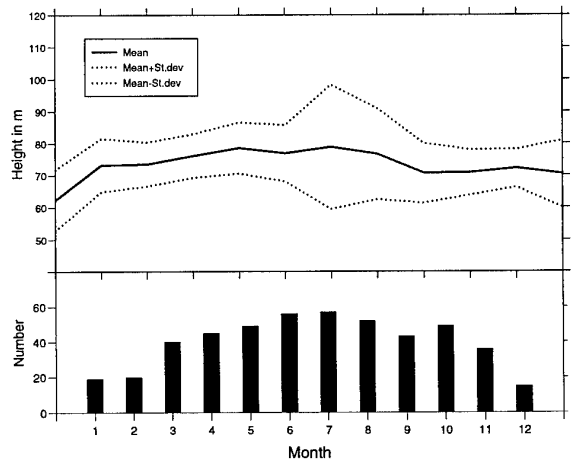


Fig. 12. Number of ducts and duct heights at Bodø 1993

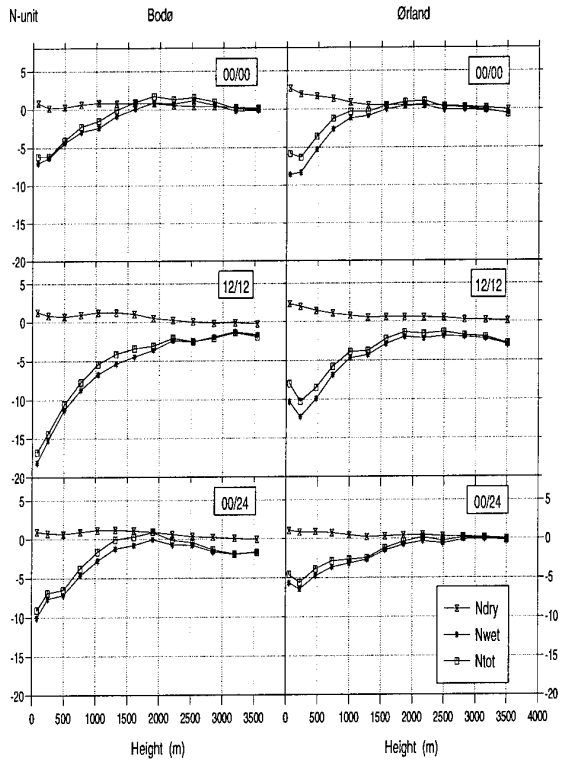


Fig. 13. Difference in refractivity obtained by the radiosondes and LAM

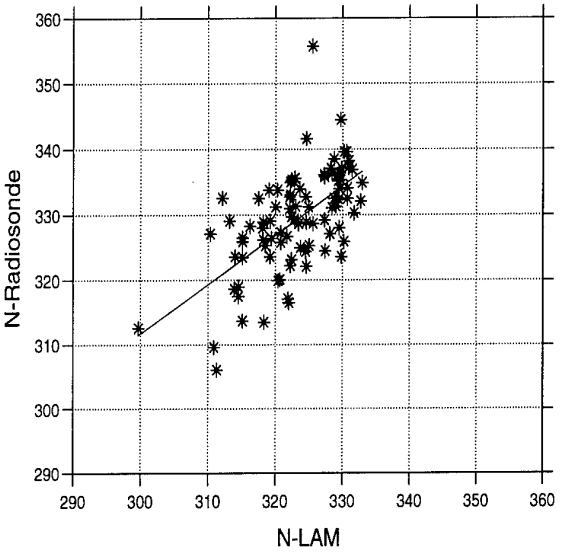


Fig. 14. Difference in refractivity obtained by the radiosonde of Ørland and LAM at surface (first grid height)

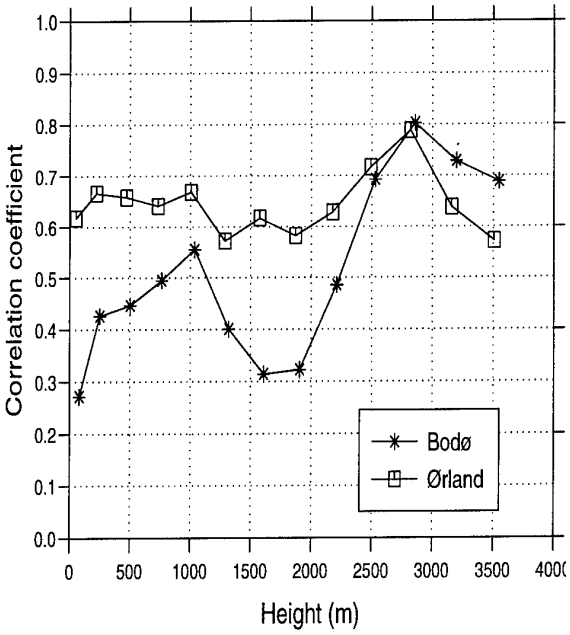


Fig. 15. Correlation radiosondes and LAM

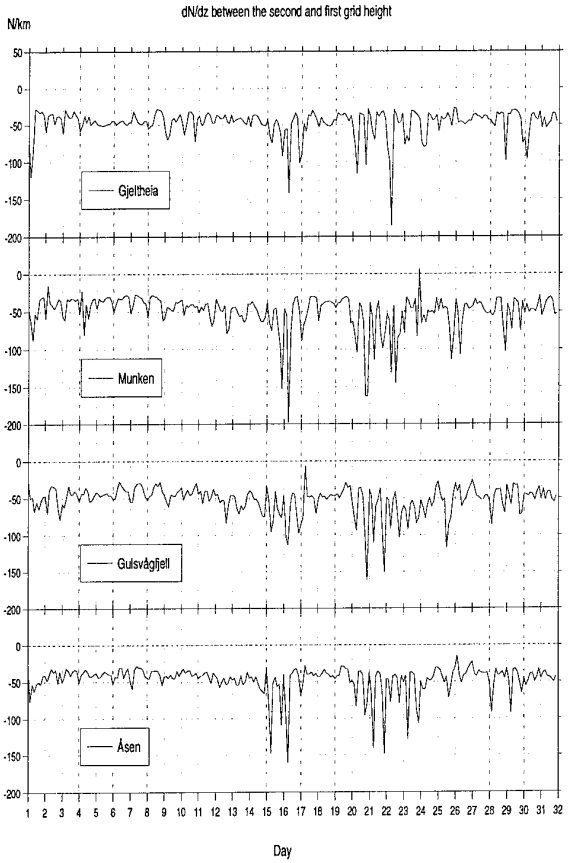


Fig. 16. dN/dz timeseries obtained from the first and second grid heights of LAM for the link stations

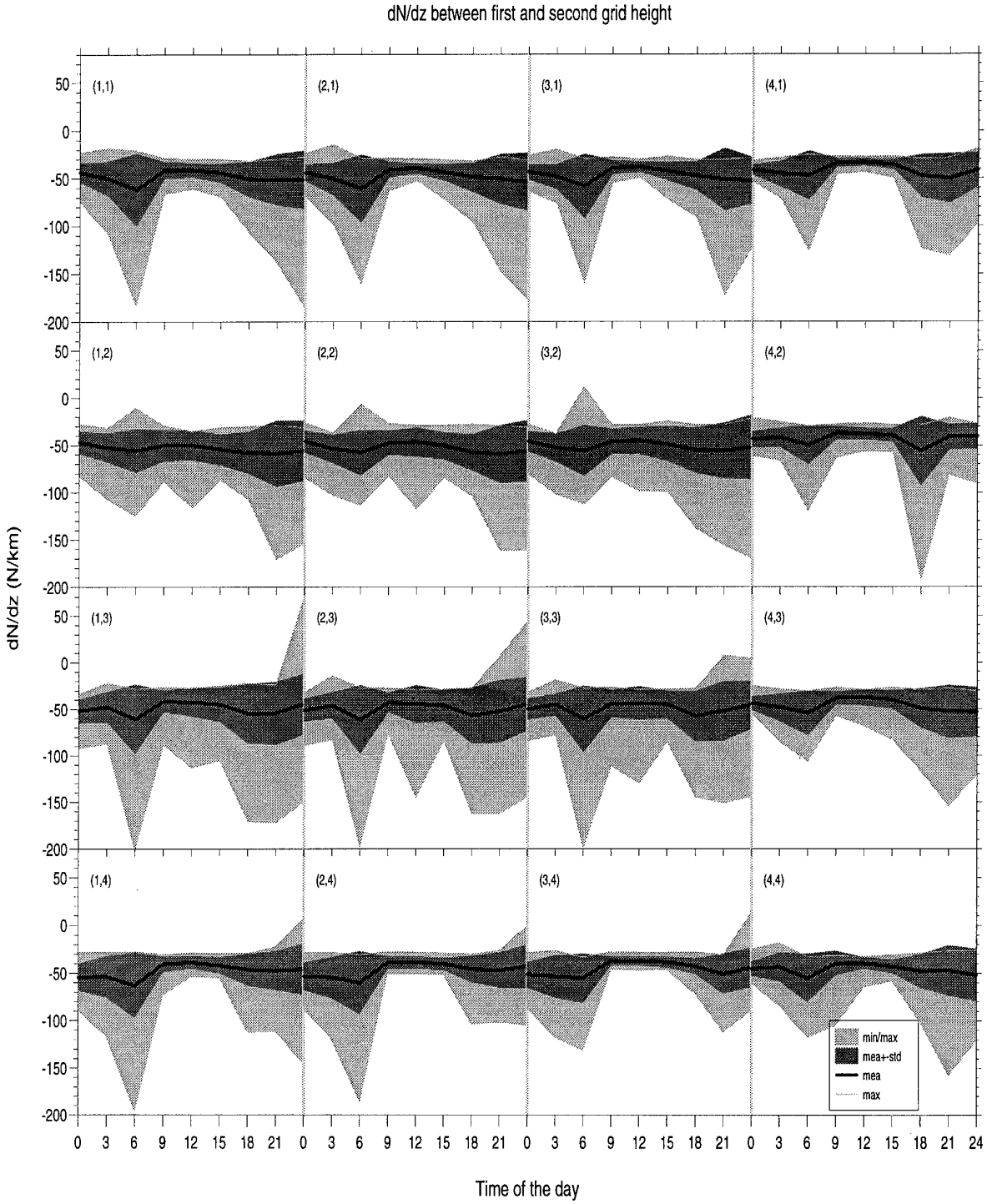


Fig. 7. dN/dz obtained from the first and second grid height of LAM for the defined sub-grid in Table III

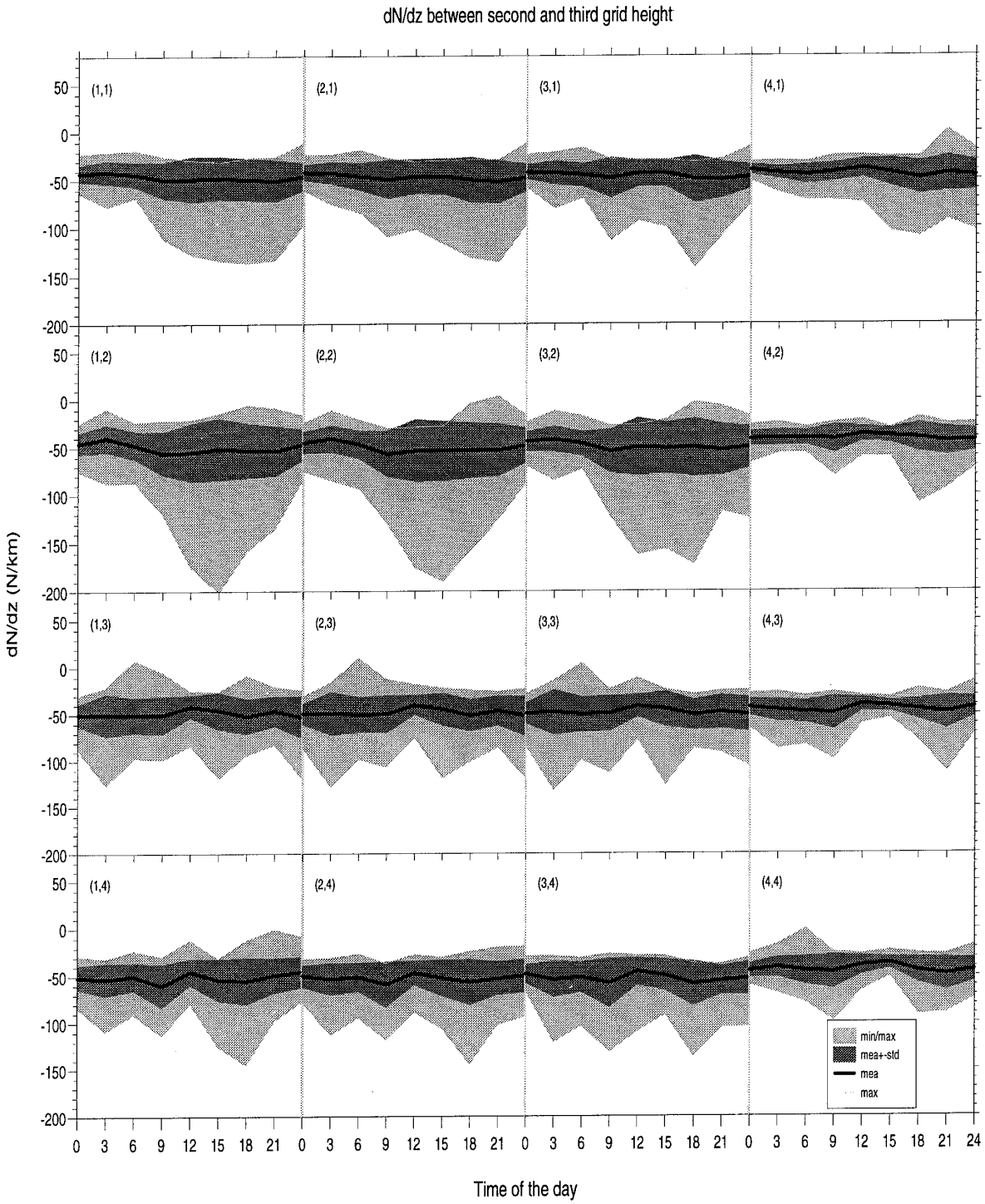


Fig. 8. dN/dz obtained from second and third grid height of LAM for the defined sub-grid in Table III

## DISCUSSION

**W. OLSEN**
What was the synoptic pattern during the anomalous refractive period, (19-23 Jul I think) during which the LAM 5 output also showed the pronounced dN/dz correlating to signal reduction?

**AUTHOR'S REPLY**
For the month, the weather was mainly anticyclonic with dry, warm air emerging from east. Temperatures for the month were well above normal for the whole month. For the mentioned days we plan to produce the relevant weather maps (S. Lystad) and give the information in future publications.

**C.R. PHILBRICK**
Could you and the previous author, Dr. Burk, please elaborate on the future direction for the mesoscale models? It is obvious that the future useful tool is the combination of measurements and models; what is needed to advance the data assimilation mesoscale models? more layers? different grid? particular data?

**AUTHORS' REPLY**
**T. TJELTA:**
Better parameterization of the active surface layer (i.e. moisture sources and transport) together with a "manageable" increase in low level layers and inclusion of better topographic information would improve results, but this is surely dependent on the amount of data for initialization/assimilation.

**S. BURK:**
In complex forecast systems such as these, one must always seek the "weakest link" and attempt to make improvements there. Based on our VOCAR experimental results, it is my feeling that the weakest link in our mesoscale model (in so far as refractivity forecasting is concerned) is the need for a better analysis of the moisture field. Moisture tends to be a highly structured 3-D field which is only poorly sampled. Therefore, there is the need for better initialization techniques and to improve the extraction of moisture fields from satellite observations, etc.

**U. LAMMERS**
Did you imply in your paper that the observed multi-path propagation on the long links was likely due to surface reflection? Using a vertically scanning receive beam of .15° half power width, we observed multiple beams on a 100 km reflectively perturbed line-of-sight path which definitely originated in the atmosphere, not on the mountainous, rough terrain below.

**AUTHOR'S REPLY**
I believe we see a combined atmospheric and ground reflection effect. The atmospheric duct creates a condition for deep fading allowing blocked sea-reflections to have an influence. On the northern link, Åsen to Gulsvaagfjell, we observe less fading activity. If atmospheric multi-path dominated we would have seen more activity on this link than actually observed.

# A MICROWAVE PROPAGATION MODEL COUPLED TO AN AIR MASS TRANSFORMATION MODEL

G.E. Grandin
Military Weather Service
Swedish Air Force Headquarter
S-107 95 Stockholm, SWEDEN

SUMMARY

Since 1985 a project in order to improve microwave propagation forecasts has been run in the Swedish Military Weather Service. The purpose has been to test if there are computer-based models that are more useful than earlier manual methods. Until now two different kinds of models have been tested: The first one is a simple refractive index model for use on board warships. The second kind of model is a refractive index model coupled to a one-dimensional boundary layer model connected to a horizontal trajectory in order to describe horizontal advection.
The result is presented by ray tracing diagrams in order to give advices for tactical descisions at military aircrafts, warships and radar stations.
Experiments with those two models have been made mainly over the Baltic Sea. During 1987-1992 the "simple" model was tested on board a warship. During the same period the other model was tested on nine sites in Sweden. There have been three "intense" periods where extra efforts in personel, measurements and verifications were made.
The experiments showed that computer-based radar range forecasts are only usable in the Baltic Sea if:

A. There is input data with high quality

B. The weather situation is homogeneous

C. The operators are educated

## 1. INTRODUCTION

The Baltic Sea is a very important sea for Sweden. It was and is still very important for Sweden from military point of view. Of special interest for us is of course to measure and predict the microwave propagation conditions over the Baltic Sea both for some hours and for some days ahead.

Since 1985 a project in order to improve microwave propagation forecasts has been run in the Swedish Military Weather Service. The pupose has been to test if there are computer-based models that are more useful than earlier manual methods. The project was preceded by a study directed by Edvard Karlsson, National Defence Research Institute. Among other models he studied the IREPS developed at NOSC in San Diego.

Until now two different kinds of models have been tested: The first one is a simple refractive index model for use on board warships. The radar range conditions in this model are calculated from parameters measured only on board the warship. The second kind of model is a refractive index model coupled to a one-dimensional boundary layer model. This model is a type of an air mass transformation model since it is connected to a horizontal trajectory in order to describe horizontal advection. The input data is from radiosoundings both ordinary and low level.

The results from the models are presented by ray tracing diagrams for illustrating wave propagation in the troposphere with different kinds of ducts. The purpose is to give advices for tactical descisions at military aircrafts, warships, and radar stations (however, the first kind of model is intended only for local use on board warships).

Experiments with the two models have been made mainly over the Baltic Sea. During 1987 - 1992 the "local" model was tested on board a warship. During the period the other model has been tested on nine sites in Sweden. There have been three "intense" periods (October 1987, May 1989, and May 1992) where extra efforts in personel, measurements and verifications were made.

A summary of model descriptions, experiments, and results follows here.

## 2. MODEL DESCRIPTIONS, EXPERIMENTS, AND RESULTS

### 2.1 Local refractive index model

The refractive index model for use on board has been developed to compute refractive index, ducts and microwave propagation. The calculations are based on measurements of sea surface temperature, air temperature, air humidity, and wind velocity on board the ship (see figure 1). The variations of the meteorological variables vs height are calculated with profile functions for a horizontally homogeneous, stationary surface layer of the atmosphere. Then the refractive index can be calculated and the "duct situation" can be evaluated.

Thus the only measured data are from the ship with maximum 15 meters height. To assume values for the atmosphere above, profile functions are used. Although they are only intended to be used in the surface layer they are also used for altitudes above it, sometimes for the whole boundary layer! The profile of the refractive index is estimated according to Davidson. The result is presented by a ray tracing diagram (figure 2) and a relative range percent number which is equal to calculated present radar range divided by normal radar range.

The model was programed in a PC on board a warship. Input data were taken from the measuring equipment on board the ship. The model was run daily often every hour or sometimes every 10 minutes. The calculated radar range at 15 meters height was compared with the observed range. The observed range was estimated from known distances to other ships, aircrafts, island, and coastlines. Notes were made about calculated or observed duct layers, different results in different directions from the warship and about the weather situations.

*Paper presented at the Sensor and Propagation Panel Symposium on "Propagation Assessment in Coastal Environments" held in Bremerhaven, Germany 19-22 September 1994.*

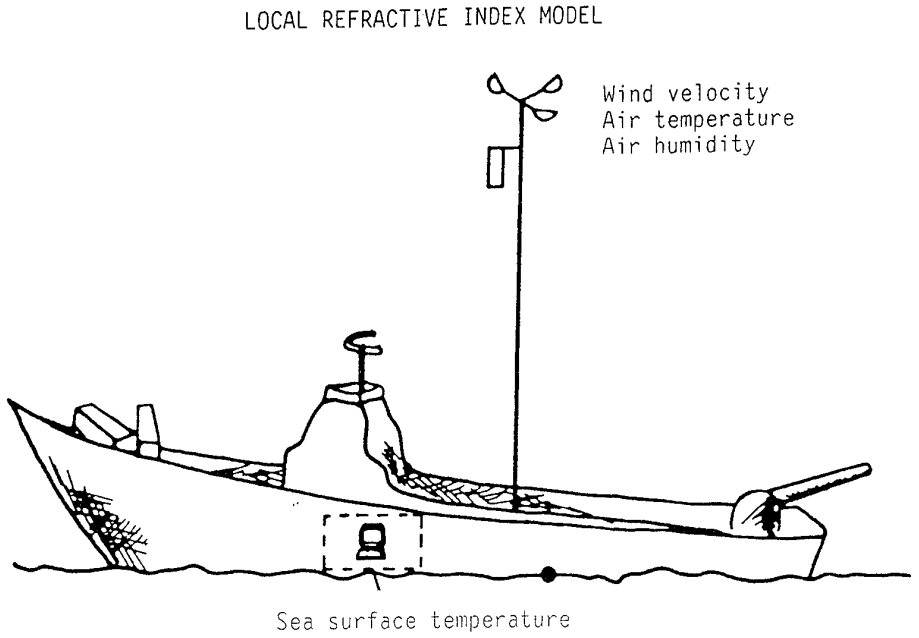


Figure 1. Measuring instruments for the local refractive index model on board a warship.

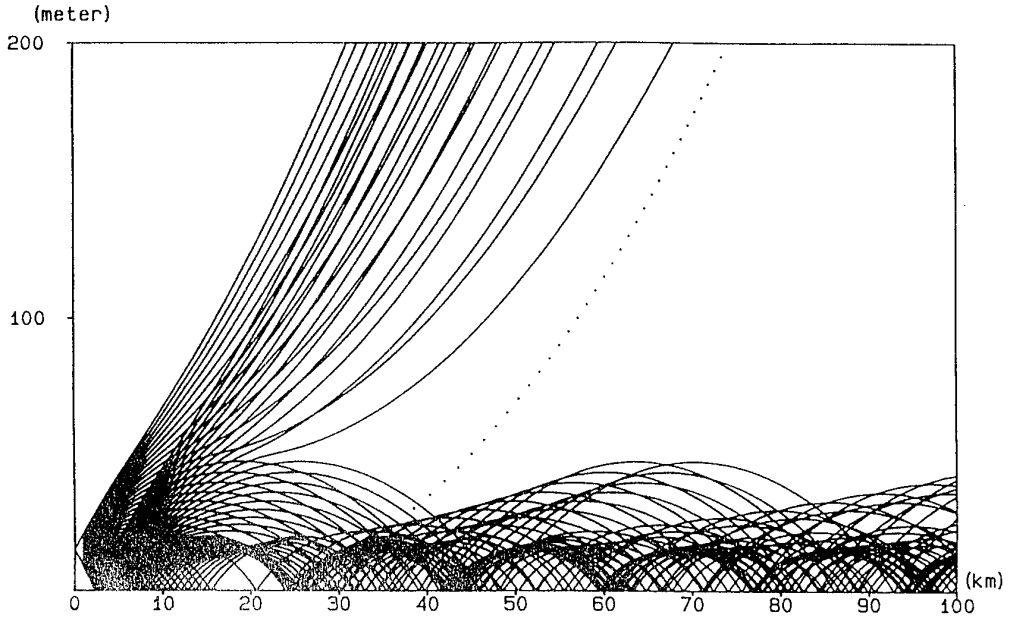


Figure 2. A ray tracing diagram is used to illustrate the wave propagation and different types of ducts. The antenna height is 15 meters above the sea surface.

| Observed radar range (%) | Estimated radar range (%) | | | Total number of cases | % "passed" results |
|---|---|---|---|---|---|
| | ≤ 80% | 90-140% | ≥ 150% | | |
| ≤ 80% | 3 | 5 | 0 | 8 | 38 |
| 90 - 140% | 9 | 45 | 8 | 62 | 73 |
| ≥ 150% | 2 | 20 | 57 | 79 | 72 |
| | | | SUM | 149 | 70 (average) |

Table 1. Verification of a local refraction index model. The table shows number of verified cases from experiments at the Baltic Sea 1987 - 1988.

The warship operated in the Baltic Sea during the tests that were made during the summer half years or 1987 and 1988 respectively. See results in table 1! The results show in average 70 % "good" agreement between the predicted and the observed ranges. But the results are bad at sub-refraction cases although the total number of such cases are rather few. Still we have decided to let this model pass to be in operational run because the long radar range situations are the most interesting ones for us.

2.2 The 1-dimensional boundary layer model along a trajectory

A one-dimensional boundary layer model (BLM) is assumed to be moved along a trajectory. The air column moves at the same speed as the wind velocity at the height where the turbulence is most intense. The BLM is a K-model with 30 vertical grid points and the top level is about 2000 meters (figure 3).

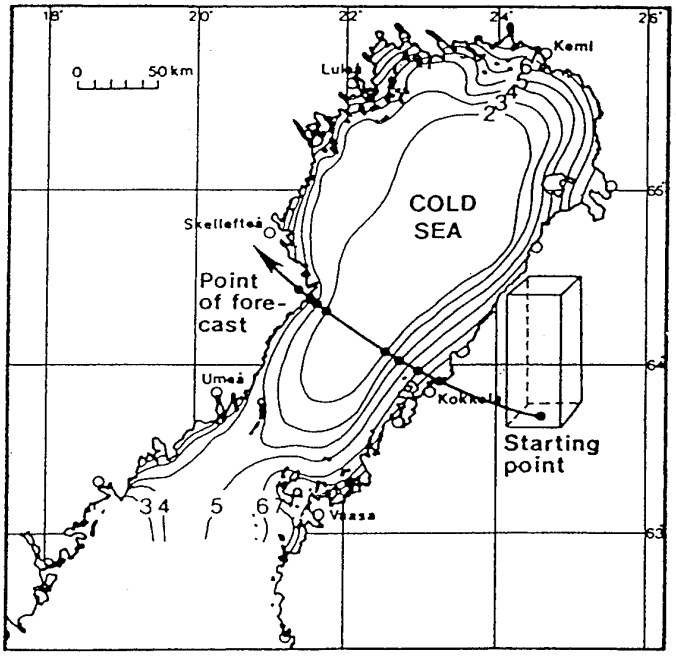


Figure 3. The air column (1-dimensional model) is moved along a trajectory.

A refractive index model is coupled to the BLM so it is possible to estimate the profiles of the refractive index along trajectories over for example the Baltic Sea. With a ray tracing model it is then possible to show the microwave propagation pattern from arbitrary radar antenna altitudes. The input data is taken from a suitable radiosounding station or from low level radiosoundings especially run for the microwave propagation project.

This model has been used in a test system that was run at 9 sites 1986-1993. From these 9 sites that were regional weather centrals or air bases it was possible to run the model with suitable radiosoundings as input data. The result was presented as ray tracing diagrams where the antenna height could be chosen.

The system was gradually built up and incresed after the start 1986 but it is still not in operational use. However, the pupose of the test system has been to provide basis to a future operational system and to gather experiences. The people at the sites (meteorologists) were instructed to make verifications continuously. The verifications were made with aircrafts, warships and radar sites at the ground and often at the coast.

We had three "intense" periods where people and equipments were mobilized. Then different types of flights were made with for example "Viggen" recce aircrafts. Figure 4 shows results from "diagram flights" one day over the Baltic Sea and a comparison with a ray tracing diagram (some data is missing to make this paper not classified).

Details from the results are classified but as a whole the results show that the 1-dimensinal BLM along a trajectory is meaningful to use 0 - 6 hours ahead over the Baltic Sea. Some improvements have to be done before the operational start of this system in 1995. For example the vertical grid will be made more course and it will be possible to take input data NWP (numerical weather predictions), for example mesoscale models.

## 3. CONCLUSIONS

Obviously, making radar range forecast is a very difficult problem. The risk is that they often can be more misleading than useful. One reason is that the atmosphere is inhomogeneos both in space and time. For example duct layers are very sensitve to that. Another reason is of course lack of appropriate input data.

Therefore we have stated:

The experiments showed that combuter-based radar range forecasts are only usable in the Baltic Sea if:

A. There is input data with high quality

B. The weather situation in the actual area is homogenous enough

C. The operators are educated enough in using radar range forecasts

## 4. PLANS

The local refractive model is alresdy in operational use at warships in Sweden. Now there are 3 equipments and the plan is to obtain one equipment to every surface warship squadron.

As I said, the 1-dimensional BLM along a trajectory with the ray tracing model is planned to be in operational use in 1995. Further on we plan to incorporate an improved presentation model, for example based on Parabolic Equation Models.

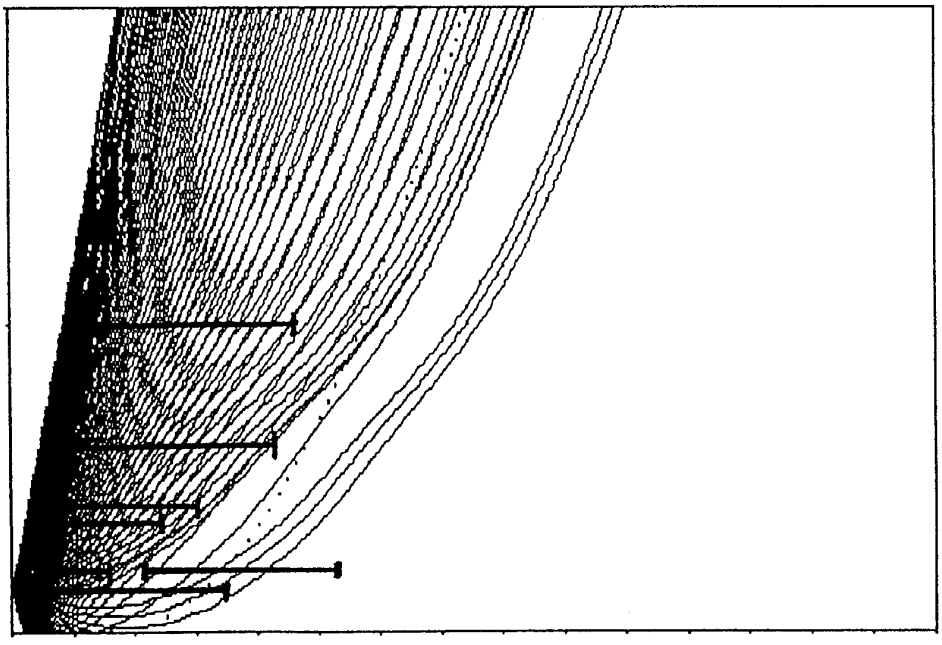

Figure 4. Comparison between the result from a ray tracing diagram and the observed positions of aircrafts from a radar site on the ground. The horizontal lines mean positions where the aircrafts were seen from the radar site.

## DISCUSSION

**D. DOCKERY**
Did radiosonde measurements indicate subrefractive conditions during those cases when the radar range was over estimated?

**AUTHOR'S REPLY**
Unfortunately I cannot answer that question because we have concentrated our studies on super-refraction. As I said, the verifications from the local refractive index model at warships showed bad agreement of observed-calculated radar range at sub-refraction cases (but no radiosondes were used here).

# Climatic Mapping of Refractivity Parameters from Radiosonde Data

**K.H. Craig and T.G. Hayton**
Radio Communications Research Unit
Rutherford Appleton Laboratory
Chilton, Didcot, OX11 0QX
U.K.

## SUMMARY

Global maps of super-refraction and duct statistics based on the analysis of radiosonde data have, for many years, been used to characterise the effects of climate in statistical radiowave propagation models. This paper describes a new analysis based on a more recent and more extensive dataset.

The sources of radiosonde data and our data reduction and validation strategy are discussed, and the statistical parameters of interest for super-refracting and ducting layer statistics are introduced. Contour maps of these parameters are given for the European region; comparisons with earlier data highlight some of the problems involved in this type of study. Comparisons of high and low resolution data analyses for the coastal site of Hemsby in the UK are made, and the influence of the boundary layer on surface duct statistics discussed. Some conclusions are drawn on the usefulness of radiosonde data for the mapping of refractivity parameters.

## 1 INTRODUCTION

Climatic mapping of refractivity parameters based on radiosonde ascents was first done by Bean et al [1] in the 1960s. This study involved 112 radiosonde stations with a time span of 5 years (with only 4 months from each year included). The results of this study still form the basis of the recommended prediction procedures for line-of-sight paths [2] and for interference between terrestrial stations [3] made by the International Telecommunication Union for civil communications.

A more extensive study of surface, super-refracting layer and ducting statistics based on 5 years of data (all calendar months) from over 900 stations was carried out in the late 1970s by L.N. Ortenburger of GTE Sylvania [4] for the US DoD. The Sylvania data was used to provide a historical electromagnetic propagation condition database for the US Navy [5].

The authors have recently begun a fresh statistical analysis based on more recent and more extensive radiosonde data in order to investigate and map physically-based refractivity parameters representative of the atmosphere during anomalous propagation conditions. Although the maps will be of interest in their own right, the longer term aim is to incorporate these parameters in statistical propagation models in order to represent the effects of climate on propagation. This stage will involve validation against radio link data. We are interested both in global climatology, and also in such regional, microclimatological factors as orographic and coastal effects.

In this paper, preliminary results are reported. In a study of this kind, much of the work involves data reduction, selection and validation, and some of the methods used, and problems encountered will be discussed. The difficulties involved in using radiosonde data to deduce refractivity statistics (for example, sensor time lags and acclimatisation) are well known, at least qualitatively; in this study, we have attempted to quantify some of these by comparing statistics based on high resolution "raw" radiosonde data, as well as on the low resolution data obtained from the global network of upper air sounding stations.

## 2 RADIOSONDE DATA SOURCES

The study is concerned with statistics of the radio refractivity $N$, or of the modified refractivity $M$, and their vertical gradients. The requirement is therefore for profiles of $N$ or $M$ against height at representative locations and times around the world.

$N$ given by the well-known formula:

$$N = 77.6\frac{P}{T} + 3.73\times10^5\frac{e}{T^2} \qquad (1)$$

where $P$ is the total atmospheric pressure (hPa), $T$ is the absolute temperature (K) and $e$ is the water vapour pressure (hPa). $M$ is simply derived from $N$ at a height $h$ (m) above the ground (or relative to sea level) by:

$$M = N + 0.157\,h \qquad (2)$$

Direct sensing of pressure, temperature and water vapour pressure (or an equivalent humidity parameter) profiles is routinely carried out by means of radiosonde balloon ascents.

*Paper presented at the Sensor and Propagation Panel Symposium on "Propagation Assessment in Coastal Environments" held in Bremerhaven, Germany 19-22 September 1994.*

| Level | Pressure (hPa) | Geopotential height (m) | Temperature (C) | Dew point depression (C) | Wind direction (deg) | Wind speed (kts) | Quality marks |
|---|---|---|---|---|---|---|---|
| 1 | 1003.0 | 99999.0 | 2.8 | 2.1 | 999.0 | 999.0 | V |
| 2 | 1000.0 | 38.0 | 3.2 | 3.1 | 999.0 | 999.0 | AA |
| 3 | 935.0 | 99999.0 | .2 | 2.5 | 999.0 | 999.0 | A |
| 4 | 921.0 | 99999.0 | 1.4 | 2.9 | 999.0 | 999.0 | A |
| 5 | 857.0 | 99999.0 | -1.3 | 2.8 | 999.0 | 999.0 | A |
| 6 | 850.0 | 1343.0 | -1.7 | 3.1 | 165.0 | 36.0 | AA A |
| 7 | 829.0 | 99999.0 | -2.3 | 4.2 | 999.0 | 999.0 | A |
| 8 | 811.0 | 99999.0 | -1.9 | 6.0 | 999.0 | 999.0 | A |
| 9 | 765.0 | 99999.0 | -4.9 | 7.0 | 999.0 | 999.0 | A |
| 10 | 700.0 | 2870.0 | -10.1 | 6.0 | 160.0 | 48.0 | AA A |
| 11 | 594.0 | 99999.0 | -19.1 | 3.5 | 999.0 | 999.0 | A |
| 12 | 515.0 | 99999.0 | -25.9 | 8.0 | 999.0 | 999.0 | A |
| 13 | 500.0 | 5380.0 | -27.7 | 8.0 | 175.0 | 48.0 | AA A |
| 14 | 407.0 | 99999.0 | -39.7 | 9.0 | 999.0 | 999.0 | A |
| 15 | 400.0 | 6940.0 | -40.7 | 10.0 | 160.0 | 48.0 | AA A |
| 16 | 334.0 | 99999.0 | -50.9 | 99.9 | 999.0 | 999.0 | A |
| 17 | 300.0 | 8830.0 | -55.9 | 99.9 | 165.0 | 44.0 | AA A |
| 18 | 279.0 | 99999.0 | -59.1 | 99.9 | 999.0 | 999.0 | TA |
| 19 | 264.0 | 99999.0 | -56.7 | 99.9 | 999.0 | 999.0 | A |
| 20 | 250.0 | 9980.0 | -57.9 | 99.9 | 180.0 | 32.0 | AA A |

Table 1: Example of radiosonde ascent data extracted from NCAR dataset

### 2.1 Low resolution data

A global network of meteorological stations gathers data on a regular basis for synoptic weather forecasting, coordinated by the World Meteorological Organisation (WMO). These data are archived and are available from several world data centres. Surface observations are made at more than 5000 sites every three hours, while routine radiosonde observations (RAOBs) are made at over 1000 stations twice daily, nominally at 0000 and 1200 UT. (The ascents are made simultaneously at all locations on the globe, rather than at the same *local* time.) The RAOBs are the most useful for calculating super-refracting and ducting layer statistics.

This WMO network of stations is the only source of data with global coverage and long time span. While other methods, such as satellite remote sensing and numerical weather prediction models, show promise for the future, particularly in the area of *forecasting*, the WMO radiosonde network is the obvious basis for global climatic mapping of statistical parameters.

All available radiosonde observation (RAOB) data for the ten years 1983–1992 were obtained from the National Center for Atmospheric Research (NCAR) in the USA. A typical ascent (up to a height of 10 km) is shown in Table 1.

The levels at which data are reported by the WMO network are of two types. All parameters are reported at *standard* levels: fixed pressure levels agreed by the WMO (1000, 850, 700, 500, 400, ... hPa). Only the 1000 hPa and 850 hPa levels are normally relevant to terrestrial radio links, the lower pressures levels being too high in altitude. Pressure, temperature and dew point are also reported at *significant* levels: heights that show significant features (such as changes of slope) in the vertical profiles of temperature or dew point. There may be several significant levels below a height of 1000 m.

These reporting levels are extracted from the "raw" *high* resolution data directly measured by the radiosonde as it ascends (with typically 10 m height resolution in modern systems) via a complex reduction process that may involve smoothing and interpolation. Indeed, until recently, significant levels were usually *manually* extracted from the raw data; and even though modern radiosonde systems automate this process, there is no universally agreed procedure for defining significant levels. We refer to the standard/significant level data as *low* resolution data; one of the purposes of this study is to examine the effects of this reduction process on the usefulness of WMO data for refractivity studies.

Referring to eqn (1) and Table 1, the parameters of interest for calculating refractivity-height profiles are:

(i) **Pressure:** values are rounded to 1 hPa (i.e. about 8 m height resolution) at levels below 100 hPa.

(ii) **Temperature**

(iii) **Dew point depression:** water vapour pressure can be obtained directly from the temperature and dew point depression by any one of a large number of formulae based either on the Goff–Gratch or Clausius–Clapeyron equations; we have used the formula of Tabata [6]. Above some height (typically 5–6 km) dew point depressions are not available (indicated by the dummy value of 99.9); at these heights the water vapour pressure can be assumed to be zero.

(iv) **Height:** Given as geopotential height at standard levels only (the value 9999.0 represents missing data). Geopotential height is related to the potential energy acquired by a unit mass on being raised

through a unit distance in a gravitational field of unit strength. It differs from the true height because the Earth's gravitational field is not constant with height. Although geopotential height is more useful in dynamical models, true height is required for refractivity analyses. The difference between the two quantities amounts to less than 1% in the first one or two kilometres above the Earth's surface, however.

Also of use in data validation are:

(v) **Quality marks:** NCAR has carried out some data validation on the RAOBs submitted to them for archiving. Each parameter has been marked with a "flag" showing the result of consistency checks applied to the data.

The wind speed and direction information has not been used in this study. If needed, wind information is available at *pilot* levels in addition to the standard levels shown. Many stations also launch pilot balloons (PIBALS) to give information on upper air winds only at the intermediate times of 0600h and 1800h.

The first reported level (level 1) in Table 1 corresponds to the station ground level. A calculation of the ground value of refractivity is clearly very important for studies of ground-based layers and surface ducts. In this context, it is important to note that *the station values are normally obtained from ground-based sensors, and not from the radiosonde itself.* This has important implications.

### 2.2 High resolution data

For modern radiosondes, the height resolution of the "raw" data from which the standard and significant levels are extracted is high: the Vaisala sondes currently used by the UK Met Office send back data every 2 seconds, giving a height resolution of about 10 m. In the UK, this high resolution data is archived in digital form.

A complete year (1991) of high resolution data from Hemsby in the UK has been obtained in order to compare radiometeorological statistics obtained from the WMO-formatted data with those obtained from the raw data. The data files contained 14 primary or derived parameters at each 2 second reporting level, the first level generally being less than 20 m above the ground. Only the pressure, temperature and dew point were used in this study.

## 3 DATA REDUCTION AND VALIDATION

One of the most time-consuming parts of the analysis of the low resolution, global, 10-year radiosonde dataset is the extraction of the relevant information in a format suitable for scientific analysis. This is due to the sheer quantity of data to be manipulated—more than 8.4 million ascents (RAOBs and PIBALs), amounting to over 6 Gbytes of data (in a compressed binary format). Validation of the extracted data is one of the most important stages, since much of the data is of low quality and careful quality control is required.

### 3.1 Extraction of station data

The compressed and encoded WMO dataset as supplied by NCAR contains radiosonde ascents that are ordered chronologically, rather than by station. Extracting and unpacking the data for all the ascents of a single radiosonde station made in a 10-year period, and saving these in a "station file" is equivalent to rotating a 6 Gbyte matrix. This was made easier by the availability of 20 Gbyte of disk space for this task. In all, 4430 station files were created, and archived by WMO region.

### 3.2 Selection of stations

Of the 4430 station files available, not all contain sufficient ascents for subsequent statistical analysis. Indeed, as Figure 1 shows, the majority of stations make (or at least report) very few ascents: about 3000 of the stations made less than 250 ascents in the 10 year period, including over 2000 that averaged less than one ascent per year! However, apart from the very large peak in the first bin, Figure 1 shows that the number of ascents per station is fairly evenly spread, with a slight increase above the 7000 figure corresponding to the "high quality" stations that report two ascents per day, except for occasional problems.

We considered two criteria based on the number of reported RAOB (0000h or 1200h) ascents for a station to be accepted for statistical analysis:

(i) it must have more than 3000 (0000h + 1200h) ascents in total;
(ii) it must have more than 1000 ascents at each of 0000h *and* 1200h.

942 stations satisfied the first criterion and 979 satisfied the second criterion; interestingly, the two criteria produced largely the same set of stations. The results to be presented are based on the first selection criterion. Figure 2 is a map of the 942 stations accepted for further analysis; the *average* number of ascents per station for these stations is 6000.

Since the meteorology of ocean and coastal regions were of particular interest, it was necessary to identify the radiosonde stations in these regions. A simple criterion based on station altitude above mean sea level produced the 299 stations shown in Figure 3.

### 3.3 Computation of height-refractivity profiles

Before statistical analyses are applied to the station files, these are processed to produce "refractivity files" i.e. a single file per station containing all height-refractivity profiles for the complete ten year time span. This is done for two reasons:

- the volume of data is much less than that of the original station files in the format of Table 1 since the refractivity files contain less parameters and only retain profiles up to a height of 3 km. The size of a refractivity file is typically 1 Mbyte.
- the station file data are incomplete (for example true height values must be calculated) and may contain invalid data.

Producing a height-refractivity profile requires, for each reported level in a station file, the calculation and validation of (a) the true height, and (b) the refractivity.

### 3.4 Calculation and validation of true height

Since heights are only reported at standard levels, the height of the radiosonde at each level must be calculated by integrating the hydrostatic equation and the equation of state of the air from the ground up to the level of interest. For accuracy, the equation of state must take account of the correct dry air/water vapour mix. True or geopotential height can be calculated depending on whether the value of gravitational acceleration used in the calculation is the sea level value (for geopotential height) or the value pertaining to the height of interest (for true height).

Ideally the integration must be carried out over sufficiently small height intervals for the true temperature and dew point temperature profiles to be adequately represented. Indeed the reported geopotential heights at standard levels are based on such an analysis of the raw, *high resolution* data; these unfortunately are not available in the low resolution data, and a reconstruction of the significant level heights must be based only on the few reported levels available. This gives rise to discrepancies between the calculated and reported values of height at the standard levels. For the refractivity profiles, we always use the calculated values of true height at the standard levels rather than convert the reported values of geopotential height to true height, in order to avoid creating artificially high gradients where there is a mismatch between a calculated significant level height and a nearby reported standard level height.

As part of the validation process, calculated and reported *geopotential* height values at the standard levels were compared. Figure 4 is a scatter plot of the differences between the calculated and reported height values at the standard levels for Hemsby in the UK for the complete 10 year period. The points are observed to be tightly clustered with a mean close to zero, although with a certain number of "outliers"; (the "drift" in the mean at the highest levels is believed to be caused by our implementation of the hydrostatic equation which ignores the effects of the tropopause; since only heights below 3 km are of interest, this effect is not important). For this station the mean "error" and standard deviation (calculated at the 1000 and 850 hPa levels) are -0.18 m and 2.64 m respectively, typical of a "reliable" station. Many stations show a much greater scatter of points.

The outliers are due to large height discrepancies at particular levels; these can be caused either by (a) errors in reported height or meteorological parameters, or (b) missing significant levels in the reported data. When calculating the height-refractivity profiles, a level (and all higher levels) is omitted if the difference between the calculated and reported values of geopotential height is greater than a predetermined limit (somewhat arbitrarily taken as 50 m).

Many stations had a mean "error" differing from zero by several standard deviations. This is believed to be due to reporting errors in the station ground height (which was used to initialise the hydrostatic equation); this can happen if the launch point has been moved since the station height was originally reported. If necessary, the calculated mean errors can be used to correct the reported station ground heights.

### 3.5 Calculation and validation of refractivity

Refractivity is calculated at each level using eqn (1). The NCAR quality marks indicate a degree of credibility to be attached to each measurement, and these are used in our validation. Our acceptance criterion is very conservative: a level is accepted only if all the meteorological parameters are present and pass the tightest consistency checks. Otherwise the level (and all subsequent levels) is rejected.

As a result of the height and refractivity validation process, the percentage of available ascents that can be used for statistical analyses below 3 km in height is generally greater than 80%, and is as high as 96% for the best stations.

### 3.6 High resolution data

The high resolution ascent data were also reduced to a (single station, one year) refractivity file of the same format as the low resolution data files (but with *all* recorded levels up to 3 km). The limited amount of data meant that a visual inspection of the plotted profiles was possible to verify that there were no gross data errors.

## 4 SUPER-REFRACTION AND DUCT LAYER STATISTICS

Bean et al [1] investigated (amongst other things) the refractivity gradients in the surface layer, defined by the difference between the refractivity value at 100 m above the surface and at the surface. The maps used by the ITU radio link performance models [2,3] show the percentage of the time that the gradient in the lowest 100 m is less than −100 N/km, denoted by $\beta_o$. This parameter can be taken as an indication of the probability of occurrence of super-refracting surface layers.

Since the strongest anomalous propagation effects are usually associated with the formation of ducts, it might be expected that the presence of ducting layers (i.e. layers with a refractivity gradient $\leq -157$ N/km) would be more appropriate. Maps of this quantity were drawn by Bean et al, but were not adopted by the ITU. One reason may be that mean gradients measured in the 100 m surface layer used in the Bean et al analysis will fail to detect the shallower ducts (caused by advection or nocturnal inversions) that can still produce very significant effects on surface links.

In this study, explicit duct statistics have been investigated as potential climatic parameters. Although the choice of the best parameters to use in statistical prediction models will ultimately be determined by testing the models against radio link data, a number of candidate parameters are suggested on physical grounds, and the climatology of these parameters is of interest in any case:

(i) for surface (S) ducts: the probability of occurrence, and statistics of duct thickness and strength;
(ii) for elevated (E) ducts: the probability of occurrence, and statistics of duct height, thickness and strength;
(iii) elevated layer, surface (ES) ducts were also included in the analysis; however their probability of occurrence was so low that the layer parameters did not have sufficient statistical significance for climatic mapping.

For each radiosonde ascent, the parameters of all ducts occurring in that ascent were extracted. (For ducts, it is more appropriate to consider height–*modified*-refractivity profiles: a ducting layer exists if the modified refractivity gradient in the layer $\leq 0$ M/km). In this process, it was of course necessary to assume that the WMO significant levels were an adequate representation of the significant levels in the refractivity profile; in particular, surface duct parameters are sensitive to the ground value of refractivity. These assumptions are considered in detail later.

Annual and monthly probability distributions of the duct layer parameters were calculated for each station, and the median values extracted. As an indication of statistical significance, the lower and upper quartiles (the points corresponding to the 25 and 75 percentiles) were used as a "confidence interval". These statistical parameters were also calculated as part of the earlier Sylvania study, allowing a comparison with the earlier data.

Figures 5 and 6 show the potential of ducting parameters as climatic variables, using stations in the Mediterranean and India. The seasonal variations of duct height at the two locations are clearly very different, while the trend in the probability of duct occurrence is similar. (The *absolute* values of duct occurrence have to be interpreted with care, as discussed later).

### 4.1 Mapping of statistics

Statistical parameters for over 100 stations in the European region have been extracted. Figures 7–10 are examples of contour maps based on these, showing annual percentage of occurrence and annual median duct strength of surface and elevated ducts. As expected, all these statistics show an increase from the continental climate in the north-east to the Mediterranean climate in the south. The influence of the coast on the probability of occurrence of surface ducts is also apparent in Figure 7.

Maps of median annual duct thickness were not found to show any useful trends.

### 4.2 Problems with surface layer incidence statistics

Comparisons between the new statistics and earlier results, where available, have been made. In many cases the agreement between the new study and the earlier results is very good; for example, duct *strength* statistics from this study agree very well with those from the Sylvania study.

However, in some cases the agreement is poor. In particular, this is the case for the percentage of the time that a super-refracting or ducting layer exists at a location. It is unfortunate that this is probably the most obvious parameter that could be used as an indicator of the incidence of anomalous propagation (for example, $\beta_0$ in the ITU prediction models). It is therefore necessary to understand why it appears to be the most difficult to derive from radiosonde ascents.

Here we give some examples, and possible reasons for the differences. A critique of the results, and implications for the use of the parameters in prediction models will be given in the next section after a consideration of the high resolution data.

Figure 11 compares the monthly and annual values of the quantity $\beta_0$ for Hemsby as given by the new results of this study, with the values taken from the maps of Bean et al [1] (only available for four months of the year). The agreement is very poor, the probability of occurrence of surface super-refracting layers being many times higher in the new data than in the earlier data.

Figure 12 compares the monthly and annual values of the probability of occurrence of surface ducts for Hemsby obtained from three datasets: (i) the Sylvania study [5] (5 years in the late 1960s and early 1970s); (ii) the new data (1983–92); (iii) an analysis based on the years 1980–89 (a slightly extended dataset was available for this station). Again the agreement is poor, although the monthly trends are similar. Even the comparison between the years 1980–89 and 1983–92 show major differences.

It is instructive to look at the annual values of the probability of occurrence of surface ducts, calculated on a year-by-year basis—Figure 13. Each "ribbon" represents the trend in this quantity during the period 1983–1992 for a single radiosonde station. Two groups are given, corresponding to stations in the UK and in Scandinavia. Of particular note is the large increase in the percentages at the UK stations after 1989.

There are three possible reasons for the differences between the newer and older studies:
(i) Climatic change
(ii) Differences in the data processing
(iii) Differences in the radiosonde systems

Climatic change clearly cannot explain such large variations, and would also be expected to affect the other statistics (such as median duct height). There may well be differences in the way we extract duct information compared to the earlier studies, but Figure 13 shows that a strong time-dependence in the statistics occurs even within our limited 10-year data span, and this cannot be explained by data processing differences.

In the cases illustrated here, the differences are almost certainly due to the fact that many stations now use improved radiosonde systems compared to those that were in use in the 1960s and 1970s when the earlier studies were carried out. For example, the UK Meteorological Office replaced its sondes with Vaisala minisonde systems in 1990. The effect of this change on the duct incidence statistics is clear in Figure 13 (although the reason for the continuing rise in succeeding years is so far unexplained).

Newer radiosondes have several improvements compared to older models. The sensors are more accurate (particularly the humidity element), with faster response times, and the sondes have better vertical resolution: older radiosondes tended to underestimate the magnitude of any refractivity changes, reducing the apparent gradients and missing thin structures. These improvements increase the probability of detecting surface layers in the first few tens of metres above the ground.

A wider comparison of the newly calculated annual values of $\beta_0$ averaged over 10 years with the values taken from the maps of [1] for 25 locations around the world was made. The correlation coefficient was very low (0.06). In the light of the above comments, it was surprising to find that almost half the stations had calculated values of $\beta_0$ *smaller* than the map-derived values. However, with the exception of a single station, all *large* differences are due to larger calculated values of $\beta_0$.

The probabilities of occurrence of surface super-refracting and ducting layers as derived from low-resolution radiosonde data are evidently dominated by instrumental and data reduction factors. Great care has to be taken in interpreting these figures, particularly if the time span of the data includes a change of instrumentation, or if results from different sites with widely different radiosonde types are compared.

It must be emphasised again that the above examples were chosen to illustrate the large differences that *can* occur when results derived from different datasets are compared. There was more consistency between the different studies in the other layer statistics.

## 5 HIGH RESOLUTION DATA ANALYSIS

One of the main reasons for obtaining the high resolution ("raw") Hemsby radiosonde data for 1991 was to investigate whether "significant" levels in refractivity (that is, those significant for ducting layer statistics) were adequately represented by the WMO-reported significant levels (of temperature and dew point) in the low resolution data.

Both an ascent by ascent comparison of the height-refractivity profiles derived from the high resolution (HIRES) and low resolution (LORES) data, and a comparison of annual duct layer statistics derived from the high and low resolution datasets for 1991 were considered.

Figure 14 shows four examples that are fairly representative of the types of situation that can occur. Since the WMO-reported significant levels were extracted from the LORES data points shown, it should be clear that the differences are due to the data processing of the LORES data, and has nothing to do with instrumental performance. Each example contains a surface duct, but in the first two cases, the LORES data misrepresents the strength and height of the ducting layer. In the last example, a (weak) elevated duct has been missed. To quantify the effect of these differences requires an examination of the statistics.

### 5.1 Comparison of statistics

### 5.2 Duct incidence statistics

The same duct detection algorithm was run on the low and high resolution data. The results for surface ducts are given in Table 1. Ideally, the off-diagonal elements of the score matrix should be zero. A large number of ascents (30%) showed a surface duct in the HIRES data, but not in the LORES data. This might have been expected to be caused by weak features in the height-refractivity profile at low heights that are not present in the low resolution data. However, it turns out that much of the effect is due to quite strong, but low level, surface ducts.

| | | Low Resolution | |
|---|---|---|---|
| | | No Duct | Duct |
| High Resolution | No Duct | 27% | 4% |
| | Duct | 30% | 39% |

Table 1: Surface duct detection scores

The small number of ascents (4%) when a surface duct was present in the low resolution, but not the high resolution, data are due to the exclusion of ES ducts from this table: occasionally a duct would be identified as ES in the high resolution data and as S in the low resolution data.

For elevated ducts, the disparity between the annual incidence of ducts in the HIRES data (69%) and the LORES data (21%) was higher than for surface ducts (69% compared to 43%). In this case the difference was due to weak features in the HIRES profiles that were not reflected in the LORES profiles. Removing all elevated ducts with a strength less than 2 M-units resulted in similar statistics for LORES and HIRES data.

### 5.3 Duct strength and thickness statistics

For surface ducts, the LORES and HIRES probability distributions of duct strength were similar. Surface duct heights derived from the LORES data were quantised in multiples of approximately 8 m, due to the rounding of pressure levels to 1 mb in the NCAR data. This makes comparison of the distributions of duct thickness (height) difficult—we concluded that it is not sensible to derive surface duct height statistics from the NCAR WMO data.

For elevated ducts, both the duct strength and thickness distributions were heavily biased towards small values in the HIRES data (Table 2). As already mentioned, this was caused by weak features in the HIRES profiles that were not reflected in the LORES profiles. Application of a low-duct strength filter restored agreement between the LORES and HIRES statistics.

| Annual median value of: | LORES | HIRES |
|---|---|---|
| Duct Strength (ΔM) | 4.3 | 0.7 |
| Duct Thickness (m) | 125 | 30 |

Table 2: Elevated duct statistics

The sensitivity of the statistics to the data resolution, and the need for conditional probability distributions (based on a weak duct "filter") is fairly obvious, but a unified approach that will deal satisfactorily with the multitude of radiosonde types will require further work.

### 5.4 Boundary layer modelling

It has already been pointed out that, of the high percentage of surface ducts seen in the Hemsby ascents, a large proportion are relatively strong features, unlikely to be caused by "noise" in the data. However, the LORES data showed that most of these apparent ducts were defined by only two points—the ground point and the first radiosonde point—as illustrated in Figure 14.

This apparent "offset" of the ground value from the value that would be expected by simple extrapolation of the radiosonde data values to the ground was responsible for the different surface layer statistics (super-refraction and ducting) obtained from different resolution datasets.

The Hemsby high (about 10 m) resolution data were used to investigate the surface layer in more detail: the first radiosonde point generally occurs at a height less than 20 m above ground level. Three possibilities for the station value "offset" were considered:

(i) calibration differences between the ground-based sensors and the radiosonde sensors;
(ii) time lags and inadequate acclimatisation of the radiosonde before launch;
(iii) boundary layer effects;

Figure 15 shows the distribution of the difference between the reported ground value and the ground value derived by extrapolating the first few radiosonde points. The distribution is strongly biased to positive values (i.e. higher refractivity measured at the ground than would be expected by extrapolating from the radiosonde data). This shows that the differences are unlikely to be due to calibration errors, which would be expected to be random.

The quality control at Hemsby is known to be good. In the great majority of the ascents, the refractivity profiles were close to linear right from the lowest radiosonde point, with only the ground value point offset from this line, so it seems unlikely that poor acclimatisation or sensor time lags are the cause of the ground value offsets.

In the atmospheric boundary layer, the lowest 50–100 m forms a surface layer in which the wind structure is determined primarily by surface friction and the vertical gradient of temperature. The vertical transport of momentum, heat and moisture in this layer occurs by turbulent mixing, and the vertical fluxes of these quantities are proportional to the mean values of the gradients of wind velocity, potential temperature and specific humidity, respectively [7]. The vertical profiles of these quantities are almost always logarithmic in the lowest part of the surface layer.

To test whether boundary layer effects contribute to the offsets of the surface values, potential temperature and specific humidity fluxes were calculated from the LORES temperature and dew point values (assuming that radiosonde point samples, rather than statistical averages, could be used for flux calculations) measured at the "station height" (taken to be 1 m above ground level) and the top of the surface duct. The fluxes were

then used to predict the full modified refractivity profile between the ground and the top of the duct, while the profile above this surface layer was assumed to be correctly represented by the low resolution data.

Figure 16 shows two examples of this type of analysis; the diamonds are the LORES values on which the flux calculations were based, and the solid curve is the reconstructed profile. The HIRES profile points (horizontal bars) are shown for comparison. Assuming that the HIRES profile can be regarded as "ground truth", the agreement with the profile reconstructed from the LORES data and boundary layer theory is good in the first example, although less so in the second example (the same ascent as in the first graph of Figure 14); in the second example, the height of the layer suggests coastal advection, rather than boundary layer mixing, as a cause of ducting, which may explain the poorer fit in this case.

It appears possible that the ground value "offsets" observed in the Hemsby data are genuine and attributable to boundary layer effects. If this can be confirmed, boundary layer modelling may provide a means of estimating the true parameters of low level surface ducts, and hence stable statistics of surface super-refracting and ducting layers independent of the resolution of the radiosonde data from which they are derived. However, further work is required. Boundary layer studies for an inland station is desirable for comparison with the coastal site at Hemsby.

## 6 CONCLUSIONS

The network of WMO synoptic radiosonde stations provides the only source of long term refractivity statistics with global coverage. Maps of ducting parameters for the European region have been drawn, based on data for the ten years 1983–92, and compared with earlier results. Large differences were found in some cases; the reasons for the differences were discussed, and further investigated by analysis of a "high resolution" dataset for Hemsby in the UK.

In summary, the apparent probability of occurrence of super-refracting and ducting layers depends strongly on:

- the accuracy and response times of the radiosonde instruments
- the resolution of the data from which the statistics are derived

Maps of probability of occurrence therefore need to be interpreted with caution, especially if the time span of the data covers changes in instrumentation, or if instruments of very different performance are included. However, the *trends* (for example monthly variation) may be a useful guide to climatic differences. Other duct statistics (such as layer strength) appear to be less sensitive to the source of the data.

It is clear that care is required in the interpretation of the meaning of duct statistics derived from radiosonde data. Of course, even "biased" results may be useful as driving parameters for prediction models, if these pseudo-duct statistics can be "normalised" semi-empirically by means of correlation studies with radio link performance data.

Work to extend the mapping beyond Europe is already in progress, together with further studies on the sensitivity of the statistics to the data sources. Other issues, such as the significance of diurnal effects on the time-sampled data, are being considered.

## 7 ACKNOWLEDGEMENTS

The study was carried out within the framework of the EU COST 235 project, and acknowledgement is due to our collaborators in Norwegian Telecom Research and CRC Canada for helpful discussions.

The work has been partly funded within the National Radio Propagation Programme by the Radiocommunications Agency of the Department of Trade and Industry in the UK.

## 8 REFERENCES

[1] B.R. Bean, B.A. Cahoon, C.A. Samson and G.D. Thayer, "A World Atlas of Atmospheric Radio Refractivity", ESSA Monograph 1, 1966.

[2] ITU-R Recommendation 530-4, "Propagation data and prediction methods required for the design of terrestrial line-of-sight systems", 1992-CCIR Recommendations, RPN series, Propagation in Non-Ionised Media, Geneva, 1992.

[3] ITU-R Recommendation 452-5, "Prediction procedure for the evaluation of microwave interference between stations on the surface of the Earth at frequencies above about 0.7 GHz", *ibid*, 1992.

[4] L.N. Ortenburger, "Radiosonde Data Analysis II", GTE/Sylvania Incorporated, 1977.

[5] W.L. Patterson, "Historical Electromagnetic Propagation Condition Database Description", NOSC Technical Document 1149, 1987.

[6] Tabata, S. "A simple but accurate formula for the saturation vapour pressure over liquid water", *J. Appl. Meteor.*, **12**, 1410–1411, 1973.

[7] J.C. Kaimal and J.J. Finnigan, "Atmospheric Boundary Layer Flows", OUP, 1994.

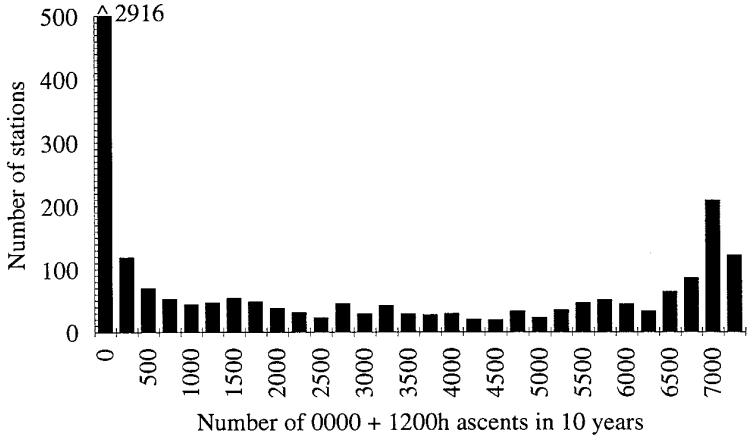


Figure 1: Distribution of the number of ascents in the 10-year dataset

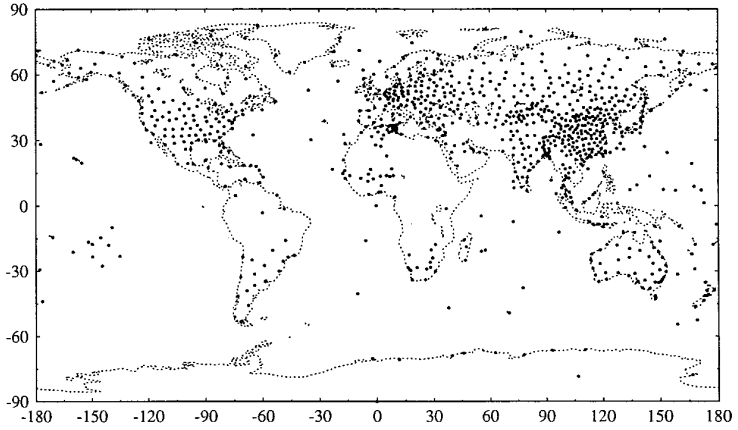


Figure 2: The 942 radiosonde stations selected for analysis

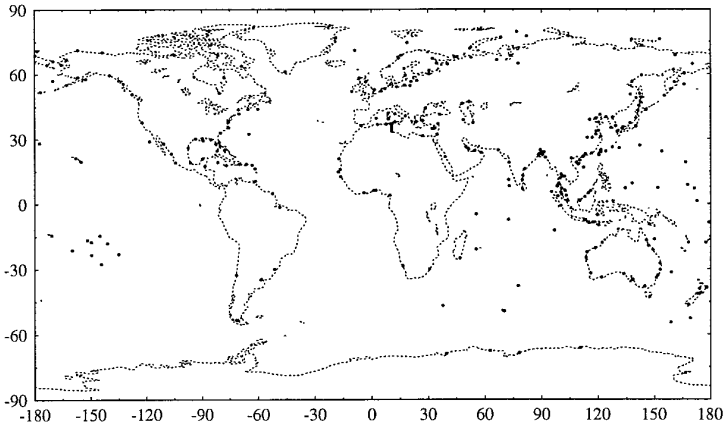


Figure 3: The 299 coastal stations

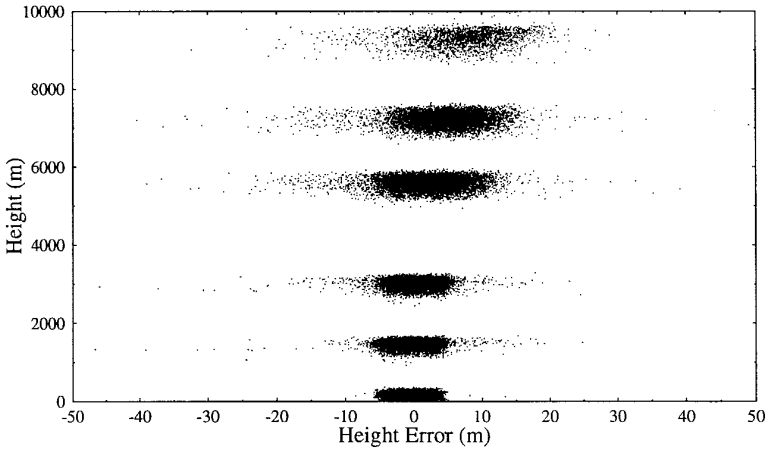


Figure 4: Scatter plot of differences between calculated and reported geopotential heights for a ten year period at Hemsby

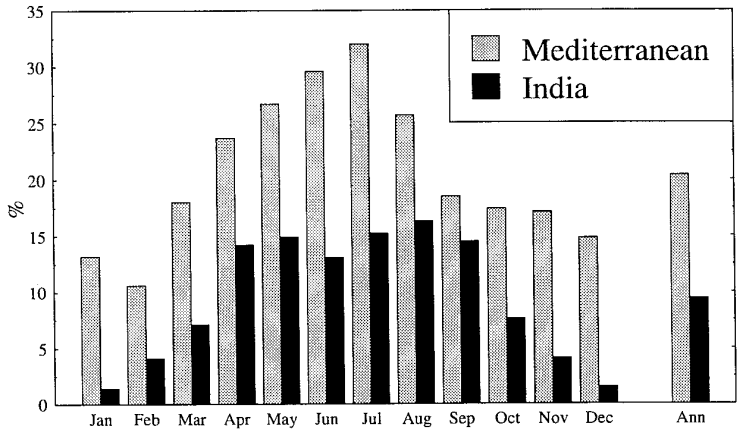


Figure 5: Monthly and annual probabilities of occurrence of surface ducts in the Mediterranean and India

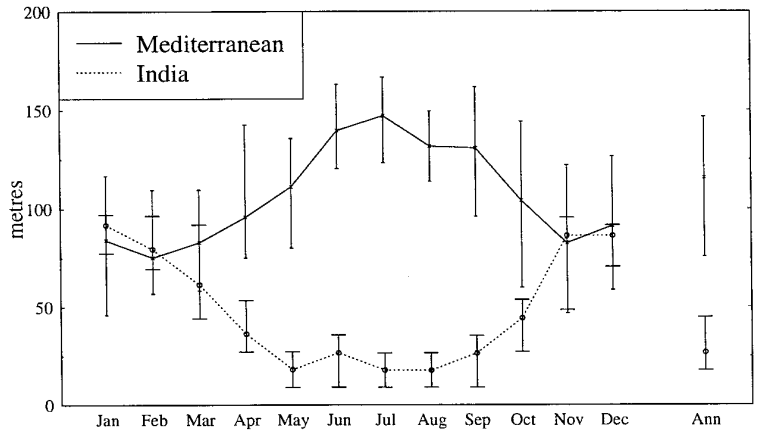


Figure 6: Monthly and annual median values of surface duct height in the Mediterranean and India

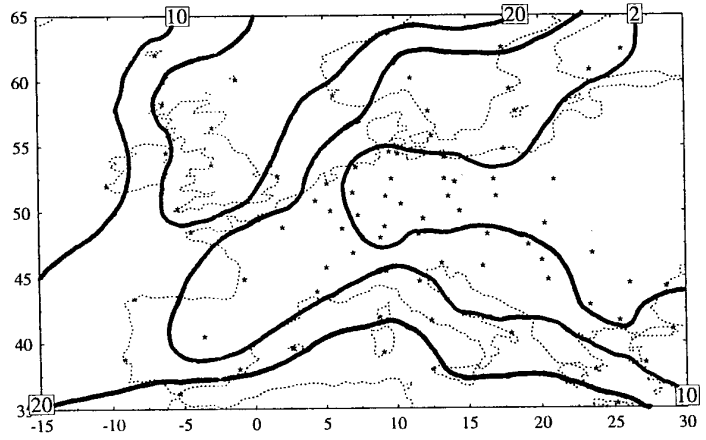


Figure 7: Annual percentage of occurrence of surface ducts

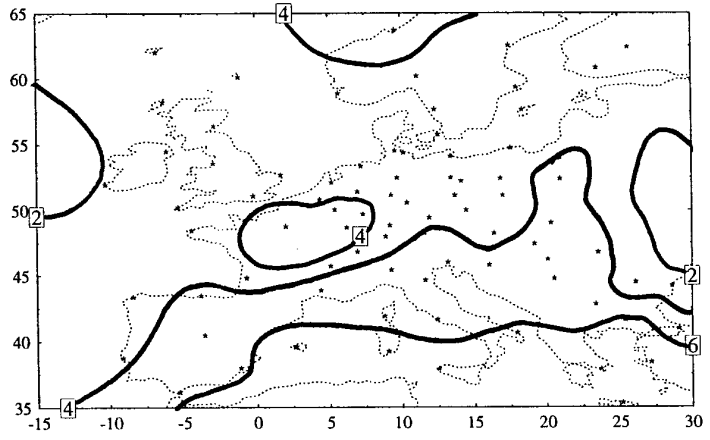


Figure 8: Annual median surface duct strength (M-units)

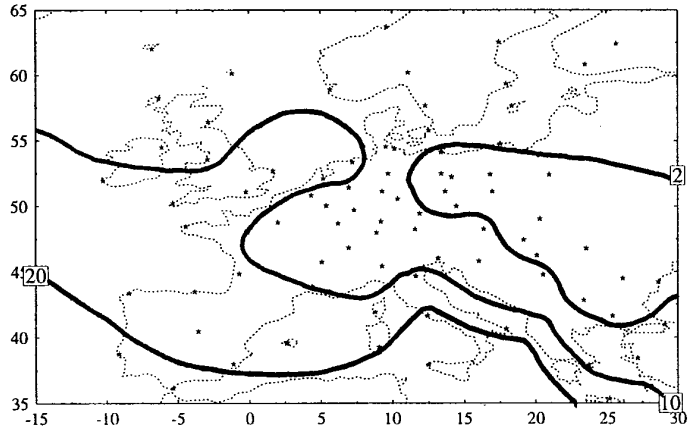


Figure 9: Annual percentage of occurrence of elevated ducts

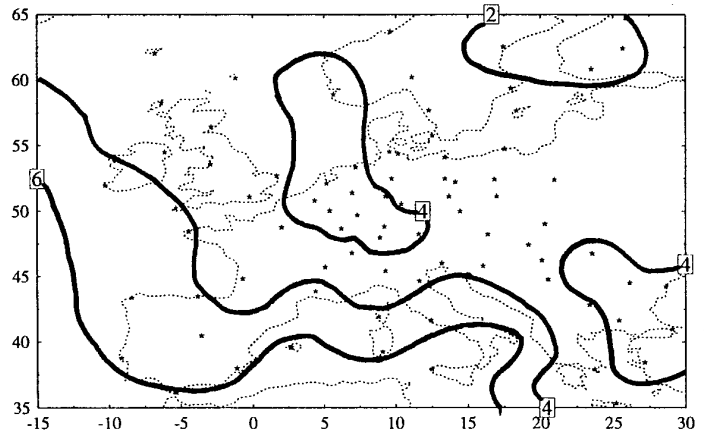


Figure 10: Annual median elevated duct strength (M-units)

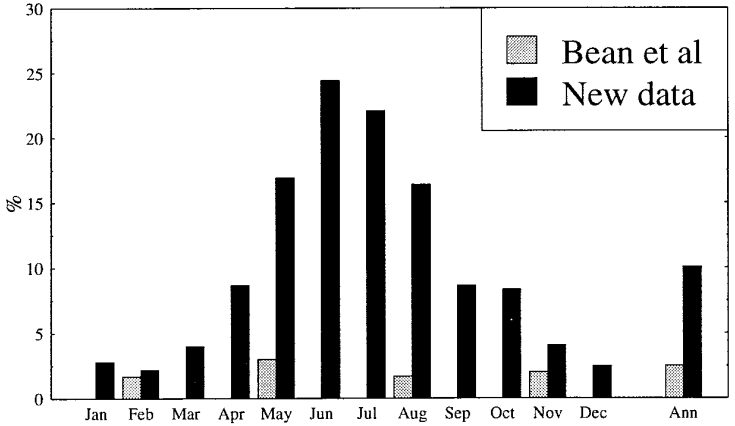


Figure 11: Monthly and annual values of $\beta_o$ for Hemsby

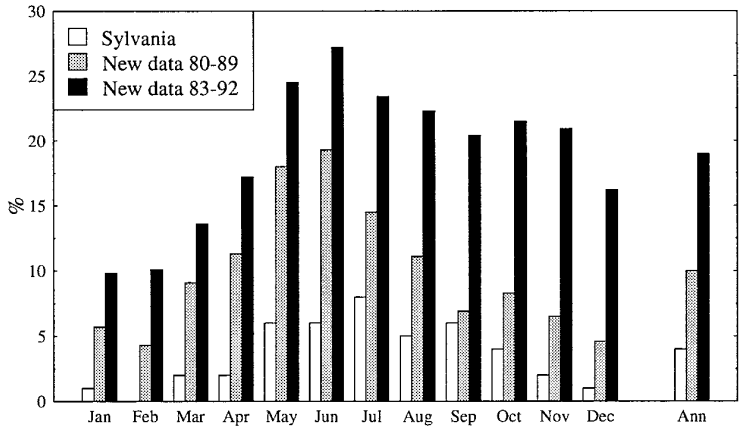


Figure 12: Monthly and annual values of the probability of occurrence of surface ducts at Hemsby

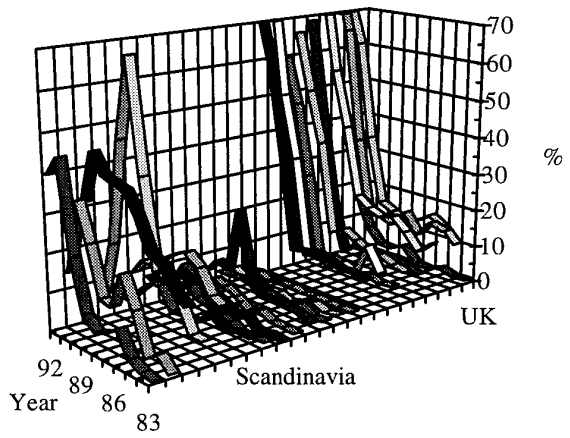


Figure 13: Year-to-year variation in the annual values of the probability of occurrence of surface ducts

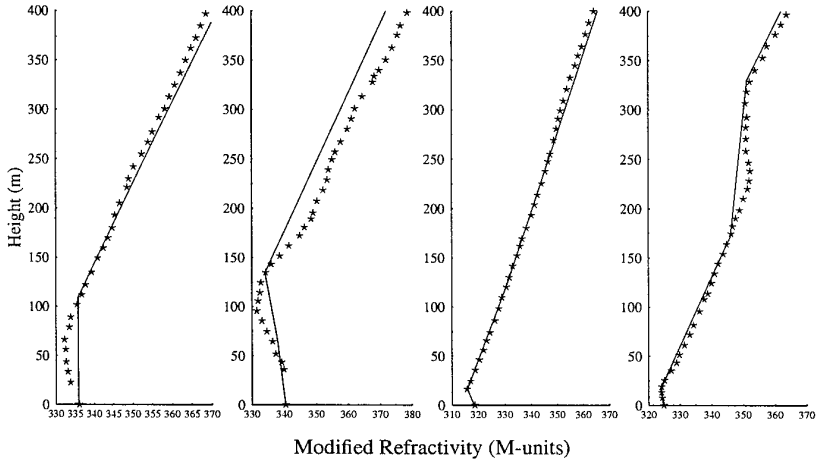


Figure 14: Modified refractivity profiles derived from low (lines) and high (points) resolution radiosonde data

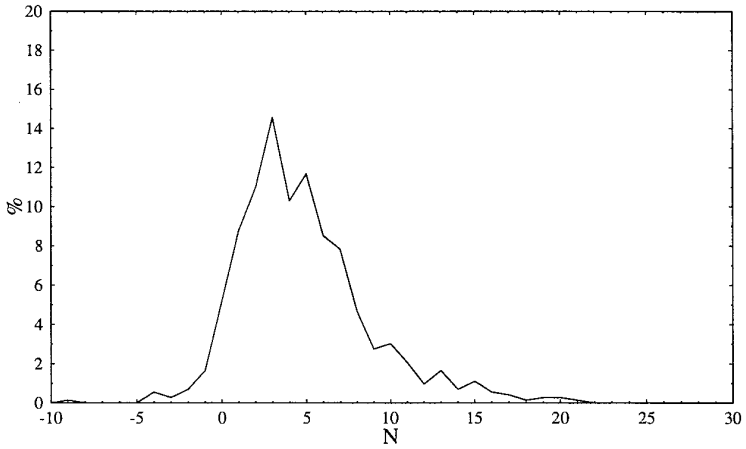


Figure 15: Distribution of radiosonde ground value offsets

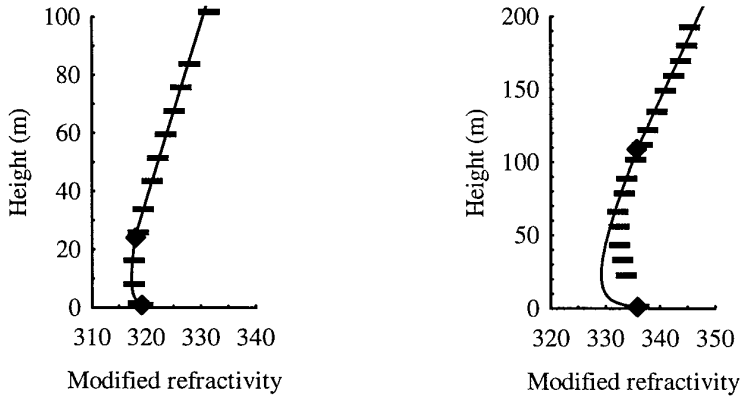


Figure 16: Examples of boundary layer modelling in the surface layer (diamonds: low resolution data; bars: high resolution data)

## DISCUSSION

**R. HELVEY**
Some years ago I discovered the existence of fictitious surface ducts during daytime in various radiosonde-derived refractive data sets - including the GTE Sylvania database. This was caused by a combination of instrumental and procedural problems. Have you been able to look for systematic diurnal differences in your statistics which might shed light on the reality of the apparent surface ducts reported?

**AUTHOR'S REPLY**
We have not looked at diurnal effects. The limited time sampling (twice a day) of WMO radiosonde launches and the longitude - dependence of the local time of launches means that diurnal variation is not very useful candidate to use as a climatic parameter, if derived from WMO sources.

**J. TURTON** (Comments)
1. I'd like to point out the existence of a recent USAF ETAC (Environmental and Technical Applications Center) global refractivity study which I have recently received. This contains an updated refractivity climatology which you may wish to see to aid some of the comparisons with previous climatologies.

2. I noted the WMO significant levels are based upon specified criteria. Many nations have systems that automatically identify significant levels according to these criteria (eg. Vaisala Digicora). In the UK, our systems (Vaisala PC-Cora) allow operator intervention in order to identify significant meteorological structure. This results in more significant levels being reported than would result just from using the WMO criteria which probably explains the recent increase in elevated duct occurrence from the UK data.

3. We do, on a number of occasions, see various near-ground low level humidity gradients in our radiosonde profiles. The reporting of these will have a detrimental effect on the derived statistics.

**AUTHOR'S REPLY**
I would be interested in the ETAC study. I note your comments on the UK systems. It is actually the surface duct occurrence that shows the biggest increase in the data from the newer instruments, no doubt due to the better resolution at the lower heights. I believe that the occurrence of steep gradients at very low heights may (at least in part) be genuine: this phenomenon has also been seen in refractometer measurements.

**J. CLAVERIE**
Did you compute surface duct height distributions?

**AUTHOR'S REPLY**
We did. However, we do not believe that the results are very useful. This is due to the 8 m "quantisation" of heights caused by the rounding of pressure levels to 1 mb in the NCAR data.

**D. DOCKERY**

Sounding in areas influenced by marine evaporative conditions will generally be unreliable below approximately 30 meters due to rapid atmospheric fluctuations. Have you considered enforcing a lower limit on the size of ducts included in your statistics?

**AUTHOR'S REPLY**

This may indeed be necessary. However since one of the main applications is (civil) terrestrial communications where low lying layers over land can be important (and the evaporation duct is absent) we would like to make some sense of the surface layer data.

# IR/RF REFRACTIVITY PROFILES OVER COASTAL WATER

**Gerrit de Leeuw, Filip P. Neele and Alexander M.J. van Eijk**
TNO Physics and Electronics Laboratory
P.O. Box 96864
2509 JG The Hague
The Netherlands

## 1. SUMMARY

In June 1992, IR/RF propagation experiments were conducted over the North Sea, at about 10 km SW from the German Island of Sylt. The experiments were a tri-lateral cooperation between institutes from Germany, Canada and The Netherlands, organized by the TNO Physics and Electronics Laboratory. The objective was a study on the complementarity of IR and radar detection systems.

In this contribution we report on the characterization of the propagation environment by the TNO Physics and Electronics Laboratory. This includes aerosol and lidar measurements to determine the extinction properties throughout the marine atmospheric boundary layer, as well as measurements of humidity and temperature profiles in the marine atmospheric surface layer to determine refractivity profiles.

Temperature and humidity profiles were measured form a jack-up barge 'Hubinsel Barbara' and on a mast. The sensors were mounted such that profiles could be measured from close to the sea surface, taking into account tidal effects and waves of 1.5 m, to heights of 10 m on the mast and 35 m on the platform. The platform data are often perturbed. Therefore, in the analysis we focussed on the temperature and humidity profiles from the mast. Effects of sensor height, wind speed and thermal stratification were considered. Deviations from the logarithmic behaviour have been observed. These are mainly ascribed to coastal influences, based on consideration of the height dependence and the effects of thermal stability. We conclude that in off-shore winds non-equilibrium situations often exist at the sensor locations, with an internal boundary layer that distorts the profiles.

## 2. INTRODUCTION

The performance of electro-optical systems for detection or identification of targets strongly depends on atmospheric conditions. A detailed knowledge of the effects of aerosols, temperature and humidity gradients, and turbulence on the propagation of electromagnetic radiation is important for both forecasting the propagation conditions (e.g., maximum range of detection of targets) and the interpretation of observations; range prediction is valuable as a TDA (tactical decision aid) for *a priori* assessment of the value of electro-optical detection systems. Over sea, IR detection systems are complementary to RF systems because of the differences in refraction properties as function of atmospheric structure.

When atmospheric conditions are such that electromagnetic waves are bent towards the Earth's surface, it is possible to observe targets beyond the geometrical horizon. In this case the atmospheric structure is super-refractive. Sub-refraction occurs when waves are bent away from the surface. Beaulieu[6] shows that for radar frequencies (RF) the dew-point-to-sea-temperature (DSTD) determines the refractive structure near the sea surface, super-refraction occurring for negative DSTD. For infra-red (IR) waves the air-to-sea-temperature difference (ASTD) is a useful parameter. Here, super-refraction occurs when ASTD is positive. Sub-refractive conditions exist when DSTD is positive (RF) or ASTD is negative (IR). In oceanic environments the thermal stratification is usually near-neutral and the DSTD generally negative (since the dew point cannot be higher than the air temperature). Therefore, conditions over sea are frequently super-refractive at RF. Furthermore, sub-refraction cannot occur for both RF and IR and, therefore, at least one frequency must be in the super-refractive domain. This indicates the synergism and complementarity of IR and RF for long-range detection.

The SYLT92 campaign was organized in a coastal marine environment to simultaneously perform propagation experiments at radar and infra-red wavelengths and measure the detailed structure of the marine atmospheric surface layer (up to 30 m above the sea surface). The objective of SYLT92 was to study the behaviour of electromagnetic radiation over sea and to validate and improve current models predicting radar or infra-red propagation. The synergism between IR and radar detection systems can then be demonstrated via the models.

The SYLT92 experiment was a trilateral cooperation between institutes from Germany, Canada and The Netherlands. The experiment took place from May 18 until June 19 at the North Sea near the German island of Sylt. The campaign was coordinated by the TNO Physics and Electronics Laboratory, that also performed radar propagation measurements and was responsible for meteorological characterization of the atmospheric surface layer. Germany hosted the experiment. WTD-71 (Germany) made available the Hubinsel Barbara, a jack-up barge that was towed to an indicated position, and a service boat. FGAN-FHP (Germany) conducted radar measurements and had a meteorological station on one of the radar reflector poles. Wave information was made available from the tide gauge at Westerland. DREV (Canada) was responsible for the optical and IR propagation measurements. The SYLT92 experiment and the individual contributions, with emphasis on the efforts by the TNO Physics and Electronics Laboratory was extensively described by De Leeuw et al.[1]

An overview of the results from the RF propagation measurements was presented by Sittrop et al.[2], an initial analysis of the IR propagation measurements was presented by Dion and Beaulieu.[3]

In this contribution the results are presented of the analysis of meteorological data collected during the SYLT92 experiment and the validation of two models predicting the refractive structure of the atmosphere at radar and infra-red

*Paper presented at the Sensor and Propagation Panel Symposium on "Propagation Assessment in Coastal Environments" held in Bremerhaven, Germany 19-22 September 1994.*

wavelengths. The models predict temperature, humidity and refractivity profiles, which are compared to observed vertical variations. Discrepancies between model predictions and observations are ascribed to the influence of the nearby coast.

## 3. EXPERIMENTAL SET-UP.

The experimental set-up is briefly described, with emphasis on the meteorological measurements. The reader is referred to De Leeuw et al.[1] for a more detailed layout of the experiment.

The experiment was centred around the German jack-up barge 'Hubinsel' Barbara, placed in the North Sea, near the German coast. Temperature and humidity sensors were placed at different heights on the west side of the platform for profile measurements, up to about 30 m above sea level. Profiles were also measured along a mast with 4 sensors, placed at 4, 5, 7 and 9.5 m above mean low sea level. The height of the lowest sensor was such, that it was well away from the waves at high tide, allowing for waves up to 1.5 m.

Figure 1 shows the locations of the barge 'Barbara' and the mast.

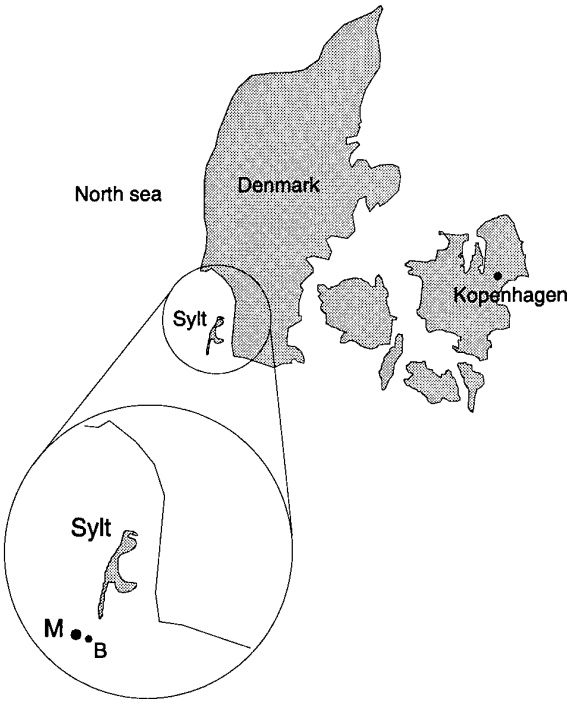


Figure 1. Locations of 'Hubinsel Barbara' and the mast.

The instruments on the mast were Rotronic Hygrometers, type YA-100 with teflon foam filter, placed in a Young shelter, shielding the sensors from sea spray and solar radiation. The instruments were placed in the prevailing wind direction, WNW to NW in June,[4] free from distortion effects from the Mast. A cup-anemometer was placed on top of the mast. Sea temperature was measured at 0.2 m below the sea surface, with a thermistor mounted on a float.

On Barbara, temperature and relative humidity were measured with Hygrophyl instruments, type G1463, mounted on the west side of the hull. In this way, the sensors would be exposed for the wind directions expected in the area. Wind speed and wind direction were measured with a cup anemometer and a wind vane, mounted in a mast on the helicopter deck, at a height of 35 m. Sea temperature was measured by two systems, each consisting of a thermistor on a float. Thus, possible contaminations from the platform could be detected.

In the mast on the helicopter deck of Barbara, also a turbulence package was mounted, consisting of a 3D sonic anemometer and an OPHIR IR hygrometer. Both these instruments measured at high frequency (25 and 20 Hz). Their results are not included in the present analysis.

Tidal data are taken from the tidal gauge at the Westerland tower, digitized from analog recordings. Correction curves have been applied to obtain the water height at the location of the mast.

## 4. DATA VALIDATION AND CALIBRATION.

### 4.1 Validation

During most of the experiment the wind came from easterly directions and most of the Barbara instrumentation was on the lee side of the platform structure. In that case the readings of these instruments were strongly affected by the platform and not representative for unperturbed open sea conditions. Therefore, they are not used in our analyses. The only instrument on Barbara that produced reliable data of both temperature and humidity was the Hygrophyl on the halfdeck (on average at 25 m above sea level). The Ophir instrument on the heli deck appeared to give unreliable humidity readings, although the temperature data seemed to be correct. Therefore the Ophir temperature is used where possible.

All of the sensors on the mast gave reliable results during the whole experiment, except for one occasion when sea spray apparently affected the lowest sensor.

### 4.2 Sensor comparison.

Temperature and humidity sensors were calibrated prior to the experiment and anemometers were compared. Nevertheless, the readings of different instruments, when calibrated, are known to be somewhat different, when a side-by-side comparison is made. However, for the evaluation of the gradients the differences between the instruments at the various levels and platforms are more important than the absolute values. Therefore, prior to installation of the instruments an intercomparison was made with all instruments mounted on the halfdeck, in the shadow of the helideck. Data were collected during a 24-hour period on May 19 and 20. These data comprise a balanced set, both at the low and at the high ends of the temperature and humidity ranges sufficient data are available to compute reliable correction curves. During the experiment, several additional comparison runs were made with the instruments placed side-by-side and whenever possible, the mast sensors were compared with a hand-held calibrated DV-2 temperature and humidity sensor. In

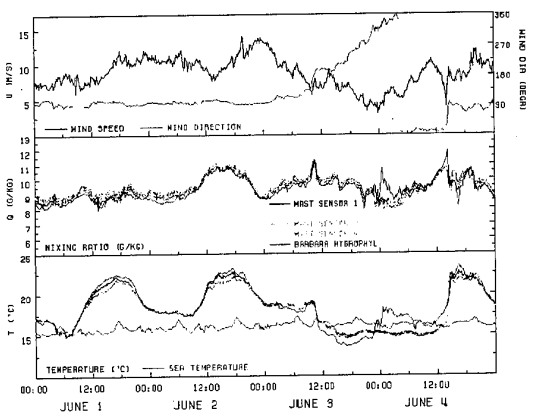


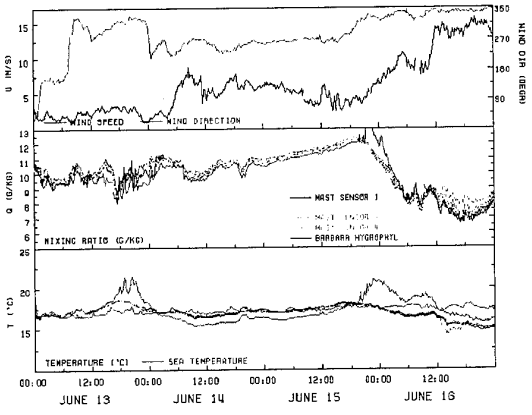


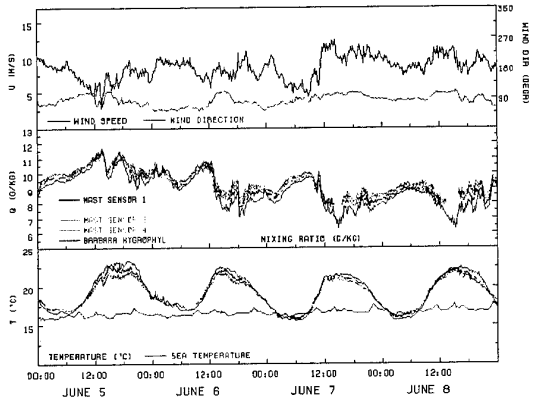


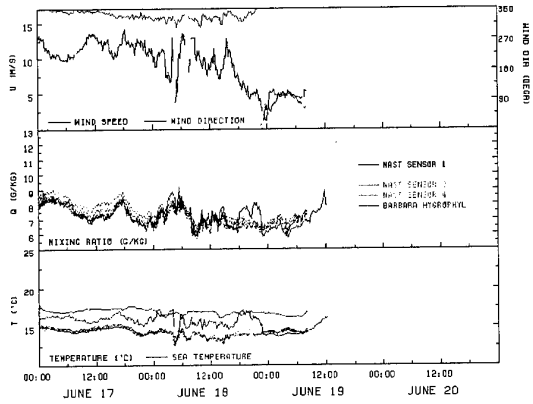


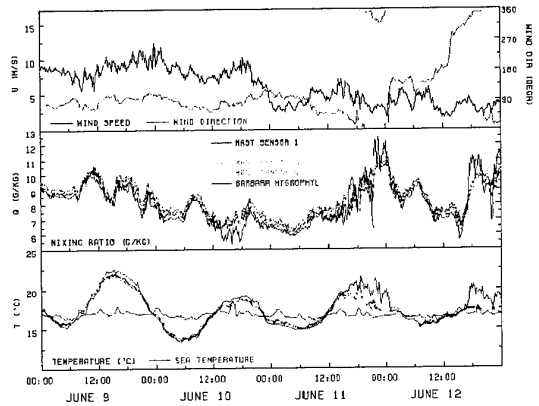


Figure 2. Overview of meteorological data measured during the SYLT92 experiment, June 1-19: upper panels show wind speed and direction, mixing ratios from the four mast sensors and the hygrophyl are shown in the middle panel, temperatures are shown at the bottom.

addition, the Barbara instruments were compared with an Assmann wet/dry bulb hygrometer, on a daily basis and sometimes several times per day.

The temperature sensor comparison data cover the temperature range 13-19 °C evenly; no data were obtained for higher temperatures. All Rotronic sensors consistently give temperatures about 0.5 to 0.8 °C lower than the three sea temperature sensors (thermistors). The latter were calibrated prior to the SYLT experiment with the thermistors in a climate chamber at TNO. For this reason, one of the sea temperature sensors of Barbara was chosen as reference.
The humidity calibration data cover a range of relative humidities from 55% to 90%. The mast hygrophyl sensors agree well; the only hygrophyl used on Barbara consistently yields lower humidities. No true calibration of the humidity sensors was made prior to the experiment, although all sensors were factory-calibrated. The sensor at the top of the mast is chosen as reference sensor, because its data compare well with the readings from hand-held instruments (Assman and DV-2).

For more details on the data comparison, the reader is referred to Neele and De Leeuw.[5]

### 4.3 Validated data.

With the data from the sensor intercomparison, described above, correction curves were computed. The (linear) corrections were applied to all data available. The validated temperature and mixing ratio data are shown in figure 2, together with wind direction and wind speed, for the period June 1 - June 19.

The first half of the measuring campaign can be characterized by a diurnal period of warming up during the afternoon and cooling during the night. This is associated with stable thermal conditions during periods of sunshine and, usually, unstable stratification during the night and morning. The wind was off-shore during this period (direction around 90°). During the stable periods, large ASTDs were observed, up to 7 °C between the lowest mast sensor and the sea surface. A stationary front between maritime and continental air masses passed the area on June 4, around 14:00h. It is marked by a abrupt increase in temperature and change in humidity; the wind direction changes from east through south to north and to east again. During the second half of the campaign, roughly from June 12 onward, onshore winds dominated. Consequently, the ASTD was smaller, around zero and negative during the last few days. Note that whenever the wind was northerly, the sensor on Barbara's half deck gave unrealistically high temperatures and unrealistically low humidities.

The sea temperature varied with the periodic heating of sea water on the tidal flats near the shore: the peaks in the sea temperature record coincide with receding tide, when warm water from the tidal flats passed the sensors.

Figure 2 shows that the various meteorological parameters are not independent. In part this is due to coastal influences. For example, large, positive ASTD occurred only for off-shore winds; for onshore winds the ASTDs were small.

## 5. IR AND RF REFRACTIVITY.

Due to vertical and horizontal variations in humidity, temperature, pressure, etc., electromagnetic waves in the atmosphere are refracted. In super-refractive conditions, velocity increases with height and a ray leaving a source horizontally is bent towards the Earth's surface. Sub-refractive conditions exist when rays are bent upward (velocity decreasing with height). Trapping of rays in a layer near the surface occurs in the former case, when the rays are bent with a curvature greater than that of the Earth. In such conditions the range of radar or infra-red observations is not limited by the geometrical horizon and can be quite large (if not limited by extinction due to aerosols or molecular species). The height at which a ray is bent such that it travels parallel to the Earth's surface is called the duct height; this height is usually taken as the top of the trapping layer.

The refractivity profile can be calculated from the observed temperature and humidity profiles, because these parameters dominate the refractive structure, or refractivity profile (see below for definitions). The refractivity structure thus obtained may be used, for example, to predict maximum visibility range for radar or, by ray-tracing, to assess the use of IR and RF systems and their limitations due to atmospheric refraction and multipath effects.

### 5.1. Calculation of RF refractivity.

Since the variations in the index of refraction $n$ are very small, the refractivity $N$ has been introduced

$$N = (n-1) \cdot 10^6$$

Following Beaulieu,[6] the refractivity $N$ for radar is calculated using the relation

$$N_{RF} = 77.6\ p / T + 3.734 \cdot 10^5\ V_p / T$$

where $p$ is atmospheric pressure in mbar, $T$ the air temperature in Kelvin and $V_p$ the partial water vapour pressure in mbar. At the length scales typically involved in radar experiments, the curvature of the Earth's surface must be taken into account. The spherical geometry can be incorporated in two ways. One is by performing all calculations in a spherical geometry. The other is by transformation of the refractivity profile, using a flat-Earth representation, to exploit the simpler expressions of a flat geometry. For radar propagation close to the sea surface, a good approximation to the transformation to a flat-Earth representation is obtained by adding 0.157 times the height to the refractivity profile. Thus, the modified refractivity M is obtained. Using the previous expression for $N$, the modified refractivity is then given by

$$M_{RF} = 77.6\ p / T + 3.7345 \cdot 10^5\ V_p / T + 0.157\ z$$

where $z$ is the height (in m) above the sea surface.

### 5.2. Calculation of IR refractivity.

The IR refractivity is found using the formula given by Edlén :[7]

$$M_{IR} = \left[ a_0 + \frac{a_1}{(1 - (v/b_1))} + \frac{a_2}{(1 - (v/b_2))} \right] \cdot \frac{p\,(T_0 + 15.0)}{p_0\,T} - \frac{p_w}{p_0} \left[ c_0 - (v/c_1) \right]$$

where $p$ is atmospheric pressure (mbar), $T$ the air temperature (Kelvin), $p_w$ the partial water vapour pressure (mbar). The wavelength dependence is incorporated in the formula through the wavenumber v:

$$v = 1 \cdot 10^4 / l$$

where $l$ is the wavelength in μm. The constants in the formula of Edlén are

$a_0 = 83.42$ $b_1 = 1.140 \cdot 10^5$ $c_0 = 43.49$
$a_1 = 183.08$ $b_2 = 6.240 \cdot 10^4$ $c_1 = 1.7 \cdot 10^4$
$a_2 = 4.11$

$T_0 = 273.15\ K$
$p_0 = 1013.25\ mbar$

We calculated the refractivity for IR wavelengths of 1.06 μm (Nd/YAG laser) and 10.59 μm ($CO_2$ laser and thermal IR systems), using the meteorological data discussed in the previous section.

### 6. MODEL VALIDATION.

With the present data set, models describing the structure of the atmospheric surface layer over water can be evaluated for a coastal area. The behaviour of temperature and humidity as a function of height above the sea level predicted by these models is generally of the logarithmic type. This is valid in near-neutral conditions, with no coastal influences. The site chosen in this experiment is close to the German coast; the effect of nearby land is expected for easterly winds.

The following sections deal with the validation of two models, LKB[8] and EVAP.[9] Discrepancies between observations and model are related to specific weather parameters.

#### 6.1 The models

##### 6.1.1 LKB model

The LKB model[8] is based on a bulk parameterization of the fluxes of heat, moisture and momentum between atmosphere and ocean. An interfacial sublayer, a thin layer above the sea surface where molecular diffusion processes are important, is incorporated in the model. It is applicable in approximately stationary and horizontally homogeneous conditions, over an open fetch of water and with moderate wind speeds. The model incorporates the effect of wind-generated waves on the local roughness (effects of swell are not included in the model). The authors expect that at high winds the model breaks down, as breaking waves disturb the interfacial sublayer and sea spray affects the temperature and humidity in the surface layer.

The model calculates the profiles of temperature and humidity from the measured values at a single height. With these profiles, the refractive structure (see previous section) can be calculated; the duct height is then simply the minimum in the modified refractivity profile.

In this study the implementation of the LKB model by Liu & Blanc[10] is used, extended with a routine to find $M(z)$.

##### 6.1.2 EVAP model

The EVAP model[9] is based on the theory developed by Jeske.[11] This model directly estimates the duct height from the bulk meteorological measurements. The method approximates the gradients of temperature and humidity by their vertical differences (sensor height - surface). This is justified when the gradients are small (near neutral conditions), but may lead to under- or overestimating of the duct height for highly (un)stable stratification. For such conditions, no generally accepted models exist.[11] The theory does not incorporate an interfacial sublayer and assumes a constant roughness length $z_0$. Geernaert[12] showed that $z_0$ depends on wave state (and wind stress).

The theory on which the EVAP model is based, does not incorporate a molecular diffusion layer, like the LKB model. Starting from the flux-gradient relations from turbulence theory for temperature and humidity, the M-profile is developed. Jeske[11] and Paulus[9] do not present explicit formulae for the temperature and humidity profiles. Their formulation differs from that of Liu et al. (1979) in the approximation of the vertical gradients by a different formula. The stability function $\Phi$ is also formulated in a different way.

The original EVAP model[9] assumes that the measurements are made at a height of 6.5 m above mean sea level (AMSL). For the present study, the model has been modified to accept any measurement height. For the present situation, the difference is small, as the height of the highest mast sensor (used as reference) is around 10 meters. Nevertheless, the modified model yields results that are in better agreement with observations than the original EVAP model.

#### 6.2 Validation of temperature and humidity profiles

##### 6.2.1 Temperature

The readings from the highest sensor on the mast, together with the wind speed and the sea temperature data, are used in the LKB and EVAP models to compute the profiles of temperature and relative humidity. A comparison between observed and computed temperature profiles is shown in Figure 3. The time period presented in the figure is June 3 and 4. Temperature profiles are plotted every hour; the temperature axis is horizontal, increasing to the right. The logarithm of height is plotted on the vertical axis. Throughout June 3 and most of June 4 almost purely logarithmic profiles are observed. The sudden change in the profiles around 14:00h on June 4 is due to the passage of the stationary front. At that time, the conditions changed from unstable to stable, with ASTD > 5°C. The LKB model predicts a temperature gradient that is too high (solid lines), where the EVAP profiles compare better with observations. For near-neutral conditions, as observed in the second half of the measuring period, the temperature profiles are almost purely logarithmic and the two models agree very well (not shown). The largest discrepancies appear for large, positive ASTD. Jeske[11] (1973) already noted that in these cases the assumptions in the EVAP model break down.

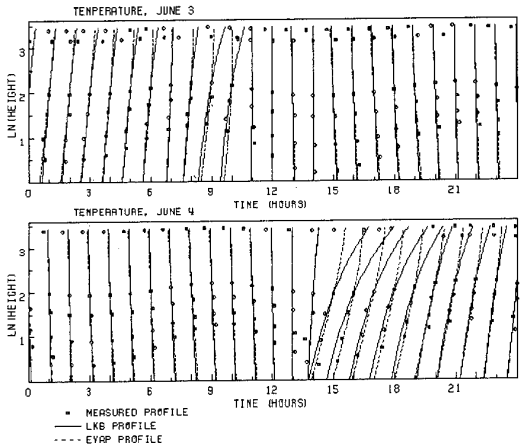


Figure 3. Comparison of temperature profiles computed with the LKB and EVAP models with experimental data. See text for explanation.

The difference between the modelled values for temperature or humidity and the respective observed values at the lowest sensor is used as a measure of the misfit between model and observations. Since the lowest sensor is furthest away from the reference sensor, deviations of the computed profile from the observed one show up clearest at this sensor. The data (i.e., differences between model and observation) are presented in scatter plots, organised as a function of wind speed, wind direction, tide or ASTD. Figure 4 shows an example of a scatter plot, obtained for the LKB model. The data are plotted as a function of wind speed, in different panels corresponding to increasing ASTD. Error bars are obtained by binning the data (in the case of Figure 6 in bins 1 m/s wide) and computing the mean and standard deviation. For this a robust technique of iterative residual down-weighting[13] is used. This method iteratively downweights all data that lie further than a specified number of standard deviations from the mean; in this case 1.5 standard deviations is used.

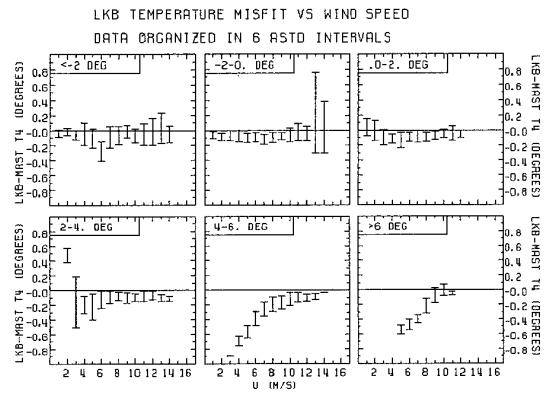


Figure 4. Scatter plot of temperature misfit against wind speed. Temperature misfit is defined as LKB-computed minus temperature observed at the position of the lowest sensor on the mast. Input for the LKB model were the observations from the highest sensor on the mast. Data are arranged in intervals of increasing ASTD.

In this way, outliers in the data set have a minimized influence on the mean temperature or humidity. The uncertainty in the individual measurements is 0.2°C, which compares well with the error bars in Figure 4. As noted before, large positive air-sea temperature differences occur in off-shore winds. In these cases a clear trend is visible of increasing model misfit as the wind speed is lower (cf. the data in the panels where ASTD > 4°C).

Figures 5 and 6 are similar to Figure 4, but now the data for increasing height AMSL of the lowest sensor are plotted as a function of wind speed. The height variations are caused by tidal effects. Data plotted are for off-shore winds only (wind directions between 60° and 120°), and ASTD greater than 3°C. It is clear that the trend increases with decreasing distance from the sea surface. At heights above 3.5 m the model compares favorably with experimental data. The data in Figure 5 are for the LKB model, those in Figure 6 are for the EVAP model. The EVAP model predicts temperatures near the sea surface that are too high. This is probably due to the absence of a surface boundary layer in the EVAP model. As the LKB model is the more complete of the two models tested here, it seems that the LKB model is more likely to represent the behaviour of open ocean atmosphere.

Figures 4 and 5 strongly suggest the existence of an additional boundary layer, formed for off-shore winds, when relatively warm air masses from land move over a cold sea surface. In this new boundary layer the temperature is higher than expected (temperature difference negative) from the model predictions. The thickness of this boundary layer would be about 3 m for low wind speeds, estimated from the maximum height above the sea at which the effect is visible in figure 5. At high winds the boundary layer disappears completely. Such an inverse relation of boundary layer thickness with flow speed is expected.[14]

Note in the figures that the LKB model tends to underestimate the temperature at the position of the lowest sensor. This is apparent from a bias toward negative temperature misfits in figure 4. A problem with the present data set is the measurement of the sea temperature. The sea temperature sensor measured the temperature at about 0.2 m below the sea surface. This temperature may deviate from the skin temperature by up to 0.5 °C (see, e.g., Roll[15] and Soloviev[16]). However, the LKB and EVAP models require the skin temperature as input. The effect of using the sub-surface sea temperature is difficult to assess. Roll[17] noted the existence of a 'cold film' on the sea surface, due to cooling by evaporation. In temperate environments the sea nearly always acts as a source of water vapour and this 'cold film' would be expected to be present. The magnitude of the temperature drop in this film is not quite clear. Liu et al.[8] note that the error introduced by using the sub-surface temperature would be largest for ASTD near zero.
In general, the largest scatter of model temperature minus observed temperature occurs for stable conditions, which arise almost exclusively for off-shore winds. This shows that coastal effects may reduce the applicability of the models tested here.

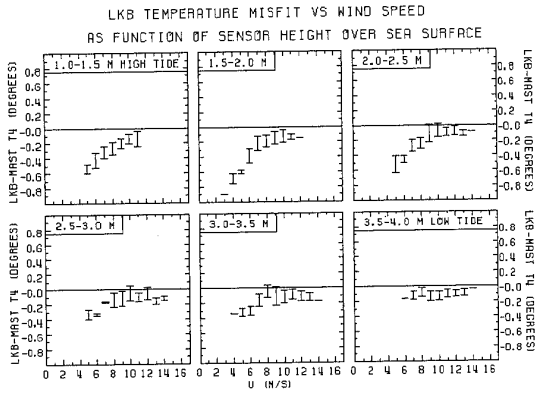


Figure 5. As figure 4, now only for wind directions between 60° and 120° (off-shore winds). Parameter is the height AMSL. The misfits show a trend of decreasing misfits with increasing wind speed. This trend is largest when lowest sensor on the mast is close to the sea surface (high tide) and disappears when sensor is more than about 3 m over the sea surface.

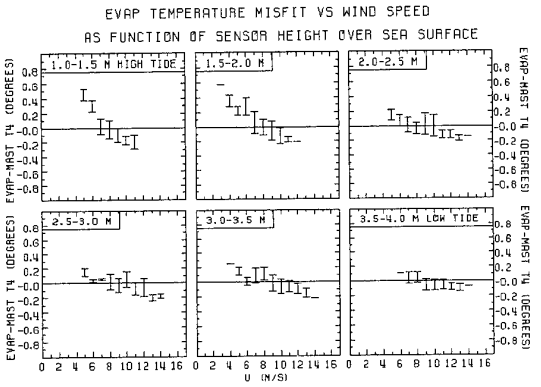


Figure 6. As figure 5, now for the EVAP model. The misfits for this model show a trend that is opposite to that in figure 5. The lack of an interfacial sublayer in this model may be the cause for this.

### 6.2.2 Humidity

The shortcomings of the EVAP model are most obvious in the humidity profiles (mixing ratio). An example is shown in Figure 7, for June 13 and 14. Both experimental data and profiles computed from the two models used in this study are shown. The EVAP model predicts dramatical increase or decrease in the humidities with height. The weather conditions on June 13 include ASTD near 0°C and low wind speeds (below 2 m/s). For such low wind speeds the flow is smooth, rather than rough. The smooth flow results in very small $L'$ (Monin-Obukhov lengths corrected for stability, as used in the EVAP model) and hence large values of $z/L'$. The stability function $\Phi$ used in the EVAP model is valid for small values of its argument $z/L'$, yet the small value of $L'$ leads to unreliable results. The LKB model uses a different formulation of the Monin-Obukhov length, which does not approach zero for low winds. Therefore, this model predicts humidity profiles that are much closer to the observed profiles.

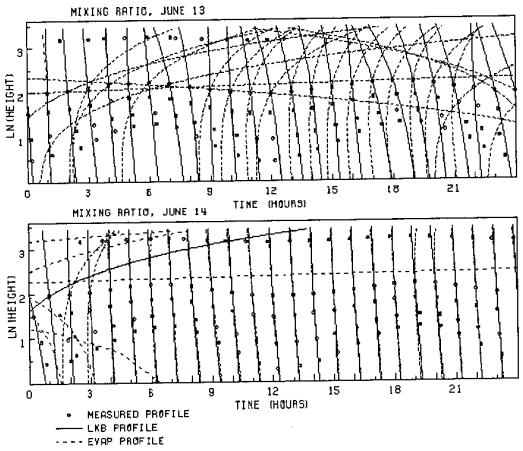


Figure 7. As figure 3, now for mixing ratio in the two-day period June 13 and June 14. The predictions from the EVAP model are unreliable, due to low wind speeds.

Brutsaert[18] (1992) presents alternative approximations for the stability function $\Phi$, that are valid for a much larger range of its argument, but these have not been tested here. It should also be noted that the formulations used for $\Phi$ are based on data collected over land. Schacher et al.[19] showed that over water different relations apply. For unstable conditions over water, McBean and Elliot[20] derived a relation yielding better results than a relation valid for over-land experiments; no such relations are available for unstable or neutral conditions over water. The results of Davidson and Boyle[21] also suggest that such relations are needed for over-water experiments.

### 6.3 Refractive structure of the atmosphere

Using the theory presented in section 5 and the profiles of temperature and humidity, the refractive structure of the surface layer can be calculated. It should be kept in mind that in this experiment the temperature and humidity profiles have been measured locally. Spatial variation of $T$ and $Q$ do occur in this coastal area with off-shore winds but have not been measured. These spatial variations may have a stronger effect on the propagation of electromagnetic radiation than vertical gradients, especially in the present coastal environment. For onshore winds, such gradients are expected to be relatively small, as the air masses have been mixed thoroughly.

### 6.3.1 Radar refractivity

Figure 8 shows some results for the radar refractivity profiles, for June 1 and June 13, respectively. Profiles are shown every hour; horizontal axis is height, vertical is modified refractivity $M$. During the first part of the experiment, the two models give similar results. The LKB model predicts profiles that increase more rapidly with height than EVAP; this agrees with the data from the Hygrometer on Barbara's half deck. The weather conditions on June 13, as discussed above, are such that the EVAP model predicts non-ducting conditions during most of the day. This is in clear disagreement with the data. The LKB model yields profiles that are in better agreement with the experimental data.

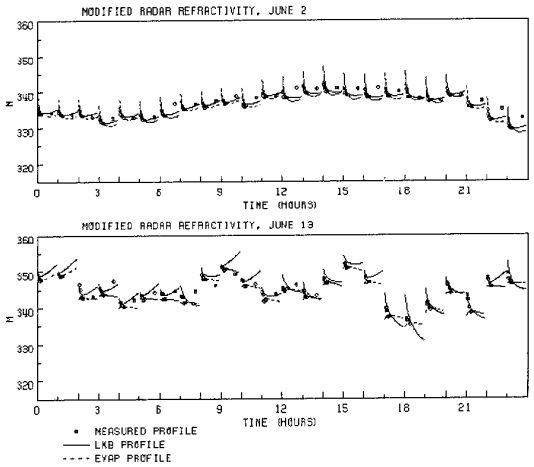


Figure 8. As figure 3, now for modified radar refractivity, for June 2 and June 13. Whereas both the LKB and EVAP model give good results during June 2, the low wind speeds on June 13 cause a break-down of the EVAP model.

The data in Figure 8 are an ilustration of the common occurrence of super-refractive conditions for radar frequencies. Both data and model predictions indicate that during the greater part of the experiment the conditions were such that radar waves are trapped near the surface. Such conditions are favourable for radar detection over long ranges.

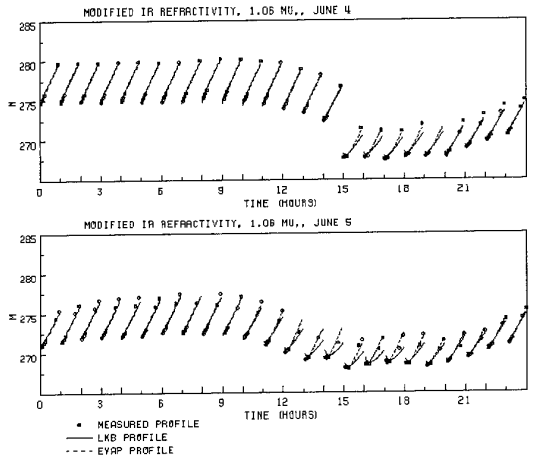


Figure 9. As figure 3, now for modified refractivity at the infra-red wavelength of 1.06 μm. Period displayed is June 4 and 5. Sub-refractive conditions prevail, indicated by monotonously increasing *M*. During the afternoon on both days, the infra-red refractivity enters the sub-refractive domain.

### 6.3.2 Infra-red refractivity

The conditions for infra-red wavelengths are the opposite to those of radar. Some refractivity profiles are shown in figure 9, for a wavelength of 1.06 μm. The results for a wavelength of 10.59 μm are similar. The period covered is June 4-5. It is evident from Figure 9 that most of the time sub-refractive conditions prevail, indicated by the monotonously increasing $M(z)$. Super-refractive conditions exist only during the afternoon, when the ASTD is positive.

### 6.4 Duct heights

As described above, the height at which the modified refractivity profile has zero gradient is defined as the duct height. The observed duct height is found by fitting a linear+logarithmic function to the observed refractivity profile. The log-linear profile shape is suggested by the LKB and EVAP models. However, this fitting procedure amounts to introducing *a priori* knowledge about the shape of the refractivity function and leads to (unknown) errors if the true shape of this profile cannot be adequately described by a linear+logarithmic function. Fitting the observed profile with a different function (e.g., a second order polynomial) does not solve this problem.

For the determination of duct heights, the half-deck sensor on Barbara is used as well as the mast sensors. This is because it is essential for a reliable duct height estimate to have a measurement at some height above the mast. However, whenever the Barbara sensor gave unreliable

### 6.4.1 Radar (RF) ducts

Figure 10 shows the observed RF duct heights as a function of time, at 20-minute intervals, for the whole experiment. Also shown are the duct heights from the LKB and EVAP models. A clear diurnal pattern caused by heating and cooling is seen from June 5 to June 10. During the night, unstable conditions prevail and ducts are observed below 10 m height (evaporation duct). In the afternoon, when the atmosphere is warmed up by solar irradiation, stable conditions exist and no duct below the Barbara sensor is observed (leaving open the possibility of an elevated duct). The data show that for radar frequencies the conditions are predominantly super-refractive. During periods of stable conditions (warm air over cold sea), the models fail to produce reliable duct heights. For unstable conditions good performance is obtained. This result is supported by the data obtained from radar measurements.[1] During stable conditions radar cross sections show significantly larger scatter than when conditions are unstable. The LKB model seems to predict duct heights that are closer to the observed heights than the EVAP model, which is biased to too high ducts.

This result is shown in figure 11, which is a scatter plot of LKB and EVAP vs. observed duct heights. The high ducts predicted by LKB (above 20 m) all correspond to stable conditions.

### 6.4.2 Infra-red ducts

It has been noted that IR and RF are complementary in the sense that usually at least one of the two is in the super-refractive domain.[1,8] This allows one to be able to look beyond the geometrical horizon when sensor systems are available for both the IR and RF bands.

Figure 12 shows the duct heights at infra-red wavelength of 1.06 μm for June 5-8. The conditions are predominantly sub-refractive, the energy being bent away from the Earth's surface. During the first 8 days of the experiment, ducting is present during the afternoon. Similar results are obtained for a wavelength of 10.6 μm.

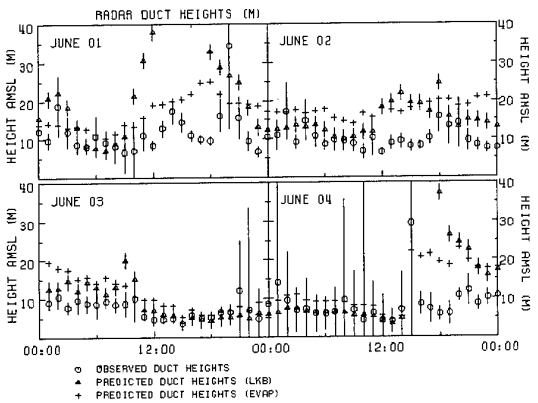


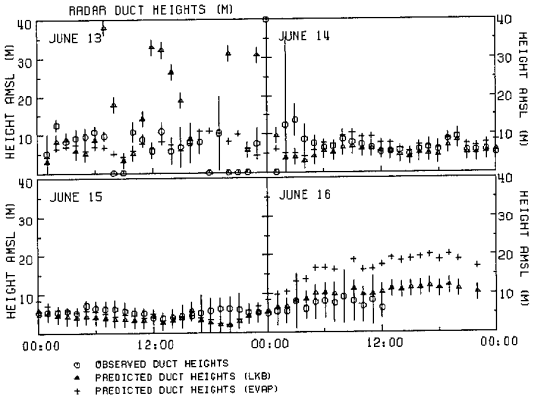


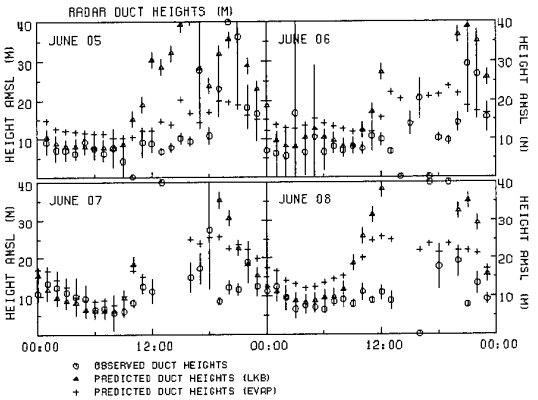


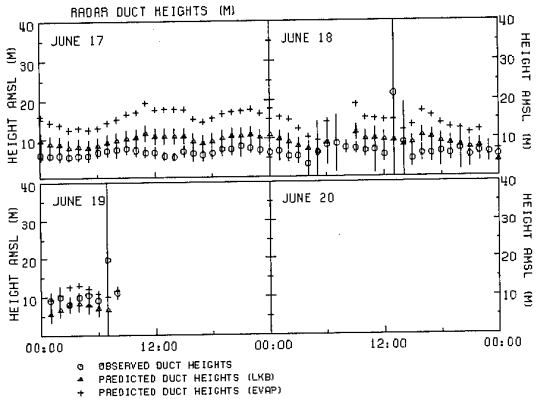


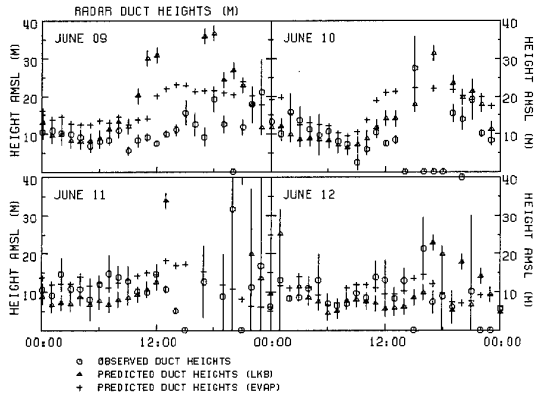


Figure 10. Variation of duct height at radar frequencies with time. Circles: observed duct height, triangles: LKB-predicted duct height and crosses: EVAP-predicted duct height.

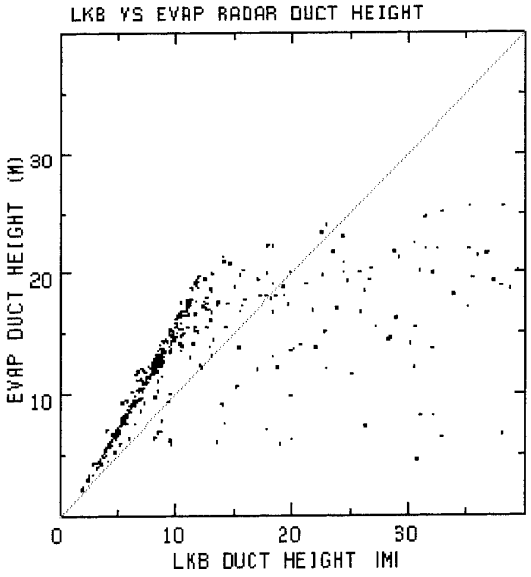


Figure 11. Scatter plot of duct heights predicted by the EVAP model vs. duct heights predicted by LKB model. The EVAP model is biased to high ducts, compared to the LKB model. All points where LKB predicts a duct height much larger than the EVAP model are associated with thermally stable conditions and offshore winds.

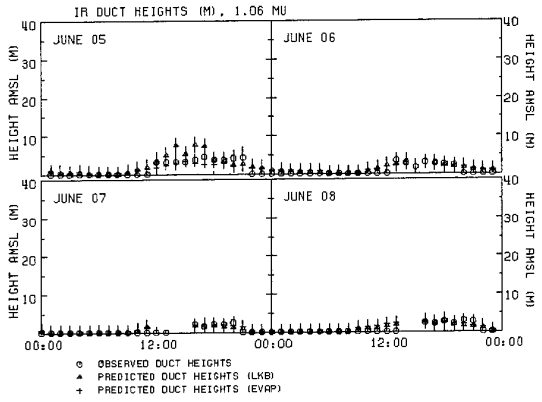


Figure 12. As figure 10, now for infra-red wavelength 1.06 μm, and the four-day period June 5 - 8.

A few times during the experiment a mirage effect has been observed visually. At these times the infra-red refractivity profiles show no sign of complexity or super-refraction. This is probably due to horizontal inhomogeneity of the atmosphere (the line of sight being in the direction of land) and the instruments being placed outside the complex zone.

Figures 10 and 12 are an indication of the complementarity of radar and infra-red with respect to super-refraction. Beaulieu[6] noted that always one or both of radar or infra-red is in the super-refractive domain. During the afternoon, when at radar frequencies no duct is detected within the height range of the sensors, the propagation conditions at infra-red wavelengths are super-refractive. This observation is a clear illustration of the value of combining RF and IR for long-range observation.

## 7. CONCLUSIONS.

The results presented in this report lead to the following conclusions.

The LKB model predicts reliable temperature and humidity profiles for both stable and unstable conditions, although for very stable stratifications the predicted gradients are too large. Duct heights produced by the model are in good agreement with observations for unstable conditions.

The EVAP model is based on more assumptions about the structure of the atmospheric surface layer and simplifications in the theory than the LKB model. This results in duct heights that are biased to values that are too high as compared with observations. This is not due to the fixed measuring height, that was part of the original EVAP model; the model has been modified to accept the actual measuring height. The EVAP model produces unrealistic profiles of temperature and humidity for warm air moving over a cold sea surface, especially during light winds. This combination leads to unreliable duct heights, the cause for which must be sought in a small value of the Monin-Obukhov length used in the model. This results in a breakdown of the stability function $\Phi$. This presents less of a problem in the LKB model, which uses a different formulation of the Monin-Obukhov length. For unstable conditions the EVAP model produces results that are in good agreement with observations, although it is biased to too high ducts.

In general, for unstable to neutral conditions, which in this experiment occur mostly for air masses with an oceanic origin, the data show that current models reliably predict the profiles of temperature and humidity in the atmospheric surface layer over the ocean, given a measurement at a single height. The fact that for stable conditions both models fail to reproduce the observations can be attributed to coastal influences. Stable conditions almost invariably occurred during the afternoon, when the wind was off-shore. The mast was located about 15 km off-shore, which is much closer than the estimated 60 km over which coastal influence has been shown to be present.[22] The high ASTD (up to 7°C between the lowest mast sensor and the sea surface) observed for off-shore winds indicate that these air masses have been warmed up over land and travelled a relatively short distance over the sea.

Thus, the data collected during SYLT92 strongly suggest that, for prediction of the behaviour of electro-optical and radar systems in coastal environments, current models of the atmospheric surface layer over the ocean need to be extended to include effects of nearby land. The possibly large temperature differences between the land and sea surfaces may give rise to a turbulence, stronger than expected if an oceanic origin is assumed for the air masses. Although the present data do not explicitly show this, strong horizontal gradients are expected in coastal areas for off-shore winds. Such gradients must be accounted for in any model predicting infra-red or radar propagation close to the sea surface in coastal regions.

## ACKNOWLEDGEMENTS

Our participation in the Sylt92 experiments were supported by the Dutch Ministry of Defence, assignments A92KM609 and A92KM638. Hubinsel Barbara was made available through BWB-FFV-4, Koblenz and WTD-71. The support and advice of many colleagues at TNO Physics and Electronics Laboratory and elsewhere is gratefully acknowledged.

## REFERENCES.

1. De Leeuw, G., Sittrop, H. and H.J.M. Heemskerk, First impressions and some qualitative results from the SYLT92 experiment, *TNO report 92-A363*, 1992.

2. Sittrop, H., H. Gravesteijn and H.J.M. Heemskerk. The influence of the evaporation duct on the angle of arrival and amplitude of the backscattered signal from targets low above the sea. in: Atmospheric propagation effects through natural and man-made obscurants for visible to mm-wave radiation. AGARD CP 542, paper 4 (13 pp.). 1993.

3. Dion, D. and A.J. Beaulieu. Sylt'92 campaign: the complementarity of radar and eo sensors. Defence Research Establishment Valcartier, Quebec, Canada, 1993.

4. Korevaar, C.G., *North Sea Climate, based on observations from ships and light vessels*, Kluwer, Dordrecht, The Netherlands, 1990.

5. F.P. Neele and G. de Leeuw. Temperature and humidity profiles from SYLT92: validation of RF and IR propagation models. TNO Physics and Electronics Laboratory, Report, 1994, in print.

6. Beaulieu, A.J., Atmospheric refraction model, Canada National Defence Research Establishment Valcartier, Québec, Rep. 4661/92, 1992.

7. Edlén, B., The dispersion of standard air, *J. Opt. Soc. Am.*, 43, 339-343, 1953.

8. Liu, W.T., Katsaros, K.B. and J.A. Businger, Bulk parameterization of air-sea exchanges of heat and water vapour including the molecular constraints at the interface, *J. Atmos. Sc.*, 36, 1722-1735, 1979.

9. Paulus, R.A., Specification for environmental measurements to assess radar sensors, NOSC TD 1685, San Diego, 1989.

10. Liu, W.T. and T.V. Blanc, The Liu, Katsaros and Businger (1979) bulk atmospheric flux computational iteration program in Fortran and Basic, NRL Memorandum Report 5291, 1984.

11. Jeske, H., State and limits of prediction methods of radar wave propagation conditions over sea, in *Modern Topics in microwave propagation and air-sea interaction*, A. Zancla (editor), p. 130-148, Reidel, 1973.

12. Geernaert, G. Bulk parameterizations for the wind stress and heat fluxes. In: G.L. Geernaert and W.J. Plant (Eds.): Surface waves and fluxes, Volume I - Current theory. Kluwer, Dordrecht, 1990.

13. Huber, P.J. *Robust Statistics*, John Wiley, New York, 1981.

14. Montgomery, R.B., Observations of vertical humidity distribution above the ocean surface and their relation to evaporation, *Papers in Phys. Oceanog. and Met.* v. 7, no. 4, 30 pp., 1940.

15. Roll, H.U., Über die vertikale Temperaturverteilung in der wassernahen Luftschicht, *Ann. Meteorol.*, 7, 4, 1948.

16. Soloviev, A.V., Coherent structures at the ocean surface in convectively unstable conditions, *Nature*, 346, 157-160, 1990.

17. Roll. H.U., Physics of the marine atmosphere, Academic Press, New York, 1965.

18. Brutsaert, W., Stability correction functions for the mean wind speed and temperature in the unstable surface layer, *Geophys. Res. Lett.*, 19, 469-472, 1992.

19. Schacher, G.E., Davidson, K.L., Houlihan, T. and C.W. Fairall, Measurements of the rate of dissipation of turbulent kinetic energy over the ocean, *Boundary Layer Meteorol.*, 20, 321-330, 1981.

20. McBean, G.A. and J.A. Elliot, The vertical transports of kinetic energy by turbulence and pressure in the boundary layer, *J. Atmos. Sci.*, 32, 753-766, 1975.

21. Davidson, K.L., and P.J. Boyle. Overwater results on the dimensionless TKE dissipation rate. Proc. Ninth Symp. on Turbulence and Diffusion, Roskilde, Denmark, April 30-May 5 1990, 51-53.

22. EPRF (Environmental Prediction Research Facility), Coastal sea-air interactions and the extent of coastal influence, Techn. Note, 72-2, Naval Postgraduate School, Oceanographic Dept., Monterey, 1972.

## DISCUSSION

**J.H. RICHTER** (Comment)
The importance of the horizontal variability of surface layer properties (such as the effect of air-sea temperature differences on refractivity) is generally different for infrared as opposed to microwave operational applications. In the microwave case, usually ranges of tens to hundreds of kilometers are of interest while infrared systems are mostly used for ranges that are an order of magnitude smaller. This may result in different sampling and prediction requirements for infrared and microwave applications.

**R. PAULUS**
The EVAP model operates in terms of potential refractivity. How is mixing ratio extracted from that?

**AUTHOR'S REPLY**
The EVAP model is based on Jeske (1973) and we have used his formulation for surface layer profiles in our calculations. The equation for direct calculation of refractivity profiles in the EVAP model is based on the explicit gradients of temperature and humidity.

**D. DION**
Even though discrepancies are observed between measured and predicted values for the lowest probes, don't you think that the real question is which profiles lead to better predictions of propagation effects? What do the results say?

**AUTHOR'S REPLY**
Of course, the real question is which profiles lead to better predictions of propagation effects. However, models are based on theoretical formulations that have to be tested with experimental data. Our aim of this analysis was to study the effect of waves and thermal stratification on model formulations. The results have been presented here. From the same experiment, also RF and IR-propagation measurements are available. The analysis of the RF propagation measurements has shown some unexpected effects which could be qualitatively explained with the meteorological observations. The quantitative test of the propagation models with these RF propagation data is outside the scope of the present paper.

**S. BURK**
You encountered trouble with low winds speeds in the Liu, Katsaros, Businger formulation. Have you tested artificially constraining the wind speed to be no smaller than some value, say 2 m/s, and see what results from such calculations?

**AUTHOR'S REPLY**
We have not tested with artificial constraints. The discrepancy between LKB model predictions and observations are only found for very large values of ASTD and low wind speeds, i.e., a very stable atmosphere. If only the wind speed is low, but the thermal stratification is unstable or neutral, the LKB model gives much better predictions. Hence, we infer that the observed discrepancies cannot be attributed to a general failure of LKB in low wind speed conditions, rather we ascribe the discrepancies to the occurrence of a non-equilibrium situation of warm air flowing out over a cold sea surface. This gives rise to an internal boundary layer for which models are presently not available.

# REPORT DOCUMENTATION PAGE

| 1. Recipient's Reference | 2. Originator's Reference | 3. Further Reference | 4. Security Classification of Document |
|---|---|---|---|
| | AGARD-CP-567 | ISBN 92-836-0013-4 | UNCLASSIFIED/ UNLIMITED |

**5. Originator** Advisory Group for Aerospace Research and Development
North Atlantic Treaty Organization
7 rue Ancelle, 92200 Neuilly-sur-Seine, France

**6. Title**
Propagation Assessment in Coastal Environments

**7. Presented at**
the Sensor and Propagation Panel Symposium, held in Bremerhaven, Germany 19-22 September 1994

| 8. Author(s)/Editor(s) | 9. Date |
|---|---|
| Multiple | February 1995 |
| **10. Author's/Editor's Address** | **11. Pages** |
| Multiple | 364 |

**12. Distribution Statement** There are no restrictions on the distribution of this document. Information about the availability of this and other AGARD unclassified publications is given on the back cover.

**13. Keywords/Descriptors**

Coasts
Electromagnetic wave propagation
Radio waves
Electrooptics
Remote sensing
Detecting
Sensor characteristics
Integrated systems
Modelling

**14. Abstract**

This publication reports the unclassified papers at a specialists' meeting held by the Sensor and Propagation Panel at its Fall 1994 meeting.

The topics covered on the occasion of that symposium on the subject of "Propagation Assessment in Coastal Environments" included:

— Radio Propagation Modeling
— Electro-optical Propagation Modeling
— Remote and Direct Sensors and Sensing Techniques
— Modeling and Prediction of the Propagation Environment
— Sensor Technology and Systems Aspects
— Measurement Campaigns

AGARD

NATO OTAN

7 RUE ANCELLE • 92200 NEUILLY-SUR-SEINE

FRANCE

Télécopie (1)47.38.57.99 • Télex 610 176

**DIFFUSION DES PUBLICATIONS**

**AGARD NON CLASSIFIEES**

Aucun stock de publications n'a existé à AGARD. A partir de 1993, AGARD détiendra un stock limité des publications associées aux cycles de conférences et cours spéciaux ainsi que les AGARDographies et les rapports des groupes de travail, organisés et publiés à partir de 1993 inclus. Les demandes de renseignements doivent être adressées à AGARD par lettre ou par fax à l'adresse indiquée ci-dessus. *Veuillez ne pas téléphoner.* La diffusion initiale de toutes les publications de l'AGARD est effectuée auprès des pays membres de l'OTAN par l'intermédiaire des centres de distribution nationaux indiqués ci-dessous. Des exemplaires supplémentaires peuvent parfois être obtenus auprès de ces centres (à l'exception des Etats-Unis). Si vous souhaitez recevoir toutes les publications de l'AGARD, ou simplement celles qui concernent certains Panels, vous pouvez demander à être inclu sur la liste d'envoi de l'un de ces centres. Les publications de l'AGARD sont en vente auprès des agences indiquées ci-dessous, sous forme de photocopie ou de microfiche.

CENTRES DE DIFFUSION NATIONAUX

ALLEMAGNE
Fachinformationszentrum,
Karlsruhe
D-76344 Eggenstein-Leopoldshafen 2

BELGIQUE
Coordonnateur AGARD-VSL
Etat-major de la Force aérienne
Quartier Reine Elisabeth
Rue d'Evere, 1140 Bruxelles

CANADA
Directeur, Services d'information scientifique
Ministère de la Défense nationale
Ottawa, Ontario K1A 0K2

DANEMARK
Danish Defence Research Establishment
Ryvangs Allé 1
P.O. Box 2715
DK-2100 Copenhagen Ø

ESPAGNE
INTA (AGARD Publications)
Pintor Rosales 34
28008 Madrid

ETATS-UNIS
NASA Headquarters
Code JOB-1
Washington, D.C. 20546

FRANCE
O.N.E.R.A. (Direction)
29, Avenue de la Division Leclerc
92322 Châtillon Cedex

GRECE
Hellenic Air Force
Air War College
Scientific and Technical Library
Dekelia Air Force Base
Dekelia, Athens TGA 1010

ISLANDE
Director of Aviation
c/o Flugrad
Reykjavik

ITALIE
Aeronautica Militare
Ufficio del Delegato Nazionale all'AGARD
Aeroporto Pratica di Mare
00040 Pomezia (Roma)

LUXEMBOURG
*Voir* Belgique

NORVEGE
Norwegian Defence Research Establishment
Attn: Biblioteket
P.O. Box 25
N-2007 Kjeller

PAYS-BAS
Netherlands Delegation to AGARD
National Aerospace Laboratory NLR
P.O. Box 90502
1006 BM Amsterdam

PORTUGAL
Força Aérea Portuguesa
Centro de Documentação e Informação
Alfragide
2700 Amadora

ROYAUME-UNI
Defence Research Information Centre
Kentigern House
65 Brown Street
Glasgow G2 8EX

TURQUIE
Millî Savunma Başkanliği (MSB)
ARGE Dairesi Başkanliği (MSB)
06650 Bakanliklar-Ankara

**Le centre de distribution national des Etats-Unis ne détient PAS de stocks des publications de l'AGARD.**
D'éventuelles demandes de photocopies doivent être formulées directement auprès du NASA Center for AeroSpace Information (CASI) à l'adresse ci-dessous. Toute notification de changement d'adresse doit être fait également auprès de CASI.

AGENCES DE VENTE

NASA Center for
AeroSpace Information (CASI)
800 Elkridge Landing Road
Linthicum Heights, MD 21090-2934
Etats-Unis

ESA/Information Retrieval Service
European Space Agency
10, rue Mario Nikis
75015 Paris
France

The British Library
Document Supply Division
Boston Spa, Wetherby
West Yorkshire LS23 7BQ
Royaume-Uni

Les demandes de microfiches ou de photocopies de documents AGARD (y compris les demandes faites auprès du CASI) doivent comporter la dénomination AGARD, ainsi que le numéro de série d'AGARD (par exemple AGARD-AG-315). Des informations analogues, telles que le titre et la date de publication sont souhaitables. Veuiller noter qu'il y a lieu de spécifier AGARD-R-nnn et AGARD-AR-nnn lors de la commande des rapports AGARD et des rapports consultatifs AGARD respectivement. Des références bibliographiques complètes ainsi que des résumés des publications AGARD figurent dans les journaux suivants:

Scientific and Technical Aerospace Reports (STAR)
publié par la NASA Scientific and Technical
Information Division
NASA Headquarters (JTT)
Washington D.C. 20546
Etats-Unis

Government Reports Announcements and Index (GRA&I)
publié par le National Technical Information Service
Springfield
Virginia 22161
Etats-Unis
(accessible également en mode interactif dans la base de
données bibliographiques en ligne du NTIS, et sur CD-ROM)

*Imprimé par le Groupe Communication Canada*
*45, boul. Sacré-Cœur, Hull (Québec), Canada K1A 0S7*

AGARD

NATO OTAN

7 RUE ANCELLE • 92200 NEUILLY-SUR-SEINE

FRANCE

Telefax (1)47.38.57.99 • Telex 610 176

**DISTRIBUTION OF UNCLASSIFIED**

**AGARD PUBLICATIONS**

AGARD holds limited quantities of the publications that accompanied Lecture Series and Special Courses held in 1993 or later, and of AGARDographs and Working Group reports published from 1993 onward. For details, write or send a telefax to the address given above. *Please do not telephone.*

AGARD does not hold stocks of publications that accompanied earlier Lecture Series or Courses or of any other publications. Initial distribution of all AGARD publications is made to NATO nations through the National Distribution Centres listed below. Further copies are sometimes available from these centres (except in the United States). If you have a need to receive all AGARD publications, or just those relating to one or more specific AGARD Panels, they may be willing to include you (or your organisation) on their distribution list. AGARD publications may be purchased from the Sales Agencies listed below, in photocopy or microfiche form.

NATIONAL DISTRIBUTION CENTRES

BELGIUM
Coordonnateur AGARD — VSL
Etat-major de la Force aérienne
Quartier Reine Elisabeth
Rue d'Evere, 1140 Bruxelles

CANADA
Director Scientific Information Services
Dept of National Defence
Ottawa, Ontario K1A 0K2

DENMARK
Danish Defence Research Establishment
Ryvangs Allé 1
P.O. Box 2715
DK-2100 Copenhagen Ø

FRANCE
O.N.E.R.A. (Direction)
29 Avenue de la Division Leclerc
92322 Châtillon Cedex

GERMANY
Fachinformationszentrum
Karlsruhe
D-76344 Eggenstein-Leopoldshafen 2

GREECE
Hellenic Air Force
Air War College
Scientific and Technical Library
Dekelia Air Force Base
Dekelia, Athens TGA 1010

ICELAND
Director of Aviation
c/o Flugrad
Reykjavik

ITALY
Aeronautica Militare
Ufficio del Delegato Nazionale all'AGARD
Aeroporto Pratica di Mare
00040 Pomezia (Roma)

LUXEMBOURG
*See* Belgium

NETHERLANDS
Netherlands Delegation to AGARD
National Aerospace Laboratory, NLR
P.O. Box 90502
1006 BM Amsterdam

NORWAY
Norwegian Defence Research Establishment
Attn: Biblioteket
P.O. Box 25
N-2007 Kjeller

PORTUGAL
Força Aérea Portuguesa
Centro de Documentação e Informação
Alfragide
2700 Amadora

SPAIN
INTA (AGARD Publications)
Pintor Rosales 34
28008 Madrid

TURKEY
Millî Savunma Başkanliği (MSB)
ARGE Dairesi Başkanliği (MSB)
06650 Bakanliklar-Ankara

UNITED KINGDOM
Defence Research Information Centre
Kentigern House
65 Brown Street
Glasgow G2 8EX

UNITED STATES
NASA Headquarters
Code JOB-1
Washington, D.C. 20546

**The United States National Distribution Centre does NOT hold stocks of AGARD publications.**
Applications for copies should be made direct to the NASA Center for AeroSpace Information (CASI) at the address below.
Change of address requests should also go to CASI.

SALES AGENCIES

NASA Center for
AeroSpace Information (CASI)
800 Elkridge Landing Road
Linthicum Heights, MD 21090-2934
United States

ESA/Information Retrieval Service
European Space Agency
10, rue Mario Nikis
75015 Paris
France

The British Library
Document Supply Centre
Boston Spa, Wetherby
West Yorkshire LS23 7BQ
United Kingdom

Requests for microfiches or photocopies of AGARD documents (including requests to CASI) should include the word 'AGARD' and the AGARD serial number (for example AGARD-AG-315). Collateral information such as title and publication date is desirable. Note that AGARD Reports and Advisory Reports should be specified as AGARD-R-nnn and AGARD-AR-nnn, respectively. Full bibliographical references and abstracts of AGARD publications are given in the following journals:

Scientific and Technical Aerospace Reports (STAR)
published by NASA Scientific and Technical
Information Division
NASA Headquarters (JTT)
Washington D.C. 20546
United States

Government Reports Announcements and Index (GRA&I)
published by the National Technical Information Service
Springfield
Virginia 22161
United States
(also available online in the NTIS Bibliographic
Database or on CD-ROM)

*Printed by Canada Communication Group*
*45 Sacré-Cœur Blvd., Hull (Québec), Canada K1A 0S7*

ISBN 92-836-0013-4